EPR Investigations of Iron-Sulfur Cluster Relays in Enzymes



Maxie M. Rößler

St. John's College

Michaelmas Term 2011

A thesis submitted to the Board of the Faculty of Physical Sciences,

for the degree of Doctor of Philosophy, University of Oxford

EPR Investigations of Iron-Sulfur Cluster Relays in Enzymes

Maxie M. Rößler, St. John's College, University of Oxford
A thesis submitted for the degree of DPhil, Michaelmas Term 2011

Electron paramagnetic resonance (EPR) spectroscopy is a powerful tool for obtaining structural information about chemical centres with unpaired electrons. In complex biological systems, EPR spectroscopy can be used to probe these paramagnetic centres and the long-range interactions between them. This thesis investigates two important types of enzymes, and in particular the role of the iron-sulfur electron-transfer centres they contain, with a variety of EPR techniques.

Complex I (NADH:Ubiquinone Oxidoreductase) plays a key role in the electron-transfer chain essential to the formation of ATP, and its malfunction has been related to numerous human diseases. It is a giant enzyme that contains the longest relay of iron-sulfur clusters known. EPR experiments conducted on complex I from bovine mitochondria yield crucial insight into the mechanism of efficient long-range electron transfer and bring us a step closer to understanding the functioning of this important complex.

Hydrogenases are produced by micro-organisms and catalyse the reversible oxidation of H_2. Most hydrogenases, including Hyd-2 from *Escherichia coli*, are very air-sensitive, but some, including *E. coli* Hyd-1 and *Salmonella* Hyd-5, are able to function in the presence of atmospheric levels of O_2. Understanding the origins of this 'O_2-tolerance' is of paramount importance if hydrogenases are to be exploited in future energy technologies. In this thesis, native *E. coli* Hyd-1 and Hyd-2, *Salmonella* Hyd-5, as well as O_2-tolerant and O_2-sensitive variants of *E. coli* Hyd-1 are characterised using EPR. The EPR investigations elucidate properties of the active site and the electron-transfer relay and, in conjunction with other techniques, reveal structural and mechanistic details of how a highly unusual iron-sulfur cluster in the electron-transfer chain enables some hydrogenases to sustain catalytic activity in the presence of O_2.

Collaborations

Many of the EPR studies and spectral analyses were carried out in collaboration with Dr. Jeffrey Harmer, in particular the work described in Chapters 4 and 7. Complex I samples were made by Dr. Martin King in the research group of Dr. Judy Hirst. The electrochemistry experiments shown in the introduction of Chapters 5 and 6 were carried out by Dr. Alison Parkin and Dr. Rhiannon Evans. All molecular biology to generate the *E. coli* Hyd-1 variants was carried out by Dr. Michael Lukey and Dr. Rhiannon Evans. Some of the experiments in Chapters 5 and 6 were carried out by Rosalind Davies under my supervision. The crystal structures of *E. coli* Hyd-1 were provided by Professor Fontecilla-Camps and Dr. Anne Volbeda. The computational calculations referred to in Chapter 7 were performed by Dr. Patricia Amara and Dr. Jean-Marie Mouesca.

Acknowledgements

My foremost thanks must go to Professor Fraser Armstrong. Thank you Fraser for your unfailing encouragement, enthusiasm and trust that things will eventually work out. Thank you for reminding me of the bigger picture and for sharing some of your vast knowledge on proteins. Last but not least, thank you for finding the funding for numerous expensive EPR tubes and for generous contributions towards conference attendance.

Much of this work would not have been possible without Dr. Jeffrey Harmer. Thank you Jeff for finding the time in your busy schedule to help me out and for teaching me so much. Your sarcasm and humour have been uplifting. I might try to go skiing with a cricket bat one day! Thank you also for coping with reading so much of this thesis.

I am grateful to Dr. Judy Hirst, Dr. Martin King and Dr. Alan Robinson at the Mitochondrial Biology Unit in Cambridge for a very fruitful collaboration on the complex I work.

In Oxford, to the electrochemistry and molecular biology teams: Mike, Alison and Non, it has been great working with you. Thank you also to Rosie: I could not have hoped for a better Part II student and it was fun to work with you. A big thank you must also go to Elena Nomerotskaia; the production of (milli)litres of hydrogenase has become so much more bearable since you joined the group!

I am also thankful to the Grenoble team: Professor Juan Fontecilla-Camps, Dr. Anne Volbeda, Dr. Patricia Amara and Dr. Jean-Marie Mouesca; thank you for much insight on the structural and computational side of the *E. coli* project.

The team at the National EPR Research Facility & Service in Manchester, in particular Professor David Collison, Daniel Sells and Dr. Floriana Tuna, are gratefully acknowledged. Thank for your help and for giving me much freedom in the lab during my stay.

My thanks also go to Professor Leslie Dutton for hosting me for a week in his lab in Philadelphia.

To the ICL research support staff: thank you Terri and Martyn for making such intricate glass structures, Nenad and Paul for replacing the CW cryostat fuse and dealing with all sorts of electronic trouble, Tom for fixing various computer bugs, Les and Charlie from the PTCL workshop for making the UV-vis 'adapter' for the CW resonator, Ashleigh for too many jobs to list.

Dr. Kevin Henbest is gratefully acknowledged for providing his UV-vis lamp and filter selection.

I am indebted to my proofreaders: Jeff, Alison, Non, Bonnie, Mike, Alice and Fraser. Thank you so much for your time and helpful comments! Many thanks also to Philip for introducing me to LaTeX and for much appreciated help with troubleshooting.

To everyone in the Armstrong group: thank you all for making the group such a friendly place in which to work, for support in difficult times and for much fun in and outside the lab. Special thanks to Alison for being a port of advice throughout the years and to Bonnie for being a great lab-mate.

I am also thankful to St. John's college for generous financial support to participate in several international conferences.

Finally, in memory of my mother, and my most heartfelt thanks to my father and the rest of my family, my friends and especially my husband Chiu Fan: you are the pillars upon which I stand.

Publications

Evans, R.M.; Parkin, A.; **Roessler, M.M.**; Murphy, B. J.; Adamson, H., Lukey, M. J.; Volbeda, A.; Fontecilla-Camps, J.; Armstrong, F. A.; The Principles of Sustained Enzymatic Hydrogen Oxidation in the Presence of Oxygen – the Crucial Influence of High Potential Fe-S Clusters in the Electron Relay of [NiFe]-hydrogenases, *Journal of the American Chemical Society*, Volume 135, Issue 7, pp. 2694-2707, 2013

Roessler, M.M.; Evans, R.M.; Davies, R.A.; Harmer, J.; Armstrong, F.A; EPR spectroscopic studies of the Fe-S clusters in the O_2-tolerant [NiFe]-hydrogenase Hyd-1 from *E. coli*, and characterisation of the unique [4Fe-3S] cluster by HYSCORE, *Journal of the American Chemical Society*, Volume 134, Issue 37, pp. 15581-15594, 2012

Volbeda A.; Amara P.; Darnault C.; Mouesca, J.-M.; Parkin A.; **Roessler, M.M.**; Armstrong F.A.; Fontecilla-Camps, J.C.; X-ray crystallographic and computational studies of the O_2-tolerant [NiFe]-hydrogenase 1 from *Escherichia coli*; *Proceedings of the National Academy of Sciences of the United States of America*, Volume 109, Issue 14, pp. 5305-5310, 2012

Parkin, A.P.; Bowman, L.; **Roessler, M.M.**; Davies, R.A.; Palmer, T.; Armstrong, F.A.; Sargent, F.; How *Salmonella* oxidises H_2 under aerobic conditions, *FEBS letters*, Volume 586, Issue 5, pp. 536-544, 2012

Lukey, M.J.; **Roessler, M.M.**; Parkin, A.; Evans, R., Davies, R.; Lenz, O.; Friedrich, B.; Sargent, T.; Armstrong, F.A Oxygen Tolerant [NiFe]-Hydrogenases: the Individual and Collective Importance of Supernumerary Cysteines at the Proximal Fe-S Cluster, *Journal of the American Chemical Society*, Volume 133, Issue 42, pp. 16881-92, 2011

Roessler, M.M.; King, M.S.; Robinson, A.J.; Armstrong, F.A.; Harmer, J.; Hirst, J., Direct assignment of EPR spectra to structurally defined iron-sulfur clusters in complex I by double electron-electron resonance, *Proceedings of the National Academy of Sciences of the United States of America*, Volume 107, Issue 5, pp. 1930-1935, 2010

Lukey, M.J.; Parkin, A.; **Roessler, M.M.**; Murphy, B.J.; Harmer, J.; Palmer, T.; Sargent, T.; Armstrong, F.A., How E. coli is equipped to oxidize hydrogen under different redox conditions, *Journal of Biological Chemistry*, Volume 285, Issue 6, pp. 3928-3938, 2009

Lee, C.-Y.; Stevenson, G. P.; Parkin, A.; **Roessler, M.M.**; Baker, R.E.; Gillow, K.; Gavaghan, D.J.; Armstrong, F.A.; Bond, A.M., Theoretical and experimental investigation of surface-confined two-center metalloproteins by large-amplitude Fourier transformed ac voltammetry, *Journal of Electroanalytical Chemistry*, Volume 656, Issue 1, pp. 293-304, 2010

The work in this publication is not featured in this thesis.

Contents

Abstract i

Collaborations iii

Acknowledgements v

Publications vii

Nomenclature xiii

1 Introduction 1
- 1.1 Iron-sulfur clusters . . . 2
- 1.2 Two intriguing Fe-S cluster electron-transfer relays . . . 8
  - 1.2.1 Electron-transfer relays . . . 8
  - 1.2.2 Hydrogenases . . . 9
  - 1.2.3 Complex I: The longest Fe-S cluster relay known . . . 16
- 1.3 Structure of this thesis . . . 21

2 EPR Theory & Methods 23
- 2.1 The g factor and resonance . . . 25
- 2.2 The g matrix & g anisotropy . . . 29
  - 2.2.1 The deviation of g from g_e . . . 34
- 2.3 The Spin Hamiltonian . . . 35
  - 2.3.1 Electron Zeeman interaction . . . 36
  - 2.3.2 Nuclear Zeeman interaction . . . 36
  - 2.3.3 Hyperfine interactions . . . 37
  - 2.3.4 Nuclear quadrupole interactions . . . 38
  - 2.3.5 Zero-field splitting . . . 38
- 2.4 Weak electron-electron interactions . . . 41
- 2.5 Continuous wave EPR . . . 43
- 2.6 Pulse EPR . . . 46
  - 2.6.1 The Hahn echo and the stimulated echo . . . 47
  - 2.6.2 Electron spin-echo envelope modulation . . . 48
  - 2.6.3 4-pulse ESEEM: HYSCORE . . . 49
  - 2.6.4 Electron nuclear double resonance (ENDOR) . . . 52
  - 2.6.5 Double electron-electron resonance (DEER) . . . 53
  - 2.6.6 Relaxation and saturation . . . 55

3 Methods **59**
3.1 Electrochemistry of bulk enzyme solutions . . . 60
3.2 Preparation of EPR samples at defined potentials . . . 63
3.3 Determining the number of spins in an EPR sample . . . 69
3.4 Protein Film Electrochemistry . . . 70
3.5 EPR measurements . . . 72
3.5.1 Spectrometers and resonators . . . 72
3.5.2 Field calibration . . . 73
3.5.3 Background Cu^{2+} and Mn^{2+} at W-band . . . 74
3.6 Preparation of protein samples . . . 79
3.6.1 Complex I from bovine heart mitochondria . . . 79
3.6.2 Hyd-1 and Hyd-2 from *E. coli* and Hyd-5 from *Salmonella enterica* . 80
3.7 Determination of protein concentration . . . 81
3.8 Buffers . . . 81
3.9 Images of three-dimensional protein structures . . . 83

4 Direct assignment of EPR spectra to structurally defined iron-sulfur clusters in complex I by double electron-electron resonance **85**
4.1 Introduction: The iron-sulfur cluster relay in complex I . . . 88
4.2 Double electron-electron resonance spectroscopy with iron-sulfur clusters . 93
4.2.1 The local spin model . . . 93
4.2.2 Orientation selection . . . 97
4.3 Experimental Methods . . . 99
4.3.1 EPR Spectroscopy . . . 99
4.3.2 Preparation of EPR Samples of *B. taurus* complex I . . . 100
4.4 Results . . . 101
4.4.1 Determination of the simulation input parameters . . . 102
4.4.2 Overlap of Fe-S cluster spectra . . . 107
4.4.3 Analysis of DEER traces . . . 108
4.5 Conclusions . . . 117
4.6 Discussion . . . 120

5 The EPR-visible states of the active site in the O_2-tolerant *E. coli* Hyd-1 and the O_2-sensitive *E. coli* Hyd-2 [NiFe]-hydrogenases **125**
5.1 Introduction . . . 128
5.1.1 EPR-visible states of the active site in [NiFe]-hydrogenases . . . 128
5.1.2 The EPR-active states of the electron transfer relay in standard [NiFe]-hydrogenases . . . 131
5.1.3 *Escherichia coli* synthesises two H_2 uptake hydrogenases with highly contrasting properties . . . 132
5.2 Experimental procedures . . . 137
5.2.1 Preparation of EPR samples . . . 138
5.2.2 EPR measurements . . . 139
5.2.3 Electrochemical experiments . . . 139
5.3 Results . . . 140
5.3.1 The EPR-visible oxidised states in *E. coli* Hyd-1 & Hyd-2 . . . 140

5.3.2 The EPR-active reduced Ni states in *E. coli* Hyd-1 and Hyd-2 . . . 142
5.3.3 The temperature & frequency dependence of Ni-C in *E. coli* Hyd-2 148
5.3.4 Ni-C *vs* Ni-L in *E. coli* Hyd-2 . . . 152
5.3.5 The EPR-active reduced state in *E. coli* Hyd-1: Outlook . . . 160
5.4 Discussion and future work . . . 161

6 O_2-tolerance in [NiFe]-hydrogenases and the role of supernumerary cysteines at the proximal Fe-S cluster 167
6.1 Introduction . . . 170
6.1.1 Background to O_2 tolerance in [NiFe]-hydrogenases . . . 170
6.1.2 Electrochemical characterisation of the proximal cluster of native *E. coli* Hyd-1 and variants C19G, C120G and C19G/C120G . . . 174
6.2 Methods . . . 178
6.2.1 Preparation of native and variant *E. coli* Hyd-1 EPR samples . . . 178
6.2.2 Preparation of *Salmonella* Hyd-5 EPR samples . . . 179
6.2.3 EPR measurements . . . 179
6.3 Results . . . 180
6.3.1 The active site and O_2-tolerance . . . 180
6.3.2 The high potential centre and O_2-tolerance . . . 184
6.3.3 The C19G variant . . . 192
6.3.4 The C120G variant . . . 194
6.3.5 Summary of the supernumerary cysteine variants . . . 196
6.3.6 The EPR properties of an O_2-tolerant [NiFe]-hydrogenase from *Salmonella enterica* . . . 202
6.4 Discussion and future work . . . 204

7 Characterisation of the unique [4Fe-3S]$^{5+}$ cluster in O_2-tolerant hydrogenases by HYSCORE 211
7.1 Introduction . . . 214
7.2 Methods . . . 217
7.2.1 Preparation of EPR samples . . . 218
7.2.2 EPR measurements and analysis of HYSCORE spectra . . . 219
7.3 Results . . . 219
7.3.1 Potential titrations of *E. coli* native and P242C variant Hyd-1 . . . 219
7.3.2 Comparison of the EPR spectra of native Hyd-1 and the P242C, C19G/C120G/P242C and C19G/C120G variants . . . 223
7.3.3 Detection of strong nitrogen couplings in high-potential Hyd-1 P242C 226
7.3.4 HYSCORE measurement of Hyd-1 P242C reveal three ^{14}N couplings 229
7.3.5 Model of the 'superoxidised' P242C EPR spectra . . . 240
7.4 Discussion . . . 243

8 The spin state of the distal iron-sulfur cluster in O_2-tolerant [NiFe]-hydrogenases 249
8.1 Introduction . . . 252
8.1.1 Previous studies of the Fe-S cluster relay at low potentials . . . 252
8.1.2 Previous site-directed mutagenesis studies of the electron transfer relay . . . 257

8.2 Methods . . . 259
8.2.1 EPR sample preparation . . . 259
8.2.2 EPR measurements . . . 261
8.3 Results (Part I) . . . 261
8.3.1 Native and variant *E. coli* Hyd-1 and *Salmonella* Hyd-5 compared at low potentials . . . 261
8.3.2 Potential titrations of *E. coli* native and P242C variant Hyd-1 . . . 264
8.3.3 Interactions with the active site Ni species . . . 267
8.3.4 Temperature dependence of the low-potential signal in native Hyd-1 and Hyd-1 P242C . . . 274
8.4 Results (Part II) . . . 279
8.4.1 X-band and W-band field sweeps . . . 279
8.4.2 Wide X-band field sweeps of the proximal cluster variants . . . 286
8.4.3 There is no direct evidence for the reduced distal cluster contributing to the low-potential Fe-S spectrum . . . 289
8.4.4 Are there dipolar interactions between the proximal and distal clusters? . . . 298
8.5 Discussion and further work . . . 299

9 Summary and Conclusions **307**

10 Appendices **311**
10.1 The Nernst equation . . . 312
10.2 Appendix to Chapter 5 . . . 314
10.3 Appendix to Chapter 6 . . . 315
10.4 Appendix to Chapter 7 . . . 318
10.5 Appendix to Chapter 8 . . . 319

Bibliography **325**

Nomenclature

2pe	two-pulse echo-detected
A. vinosum	*Allochromatium vinosum*
Aa Hase I	*Aquifex aeolicus* [NiFe]-Hydrogenase 1
D. fructosovorans	Desulfovibrio fructosovorans
D. gigas	*Desulfovibrio gigas*
D. vulgaris	*Desulfovibrio vulgaris*
E. coli	*Escherichia coli*
H. marinus	Hydrogenovibrio marinus
R. eutropha	*Ralstonia eutropha*
Re-MBH	*Ralstonia eutropha* membrane-bound [NiFe]-hydrogenase
ATP	Adenosine triphosphate
CODH	Carbon monoxide dehydrogenase
CW	continuous wave
DEER	Double electron-electron resonance
DFT	Density functional theory
ENDOR	Electron-nuclear double resonance
EPR	electron paramagnetic resonance
FID	Free induction decay
FMN	Flavin mononucleotide
FTIR	Fourier-transform infrared
HiPIP	High-potential iron-sulfur protein
HYSCORE	Hyperfine sublevel correlation spectroscopy

IR	infrared
mw	microwave
NAD	nicotinamide adenine dinucleotide
NADH	nicotinamide adenine dinucleotide, Hydrogen reduced
NMR	Nuclear magnetic resonance
PFE	protein film electrochemistry
QM/MM	Quantum Mechanics/Molecular Mechanics
REFINE	Relaxation Filtered Hyperfine spectroscopy
ROS	Reactive oxygen species
SCE	saturated calomel electrode
SDSL	site-directed spin labeling
SHE	Standard hydrogen electrode
SOMO	singly occupied molecular orbital
SPF	Spin projection factor
SRT	shot repetition time

List of Tables

3.1 Mediators and their reduction potentials 68
3.2 EPR tubes and their application 68
3.3 Resonators and their application 73

4.1 Redox potentials of the observed Fe-S cluster signals in *B. taurus* complex I 91
4.2 Principal g values, g-strain parameters, and relative intensities of spectra from the four reduced Fe-S clusters observed in *B. taurus* complex I 103
4.3 Spin projection factors for $[2Fe\text{-}2S]^{+}$ and $[4Fe\text{-}4S]^{+}$ clusters 105
4.4 Intercluster distances for models A, B and C 109
4.5 Combination of cluster pairs tested in simulations of the experimental DEER traces and the respective intercluster distances 113

5.1 Rate constants for the conversion of Ni-L to Ni-C in *E. coli* Hyd-2 153
5.2 Comparison of the activation energies/enthalpies for the interconversion between Ni-L and Ni-C in standard [NiFe]-hydrogenases 155

6.1 Comparison of the potentials of the EPR-visible active site species in [NiFe]-hydrogenases from different species 192
6.2 Midpoint potentials of the EPR-active Fe-S clusters observed in native Hyd-1 and the supernumerary cysteine variants 199

7.1 Hyperfine and nuclear-quadrupole parameters for ^{14}N of H-bonded His to the active site [NiFe]-bridging Cys in *E. coli* Hyd-1 compared to other [NiFe]-hydrogenases 235
7.2 Hyperfine and nuclear-quadrupole parameters for $^{14}N_{C20}$ coupling to Fe_4 in *E. coli* Hyd-1 P242C and comparison with other strongly coupled ^{14}N nuclei reported in the literature 240
7.3 g values for the proximal $[4Fe\text{-}3S]^{5+}$ cluster and exchange interaction with the active site in O_2-tolerant [NiFe]-hydrogenases 241

8.1 Midpoint potentials of Fe-S clusters in standard [NiFe]-hydrogenases 253
8.2 Midpoint potentials of Fe-S clusters in O_2-tolerant [NiFe]-hydrogenases . . 256
8.3 Spin integrations of Fe-S cluster signals of native Hyd-1 and the P242C variant at high and low potentials 266
8.4 Midpoint potentials of the EPR-active Fe-S clusters observed in native Hyd-1 and Hyd-1 P242C 267
8.5 Temperature dependence of Hyd-1 native and P242C double integrals of low-potential CW EPR spectra 277

List of Figures

1.1 Oxidation states and (de)localisation of electrons in ferredoxin-type Fe-S clusters . . . 3
1.2 Examples of the structural variety of Fe-S clusters . . . 6
1.3 Structure of the [NiFe]-hydrogenase from *D. fructosovorans* . . . 9
1.4 Photosynthetic H_2 production . . . 13
1.5 Structure of the [NiFe]-hydrogenase from *H. marinus* . . . 15
1.6 Crystal structure of the hydrophilic domain of complex I from *Thermus thermophilus* . . . 18
1.7 The role of complex I . . . 19

2.1 Energies of the spin states of an electron in a magnetic field . . . 28
2.2 Nutation of the magnetisation vector about the effective magnetic field . . . 30
2.3 The relative orientation between the principal axes frame (x, y, z) and the laboratory frame (X, Y, Z) as defined by the Euler angles . . . 31
2.4 Schematic representation of molecules with axial and rhombic symmetries and orientations resulting in the same g values . . . 32
2.5 Simulated powder EPR spectra with an axial and a rhombic g matrix . . . 33
2.6 Sphere representing the probability of $\mathbf{g}$ matrix orientations at a particular field position . . . 34
2.7 Dipolar interaction between two spins parallel to the magnetic field . . . 41
2.8 Energy level diagram exemplifying a weak exchange interaction between two electron spins . . . 43
2.9 Pulse sequences resulting in the Hahn echo and the stimulated echo . . . 47
2.10 ESEEM pulse sequences . . . 50
2.11 Schematic representation of the peaks observe in HYSCORE spectra . . . 51
2.12 Energy level diagram for a $S = 1/2$, $I = 1$ system when $\nu_I \approx |A|/2$ (exact cancellation condition) . . . 52
2.13 Davies and Mims ENDOR pulse sequences . . . 53
2.14 DEER pulse sequences . . . 55

3.1 Nernst curves for one-electron and two-electron processes and experimental data for a redox centre A with $E_{mA} = +215$ mV. . . . 62
3.2 Set-up for the preparations of EPR samples at well-defined potentials . . . 64
3.3 Different glass cells used for the preparation of potential-equilibrated EPR samples . . . 66
3.4 Chronopotentiometry traces for the titration of a Hyd-1 variant . . . 67
3.5 Calibration curves using $Cu(ClO_4)_2$ as a standard for 'spin counting' . . . 70

3.6 Schematic showing the principles of a protein film electrochemistry experiment . . . 71
3.7 Schematic showing a typical electrochemical cell used in PFE experiments 72
3.8 Two-pulse echo detected field sweeps of a sample of Hyd-1 P242C and the resonator background . . . 74
3.9 Two-pulse echo detected field sweeps of W-band resonator background . . 75
3.10 T_1 measurements of Mn^{2+} in W-band resonator *vs* Hyd-1 P242C $[4Fe\text{-}4S]^+$ 76
3.11 T_2 measurements of Mn^{2+} in W-band resonator *vs* Hyd-1 P242C $[4Fe\text{-}4S]^+$ 77
3.12 Mn^{2+} measurements at W-band with different flip angles . . . 78
3.13 Example calibration line in a Bradford assay . . . 82

4.1 Arrangement of redox cofactors in *B. taurus* complex I . . . 89
4.2 Temperature dependence of CW EPR spectra of *B. taurus* complex I reduced to −0.4 V with NADH . . . 90
4.3 Schematic representation of the g-matrices for each Fe in an Fe-S cluster . 94
4.4 Representation of orientation selection of the mw pulses for the N4 and N2 spectra . . . 98
4.5 Orientation selective DEER simulation parameters for a [2Fe-2S]-[4Fe-4S] cluster pair . . . 99
4.6 EPR spectra of complex I from *B. taurus*, and simulations for N1b, N2, N3 and N4 . . . 103
4.7 DEER trace illustrating typical oscillation period . . . 108
4.8 Comparison of DEER trace obtained from -0.4 V and -0.3 V samples measured under the same conditions . . . 110
4.9 X-band echo-detected EPR spectra of complex I reduced to -0.4 V (A) and -0.3 V B) recorded at 10 K, simulated with the components N1b, N2, N3 and N4 . . . 111
4.10 DEER spectra from *B. taurus* complex I reduced to -0.4 V and -0.3 V measured at 10 K, with the best fit simulations for SPFs $k_{1,2}$ = +1.17 and $k_{3,4}$ = -0.67 . . . 114
4.11 DEER spectra from *B. taurus* complex I reduced to -0.4 V and -0.3 V measured at 10 K, with the best fit simulations for SPFs $k_{1,2}$ = +1.35 and $k_{3,4}$ = -0.85 . . . 115
4.12 DEER spectra from *B. taurus* complex I reduced to -0.4 V and -0.3 V measured at 10 K, including the best fit simulations with exponential baseline for SPFs $k_{1,2}$ = +1.17 and $k_{3,4}$ = -0.67 . . . 116
4.13 DEER spectra from *B. taurus* complex I reduced to -0.4 V and -0.3 V measured at 10 K, including the best fit simulations with no baseline correction for SPFs $k_{1,2}$ = +1.17 and $k_{3,4}$ = -0.67 . . . 117
4.14 Schematic representation of the $g-$axis orientations and four possible SPF assignments in clusters 4Fe[TY]1 (signal N4) and 4Fe[PS] (signal N2) . . . 119
4.15 Representation of the alternating cluster occupancy in complex I postulated during turnover . . . 122
4.16 Electron transfer reactions in complex I . . . 124

5.1 Schematic diagram of the redox states of the active site of catalytic [NiFe]-hydrogenases and structure of the active site . . . 130

5.2 Arrangement of the Fe-S clusters relative to the active site in [NiFe]-hydrogenases and schematic diagram of the redox states of the Fe-S cluster relay in standard hydrogenases . . . 132
5.3 *E. coli* Hyd-1, Hyd-2 and Hyd-3 . . . 133
5.4 The activity of *E. coli* Hyd-1 & Hyd-2 on a pyrolytic graphite edge electrode. 135
5.5 A comparison of the O_2 tolerance of *E. coli* Hyd-1 and Hyd-2 . . . 136
5.6 X-band CW EPR spectra of as-isolated Hyd-1 and Hyd-2 . . . 141
5.7 X-band CW EPR spectra showing the conversion of Ni-L to Ni-C in H_2-reduced Hyd-2 . . . 143
5.8 X-band CW EPR spectra comparing the Ni species in low-potential Hyd-1 and Hyd-2 . . . 145
5.9 The kinetic isotope effect in *E. coli* Hyd-1 *vs* Hyd-2 . . . 147
5.10 X-band CW EPR spectra showing the temperature dependence of Hyd-2 Ni-C . . . 149
5.11 Comparison of oxidised and reduced Hyd-2 at X-band and W-band frequencies . . . 151
5.12 Conversion of Ni-L to Ni-C in Hyd-2, monitored through the increasing peak intensity of Ni-C g_x . . . 152
5.13 Arrhenius plot for the conversion of Ni-L to Ni-C in H_2-reduced Hyd-2 . . . 154
5.14 X-band HYSCORE spectra ($^{14}N/^{2}H$ region) of Ni-C in H_2-reduced and D_2-reduced *E. coli* Hyd-2 at g_y and g_x orientations . . . 157
5.15 Multiple sequence alignment showing sections of the large subunits in *E. coli* Hyd-2, *D. vulgaris* Miyasaki F and *A. aeolicus* Hase I . . . 158
5.16 X-band HYSCORE spectra (^{1}H region) of Ni-C and Ni-L in H_2-reduced and D_2-reduced *E. coli* Hyd-2 at the g_x orientation . . . 159
5.17 X-band CW EPR spectra of *E. coli* Hyd-1 native and C19G/C120G at low potentials and HYSCORE spectrum of Ni-L* in Hyd-1 C19G/C120G (g_y orientation) . . . 160
5.18 Mechanism for H_2 cleavage in [NiFe]-hydrogenases proposed by Lill and Siegbahn based on theoretical work . . . 165

6.1 The proximal cluster and active site and their amino acid environment in *D. fructosovorans* [NiFe]-hydrogenase and *E. coli* Hyd-1 . . . 171
6.2 Multiple sequence alignment of key sections of the small subunit in a selection of catalytic [NiFe(Se)]-hydrogenases. . . . 173
6.3 Chronoamperometry experiments showing the response of native Hyd-1 and the proximal cluster variants to varying amounts of O_2 . . . 176
6.4 Cyclic voltammograms showing re-activation of the anaerobically generated (left panel) and aerobically generated (right panel) inactive states of native Hyd-1 and the proximal cluster variants . . . 177
6.5 X-band CW EPR spectra of as-isolated native Hyd-1 and the proximal cluster variants, 80 K . . . 180
6.6 X-band CW EPR spectra of anaerobically inactivated native Hyd-1 and the proximal cluster variants, 80 K . . . 182
6.7 X-band CW EPR spectra of aerobically inactivated native Hyd-1 and the proximal cluster variants, 80 K . . . 183

6.8 X-band CW EPR spectra of potential titration of native Hyd-1 at 15 K . . 185
6.9 X-band CW EPR spectra at 15 K and 80 K of native Hyd-1 poised at 385 mV, 145 mV and 36 mV 186
6.10 X-band CW EPR spectra of potential titration of Hyd-1 C19G/C120G at 15 K 188
6.11 X-band CW EPR spectra of potential titration of Hyd-1 C19G/C120G at 70 K (left) and corresponding Nernst plots of the observed Ni species (right) 190
6.12 X-band CW EPR spectra of potential titration of Hyd-1 C19G at 15 K (left) and at 80 K (right) 193
6.13 X-band CW EPR spectra of potential titration of Hyd-1 C120G at 15 K . 195
6.14 Potentiometric titrations of the EPR-active Fe-S cluster species observed in native Hyd-1, C19G/C120G, C19G and C120G 197
6.15 Comparison of the 9.39 GHz CW EPR spectra at 15 K of Hyd-1 and proximal cluster variant 'as-isolated' enzyme samples poised at high potentials 201
6.16 CW EPR spectra of *Salmonella* Hyd-5 poised at different potentials 202
6.17 The proximal cluster in its oxidised and reduced form in *E. coli* Hyd-1 . . . 209

7.1 The proximal cluster in its oxidised and reduced form in *E. coli* Hyd-1 . . . 214
7.2 Different models proposed for the proximal cluster in its oxidised form in *E. coli* Hyd-1 215
7.3 CW EPR spectra of potential titrations of native Hyd-1 and the P242C variant 221
7.4 Potentiometric titrations of the EPR-active species observed in native Hyd-1 and the P242C variant 222
7.5 X-band CW EPR spectra of native Hyd-1, P242C, C19G/C120G/P242C and C19G/C120G poised at high potentials 224
7.6 X-band echo-detected and CW spectra of native Hyd-1 and the P242C variant poised at high potential 227
7.7 X-band HYSCORE spectra of native Hyd-1, Hyd-1 P242C and deuterated P242C samples poised at high potential 228
7.8 X-band HYSCORE spectra showing the three different ^{14}N nuclei (N1, N2 & N3) observed in P242C at high potential. 230
7.9 Energy level diagram for a $S_1 = 1/2$, $S_2 = 1/2$ and $I = 1$ (^{14}N) system with an exchange interaction J between spins 1 and 2 and dependence of nuclear energy levels on J 231
7.10 X-band HYSCORE spectrum of P242C at high potential at $B_0 = 326.0$ mT with cross-peak position simulations as a function of the exchange coupling J between the superoxidised proximal cluster and the active site Ni-A/Ni-B species 233
7.11 The active site of *E. coli* Hyd-1 showing the H-bonding between bridging Cys579 and Nϵ of His83 and multiple sequence alignment of key regions of the large subunit in different [NiFe]-hydrogenases 234
7.12 X-band HYSCORE spectrum of P242C at high potential, at $B_0 = 348.2$ mT, with simulations of only the dq cross-peaks as a function of the exchange coupling J between the proximal cluster and the active site Ni-A/Ni-B species 237

7.13 X-band HYSCORE spectra of P242C poised at high potential showing the field dependence of the N2 & N3 couplings . . . 238
7.14 X-band HYSCORE spectra of P242C poised at high potential showing the field dependence of the N1 coupling. . . . 239
7.15 Simulation of EPR spectra of P242C poised at high potential in terms of a four component model. . . . 242

8.1 Comparison of the midpoint potentials of the Fe-S cluster in standard and O_2-tolerant [NiFe]-hydrogenases . . . 257
8.2 Comparison of the X-band CW EPR spectra at 15K of native Hyd-1 and proximal variant enzyme samples after activation under H_2 . . . 262
8.3 Comparison of the low potential CW EPR spectra of *E. coli* Hyd-1 native and P242C variant, and *Salmonella* Hyd-5 . . . 264
8.4 CW EPR spectra of potential titrations of native Hyd-1 and the P242C variant . . . 265
8.5 Potentiometric titrations of the EPR-active species observed in native Hyd-1 and the P242C variant . . . 267
8.6 CW EPR spectra of Ni signals of native Hyd-1 (15 K) and Hyd-1 P242C (20 K) at selected potentials . . . 268
8.7 CW EPR spectra of Ni signals of native Hyd-1 and Hyd-1 P242C at selected potentials (80 K) . . . 270
8.8 X-band CW EPR spectra of native Hyd-1 and variants comparing low-potential Ni signals . . . 272
8.9 15 K and 80 K X-band CW EPR spectra of native Hyd-1 and proximal cluster variants poised at 77±2 mV . . . 274
8.10 Native Hyd-1: temperature dependence of low-potential species . . . 275
8.11 Hyd-1 P242C: temperature dependence of low-potential species . . . 276
8.12 Temperature dependence of low potential native Hyd-1 X-band CW EPR spectra scaled by the Boltzmann distribution . . . 278
8.13 Temperature dependence of H_2-reduced native Hyd-1 X-band two-pulse echo-detected field sweeps . . . 280
8.14 T2 measurements of low-potential native Hyd-1 and the P242C variant at X-band (3 K) . . . 281
8.15 H_2-reduced native Hyd-1 X-band two-pulse echo-detected field sweeps with variable τ at 2.7 K . . . 282
8.16 Reduced Hyd-1 P242C X-band two-pulse echo-detected field sweeps with variable τ at 7 K . . . 283
8.17 Comparison of X- and W-band field sweeps of low-potential native Hyd-1 and the P242C variant . . . 284
8.18 X-band two-pulse echo-detected wide field sweeps of native Hyd-1 and variants (2.7 K) . . . 287
8.19 Echo intensity of low-potential Hyd-1 C19G/C120G as a function of temperature (X-band) . . . 288
8.20 X-band two-pulse echo-detected field sweeps of native Hyd-1 and Hyd-1 P242C poised at low potential . . . 290
8.21 X-band HYSCORE spectra of H_2-reduced native Hyd-1 (- 355 mV) . . . 292

8.22 X-band HYSCORE spectra of reduced Hyd-1 P242C (- 250 mV) 293
8.23 X-band HYSCORE spectra in reduced native Hyd-1 and Hyd-1 P242C and simulations of ^{14}N peaks 295
8.24 X-band HYSCORE spectra of reduced native Hyd-1 and Hyd-1 C19G at 500 mT 297
8.25 Distance between the proximal and distal clusters in *E. coli* Hyd-1 298

10.1 E_{switch} at 37 ^{o}C and 10 ^{o}C of *E. coli* Hyd-1 and Hyd-2 at pH 6 314
10.2 X-band 9.39 CW EPR spectra of C19G/C120G samples following anaerobic and aerobic inactivation, 15 K 315
10.3 Calculated one-electron Nernst plot for HP with E_m +230 mV and deduced plot for medial cluster based on the information that at E_1 the spin integration of the FeS cluster signals is 0.9 317
10.4 Nernst plots for native Hyd-1 and for P242C 318
10.5 Temperature dependence of $Cu(ClO_4)_2$ CW EPR spectra 319
10.6 X-band two-pulse echo-detected wide field sweeps of native Hyd-1 and variants (2.7 K) 320
10.7 X-band HYSCORE spectra of H_2-reduced native Hyd-1 (- 355 mV) 321
10.8 X-band HYSCORE spectra of reduced Hyd-1 P242C (- 250 mV) 322
10.9 X-band HYSCORE spectra of reduced Hyd-1 P242C (- 250 mV) 323
10.10Sequence alignment of the small subunit O_2-tolerant [NiFe]-hydrogenases . 324

Chapter 1

Introduction

1.1 Iron-sulfur clusters

In 1964, when Helmut Beinert first presented the now well-known '$g = 1.94$' EPR signal and evidence that it had to result from iron in submitochondrial fractions [1, 2], it was a puzzle how an Fe complex could have a g value below 2.00. In 1966, Gibson *et al.* [3] showed that in spinach ferredoxin such an EPR signal could arise from an antiferromagnetic exchange interaction between two Fe atoms in the +2 and the +3 oxidation states. As we now know, spinach ferredoxin contains a [2Fe-2S] cluster in which the two Fe atoms are indeed coupled antiferromagnetically. Since then it has been recognised that iron-sulfur clusters are ubiquitous in nature [4] and they are not only present in small electron-transfer proteins such as ferredoxins, but also in large complex enzymes such as those of the mitochondrial respiratory chain.

The variety of Fe-S cluster structures observed reflects the chemical versatility of both Fe and S [4, 5]. The simpler clusters, [2Fe-2S], [3Fe-4S] and [4Fe-4S] centres (Fig. 1.1), are involved in many one-electron transfer reactions, the first role of Fe-S clusters to be recognised [6]. Contrary to the localised Fe^{2+} and Fe^{3+} states in [2Fe-2S] clusters, [4Fe-4S] and [3Fe-4S] clusters have mixed valence states in which an electron can be 'shared' between two Fe subsites [7], as illustrated in Fig. 1.1. The electron delocalisation is thought to be crucial in enabling these centres to transfer electrons efficiently. The more efficient electron transfer of such delocalised clusters compared to a single metal site has been demonstrated both theoretically [8] and experimentally [9].

Cysteine residues are the most common ligands for Fe-S clusters (as in Fig. 1.1), but other residues are also encountered. One of the earliest examples of non-cysteine Fe ligation is the Rieske centre, in which two His residues coordinate one Fe subsite of a [2Fe-2S] cluster. These centres were first discovered in cytochrome c reductase (complex III of the respiratory chain) [10]. In the determination of the localisation/delocalisation patterns shown in Fig. 1.1, the Mössbauer technique (a γ-ray absorption spectroscopy exploiting the Doppler effect) proved to be especially important. The gamma rays emitted by excited states of the nuclei of ^{57}Fe isotopes decaying to the ground state are absorbed by

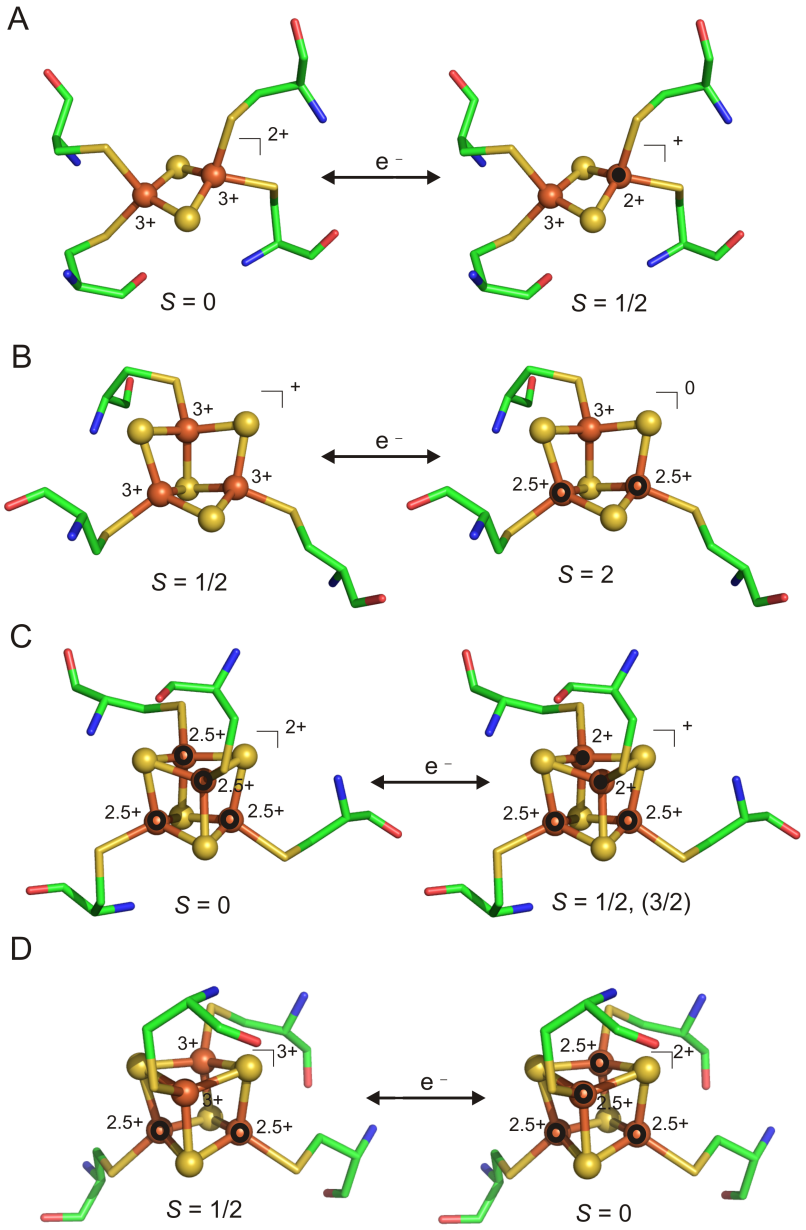


Figure 1.1: **Oxidation states and (de)localisation of electrons in all cysteine ligated ferredoxin-type Fe-S clusters.** The cluster core charges are indicated, as are the nominal charges of the Fe-subsites. (A) [2Fe-2S] cluster (2Fe[75] from *T. thermophilus* complex I, 2FUG.PDB, see Fig. 1.6, (B) [3Fe-4S] cluster (medial cluster from *E. coli* Hyd-1, 3USC.PDB), (C) [4Fe-4S] cluster showing the typical 2+ to 1+ redox transition (proximal cluster from *D. fructosovorans* [NiFe]-hydrogenase 1FRV.PDB), (D) [4Fe-4S] cluster showing the 3+ to 2+ redox transition found in high-potential iron proteins, HiPIPs (from *Thermochromatium tepidum* [NiFe]-hydrogenase 2FLA.PDB). The assignment of the charges to the Fe-subsites is arbitrary and the particular clusters chosen from different proteins (as indicated) only serve as example structures. The overall spin ground states (S) of the clusters are indicated. Colours represent the following atoms: S yellow, Fe orange, C green, N blue, O red.

the sample containing the same isotope. Because the radial distribution functions of d and s electrons overlap, this absorption gives an indirect measure of the d-orbital population. The measured absorption spectra are characterised by (1) the quadrupole splitting which results from the nuclear spin of 3/2 of ^{57}Fe splitting the observed lines into doublets, and (2) the isomer shift. Both the quadrupole splitting and the isomer shift are sensitive to the oxidation state and ligand environment of the Fe under investigation [4, 5]. For example, while [2Fe-2S]$^{+}$ clusters give rise to two doublets, oxidised [3Fe-4S]$^{+}$ clusters give rise to just one doublet (see Fig. 1.1) [5, 11, 12]. Solution NMR experiments have shown that the valence pairs observed in [4Fe-4S]$^{3+}$ clusters are not located on one face of the cubane (on the time scale of the NMR experiment, 10^{-5} s), but exist in an equilibrium between different forms where pairs reside on different faces [13]. However, in the frozen solutions studied with EPR at low temperatures (typically 10-40 K), the different valence pairs are, to a good approximation, located on specific Fe subsites. This allows the determination of the overall spin ground state of the clusters in different oxidation states, as indicated in Fig. 1.1. In short, two Fe atoms within a valence pair couple ferromagnetically, and different valence pairs then couple antiferromagnetically [7, 14] (see Chapter 2, Section 2.3.5).

[4Fe-4S] clusters most commonly cycle between the +2 and +1 oxidation states (the oxidation states used throughout this thesis indicate the charge of the core cluster, without ligands). Cycling between the +3 and +2 oxidation states occurs in HiPIPs (high-potential iron-sulfur proteins), which are common in purple photosynthetic bacteria. However, [4Fe-4S] clusters do not appear to cycle between all three oxidation states physiologically; although Heering *et al.* [15] were able to reversibly super-reduce [4Fe-4S]$^{3+}$ from *Rhodophila globiformis*, this super-reduction was very slow and accompanied by a conformational change. Furthermore, the reduction potentials of the two redox couples spanned more than 1 V [15]. Most recently, the Fe-S cluster in closest proximity to the active site in a subclass of [NiFe]-hydrogenases (Section 1.2.2) which are able to sustain catalysis in the presence of O_2, was found to be able to cycle reversibly between three oxi-

dation states over a narrow range [16] while undergoing a conformational change [17, 18]. This [4Fe-3S] cluster can be seen as fulfilling two roles: catalytic electron transfer to and from the active site, and 'rescuing' the active site from permanent O_2 damage. The work presented in this thesis contributes to our understanding of this highly unusual cluster in O_2-tolerant [NiFe]-hydrogenases (Chapters 6, 7, 8). $[3Fe\text{-}4S]^0$ clusters have been observed *via* electrochemistry to 'hyper-reduce' to $[3Fe\text{-}4S]^{2-}$ in a cooperative 2-electron reduction with concomitant protonation, but whether there is a biological role of this chemistry is uncertain [19, 20].

While an understanding of the biogenesis of Fe-S clusters is just beginning to emerge [21–23], [2Fe-2S], [3Fe-4S] and [4Fe-4S] clusters were chemically synthesised *via* relatively simples routes, from Fe^{3+}, thiols and sulfides, as early as the 1970s [24, 25]. Although *in vitro* synthesis demonstrated that these clusters are stable without the encasing protein structure, the cluster environment certainly influences the properties of the cluster. This is demonstrated by the much higher reduction potential of the [4Fe-4S] cluster of HiPIPs compared to ferredoxins. Although both contain [4Fe-4S] clusters entirely ligated by cysteine residues, the cysteine-ligand dihedral angles and positions of hydrogen bonds differ substantially [15]. Single crystal EPR studies of increasingly elaborate models compounds seek to understand the electronic properties of the clusters in different oxidation states, and g-tensor[1] orientations have been determined [26–28]. The guidelines established for g-tensor orientations can be useful for data analysis when this information cannot be acquired experimentally (see Chapter 4). Efforts have also been made to reproduce, synthetically, the asymmetry found in the [4Fe-4S] cluster in the enzyme aconitase (Fig. 1.2), and experiments have been conducted to understand the effects on spin states and g-tensor orientations [29], in comparison with experimental data [30].

The [4Fe-4S] cluster in aconitase illustrates another important role that some Fe-S clusters fulfill: participation in catalysis. Aconitase forms part of the citric acid cycle and catalyses the interconversion between citrate and isocitrate through an intermediate

[1] see Chapter 2

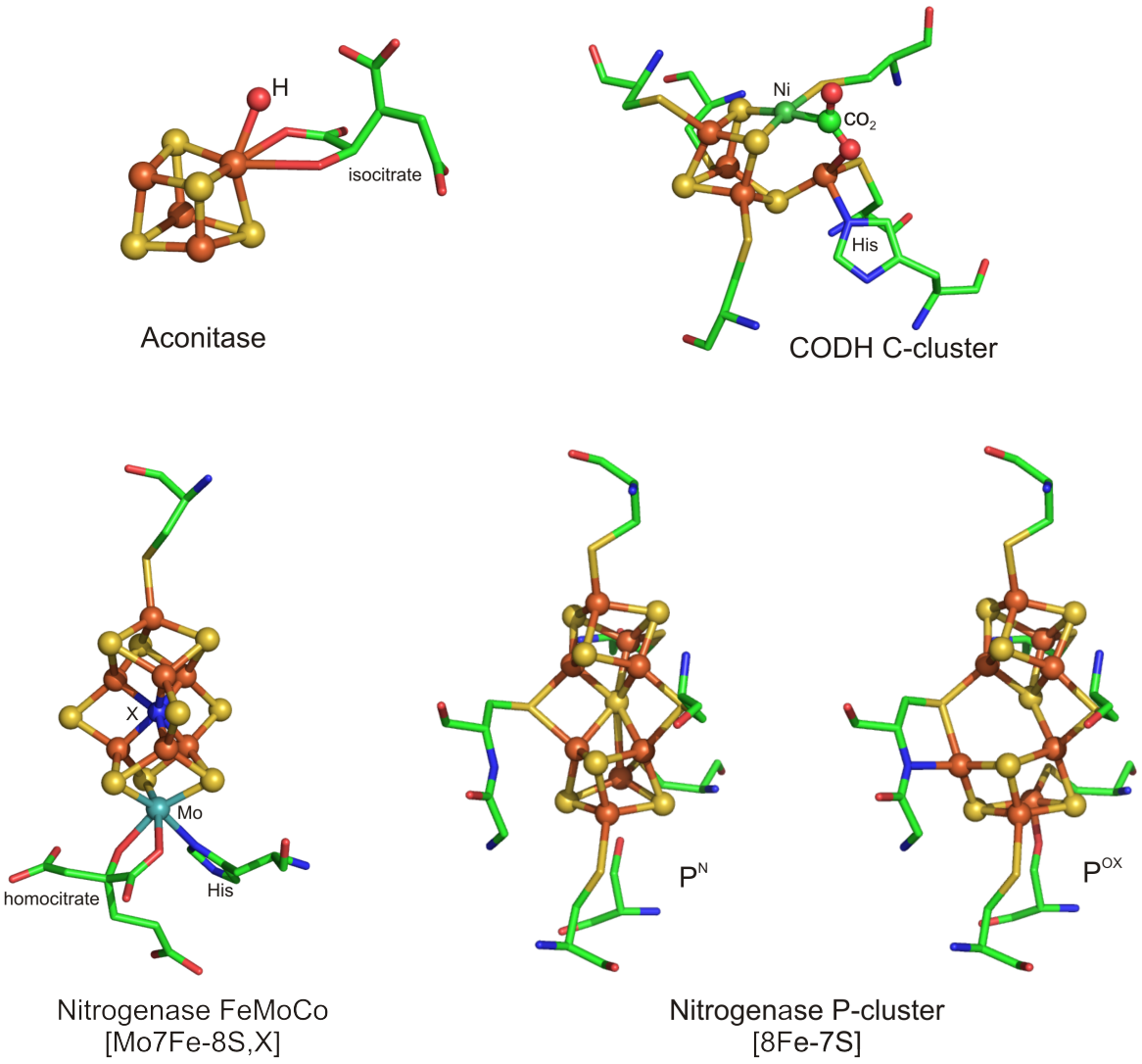


Figure 1.2: **Examples of the structural variety of Fe-S clusters.** Active aconitase 1C97.PDB [31], carbon monoxide dehydrogenase (CODH) 3B52.PDB [32], nitrogenase FeMoCo (1M1N.PDB) [33] and P-cluster (P^N 1M3N.PDB; P^{OX} 1M2N.PDB) [34]. Colours represent the following atoms: S yellow, N blue, Fe orange, O red, C green, Mo light blue; X = C, N or O.

aconitate [35, 36]. Fig. 1.2 shows the active form of the enzyme with isocitrate bound at one of the Fe subsites of the [4Fe-4S] cluster, the site of catalysis. This Fe is also bound by OH or a water molecule, making it six-coordinate [30]. The binding of the carboxylate group of the substrate was demonstrated by ^{17}O ENDOR (Electron-nuclear double resonance, Section 2.6.4 in Chapter 2) [37], and Mössbauer studies supported a mechanism in which changes in the coordination environment of one of the Fe subsites

occur upon substrate binding [30]. The first crystal structure of the active enzyme confirmed the presence of the OH or H_2O ligand [38], and a later structure showed substrate binding (see Fig. 1.2), confirming the conclusions reached from the spectroscopic investigations [31]. A plausible mechanism is thus that substrate binding Fe acts as a Lewis acid, abstracting a hydroxyl group from citrate concomitantly with proton abstraction by the bound hydroxide; the resulting aconitate then swings around and OH and H are reinserted to yield isocitrate [4, 35]. The OH-coordinated Fe is labile and lost when the active enzyme is exposed to air, *i.e.* the [4Fe-4S] cluster degrades into a [3Fe-4S] cluster [39].

Other examples of Fe-S clusters constituting the active site of an enzyme are Ni carbon monoxide dehydrogenases (CODHs) which catalyse the interconversion between CO_2 and CO [40]. In this case the active site is a modified Fe-S cluster (Fig. 1.2). Insights into the active site catalytic mechanism have mainly resulted from crystallographic studies [32] and the CO_2-binding structure is shown in Fig. 1.2. Besides their importance in biology, CODHs have been exploited for photo-induced CO production from CO_2 [41], and in an enzyme driven water-gas shift reaction ($CO + H_2O \rightarrow H_2 + CO_2$) [42].

Nitrogenase, an essential enzyme in the nitrogen cycle, and responsible for the 'activation' of N_2, contains some of the most intricate Fe-S structures (Fig. 1.2). The 'P-cluster', composed of two [4Fe-3S] modules linked by cysteines, is thought to be involved in electron transfer and undergoes a dramatic conformational change between its reduced (P^N) and oxidised (P^{OX}) states [34] (Fig. 1.2), while 'FeMoCo' (FeMo cofactor) is postulated to be the site of N_2 reduction to NH_3 [43]. The central 'X' ligand (C, N or O) in the latter was discovered many years after the first crystal structure of nitrogenase appeared [33] − until then the apparent 3-coordinate six central Fe atoms were a mystery. Understanding how biological nitrogen fixation can occur at ambient temperature and pressure (although 16 ATP are consumed) is intriguing given the high energetic cost of the industrial Haber process used to convert N_2 and H_2 to NH_3.

The facile conversion between different types of 'simple' Fe-S clusters gives rise to

another important role: their ability of function as sensors. A prominent example is the fumarate nitrate regulator (FNR). Under anaerobic conditions FNR contains a [4Fe-4S] cluster and binds DNA, resulting in the transcription of enzymes which are necessary in the absence of O_2. When O_2 is introduced, the [4Fe-4S] cluster degrades to a [2Fe-2S] cluster, as shown by Mössbauer studies [44, 45], causing FNR to no longer be able to bind to DNA and resulting in the transcription of enzymes required under aerobic conditions [35].

1.2 Two intriguing Fe-S cluster electron-transfer relays

1.2.1 Electron-transfer relays

The first evidence that Fe-S compounds play a significant role in what we now call hydrogenases was published by Otto Warburg in 1949 [4, 46]. In 1995, the crystal structure of the [NiFe]-hydrogenase from *Desulfovibrio gigas* [47] revealed the relay arrangement of the electron-transfer Fe-S clusters. Such a nearly linear relay arrangement of electron-transfer cofactors was subsequently revealed in many other enzymes, including fumarate reductase (1999) [48], CODH (2001) [49], nitrate reductase (2003) [50] and complex I (2006) [51] (section 1.2.3). The great number of Fe-S clusters, up to 9 in complex I, found in these enzymes was rather puzzling until Dutton and co-workers [52] proposed the now well-known '14 Å rule'. The correlation of distance between electron-transfer centres and the rate of substrate redox reactions in a very large number of proteins led Page *et al.* to the conclusion that the most crucial characteristic for efficient electron tunneling was the positioning of centres within 14 Å of each other [52]. Over distances shorter than 14 Å, electron transfer is very fast, much faster than chemical reactions at the active site in enzymes. Thus electron transfer is not rate limiting, even if the relay contains a thermodynamically 'uphill' (positive ΔG) step [52].

Although the model proposed by Dutton and co-workers [52] serves as a very useful guide, more sophisticated models are likely necessary to account for and accurately calculate observed electron-transfer rates. Investigations into long-range electron transfer span many different systems and employ both experimental and theoretical methods [53–57].

1.2.2 Hydrogenases

As can be seen from the structure of *Desulfovibrio fructosovorans* [NiFe]-hydrogenase in Fig. 1.3 [58, 59], [NiFe]-hydrogenases comply to the 14 Å rule. The medial [3Fe-4S] cluster is an electron 'sink' that gives rise to an uphill step because it usually has a much more positive reduction potential compared to the proximal and distal [4Fe-4S] clusters

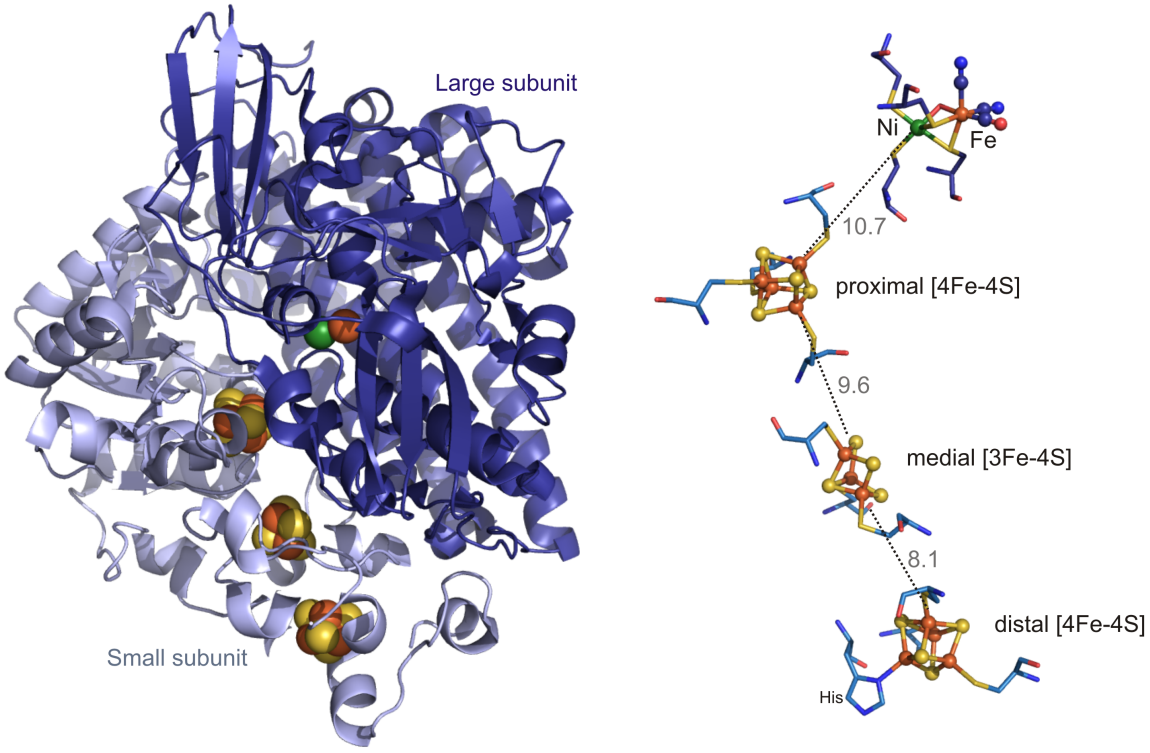


Figure 1.3: **Structure of the [NiFe]-hydrogenase from *D. fructosovorans* (1FRV.PDB).** The large subunit housing the [NiFe] active site and the small subunit housing the Fe-S clusters are shown in different colours. The electron-transfer relay is shown with the ligands directly coordinating the Fe-S clusters and the active site Ni and Fe atoms. Edge-to-edge distances are given in Å. Colours represent the following atoms: S yellow, N blue, Fe orange, O red, Ni green.

(the introduction to Chapter 8 provides an overview of the redox potentials reported for different [NiFe]-hydrogenases). Substitution of the medial [3Fe-4S] cluster for a [4Fe-4S] cluster through site-directed mutagenesis in *D. fructosovorans* [NiFe]-hydrogenase only had a very small effect on the catalytic activity, even though the potential of the cluster is reported to have decreased by $\approx$ 300 mV [58]. As well as distances, the direct environment of the clusters also appears to play an important role in determining electron transfer rates. As shown in Fig. 1.3, the distal [4Fe-4S] cluster exhibits unusual ligation by three cysteines and one histidine residue. The substitution of this His residue for a cysteine almost entirely abolished catalytic activity even though the cluster potential did not change significantly [60].

The Fe-S cluster relay in the small subunit of hydrogenases transfers electrons to the deeply buried active site which sits in the large subunit and catalyses the simple but fundamental reaction

$$H_2 \rightleftharpoons 2H^+ + 2e^- \quad E^0 = 0\ V,\ E^{\ominus}_{pH7} = -0.413\ V. \tag{1.1}$$

Three different types of hydrogenases are produced by bacteria and all carry out the interconversion between molecular hydrogen and protons. These enzymes are the result of convergent evolution and they all employ highly unusual CO ligands in the active site (Fig. 1.3) that are otherwise unknown in biology [61, 62]. The three types have been named according to their active site metal content as [NiFe]-, [FeFe]- and [Fe]-hydrogenases. Only [NiFe]-hydrogenases are studied in this thesis. In a subclass of the [NiFe]-hydrogenases one of the terminal cysteine ligands of the active site Ni (Fig. 1.3) is replaced by a selenocysteine and these enzymes have thus been named [NiFeSe]-hydrogenases [63]. The electron transfer relay in [NiFeSe]-hydrogenases contains three [4Fe-4S] clusters [63]. The active site in [NiFe(Se)]-hydrogenases cycles through a variety of oxidation states that are most unusual in coordination chemistry [64] and these are introduced in detail in Chapter 5.

While the pathway for electron delivery to the active site undoubtedly involves the Fe-S cluster relay, proton and H_2 transfer to and from the active site are less well understood. The first experimental evidence for the existence of so-called gas-channels resulted from a crystallographic study by Fontecilla-Camps and co-workers who were able to trap Xe atoms within the [NiFe]-hydrogenase crystal from *D. fructosovorans* exposed to high pressures of Xe gas [65]. Molecular dynamics simulations also support the idea that H_2 preferentially occupies certain gas channels [66]. However, such simulations also show that the small H_2 molecule is able to diffuse through the protein without the need of special hydrophobic gas channels [67, 68]. Proton transfer requires a series of protonations and deprotonations of amino acid residues with suitable pK_a values which are difficult to identify; a number of pathways are potentially feasible [59, 69].

In the search for renewable and sustainable forms of energy, hydrogenases − with cheap and abundant Ni and Fe at their active site − have attracted much attention both as a potential source of H_2 as a fuel, and as inspiration for synthetic systems capable of producing H_2 sustainably, cheaply and at high turnover frequencies. Currently, industrial production of H_2 mainly relies on natural gas (methane) through steam reforming − a high-temperature, costly process that also produces both CO and CO_2. Although platinum is an efficient catalyst for the interconversion of H_2 and protons under mild conditions (with turnover rates comparable to [NiFe]-hydrogenases [70]), it is a rare and expensive metal that is irreversibly poisoned by CO [71] and therefore neither viable economically nor sustainable. Recent successes in the synthetic approach to H_2 production include the covalent attachment of a nickel bisdiphosphine complex onto carbon nanotubes, resulting in high activity and stability of H_2 cycling [72]. DuBois and co-workers synthesised a Ni compound inspired by features of both [NiFe]- and [FeFe]-hydrogenases, capable of turnover rates in the excess of 100000 per second, although this is achieved only at a large overpotential [73].

[NiFeSe]-hydrogenases have been exploited in solar driven H_2-production through their attachment to conducting nanoparticles together with a photosensitiser [74, 75]. However,

this system only functions under anaerobic conditions, or at best in very low levels of O_2 (1 %) − a major practical drawback. Furthermore, the ultimate aim is to eliminate the required sacrificial electron donor and achieve sunlight-powered conversion of water to H_2 and O_2. In nature, the latter is achieved as illustrated in Fig. 1.4 *via* the light harvesting photosystem II (PSII) complex which splits water into O_2 and electrons. The electrons are passed through photosystem I (PSI) and can be used by hydrogenases for H_2 production under anaerobic or fermentative conditions, and are used for CO_2 reduction ('carbon fixation') under normal conditions [76].

Recently, in an approach inspired by the natural bio-photosynthetic machinery, a [NiFe]-hydrogenase [77] and a [FeFe]-hydrogenase [78, 79] 'tethered' to PSI were shown to be active in light-induced H_2 production. The [NiFe]-hydrogenase/PSI complex constitutes the highest known rate of *in vivo* light-driven H_2 production [76, 77]. The electron supply was a gold electrode in the [NiFe]-system and an electron donor such as cytochrome in the [FeFe]-system. However, if electrons were to be supplied by photosystem II, the [NiFe]-hydrogenase system is challenged by its low inherent H_2 production capacity, and the [FeFe]-hydrogenase system would suffer from its high sensitivity to O_2 [76].

The systems described above illustrate two important issues in employing hydrogenases for technological H_2 production: O_2 sensitivity and 'catalytic bias'. The latter term refers to the inherent ability of the enzyme to catalyse H_2 oxidation over proton reduction; [FeFe]-hydrogenases are generally classified as H_2 producers while [NiFe]- and [NiFeSe]-hydrogenases are mainly biased towards H_2 oxidation. With the goal of exploiting hydrogenases for H_2 production *in air*, it is unfortunate that most hydrogenases, in particular the [FeFe]-hydrogenases, are highly sensitive to O_2. Some H_2-sensing regulatory [NiFe]-hydrogenases appear to be unaffected by O_2, but their catalytic activity is two orders of magnitude lower than that of the membrane-bound respiratory [NiFe]-hydrogenases [76]. The O_2-coping strategy of regulatory enzymes has been shown to lie in their ability to limit the access of O_2 to the active site through a 'gate' of bulky amino acid residues [80, 81]. A growing number of the more active respiratory [NiFe]-hydrogenases have been

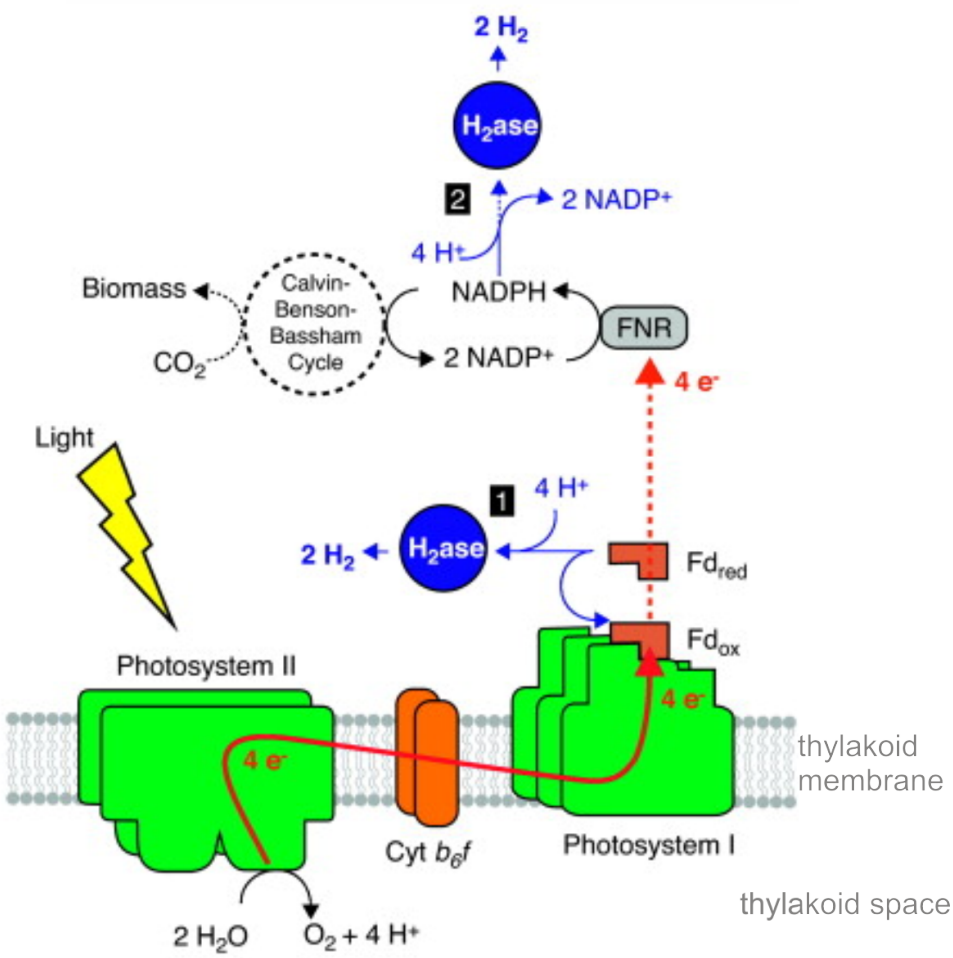


Figure 1.4: **Photosynthetic H_2 production.** The light harvesting photosystem II complex splits water into O_2 and electrons, which are passed through cytochrome b_6f (Cyt b_6f) to photosystem I. This complex passes electrons to ferredoxin (Fd_{ox}), and reduced ferredoxin (Fd_{red}) donates electrons to $NADP^+$, catalysed by FNR (ferredoxin:$NADP^+$ oxidoreductase). Electrons are finally used to reduce CO_2, but under anaerobic conditions highly air-sensitive [FeFe]-hydrogenases can withdraw electrons (1) and under fermentative conditions cyanobacterial [NiFe]-hydrogenases use NADPH as a reductant for H_2 production (2). Reprinted from ref. [76] with permission from Elsevier.

found to be able to sustain catalysis (with a bias towards H_2 oxidation) in the presence of O_2 [82–85]. The ability of these enzymes to survive O_2 does *not* appear to arise from preventing O_2 from reaching the active site [86]. Understanding the origin of O_2 tolerance in this family of respiratory [NiFe]-hydrogenases is of paramount importance in the search for an efficient H_2 producer with high turnover rates under ambient conditions.

Two crystal structures of membrane-bound O_2-tolerant [NiFe]-hydrogenases were re-

cently published from *Hydrogenovibrio marinus* [17] and from *Ralstonia eutropha* [87], the former is shown in Fig. 1.5. Overall, the structure is very similar (see Fig. 1.5, bottom) to that of other O_2-sensitive (henceforth 'standard') [NiFe]-hydrogenases, such as the *D. fructosovorans* enzyme (Fig. 1.3). The full dimer of heterodimers is shown in Fig. 1.3 because Shomura *et al.* [17] consider the dimerisation to be biologically significant (unlike in standard [NiFe]-hydrogenases). This is because the contact area between the proteomers is high, and the C-termini and distal [4Fe-4S] clusters face the same side (*in vivo* the C-terminus is in close proximity to cytochrome *b*, to which the distal cluster transfers electrons), see Fig. 1.5. However, the most notable difference is the unusual structure and coordination of the proximal cluster, which plays a crucial role in conferring O_2 tolerance on this family of enzymes [16, 88, 89] (Chapters 6 and 7).

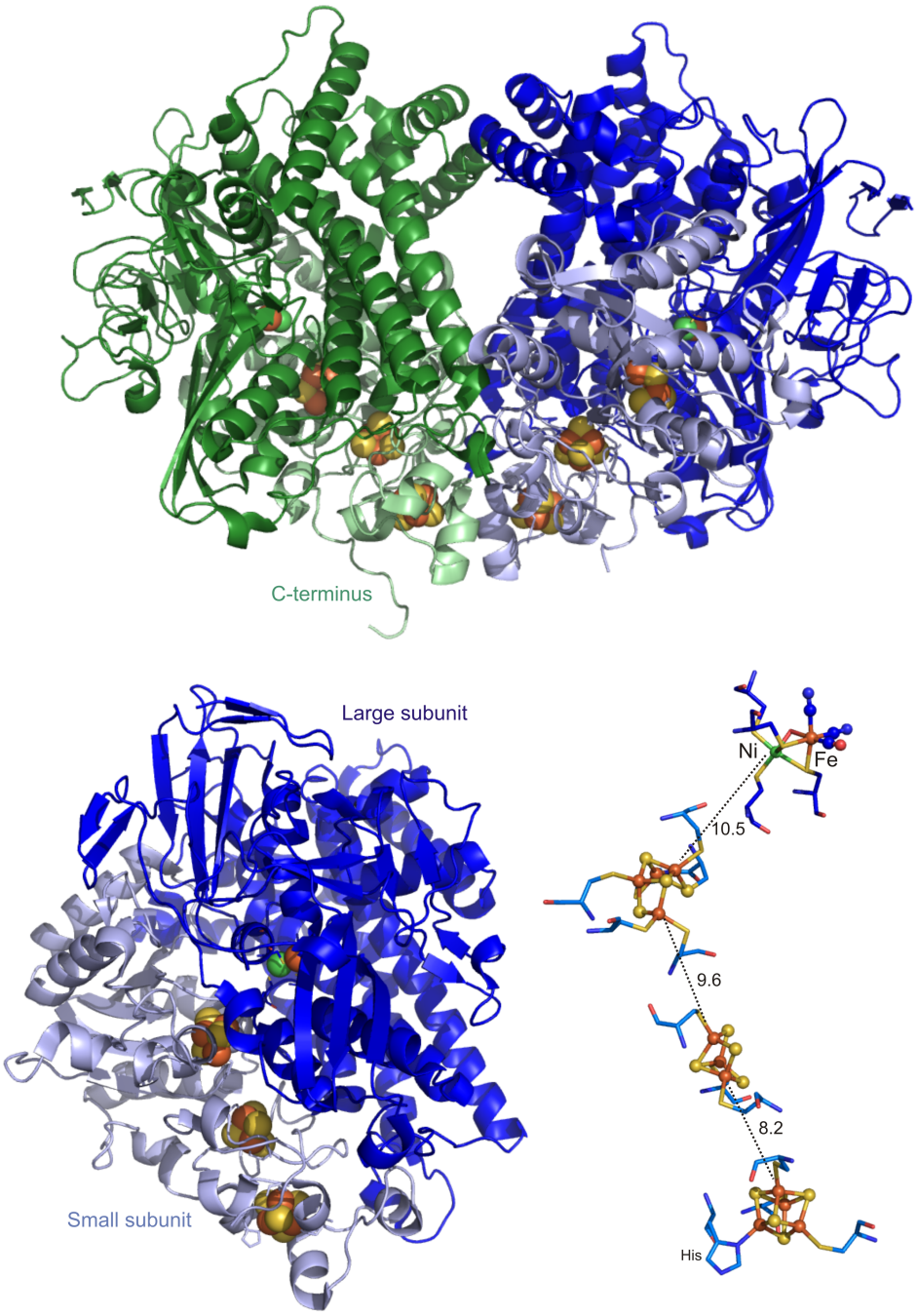


Figure 1.5: **Structure of the [NiFe]-hydrogenase from *H. marinus* (oxidised structure, 3AYZ.PDB).** (*Left*) dimer of heterodimers; (Centre) heterodimer shown in a different orientation compared to the dimer of heterodimers but in the same orientation as that from the *D. fructosovorans* enzyme (Fig. 1.3); (*Right*) Electron transfer relay, with the ligands directly coordinating the Fe-S clusters and the active site Ni and Fe atoms. Edge-to-edge distances are given in Å. Colours represent the following atoms: S yellow, N blue, Fe orange, O red, Ni green.

1.2.3 Complex I: The longest Fe-S cluster relay known

One of the most intriguing Fe-S cluster electron-transfer relays is found in complex I, the first enzyme of the respiratory chain. In eukaryotes, complex I is one of five complexes positioned in the inner mitochondrial membrane: NADH:ubiquinone oxidoreductase or NADH dehydrogenase (complex I), succinate:ubiquinone oxidoreductase or succinate dehydrogenase (complex II), ubiquinol:cytochrome c oxidoreductase or cytochrome bc1 (complex III), cytochrome c oxidase (complex IV), and ATP synthase (complex V). Electron flow through complexes I, III and IV results in the pumping of protons out of the mitochondrial matrix into the intermembrane space and ATP synthase uses the generated proton motive force to make adenosine triphosphate (ATP) [36]. The final electron acceptor, O_2, is converted to water by the last of the proton pumps, cytochrome c oxidase.

Complex I catalyses the two-electron oxidation of NADH (the reduced form of nicotinamide adenine dinucleotide) and the two-electron reduction of quinone (Q) in a thermodynamically very favourable reaction with a potential difference of 0.4 V [90]:

$$\begin{aligned} NAD^+ + 2H^+ + 2e^- &\rightleftharpoons \quad NADH + H^+ \quad E_{pH7} = -0.33\ V \\ Q + 2H^+ + 2e^- &\rightleftharpoons \qquad QH_2 \qquad\ E_{pH7} = 0.07\ V\ . \end{aligned} \tag{1.2}$$

For each two-electron oxidation of a NADH molecule, it is generally accepted that 4 H^+ are translocated from the mitochondrial matrix (or cytoplasm in bacteria) to the intermembrane space (or periplasm), and 2.5 molecules of ATP are generated [90].

The complex I enzyme from bovine heart mitochondria has a mass of approximately 980 kDa, resulting from 45 subunits [91]. This makes complex I the largest of the respiratory complexes, and one of the largest enzymes known. The central 14 subunits are present in both prokaryotic and eukaryotic complex I from different species [92]. Despite its huge size, complex I is only just visible under an electron microscope. However, the basic L-shape (in eukaryotic complex I composed of the membrane domain embedded in the inner mitochondrial membrane and a hydrophilic domain projecting into the mitochon-

drial matrix), is similar in enzymes from bacterial and mammalian species [93]. Amongst the complexes of the respiratory chain, complex I is probably the least well understood. The 3.3 Å resolution structure of the peripheral hydrophilic arm of bacterial complex I from *Thermus thermophilus* [51] revealed the arrangement of the FMN (flavin mononucleotide), the site of NADH oxidation, and the Fe-S cluster arrangement (Fig. 1.6). The [4Fe-4S] cluster in the Nqo3 subunit in *T. thermophilus* (indicated with a dotted circle in Fig. 1.6) is not conserved in the enzyme from *Bos taurus*.

Electrons enter the chain at FMN, the site of NADH oxidation (see Fig. 1.7), in a reaction that proceeds *via* a hydride transfer [95], thus avoiding unstable $NAD^{\bullet}$ [90]. The reaction at the other end of the electron-transfer chain, the reduction of the electron carrier ubiquinone (or coenzyme Q10) to ubiquinol, is much less understood. Part of the difficulty lies in the extreme hydrophobicity of ubiquinone (unsurprisingly, given its location in the lipid bilayer), which precludes the possibility of studying the natural substrate with isolated complex I [96]. A possible binding site was revealed by the crystal structure and is indicated in Fig. 1.6. It is interesting to note that parts of what is thought to be the quinone-reducing catalytic core (the 49 kDa and PSST subunits, Fig. 1.6), are thought to have evolved from [NiFe]-hydrogenases (see Section 1.2.2) [92]. Conserved residues may participate in dynamic proton transport in both enzymes [59].

Although the mechanism of proton translocation is far from understood, important clues are provided by the crystal structures of the entire complex I, including the membrane and hydrophilic domains. This was recently solved at 4.5 Å resolution for the enzyme from the bacterium *Thermus thermophilus* [97] and at 6.3 Å resolution for the enzyme from *Yarrowia lipolytica* (an aerobic yeast) [98]. Despite resolutions far from atomic level, there is now little doubt that conformational changes play an important role in proton translocation. The model proposed by Efremov *et al.* [97] is depicted in Fig. 1.7.

Sazanov and co-workers compared complex I to a steam-engine "where the electron transfer is used to move a piston, which then drives [...] a set of discontinuous helices"

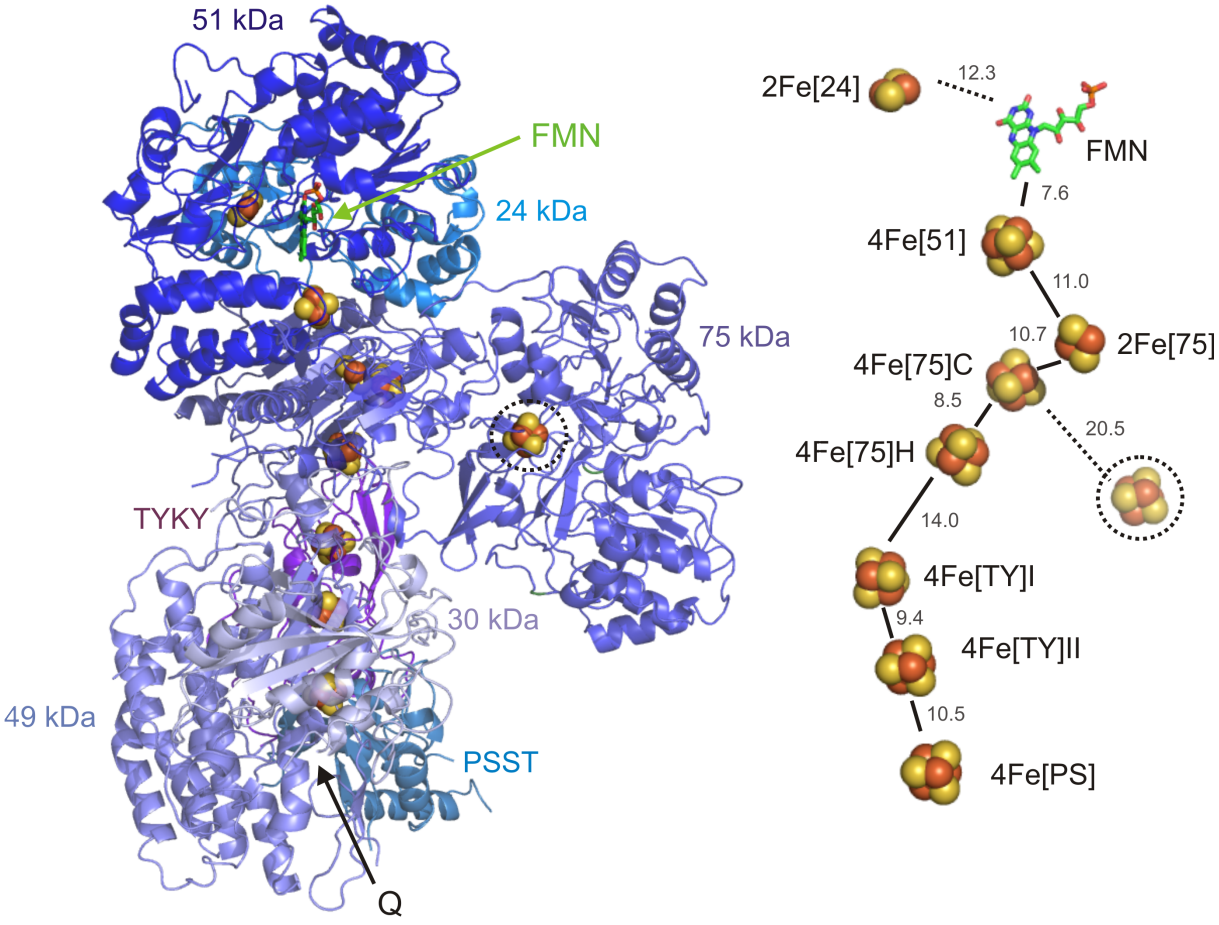


Figure 1.6: **Crystal structure of the hydrophilic domain of complex I from *Thermus thermophilus*(2FUG.PDB).** Fe-S clusters are shown as red and yellow spheres; the flavin mononucleotide (FMN) is shown with a green carbon core and a possible quinone (Q) binding site is indicated [51]. (Left) Different subunits are shown in shades of blue and are labelled according to the nomenclature for *Bos taurus* complex I [90]. The circled [4Fe-4S] cluster is only present in complex I from some bacterial species, including *T. thermophilus*; it is not present in the eukaryotic *Bos taurus* complex I. (Right) Edge-to-edge distances between the redox cofactors in Å. The dotted line indicates there is most probably no electron transfer pathway between these centres (see text). The structure of the cofactors is shown at a slightly different angle compared to the whole structure of the hydrophilic domain (left) for clarity. Clusters are labelled according to the standard nomenclature for the *B. taurus* enzyme, according to their cluster type ([2Fe-2S] or [4Fe-4S]) and their subunit (PS = PSST, TY = TYKY, 24 = 24 kDa, 75 = 75 kDa. H indicates that the cluster is ligated by one histidine residue; C indicates that the cluster is all cysteine ligated. Adapted from ref. [94].

[97]. This is illustrated in Fig. 1.7 where the piston, powered by electron transfer through a long chain of Fe-S clusters, is the amphipathic HL helix which spans almost the entire

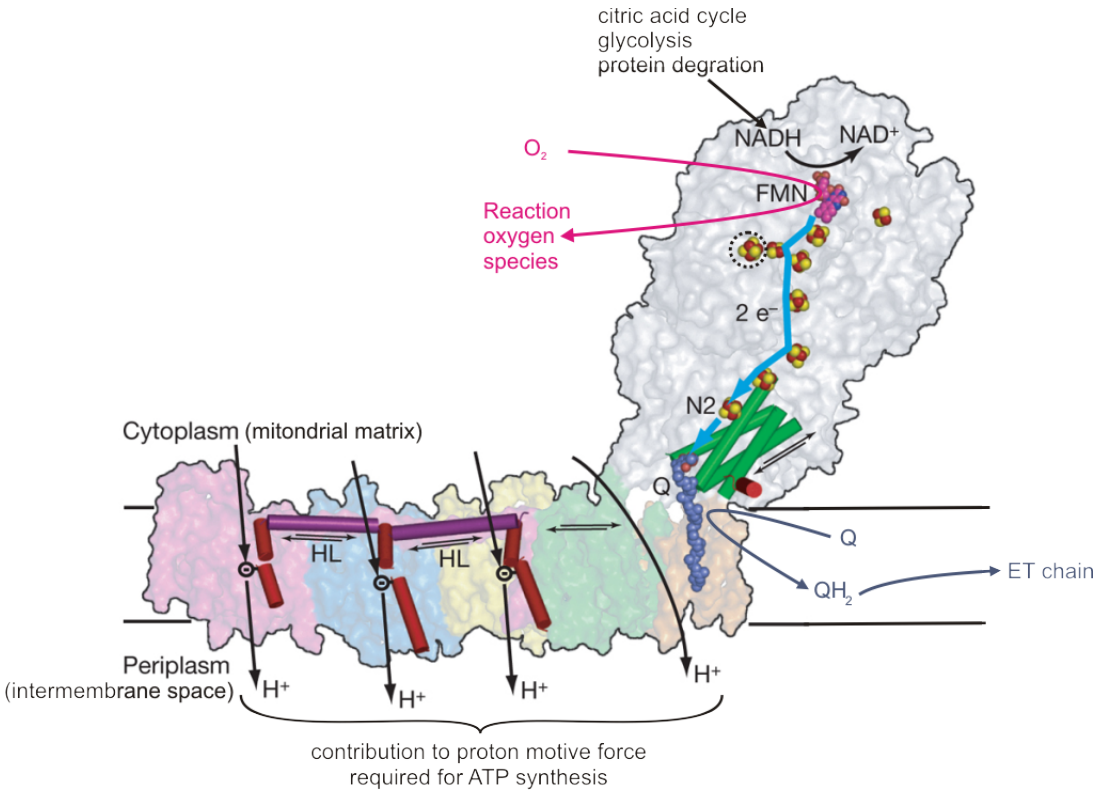


Figure 1.7: **Role of complex I and model proposed by Efremov *et al.* [97] for proton translocation based on the structure from *Thermus thermophilus*.** Figure adapted by permission from Macmillan Publishers Ltd: Nature [97], copyright 2010. NADH generated in the citric acid cycle, *via* glycolysis or protein degradation, is oxidised to NAD^+ and two electrons are transferred by the chain of Fe-S clusters to reduce ubiquinone to ubiquinol, which carries electrons to complex III and eventually the reduction of O_2 to H_2O by complex IV. Proton translocation across the membrane contributes to a proton motive force necessary for the synthesis of ATP. Reduced FMN can also reduce O_2 to reactive oxygen species such as superoxide, which are a cause of cellular oxidative stress. The Fe-S cluster surrounded with a dotted circle is not present in *Bos taurus* complex I. The hydrophilic domain is in grey (located in the cytoplasm in bacterial complex I and in the mitochondrial matrix in eukaryotic complex I). The amphipathic helix HL spans almost the entire membrane domain. Conformational changes are indicated with double arrows. ET stands for electron transfer.

membrane domain, and the resulting conformational change of the three discontinuous helices (in red) each drives one proton transfer across the membrane. The mechanism for translocation of the fourth proton appears to be less clear. Possibilities include a conformational change induced by subunits Nqo7, 10, 11 (green domain in Fig. 1.7) [97, 99]. The 'tandem' cysteines ligating cluster N2, the 'last' cluster of the chain and electron donor to quinone, have also been proposed to play a role in coupling electron and proton

transfer [95]. However, such a direct pathway is somewhat questionable given the distance of cluster N2 from the membrane ($\approx$ 30 Å in *Y. lipolytica* complex I [98]).

In addition to the remaining mysteries regarding proton translocation, the questions of how electron transfer is operated efficiently, and why the electron-transfer chain is so long, remain to be answered. One step towards this goal is to gain an understanding of the 'energy landscape' of the electron transfer relay, which consists of ferredoxin-type [2Fe-2S] and [4Fe-4S] clusters (Figs. 1.1 and 1.6). This in turn requires an unambiguous assignment of the known reduction potentials of redox cofactors to the structurally defined clusters, a significant challenge because of the great number of Fe-S centres present in this enzyme. This challenge is addressed in Chapter 4, where our current knowledge of the Fe-S cluster relay is introduced in more detail.

Beyond intellectual curiosity, the number of human diseases associated with the malfunctioning of complex I [100, 101] also justifies the numerous studies aimed at elucidating the mechanism of this enzyme. Remarkably, mutations in one of the subunits of complex I lead to approximately 50 % of known mitochondrial disorders [92, 102]. Parkinson's disease has been associated with the production of reactive oxygen species (ROS) by complex I [103]. Because ROS damage mitochondrial DNA, they have also been associated with aging [104]. Reactive oxygen species can be produced by the reaction of molecular O_2 with the reduced FMN (see Fig. 1.7). Kussmaul *et al.* [105] have shown that in the bovine enzyme, which has high sequence identity with human enzyme [91], it is the fully reduced FMN (rather than a partially reduced flavosemiquinone) that reacts with O_2. Because the ROS generated is superoxide rather than peroxide, the fate of the second electron from reduced FMN remains unclear. One possibility is that the [2Fe-2S] cluster on the other side of the flavin relative to the other clusters (see Fig. 1.6), which does not participate in electron transfer from FMN to quinone [106, 107], accepts this electron [51, 108] thereby acting a radical buffer. However, it is also possible that this unusual cluster is simply an 'evolutionary remnant' with no particular role [90].

1.3 Structure of this thesis

In the study of Fe-S clusters, to which much of the work in this thesis is devoted, EPR spectroscopy is an indispensable tool. The increasing usefulness of this technique partially stems from the recent technological and computational advances that allow pulsed EPR to be commercially available, and thus more widely applicable. EPR is the primary technique employed in this thesis and Chapter 2 provides a theoretical foundation and introduction to the different EPR experiments used.

The preparation of adequate biological samples for EPR measurements can be a major challenge. Because of the redox activity of Fe-S clusters, as well as the [NiFe] active site in the hydrogenases studied, potential control is paramount. Chapter 3 describes the titration technique that was set up to achieve precise potential control of large quantities of hydrogenase. A single technique is seldom sufficient to answer a particular question in biology and a major limitation of EPR is that it does not give any information about the reactivity of the enzyme studied. In this respect, protein film electrochemistry (PFE) is one of the most useful techniques and its most important aspects are introduced in Chapter 3. In some cases, especially the work described in Chapter 6, PFE experiments carried by other members of Prof. Fraser Armstrong's group, Drs. Michael Lukey, Alison Parkin and Rhiannon Evans, have guided the design of my EPR experiments. Site-directed mutagenesis has also proved to be an indispensable tool, and the variants studied in this thesis were constructed by Dr. Michael Lukey and Dr. Rhiannon Evans.

In a collaborative project with the Hirst group at the Medical Research Council in Cambridge, Chapter 4 aims to resolve a long standing uncertainty over how to assign the observed Fe-S EPR signals in reduced complex I from *Bos taurus* to structurally defined clusters. This work primarily makes use of double electron-electron resonance (DEER) spectroscopy, a pulsed EPR technique which relies on dipolar interaction between paramagnetic centres.

The O_2-tolerant Hydrogenase-1 (Hyd-1) and O_2-sensitive Hydrogenase-2 (Hyd-2) from the common bacterium *Escherichia coli* are introduced in Chapter 5 and their contrasting

EPR characteristics are presented. Reduced Hyd-1 is found to exhibit unusual Ni signals from the [NiFe]-active site and by comparison with Hyd-2, hyperfine spectroscopy is employed with the aim of structurally defining the observed active-site state, which may form part of the catalytic cycle.

Chapter 6 shows that both *E. coli* Hyd-1 and *Salmonella enterica* Hyd-5 exhibit the Fe-S cluster EPR fingerprints common to O_2-tolerant [NiFe]-hydrogenases. In conjunction with site-directed mutagenesis and PFE, the origins of the usual high-potential EPR signals and their connection with O_2 tolerance are investigated. With the aid of the crystal structure of *E. coli* Hyd-1, determined in the laboratory of Professor Juan Fontecilla-Camps in Grenoble, the work in Chapter 7 aims to unravel details of the unusual coordination of the proximal cluster, to provide further understanding of how this new type of Fe-S cluster helps protect the enzyme from the detrimental effects of O_2 attack. Hyperfine sublevel-correlation spectroscopy (HYSCORE) serves as the main technique here, and investigations of different variants of *E. coli* Hyd-1 in addition to the native enzyme prove to be of great importance.

Finally, the Fe-S cluster signals exhibited by O_2-tolerant membrane-bound [NiFe]-hydrogenases at *low* potentials are investigated through a variety of EPR techniques (Chapter 8). Work in previous Chapters points towards the possibility that the reduced distal cluster does *not* contribute to these signals, contrary to the current consensus. This possibility is explored through the study of both native and variant *E. coli* Hyd-1 enzymes.

The findings of the work presented in this thesis are summarised and put into perspective in Chapter 9.

Chapter 2

EPR Theory & Methods

Several EPR textbooks were used for the introduction to EPR theory presented here [109–112]. In addition, I have found the lecture course script written by Professor Gunnar Jeschke [113] in 2007 for the introduction to EPR spectroscopy at the University of Konstanz very helpful. This script is in German and I hope that some of the material from this course which I endeavoured to integrate here will be useful to non-German speakers.

2.1 The g factor and the resonance condition

The experiment performed by Stern and Gerlach in 1922, in which an inhomogeneous magnetic field split a beam of silver atoms into two components, was the first observation of the effect of an electron spin. This observation, which was difficult to rationalise at the time, was explained by Goudsmit and Uhlenbeck by ascribing half-integral angular momentum to an intrinsic spin of the electron. The transcript of the witty and insightful lecture by Goudsmit on the discovery of the electron spin (translated by J.H. van der Waals), which he held at the 50^{th} anniversary celebration of the Dutch Physical Society in 1971, is given in reference [114].

The magnetic moment of the one unpaired electron of the silver atom cannot result from orbital angular momentum because the electron is in an s-orbital. The Stern-Gerlach experiment showed that the magnetic moment of the unpaired electron could only adopt one of two orientations; that it is quantised. Because magnetic moments result from angular momentum, the electron must have a quantised intrinsic angular momentum, called 'spin'. That is, the electron has an internal degree of freedom with the properties of angular momentum, as formulated by Dirac. For a single electron, the spin angular momentum quantum operator $\hat{\vec{S}}$ has a spin quantum number $S = 1/2$. The eigenstate with a parallel orientation of the spin relative to the magnetic field is denoted α with a magnetic quantum number $m_s = +1/2$ and the eigenstate with the antiparallel orientation is denoted β with $m_s = -1/2$. The magnetic moment the electron spin is

$$\vec{\mu}_e = -g_e \mu_B \hat{\vec{S}}. \tag{2.1}$$

The magnetic moment is therefore antiparallel to the electron spin and β is the lower energy state (the spin is antiparallel to the magnetic field but the magnetic moment is parallel to the field, see equations 2.6 and 2.10). The Bohr magneton, μ_B, is given by correspondence with classical physics where a particle with a charge q, a mass m and a

magnetic moment $\vec{l}$ has a magnetic moment $\vec{\mu} = q\vec{l}/(2m)$. Hence

$$\mu_B = \frac{e\hbar}{2m_e}, \tag{2.2}$$

where e is the elemental charge, $\hbar = h/2\pi$ and m_e is the mass of the electron. However, the correspondence principle does not apply entirely to the electron because $g \approx 2$. This g value is predicted by Dirac's quantum theory; it cannot only be measured with great accuracy but is also predicted with great accuracy by quantum electrodynamics ($g_e = 2.0023193043737$).

Similarly, the nuclear magnetic moment can be written as

$$\vec{\mu}_N = g_N \mu_N \vec{\hat{I}}, \tag{2.3}$$

where $\vec{\hat{I}}$ is the angular momentum operator and μ_N is the nuclear magneton

$$\mu_N = \frac{e_p\hbar}{2m_p}. \tag{2.4}$$

The proton charge and mass are e_p and m_p, respectively, and g_N is the nuclear g value which is characteristic of a particular isotope. Usually, the nuclear magnetogyric ratio γ_N is used, and equation 2.3 becomes

$$\vec{\mu}_N = \gamma_N \vec{\hat{I}}. \tag{2.5}$$

The greater sensitivity of EPR compared to NMR spectroscopy results from μ_B being much greater than μ_N, owing to the much smaller mass of the electron compared to the proton. Note that for an $I = 1/2$ nucleus with positive γ_N (e.g. a proton), α is the lowest energy state (both the magnetic moment and the spin are parallel to the applied field).

Classically, the energy of a magnetic moment $\vec{\mu}$ in a field $\vec{B}$ is

$$E = -\vec{\mu}^T \vec{B}. \tag{2.6}$$

For a quantum mechanical system, the Hamiltonian for a free electron in a magnetic field $\vec{B}$ is given by

$$\mathcal{H} = g_e \mu_B \vec{B}^T \vec{\hat{S}} \tag{2.7}$$

where the spin operator vector $\vec{\hat{S}}^T = [\hat{S}_x, \hat{S}_y, \hat{S}_z]$, with

$$\hat{S}_x = \frac{1}{2}\begin{pmatrix} 0 & 1 \\ 1 & 0 \end{pmatrix}, \quad \hat{S}_y = \frac{1}{2i}\begin{pmatrix} 0 & 1 \\ -1 & 0 \end{pmatrix}, \quad \hat{S}_z = \frac{1}{2}\begin{pmatrix} 1 & 0 \\ 0 & -1 \end{pmatrix}. \tag{2.8}$$

If the magnetic field is in the z-direction, equation 2.7 simplifies to

$$\mathcal{H} = g_e \mu_B B_0 \hat{S}_z \tag{2.9}$$

where B_0 is the magnitude of $\vec{B}$. The eigenvalues of the Hamiltonian are

$$E = g_e \mu_B B_0 m_s. \tag{2.10}$$

Since $m_s = \pm\ 1/2$, the energy difference between to two spin states α and β in a static magnetic field is

$$\Delta E = g_e \mu_B B_0. \tag{2.11}$$

Through the Bohr frequency condition ($\Delta E = h\nu$)

$$h\nu = g_e \mu_B B_0, \tag{2.12}$$

yielding the Larmor frequency ω_0 (in angular momentum units)

$$\omega_0 = \frac{g_e \mu_B B_0}{\hbar}. \tag{2.13}$$

The energy difference ΔE, or Zeeman splitting, between the α and β eigenstates of a free electron is therefore determined by the strength of the applied magnetic field, B_0

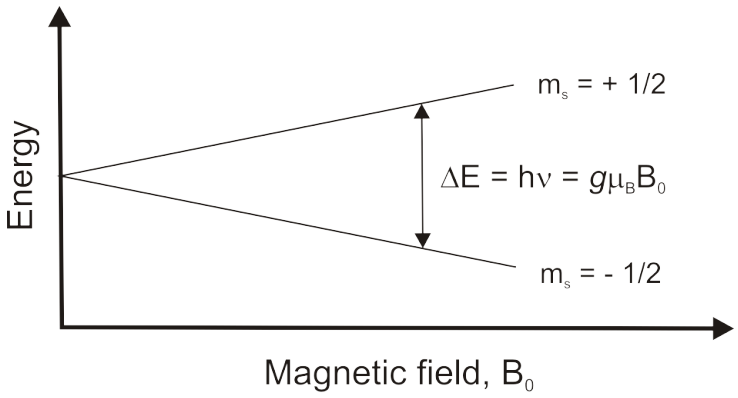


Figure 2.1: **Energies of the spin states of an electron in a magnetic field.** When the resonance condition is fulfilled, an EPR allowed transition is observed.

(Fig. 2.1). For example, a magnetic field of 350 mT and $g = 2$ corresponds to $\nu = 9.8$ GHz (in the laboratory, frequencies rather than angular frequencies are used) − this is a typical so-called X-band frequency. Larger magnetic fields can be achieved with superconducting magnets; a 3.5 T field corresponds to a frequency of ≈ 98 GHz (W-band frequency). In EPR spectroscopy, magnetic transitions can therefore be induced with microwaves (as opposed to radiofrequencies in the MHz range used in NMR spectroscopy).

EPR spectra are usually recorded from macroscopic samples rather than individual spins. Classically, the magnetised sample (induced by the static B_0 field applied along the z axis in the laboratory frame) interacts with the applied magnetic field (B_1) of the microwave radiation. The induced equilibrium magnetisation of the sample, which is proportional to the sum of the magnetic moments of the individual spins, is determined by the Boltzmann distribution; only the difference in population of the α and β states contributes to the net magnetisation. When the net magnetisation vector is parallel with B_0 along the z axis (as is the case in thermal equilibrium), the magnetisation is time-independent. However, if the magnetisation is diverged from the z direction, it precesses around the z axis and induces an oscillating magnetic field that can be detected. This precession frequency is the Larmor frequency given by equation 2.13. In an EPR experiment, the diversion of the magnetisation from the z axis is usually achieved by applying a linearly polarised oscillating field (microwave radiation) along, for instance,

the x axis. When the applied microwave frequency is equal to the Larmor frequency (the microwave radiation is said to be 'resonant'), the magnetisation vector precesses around the x axis at a frequency ω_1 (in the rotating frame, which rotates anticlockwise with the microwave frequency)[1]:

$$\omega_1 = \frac{g_x \mu_B B_1}{\hbar}. \tag{2.14}$$

When $\omega_{mw} \neq \omega_0$, the resonance offset Ω_S of the electron spin S is given by

$$\Omega_S = \omega_0 - \omega_{mw} \tag{2.15}$$

and the magnetisation vector precesses both with frequency Ω_S around the z axis and with frequency ω_1 around the x axis. It is itself a precession, with a nutation frequency ω_{nut}

$$\omega_{nut} = \sqrt{\Omega_S^2 + \omega_1^2} \tag{2.16}$$

about an axis defined by the angle θ (see Fig. 2.2)

$$\theta = arctan\left(\frac{\omega_1}{\Omega_S}\right). \tag{2.17}$$

When the resonance offset is very large ($\Omega_S >> \omega_1$) the magnetisation vector is not significantly diverged from the thermal equilibrium situation, but when $\Omega_S = 0$, $\theta = 90°$ and $\omega_{nut} = \omega_1$.

2.2 The g matrix and g anisotropy

The value of g deviates from the free electron value g_e because of spin-orbit coupling. Normally the orbital angular momentum vanishes in the ground state and mixing of orbital angular momentum from excited states into the ground state therefore contributes to the spin-orbit coupling. The extent of spin-orbit coupling depends on the molecule.

[1] Descriptions for the need (and convenience) of the rotating frame are given elsewhere, see for example refs. [113] and [115].

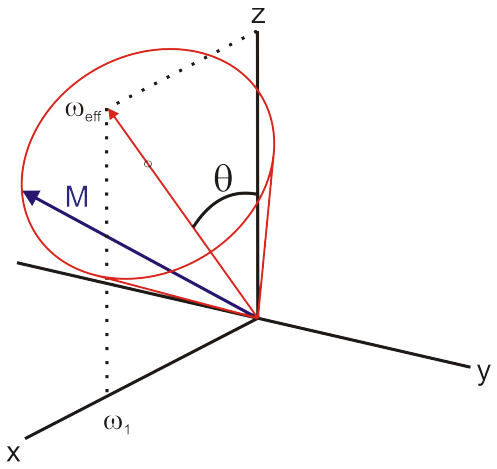


Figure 2.2: **Nutation of the magnetisation vector M about the effective magnetic field.** Figure reproduced from ref. [113].

The information g can give on the surrounding structure of the unpaired electron is partly what makes EPR spectroscopy a useful technique. The anisotropy of the interaction of the spin with the magnetic field (*i.e.* the orientation dependence of the spin in the magnetic field) is reflected in the **g** matrix

$$\mathbf{g} = \begin{pmatrix} g_{xx} & g_{xy} & g_{xz} \\ g_{yx} & g_{yy} & g_{yz} \\ g_{zx} & g_{zy} & g_{zz} \end{pmatrix}. \tag{2.18}$$

In the eigenframe of **g** (or principal axes system), **g** only contains diagonal elements

$$\mathbf{g}^{(E)} = \begin{pmatrix} g_x & 0 & 0 \\ 0 & g_y & 0 \\ 0 & 0 & g_z \end{pmatrix} \tag{2.19}$$

where the g values each correspond to the three mutually perpendicular axes of the molecule under investigation. The superscript E denotes that the g matrix has this form in the eigenframe. The orientation of the molecule in the laboratory frame is defined by three Euler angles α, β and γ, which 'transfer' the principal axes frame to the laboratory frame (Fig. 2.3).

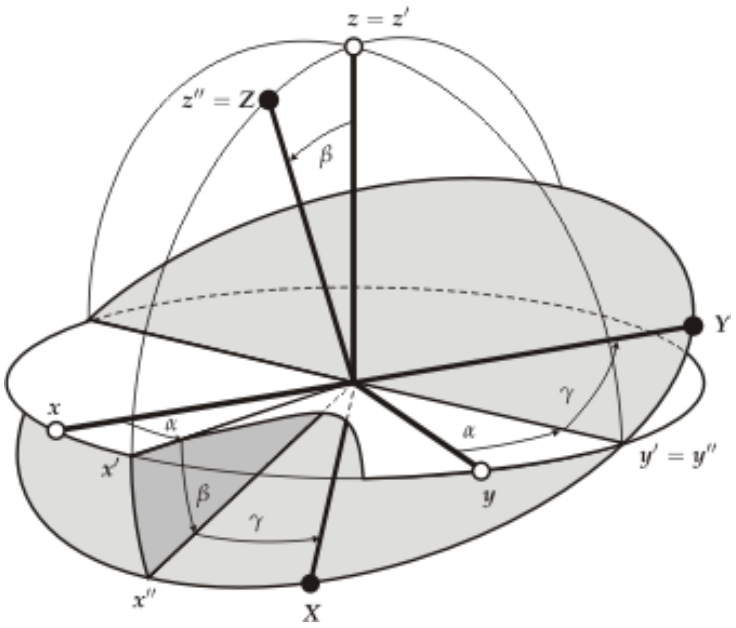


Figure 2.3: **The relative orientation between the eigenframe (x, y, z) and the laboratory frame (X, Y, Z) as defined by the Euler angles.** α rotates x, y, z counterclockwise around its z axis to give x', y', z'. β rotates x', y', z' counterclockwise around its y' axis to give x'', y'', z''. γ rotates x'', y'', z'' counterclockwise around its z'' axis to give the final X, Y, Z. Mathematically, the rotations are expressed through rotation matrices. In EasySpin [116], the function erot calculates rotation matrices from Euler angles and the function eulang calculates Euler angles from rotation matrices. Figure taken from ref. [117].

In the eigenframe, the effective g value is given by

$$g(\theta, \phi) = \sqrt{g_x^2 sin^2\theta cos^2\phi + g_y^2 sin^2\theta sin^2\phi + g_z^2 cos^2\theta}. \tag{2.20}$$

In solution, the anisotropy of the g value averages out in the fast isotropic tumbling limit and only the isotropic g value ($g_{iso} = (g_x + g_y + g_z)/3$) is observed. In frozen solutions (studied exclusively in this thesis), the molecules are randomly oriented with respect to the magnetic field B_0. The measured 'powder EPR spectra' are therefore a sum of the EPR spectra of each individual molecule 'on resonance' at a particular field, with a particular g value (*i.e.* giving rise to single sharp lines) - g anisotropy therefore makes the measured spectrum broad. At a particular resonance field, different numbers of molecules contribute. This distribution can be understood qualitatively by considering the number

of different orientations of a particular molecule that have the same g value. Figure 2.4 is a schematic diagram of a molecule with axial symmetry (A), for which $g_x = g_y \neq g_z$, and a molecule with rhombic symmetry (B), for which $g_x \neq g_y \neq g_z$. The length of a line from the centre of the ellipse to the surface represents a particular g value (or B_0 field and mw value) and the number of lines of the same length represents the number of orientations of the molecule contributing to the EPR intensity at the same B_0 field.

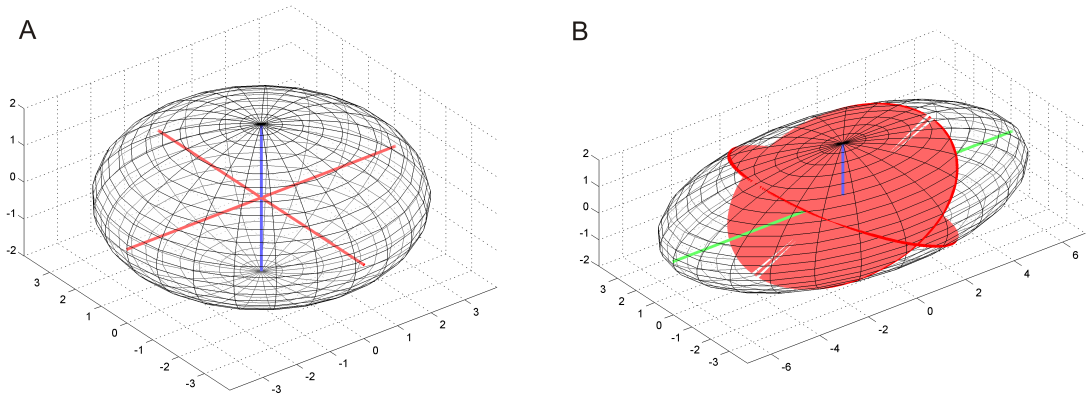


Figure 2.4: **Schematic representation of molecules with axial (A) and rhombic (B) symmetries and orientations resulting in the same g values.** Lines of the same colour are of the same length and represent orientations of the molecule which give rise to the same g values (see text).

Simulated power EPR spectra for an axial **g** matrix and a rhombic **g** matrix are given in Fig. 2.5. The absorption spectrum can be obtained with pulsed EPR methods, whereas the derivative spectrum is measured in continuous wave EPR (see below).

Alternatively, the appearance of the power spectra can be understood, and quantitatively described, by examining the dependence of the resonance field on the g-matrix orientation (equation 2.20). For an axial **g** matrix, $g_\perp = g_z$ and $g_\parallel = g_x = g_y$, and equation 2.20 becomes $g(\theta) = \sqrt{g_\perp^2 sin^2\theta + g_\parallel^2 cos^2\theta}$. Consequently B_0 only depends on θ

$$B_0(\theta) = \frac{h\nu_{mw}}{g\mu_B} = \frac{h\nu_{mw}}{\sqrt{g_\perp^2 sin^2\theta + g_\parallel^2 cos^2\theta}}. \tag{2.21}$$

Every field position in Fig. 2.5 (left) can therefore be ascribed to a particular value of θ

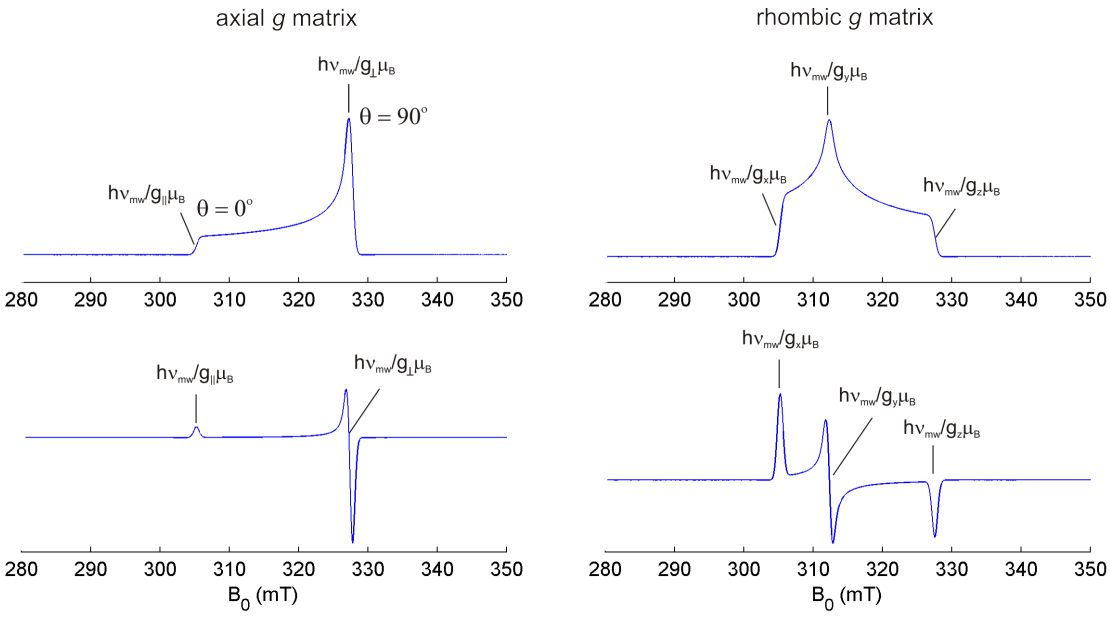


Figure 2.5: **Simulated powder EPR spectra with an axial and a rhombic g matrix.** Simulations used the program EasySpin [116], with the following parameters: mw frequency 9.4 GHz, $g_\perp = 2.05$, $g_\parallel = 2.2$ (left, axial g matrix), $g_x = 2.05$, $g_y = 2.15$, $g_z = 2.20$ (right, rhombic g matrix). Both absorption (top) and derivative (bottom) spectra are shown.

and the maximum spectral intensity corresponds to the $g_\perp$ resonance field position when $\theta = 90^o$. The spectral intensity dependence on $sin\theta$ can been visualised by inspecting the probabilities of orientations on a unit sphere in which the labelled z axis corresponds to the z axis in the eigenframe, and the orientation of the **g** matrix in the magnetic field is characterised by the polar angle θ between the z axis and $\vec{B}_0$ (Fig. 2.6).

The number of orientations at a given angle θ varies with $sin\theta$ because it corresponds to the circumference ($2\pi sin\theta$) on the unit sphere, where the magnitude of $\vec{B}_0$ is taken to be 1. For a rhombic **g** matrix, the orientations are distributed over the unit sphere in a more complicated way because g, and therefore ν_{mw}/B_0, now depends on two polar angles, θ and ϕ (where ϕ is the angle between the projection of $\vec{B}_0$ onto the xy plane of the eigenframe and the x axis of the eigenframe).

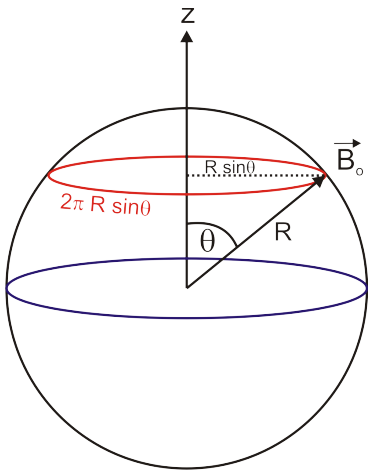


Figure 2.6: **Sphere representing the probability of molecular orientations at a particular field position.** The probability of molecular orientations with angle θ is proportional to $sin\theta$ (red circumference). The blue circumference corresponds to the angle $\theta = 90^o$ with the most contributing orientations. In the unit sphere $R = 1$. $\vec{B_0}$ is the magnetic field vector and z is in the direction of the z axis in the eigenframe. This representation applies to a **g** matrix with axial symmetry (see text). Figure reproduced from ref. [113].

2.2.1 The deviation of g from g_e

As mentioned above, the deviation of g from g_e is due to spin-orbit coupling. The **g**-matrix elements can be expressed as [109, 110]

$$g_{ij} = g_e\delta_{ij} + 2\lambda \sum_{m \neq n} \frac{\langle n|\hat{l}_i|m\rangle\langle m|\hat{l}_j|n\rangle}{E_n - E_m}. \tag{2.22}$$

The wavefunctions n and m describe the ground state occupied by the unpaired electron with corresponding energy E_n, and an excited state with corresponding energy E_m, respectively. The Kronecker δ symbol is given by $\delta_{ii} = 1$ and $\delta_{ij} = 0$; g_e therefore does not contribute to the off-diagonal elements of the g matrix. λ is the effective spin-orbit coupling constant

$$\lambda = \pm\frac{\zeta}{2S} \tag{2.23}$$

and ζ is the spin-orbit coupling constant, which is the same for orbitals of the same l and can be estimated from atomic spectra. Importantly, λ is positive when the shell is less than half-full and negative when it is more than half-full. For example, in Ni complexes

(which are studied in this thesis) λ is clearly negative and the g values are therefore positively shifted compared to g_e. For Ni^{3+} in a square pyramidal crystal field, such as in the Ni-C state of [NiFe]-hydrogenases [118], the singly occupied molecular orbital (SOMO) is d_z^2. In equation 2.22 n then denotes the d_z^2 orbital and m denotes any of the other d-orbitals. Although there is no simple correlation, the generally increasing value of λ with increasing mass [113] means that the **g** anisotropy in transition metal ions is much larger than that in organic radicals, *i.e.* the spin-orbit coupling is larger in transition metal ions because excited states are closer to the ground state. The dependence of g on the ligand coordination and environment of the metal ion means that the observed g values in an EPR spectrum can often be used as fingerprints to identify an unknown paramagnetic centre.

2.3 The Spin Hamiltonian

Besides the magnetic field, electron spins can also interact with each other and with nuclear spins. Such interactions lead to additional spectroscopic transitions because the energy levels are split further. The spin Hamiltonian operator[2] was developed by Abragam and Pryce [119] and describes how the energy level positions depend on these interactions:

$$\mathcal{H}_0 = \mathcal{H}_{EZ} + \mathcal{H}_{NZ} + \mathcal{H}_{HF} + \mathcal{H}_{NQ} + \mathcal{H}_{ZFS} + \mathcal{H}_{NN} \tag{2.24}$$

where $\mathcal{H}_{EZ}$ and $\mathcal{H}_{NZ}$ are the electron and nuclear Zeeman interactions, $\mathcal{H}_{HF}$ is the hyperfine interaction, $\mathcal{H}_{NQ}$ is the nuclear quadrupole interaction (for spins with nuclear quantum numbers $I > 1/2$), $\mathcal{H}_{ZFS}$ is the zero-field splitting, and $\mathcal{H}_{NN}$ is the spin-spin interaction between a pair of nuclear spins. The latter interaction is too small to be resolved in EPR spectra of frozen solutions and will not be discussed further here. The other terms are briefly introduced below [111]. All energies are given angular frequency

[2]The spin Hamiltonian is so-called because it only takes into account the degrees of freedom of the electron spin, rather than those of the entire system.

units.

2.3.1 Electron Zeeman interaction

The electron Zeeman interaction was already discussed above and Fig. 2.1 exemplified this interaction for a spin system with $S = 1/2$. In summary

$$\mathcal{H}_{EZ} = \frac{\mu_B}{\hbar} \vec{B}_0^T \mathbf{g} \vec{\hat{S}}. \tag{2.25}$$

To account for orbital angular momentum from excited states mixing into the ground state, this Hamiltonian becomes

$$\mathcal{H}_Z + \mathcal{H}_{LS} = \frac{\mu_B}{\hbar} \vec{B}_0^T (\vec{\hat{L}} + g_e \vec{\hat{S}}) + \lambda \vec{\hat{L}}^T \vec{\hat{S}}. \tag{2.26}$$

where $\mathcal{H}_Z$ is the electron Zeeman term including orbital angular momentum ($\vec{\hat{L}}$) and $\mathcal{H}_{LS}$ is the spin-orbit interaction. Other terms in equations 2.25 and 2.26 have been defined previously (see equations 2.2, 2.8, 2.18, 2.23).

2.3.2 Nuclear Zeeman interaction

Analogous to the electron Zeeman interaction, the nuclear Zeeman interaction describes the coupling of a nuclear spin I to B_0

$$\mathcal{H}_{NZ} = -\frac{g_N \mu_N}{\hbar} \vec{B}_0^T \vec{\hat{I}} = -\frac{\gamma_N}{\hbar} \vec{B}_0^T \vec{\hat{I}} \tag{2.27}$$

where g_N (see equation 2.3) and the spin quantum number I are inherent properties of a nucleus. For the proton, $g_N = 5.58$ so that the nuclear Zeeman interaction is only 1/658 of the electron Zeeman interaction. Because absolute values of g_N are even smaller for other nuclei, the nuclear Zeeman interaction is then even less.

2.3.3 Hyperfine interactions

For an electron spin couped to a single nuclear spin, the Hamiltonian is given by

$$\mathcal{H}_{HF} = \vec{\hat{S}}^T \mathbf{A} \vec{\hat{I}} \tag{2.28}$$

where $\mathbf{A}$ is the hyperfine tensor. The Hamiltonian can also be written as the sum of the isotropic Fermi contact interaction $\mathcal{H}_F$ and the anisotropic electron-nuclear dipole-dipole coupling $\mathcal{H}_{DD}$

$$\mathcal{H}_F + \mathcal{H}_{DD} = a_{iso} \vec{\hat{S}}^T \vec{\hat{I}} + \vec{\hat{S}}^T \mathbf{T} \vec{\hat{I}}. \tag{2.29}$$

The hyperfine interaction is therefore independent of the applied magnetic field B_0. a_{iso} is the isotropic hyperfine coupling constant

$$\begin{aligned} a_{iso} &= \frac{2\mu_0}{3\hbar} g_e \mu_B \gamma_N |\psi_0(0)|^2 \\ &= \frac{Tr(\mathbf{A})}{3} \end{aligned} \tag{2.30}$$

and $|\psi_0(0)|^2$ is the electron spin density at the nucleus. The finite probability of an electron being found at the nucleus thus gives rise to the Fermi contact interaction. The anisotropic part can be described by correspondence with classical mechanics if the distance r between the electron and nucleus is large compared to their size (which is not true for s orbitals)

$$\begin{aligned} \mathcal{H}_{DD} &= \frac{\mu_0}{4\pi\hbar} g_e \mu_B \gamma_N \left(\frac{3(\vec{\hat{S}}^T \vec{r})(\vec{r}^T \vec{\hat{I}})}{r^5} - \frac{\vec{\hat{S}}^T \vec{\hat{I}}}{r^3} \right) \\ &= \vec{\hat{S}}^T \mathbf{T} \vec{\hat{I}}. \end{aligned} \tag{2.31}$$

The dipolar coupling constant $\mathbf{T}$ is a traceless symmetric tensor with elements

$$T_{ij} = \frac{\mu_0}{4\pi\hbar} g_e \mu_B \gamma_N \left\langle \psi_0 \left| \frac{3 r_i r_j - \delta_{ij} r^2}{r^5} \right| \psi_0 \right\rangle \tag{2.32}$$

provided that the electron-nuclear dipole-dipole coupling is spin-only.

2.3.4 Nuclear quadrupole interactions

Nuclei with $I > 1/2$ have a non-spherical charge distribution, described by the nuclear electrical quadrupole moment Q. The Hamiltonian

$$\mathcal{H}_{NQ} = \vec{\hat{I}}^T \mathbf{P} \vec{\hat{I}} \tag{2.33}$$

describes the interaction of Q with the electric field gradient caused by nearby electrons and nuclei. The nuclear quadrupole tensor $\mathbf{P}$ is traceless and in the eigenframe is given by

$$\begin{aligned} \mathcal{H}_{NQ} &= P_x \hat{I}_x^2 + P_y \hat{I}_y^2 + P_z \hat{I}_z^2 \\ &= \frac{e^2 qQ}{4I(2I-1)\hbar} \left[(3\hat{I}_z^2 - I(I+1)^2 + \eta(\hat{I}_x^2 + \hat{I}_y^2) \right] \end{aligned} \tag{2.34}$$

where eq is the electric field gradient, $\eta = (P_x - P_y)/P_z$ is the asymmetry parameter with $0 < \eta < 1$ (for rhombic symmetry $\eta = 1$ and for axial symmetry $\eta = 0$) and $|P_z| \geq |P_y| \geq |P_x|$. In the literature, the two quantities $e^2qQ/\hbar$ and η are usually provided, or the diagonal elements of $\mathbf{P}$ (in the principal axes system) are given as $[P_x, P_y, P_z] = [-K(1-\eta), -K(1+\eta), 2K]$ where $K = \frac{e^2qQ}{4I(2I-1)\hbar}$.

2.3.5 Zero-field splitting

The magnetic moments of several unpaired electrons can couple so strongly with each other that the overall spin state is best described with an effective spin $S > 1/2$. In weak ligand fields, all individual n electron spins are parallel and this high-spin state is described by $S = n/2$, for example for high-spin Fe^{3+} where $S = 5/2$. Low-spin Fe^{3+} in a strong octahedral ligand field yields an effective spin of $S = 1/2$. The interaction between two or more unpaired electrons causes energy levels with different spin quantum numbers S as well as energy levels with different magnetic quantum number m_s to split. Because this interaction is also present at zero field, it is called zero-field splitting and

the Hamiltonian in its eigenframe is given by

$$\begin{aligned}\mathcal{H}_{ZFS} &= \vec{\hat{S}}^T \mathbf{D} \vec{\hat{S}} \\ &= D_x \hat{S}_x^2 + D_y \hat{S}_y^2 + D_z \hat{S}_z^2 \\ &= D\left[(\hat{S}_z^2 - \frac{1}{3}S(S+1)\right] + E(\hat{S}_x^2 - \hat{S}_y^2) \end{aligned} \tag{2.35}$$

where the tensor $\mathbf{D}$ is traceless (*i.e.* there is no isotropic part to the zero-field splitting) and

$$\begin{aligned} D &= \frac{3}{2}D_z \\ E &= \frac{1}{2}(D_x - D_y), \end{aligned} \tag{2.36}$$

D and E are the axial and rhombic zero-field splitting parameters, so-called because for cubic symmetry $D = E = 0$; for axial symmetry $D \neq 0$ and $E = 0$ and for rhombic systems $D \neq 0$ and $E \neq 0$. The rhombicity E/D is defined such that $0 \leq E/D \leq 1/3$, where 0 represents a completely axial system and 1/3 a completely rhombic system. The zero-field splitting can be viewed as an electronic quadrupole interaction. In transition metals, its origin is mainly spin-orbit coupling (similar to the deviation of g from g_e). The allowed $|-1/2\rangle \leftrightarrow |+1/2\rangle$ transition in systems with an effective half-integer spin is to a first approximation unaffected by the zero-field splitting. Furthermore, often $D >> h\nu$ at conventional mw frequencies, so that the energy of the mw radiation is not large enough to induce transitions between different m_s manifolds and only intra-manifold transitions are observed. Such $|-m_s\rangle \leftrightarrow |+m_s\rangle$ transitions with $\Delta m_s \neq 1$ can then also be allowed. A prominent example is the high-spin $S = 5/2$ purely rhombic Fe^{3+} hexaaquo ion, which even when at very low concentration gives rise to a sharp EPR signal at $g = 4.3$. The reason is that all three effective g values of the $m_s = 3/2$ doublet are coincident at 4.29 when $E/D = 1/3$ (*i.e.* there is no anisotropy) [120]. Consequently, this '$g = 4.3$' signal is observed in many EPR spectra of biological samples [120].

Integer spin systems are usually 'EPR silent' because the large zero-field splitting means that inter-manifold transitions cannot be observed because of insufficiently high mw frequencies, and intra-manifold transitions are forbidden. Intra-manifold transitions can become allowed in rhombic systems but the energy separation between these levels is then usually too large for a transition to be induced by the mw radiation. However, at high field and high mw frequencies such transitions may be observed with EPR. Parallel mode EPR, in which mw radiation is *parallel* to the magnetic field and requires a different cavity to the standard perpendicular-mode cavity, allows observation of $\Delta m_s = 0$ transitions which tend to have a greater probability among $m_s = \pm n$ states (where n is an integer) [121].

Iron-sulfur clusters

In iron-sulfur clusters, which are extensively studied in this thesis, the individual iron ions are nominally high spin ($S = 5/2$ for Fe^{3+} and $S = 2$ for Fe^{2+}). In the reduced $[2Fe\text{-}2S]^+$ cluster, Fe^{2+} and Fe^{3+} coupled antiferromagneticaly to give an overall spin $S = 1/2$. [3Fe-4S] and [4Fe-4S] clusters often exhibit delocalised valence pairs in which two Fe ions couple ferromagnetically, and this pair is then antiferromagnetically coupled to another pair, or another Fe ion. For example, reduced $[3Fe\text{-}4S]^0$ clusters appear to be composed of a $Fe^{2.5+} - Fe^{2.5+}$ pair ($S = 9/2$) antiferromagnetically coupled to Fe^{3+} ($S = 5/2$), resulting in an effective spin $S = 2$. Similarly, a $[4Fe\text{-}4S]^{2+}$ cluster contains two delocalised $Fe^{2.5+} - Fe^{2.5+}$ pairs, whose antiferromagnetic coupling results in a total spin of $S = 0$. $[4Fe\text{-}4S]^{3+}$ and $[4Fe\text{-}4S]^+$ clusters exhibit many spin and electronic states, but it is noteworthy that the $S = 1/2$ ground state of the former is well separated from higher spin states, whereas the latter may have a $S = 1/2$, $3/2$ and $7/2$ ground state (or mixtures of these), with the excited states lying at lower energy compared to the higher oxidation counterparts [7].

2.4 Weak electron-electron interactions

Two weakly interacting unpaired electrons or group spins (as described in section 2.3.5) are characterised by their individual spin S_1 and S_2 and exchange and dipolar coupling between them:

$$\mathcal{H}_0(S_1, S_2) = \mathcal{H}_0(S_1) + \mathcal{H}_0(S_2) + \mathcal{H}_{exchange} + \mathcal{H}_{dd}. \tag{2.37}$$

The anisotropic dipolar coupling between two electron spins is analogous to that between an electron and a nuclear spin, that is, to the anisotropic part of the hyperfine interaction (section 2.3.3):

$$\begin{aligned} \mathcal{H}_{dd} &= \vec{\hat{S}}_1^T \mathbf{D} \vec{\hat{S}}_2 \\ &= \frac{\mu_0}{4\pi\hbar} g_1 g_2 \mu_B^2 \left(\frac{3(\vec{\hat{S}}_1^T \vec{r}_{12})(\vec{r}_{12}^T \vec{\hat{S}}_2)}{r_{12}^5} - \frac{\vec{\hat{S}}_1^T \vec{\hat{S}}_2}{r_{12}^3} \right) \end{aligned} \tag{2.38}$$

where $\vec{r_{12}}$ is the vector connecting the two electron spins, $r_{12} = |\vec{r_{12}}|$, and g_1 and g_2 are the g values of the two electron spins. When the two spin are parallel to each other and to the applied magnetic field, then equation 2.38 becomes

$$\mathcal{H}_{dd} = \frac{\mu_0}{4\pi\hbar} g_1 g_2 \mu_B^2 \left(\frac{1 - 3cos^2\theta}{r_{12}^3} \right) \vec{\hat{S}}_{1z}^T \vec{\hat{S}}_{2z} \tag{2.39}$$

where θ is the angle between B_0 and $\vec{r_{12}}$ (Fig. 2.7).

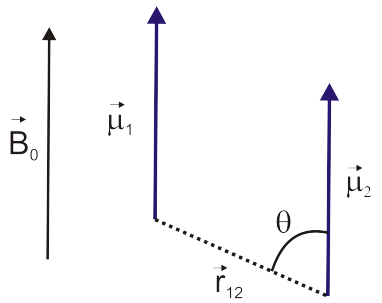


Figure 2.7: **Dipolar interaction between two spins with magnetic moments μ_1 and μ_2, oriented parallel to the applied magnetic field B_0.**

This approximation holds true when the anisotropy of **g** is small and when the electron

Zeeman interaction is much larger than the electron-electron dipolar interaction. Additionally, in equation 2.39 the spins are treated as point dipoles, which is not strictly true because spins exhibit a spatial distribution. This is a good approximation provided that the distance between the two spins is large compared to their individual spacial distribution. When a group of spins results in an overall spin ground state, such as in iron-sulfur clusters, equation 2.39 has to be modified, as discussed in Chapter 4, Section 4.2.1. Because of the $1/r^3$ dependence of the dipolar interaction, it can be used to measure the distance between spins 1 and 2 (Section 2.6.5).

When the orbitals to the two spins overlap significantly, the Heisenberg exchange interaction becomes relevant:

$$\mathcal{H}_{exchange} = \vec{\hat{S}}_1^T \mathbf{J} \vec{\hat{S}}_2 \tag{2.40}$$

where $\mathbf{J}$ contains an isotropic and an anisotropic part. The latter becomes important when spin-orbit coupling is large, but the isotropic part generally dominates, so that

$$\mathcal{H}_{exchange} = J_{iso} \vec{\hat{S}}_1^T \vec{\hat{S}}_2 \tag{2.41}$$

where

$$\begin{aligned} J_{iso} &= \frac{Tr(\mathbf{J})}{3} \\ &= -\frac{2e^2}{4\pi\hbar\epsilon_0} \left\langle \psi_1(r_1)\psi_2(r_2) \left| \frac{1}{r_{12}} \right| \psi_1(r_2)\psi_2(r_1) \right\rangle . \end{aligned} \tag{2.42}$$

ψ_1 and ψ_2 are isolated orbitals on the spins 1 and 2. Because the exchange interaction decays exponentially with r_{12} as the wavefunctions of the overlapping orbitals decay, in general at distances greater than ≈ 15 Å $J_{iso} \to 0$ and the dipole interaction will dominate the coupling between two electron spins.

A schematic energy diagram showing how two EPR lines are split into four lines through a weak isotropic exchange interaction (J) is given in Fig. 2.8.

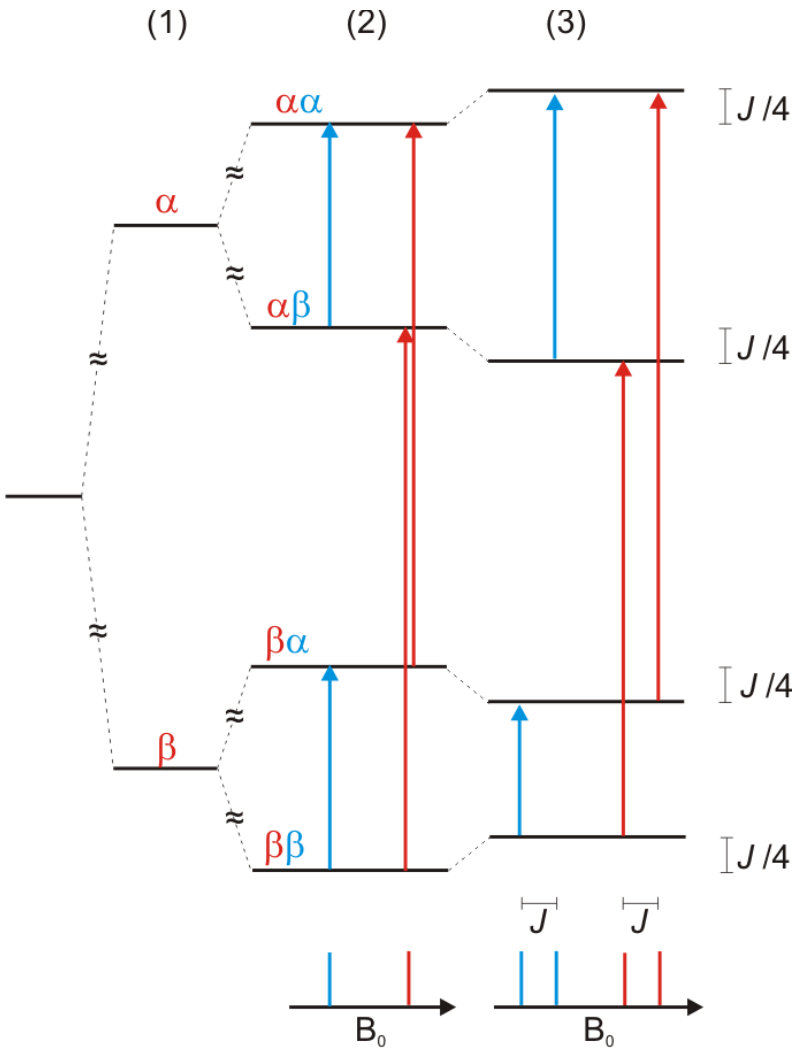


Figure 2.8: **Energy level diagram exemplifying a weak exchange interaction between two electron spins for $J > 0$.** (1) Zeeman splitting of the energy levels of an isolated spin, (2) energy levels to two isolated spins, (3) energy levels of two spins weakly coupled through an exchange interaction ($J > 0$). The expected resulting powder spectrum is shown below the energy levels diagrams. Energy level shifts due to J are greatly exaggerated.

2.5 Continuous wave EPR

The simplest EPR experiment is based on the continuous application of a constant microwave frequency (ν_{mw}) and is therefore called continuous wave EPR (CW EPR). The spectrum is obtained through measurement of the microwave absorption by the sample as a function of the applied magnetic field B_0. Unusually compared to other spectroscopic methods, the CW EPR signal is recorded as a harmonic (see Fig. 2.5, bottom row). The

reason is that the mw-diode, which detects the reflected microwaves from the resonator, is sensitive over a wide frequency range and also detects noise or interference rather than just the frequency encoding the EPR signals. To circumvent this problem, modulation coils operating with alternating current (typically at 100 KHz) are attached near the resonator which produce an additional oscillating magnetic field. The microwaves reflected from the cavity (*i.e.* the EPR signal) are then modulated at a particular frequency which is selectively filtered out by a phase sensitive detector; any other frequency signals are suppressed. The sensitivity through this modulation-amplitude detection method is thereby greatly improved. Although the intensity of the detected EPR signals increases with increasing modulation amplitude, the EPR lineshape can become distorted when the modulation amplitude is too large. To obtain 'true' lineshapes, the modulation amplitude should be less than one third of the peak-to-peak intrinsic linewidth. The sensitivity of the CW EPR experiment is further increased by using a mw cavity which stores mw energy very efficiently. This efficiency is indicated by Q, the quality factor.[3] When a sample is introduced, mw radiation that is *not* resonant with the electron spins should not be reflected and reach the detection diode; this is achieved by adjusting the mw frequency to the resonator frequency ν_R (called 'critical coupling'). The resonator bandwidth $\Delta\nu_R$ is inversely proportional to Q:

$$\Delta\nu_R = \frac{\nu_R}{Q}. \tag{2.43}$$

The sensitivity of the CW EPR measurement is directly proportional to Q and measurements are therefore usually carried out with Q as high as possible.

Besides the modulation amplitude, another important experimental factor to consider is the applied microwave power, which can be regulated by an attenuator. The EPR signal intensity grows as the square root of the power provided that the mw power is not too high. Following mw absorption, the Boltzmann distribution of the ground and excited states is maintained through depopulation of the excited states *via* spin-lattice relaxation T_1 (spontaneous emission is negligible at mw frequencies). In this mw power

[3]Strictly, this is the *loaded* quality factor.

regime the double integral of the EPR signal is proportional to the spin concentration of the sample. When higher mw power is applied, the populations of the ground and excited states equalise and no net mw radiation is absorbed. This effect is known as 'saturation' and is dependent on T_1. T_1 is inherent to the sample and is temperature dependent. When T_1 is short, as for iron-sulfur clusters (said to 'relax fast'), lower temperatures are required to study such samples compared to samples with longer T_1, such as Ni complexes. To avoid saturation, Ni species therefore usually have to be measured at high temperatures (70-80 K), whereas iron-sulfur clusters are measured at temperatures below 30-40 K.

The spin-spin relaxation time, T_2, contributes to the EPR spectra through homogeneous line broadening. If only T_2 contributes to line broadening, the peak-to-peak line width is proportional to $1/T_2$ and the lineshape is the derivative of a Lorentzian line; T_2 can then be determined from measurements of the CW EPR linewidth. Because the product T_1T_2 can be obtained from saturation measurements, T_1 can then also be determined. In practice, spectra are usually also inhomogeneously broadened, for example through unresolved hyperfine couplings, and the lineshape is then the derivative of a Gaussian line. T_1 and T_2 are then difficult to determine accurately *via* CW EPR.

2.6 Pulse EPR

The different interactions contributing to the spin Hamiltonian (see equation 2.24) are difficult to resolve with CW EPR and the separation of these interactions is only possible with pulse EPR methods. Pulse EPR is also more suited for the separate measurement of the relaxation times T_1 and T_2. However, contrary to pulse NMR spectroscopy, pulses are often not able to excite the entire spectrum of the electron spin. In order to match the resonator bandwidth to the desired excitation width of the pulses, a lower Q is necessary (achieved through lower Q cavities and 'overcoupling' for the pulse experiment). Furthermore, a high Q is also undesirable in pulse experiments because it leads to a longer 'deadtime' (t_D), the time during which no signals can be detected following a mw pulse ($t_D = 16/(\pi\Delta\nu_R)$ [122]). The requirements for a lower Q are competing effects with a *higher* Q necessary to obtain a high B_1 field and a high signal-to-noise ratio (both are proportional to $\sqrt{Q}$). The lower Q leads to lower sensitivity compared to CW EPR,[4] so that the latter still remains the method of choice for a first characterisation of a sample. Consequently, higher sample concentrations are usually necessary for pulse X-band compared to CW X-band measurements. At high frequencies, for example at W-band (95 GHz), both CW and pulse measurements are carried out in the same resonator, with high Q. A higher Q is acceptable (and desirable since S/N $\propto \sqrt{Q}$) because the resonator bandwidth remains sufficiently large, although it is smaller than at X-band, through the higher frequency ν_R (equation 2.43). The deadtime therefore also remains sufficiently low. The gain in signal-to-noise through the higher mw frequency and Q (S/N $\propto \sqrt{\nu_{mw}^3 Q}$ [122]) is somewhat offset by the much smaller sample volume required because of the higher mw frequency. Especially for broad spectra, such as Fe-S clusters, even more concentrated samples are therefore usually desirable to obtain a good S/N ratio at W-band.

[4] The lower Q is partially compensated by a larger proportionality constant c (mainly describing the resonator dimensions) of pulse resonators (S/N $= c\sqrt{Q}$).

2.6.1 The Hahn echo and the stimulated echo

The simplest echo experiment employs only two mw pulses and produces the Hahn or primary echo (Fig. 2.9, top). Before any pulse is applied, the magnetisation vector (red arrow in Fig. 2.9) is oriented along the $+z$ axis, parallel to the magnetic field B_0. The $\pi/2$ pulse is applied along the $+x$ axis in the rotating frame and causes the magnetisation vector to rotate by 90^o anticlockwise around the x axis so that it is oriented along the $-y$ axis. In the following time period τ, the 'evolution period', the magnetisation vector of individual spin packets (blue and green arrows) precesses around the z axis at different resonance offset frequencies (in Fig. 2.9 the green spin packets have higher frequency than the blue spin packets). At time τ, a π pulse applied along the $+x$ axis rotates all the magnetisation vectors of the spin packets by 180^o around the x axis, and after a time 2τ after the $\pi/2$ pulse all spin packets are once again in phase (refocused) along the $+y$ axis. The overall magnetisation has decreased because of transverse relaxation (T_2).[5]

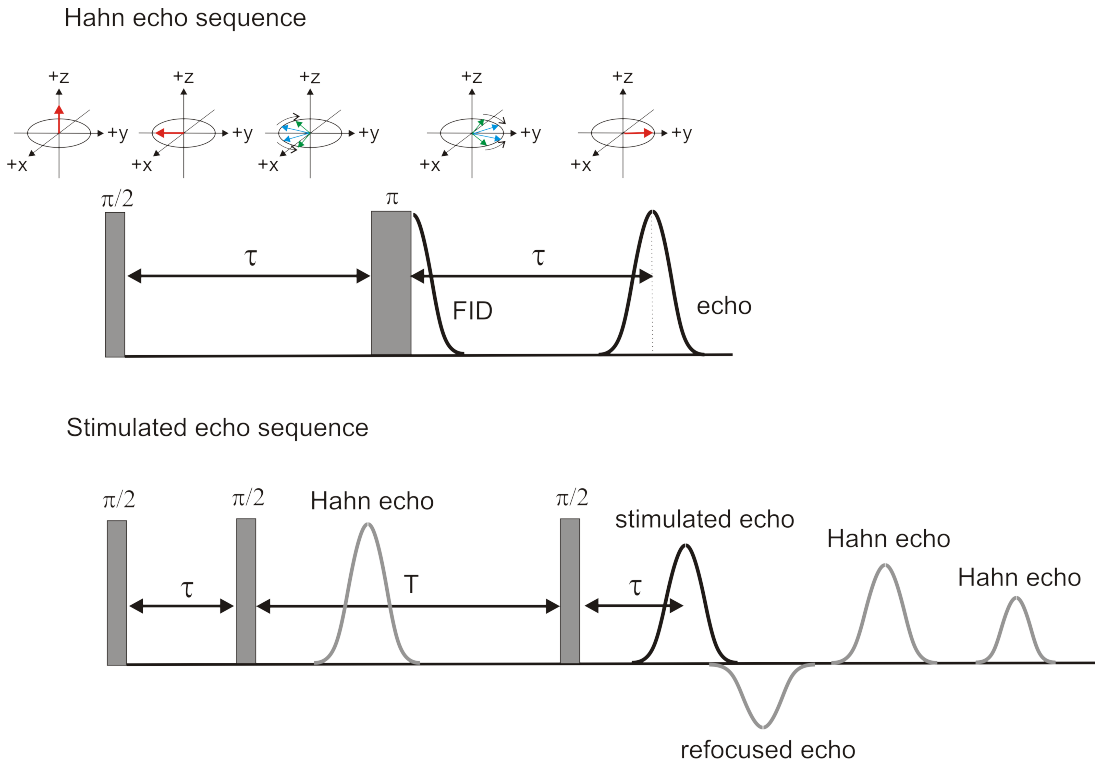


Figure 2.9: **Pulse sequences resulting in the Hahn echo and the stimulated echo.**

[5]Strictly, T_2 should be the phase-memory time, T_m, see section 2.6.6.

In principle, an FID (free induction decay) detected spectrum (the FID after the first $\pi/2$ pulse) gives similar information as a two-pulse echo-detected (Hahn echo-detected) spectrum. However, FIDs of very broad spectra decay very quickly, often within the deadtime period after the mw pulse. The primary echo sequence therefore allows the signal to be recovered − provided T_2 is not too short. A temperature at which T_2 is sufficiently long can usually be found and a two-pulse echo-detected field sweep is often equivalent to the integrated CW EPR spectrum of the same sample. Because the phase of the primary echo depends on the phase of the π (or inversion) pulse, it is possible to suppress the FID from the π pulse by applying a two-step phase cycle: subtraction of two signals obtained with $\pi/2_{(+x)}$ and $\pi/2_{(-x)}$ pulses (where the subscript indicates the direction in which the $\pi/2$ pulse is applied) removes the FID from the π pulse whose phase does not change, but the echo remains because it is of opposite sign in the two experiments. When longer pulse sequences are employed, producing numerous echoes as well as FIDs, phase cycles are mandatory to be able to observe the echo of interest exclusively.

The pulse sequence resulting in a stimulated echo (as well as three Hahn echoes and a refocused echo) is shown in Fig. 2.9. Here, the π pulse of the Hahn echo is essentially split into two $\pi/2$ pulses and this allows 'storage' of the magnetisation parallel to the z axis. This echo forms the basis of ESEEM experiments (see below) and is important because it decays with T_1, which is usually much longer than T_2, so that the echo decays more slowly. Because part of the magnetisation is stored along the z axis during the delay T, T can be adjusted according to T_1 of the sample.

2.6.2 Electron spin-echo envelope modulation (ESEEM)

The presence of nuclear spins weakly coupled to the electron spin causes the intensity of the echo to be modulated (as shown in Fig. 2.10) at the nuclear frequencies of the interacting nucleus. In the 2-pulse ESEEM experiment, τ is varied while in the 3-pulse ESEEM experiment T is varied. Similarly to the two-pulse Hahn echo sequence, the two-

pulse ESEEM experiment is often limited by the short T_2 relaxation time. Because of its dependence on T_1, the 3-pulse ESEEM experiment usually gives better resolution than the two-pulse experiment; the nuclear coherence decays with the nuclear relaxation time which is usually much longer than the T_2 (or T_m). The $\pi/2$-τ-$\pi/2$ sub-sequence is commonly used to generate nuclear coherence. However, 3-pulse ESEEM exhibits so-called blind spots at frequencies $2\pi n/\tau$ (where n=0,1,2,...), at which the modulation vanishes. Often many spectra measured with different τ values are added to avoid blind-spot artifacts.

2.6.3 4-pulse ESEEM: HYSCORE

The final sequence shown in Fig. 2.10 corresponds to the hyperfine sublevel correlation spectroscopy (HYSCORE) experiment. In this 4-pulse ESEEM experiment, the 3-pulse sequence is supplemented by a mw mixing π pulse after the nuclear coherence generator, and this pulse interchanges nuclear coherences between the electron-spin α and β manifolds (where α and β are different m_s manifolds). The free evolution times of nuclear coherence, t_1 and t_2, are varied independently. After the final $\pi/2$ pulse, nuclear coherences are transferred to electron coherence and detected as an electron-spin echo modulated by the nuclear frequencies. A 2D Fourier transformation of the time domain signal leads to a 2D frequency domain spectrum in which the nuclear frequencies of the α manifold are correlated with those of the β manifold. A schematic representation of the peaks obtained in a HYSCORE spectrum is shown in Fig 2.11. In the weak coupling case, $|A| < 2|\nu_I|$ (were A is the hyperfine coupling and ν_I is the nuclear Zeeman frequency), cross-peaks are observed in (+,+) (and (−,−)) quadrant (shown as blue dots). Additional (unwanted) peaks are also often observed due to polarisation (two-spin order) transfer to nuclear coherence and *vice versa* (axial peaks, shown as open circles), which cannot be removed by phase-cycling. The non-ideality of the mixing π pulse causes diagonal peaks (grey circles). In the strong coupling case, $|A| > 2|\nu_I|$, cross-peaks are observed in (−,+) (and (+,−)) quadrant. Intermediate couplings result in cross-peaks in both quadrants. Similar to the 3-pulse ESEEM experiment, the HYSCORE experiment exhibits blind

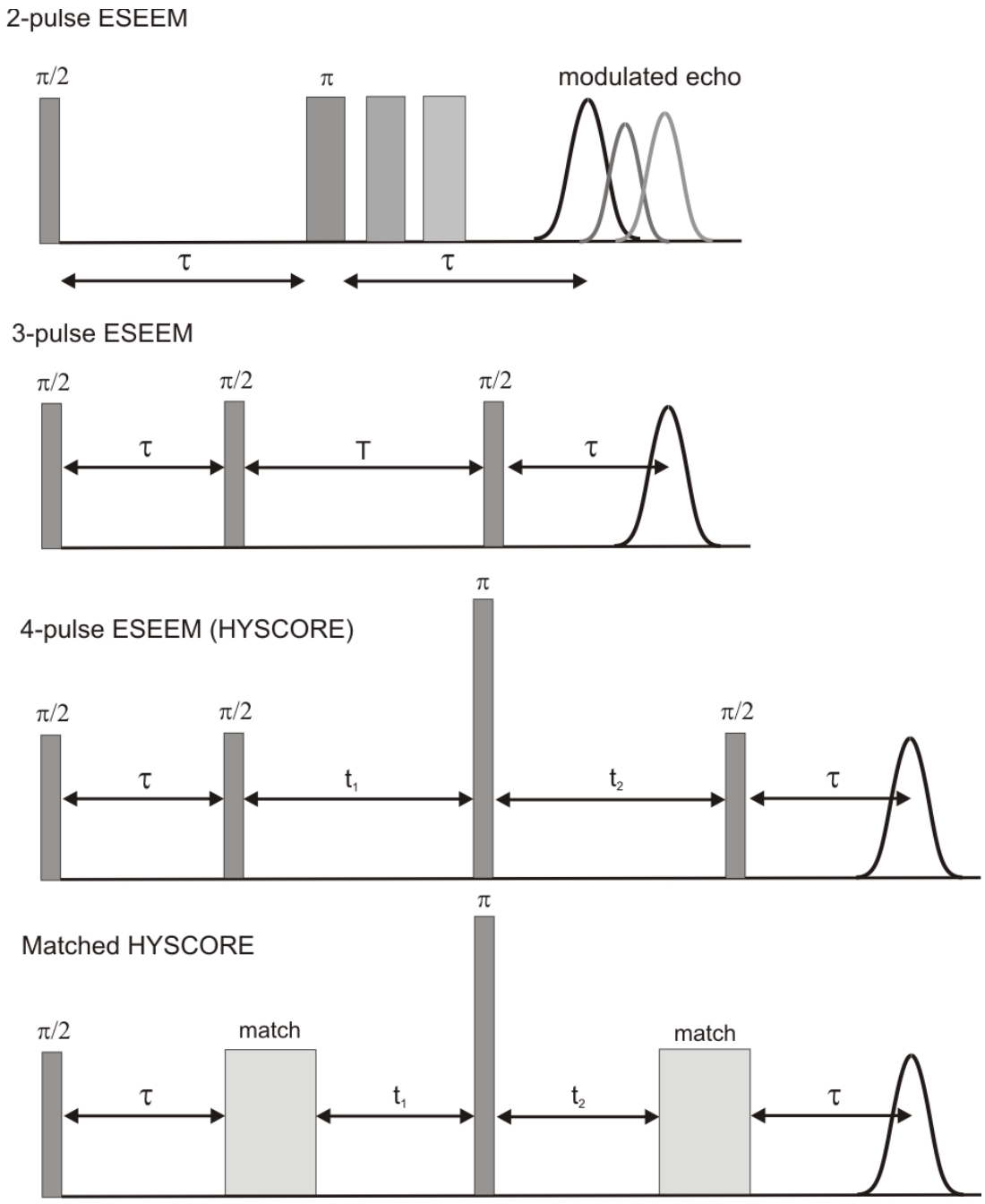


Figure 2.10: **ESEEM pulse sequences.**

spots ($A_{blind} = n/\tau$ where n = 0,1,2...).

A variation of the HYSCORE experiment which uses 'matched' pulses (Fig. 2.10, bottom) can provide a much enhanced sensitivity compared to standard HYSCORE [111, 123, 124]. In matched HYSCORE experiments the second and fourth pulses are non-selective, with a B_1 strength and length chosen to excite the forbidden transitions and

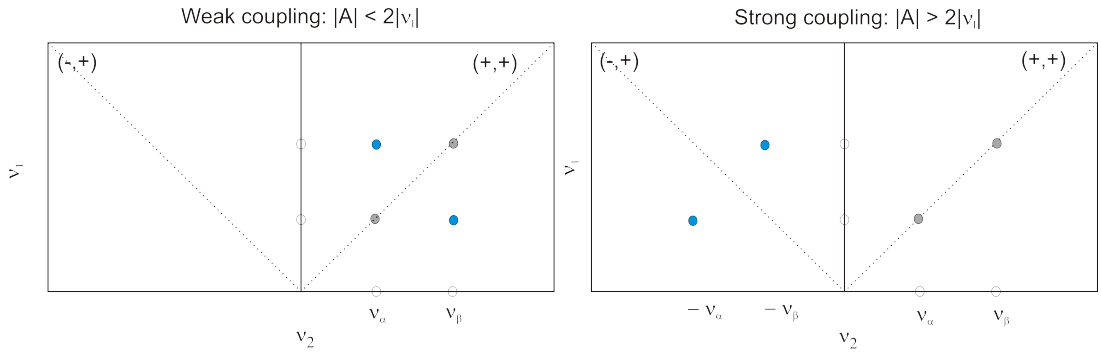


Figure 2.11: **Schematic representation of the peaks observe in HYSCORE spectra for the weak and strong coupling cases.** Blue circles represent the wanted cross-peaks; grey circles represent the diagonal peaks resulting from non-ideality of the π pulse and the open circles represent axial peaks due to nuclear coherence transfer to polarisation and *vice versa*.

thus generate nuclear coherence. In particular, it has been shown that the signal-to-noise improvement can be more than an oder of magnitude for strongly coupled nitrogens and for proton combination peaks [123].

The nuclear Zeeman and hyperfine interactions in exact cancellation

Sometimes the nuclear Zeeman and hyperfine interaction for a particular $I = 1$ nucleus (often ^{14}N) cancel each other out in one of the electron-spin manifolds, *i.e.* $|A| \approx 2|\nu_1|$. The nuclear frequencies observed in this manifold then directly correspond to the nuclear quadrupole frequencies. This situation is illustrated in the energy level diagram in Fig. 2.12.

Three diagonal peaks can then be observed in the HYSCORE spectra corresponding to the nuclear quadrupole resonance frequencies [111, 125]

$$\begin{aligned} \nu_0 &= 2K\eta \\ \nu_- &= K(3-\eta) \\ \nu_+ &= K(3+\eta) \end{aligned} \tag{2.44}$$

where $K = e^2qQ/(4h)$ and η is the asymmetry parameter (see section 2.3.4). The only

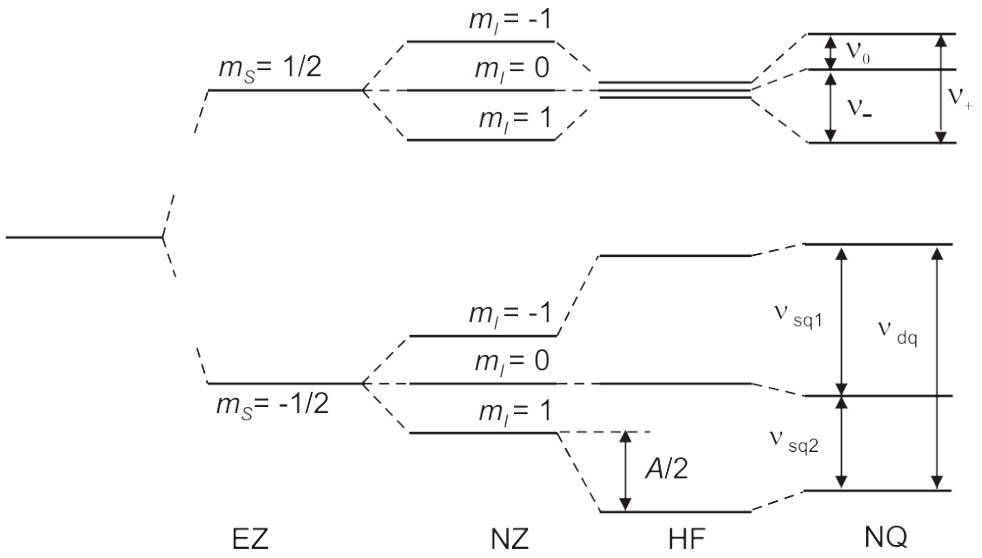


Figure 2.12: **Energy level diagram for a $S = 1/2$, $I = 1$ system when $\nu_I \approx |A|/2$ (exact cancellation condition).** ν_+, ν_0 and ν_- are given by equation 2.44. In the 'non-cancelled' manifold, dq stands for double quantum and sq for single quantum transitions.

observable sharp peak from the other manifold in which the nuclear Zeeman and hyperfine interaction are additive (the β manifold in Fig. 2.12) is often only the double quantum transition (ν_{dq}) since to first order it is free of broadening by the nuclear quadrupole interaction.

2.6.4 Electron nuclear double resonance (ENDOR)

Electron nuclear double resonance probes the nuclear transitions directly. ENDOR is not extensively used in this thesis and is only introduced very briefly. Both Davies and Mims ENDOR rely on polarisation transfer between electron and nuclear transitions. Davies ENDOR is based on selective pulses (Fig. 2.13). The first π pulse inverts the polarisation of a particular EPR transition. The population of the electron spin-echo observer transition will be affected every time the RF (radiofrequency) pulse, which is incremented over the desired frequency range, is in resonance with one of the nuclear transitions. A two-pulse Hahn echo sequence monitors the primary echo intensity.

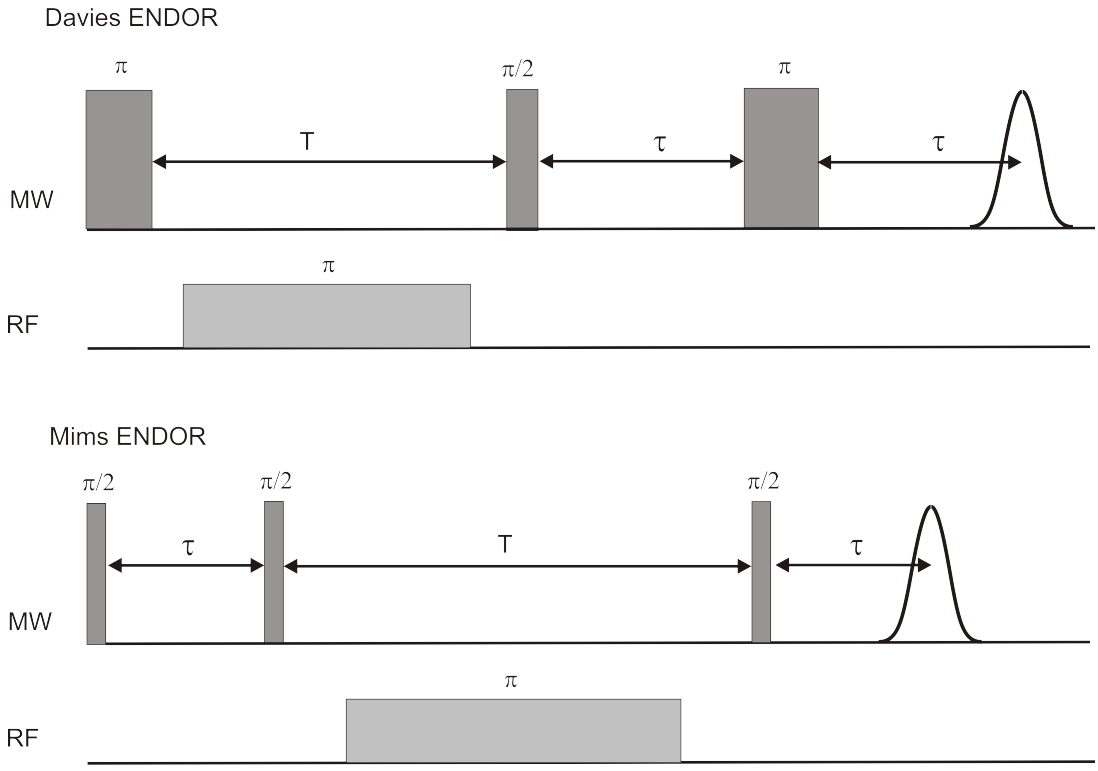


Figure 2.13: **Davies and Mims ENDOR pulse sequences.**

The Mims ENDOR experiment is based on the stimulated echo sequence with non-selective mw $\pi/2$ pulses and is often used for small hyperfine interactions [126]. The echo is monitored as a function of the (selective) radiofrequency pulse which interacts with the polarisation grid created by the $\pi/2$ - τ - $\pi/2$ sub-sequence. Polarisation is shifted by the hyperfine coupling A provided the RF pulse is on resonance. The final $\pi/2$ pulse allows detection of the EPR polarisation. Similar to the HYSCORE experiment, Mims ENDOR exhibits blind spots which now depend on the hyperfine coupling constant A. For large hyperfine couplings Davies ENDOR is therefore usually preferable.

2.6.5 Double electron-electron resonance (DEER)

Double electron-electron resonance (DEER), or PELDOR, has become the most commonly used technique for distance measurements in EPR. The DEER experiment is designed to single out the dipolar interaction from all other spin Hamiltonian parameters and this is achieved by using two different mw frequencies (ω_A and ω_B).

The 3-pulse DEER experiment was first developed by Milov *et al.* [127]. It suffers from a deadtime which can prevent full characterisation of broad distance distributions (and distorts the shape of the dipolar spectrum) [111]. The problem of the deadtime is circumvented by observing the refocused rather than the primary echo. The dead-time free 4-pulse DEER experiment (Fig. 2.14) is almost exclusively employed in this thesis. The mw detection subsequence at ω_A is applied to the detection (A) spins. In the absence of a π pulse at frequency ω_B, the primary echo at time $2\tau_1$ would just refocus at time $2(\tau_1 + \tau_2)$. However, when the pump pulse at frequency ω_B is applied to the pump (B) spins, the B spins (ideally) flip from the α to the β state or *vice versa*. This inverts the local magnetic field and changes the frequencies of the A-spins, which cannot refocus, and the echo is thus modulated. The π-pulse is shifted in time, causing a modulation of the refocused echo intensity which is inversely proportional to the cubed distance between the A- and B-spins (see equation 2.39). Measurement of the refocused-echo intensity as a function of t produces the DEER trace.

The application of DEER to distance measurements between iron-sulfur clusters is detailed in Chapter 4, Section 4.2.

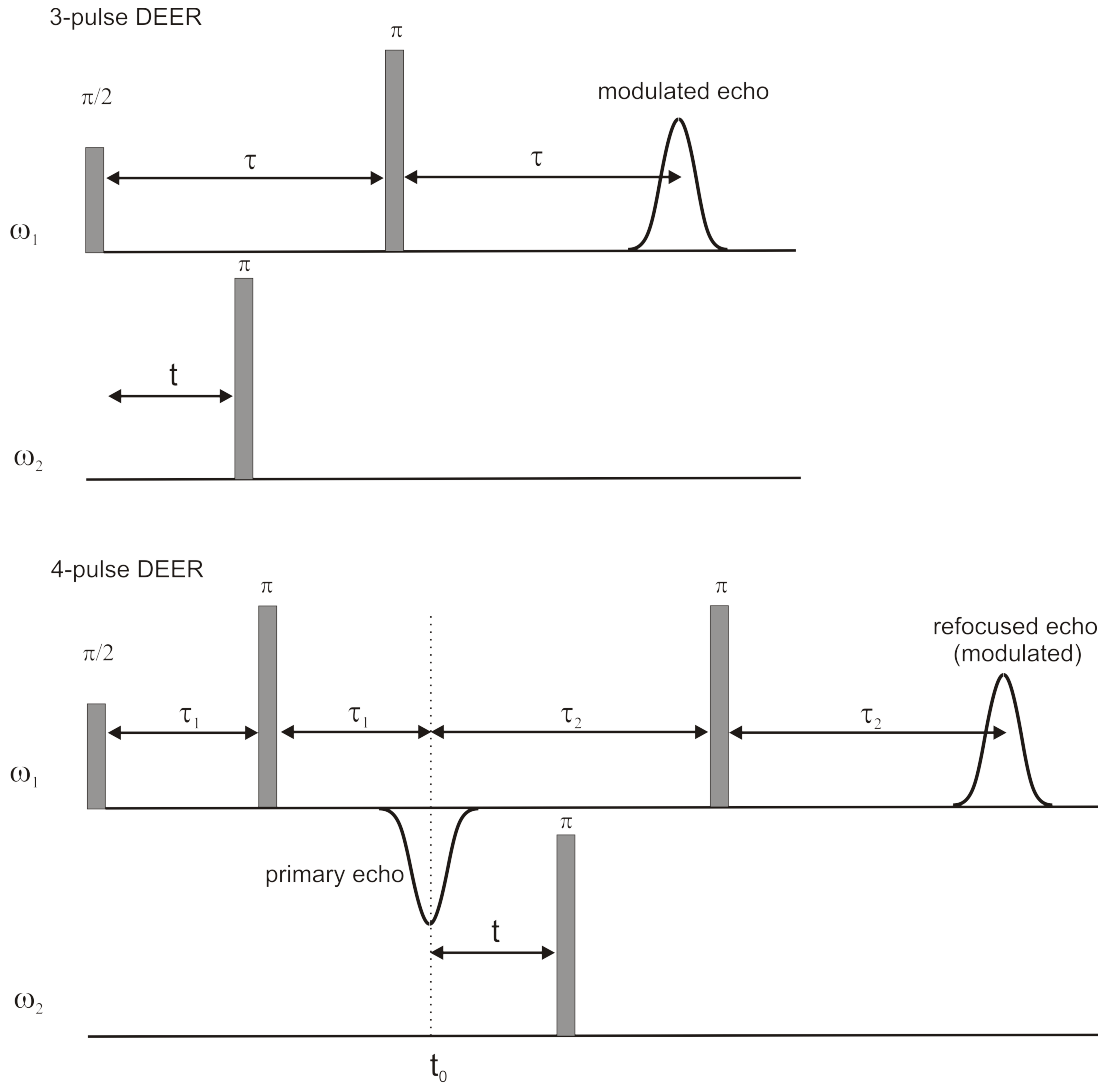


Figure 2.14: **DEER pulse sequences.** The mw detection subsequence at ω_A is applied to the detection (A) spins, and the pump pulse at frequency ω_B is applied to the pump (B) spins. In the 4-pulse sequence, the refocused echo from the detection spins at time $2\,(\tau_1+\tau_2)$ is observed as a function of time (t), where $t_0 = 2\tau_1$ is outside the spectrometer deadtime (≈ 100 ns).

2.6.6 Relaxation and saturation

When the magnetisation is rotated into the xy plane, it does not remain there forever: relaxation causes it to decay and realign with the z axis. How quickly the magnetisation returns to the z axis to re-establish thermal equilibrium is described by the spin lattice relaxation time, T_1, so called because it relies on coupling between the spin system and the surrounding lattice. The disappearance of the magnetisation in the xy plane is described

by the transverse relaxation time T_2.

T_1 can be measured by applying a π pulse (or an inversion pulse, since this pulse inverts the magnetisation), followed by a two-pulse Hahn echo sequence (*i.e.* similar to the Davies ENDOR experiment without the RF pulse, see Fig. 2.13). This is called the inversion recovery experiment because the return of the magnetisation to the z axis is monitored. After a π pulse, the magnetisation is (ideally) described by

$$M_z(t) = M_0(1 - 2e^{-(1/T_1)}) \tag{2.45}$$

or

$$M_z(t) = M_0(1 - e^{-(1/T_1)}) \tag{2.46}$$

after a $\pi/2$ pulse.

In a pulse experiment, even if T_1 is not explicitly determined through the inversion recovery experiment, the shot repetition time (SRT) − the time between individual experiments − gives an indication of order of magnitude of T_1. Conversely, it is important to adjust the SRT such that the magnetisation has time to return to the z axis between experiments − otherwise the FID or echo will decrease to an intensity that is smaller than the initial (unsaturated) intensity. 99% of the magnetisation will be recovered before the next experiment if SRT = 5 T_1 ($M_z(SRT) = M_0(1 - e^{-\frac{SRT}{T_1}})$ [122].

The transverse relaxation rate T_2 is given by

$$\frac{1}{T_2} = \frac{1}{T_2'} + \frac{1}{2T_1} \tag{2.47}$$

where T_2' is the spin-spin relaxation time, originating from a flip-flop process in which a spin changes from α to β thereby causing as second spin to change from β to α. It contributes to the faster fanning out of the magnetisation in the xy plane and the decay of the transverse magnetisation (FID) from this mechanism is generally exponential. Equation 2.47 implies that $2T_1 \geq T_2$. $1/(2T_1)$ is also called lifetime broadening. Because

relaxation processes other than T_2 (for example spectral diffusion) also contribute to the decay of the primary echo as τ is increased, an empirical parameter T_m, the phase-memory time, is convenient. It corresponds to the inverse homogeneous linewidth. Nonetheless T_m is often approximated with T_2. Inhomogeneous broadening also contributes to the decay of the magnetisation in the xy plane. It originates from different spin packets experiencing slightly different magnetic fields and results in Gaussian lineshapes.

Chapter 3

Methods

3.1 Electrochemistry of bulk enzyme solutions

One of the principal methods used in this thesis is the preparation of hydrogenase EPR samples at defined potentials. The purpose of the preparation of such samples is to 'trap' particular states of the active site or the Fe-S clusters, so that these can be examined *via* EPR, and further to determine the reduction potential (or midpoint potentials) of the EPR-active redox centres.

Setting the potential directly by means of an electrode, as in protein film electrochemistry (PFE, see Section 3.4), is not currently possible because the quantity of enzyme required for EPR is too large to enable all enzyme molecules to 'sense' the electrode potential simultaneously. An additional complication is that EPR samples would have to be frozen in the presence of the electrode to avoid potential drift between sample making and freezing. Instead, the potential of a bulk solution of enzyme is set *chemically* by means of addition of oxidising and reducing agents, and electrodes are only used to *measure* the solution potential (at zero current). The principles of this technique were previously summarised [128] and are based on the method first developed by Dutton [129]. The most important aspects, specific to the preparation of EPR samples at defined potentials ('EPR titrations'), are now explained.

A mixture of several redox-active mediators, small (often organic) molecules, covering the relevant range of reduction potentials, are used to communicate the potential of the enzyme/mediator solution to the working electrode. These mediators must be chosen carefully, such that they (1) react reversibly with both the working electrode and the enzyme's redox component, (2) do not decompose, (3) do not modify the enzyme's redox component, (4) do not interfere with the measurement (in this case EPR measurements). In theory, the redox potential of the enzyme solution should be a measurement at equilibrium. However, for hydrogenases this is sometimes not the case because it is impossible to deprive the enzyme of its substrate (H^+), and thus catalytic activity prevents equilibration at low potential. The EPR titrations in this thesis are all performed on hydrogenases that are 'biased' towards H_2 oxidation (*i.e.* they essentially produce no H_2 even at very

low potentials), so that it is possible to achieve (near) equilibrium conditions.

For a redox component in the enzyme, A, undergoing the n-electron reduction

$$A_{ox} + ne^- = A_{red} \tag{3.1}$$

the reduction potential of A, E_A is given by the Nernst equation (Appendix 10.1):

$$E_A = E_{mA} - \frac{RT}{nF}\ln\frac{[A_{red}]}{[A_{ox}]}. \tag{3.2}$$

In equation 3.2 E_{mA} is the midpoint potential of A at which $[A_{red}] = [A_{ox}]$ at the pH of the experiment (which has to be specified). Strictly, E_{mA} should be E_{0A}, which is the standard reduction potential of A at which A_{red} and A_{ox} have unit activity at pH = 0. However, these conditions are impossible to achieve in practice; pH = 0 cannot generally be used for work with biological systems and extrapolation from higher pH values is often unreliable [129].

In an EPR titration, E_A is varied by changing the ratio of $[A_{red}]/[A_{ox}]$ through the addition of oxidising or reducing agents. To determine E_{mA}, either $[A_{red}]$ or $[A_{ox}]$ are monitored. Assuming that $[A_{ox}]$ can be monitored by plotting the peak intensity of its EPR signal (*e.g.* the [3Fe-4S]$^+$ cluster EPR signal) and if $[A_{ox}]$ is taken as the fraction of oxidised A, then

$$[A_{red}] = 1 - [A_{ox}] \tag{3.3}$$

and equation 3.2 becomes

$$[A_{ox}] = \frac{1}{1 + \exp\{-\frac{nF}{RT}(E_A - E_{mA})\}}. \tag{3.4}$$

An example is given in Fig. 3.1 for the oxidation of the [3Fe-4S] cluster in the C19G/C120G variant of *E. coli* hydrogenase-1. Calculated Nernst curves with $n = 1$ and $n = 2$ show that the oxidation of this cluster is a one-electron process.

In this thesis, all EPR titrations are carried out at pH 6, but it should be noted that

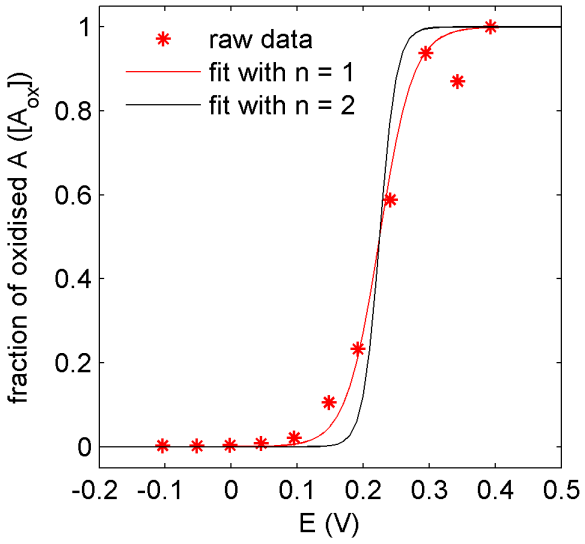


Figure 3.1: **Nernst curves for one-electron and two-electron processes and experimental data for a redox centre A with $E_{mA} = +215$ mV.** In this case A is the medial [3Fe-4S] cluster of the C19G/C120G variant of hydrogenase-1 from *E. coli*. The data were measured at pH 6.

some redox processes are pH dependent, for example the $[3Fe\text{-}4S]^{+/0}$ reduction potential. For a one-electron reduction process

$$A_{red}H = A_{ox} + e^- + H^+ \tag{3.5}$$

the Nernst equation becomes

$$\begin{aligned} E_A &= E_{mA} - \frac{RT}{F}\ln\frac{[A_{red}]}{[A_{ox}][H^+]} \\ &= E_{mA} + 2.3\frac{RT}{F}\log\frac{[A_{ox}]}{[A_{red}]} - 2.3\frac{RT}{F}\text{pH}. \end{aligned} \tag{3.6}$$

At 20°C, E_{mA} therefore decreases by 58 mV per increase in pH unit when $pK_{red} >$ pH $> pK_{ox}$ (where pK are the values for proton association to the reduced and oxidised forms of A).

Obtaining Nernst curves from EPR redox titrations

Peak intensities of spectra resulting from EPR samples poised over a range of potentials (see below) were monitored as follows: the height of a peak at a particular field position (g value) was determined by averaging the values within a small range either side of the peak, the spectrum in which this averaged height was maximal was normalised to 1 and the peak heights in other spectra were normalised accordingly. Field (g value) positions belonging to the same species, which give rise to similar peak-intensity *vs* potential plots ('Nernst curves' or 'Nernst plots'), are indicated by vertical dotted lines of the same colour. For clarity, the Nernst plot for only one of the lines of the same colour is shown. Solid lines obtained using the one-electron Nernst equation were fitted to the experimental data points by inspection. The error of the fit was also determined by eye, following inspection of several Nernst plots resulting from monitoring peak intensities at different field positions (g values) of the same species.

3.2 Preparation of EPR samples at defined potentials

For preparing EPR samples at well-defined potentials, a set-up (Fig. 3.2) was designed and implemented based on that first described by Dutton [129] for spectroelectrochemical titrations monitored *via* visible spectroscopy and later adapted for the preparation of EPR samples by Cammack [128].

The enzyme solution and redox mediators are introduced into the cell and the potential is adjusted by substoichiometric additions of a non-specific chemical reductant or oxidant. A two-electrode system is used to determine the equilibrium solution potential. The working electrode is the platinum ring of a combination electrode (Mettler Toledo, InLab Redox Micro) and the reference electrode is a micro Ag/AgCl electrode (WPI, DRIREF-2).[1] Potential is monitored using an electrochemical analyser (Autolab PG-10) controlled by NOVA software (EcoChemie) or GPES software (General Purpose Electrochemical

[1]The reference electrode of the combination electrode was not used because the electrode 'anatomy' required a large minimum volume of solution to read the potential.

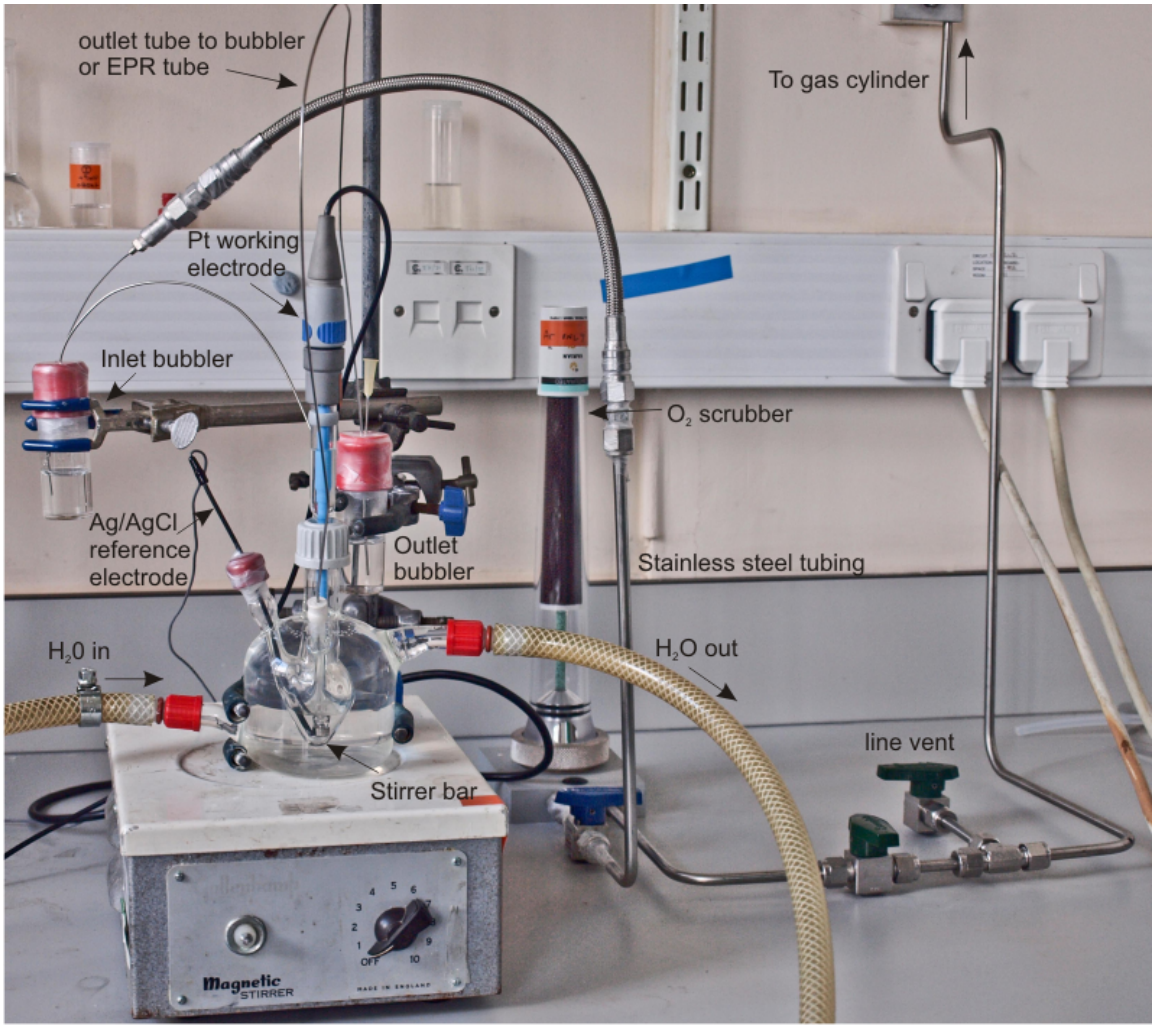


Figure 3.2: **Set-up for the preparations of EPR samples at well-defined potentials.** In the picture, the cell contains buffer. The set-up is based on that first described by Dutton [129].

System, Version 4.9). The maintenance of strictly anaerobic conditions is paramount and Ar gas (BOC gases) or H_2 gas (Premier Grade, Air Products) is passed though an O_2-scrubber (Gas Clean Filters, Varian) and a thoroughly degassed inlet bubbler solution (to wet the gas and monitor the flow rate) before entering the cell, which is kept under positive gas pressure. Stainless steel tubing and custom-made glass vessels are used for the entire set-up and rubber bungs (Subaseal & rubber septa cap 5-6 mm O.D., Sigma Aldrich) are covered with Nescofilm (Alfresa Pharma Corporation, Japan). The apparatus was tested for leakage of atmospheric O_2 into the enzyme solution: 50 μM benzyl viologen and 50 μM phenosafranine (which changes colour from blue to pink at -260 mV [128])

in pH 7 buffer (Fisher, buffer solution pH 7), were reduced with sodium dithionite until the solution just turns blue, under a flow of Ar, and the solution remained blue for 1 h, showing that no O_2 leaks into the cell. Constant mixing of the enzyme solution is ensured with a tiny stirrer bar (Fisher) and the cell is water jacketed for precise temperature control. EPR samples are withdrawn by removing the outlet tube from the outlet bubbler and transferring it to an EPR tube; after degassing the EPR tube for 2-3 minutes with the gas mixture of the cell, the other end of the outlet tube is dipped into the enzyme solution briefly, forcing enzyme solution through the outlet tube into the EPR tube, and the enzyme sample is flash-frozen in an isopropanol slush (isopropanol stirred over liquid N_2). For the preparation of W-band EPR samples, the set-up shown in Fig. 3.2 was transferred to an anaerobic glove box (Glove box technologies) containing N_2 atmosphere ($O_2 < 1$ ppm), and potential-equilibrated enzyme solution was transferred to the EPR tube using a syringe (Hamilton gas-tight 2.5 μL or 10 μL). Because of the small diameter of W-band EPR tubes (0.7 mm inner diameter), the 'shooting' method for enzyme sample withdrawal described above was not suitable. W-band tubes were taken into the glove box well in advance of the experiment to remove traces of O_2. Despite preparation of W-band samples in the glove box, the potential of W-band samples was found to be difficult to reproduce, contrary to X-band samples. In order to prevent evaporation of the enzyme solution throughout a long titration procedure (several hours), the cell solution volume was monitored over several hours under flushing with Ar with varying concentrations of glycerol. At 20 ^{o}C, the addition of 10% glycerol to the enzyme solution as well as the inlet bubbler (containing the buffer of the enzyme solution), was found to provide the necessary balance between evaporation and increased hygroscopy of the solution. A significantly higher percentage resulted in an increase of the cell volume, whereas a lower percentage resulted in reduction of the cell volume. The addition of glycerol also prevents formation of ice-crystals in the enzyme samples upon freezing.

Different glass cells are suitable for the potential adjustment of small and large enzyme solution volumes (Fig. 3.3). For titrations, typically between 5.5 and 7.5 mL were required

and cell B was used. Concentrated samples for pulse EPR measurements were made in cell A, in which a minimal volume of ≈ 150 μL is required for a potential reading.

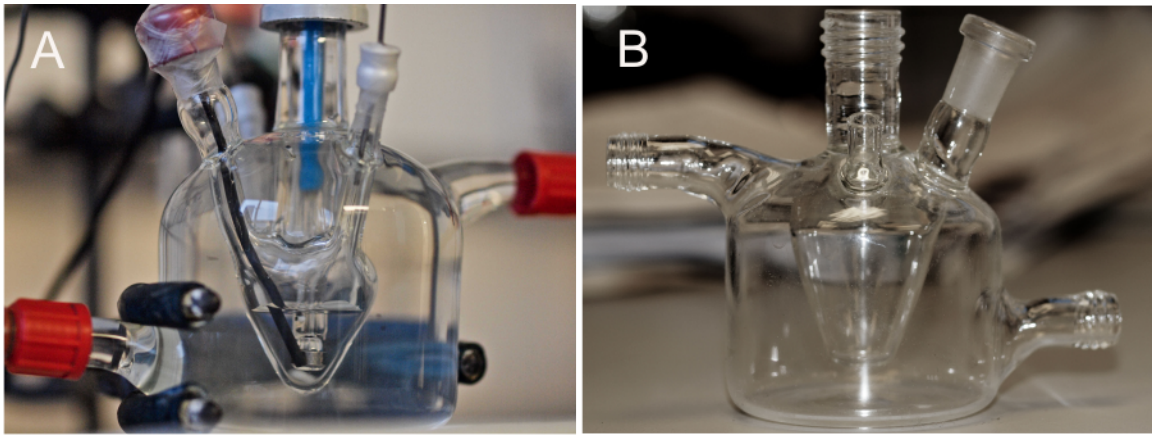


Figure 3.3: **Different glass cells used for the preparation of potential-equilibrated EPR samples.** Cell A here is shown 'in action' containing a buffer solution and was used for small volumes of enzyme solution (from a minimum of 150 μL to a maximum of ≈ 500 μL). Cell B was used for full EPR-titrations (minimum volume ≈ 350 μL, maximum volume ≈ 8 mL). These cells were made by Martyn Miles (cell A) and Terri Adams (cell B) (Inorganic Chemistry, University of Oxford).

An example of a typical chronopotentiometry trace for the titration of a variant of Hyd-1 (C19G/C120G/P242C) is given in Fig. 3.4. The withdrawal of EPR samples is marked with asterisks.

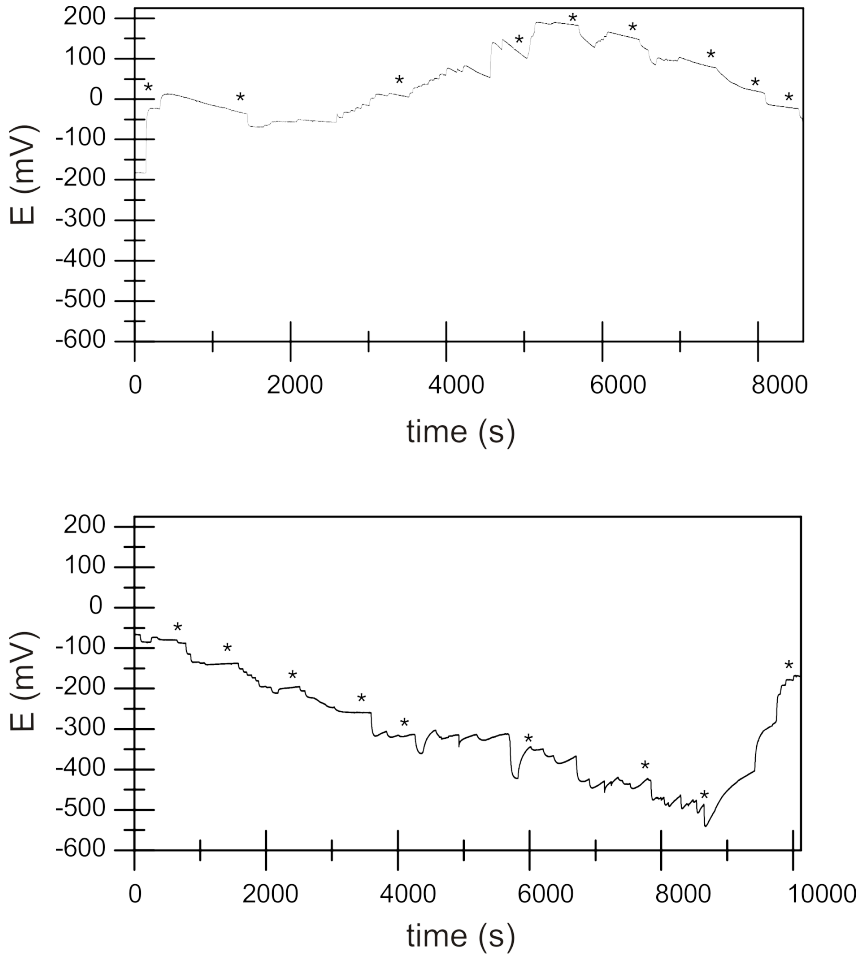


Figure 3.4: **Chronopotentiometry traces for the titration of a Hyd-1 variant (C19G/C120G/P242C).** The withdrawal of EPR samples is marked with asterisks. Mediators were added to the titration cell (Fig. 3.3 B) containing the enzyme solution prior to time 0 of the top trace. Potential steps represent the addition of 0.05 μL or 0.1 μL of 400 or 200 mM potassium ferricyanide or sodium dithionite.

Redox mediators and oxidising and reducing agents

All full titrations in this thesis were carried out in the presence of 40 μM each of methyl viologen (MV), benzyl viologen (BV), phenazine methosulfate (PMS), indigotetrasulfonate (ITS), 1,2-naphthoquinone (NQ) and 2-hydroxyl-1,4-naphthoquinone (OHNQ) (Table 3.1). The MV and BV stock solutions were prepared in deionised water; all other mediator stock solutions were prepared in dimethyl sulfoxide. Safranine and phenosafranine were judged to be unsuitable mediators because they were found to adhere to the platinum electrode. Solutions of sodium dithionite (Sigma Aldrich) in pH 8 borate buffer

Table 3.1: **Mediators used in this thesis and their reduction potentials.**

Mediator	abbreviation	E_m (mV) *vs* SHE [130, 131]
1,2-naphthoquinone	NQ	+145
Phenazinemethosulfate	PMS	+90
Indigo tetrasulfonate	ITS	−46
2-hydroxy-1,4-naphthoquinone	OH-NQ	−137
Benzyl viologen	BV	−345
Methyl viologen	MV	−430

(400 mM and 200 mM), prepared immediately prior to being required, were used as reductant. The solutions were prepared in an aerobic vessel and kept on ice during full redox titrations. Solutions of potassium ferricyanide (Sigma Aldrich), 400 mM and 200 mM, prepared in water, were used as oxidant.

EPR tubes and sample volumes

Different EPR tubes are required for different EPR measurements, and this is detailed in table 3.2.

Table 3.2: **EPR tubes and their application.** O.D. = outer diameter, I.D. = inner diameter, W = Wilmad, pr. = precision, res. = resonator, V = volume, titr. = titration, quant. = quantification. Details of the EPR resonators are given in Section 3.5.1.

EPR tube name	O.D.	I.D.	supplier	sample V comments	application &
4 mm high pr.	4.00 ±0.013	3.20 ±0.013	W 714-PQ-7	≈ 300 μL	X-band titr. & spin quant.
4 mm low pr.	4	3	W 707-SQ	≈ 100 μL	X-band CW
3.8 mm	3.80 ±0.013	2.79 ±0.013	W 706-PQ	≈ 80 μL	pulse X-band (MD4 res.)
3 mm	3.0 ±0.25	2.7 ±0.15	CE-MAT PN99553627	≈ 50 μL	pulse X-band (MS3 res.)
0.87 mm	0.87	0.70	W S-.7X.87	1-2 μL	W-band

For W-band measurements Suprasil quartz tubes were found to give a better signal to noise ratio than standard quartz tubes. All other measurements employed standard (cheaper) quartz tubes.

Calibration of reference electrode

The Ag/AgCl reference electrode (WPI, DRIREF-2) was calibrated using quinhydrone (Aldrich) at pH 4 and pH 7 (Fisher buffer solutions pH 4 and pH 7). Potentials are quoted with respect to SHE using the correction

$$E_{SHE} = E_{Ag/AgCl} + 0.195 \text{ V or } E_{SHE} = E_{Ag/AgCl} + 0.201 \text{ V at } 20^{o}\text{C}. \quad (3.7)$$

The potential of the reference electrode was found to drift very little with time (6 mV in two years).

3.3 Determining the number of spins in an EPR sample

Spin quantification was carried out using $Cu(ClO_4)_2$ samples as a standard. Samples were prepared using anhydrous $CuSO_4$ (BDH laboratory supplies) at concentrations of 200 μM, 150 μM, 100 μM, 50 μM and 10 μM in 2 M $NaClO_4$(aq), adjusted to pH 1.22 with HCl (BDH laboratory supplies). 300 μL of each solution was transferred to a 4 mm high precision EPR tube and the samples were measured under strictly non-saturating conditions at both 15 K and 80 K. The empty-resonator baseline was recorded under identical conditions (but field corrected) and subtracted. The total areas of the resultant spectra were plotted as a function of the number of spins in the sample to produce spin calibration plots as shown in Fig. 3.5.

The areas in Fig. 3.5 were scaled by microwave power and there is a 5.3-fold increase in area from 80 K to 15 K. This is expected since the temperature dependence of $Cu(ClO_4)_2$ follows the Boltzmann distribution (see Chapter 8, Section 8.3.4 as well as appendix Fig. 10.5). Either calibration curve can therefore be used to determine the number of spins in a sample, which can be measured at different mw power, different modulation amplitude, different scan rates and different video gains, as long as these changes are accounted for in the determination of the area. For example, if the sample under investigation is measured

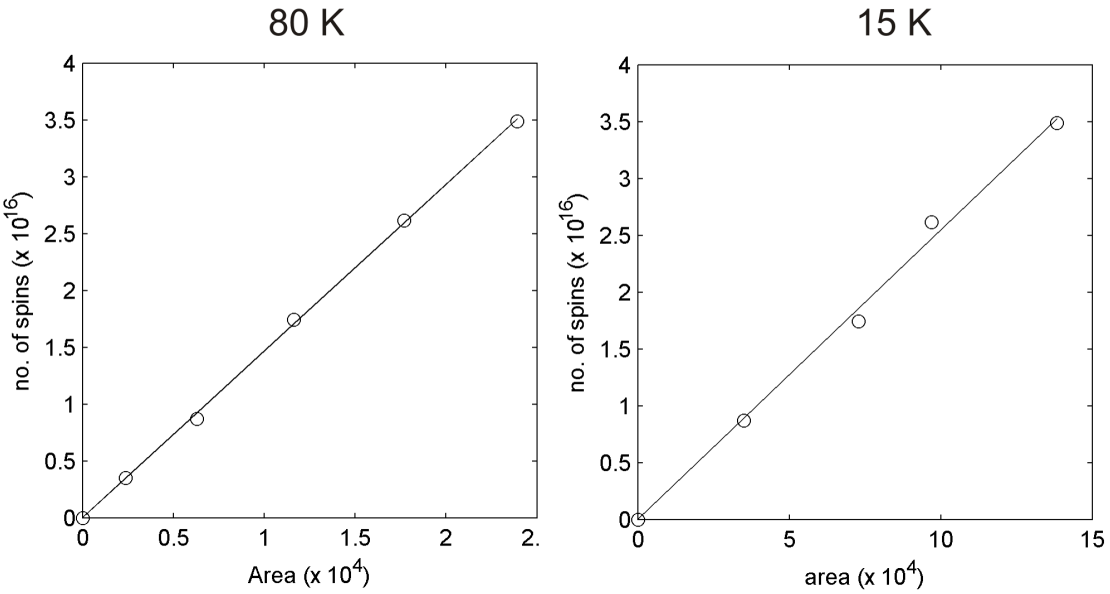


Figure 3.5: **Calibration curves obtained at 80 K and at 15 K using $Cu(ClO_4)_2$ as a standard for 'spin counting'.** Measurement conditions: (80 K) mw power 2 mW, modulation amplitude 1 mT; (15 K) mw power 8 μW, modulation amplitude 1 mT; the 10 μM sample could not be measured with sufficient signal-to-noise ratio under these conditions and is therefore omitted in the 15 K plot (right).

at 1 mW but otherwise the conditions are the same as those used for the $Cu(ClO_4)_2$ samples at 80 K in Fig. 3.5, the area of the sample has to be multiplied by 2 when compared to the areas (and therefore number of spins) in the calibration plot.

3.4 Protein Film Electrochemistry

Protein film electrochemistry (PFE) is very different from the solution electrochemistry (potentiometry) experiments described in Section 3.1. In PFE, current is measured as a function of the applied electrode potential (rather than measuring a potential at zero current of a system at equilibrium). This is possible by 'wiring' a monolayer of enzyme molecules to the electrode surface, so that reversible electron transfer an occur between the enzyme and the electrode (Fig. 3.6). The measured current gives direct information on the catalytic activity of the enzyme [132]. For the experiments described in this thesis, the electrode is pyrolytic graphite, the 'edge' of which has proven to provide a suitably rough surface able to adsorb many enzymes non-covalently [132], including the hydrogenases

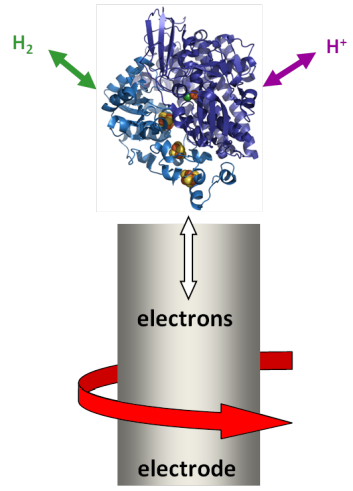


Figure 3.6: **Schematic showing the principles of a protein film electrochemistry experiment.** The attachment of a hydrogenase molecule is shown here but many different proteins have been studies *via* PFE [132]. The chemistry is controlled by modulating the electrode potential and through electrode rotation (red arrow). The current gives a direct measure of catalytic activity of the enzyme.

studied here.

Contrary to the EPR titration experiments described above, which requires many millilitres at tens of micromolar concentration, a PFE experiment typically needs less than a picomole of enzyme. Furthermore, PFE is extremely well-suited for studying the reactions of hydrogenases (and other enzymes): substrate concentration can be easily and precisely varied by varying the gas mixtures passing through the electrochemical cell's headspace and inhibitors can be supplied and removed. A schematic of a typical electrochemical cell is shown in Fig. 3.7.

In this thesis, two types of PFE experiments are employed: cyclic voltammetry and chronoamperometry. In cyclic voltammetry, the potential is linearly swept at a constant rate between two limits, in a cyclic fashion, and the current response is recorded. The current is then typically displayed as a function of potential. Chronoamperometry is a measure of current as a function of time. The potential is kept constant or varied in potential steps. Importantly, chronoamperometry allows measurement of catalytic activity as a function of time alone and therefore enables the determination of rates of reactions, because the current response is not convoluted by both potential *and* time, as

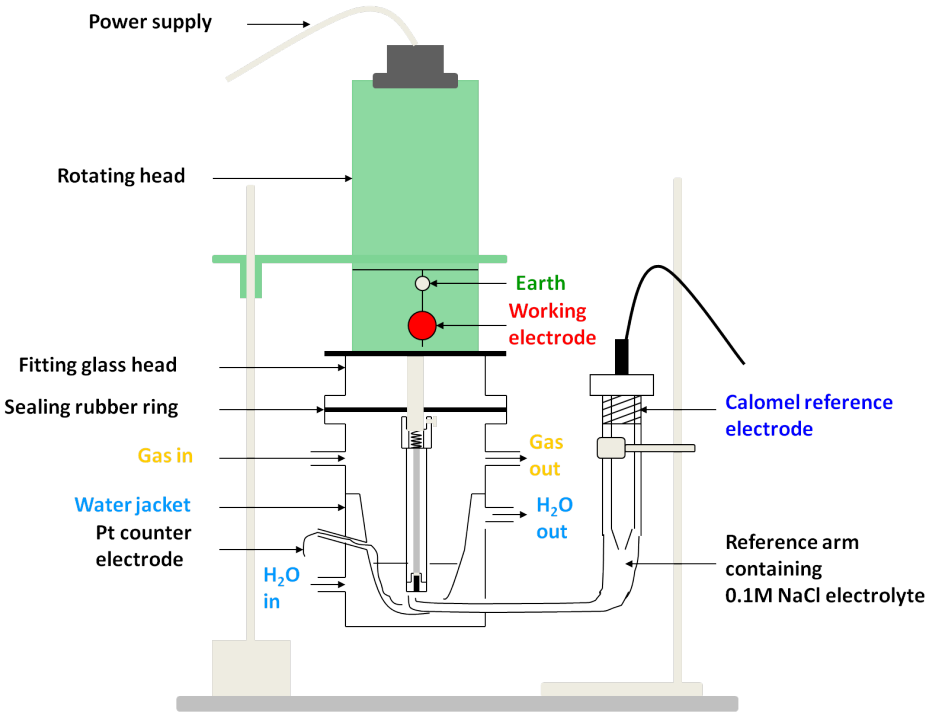


Figure 3.7: **Schematic showing a typical electrochemical cell used in PFE experiments.**

is the case in cyclic voltammetry.

The saturated calomel electrode (SCE) in the side arm is linked to the main compartment of the electrochemical cell through a Luggin capillary and therefore remains at room temperature. All potential values were corrected for the standard hydrogen electrode (SHE) scale using the relationship [133]

$$E_{SHE} = E_{SCE} + 0.241 \text{ at } 25\ ^{o}\text{C}. \tag{3.8}$$

3.5 EPR measurements

3.5.1 Spectrometers and resonators

All EPR measurements were performed on spectrometers with resonators (made by Bruker GmbH, Germany) which were part of the CAESR ESR facilities in Oxford.

Spectrometers

EMX (X-band CW EPR spectrometer)

ElexSys 680 (X/W-band pulse/cw spectrometer)

Resonators

Table 3.3: **Resonators and their application.** All Resonators are made by Bruker GmbH, Germany.

Resonator	Description	Applications in this thesis
X-band Super High Sensitivity	X-band CW	CW measurements
X-band EMX High Sensitivity	X-band CW	CW measurements
EN 4118-MD4	X-band Pulse-ENDOR Dielectric	Field sweeps, HYSCORE, ENDOR, ESEEM
EN 4118X-MS3	X-band Split-Ring	DEER measurements
EN 4118-MD5	X-band Dielectric	Field Sweeps
EN 600-1021H TeraFlex	W-band Pulsed ENDOR	W-band measurements

Details of the experiments (*e.g.* mw power, pulse lengths etc.) are provided in the methods section of the individual chapters or in figure legends. The resonator background (measured under identical conditions as the sample) was subtracted from all CW EPR measurements.

3.5.2 Field calibration

The magnetic field was generally calibrated on the CW EMX spectrometer at room temperature with 2,2-diphenyl-1-picrylhydrazyl as external standard ($g = 2.0036$) because this spectrometer is equipped with a frequency counter. Pulse measurements on the ElexSys instrument could usually be calibrated by comparison with CW measurements of the same sample. When the spectra at X-band and W-band were too different (*e.g.* due to a large exchange interaction between two observed paramagnetic centres), the W-band field was calibrated *via* a MIMS ENDOR measurement from which the proton nuclear frequency could be extracted and compared to the calculated nuclear frequency.

3.5.3 Background Cu^{2+} and Mn^{2+} at W-band

The Cu^{2+} and Mn^{2+} signals from the W-band resonator are significant, as shown in the echo-detected field sweeps of a ≈ 300 μM sample of Hyd-1 P242C (Chapter 7) compared with the background (Fig. 3.8). The multiplet of the manganese ion, often indiscernible at X-band, is well-resolved at W-band. The six sharp lines arise from $I = 5/2$ of Mn^{2+} in the $m_s = -1/2 \leftrightarrow +1/2$ transition, which to a first approximation is free of zero field splitting; other transitions are broad and are usually not observed.

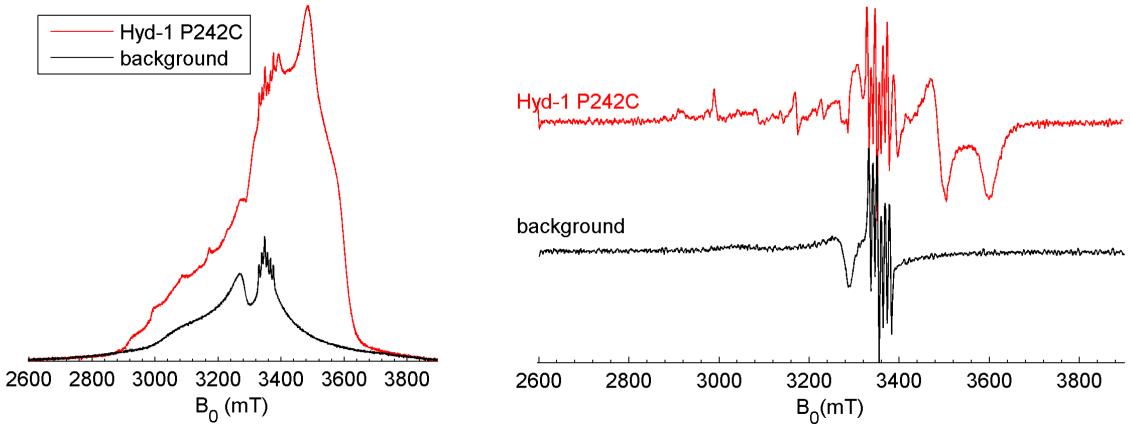


Figure 3.8: **Two-pulse echo detected field sweeps of a sample of Hyd-1 P242C and the resonator background measured under identical conditions.** (Left) Absorption spectrum; (right) numerical first derivative. 'Hyd-1 P242C' refers to a reduced sample at $\approx 300\mu$M concentration; 'background' refers to the empty resonator. Measurement conditions: 5 K, $\pi/2 = 28$ ns, $\tau = 180$ ns, 93.859 GHz (black), 93.849 GHz (red), shot repetition time 5 ms. Measurements included a 2-step phase cycle.

As shown by the black and blue spectra in Fig. 3.9, which correspond to the field sweeps of the empty resonator and a control sample using the same buffer and type of tube used for enzyme samples, the buffer used for sample preparations does not contribute to the observed Cu^{2+} and Mn^{2+} signals in the background. Unfortunately, the manganese contamination in the resonator was found to deteriorate with time (cyan and green traces). Following resonator cleaning by Bruker the copper background improved, but not the Mn^{2+} contribution. With manganese impurities of this magnitude it is extremely difficult to subtract the background successfully from the spectra of the enzyme sample, and

important signals potentially remain masked in the $g = 2$ region under the Mn^{2+} multiplet peaks. Other methods for removing the Mn^{2+} contribution from the enzyme sample spectra were therefore explored.

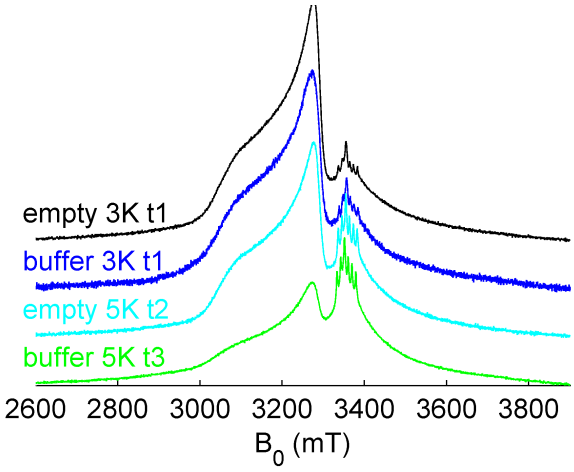


Figure 3.9: **Change of W-band background with time: two-pulse echo-detected field sweeps.** 'Empty' designates a measurement of the empty resonator, 'buffer' refers to pH 6 buffer (100 mM Mes, 100 mM NaCl, 10 % glycerol) in a suprasil tube. t1, t2 and t3 refer to the times at which the spectra were taken t1 = 02/2011, t2 = 04/2011, t3 = 08/2011). Measurement conditions: (black) 93.860 GHz, 3 K, $\pi/2 = 32$ ns, $\tau = 180$ ns; (blue) 93.900 GHz 3 K, $\pi/2 = 32$ ns, $\tau = 180$ ns; (cyan) 93.849 GHz 5 K, $\pi/2 = 28$ ns, $\tau = 180$ ns; (green) 93.905 GHz 5 K, $\pi/2 = 28$ ns, $\tau = 180$ ns. Measurements included a 2-step phase cycle.

First, if the Mn^{2+} impurity and the Fe-S cluster species under investigation have very different spin-lattice relaxation times (T_1), a 'relaxation filter' (an inversion pulse) can be introduced, followed by a delay equal to the time at which no Hahn echo is observed from Mn^{2+} (the time at which the inversion recovery trace of Mn^{2+} crosses zero), before the normal two pulse Hahn-echo sequence. Inversion recovery traces at 5 K of Mn^{2+}, obtained from the empty W-band resonator, and the reduced Hyd-1 P242C Fe-S cluster species measured at a field position where Mn^{2+} is off-resonance, are presented in Fig. 3.10 (the 'spikes' in the first μs are due to other echoes since no phase cycle was applied). At approximately 4.8 μs no Hahn-echo is observed from the Mn^{2+} centre. While T_1 for Mn^{2+} is on the order of 10-100 μs, that of the $[4Fe\text{-}4S]^+$ is on the order of 10 ms. Given that the spin-lattice relaxation times differ by 1-2 orders of magnitude, a relaxation-filtered two-pulse echo measurement of the reduced Hyd-1 P242C sample with a time delay of

4.8 μ after the initial inversion pulse should eliminate the Mn^{2+} contribution from the spectra. While this was indeed found to be the case, unfortunately most of the sample spectrum also disappeared (not shown). This is almost certainly because the initial π pulse is not strong enough to fully invert the magnetisation at time zero. With the further decrease in inverted echo intensity after 4.8 μs, only a fraction of the full echo intensity remains. Measurements with such a relaxation filter are not feasible because extremely long accumulation times would be required to obtain a sufficiently good signal to noise ratio. A better scenario would be to measure the *recovered* echo intensity (*i.e.* T_1 of the sample would have to be much *smaller* than that of Mn^{2+}), so that incomplete inversion of magnetisation at time zero is not crucial. However, given the typically exponential decrease of the echo intensity with increasing temperature of the samples investigated in this thesis, increasing the temperature to a point a which this scenario might arise was not an option, *i.e.* the temperature range for measurement of Fe-S signals is limited.

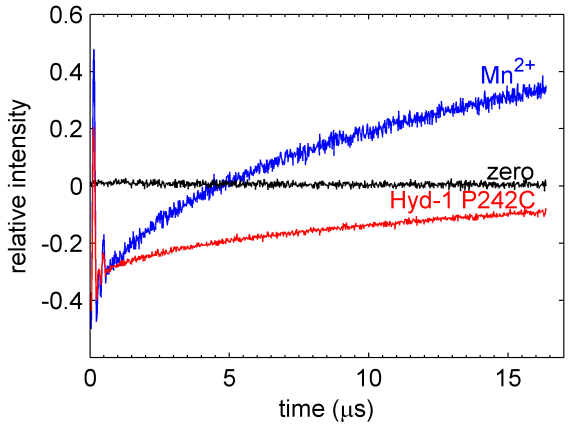


Figure 3.10: T_1 **measurements of Mn^{2+} in W-band resonator *vs* Hyd-1 P242C [4Fe-4S]$^+$(5 K).** The Mn^{2+} measurement refers to the empty resonator, 3352.7 mT, 93.910 GHz. The zero line was determined by measurement at zero mw power. The Hyd-1 P242C trace refers to a measurement at 3491.0 mT (maximum intensity of the [4Fe-4S]$^+$ cluster signal, but off-resonance for Mn^{2+}). The inversion pulse was 56 ns, followed by an initial delay of 200 ns, with 16 ns increments. The detection employed $\pi/2 = 28$ ns, $\pi = 56$ ns, $\tau = 300$ ns. No phase cycle was used and the initial spikes therefore reflect the other two (unwanted) echoes of the pulse sequence.

Next, the difference in T_2 relaxation times was investigated in order to establish

whether Mn^{2+} and the sample Fe-S cluster species can be separated by carefully choosing the τ value in the echo-detected field sweeps. Unfortunately this also proved to be impossible since the spin-spin relaxation times were found to be almost identical (Fig 3.11). The T_2 relaxation trace of the enzyme sample was measured at a field position where Mn^{2+} transitions are off-resonance.

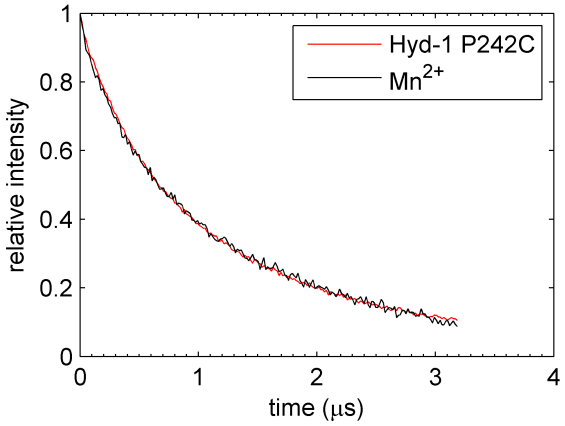


Figure 3.11: T_2 **measurements of Mn^{2+} in W-band resonator *vs* Hyd-1 P242C $[4Fe\text{-}4S]^+$ (5 K).** The Hyd-1 P242C trace refers to a measurement at 3476.0 mT (maximum intensity of the $[4Fe\text{-}4S]^+$ cluster signal, but off-resonance for Mn^{2+}), 93.850 GHz, shot repetition time 5 μs. The Mn^{2+} measurement refers to the empty resonator, 3356.0 mT, 93.906 GHz, shot repetition time 5 μs. Pulse sequence: $\pi/2 = 28$ ns, $\pi = 56$ ns, $\tau = 180$ ns, 8 ns increments.

The final possibility explored was to make use of the different flip angles of a given pulse for species with different spins S. However, this approach is not very likely to be successful since the Mn^{2+} impurity is present in the cavity and therefore at a different position than the sample. Flip angles are determined by the duration of the pulse and the Rabi frequency ω_1. If only one EPR transition (for species with $S > 1/2$) is considered and other transitions are assumed to be off-resonance because of additional interactions such as zero field splitting, the Rabi frequency for the precession about the x axis is given by [134]:

$$\omega_1 = \gamma B_1 \sqrt{S(S+1) - m_s(m_s+1)} \tag{3.9}$$

where γ is the gyromagnetic ratio and B_1 is the applied magnetic field (in the rotating

frame). Considering the $m_s = -1/2 \leftrightarrow +1/2$ transitions of both the $S = 1/2$ and $S = 5/2$ systems, the Rabi frequency for an $S = 5/2$ system is then 3 times larger than that of a $S = 1/2$ system, so that a 90^o pulse for the $S = 1/2$ system corresponds to a 270^o pulse for the $S = 5/2$ system and the generated free induction decays differ in sign [134]. The echoes resulting from a $\pi/2 - \tau - \pi - \tau -$ echo sequence are therefore also of opposite signs. Long selective pulses are required to separate contributions from different species to the echo. Hofbauer and Bittl [134] studied the best possible combinations of flip angles, the time τ between the pulses and the integration time window over the echo both theoretically and experimentally to separate an inorganic exchange-coupled system with overall $S = 1/2$ ground state from Mn^{2+} impurities. Their approach was tested here on the empty W-band resonator containing Mn^{2+} (and Cu^{2+}) contaminations only. Figure 3.12 shows the two-pulse echo-detected field sweeps (in the Mn region only) for a nominal 90^o pulse, which exhibits clear multiplet lines, and 231^o $\pi/2$ pulse, in with the presence of Mn^{2+} is hardly discernible. The conditions which result in the most successful suppression of the Mn^{2+} peaks were similar to those reported by Hofbauer and Bittl [134].

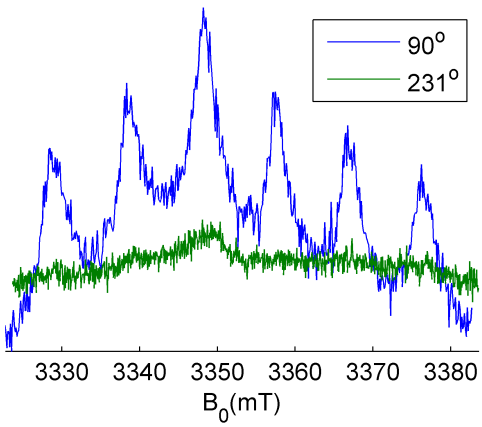


Figure 3.12: **Mn^{2+} measurements at W-band with nominal flip angles of 90^o and 131^o (5 K).** (Blue) $\pi/2 = 28$ ns, $\pi = 56$ ns, $\tau = 180$ ns, (Green) $\pi/2 = 76$ ns, $\pi = 152$ ns, $\tau = 300$ ns, 93.912 GHz

Applying the same flip angle, τ value and integration window to the Hyd-1 P242C samples did not eliminate the Mn^{2+} signals (spectrum not shown). While the quality

factor changes when the sample is introduced into the resonator, and adjustments are expected to be necessary, removal of the $S = 5/2$ contribution also resulted in removal of most of the $S = 1/2$ contribution although theoretically with the chosen pulse lengths and time delay this would not be expected to happen [134]. Practically, it is not surprising that the separation of the two spin systems through flip angle adjustments was not possible given their different location with respect to the incoming mw radiation.

In summary, much of the problem of eliminating Mn^{2+} cavity impurity contributions originates from the very broad spectra of the Fe-S cluster species studied in this thesis (1300 mT at W-band). This means that even very high protein concentrations close to 1 mM are insufficient to allow measurement conditions which result in significant loss of the echo intensity compared to that obtained from a simple Hahn echo sequence with 90^o pulses and a τ value as short as possible. The W-band absorption or derivative spectra shown in this thesis are therefore the results of background subtractions in which the empty resonator or a buffer sample was measured under as much the same conditions as possible and subtracted from the enzyme sample spectrum. With the augmenting Mn^{2+} contamination in the resonator with time (see Fig. 3.9), this could be achieved with increasingly less success.

3.6 Preparation of protein samples

3.6.1 Complex I from bovine heart mitochondria

Isolation of *Bos taurus* complex I and the preparation of EPR samples (Chapter 4) was carried out by Dr. Martin King (Mitochondrial Biology Unit, MRC, Cambridge), as described in reference [135].

3.6.2 Hyd-1 and Hyd-2 from *E. coli* and Hyd-5 from *Salmonella enterica*

The bacterial strains used, growth and isolation of the membrane-bound Hydrogenase-1 and Hydrogenase-2 enzymes from *E. coli* were carried out as described in ref. [83] and Dr. Michael Lukey's PhD thesis ([136]) with some modifications: membranes were solubilised with 3% Triton X-100 (Fisher) for 40 minutes; the His-trap column was equilibrated in 20 mM Tris, pH 7.2, 350 mM NaCl and 60 mM imidazole, 1 mM dithiothreitol, 0.02% Triton X-100 (Fisher), and the enzyme eluted with a linear gradient to a final concentration of 750 mM imidazole. Fractions containing purified Hyd-1 or Hyd-2 (as judged by absorption at 280 and 420 nm and ascertained by SDS-PAGE and Coomassie blue staining) were concentrated by centrifugal ultrafiltration, and an anaerobic buffer exchange to MES buffer (Section 3.8) was carried out in a glove box (O_2 $<$ 2 ppm) using a size-exclusion column (GE Healthcare, PG-10 columns) pre-equilibrated with MES buffer. Traces of O_2 in the column resin were removed prior to equilibration with MES buffer containing 1-2 mM dithiothreitol. Protein in MES buffer was snap-frozen anaerobically and stored in liquid nitrogen. The *E. coli* K-12 strains used for the expression of the Hyd-1 variants P242C, C19G/C120G, C120G and C19G were ML22, ML23, ML24 and ML25, respectively and were constructed by Dr. Michael Lukey (see refs. [89, 136]). The strain used for the expression of Hyd-1 C19G/C120G/P242C was made by Dr. Rhiannon Evans (Oxford) and is named sRME3. The pBS plasmid containing the double proximal mutation (pML23) was used to make the additional mutation at the medial cluster using the same P242C primers as were used to make the P242C single variant.[2] Growth and purification was carried out in the same way as for native Hyd-1 (strain FTH004 [137]) and yields were similar from all strains ($\approx$ 0.15 mg per gram of cells) with the exception of ML24 (encoding for the C120G HyaA protein) which was 2-3 times lower. Some growths and purifications of Hyd-1, Hyd-1 variants and Hyd-2 were carried out with the help of

[2]Personal communication with Dr. Rhiannon Evans, who carried out all the molecular biology for this variant.

Elena Nomerotskaia (University of Oxford).

The genetic approach which allowed an affinity-tagged version of *Salmonella enterica* Hyd-5 to be isolated, as well as the protocol for the bacterial growth and protein purification are described in ref. [138]. Growth and purification of the Hyd-5 enzyme ([138]) used in this thesis (Chapter 6, Section 6.2.2) were carried out by Dr. Alison Parkin and Elena Nomerotskaia, University of Oxford.

3.7 Determination of protein concentration

Protein concentrations were estimated spectroscopically using the Bradford method [139]. It was found that estimating the protein concentration by simply measuring the absorbance at 280 nm was not sufficiently accurate because cytochrome *b* is partially co-purified with *E. coli* Hyd-1 (Section 5.1.3). Consequently, although only a small fraction of Hyd-1 molecules contain cytochrome *b*, its large extinction coefficient at 280 nm leads to a gross overestimate of the enzyme concentration.

A typical calibration plot obtained with bovine serum albumin (BSA, Sigma Aldrich) and the determination of the concentration of a sample (in this case a variant of *E. coli* Hyd-1) is shown in Fig. 3.13. The measured absorbances of the sample are fitted to a straight line approximately coincident with the calibration plot, and the average concentration of the samples is thus determined.

3.8 Buffers

Buffer solutions were prepared with Millipore water with a resistivity of greater than 18 $M\Omega cm^{-1}$. The pH meter (Fisher, Accumet 950) was calibrated at the experimental temperature immediately prior to measurement of the buffer pH.

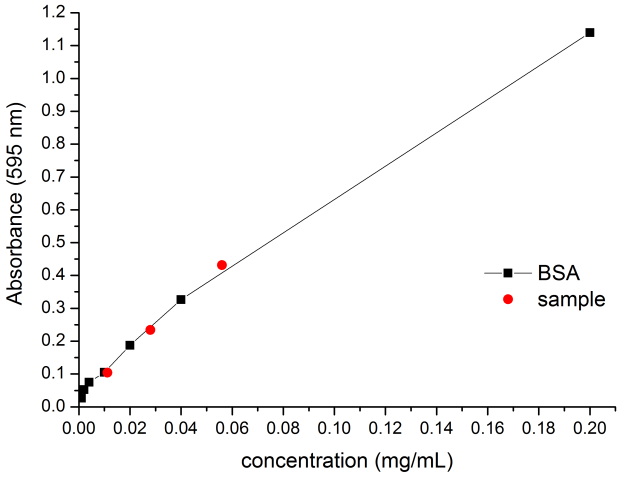


Figure 3.13: **Example calibration line in a Bradford assay.** A 2 mg/mL BSA standard was used and diluted to the concentrations shown. The red points corresponding to the protein sample of unknown concentration were diluted 1000, 2000 and 5000-fold. The concentration was thus determined to be 56 mg/mL.

MES buffer

In order to make the experiments between different enzymes as comparable as possible, most EPR samples were prepared with the same buffer, referred to as 'MES buffer'. This buffer contained 100 mM MES (Melford Laboratories), 100 mM NaCl (Fischer Scientific) and was adjusted to pH 6.00 at 20^{o}C by addition of μL quantities of a $NaOH_{aq}$ (GPR) solution. 10 % glycerol (Fisher) was added to the final solution. Deuterated MES buffer was made by preparing 100 mM MES, 100 mM NaCl in D_2O (Apollo Scientific, >99.92 atom % D) and adjusting the pH to 5.4 (pD = 6) [140] using NaOH pellets dissolved in D_2O for adjustment to pH 6.00. 10 % glycerol was added to the final solution. MES buffer is a suitable buffer for EPR experiments because it is not reported to change pH upon freezing [141].

Phosphate buffer

This buffer was used for the electrochemical experiments in Chapter 5, Section 5.3.2. Monosodium phosphate (Fisher) and disodium phosphate(Fisher) were used in the ap-

propriate ratio to give 100 mM phosphate buffers at pH 6.00 and at pH 7.50, both at 10 ^{o}C and at 27 ^{o}C.

3.9 Images of three-dimensional protein structures

Images of three-dimensional structures were generated from structure files deposited in the protein data bank (PDB, http://www.rcsb.org) using the program PyMOL (DeLano Scientific, 2002).

Chapter 4

Direct assignment of EPR spectra to structurally defined iron-sulfur clusters in complex I by double electron-electron resonance

The work described in this chapter was carried out in collaboration with the group of Dr. Judy Hirst at the Medical Research Council (Mitochondrial Biology Unit), Cambridge, and has been published [135]. Dr. Martin King performed all the complex I purifications and prepared all the EPR samples. The structural modeling of *B. taurus* complex I was done by Dr. Alan Robinson (Mitochondrial Biology Unit, Cambridge). The orientation selective DEER program was written by Dr. Jeffrey Harmer (CAESR, Oxford) and the procedure has been published [142]. All EPR measurements, analysis and simulations building up on the orientation selective DEER program were carried out by myself, but I am indebted to Dr. Jeffrey Harmer for help and advice.

Abstract

In oxidative phosphorylation, complex I (NADH:ubiquinone oxidoreductase) couples electron transfer to proton translocation across an energy-transducing membrane. Complex I contains a flavin mononucleotide to oxidize NADH, and an unusually long series of iron-sulfur (FeS) clusters, in several subunits, to transfer the electrons to quinone. Understanding coupled electron transfer in complex I requires a detailed knowledge of the properties of individual clusters and of the cluster ensemble, and so it requires the correlation of spectroscopic and structural data: This has proved a challenging task. EPR studies on complex I from *Bos taurus* have established that 3 EPR signals N1b, N2 and N3 arise from the 2Fe cluster in the 75 kDa subunit, and from 4Fe clusters in the PSST and 51 kDa subunits respectively (positions 2, 7, and 1 along the seven-cluster chain extending from the flavin). The other clusters have either evaded detection or definitive signal assignments have not been established.

In this study, double electron-electron resonance (DEER) spectroscopy on *Bos taurus* complex I is combined with the structure of the hydrophilic domain of *Thermus thermophilus* complex I. By considering the magnetic moments of the clusters and the orientation selectivity of the DEER experiment explicitly, signal N4 is assigned to the first 4Fe cluster in the TYKY subunit (position 5), and N5 to the all-cysteine ligated 4Fe cluster in the 75 kDa subunit (position 3). The implications of this assignment for the mechanisms of electron transfer and energy transduction by complex I are discussed.

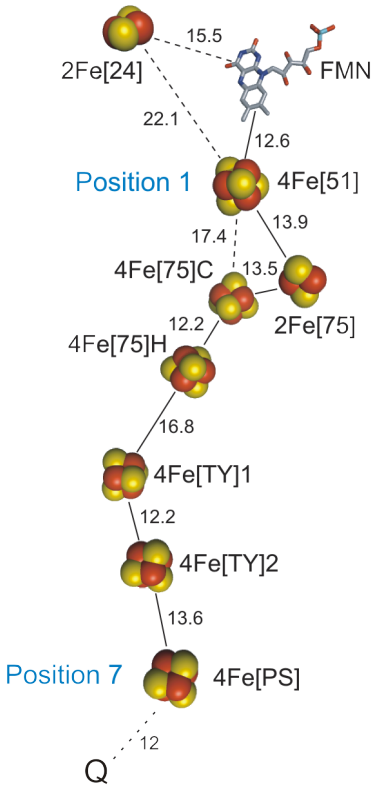
4.1 Introduction: The iron-sulfur cluster relay in complex I

The exceptionally long Fe-S cluster relay in complex I introduced in Chapter 1 (Section 1.2.3) is now discussed in more detail. Out of the eight Fe-S clusters present in *B. taurus* complex I, seven (one [2Fe-2S] cluster and six [4Fe-4S] clusters) form a chain between the two actives sites: the site of NADH oxidation and the site of ubiquinone reduction, which are more than 70 Å apart [51]. The role of the eighth cluster (the [2Fe-2S] cluster in the 24kDa subunit, see Fig. 4.1 (left)) on the opposite side of the FMN is unknown, but its location suggests that it is unlikely to be involved in energy transduction in complex I. A ninth cluster is observed in a few species, including *E. coli* and *T. thermophilus*. This [4Fe-4S] cluster is more than 20 Å away from the main chain and does not participate in electron transfer [106, 107].

Continuous wave EPR has proved to be the most useful technique for obtaining information about the redox cofactors in complex I, such as their reduction potentials. In order to obtain a basis for the free energy profile for electron transfer along the chain, it is essential to assign the set of spectroscopically determined cluster properties to the structurally defined clusters. This is a challenging task and the following gives an overview of the current knowledge from over thirty years of research.

Complex I from bovine heart is by far the best characterised eukaryotic complex I [94, 143–145]. It is the focus of this study and unless otherwise stated, the following statements refer to complex I from *B. taurus*. When complex I is reduced with NADH, EPR signals are observed that can be attributed to at most five Fe-S clusters (named N1b, N2, N3, N4 and N5). The g values of these five clusters could be established by examining samples poised at different potentials, measured at different temperatures and microwave powers [143, 145].

Signal N1b can be singled out by raising the temperature of a sample reduced to -0.4 V (or lower potential) to more than 30 K. As the temperature is lowered, increasingly more



	Ohnishi	Hirst		
	A	B	C	Position
2Fe[24]	N1a	N1a	N1a	
4Fe[51]	N3	N3	N3	1
2Fe[75]	N1b	N1b	N1b	2
4Fe[75]C	N4	N5	N5	3
4Fe[75]H	N5			4
4Fe[TY]1		N4		5
4Fe[TY]2			N4	6
4Fe[PS]	N2	N2	N2	7

Figure 4.1: **Arrangement of cofactors in *B. taurus* complex I, based on the structure from *T. thermophilus*, and possible assignments of EPR signals to clusters.** (*Left*): Fe-S clusters in the structure of the hydrophilic arm of *T. thermophilus* complex I (2FUG.PDB [51] conserved in *B. taurus*, named according to their type (2Fe or 4Fe), subunit (according to the standard nomenclature for *B. taurus*, 75 = 75 kDa subunit, 51 = 51 kDa subunit, 24 = 24 kDa subunit, PS = PSST subunit, TY = TYKY subunit [146], see also Fig. 1.6), and differentiated when necessary by C (all Cys ligated) or H (one His ligand), or as cluster 1 or 2. Distances are center-to-center for the Fe-S clusters, the central ring of the isoalloxazine system (FMN), or to the bound ubiquinone (Q, [147]) The positions of the clusters in the chain with respect to the FMN are given in blue. (*Right*): Extant assignments of the five EPR signals observed in *B. taurus* complex I reduced by NADH [94, 143, 145]. Unambiguous assignments are shown in black. N1a is shown in gray as it has never been observed in the intact enzyme (see text). The disagreement over the assignment of N4 and N5 is highlighted in red. Cluster positions in the electron transfer chain are given in blue. Adapted from ref. [135].

Fe-S clusters are visible (see Fig. 4.2 and ref. [143]) and the relaxation rates follow the order N1b<N2<N3<N4<N5 [94, 143]. Signal N5 is only observed below 5 K [143, 145]. The different relaxation behaviour has been used to separate the spectral contributions of N1 and N2 in complex I from *Y. lipolytica* by employing Relaxation Filtered Hyperfine (REFINE) spectroscopy [148]. Although this technique has been successfully applied to

separate three spectrally overlapping species in a model compound [149], it has proven very difficult when more than two spectrally overlapping species with similar relaxation rates need to be deconvoluted, as is the case in complex I [150].

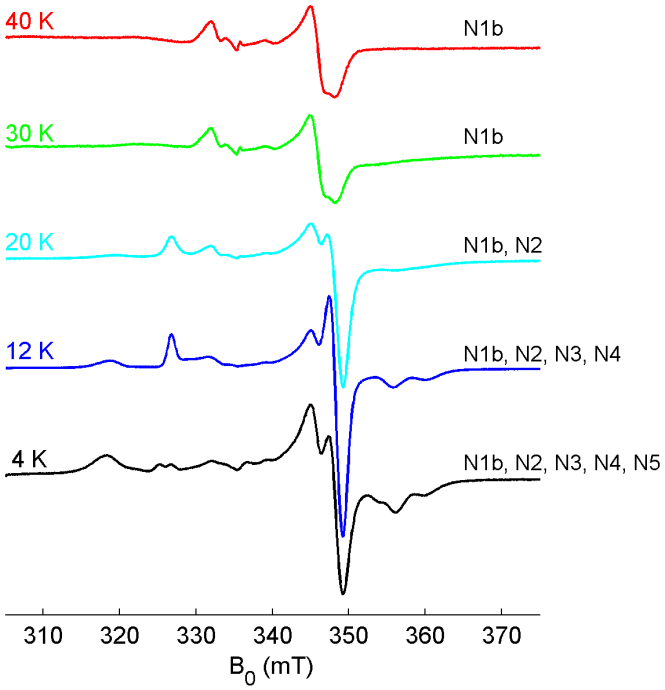


Figure 4.2: **CW EPR spectra of *B. taurus* complex I reduced to -0.4 V with NADH, showing the appearance of more Fe-S clusters as the sample temperature is decreased.** The sample temperature in indicated to the left of the spectra and the observed Fe-S cluster species are labeled to the right. Other measurement conditions are as follows: microwave power 0.5 mW, modulation amplitude 0.5 mT, microwave frequency 9.393 GHz. Note that because of the different relaxation behaviour of the clusters, many signals are inevitably saturated [145]. See section 4.4.1 for a detailed analysis for the Fe-S cluster species present in this sample.

The small range of reduction potentials exhibited by the observed clusters (Table 4.1) means that the only signal which can be observed alone at all temperatures is N2 when the potential is adjusted to -0.1 V. At -0.3 V and 12 K, overlapping signals from N2, N3 and N4 are observed [143, 145] as N1b remains oxidised. After NADH reduction to -0.4 V, EPR signals from N1b, N2, N3 and N4 are visible at 12 K. Although Ohnishi originally reported [143] N1b, N2, N3 and N4 to be present in a 1:1:1:1 ratio, Hirst and coworkers later found that determining the relative stoichiometries of the clusters is extremely difficult because

it is not possible to make all the individual spectra of the clusters unsaturated within one single spectrum [145]. N5 becomes visible in NADH reduced samples at temperatures below 5 K (Fig. 4.2) and Ohnishi reported its spin concentration to be only ≈ 0.25, raising the possibility that 75 % of the N5 spins are in the $S = 3/2$ ground state [143].

Reduction to -1 V with Eu^{2+}-DTPA resulted in additional signals which were tentatively attributed to two interacting reduced clusters, but these are highly unlikely to result from the *three* 'missing' reduced clusters [145]. However, several other interesting observations were made at this low potential [145]. Firstly, the relative intensity of N1b increased (more than 3-fold, compared to a 1.9- and 1.2-fold increase of N3 and N4, respectively, all relative to N2), supporting the extended potential dependence of N1b found in *E. coli* complex I [151]. Secondly, the relaxation rate of signal N5 was found to be *slower* at -1 V compared to -0.4 V and a conformational change affecting the properties of the cluster, or the existence of two clusters with the same g values, but different relaxation properties, was postulated [145].

Table 4.1: **Redox potentials of the observed Fe-S cluster signals in *B. taurus* complex I.** [a] Midpoint potentials of clusters N2, N3, N4 and N5 were determined from redox titrations [143, 152]
[b] Due to confusion between signals N1b and N1a, there are some reports of N1a observed in intact bovine complex I in the literature.

EPR signal name	E_{pH7} $(V)^a$	Comments
N1a	est. -0.5	not observed in complete *B. taurus* complex I [b]
N1b	est. -0.4	only partially reduced by NADH [145]
N2	-0.15	spin interactions with ubisemiquinones [147]
N3	-0.25	spin interactions with flavosemiquinone [153]
N4	-0.25	
N5	-0.26	very fast relaxing

Assignment of the EPR signals from the five reduced clusters observed in the reduced intact enzyme has proven to be extremely difficult. Over-expression of individual subunits and studies of enzyme fragments have led to much insight and were crucial in determining the number of Fe-S clusters per subunit before the crystal structure of the hydrophilic domain was solved in 2006 [51]. The flavoprotein-subcomplex (24 + 51 kDa subunits) and

the 24 kDa subunit give rise to a [2Fe-2S] signal (named N1a) which must result from the 2Fe[24] cluster (see Fig. 4.1 for nomenclature of the clusters). Signal N1a has never been observed in the intact bovine enzyme, not even when the enzyme is reduced to -1 V [145]. (In complex I from *E. coli*, signal N1a has been observed in the complete enzyme [154] as the 2Fe[24] cluster has a higher reduction potential in *E. coli* than in *B. taurus*. The potential in the latter was determined electrochemically [155].) Over-expression of the 75 kDa subunit in *Paracoccus denitrificans* complex I enabled assignment of signal N1b to cluster 2Fe[75] (position 2 in the electron transfer chain, see Fig. 4.1) since the observed [2Fe-2S] signal was very similar to that observed in the intact enzyme [156], which does not exhibit the N1a signal. Signal N2 could be assigned to the 4Fe[PS] cluster (position 7 in the chain) because spin-spin interactions were observed to the ubisemiquinone species, determined to be about 12 Å away [147, 157]. The spin relaxation of the flavosemiquinones has been observed to be very fast (compared to flavodoxin, which contains no transition metal ions in close proximity to the flavin) due to interaction with a nearby Fe-S cluster which could only be 4Fe[51] (signal N3, position 1) [153]. The question which clusters to assign to signals N4 and N5 remains highly controversial and relies on data from enzyme fragments, overexpressed subunits and point mutations. The three contending assignments are presented in Fig. 4.1. Ohnishi's model (A) assigns N4 to the 4Fe[75]C cluster (position 3) and N5 to 4Fe[75]H (position 4). Hirst's model proposes N5 to arise from cluster 4Fe[75]C (position 3) and N4 is assigned to either 4Fe[TY]1 (position 5) or 4Fe[TY]2 (position 6), or both clusters of the TYKY subunit [94, 143, 144] (see Fig. 4.1).

The aim of this work is to assign signal N4 directly by DEER spectroscopy on samples of the complete complex I enzyme from *B. taurus*, through simulations of the DEER traces for the three proposed models A, B and C, and comparison to the experimentally obtained data. With the assignment of N4, the origin of signal N5 can be deduced.

4.2 Double electron-electron resonance spectroscopy with iron-sulfur clusters

DEER spectroscopy (see Section 2.6.5) is well established to measure the distance between organic radicals, such as spin labels [158, 159]. Such spin labels, which contain an $NO^{\bullet}$ group and have an $S = 1/2$ ground state, can be introduced at well-defined positions in a protein molecule through engineering of specific amino acids in a technique known as site-directed spin labeling (SDSL). DEER has been used extensively to measure distances in proteins between such spin labels [160, 161]. While the spin states and magnetic moments are precisely known in such organic radicals, this is not the case for Fe-S clusters. The application of DEER to metal sites in multicentered enzymes is a relatively new application that builds on the seminal work of Noodleman [7] and Bertrand [162] on the magnetic interactions in Fe-S clusters, and on the application of DEER to a [NiFe]-hydrogenase by Bittl and coworkers [163, 164]. The analysis of DEER traces resulting from dipolar coupling between Fe-S clusters is complicated for two reasons. Firstly, the magnetic moment of a cluster results from ferromagnetic and antiferromagnetic interaction between the Fe subsites (Chapter 2, Section 2.3.5) and varies with the cluster type and environment [162]. Secondly, the microwave pulse excitation profiles in the DEER sequence are much narrower than the broad Fe-S cluster EPR spectra, so that each pulse only selects a limited rage of molecular orientations. These two complications are addressed in the following sections.

4.2.1 The local spin model

In the local spin model, the spin Hamiltonian for a pair of clusters (A and B) can be written in terms of the intracluster spin-spin coupling interactions $\mathcal{H}_{int}$, the electron Zeeman interaction $\mathcal{H}_Z$, the exchange interaction $\mathcal{H}_{exchange}$ and the dipolar interaction $\mathcal{H}_{dd}$:

$$\mathcal{H} = \mathcal{H}_{int} + \mathcal{H}_Z + \mathcal{H}_{exchange} + \mathcal{H}_{dd}. \tag{4.1}$$

The Hamiltonian in equation 4.1 is dominated by the intracluster coupling $\mathcal{H}_{int}$. Reduced [4Fe-4S] clusters, which formally consist of three Fe^{2+} and one Fe^{3+}, exhibit delocalised valence electron distributions over specific $Fe^{2.5+}$ and Fe^{2+} dimers due to ferromagnetic and antiferromagnetic coupling between the Fe subsites [7]. The four individual spins of the Fe ions in clusters A and B couple to give an effective spin for cluster A of $\vec{\hat{S}}_A$ and $\vec{\hat{S}}_B$ for cluster B (equation 4.2), where $\vec{\hat{S}} = [\hat{S}_x, \hat{S}_y, \hat{S}_z]$ is the electron spin operator (Section 2.1).

$$\vec{\hat{S}}_A = \sum_i \vec{\hat{S}}_{Ai} \quad \text{and} \quad \vec{\hat{S}}_B = \sum_j \vec{\hat{S}}_{Bj}. \tag{4.2}$$

For the clusters in complex I, the Fe spins couple to give an $S = 1/2$ ground state that is well separated from the excited states [165]. The individual spin of each iron ion $\vec{\hat{S}}_{Ai}$ or $\vec{\hat{S}}_{Bi}$ can therefore be expressed in terms of the spin projection factors (k_i and k_j, discussed in more detail in section 4.4.1) and the effective spin of the cluster $\vec{\hat{S}}_A$ and $\vec{\hat{S}}_B$ according to the Wigner-Eckart theorem [166]:

$$\vec{\hat{S}}_{Ai} = k_i \vec{\hat{S}}_A \quad \text{and} \quad \vec{\hat{S}}_{Bi} = k_j \vec{\hat{S}}_B. \tag{4.3}$$

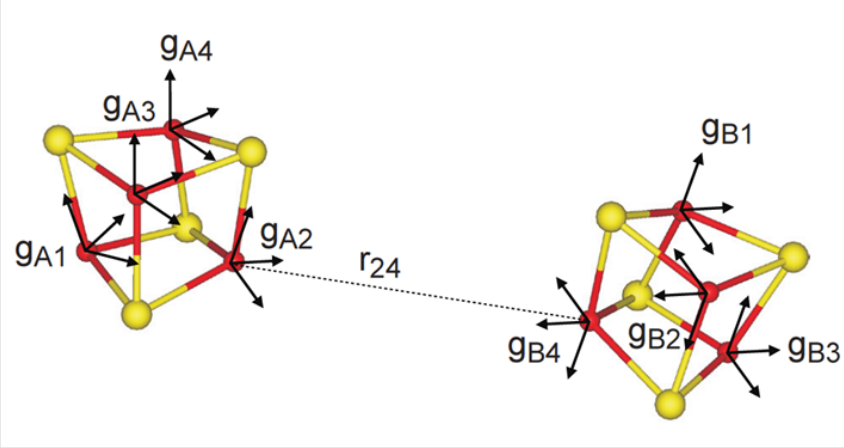


Figure 4.3: **Schematic representation of the g-matrices for each Fe in an Fe-S cluster, as required in a local spin model of the intracluster magnetic interactions.** Each Fe has an independent **g**-matrix (and spin projection factor). Taken from supporting information of ref. [135].

The matrices $\mathbf{g_A}$ and $\mathbf{g_B}$ are measurable and result from a weighed sum of the **g**-matrix

contributions of the individual Fe centers $\mathbf{g}_{Ai}$ and $\mathbf{g}_{Bj}$ (Fig. 4.3):

$$\mathbf{g}_A = \sum_i k_i \mathbf{g}_{Ai} \quad \text{and} \quad \mathbf{g}_B = \sum_j k_j \mathbf{g}_{Bj}. \tag{4.4}$$

The electron Zeeman interaction in equation 4.1 is given by:

$$\mathcal{H}_Z = -\sum_i \vec{\mu}_{Ai}^T \vec{B} - \sum_j \vec{\mu}_{Bj}^T \vec{B} \tag{4.5}$$

where the magnetic dipoles of the individual Fe ions are $\vec{\mu}_{Ai} = -\mu_B \mathbf{g}_{Ai} \vec{\hat{S}}_{Ai}$ and $\vec{\mu}_{Bj} = -\mu_B \mathbf{g}_{Bj} \vec{\hat{S}}_{Bj}$. Substituting equations 4.3 and 4.4 yields an expression of the Zeeman interaction with measurable quantities in which the spin projection factors cancel out:

$$\mathcal{H}_Z = \mu_B (\mathbf{g}_A \vec{\hat{S}}_A)^T \vec{B} + \mu_B (\mathbf{g}_B \vec{\hat{S}}_B)^T \vec{B}. \tag{4.6}$$

The exchange interaction

$$\mathcal{H}_{exchange} = -2 \sum_i \sum_j \vec{\hat{S}}_{Ai}^{\,T} \mathbf{J}_{ij} \vec{\hat{S}}_{Bj} \tag{4.7}$$

has an exponential distance dependence [167] and can be neglected in this analysis because it is usually very small when the distance between the paramagnetic clusters is greater than 10 Å. This assumption is also validated experimentally in section 4.4.1.

The dipolar coupling is described by:

$$\mathcal{H}_{dd} = \frac{\mu_0}{4\pi} \sum_i \sum_j \frac{\vec{\mu}_{Ai}^{\,T} \vec{\mu}_{Bj} - 3(\vec{n}_{Ai}^{\,T} \vec{\mu}_{Ai})(\vec{n}_{Bj}^{\,T} \vec{\mu}_{Bj})}{r_{ij}^3} \tag{4.8}$$

where r_{ij} is the distance between the ith Fe of cluster A and the jth Fe of cluster B and $\vec{n}_{ij}$ is the unit column vector. Substituting the expression for the magnetic dipoles gives:

$$\mathcal{H}_{dd} = \frac{\mu_0 \mu_B^2}{4\pi} \sum_i \sum_j \vec{\hat{S}}_{Ai}^{\,T} \frac{\mathbf{g}_{Ai}^T \mathbf{g}_{Bj} - 3(\mathbf{g}_{Ai}^T \vec{n}_{ij})(\vec{n}_{ij}^{\,T} \mathbf{g}_{Bj})}{r_{ij}^3} \vec{\hat{S}}_{Bj}. \tag{4.9}$$

The dipolar frequencies in a DEER experiments result from the dipolar Hamiltonian (equation 4.9). Because the g matrices of the individual Fe of the clusters are not available experimentally, they must be estimated from values for isolated Fe^{3+} and Fe^{2+} and from theoretical work (for $Fe^{2.5+}$). The $\mathbf{g}$ matrices for Fe^{3+} are essentially isotropic and close to the free electron value $g_e = 2$ [168]. The principal g values for Fe^{2+} also do not deviate significantly from 2; for example for *Clostridium pasteurianum* rubredoxin $g = [2.11, 2.19, 2.00]$ [169] and for *Desulfovibrio gigas* desulforedoxin $g = [2.08, 2.02, 2.00]$ [170]. A similar assumption can be applied to the Fe^{2+}-Fe^{2+} and $Fe^{2.5+}$-$Fe^{2.5+}$ valence pairs [171] in [4Fe-4S] clusters. The experimentally observed g values for the Fe-S clusters in complex I support these assumptions (section 4.4.1) since they are close to the free electron g value and the largest deviation is $\Delta g_e = 0.1$ (for the cluster giving rise to signal N4). Because the intrinsic g values for Fe^{2+} and $Fe^{2.5+}$ are close to each other and to $g = 2$, they are all set equal to the average experimental value, i.e., $\mathbf{g}_{A1/A2} = \mathbf{g}_{A3/A4}$, and $\mathbf{g}_{B1/B2} = \mathbf{g}_{B3/B4}$. The dipolar Hamiltonian then becomes:

$$\mathcal{H}_{dd} = \frac{\mu_0 \mu_B^2}{4\pi} \sum_i \sum_j k_{Ai} k_{Bj} \vec{\hat{S}}_A{}^T \frac{\mathbf{g}_A{}^T \mathbf{g}_B - 3(\mathbf{g}_A{}^T \vec{n}_{ij})(\vec{n}_{ij}{}^T \mathbf{g}_B)}{r_{ij}^3} \vec{\hat{S}}_B. \tag{4.10}$$

The $\mathbf{g}$ matrices $\mathbf{g}_A$ and $\mathbf{g}_B$ used in the DEER simulations are the experimentally determined g values, equivalent to taking an average value over all four Fe subsites in a cluster (equation 4.4). The 'average' error introduced by this simplification can be considered as being introduced into the spin projection factors. The dipolar frequency, ω_{dd}, measured at a particular orientation, is directly proportional to the g value, so that the maximum error introduced is approximately $(g_{max} - g_{avg})/g_{avg} = (2.1 - 2)/2 = 5\%$. With the aim to discriminate between the different cluster assignments in complex I, this is an acceptable error.

Finally, the non-secular terms ($\hat{S}_x \hat{S}_y$, etc.) can be neglected because the intracluster distances between the Fe ions are small compared to the intercluster distances (the individual dipolar tensors are diagonal in principal axis systems because of their dependence

on r_{ij}) [163, 164]. This reduces the dipolar coupling to the following expression:

$$\omega_{dd}^{m} = \frac{\mu_0 \mu_B^2}{2h} g_A^m g_B^m \sum_i \sum_j k_{Ai} k_{Bi} \frac{3\cos^2 \psi_{ij}^m - 1}{r_{ij}^3}. \tag{4.11}$$

ω_{dd} is the dipolar coupling frequency, g_A^m and g_B^m are the experimental g values of the two clusters, observed at the orientation of the unit magnetic field vector $\vec{B}_0^m(\theta, \phi)$, defined in the molecular frame by the polar angle θ and the azimuthal angle ϕ. Angle ψ_{ij}^m defines the angle between $\vec{B}_0^m(\theta, \phi)$ and the Fe_{Ai}-Fe_{Bj} unit vector $\vec{n}_{ij}$. The superscript m refers to a single orientation of the unit magnetic field vector $\vec{B}_0^m(\theta, \phi)$ with respect to the molecular frame for a representation of the polar angles θ and ϕ; ψ_{ij}^m defines the angle between $\vec{B}_0^m(\theta, \phi)$ and the Fe_{Ai}-Fe_{Bj} unit vector $\vec{n}_{ij}$ (see Fig. 4.5).

4.2.2 Orientation selection

X-band frozen solution (powder) field-sweep EPR spectra of Fe-S spin systems are much wider than the mw pulse excitation bandwidth. Only a fraction of the spectrum of the Fe-S cluster is therefore excited, and many orientations of a particular cluster with respect to $\vec{B}_0^m(\theta, \phi)$ have resonances that are not excited by the mw pulses. This is referred to as orientation selection. Many DEER experiments at different fields and frequencies need to be combined to obtain the complete dipolar spectrum and therefore the distance between two Fe-S clusters. Each frequency combination for the pump and detection ω_A and ω_B selects different sets of orientations of a cluster pair with respect to the spectrometer's magnetic field, $\vec{B}_0$ and this is illustrated in Fig. 4.4 for clusters N2 and N4 in complex I.

The coloured rings in the two half-spheres represent the orientations of clusters N2 and N4 resonant with the mw pulses in the molecular frame. A DEER modulation occurs where the coloured rings overlap and each DEER trace comprises a set of dipolar frequencies, ω_{dd}, from the contributing cluster pair orientations. In the case of complex I, there could be more than one set of cluster pairs contributing to the DEER trace because all the Fe-S cluster EPR spectra overlap, and this will be addressed in section 4.4.2. For

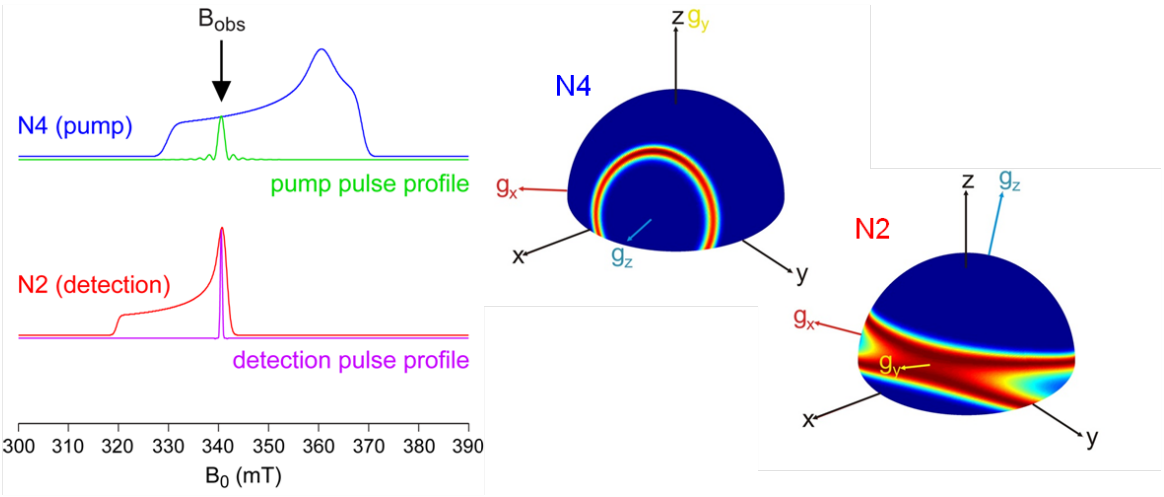


Figure 4.4: **Representation of orientation selection of the mw pulses for the N4 and N2 spectra.** (*Left*): The pump pulse excitation profile for a 20 ns π-pulse at frequency $\omega_B/2\pi = 9.727$ GHz (green) is applied to N4 (blue). The detection pulse excitation profile for a 40 ns π-pulse at $\omega_B/2\pi = 9.189$ GHz (magenta) is applied to N2 (red). The widths of the spectra reflect the molecular orientations in the frozen solution, and only a fraction of each spectrum is excited by the mw pulses. The fixed field position of the DEER measurement, $B_{obs} = 340.5$ mT, is indicated. Taken from supporting information of ref. [135]. (*Right*): The two half-spheres represent orientations resonant with the mw pulses in the molecular frame (black). The coloured rings represent the resonant orientations; off-resonant orientations are blue. The coloured frame is the g tensor of the cluster.

just one cluster pair (e.g. N2 and N4) the dipolar frequencies for a particular pump and detection pulse frequency combination are given in equation 4.11.

To account for the random distribution of molecules in the frozen-solution samples, a summation has to be performed over all orientations of $\vec{B}_0^m(\theta, \phi)$ with respect to the molecular frame. Half a unit sphere ($\theta = 0 - \pi/2$, $\phi = 0 - 2\pi$) is sufficient for the general case since the spin Hamiltonian has inversion symmetry. This was easier to implement in the DEER algorithm than rotating the complex I molecule over half a sphere while keeping the magnetic field constant. A general method for analysing orientation selective DEER traces was published by Harmer and coworkers [142], and the DEER algorithm presented in this publication was applied to this work.

Finally, the simulated DEER time domain signal also depends on the extent to which the detection spin (A-spins) are excited by the DEER detection pulse sequence for the

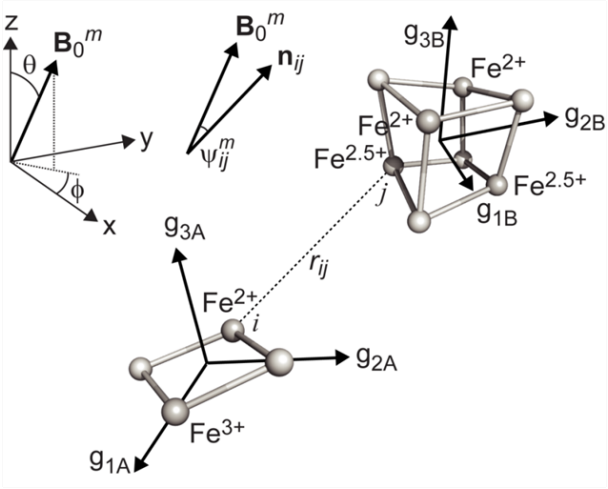


Figure 4.5: **Orientation selective DEER simulation parameters for a [2Fe-2S]-[4Fe-4S] cluster pair.** The unit magnetic field vector, $\vec{B}_0^m(\theta, \phi)$, is defined with the polar angles θ and ϕ. $\mathbf{n}_{ij}$ is the unit vector between Fe ions i and j of the two clusters, r_{ij} is the distance between them, and ψ_{ij}^m is the angle between $\vec{B}_0^m(\theta, \phi)$ and n_{ij}. The g_3-axis from the [2Fe-2S] spin point along the Fe-Fe vector. The g_3-axis from the [4Fe-4S] spin is normal to the faces assigned to the Fe^{2+} and the $Fe^{2.5+}$ pairs, in this example, the g_1 and g_2 are normal to the Fe^{2+}-$Fe^{2.5+}$ containing faces. Taken from ref. [135].

field orientation $\vec{B}_0^m(\theta, \phi)$ and this is described by the term f_A^m in equation 4.12. The corresponding modulation or oscillation depth, c_{mod}^m, describes the extent to which the pump pulse is resonant with the pump spin (B-spin) for the orientation $\vec{B}_0^m(\theta, \phi)$. The section in curly brackets in equation 4.12 refers to the unmodulated part of the DEER trace, the cosine term refers to the modulated part.

$$y_{sim}(t) = \sum_m f_A^m(\{1 - c_{mod}^m\} + c_{mod}^m \cos(\omega_{dd}^m t)). \tag{4.12}$$

4.3 Experimental Methods

4.3.1 EPR Spectroscopy

All DEER measurements employed a four pulse sequence, $\pi/2{-}\tau_1{-}\pi{-}\tau_1{-}\tau_2{-}\pi{-}\tau_2{-}echo$, for the detection pulses at frequency ω_A, and a single pump pulse at frequency ω_B moved within the refocused echo sequence. The detection pulses were phase cycled according

to [+x, +y, +y, +, x, +y, +y, -], and employed lengths of $t_\pi/t_{\pi/2}$ = 40 ns / 40 ns. The pump pulse (t_π) had a duration of either 16, 20 or 24 ns, depending on the achievable B_1-field. A variable τ_1 time (from 140-164 ns, or from 180-204 ns) was applied to dampen nuclear modulations, and time τ_2 was 1.1-1.6 μs. Given that the oscillation period in all DEER traces was between 0.5 and 0.7 μs (Fig. 4.7), the τ_2 chosen were sufficiently long to allow at least two oscillation periods to be observed and the background decay to be assessed. Measurements with longer τ_2 times would be necessary if larger distances (well beyond 40 Å , see Section 4.4.3) dominated; since this is not the case, longer τ_2 times would unnecessarily increase the data accumulation time. The DEER field positions, ω_A, and ω_B, are reported in the figure legends. Echo-detected EPR spectra were recorded by integrating the echo intensity either from a refocused echo (using the same parameters as in the DEER experiments), or from the pulse sequence $\pi/2 - \tau - \pi - \tau - echo$, with $t_\pi/2$ = 48 ns, t_π = 96 ns and τ = 200 ns at X-band, and with $t_\pi/2$ = 24 ns, t_π = 48 ns and τ = 140 ns at W-band. All pulsed X-band experiments were carried out at 10 K with a repetition time of 2 ms, and W-band measurements were performed at 8.5 K with a repetition time of 1.5 ms.

4.3.2 Preparation of EPR Samples of *B. taurus* complex I

All complex I samples analysed in this work were prepared by Dr. Martin King (Mitochondrial Biology Unit, Cambridge). Complex I was isolated from *B. taurus* heart tissue as described previously [172], except ethylene glycol, not glycerol, was used in the membrane preparation, phenylmethanesulphonyl fluoride was omitted, and asolectin was omitted from the ion-exchange chromatography. Where possible ultrapure chemicals (Fluka) were used, to minimize contamination by manganese and eliminate the Mn^{2+} signal from W-band EPR spectra. The ultrapure chemicals were dithiothreitol (Mn $\leq$ 5 ppm), ethylenediaminetetraacetic acid (Mn $\leq$ 5 ppm), ethylene glycol (Mn $\leq$ 0.05 ppm), KCl (Mn $\leq$ 0.01 ppm), NaCl (Mn $\leq$ 0.01 ppm), and Trizma base (Mn $\leq$ 5 ppm). Purified complex I was concentrated to 70 mg mL^{-1} (quantified by the Pierce bicinchoninic acid

assay) using Vivaspin centrifugal concentrators with a 100 kDa cutoff, and imported into an anaerobic glovebox ($O_2 \sim 2$ ppm). Typically, it was reduced by 10 mM NADH (to ca. -0.4 V), or by 140 mM NAD^+ and 2 mM NADH (to ca. -0.3 V), to a final concentration of 55 mg mL^{-1} (~ 55 μM), then the samples were frozen anaerobically in liquid nitrogen.

4.4 Results

In this section, the results of the experimentally obtained DEER traces from samples reduced to -0.3 V and -0.4 V will be compared to the simulated DEER traces calculated for models A, B and C. The redox potentials of the EPR active clusters in complex I (see Table 4.1) are such that it impossible to selectively reduce only two clusters - which would make the interpretation of the DEER traces much simpler. Signal N5 could not be detected in any echo-detected EPR spectra, not even below 5 K, presumably because it relaxes too fast (section 4.1). However, since the origin of N5 can be deduced once signal N4 is assigned, the 'absence' of N5 in pulse EPR spectra is actually advantageous: In samples reduced to -0.4 V, dipolar interactions can therefore potentially arise from the clusters giving rise to signals N1b, N2, N3 and N4; whereas in samples reduced to -0.3 V, N1b is largely oxidised and a DEER effect can only result from N2, N3 and N4. The temperature dependence of N1b, N2, N3 and N4 was found to be similar in X-band echo-detected experiments compared to X-band CW experiments. Consequently, raising the temperature allows selection of N1b and N2 only, but this is not useful since these two signals could already be assigned unambiguously. Selection of N3 and N4 only - which would be useful - cannot be achieved either through adjustment of the potential nor through adjustment of the sample temperature.

In order to be able to simulate DEER traces for models A, B and C, equation 4.11 shows that the following have to be established: (1) Spin Hamiltonian parameters for all the clusters, (2) the g-axis orientations for each cluster, (3) the spin projection factors k_{Ai} and k_{Bi} for each Fe ion in each cluster, (4) the coordinates for Fe ion in each cluster

to determine r_{ij}. Each of these points will be discussed in detail in section 4.4.1 below. The problem of overlapping Fe-S cluster spectra, and hence the problem of simulating orientation selective DEER traces arising from dipolar interactions between several cluster pairs, will be tackled in section 4.4.2. Qualitative and quantitative analyses of the experimentally obtained DEER traces will conclude this section.

4.4.1 Determination of the simulation input parameters

Fe-S cluster principal g-values and g-strain values

In order to obtain a reliable set of g values and g-strain values, W-band measurements were carried out and compared to X-band CW measurements. Fig. 4.6 shows the spectra overlaid on a g-value scale to remove the mw frequency and magnetic field dependence. All spectral peak positions are the same at the two different mw frequencies, indicating that they correspond to the principal g values of the observed reduced clusters. Furthermore, any dipolar or exchange interactions between the EPR visible clusters must therefore be less than about 50 MHz (the X-band linewidth), so that distances between the observed clusters are greater than approximately 10 Å (depending on the spin projection factors (SPFs), see below).

The set of g values and g strain values that describe the data at both X-band and W-band (see simulations in Fig. 4.6, shown in red) is presented in table 4.2. The g values obtained here are also in good agreement with those previously reported for *B. taurus* complex I [143].

As expected from their reduction potentials (see Table 4.1) N2, N3 and N4 contribute significantly at both -0.4 V and -0.3 V, whereas N1b is substoichiometric (its intensity is small at -0.4 V and essentially absent at -0.3 V). The X-band CW signal amplitudes are summarised in Table 4.2.

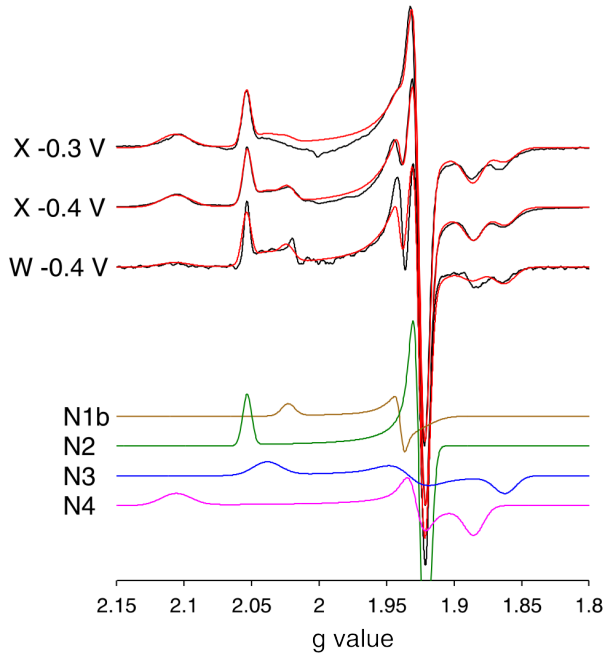


Figure 4.6: **EPR spectra of complex I from B. taurus, and simulations for N1b, N2, N3 and N4.** X-band CW EPR spectra of complex I reduced to -0.4 V and -0.3 V were recorded at 12 K, at 9.408 and 9.393 GHz, respectively. The W-band (93.875 GHz) echo-detected EPR spectrum (numerical 1^{st} derivative representation) of complex I reduced to -0.4 V was recorded at 8.5 K. The three spectra (black) are compared to one another and to their simulated spectra (*red*, comprising N1b, N2, N3 and N4, see Table 4.2), by plotting all the spectra on the g-value scale. N1b, N2, N3 and N4 are shown for the -0.4 V X-band spectrum. At -0.3 V N1b is essentially absent. See section 4.3.1 for the measurement parameters. Taken from ref. [135].

Table 4.2: **Principal g values, g-strain parameters, and relative intensities of spectra from the four reduced Fe-S clusters observed in *B. taurus* complex I.** [a] Principal g values and g-strain values are derived from modeling X- and W-band spectra (see Fig.4.6). [b] Relative amplitudes are from CW X-band and echo-detected spectra using the DEER detection-pulse sequence. Amplitude % values from -0.4 V samples are next to those from -0.3 V samples (in brackets). The echo amplitude is dependent upon the electron-spin decay (phase memory) time, so the amplitudes may not equate to the stoichiometries of the reduced clusters. Taken from ref. [135].

Signal	Principal g value[a]			g strain[a]			Amplitude (%)[b]	
	g_x	g_y	g_z	g_x	g_y	g_z	EPR	DEER
N1b	1.927	1.939	2.023	0.029	0.005	0.011	9(3)	4(1)
N2	1.921	1.927	2.054	0.009	0.008	0.008	32(34)	61(55)
N3	1.863	1.934	2.039	0.018	0.027	0.024	26(23)	9(13)
N4	1.886	1.928	2.107	0.017	0.012	0.026	33(40)	26(31)

Fe-S cluster g-axes orientations

The only observed [2Fe-2S] cluster (2Fe[75]) has an axial **g**-matrix (signal N1b). Two g_3-axis orientations are considered here: one along the Fe-Fe axis (see Fig. 4.5), as found in some Rieske-type [2Fe-2S] clusters [173, 174], and one normal to the [2Fe-2S] plane, as found in ferredoxin [2Fe-2S] clusters [173, 175]. g_1 and g_2 can take any direction perpendicular to the g_3 axis without changing the simulations.

For ferredoxin-type [4Fe-4S] clusters (as is the case in complex I), several studies report the g_3 axis to be perpendicular or very nearly perpendicular to the Fe^{2+}-Fe^{2+} and $Fe^{2.5+}$-$Fe^{2.5+}$ vectors, as shown by single crystal EPR studies of a model $(Et_4N)_2[Fe_4S_4(SBenz)_4]$ compound [27] and single crystal EPR of the two terminal iron-sulfur centres F_A and F_B in Photosystem I from *Synechococcus elongatus* [176]. For the reduced proximal [4Fe-4S] cluster in *D. gigas* [NiFe]-hydrogenase, the axis perpendicular to the ferrous and mixed valence pairs was found to be the g_2 axis [177]. In all cases, the principal g_3 axis points through the faces of the Fe-S clusters.

Signal N2 is close to axial, so that as in N1b the g_1 and g_2 axes can take any direction perpendicular to g_3. Consequently, three possibilities of arranging the g axes in cluster 4Fe[PS] (N2) need to be considered. The orientations of g_1 and g_2 are important when the **g** matrix is rhombic, as is the case for N3 and N4. Two generally accepted possibilities were included in the simulations: g_1 and g_2 point along the Fe^{2+}-Fe^{2+} and the $Fe^{2.5+}$-$Fe^{2.5+}$ vectors, or they are rotated by 45^o to be normal to the faces that contain an Fe^{2+} and an $Fe^{2.5+}$ (as shown in 4.5). For N3 and N4, there are therefore 12 possibilities of arranging the g axes.

Spin projection factors

The spin projection factor (SPF), k_i, gives the projection of the 'local' spin onto the spin of the entire cluster. It is assumed that the zero-field splitting of the individual Fe ions is much smaller than the spin coupling between two Fe ions (strong coupling limit)

[168, 178, 179], so that a simple theorem applies [180]:

$$\sum_i k(\mathsf{Fe}_i) = 1. \tag{4.13}$$

Knowledge of some of the SPFs therefore often allows calculation of the others. Different coupling schemes result in different SPFs. As confirmed by Mössbauer spectroscopy, $[2Fe\text{-}2S]^+$ clusters contain an Fe^{3+} and an Fe^{2+} ion [181]. For simple 2Fe ferredoxin-type clusters (such as 2Fe[75] (N1b) in complex I), only strong antiferromagnetic coupling between the $S = 5/2$ ferric ion (Fe^{3+}) and the $S = 2$ ferrous ion (Fe^{2+}) results in the experimentally observed $S_{total} = 1/2$ ground state, which is well separated from the excited states. In this case $k(Fe^{3+}) = k_2 = +7/3$ and $k(Fe^{2+}) = k_1 = -4/3$ [3] (see Table 4.3). However, there are two possible assignments for k_1 and k_2 since the Fe^{2+} and the Fe^{3+} could be in either subsite.

Table 4.3: **Spin projection factors for $[2Fe\text{-}2S]^+$ [3] and $[4Fe\text{-}4S]^+$ clusters [180].** Notation for spin states: |spin state of $Fe^{2.5+}$ pair or of Fe^{3+} | spin state of Fe^{2+} pair or of Fe^2 | spin ground state of cluster ⟩

$[2Fe\text{-}2S]^+$	Spin state	k_1 (Fe^{2+})	k_1 (Fe^{2+})	
	$\|5/2\|2\|1/2\rangle$	-4/3	+7/3	
$[4Fe\text{-}4S]^+$	Spin state	k_3 (Fe^{2+})	k_4 ($Fe^{2.5+}$)	
	$\|5/2\|2\|1/2\rangle$ & $\|7/2\|3\|1/2\rangle$	+1.35	-0.85	ferredoxin-type clusters
	$\|5/2\|2\|1/2\rangle$	+1.17	-0.67	ferredoxin-type clusters
	$\|7/2\|3\|1/2\rangle$	+1.50	-1.00	aconitase-type clusters
	$\|9/2\|4\|1/2\rangle$	+1.83	-1.33	aconitase-type clusters

Many different couplings are possible in reduced 4Fe clusters between the (formally) three Fe^{2+} and one Fe^{3+} [5]. Experimental isotropic hyperfine constants obtained *via* Mössbauer spectroscopy [182] and theoretical calculations performed on models of 1Fe, 2Fe and 4Fe compounds [7] have indicated that $[4Fe\text{-}4S]^+$ clusters contain delocalised valence electrons over a Fe^{2+}-Fe^{2+} and a $Fe^{2.5+}$-$Fe^{2.5+}$ pair. Mouesca *et al.* [180] compiled

a set of calculated and semi-empirical SPFs based on a large survey of the measurements for many different systems containing Fe-S clusters in various oxidation states and with different spin-coupling schemes. These different schemes for 4Fe clusters, and the resulting SPFs are summarised in Table 4.3 (notation for spin states: |spin state of $Fe^{2.5+}$ pair | spin state of Fe^{2+} pair | spin ground state of cluster $\rangle$). Note that the $|5/2|2|1/2\rangle$ and the $|7/2|3|1/2\rangle$ states, and the mixed state resulting in average (semi-empirical) SPF values relate to ferredoxin-type clusters, whereas the SPFs resulting from the $|9/2|4|1/2\rangle$ state are more appropriate for aconitase-type clusters. The latter are named after the unusual 4Fe cluster found in the activated aconitase enzyme in which one of the Fe has a water or hydroxyl ligand (the remaining three Fe coordinate cysteines) [38], making the coordination of the cluster unusual and less symmetric. The last set of SPFs was therefore only included as a sensitivity test in the calculations, since the Fe-S clusters in complex I are ferredoxin-type clusters (all cysteine ligated, with the exception of cluster 4Fe[75] which has one ligating histidine, but this cluster is not involved in this analysis).

For each set of SPFs, there are six possible arrangements since it is not known which irons are the ferrous pair which are the mixed valence pair. To ensure a manageable computation time, the set of SPFs of each 4Fe cluster was the same in any given simulation.

In summary, the number of possible SPFs and *g*-axis orientations combinations for any given set of 4Fe SPFs are: N1b (4), N2 (18), N3 (72), N4 (72). For example, for the N2-N4 pair (Fig. 4.5), there are 18 x 72 x 4 = 5184 possible combinations.

Intercluster distances

The structure of the hydrophilic domain of *T. thermophilus* complex I [51] is used as a basis for interpreting the DEER data from the *B. taurus* enzyme and a detailed analysis can be found in ref. [135]. To evaluate the validity of taking the cofactor arrangement in *T. thermophilus* to determine the intercluster distances required for simulation of the DEER traces, the sequences of *E. coli*, *T. thermophilus* and *B. taurus* were compared

and a structural model of the *B. taurus* enzyme was generated.[1] It was found that any mismatches of the bovine structure compared to the *T. thermophilus* structure are almost exclusively confined to the surface, and that the majority occur in the large domain of the 75 kDa subunit, which do not have to be considered here because the bovine enzyme lacks the 4Fe cluster in this subunit. Furthermore the sequence conservation within 10 Å of the conserved Fe-S clusters is very high (50-80%) - much higher compared to the rest of the protein (20-50%) - reflecting the importance of the cofactors in enzyme catalysis. Although residue differences close to one or more clusters will affect their spectra and/or their reduction potentials - indeed the EPR spectra of *T. thermophilus*, *E. coli* and *B. taurus* complex I differ and midpoint potentials of the clusters do vary - they are highly unlikely to affect the structure. Consequently, the cofactor arrangement in *T. thermophilus* is considered to be an excellent model for the interpretation of the DEER data from the bovine enzyme.

4.4.2 Overlap of Fe-S cluster spectra

Because of the spectral overlap of the observed clusters in complex I, each DEER trace is the weighed sum of the refocused echo intensity from each paramagnetic cluster:

$$y_{sim}^{Tot}(t) = A^{N2} y_{sim}^{N2}(t) + A^{N3} y_{sim}^{N3}(t) + A^{N4} y_{sim}^{N4}(t) + A^{N1b} y_{sim}^{N1b}(t). \tag{4.14}$$

The term A^{Nx} is the refocused echo intensity of the detection spin Nx, obtained using the DEER detection pulse sequence. Although A^{Nx} depends on $\vec{B}_0$, it is a constant in equation 4.14 because $\vec{B}_0$ is unchanged during an experiment. The simulated DEER trace of the detection spin is given by $y_{sim}^{Nx}(t)$ and is obtained from equation 4.12. In principle three pairs can contribute to any one $y_{sim}^{Nx}(t)$. For example for $y_{sim}^{N2}(t)$ the contributing pairs are N2-N3, N2-N4 and N2-N1b. However, this can be greatly simplified as will be explained in section 4.4.3.

[1]The structural modeling of *B. taurus* complex I was done by Dr. Alan Robinson, Mitochondrial Biology Unit, MRC, Cambridge.

In the simulations each detection spin is coupled only to one pump spin so that equation 4.14 only contains four terms. The possibility of a single detection spin being influenced simultaneously by two pump spins is not considered. Three-spin correlations contain sum and difference frequencies because the local field at the detection spin is changed by flipping two pump spins. Because the **g**-matrix anisotropies of the Fe-S clusters observed in complex I are large, the resonances from each cluster will in general occur at different frequencies for a particular orientation of $\vec{B}_0$. Three interacting spins are therefore highly unlikely to be a major influence in the dipolar frequencies observed in complex I. Three-spin correlation in DEER has been investigated in model spin systems contain nitroxide radicals, in which there is (at X-band) essentially no mw pulse orientation selection [183].

4.4.3 Analysis of DEER traces

Qualitative analysis

The intercluster distances can be estimated from the dominant period of oscillation, ranging from 0.5 to 0.7 μs ($\omega_{dd}/2\pi = 2.0 - 1.4$ MHz) in all DEER traces and as exemplified by the trace given in Fig. 4.7.

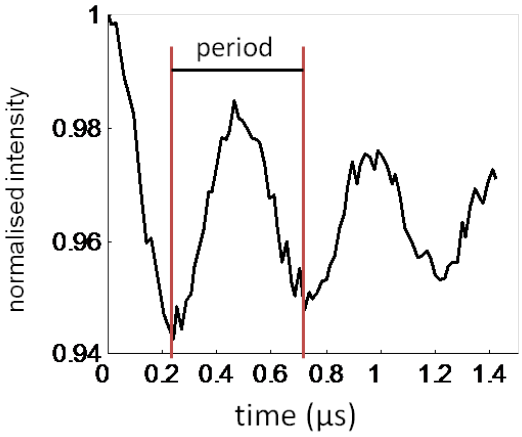


Figure 4.7: **DEER trace illustrating typical oscillation period.** The trace results from the sample reduced to -0.4 V, $B_0 = 337.7$, $\omega_A = 9.1104$, $\omega_B = 9.7269$. The oscillation period is 0.5 μs in this case, but similar oscillation periods varying between $0.5-0.7$ μs were observed in all DEER measurements taken. See section 4.3.1 for measurement parameters.

Assuming that the dominant oscillations corresponds to the intense (perpendicular) feature in the powder-averaged dipolar spectrum (the Pake pattern), and taking reasonable values for the SPFs ($k_{1,2} = 1.35$ and $k_{3,4} = -0.85$, see Table 4.3), then 10 Å equates to 70-150 MHz, 20 Å to 2-5 MHz, 30 Å to 1-3 MHz and 40 Å to 0.7-1.3 MHz. Even though the exact values depend on the assignment of the SPFs, this rough analysis shows that the intercluster distances approximately fall into the range of 20 to 35 Å. Table 4.4 summarises the intercluster distances for models A, B and C. Distances that would contribute to higher frequency oscillations than are observed are shown in gray. Long intercluster distances which at most contribute an indiscernible monotonic decay (but no oscillation) are in blue. The cluster giving rise to N5 also only contributes at most to the signal decay because its DEER electron-spin echo is not observed at 10 K (Table 4.2). Models A and C have no intercluster distances between 20 and 35 Å , whereas model B does (highlighted in red), indicating that model B is most likely to be correct. However, given the sensitivity of the dipolar frequencies to the SPF arrangements, a quantitative analysis is indispensable to ascertain the correct model.

Table 4.4: **Intercluster distances for models A, B and C.** Short distances that would yield higher frequency oscillations that are not observed are in gray; long distances that would at most contribute a weak monotonic decay to the baseline are in blue; distances that fall into the predicted range from the observed DEER oscillation periods are in red.

	N2-N4	N3-N4	N1b-N4	N1b-N3	N2-N3	N1b-N2
Model A	49.1	17.4	13.5			
Model B	25.8	40.7	35.0	13.9	60.9	51.4
Model C	13.6	49.4	41.2			

The cluster pairs which contribute most intensity to the observed DEER traces can also be identified. Figure 4.8 gives an example of 'matching' DEER traces (recorded at the same pump and detection frequencies and similar field positions) from samples poised at -0.3 V and -0.4 V. Signal N1b is only observed in the -0.4 V sample (Table 4.2, last column) and the almost overlapping DEER traces obtained from the two samples with and without the reduced 2Fe[75] cluster suggests that N1b cannot contribute significantly

to the observed DEER traces. With this additional information, it is most likely the N2-N4 cluster pair (in model B) which gives rise to the observed DEER oscillations.

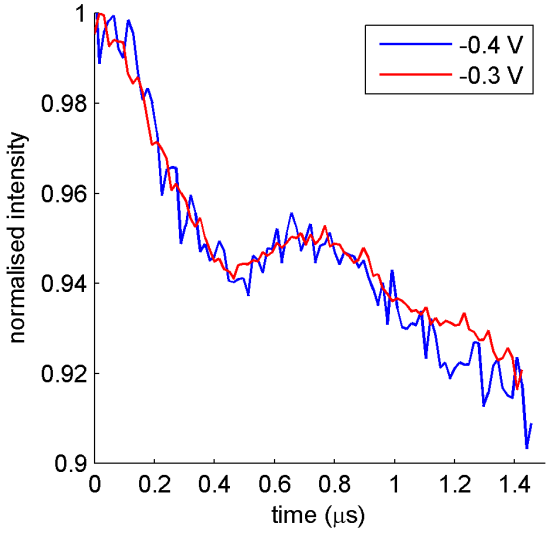


Figure 4.8: **Comparison of DEER trace obtained from reduced to -0.4 V and -0.3 V, measured under the same conditions.** -0.4 V (blue): $B_0 = 347.3$, $\omega_A = 9.3682$, $\omega_B = 9.1888$; -0.3 V (red): $B_0 = 347.3$, $\omega_A = 9.3685$, $\omega_B = 9.1889$. See section 4.3.1 for measurement parameters. The data are not background corrected.

Quantitative analysis

A quantitative evaluation of each model required simulation and analysis of a comprehensive set of DEER traces. Because the dipolar frequencies depend on the orientation of a cluster pair with respect to the spectrometer's magnetic field $\vec{B}_0$, as well as on the SPFs and on $1/r^3$, a unique description of the data is only obtained when a sufficient set of orientations are interrogated by varying the detection and pump pulse positions (Fig. 4.4). Figure 4.9 depicts the pump (red) and detection (black) pulse positions used to measure the DEER traces in Figures 4.10, 4.11, 4.13, and 4.12.

The spin Hamiltonian parameters and the procedures to account for the g-axis orientation for each paramagnetic cluster (relative to the molecular frame), the SPFs and the coordinates of each Fe in each paramagnetic cluster are described in section 4.4.1. Initially, the DEER traces for the detection spins have to be calculated ($y_{sim}^{Nx}(t)$ in equa-

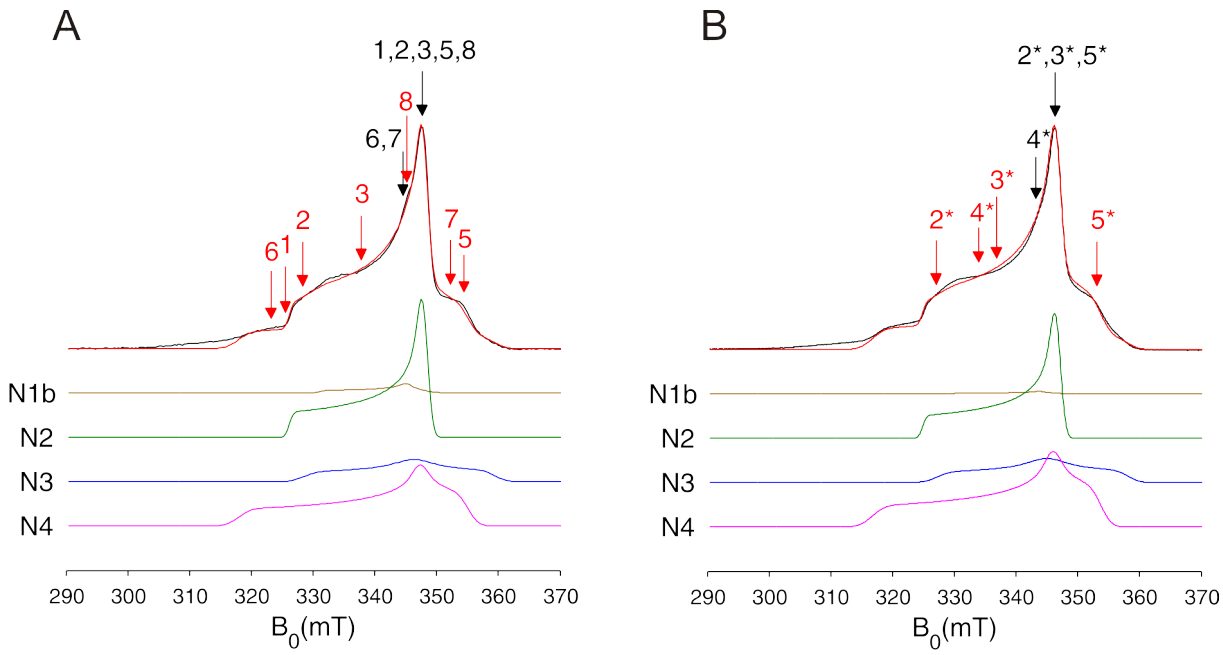


Figure 4.9: **X-band echo-detected EPR spectra of complex I reduced to -0.4 V (A) and -0.3 V (B) recorded at 10 K, simulated with the components N1b, N2, N3 and N4.** The data are in black, the simulation (see Table 4.2) is in red. The markers correspond to the pump (red) and detection (black) pulse positions at which the DEER traces in Figures 4.10, 4.11, 4.12 and 4.13 were recorded. The field positions (mT) and detection (ω_A, GHz) and pump (ω_B, GHz) frequencies were as follows: (1) $B_0 = 337.7$, $\omega_A = 9.1104$, $\omega_B = 9.7269$; (2) $B_0 = 340.5$, $\omega_A = 9.1888$, $\omega_B = 9.7267$; (3) $B_0 = 340.4$, $\omega_A = 9.1810$, $\omega_B = 9.4500$; (5) $B_0 = 347.3$, $\omega_A = 9.3682$, $\omega_B = 9.1888$; (6) $B_0 = 335.3$, $\omega_A = 9.1105$, $\omega_B = 9.7269$; (7) $B_0 = 349.0$, $\omega_A = 9.4882$, $\omega_B = 9.3083$; (8) $B_0 = 348.0$, $\omega_A = 9.3860$, $\omega_B = 9.4556$; (2*) $B_0 = 340.6$, $\omega_A = 9.1887$, $\omega_B = 9.7266$; (3*) $B_0 = 345.9$, $\omega_A = 9.3382$, $\omega_B = 9.5998$; (4*) $B_0 = 345.9$, $\omega_A = 9.3382$, $\omega_B = 9.5998$; (5*) $B_0 = 347.3$, $\omega_A = 9.3685$, $\omega_B = 9.1889$. See section 4.3.1 for measurement parameters. Taken from supporting information of ref. [135].

tion 4.14). However, some pair combinations may be omitted in light of the qualitative analysis above.

While $y_{sim}^{N2}(t)$ is comprised of the N2-N3, N2-N4 and N2-N1b pairs, the N2-N3 and N2-N1b distances (61 Å and 51 Å respectively) are too long to yield oscillations in any model A, B or C. Therefore only the N2-N4 pair needs to be considered. Regarding $y_{sim}^{N3}(t)$, the N3-N4 distance may contribute (at least in models A and B, see Table 4.4) while again the N3-N2 distance is too long. With 14 Å the N3-N1b distance is too short (higher frequency oscillations would be observed) and furthermore the modulation depth c_{mod} (see equation 4.12) of the N3-N1b contribution is low because N1b is only present

substoichiometrically. All the pairs N4-N2, N4-N3 and N4-N1b may contribute to $y_{sim}^{N4}(t)$, but like N3-N1b, the N4-N1b contribution must be of low intensity.

Any combinations involving N1b as the detection spin ($A^{N1b}y_{sim}^{N1b}(t)$) are small because A^{N1b} is very small. Furthermore the N1b-N3 (14 Å) and N1b-N2 (51 Å) distances are too short and too long respectively to merit inclusion in the simulations. Only the unknown N1b-N4 distance is worth considering, even though its contribution is expected to be negligible. All the different pair combinations tested to yield the total simulated DEER trace $y_{sim}^{Tot}(t)$ (equation 4.14) are summarised in Table 4.5.

Next, the total simulated traces have to be fitted to the experimental data. To allow simultaneous fitting of both the baseline and the DEER oscillations, the data were directly fitted in the time domain. This also avoids difficulties associated with the Fourier transformation of the DEER traces with large unmodulated contributions (which would give rise to a very large zero-frequency peak) and was done previously for nitroxide radicals [158]. Each simulated DEER trace is dampened by an exponential decay ($c_1(t)\exp(-t/T)$) to account for signal relaxation and a baseline offset is added (c_2) to account for unmodulated intensity that is not correctly described because of inaccuracies in the refocused echo intensity A^{Nx} and the g-axis orientations. The residual R is then calculated by equation 4.15 and the best fits to the experimental traces $y_{\exp}(t)$ were identified by inspecting the fits with the lowest squared residual values (the sum of R^2 over all 11 DEER traces, for every set of simulation parameters).

$$R = y_{\exp}(t) - (c_1 y_{sim}^{Tot}(t)\exp(-t/T) + c_2). \tag{4.15}$$

In order to determine the set of simulations that best fits the experimental data, an initial screen of all the data (with all of the different combinations detailed in Table 4.5) included constant c_2. This maximises the sensitivity of the fitting to the oscillation period of the experimental DEER traces, and consequently to the SPFs and intercluster distances. The initial screen ruled out approximately 95 % of the combinations. The remaining simula-

Table 4.5: **Combination of cluster pairs tested in simulations of the experimental DEER traces and the respective intercluster distances.** Each simulation was performed for four sets of SPFs: $k_{1,2} = +1.17$ and $k_{3,4} = -0.67$; $k_{1,2} = +1.35$ and $k_{3,4} = -0.85$; $k_{1,2} = +1.50$ and $k_{3,4} = -1.00$; $k_{1,2} = +1.83$ and $k_{3,4} = -1.33$. Taken from supporting information of ref. [135].

Combination	Detection - pump	Model A r (Å)	Model B r (Å)	Model C r (Å)
Ia	N2-N4	49.1	25.8	13.6
	N3-N4	17.4	40.7	49.4
	N4-N2	49.1	25.8	13.6
Ib	N2-N4	49.1	25.8	13.6
	N3-N4	17.4	40.7	49.4
	N4-N2	49.1	25.8	13.6
	N1b-N4	13.5	35.0	41.2
Ic	N2-N4	49.1	25.8	13.6
	N3-N4	17.4	40.7	49.4
	N4-N2	49.1	25.8	13.6
	N1b-N3	13.9	13.9	13.9
IIa	N2-N4	49.1	25.8	13.6
	N3-N4	17.4	40.7	49.4
	N4-N3	17.4	40.7	49.4
IIb	N2-N4	49.1	25.8	13.6
	N3-N4	17.4	40.7	49.4
	N4-N3	17.4	40.7	49.4
	N1b-N4	13.5	35.0	41.2
IIc	N2-N4	49.1	25.8	13.6
	N3-N4	17.4	40.7	49.4
	N4-N3	17.4	40.7	49.4
	N1b-N3	13.9	13.9	13.9
III	N2-N4	49.1	25.8	13.6
	N3-N4	17.4	40.7	49.4
	N4-N1b	13.5	35.0	41.2
	N1b-N3	13.9	13.9	13.9
IV	N2-N4	not tested		13.6
	N3-N1b			13.9
	N4-N2			13.6
	N1b-N4			41.2
V	N2-N4	not tested		13.6
	N3-N1b			13.9
	N4-N1b			41.2
	N1b-N4			41.2

tions were further reduced by setting $c_2 = 0$, thereby maximising the sensitivity of the fitting to the modulation depth and thus the g-axis orientations. The lowest residual fits were then inspected by eye, with and without a baseline offset. None of the remaining combinations, with any set of SPFs, g-axis orientations and cluster pair combinations, yielded any reasonable fits for models A and C. By contrast, about 1 % of the total number of simulations produced satisfactory fits for model B. The resulting 'best fits' for all three models are shown in Figures 4.10 and 4.11. These two sets of fits employed the SPFs from the $|5/2|2|1/2\rangle$ state (Fig. 4.10) and the mixed $|5/2|2|1/2\rangle$ & $|7/2|3|1/2\rangle$ state (Fig. 4.11) and include the baseline offset constant c_2 to highlight the match with the experimentally observed oscillation period.

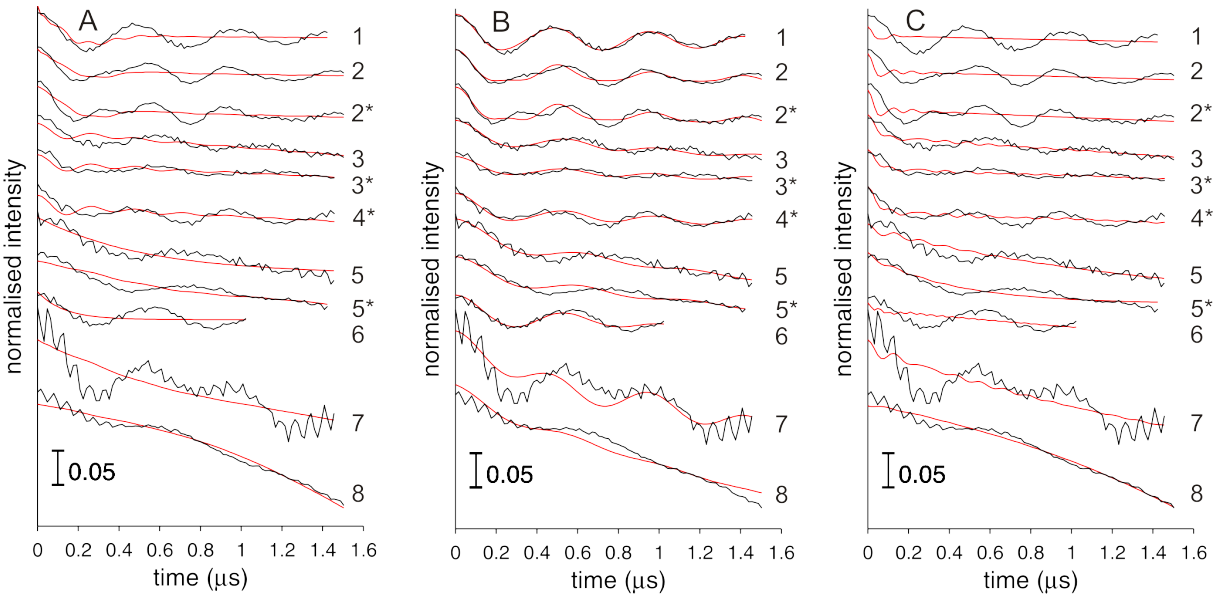


Figure 4.10: **DEER spectra from *B. taurus* complex I reduced to -0.4 V and -0.3 V measured at 10 K, with the best fit simulations for SPFs $k_{1,2}$ = +1.17 and $k_{3,4}$ = -0.67.** DEER traces (black) and best fit simulations (red) for models A, B and C. Traces marked * refer to the -0.3 V sample, all other spectra are from the -0.4 V sample. Pump and detection pulse positions are given in Fig. 4.9. All traces are normalised to the intensity at $t = 0$, and the intensity changes are denoted by the scale bar. Taken from supporting information of ref. [135].

Only model B describes the experimental data well, whereas models A and C produce simulations with completely inappropriate oscillation periods. The intercluster distances

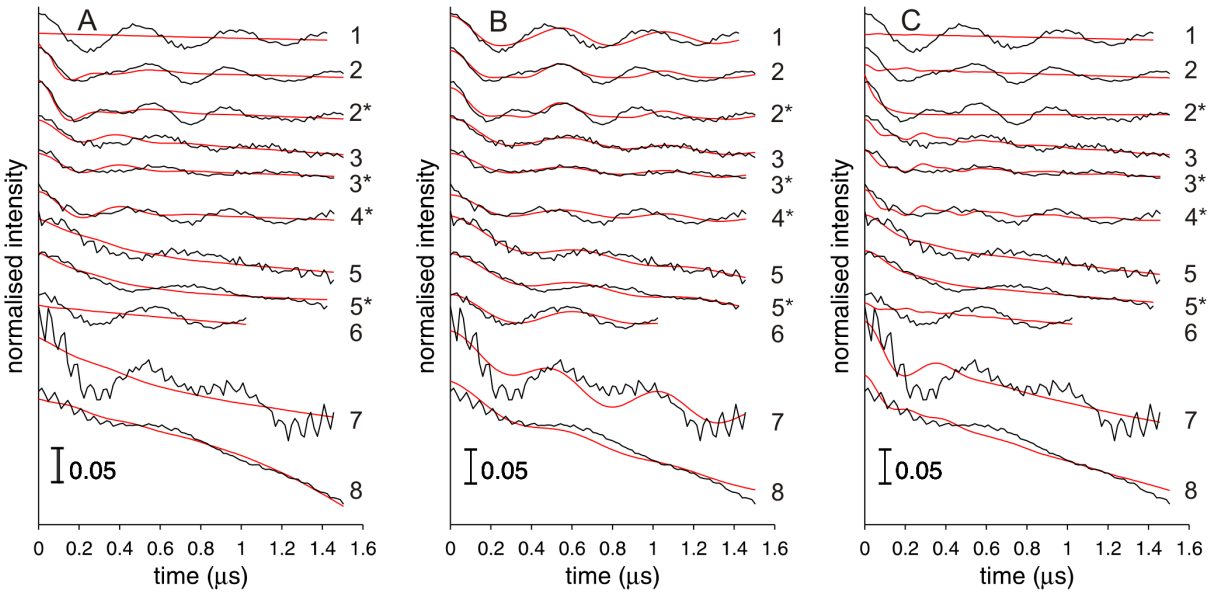


Figure 4.11: **DEER spectra from *B. taurus* complex I reduced to -0.4 V and -0.3 V measured at 10 K, with the best fit simulations for SPFs $k_{1,2}$ = +1.35 and $k_{3,4}$ = -0.85.** DEER traces (black) and best fit simulations (red) for models A, B and C. Traces marked * refer to the -0.3 V sample, all other spectra are from the -0.4 V sample. Pump and detection pulse positions are given in Fig. 4.9. All traces are normalised to the intensity at $t = 0$, and the intensity changes are denoted by the scale bar. Taken from supporting information of ref. [135].

in models A and C are therefore entirely inconsistent with the experimental data. This conclusion is supported further by Figure 4.12, which shows the best fits for each model with just an exponential decay ($c_2 = 0$). Clearly, while the g-axis orientations are not completely accurate in model B, it is meaningless to speak of any fit for models A and C.

Even when no baseline correction is done at all (i.e. equation 4.15 becomes $R = y_{\text{exp}}(t) - y_{sim}^{Tot}(t)$), the lowest residual squared fits for model B still look reasonable (Fig. 4.13). Both Figures 4.12 and 4.13 show fits with SPFs from the $|5/2|2|1/2\rangle$ state of the 4Fe clusters, but fits with SPFs from the mixed spin state yielded similar quality fits (compare Figures 4.10 and 4.11). Using SPFs from the $|7/2|3|1/2\rangle$ state produced lower quality fits and SPFs from the $|9/2|4|1/2\rangle$ state did not produce any satisfactory fits even for model B.

In the following the effect of changing the cluster pairs (see Table 4.5) on the simulations and their fit to the experimental data is discussed. As no simulations yielded any

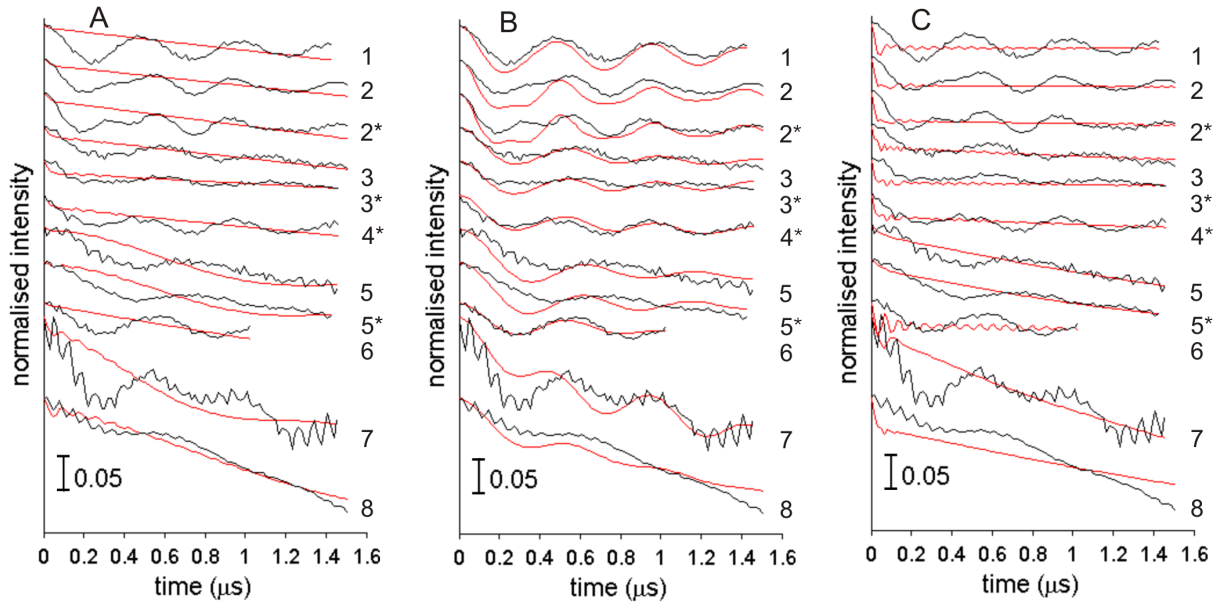


Figure 4.12: **DEER spectra from *B. taurus* complex I reduced to -0.4 V and -0.3 V measured at 10 K, including the best fit simulations with exponential baseline for SPFs $k_{1,2}$ = +1.17 and $k_{3,4}$ = -0.67.** DEER traces (black) and simulations (red) for models A, B and C. Traces marked * refer to the -0.3 V sample, all other spectra are from the -0.4 V sample. Pump and detection pulse positions are given in Fig. 4.9. All traces are normalised to the intensity at $t = 0$, and the intensity changes are denoted by the scale bar.

reasonable fits for models A and C, any references to the quality of the fit regard model B only.

As discussed above and embodied in combinations I-III, the only significant contribution to $y_{sim}^{N2}(t)$ is from the N2-N4 pair, and the only significant contributor to $y_{sim}^{N3}(t)$ is from N3-N4 - regardless of the model. Combinations Ia and IIa tested the contribution of N4-N2 and N4-N3 to $y_{sim}^{N4}(t)$, respectively, and omitted any contribution from $y_{sim}^{N1b}(t)$, which is expected to be small. Pair combinations Ia and IIa yielded very similar fits, although fit Ia was marginally better. Possible contributions from $y_{sim}^{N1b}(t)$ were added in combinations Ib, Ic and IIb, IIc. The overall fits were only very slightly improved, confirming that $y_{sim}^{N1b}(t)$ contributes little. The best fits given in the Figures above result from combination IIb for model A and combination Ib for models B and C.

Combination III was included to test the N4-N1b and N1b-N3 pair contributions, even though they will be small. The fits were slightly less satisfactory, so it was concluded that

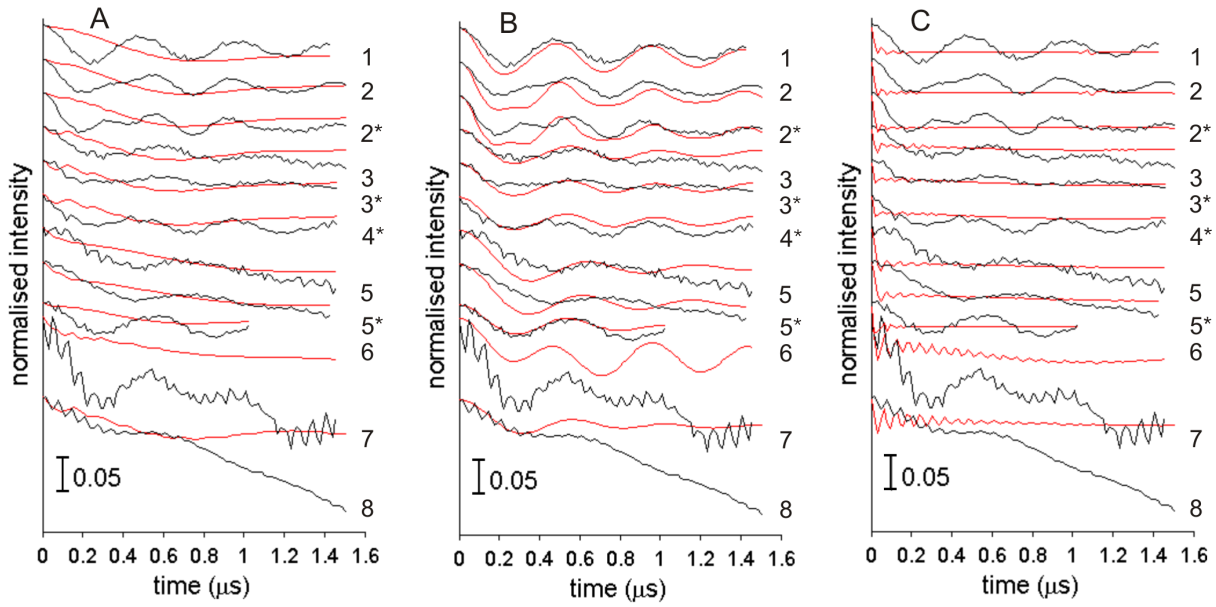


Figure 4.13: **DEER spectra from *B. taurus* complex I reduced to -0.4 V and -0.3 V measured at 10 K, including the best fit simulations with no baseline correction for SPFs $k_{1,2}$ = +1.17 and $k_{3,4}$ = -0.67.** DEER traces (black) and simulations (red) for models A, B and C. Traces marked * refer to the -0.3 V sample, all other spectra are from the -0.4 V sample. Pump and detection pulse positions are given in Fig. 4.9. All traces are normalised to the intensity at $t = 0$, and the intensity changes are denoted by the scale bar.

N4-N3 and/or N4-N2 are the main contributors to $y_{sim}^{N4}(t)$.

In model C the N3-N4 distance is very long (49.4 Å) and unlikely to be a significant contributor to the DEER trace. Combination IV and V, which take the N3-N1b pair as the contribution from $y_{sim}^{N3}(t)$ (even though N1b is of low intensity) were therefore tested. In model A and B the N3-N1b distance is farther from the experimentally observe DEER range of 20-35 Å then the N3-N4 distance, so that combination IV and V were not tested in these cases.

4.5 Conclusions

DEER is able to discriminate very clearly between the three models because of its $1/r^3$ dependence on distance. The best fits from model B do not match the experimental data perfectly because of inaccuracies in the structural model (one cluster might be tilted

slightly in *B. taurus* relative to the *T. thermophilus* enzyme, for example) and/or imprecisions in the g-axis orientations and SPFs. However, these imperfections do not detract from the unambiguous assignment of Signal N4 to the reduced cluster 4Fe[TY]1 (position 5 in the electron transfer chain, see Fig. 4.1). Model B is therefore correct.

The set of SPFs which yielded the best fits to the data were indeed those thought to best describe ferredoxin-type clusters. In all best-fit simulations with SPF sets of either $k_{1,2}$ = +1.17 and $k_{3,4}$ = -0.67 or $k_{1,2}$ = +1.35 and $k_{3,4}$ = -0.85, clusters 4Fe[PS] (N2) and 4Fe[TY]1 (N4) had the same g-axis orientations in which the g axes point through the faces of the Fe-S clusters (Fig. 4.14). As the N2 spectrum is almost axial, the orientations of the g_1 and g_2 axes for the 4Fe[PS] (N2) are tentative. Changing the g-axis orientation of 4Fe[51] (N3) was found to have little effect on the simulations, and changing the parameters for 2Fe[75] had essentially no effect, so that g-axis orientations cannot possibly be determined for these two clusters. These observations confirm that the N2-N4 distance is the major contributing distance to the observed DEER traces, as already predicted in the simple qualitative analysis.

Assignment of the SPFs is not straight forward as four combinations (Fig. 4.14) yielded good fits to the experimental data. The top left arrangement in Fig. 4.14 shows the SPF combination in which the principal g axis in clusters N2 (4Fe[PS]) and N4 (4Fe[TY]1) is perpendicular to both the Fe^{2+} pair and the $Fe^{2.5+}$ pair. This combination was judged to best describe the data and is used for the simulations of model B in Figures 4.10, 4.11 4.12, 4.13. However, it cannot be ruled out that either g_2 or g_1 are perpendicular to the ferrous and mixed valence pairs. Unsurprisingly, not all 36 possible SPF combinations yield good fits: only in a small subset do the SPF arrangements result in dipolar couplings of similar frequencies.

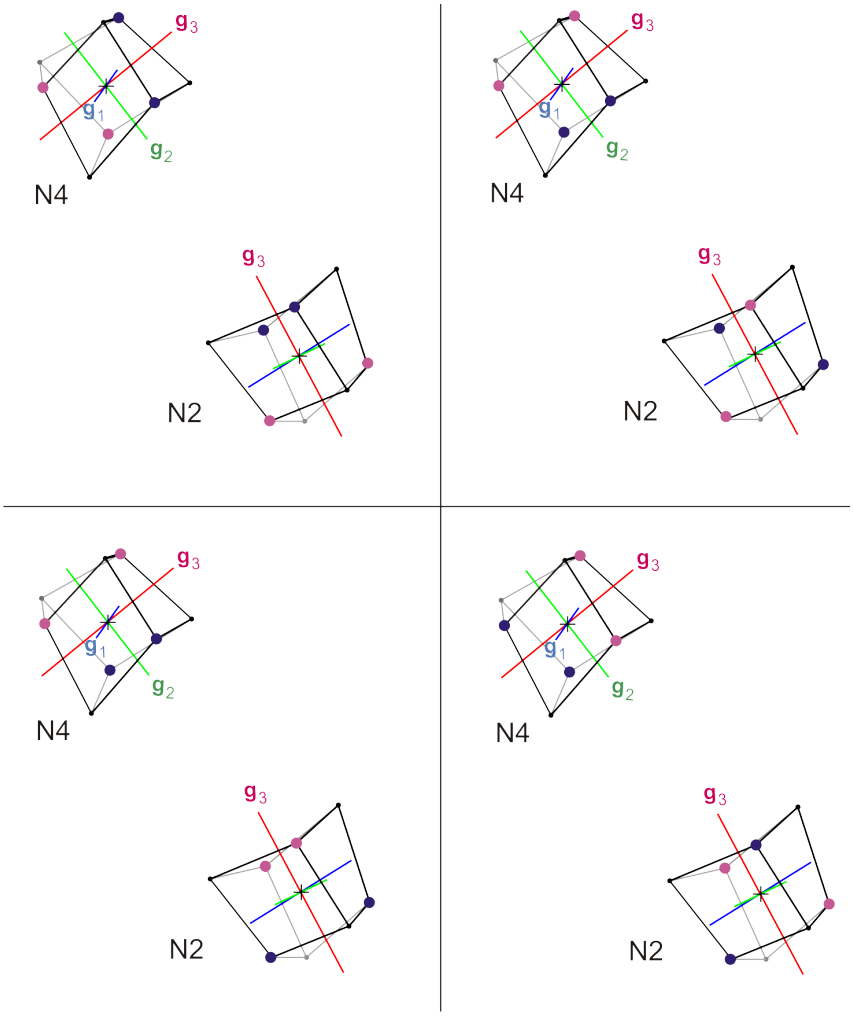


Figure 4.14: **Schematic representation of the $g-$axis orientations and four possible SPF assignments in clusters 4Fe[TY]1 (signal N4) and 4Fe[PS] (signal N2).** The $g-$axis orientations result from the best-fit simulations with either $k_{1,2}$ = +1.17 and $k_{3,4}$ = -0.67 or $k_{1,2}$ = +1.35 and $k_{3,4}$ = -0.85. The orientations of the g_1 and g_2 axes for the 4Fe[PS]/N2 are tentative since the N2 spectrum is almost axial. The Fe subsites are shown as large spheres, the S subsites as small spheres. Four arrangements of SPFs resulted in good fits to the experimental data: pink spheres represent the $k_{1,2}$ pair, and purple spheres the $k_{3,4}$ pair. The top left SPF combination is used for the simulations of model B Figures 4.10, 4.11 4.12, 4.13. The cluster coordinates are taken from the structure of the hydrophilic arm of *T. thermophilus* complex I, and the (x, y, z) coordinates used in the structure PDB file define the molecular axes. The x, y and z axes of the g matrices for N2 and N4, relative to the molecular axes, are as follows: N2, $x-$axis = $(-0.1791, -0.2317, -0.9562)$, $y-$axis = $(-0.4015, -0.1825, -0.8975)$, $z-$axis = $(-0.4895, 0.8710, 0.0419)$; N4, $x-$axis = $(-0.1791, -0.2317, -0.9562)$, $y-$axis = $(-0.6303, 0.7732, -0.0693)$, $z-$axis = $(0.7554, 0.5903, -0.2845)$.

4.6 Discussion

The application of DEER to measure the distances between complex paramagnetic metal centres is a natural extension from established studies of the distances between organic $S = 1/2$ radicals [158–161]. To date, there are few examples of DEER spectroscopy applied to Fe-S clusters. These include the binding of FAD-dependent ferredoxin reductase (which is nitroxide spin labeled) and [2Fe-2S] ferredoxin [142], and the analysis of DEER traces obtained from the active site Ni^{3+} and the [3Fe-4S] cluster in a [NiFe]-hydrogenase [163]. However, the complex magnetic interactions within Fe-S clusters (which become increasingly complicated as the cluster size increases), and the orientation selectivity of the DEER experiment resulting from the broadness of the spectra, complicates the analysis significantly for even just a single Fe-S cluster pair. *Five* such interacting paramagnetic centres (as in complex I) lead to a very complicated network of relationships. Determining the spacial relationship of the observed reduced clusters in complex I *ab initio* using DEER spectroscopy would therefore have been an unrealistic task. The successful determination of the origin of signal N4 in this work has relied on restricting the number of possible spacial arrangements of the paramagnetic centres, as well as their g-axis orientations, by making use of a the structural information available for complex I.

As the results presented here are from direct measurements of the intact enzyme, rather than on data from overexpressed subunits and enzyme fragments (which may not retain their structural or spectral integrity), a definitive assignment of the EPR signal N4 to a structurally defined cluster could be made.

The assignment of N4 to cluster 4Fe[TY]1 (position 5 in the electron transfer chain) is in agreement with the proposal by Hirst and coworkers [94] and also supports the consensus assignment of N1b to 2Fe[75] (position 2), N2 to 4Fe[PS] (position 7) and N3 to 4Fe[51] (position 1). The analysis presented here is entirely inconsistent with the assignment of N4 to 4Fe[75]C (position 3), as contended by Ohnishi *et al.* [143, 144], or with the assignment of N4 to 4Fe[TY]2, the alternative suggestion by Hirst and coworkers [94].

Although this analysis does not directly address the origin of signal N5, its assignment is implicit. The origin of N5 is also controversial, but the conclusion that model B is correct implies that N5 must arise from the 4Fe[75]C cluster (position 3). This is in disagreement with the assignment of N5 to cluster 4Fe[75]H (position 4) proposed by Ohnishi *et al.* [143]. This assignment cannot be correct as the mutation of the histidine ligand of the 4Fe[75]H cluster to alanine did not have any affect on signal N5 in *Yarrowia lipolytica* complex I (although it did prevent catalysis) [184]. By contrast, the assignment of signal N5 to 4Fe[75]C is consistent with all the extant data. It should be noted that signal N5 is rather unusual. It is observed only in a subset of eukaryotic enzymes (in the mitochondrial complexes from *B. taurus* and *Yarrowia lipolytica* but not from *E. coli*) and it relaxes very rapidly, interestingly more so at -0.4 V than at lower potential [145].

The obvious question that now remains is the implications of the assignment of signals N4 and N5 for the electron transfer in complex I. NADH oxidation is fast with respect to quinone reduction [185] and the NAD^+/NADH pool in the mitochondrial matrix is probably on average 90 % oxidised [145]. Because intramolecular electron transfer and NAD^+/NADH interconversion in complex I are fast [94], the Fe-S cluster are probably on average reduced to approximately -0.3 V, the NAD^+ potential. In the seven Fe-S cluster electron transfer chain, clusters in positions 1 (N3/4Fe[51]), 3 (N5/4Fe[75]C), 5 (N4/4Fe[TY]1) and 7 (N2/4Fe[PS]) should therefore be (at least partially) reduced. The cluster in position 2 (N1b/2Fe[75]) remains oxidised. The clusters in positions 4 (4Fe[75]H) and 6 (4Fe[TY]2) thus have unusual non $S = 1/2$ spin ground states, their EPR signals are too fast relaxing - or they could also remain oxidised. The latter possibility yields an alternating occupancy of the relay, as shown in Fig. 4.15. Notably, electrostatic interactions between the clusters would be sufficient to produce such an apparent 'roller-coaster' potential energy profile from a set of *intrinsically* essentially isopotential clusters [186]. Alternating potential energy profiles have been observed in several enzymes, including [NiFe]-hydrogenases [58], succinate dehydrogenase and fumarate reductase [187] and the photosynthetic reaction centre [188, 189]. In the latter, it has been suggested that the

presence of low potentials hemes, which essentially remain oxidised under physiological conditions, avoids electrostatic interactions by spatially separating the high potential hemes [190].

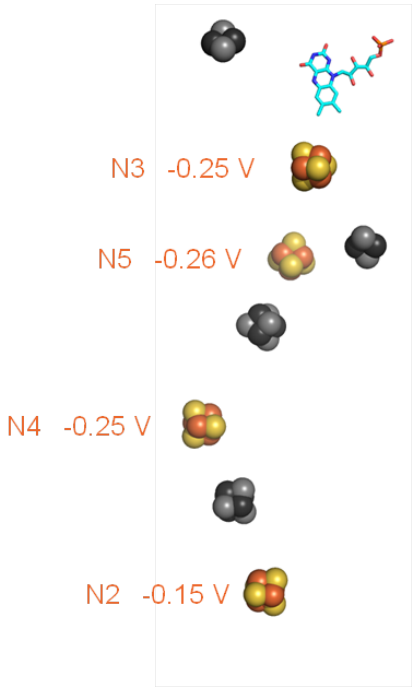


Figure 4.15: **Representation of the alternating cluster occupancy in complex I postulated during turnover.** Coloured clusters represent the four clusters that are reduced at ≈ -0.3 V; gray clusters remain oxidised. The redox potentials of the reduced clusters are indicated (see Table 4.1).

Calculations for the electron transfer rate from the FMN to the quinone therefore need to take into account the occupancy of the Fe-S cluster chain. Moser *et al.* estimated the time for one electron to pass through the chain to be about 100 μs [191]. For this calculation, potentials of -0.25 V were used for every cluster except N2 (-0.1 V) and N1a (-0.38 V) – *i.e.* an essentially isopotential energy profile. The real-time electron transfer was determined for complex I from *E. coli* using a freeze-quench approach [192]. The observed rate of N2 reduction was found to be ≈ 90 μs and is hence very close to the rate expected from Dutton's electron tunneling theory [52, 191]. Verkhovskaya *et al.* concluded that this electron transfer is unlikely to be coupled to other reactions, such as proton transfer. The second electron delivered by the NADH molecule on a similar

timescale ($\approx 90\ \mu$s) was found to reduce N1a, i.e. the cluster on the other side of the seven cofactor chain that has a much higher potential in *E. coli* complex I than in the bovine enzyme [154, 155]. Further reduction (of N1b and N4, referred to as N6b in *E. coli*) was found to be several orders of magnitude slower ($\approx$ 1-2 ms), thought to arise from the rate limiting dissociation of the first NAD^+ from its binding site, thereby preventing the entry of the next NADH molecule [192]. Given that the catalytic turnover is only $\approx$ 100-150 per second [193] (*i.e.* 200-300 electrons are transferred down the chain per second; turnover numbers vary between species, conditions of measurement, and the exact substrate used), intramolecular electron transfer appears to be much faster than the rate of catalysis.

The alternating potential profile in complex I that was first proposed by Yakovlev *et al.* [94] and now further supported by this work is consistent with fast electron transfer down the chain: More than one adjacent low potential centre would impede electron transfer much more than just a single low-potential cluster [52]. The individual electron transfer rates between the clusters for this potential energy landscape in complex I (Fig. 4.16) were analysed by Hirst in ref. [90]. Notably, the largest distance between 4Fe[75]H and 4Fe[TY]1 (N4) is compensated for by an increase in the reduction potential, so that in the forward reaction this step is very fast, whereas in the backward reaction it is two orders of magnitude slower and rate limiting [90].

Figure 4.16 B shows Hirst's model for the efficient and rapid intramolecular electron transfer in complex I: A single electron pair does not traverse the chain during a single turnover (the chain is already partially reduced), turnover only takes place when a 'poised' enzyme binds quinone, and quinone reduction and NADH oxidation occur together. The FMN remains predominantly oxidised because the extra electron is retained by the chain, most likely N1b.

The electron transfer in complex I may be compared to the Grotthus mechanism of proton transfer. Furthermore, the alternating occupancy of the chain could be key to conserving the energy of the incoming electron in the outgoing electron (in analogy to the conservation of energy in Newton's cradle). The full potential energy transfer from

NADH to bound quinone could thus be trapped in proton translocation.

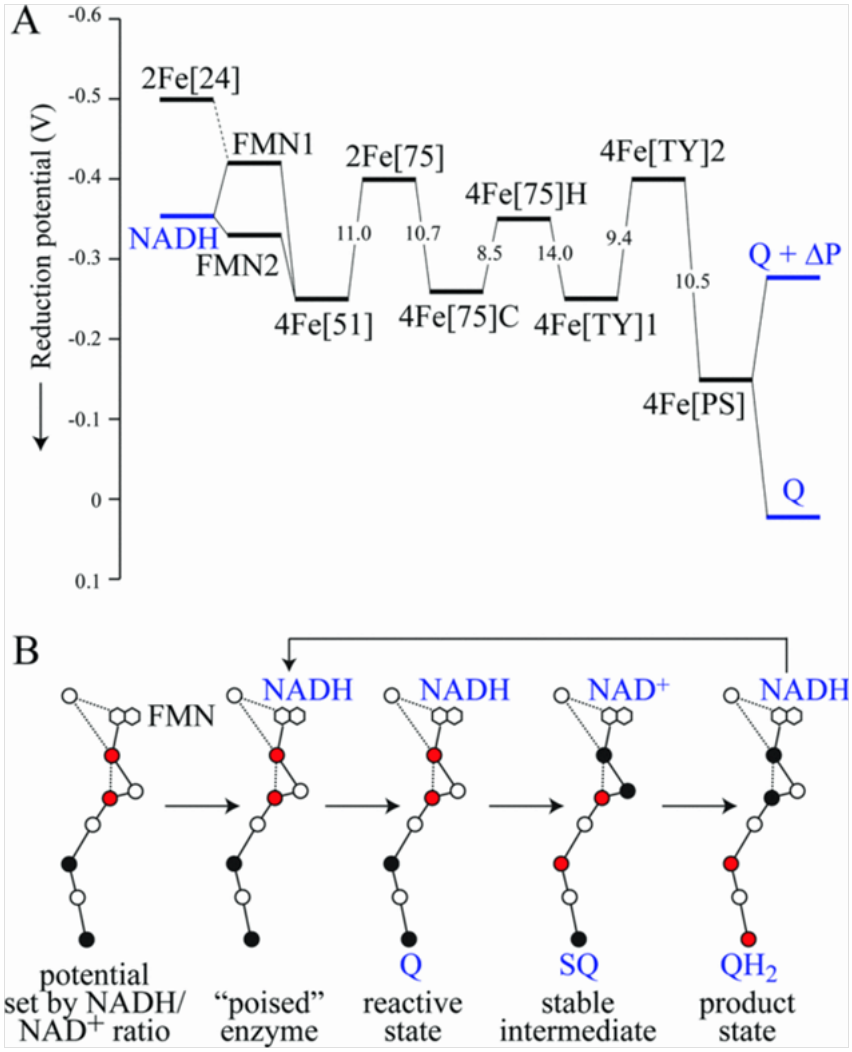


Figure 4.16: **Electron transfer reactions in complex I.** (**A**) Potential energy profile for the substrates and cofactors in complex I (based on data from *B. taurus*. The substrate potentials are two electron potentials, and two values for Q (quinone) are included, for $\Delta p = 0$ V and $\Delta p = 0.15$ V. The substrate potentials and the two flavin potentials, FMN1 (ox/semi) and FMN2(semi/red) [153] are at pH ≈7.8, and they include the coupled protonations. Cluster 4Fe[PS]/N1 is not part of the chain. Values for 4Fe[51]/N3, 4Fe[75]C/N5, 4Fe[TY]1/N4 and 4Fe[PS]/N2 are from [152]; values for other clusters are estimates. Edge-to-edge distances are indicated (in Å). (**B**) Possible scheme for the transfer of two electrons bound to quinone upon oxidation of NADH. Two electrons are highlighted in red for their identification. Figure reproduced with permission, from Judy Hirst, 2010, *Biochemical Journal*, vol. 425, pp. 327-339. © the Biochemical Society.

Chapter 5

The EPR-visible states of the active site in the O_2-tolerant *E. coli* Hyd-1 and the O_2-sensitive *E. coli* Hyd-2 [NiFe]-hydrogenases

Electrochemical experiments shown in the introduction to this chapter were carried out by Dr. Michael Lukey and Dr. Alison Parkin and have been published [83]. Isolation of the *E. coli* Hyd-1 and Hyd-2 enzymes was carried out with the help of Elena Nomerotskaia. The experiments determining the rate constants for the conversion of Ni-L to Ni-C were carried out by Rosalind Davies under my supervision. The program used for the preliminary simulation of HYSCORE spectra was written by Dr. Jeffrey Harmer. Part of the work described in this Chapter has been published [83].

Abstract

Two membrane-bound H_2-uptake [NiFe]-hydrogenases from *Escherichia coli* are compared and contrasted using EPR spectroscopy. Hydrogenase-2 (Hyd-2) belongs to the family of 'standard' [NiFe]-hydrogenases, which are highly sensitive to O_2, whereas Hydrogenase-1 (Hyd-1) belongs to the family of so-called 'O_2-tolerant' [NiFe]-hydrogenases. While Hyd-2 exhibits the EPR-detectable states of the active site typically observed in standard [NiFe]-hydrogenases, the active site EPR signals of catalytically active Hyd-1 are highly unusual. The catalytic EPR active form of [NiFe]-hydrogenases, Ni-C, typically converts to the Ni-L form when illuminated with visible light at low temperatures; such a conversion is found to occur in Hyd-2 but not in Hyd-1. Hyperfine Sublevel Correlation (HYSCORE) spectroscopy has been previously employed in a regulatory [NiFe]-hydrogenase to show that Ni-C, but not Ni-L, contains a bridging hydride [194]. In contrast, the Ni-C and Ni-L states of Hyd-2, investigated *via* HYSCORE, appear to be structurally similar in so far as the proton hyperfine couplings are concerned, and the activation energy for the conversion of Ni-L to Ni-C is found to be low compared to other catalytic [NiFe]-hydrogenases. Furthermore, Hyd-1 is found not to form the Ni-C state, but only a state with bears similarity with Ni-L and which is thus named Ni-L*. It is proposed that Ni-L − a state generally accepted as an artifact − could form part of the catalytic cycle in [NiFe]-hydrogenases.

5.1 Introduction

Hydrogenases were introduced in Section 1.2.2. The work in this chapter contributes to our understanding of why the enterobacterium *E. coli* requires *two* membrane-bound H_2 uptake [NiFe]-hydrogenases, Hyd-1 and Hyd-2. This will be investigated through their structural characterisation using EPR, in conjunction with electrochemical kinetic measurements.

Although there is no crystal structure of *E. coli* Hyd-2, sequence homologies indicate that the arrangement of the cofactors and the active site are expected to be very similar to those of other air-sensitive 'standard' [NiFe]-hydrogenases crystallised so far [136]. The structure of *E. coli* Hyd-1 has only very recently been determined [18] and while its active site appears to be very similar to that of all [NiFe]-hydrogenases crystallised to date, remarkable differences exist in the electron transfer relay, in particular at the proximal Fe-S cluster (Chapters 6, 7 and 8). The focus of this chapter are the EPR-detectable states of the active site. The oxidation states of the electron-transfer relay Fe-S clusters and in particular those of the active site are discussed below.

5.1.1 EPR-visible states of the active site in [NiFe]-hydrogenases

In 1982 Albracht *et al.* [195] showed unambiguously *via* hyperfine EPR spectroscopy of the ^{61}Ni-substituted *Allochromatium vinosum* enzyme, that Ni is a component of a class of hydrogenases now named [NiFe]-hydrogenases. In the same year, several papers reported the redox-sensitivity of the Ni, as observed by CW EPR spectroscopy [195–197]. The EPR signals were named Ni-A, Ni-B and Ni-C and now refer to particular oxidation states of the entire active site. Fernandez *et al.* [198] showed that Ni-A and Ni-B are inactive states, whereas Ni-C corresponds to a catalytically active state. Redox titrations of the EPR-detectable species established that many additional EPR-silent states of the active site also exist [196, 199–205]. The second metal in the active site, an Fe ion, was shown to be coordinated by two cyanides and one carbonyl through IR spectroscopy [206, 207]

and $^{13}C/^{15}N$ isotopic labelling [207, 208]. Unlike the nickel, the oxidation state of the iron is unchanged in all redox states of the active site, and EPR and ENDOR spectroscopies showed the iron atom to be low spin Fe(II) [209, 210], as may be predicted from the strong-field σ-donating CN^- and π-accepting CO ligands. While EPR is only able to monitor the changes in spin density located mainly on the Ni, FTIR spectroscopy monitors changes in the electron density of the Fe through changes in the vibrational frequencies of the CN and CO ligands. All states of the active site are thus 'visible' to FTIR and the first full FTIR spectroelectrochemical characterisation was carried out on the *Desulfovibrio gigas* hydrogenase [211]. The correspondence of the FTIR and EPR titrations [196, 211] lead to the conclusion that the bi-metallic active site in [NiFe]-hydrogenases behaves as an electronic ensemble. An additional EPR-active state, named Ni-L, has been observed when the Ni-C state is illuminated with visible light at cryogenic temperatures (typically below 100 K) [212–218].

The states of the active site in [NiFe]-hydrogenases are summarised in Fig. 5.1 (left). The first crystal structures of the *D. gigas* enzyme in 1995 at 2.85 Å resolution [47] and the *Desulfovibrio vulgaris* enzyme in 1997 at 1.8 Å resolution [219] revealed the presence of two cysteines bridging the Ni and Fe atoms, as well as two terminal cysteine residues ligating the Ni (Fig. 5.1 (right)). Moreover, depending on the oxidation state of the active site, an additional ligand is present between Ni and Fe (designated as X in Fig. 5.1). In early experiments with mediator dyes such as methyl viologen and the oxidant 2,6-dichloroindophenol, Fernandez *et al.* [198, 220] showed that inactive states of the enzyme correlate with EPR-defined states. Namely, the slowly activating *Unready* correlates with the EPR-defined state Ni-A and the rapidly activating *Ready*, correlates with the EPR-defined Ni-B state. However, in Chapter 6 it will be shown that while *Ready* and Ni-B can indeed be equated, *Unready* also includes other inactive states besides Ni-A. A much more detailed analysis of the reactions of hydrogenases and the active and inactive states involved has become possible through protein film electrochemistry (PFE) [132] which was introduced in Section 3.4 (Chapter 3). Spectroscopic methods and PFE are

highly complementary techniques since the former reveal structural information while the latter provides kinetic information very difficult or impossible to obtain *via* spectroscopic methods.

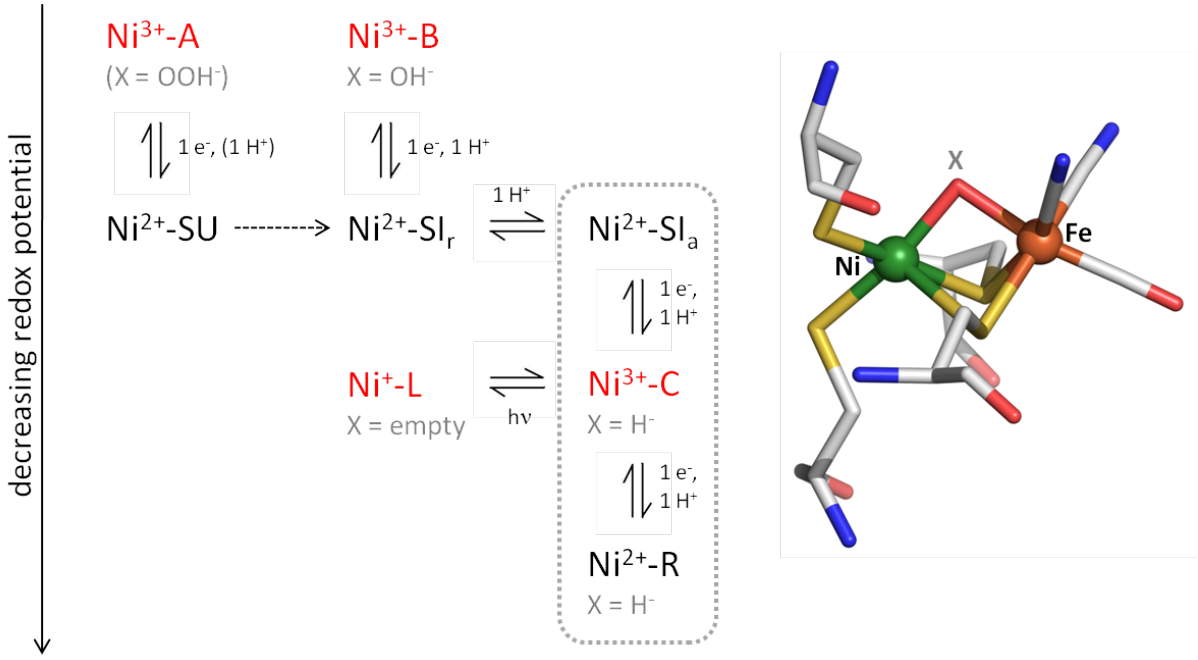


Figure 5.1: **Schematic diagram of the redox states of the active site of catalytic [NiFe]-hydrogenases (left) and structure of the active site (right).** (*Left*) Vertical lines are one-electron reduction steps that are each accompanied by a single H^+ transfer. EPR-active states are in red and EPR-silent states are in black. The vibrational frequencies of the CO and CN^- ligands bound to Fe are visible in all states with FTIR. Ni-SI_r and Ni-SI_a are in acid-base equilibrium. Illumination of Ni-C at low temperatures leads to the formation of the light-induced state Ni-L. The states commonly thought to be involved in the catalytic cycle of the enzyme are placed in a dotted box. Figure adapted from ref. [118]. (*Right*) Structure of the active site in [NiFe]-hydrogenases. Taken from the oxidised crystal structure of the hydrogenase from *Desulfovibrio fructosovorans*, 1YRQ.PDB.

The nature of ligand X bridging the Ni and Fe atoms in the inactive oxidised states was derived from crystallographic and EPR studies. While Ni-B is widely accepted to have a bridging OH^- ligand [118], the nature of ligand X in Ni-A and other Unready species remains unclear. Peroxide and oxidised sulfur species have been proposed [59, 219, 221–224] and ^{17}O ENDOR (Section 2.6.4) revealed that ^{17}O signal present in Ni-A was lost upon reduction to the active Ni-C state [225]. Both Ni-A and Ni-B contain Ni^{3+} [118, 226]. Brecht *et al.* [194] showed through HYSCORE spectroscopy (Section 2.6.3) that the Ni-C

state in the non-catalytic H_2-sensing hydrogenase from *Ralstonia eutropha* contains a bridging hydride, which disappeared in the Ni-L state of the enzyme. Furthermore, the unpaired electron in Ni^+ of Ni-L was shown to be in the d_{z^2} orbital, while it resides in the $d_{x^2-y^2}$ orbital in Ni^{3+} of Ni-C [118, 194]. Crystallography cannot detect the electron density from hydrides in these large metalloenzymes [59].

The exact mechanism of H_2 cycling in [NiFe]-hydrogenases remains elusive. As shown in Fig. 5.1, the catalytic cycle is thought to involve Ni-SI_a, Ni-C and Ni-R [118, 226, 227] (the nomenclature of the Ni states varies in the literature). In addition to experimental evidence for the intermediate states [118, 132, 226], detailed information about the energetics and possible transition states has stemmed from theoretical work [227]. Because of the detection of Ni-C with a bridging hydride, it is generally accepted that the catalytic mechanism involves heterolytic cleavage of H_2. Whether H_2 binds to Ni or Fe is still subject to debate [228]. Until Lill and Siegbahn proposed a mechanism involving oxidative addition to the Ni-L state and H_2 cleavage on Ni, all density functional theory studies invoking a heterolytic cleavage mechanism required H_2 activation on Fe [229]. The mechanism by Lill and Siegbahn is interesting not only because some experimental evidence supports cleavage at Ni [65, 230], but also because it includes, for the first time, Ni-L as an intermediate of the catalytic cycle - a redox state of the active site which is generally thought not to be functional [82, 118, 226].

5.1.2 The EPR-active states of the electron transfer relay in standard [NiFe]-hydrogenases

The oxidation states of the Fe-S clusters in standard hydrogenases are shown in Fig. 5.2. Due to their fast relaxation, Fe-S cluster EPR signals are only visible at low temperatures (typically below 30 K), while at higher temperatures (typically 80 K) only the Ni EPR signals are observable [118]. At high potential, when Ni-A and/or Ni-B are present, only the EPR signal from the oxidised [3Fe-4S] cluster is visible as the proximal and distal [4Fe-4S] clusters are EPR-silent. At low potential, when Ni-C/Ni-L are observed,

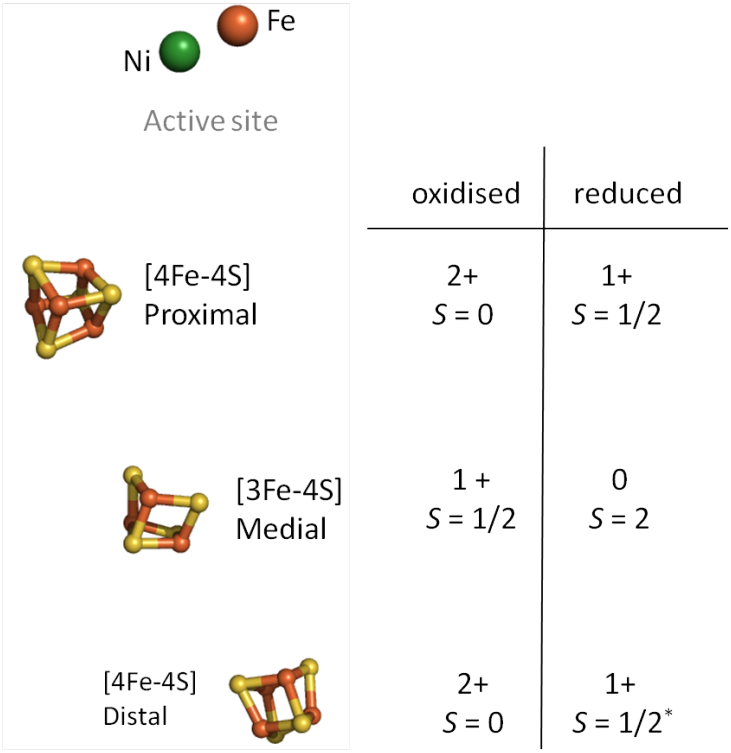


Figure 5.2: **Arrangement of the Fe-S cluster relative to the active site in [NiFe]-hydrogenases (left) and schematic diagram of the redox states of the Fe-S cluster relay in standard hydrogenases (right).** (*Left*) The Fe-S cluster structures are from the crystal structure of the hydrogenase from *Desulfovibrio fructosovorans*, 1YRQ.PDB (*Right*) The overall oxidation state of the clusters and their spin ground states are indicated. The asterisk refers to the uncertainty in the spin state of the distal cluster, which is the subject of Chapter 8.

the reduced proximal cluster interacts strongly with the active site Ni spin, causing a splitting of the Ni signals at low temperatures [118]. The electron transfer relay in O_2-tolerant hydrogenases exhibits remarkable differences to that in standard hydrogenases and this will be discussed in detail in Chapters 6 and 8.

5.1.3 *Escherichia coli* synthesises two H_2 uptake hydrogenases with highly contrasting properties

The enterobacterium *E. coli* synthesises at least three [NiFe]-hydrogenases [231] (Fig. 5.3). Hyd-1 and Hyd-2 are believed to function as 'H_2 uptake' enzymes [232, 233] and are membrane-bound periplasmic proteins. In contrast, Hyd-3 is a cytoplasmic enzyme and

as part of the formate hydrogen lyase system it is responsible for H_2 evolution under fermentative conditions [234]. Hyd-3 will not be discussed further in this thesis. In Hyd-1, the *hyaA* gene codes for the Fe-S cluster-containing β (small) subunit and *hyaB* codes for the active site binding α (large) subunit. Similarly, in Hyd-1 *hybO* codes for the small subunit and *hybC* codes for the large subunit. As seen in Fig. 5.3, a membrane-anchoring hydrophobic helix is located at the small subunit of each enzyme. Hyd-1 couples H_2 oxidation to quinone reduction *via* the transmembrane cytochrome *b* (HyaC). Preparations of Hyd-1 in this thesis include HyaA and HyaB; HyaC is also found to be attached in a fraction of the molecules (see Section 3.7). Hyd-2 uses the periplasmic ferredoxin (HybA) to reduce quinone *via* the HybB integral membrane protein [137]. Preparations of Hyd-2 include HybO, HybC and HybA.

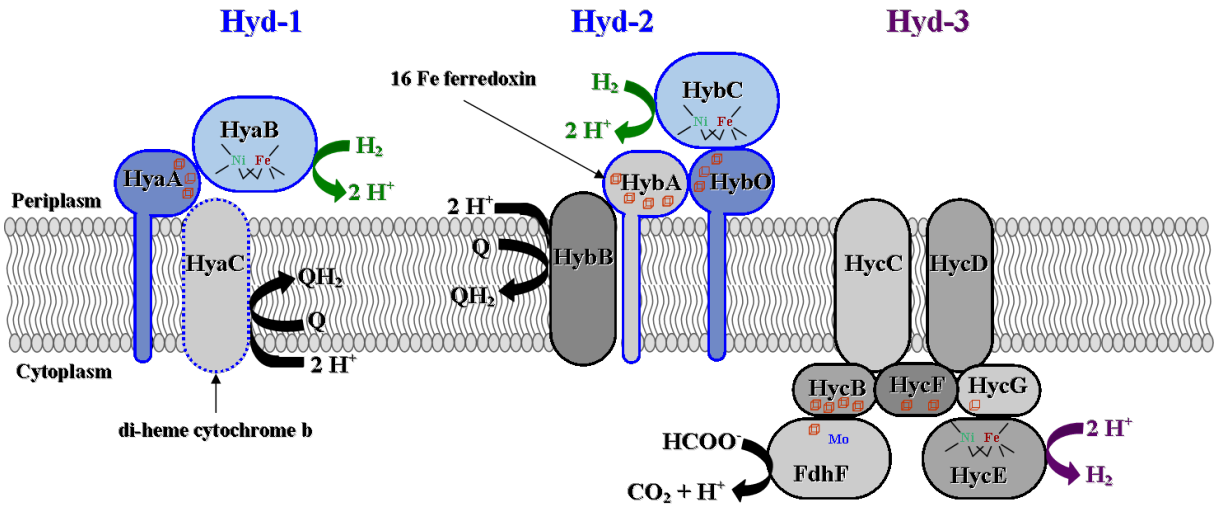


Figure 5.3: ***E. coli* Hyd-1, Hyd-2 and Hyd-3.** Solid blue contours indicate the Hyd-1 and Hyd-2 preparations used in this thesis. The dotted line around HyaC indicates that this cytochrome was only found to be attached to some of the molecules of isolated Hyd-1. The large subunit is coloured light blue and the small subunit is coloured in dark blue. Figure courtesy of Bonnie Murphy, adapted from ref. [235] by permission from Springer.

The physiological roles of Hyd-1 and Hyd-2 are believed to be rather different. Hyd-2 is thought to catalyse oxidation of extraneous H_2, with the resulting electrons eventually used by fumarate reductase to produce succinate [231]. Hyd-2 therefore allows *E. coli* to use H_2 as an energy source during growth on non-fermentable carbon compounds. The role of Hyd-1 is less clear but suggestions include the recycling of H_2 produced by Hyd-3

under fermentative conditions [234] in linking H_2 oxidation to O_2 reduction under certain conditions [236]. Indeed, conditions may exist in which Hyd-1 is expressed under high concentrations of O_2 since a fragment of Hyd-1 was isolated from aerobically grown *E. coli* [237].

Protein film electrochemistry has been used to characterise the strikingly contrasting catalytic properties of Hyd-1 and Hyd-2 under redox conditions and oxidising environments likely to be encountered by *E. coli in vivo* [83]. The most important results are now summarised.

Cyclic voltammetry experiments of Hyd-1 and Hyd-2 under 10% H_2 (Fig. 5.4) reveal that while both enzymes are capable of H_2 oxidation (net positive current is a direct measure of the net rate of steady-state H_2 oxidation), only Hyd-2 has a significant capability of H_2 production (net negative current). Furthermore, while for Hyd-2 the current trace crosses the zero line sharply and at the thermodynamic potential value predicted by the Nernst equation for the $2H^+/H_2$ couple, Hyd-1 requires an 'overpotential' for H_2 oxidation.[1] The decrease in catalytic current at high potentials relates to the formation of the inactive Ni-B/*Ready* state [238, 239], as observed in all catalytic [NiFe]-hydrogenases at high potentials under anaerobic conditions [132]. The reactivation of Ni-B is manifested by an increase in current as the potential is scanned back from positive to negative values. The midpoint of this reactivation process is defined by E_{switch} (marked with an asterisk in Fig. 5.4) and differs substantially for Hyd-1 ($E_{switch} = 0.150$ V at pH 6) and Hyd-2 ($E_{switch} = -0.085$ V at pH 6): for Hyd-1 the reactivation is sharp and complete. The Ni-B state is therefore much less favoured thermodynamically in Hyd-1 than in Hyd-2. The value for recovery from aerobic inactivation occurs at E_{switch}, *i.e.* at the same potential as recovery from anaerobic inactivation (Fig. 5.5).

The cyclic voltammograms in Fig. 5.5 A illustrate the dramatically different responses of Hyd-1 and Hyd-2 to a burst of O_2. When O_2-saturated buffer is injected during the forward scan under 100% H_2 (indicated with an arrow), a sudden decrease in current

[1] This overpotential decreases with decreasing H_2 concentration [83]

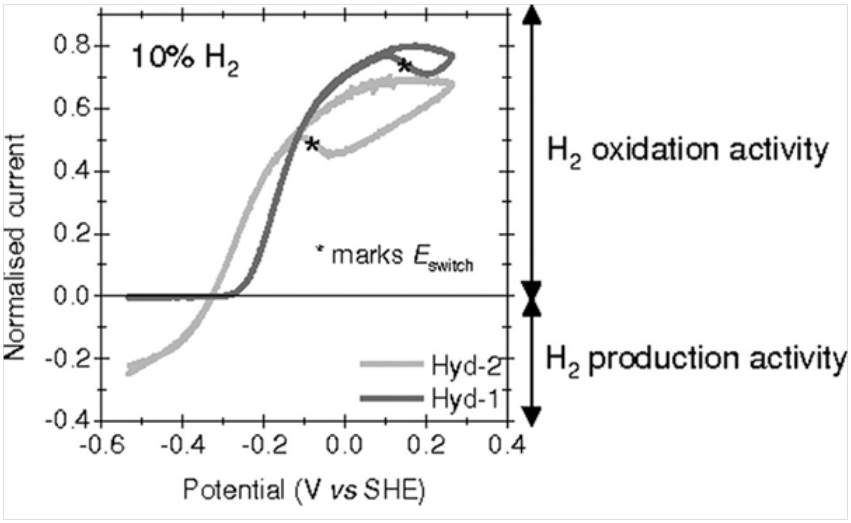


Figure 5.4: **The activity of *E. coli* Hyd-1 and Hyd-2 on a pyrolytic graphite edge electrode.** The negative current is a direct measurement of enzyme-catalyzed H_2 production, and the positive current is a direct measure of enzyme-catalyzed H_2 oxidation. Cyclic voltammograms were recorded at 30 ^{o}C, pH 6, scan rate 1 mV s^{-1}. The experiments shown in this Figure were carried out by Dr. Alison Parkin and Dr. Michael Lukey. Figure taken from ref. [83].

partially due to enzyme inhibition and partially due to temporary dilution in the H_2 concentration is observed for both Hyd-1 and Hyd-2. Hyd-1 recovers very quickly from a large burst of O_2, even during the continued forward scan to more positive potentials. In contrast, the H_2 oxidation activity in Hyd-2 is almost completely abolished when the enzyme is exposed to only one-ninth of the O_2 concentration to which Hyd-1 was exposed, and reactivation does not occur until much lower potentials are reached on the backward scan.

Potential-step experiments shown in Fig. 5.5 B allowed a deconvolution of the O_2-inhibited states formed by Hyd-1 and Hyd-2 when the active enzymes are exposed to O_2 at high potential. In the initial step, samples of Hyd-1 and Hyd-2 were held under 100% H_2 at a potential below E_{switch} at which significant H_2 oxidation activity is still observed, allowing an initial measure of the catalytic current for the particular enzyme film being studied. Next the H_2 is replaced by Ar and the current drops as the substrate is depleted. In the next step O_2-saturated buffer is injected as the potential is increased to a value well above E_{switch} and the current drops further due to aerobic inactivation. In a final step

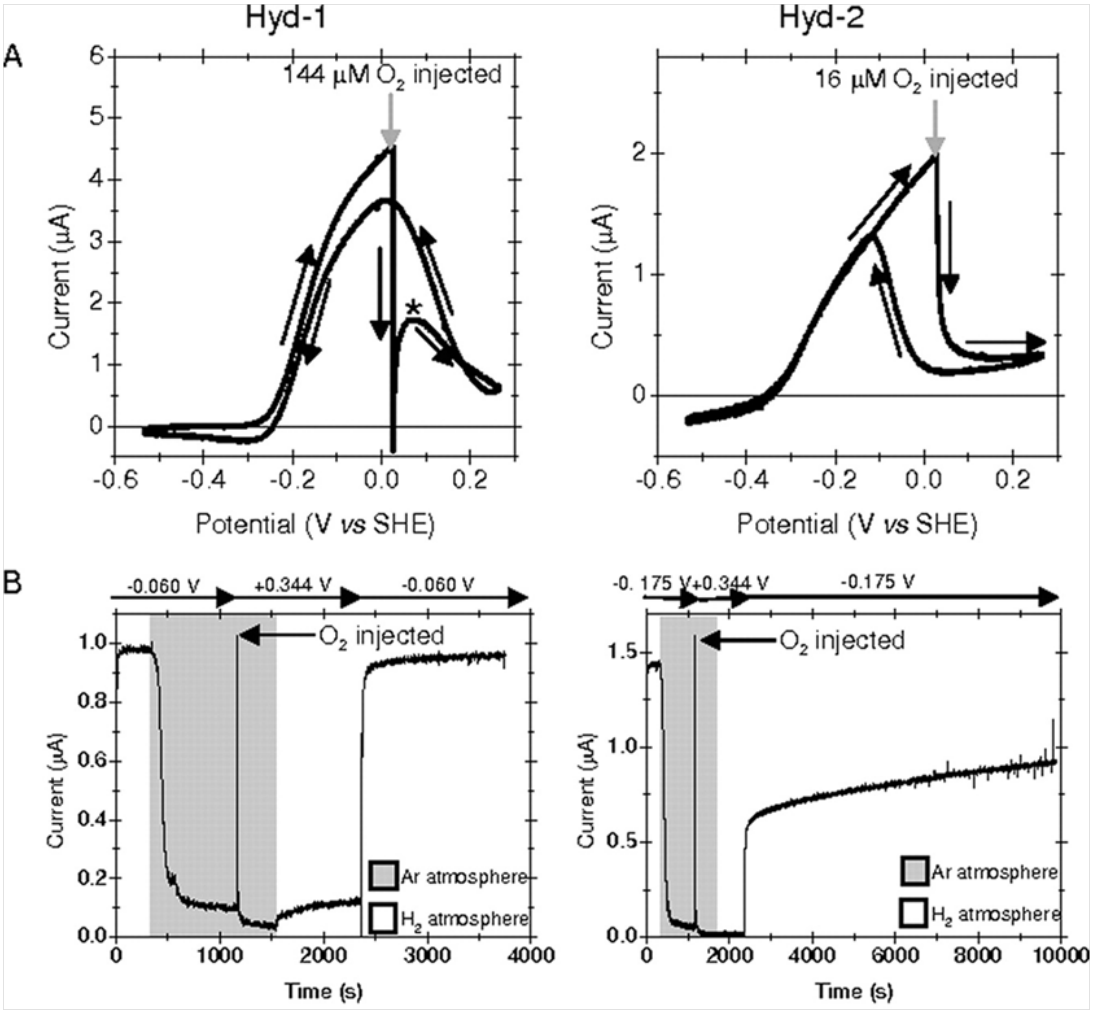


Figure 5.5: **A comparison of the O_2 tolerance of *E. coli* Hyd-1 and Hyd-2.** *A*: The cyclic voltammograms in A show the response of Hyd-1 and Hyd-2 to O_2 at high potential. At 0.03 V on the forward sweep, O_2-saturated buffer is injected into the cell solution (to give an O_2 concentration of 144 μM for Hyd-1 and 16 μM for Hyd-2). The O_2 concentration immediately begins to fall due to continued flushing of H_2; by the time the potential reaches +0.25 V and the scan direction reverses, most O_2 has been flushed from the cell. Cyclic voltammograms were recorded at 30 ^{o}C, pH 6, scan rate 1 mV s^{-1} under 100% H_2. *B*: (*Left*) A chronoamperometry experiment to investigate the inhibited active site states of Hyd-1 after exposure to O_2 at high potential in the absence of H_2. An initial measure of the H_2 oxidation activity of the film is made under 100% H_2 (white background), and the system is then equilibrated with 100% argon (gray background). For the first 1200 s, the potential is held at -0.060 V. Immediately on stepping the potential to +0.344 V, O_2-saturated buffer is injected into the cell solution to give an O_2 concentration of 325 μM. After re-equilibrating the electrochemical cell with H_2 (white background), the potential is stepped back to -0.060 V. (*Right*) A similar experiment on Hyd-2, in which all conditions are the same, except that the initial and final potential is -0.175 V instead of -0.060 V. The experiments shown in this Figure were carried out by Dr. Alison Parkin and Dr. Michael Lukey. Figure taken from ref. [83].

the potential is returned to the initial negative value, below E_{switch}. Hyd-1 immediately reaches the catalytic activity recorded prior to O_2 exposure, while Hyd-2 reactivates very slowly, not reaching the initial catalytic activity even after 7500 s. The last step of this experiment shows that upon reaction with O_2 Hyd-1 only formed the *Ready* state (which reactivates very fast), whereas the bi-phasic reactivation of Hyd-2 demonstrates that this enzyme formed both *Ready* and *Unready* states (which reactivates very slowly).

The experiments in Figures 5.4 and 5.5 classify Hyd-2 as a 'standard' hydrogenase and Hyd-1 as an 'O_2-tolerant' [NiFe]-hydrogenase [83, 240]. The catalytic biases of Hyd-1 and Hyd-2 are very different: while Hyd-2 is a bidirectional hydrogenase capable of both H_2 oxidation and production, Hyd-1 is biased towards H_2 oxidation only (with an over-potential requirement). Furthermore, the potential of reactivation, defined by E_{switch}, is much more positive in Hyd-1 than in Hyd-2. Importantly, Hyd-1 is capable of sustaining catalytic activity in the presence of O_2 and recovers very quickly and fully when O_2 is removed; Hyd-2 cannot function in the presence of O_2, forms a large amount of *Unready* state upon exposure to O_2, and reactivation is incomplete because part of the enzyme is irreversibly damaged.

5.2 Experimental procedures

The *E. coli* Hyd-1 and Hyd-2 enzymes were isolated as detailed in Chapter 3, Section 3.6.2. An additional gel filtration was carried out where specified by loading enzyme solution onto a gel filtration column (GE Healthcare, PG-10 columns) previously equilibrated with pH 6 buffer (100 mM MES, 100 mM NaCl). The enzyme was eluted with pH 6 MES buffer. No fractions contained lower molecular weight impurities as judged by SDS-PAGE, and EPR spectra of samples from different fractions were identical, both in the 'as-isolated' oxidised form and when reduced under H_2.

5.2.1 Preparation of EPR samples

As-isolated EPR samples were made by transferring ≈ 100 μL of enzyme in pH 7.5 buffer (20 mM Tris, 150 mM NaCl) to low-precision 4 mm quartz EPR tubes on the bench. Samples of reduced *E. coli* Hyd-1 or Hyd-2 were prepared in pH 6 buffer (100 mM MES, 100 mM NaCl) at 20 ^{o}C, using the titration method described in Section 3.2, in an anaerobic glove box (Glove Box Technologies, $O_2 < 1$ ppm). Approximately 150 μL of enzyme was equilibrated under a flow of H_2 or D_2 until the potential reached -355 mV (as predicted by the Nernst equation at this pH). For the Hyd-2 enzyme, equilibration required at most 1 hour. Deuterium exchange samples were prepared via buffer exchange in D_2O buffer (Section 3.8) to ensure that the aqueous composition was > 99 % D^+. Reduced Hyd-2 samples (≈ 80 μL) were transferred to 3.8 mm high-precision EPR tubes. Hyd-1 samples were titrated to the desired potential under Ar by adding benzyl and methyl viologen to the as-isolated sample such that their final concentration is in approximately a 1:1 ratio with enzyme concentration. Sodium dithionite was then added in substoichiometric quantities. Hyd-1 samples in Fig. 5.8 were transferred to high-precision 4 mm EPR tubes using the method described in Section 3.2 (≈ 250 μL, sufficient to fill the resonator height) in order to allow accurate subtraction of the spectrum of the sample poised at -323 mV from that at -200 mV. The Hyd-1 C19G/C120G variant (see Section 5.3.5 and Chapter 6) sample was prepared in a similar manner and was transferred to a 3.8 mm EPR tube.

Illumination of the H_2- or D_2-reduced Hyd-2 samples was carried out in the cavity of the EPR spectrometer using a UV/vis lamp (ORIEL instruments, 300 W Xe/HgXe) equipped with a waveguide and a < 400 nm filter to cut out UV light (Andover Corporation, UV bandpass filter 005FG9-50, N176). For experiments such as that illustrated in Fig. 5.12, spectra were recorded during illumination, and once the height of the Ni-C g_x peak remained constant (complete conversion to Ni-L is only possible at lower temperatures), the lamp was turned off and a timer started. Field sweeps of 6 mT of the Ni-C g_x peak over 120 s were measured at recorded time intervals and the maximum peak height plotted against time. For the pulsed X-band measurements in Figures 5.14 and 5.16, com-

plete conversion to the Ni-L state could be achieved by illumination of the sample inside the cavity for 15 mins at 10 K. Complete conversion to Ni-C was achieved by warming the sample in the dark to 200 K for 30 minutes. The concentration of as-isolated EPR samples for CW EPR measurements was 20 - 30 μM; pulsed X-band EPR samples were at least ten times more concentrated.

W-band EPR samples were prepared by activating approximately 50 μL of enzyme solution under H_2 for 1 h at 37 ^{o}C (the temperature was increased to concentrate the sample further through evaporation) using cell A shown in Fig. 3.3 (the potential was not monitored due to the small enzyme sample volume). After returning the temperature to 20 ^{o}C, 1-2 μL of the enzyme solution was immediately transferred to a 0.87 mm W-band EPR tube (Wilmad, suprasil Q-.7X.87) using a syringe (Hamilton, 2.5 μL). The sample for the measurements in Fig. 5.11 (left) was frozen after a delay of a few minutes whereas that in Fig. 5.11 (right) was frozen immediately. The oxidised and reduced samples in Fig. 5.11 result from different enzyme preparations and while the enzyme concentrations are not precisely known due to the method of sample preparation, the reduced sample is at least 500 μM and at least twice as concentrated as the oxidised sample.

5.2.2 EPR measurements

Continuous wave EPR measurements were carried out using the X-band Super High Sensitivity probehead. X-band pulsed measurements employed the EN4118-MD4 resonator. W-band measurements were carried out with the EN 600-1021H TeraFlex resonator. See Chapter 3 (Section 3.5) for spectrometer and resonator details. HYSCORE spectra were analysed using an in-house program written by Dr. Jeffrey Harmer; all other spectral analysis employed EasySpin [116].

5.2.3 Electrochemical experiments

The experiments in Fig. 5.9 were carried out using the method described in Chapter 3 Section 3.4. A pH 6 buffer (50 mM phosphate) was used for the electrochemical cell

solution (Section 3.8). The chronoamperometry traces were corrected for film-loss and normalised to allow direct comparison between Hyd-1 and Hyd-2. The gas flow rate through the cell was 300 standard-cubic-centimetres min^{-1} for either H_2 (Premier grade, Air Products) or D_2 (Air Products, X9S100B).

5.3 Results

5.3.1 The EPR-visible oxidised states in *E. coli* Hyd-1 & Hyd-2

In addition to their different catalytic biases and the distinct rates and potentials associated with their reactions with O_2 (Section 5.1.3), Hyd-1 and Hyd-2 are distinguished by their EPR spectra. Figure 5.6 shows the X-band CW EPR spectra of as-isolated samples of Hyd-1 and Hyd-2, each recorded at 10 K and 80 K. At 10 K, both Hyd-1 and Hyd-2 spectra are dominated by the strong signal of the $[3Fe\text{-}4S]^+$ cluster with g values (Hyd-1/Hyd-2: $g_x = 2.02/2.03$, $g_y = 2.01/2.02$, $g_z = 2.00/2.01$) consistent with those reported for [NiFe]-hydrogenases from other species (*e.g.* refs. [82, 84, 196, 241–243]). The spectrum of Hyd-1 is more complicated than that of Hyd-2 and is discussed below.

At 80 K, only the EPR signals arising from nickel are observable, and can be examined without interference from the $[3Fe\text{-}4S]^+$ cluster, which relaxes rapidly at this temperature and is not detected. The spectra show that both Hyd-1 and Hyd-2 form Ni-A and Ni-B states upon aerobic isolation. The rhombic signals characteristic of both Ni-A and Ni-B show identical g values (to two decimal places) for Hyd-1 and Hyd-2 (Ni-A, $g_x = 2.31$, $g_y = 2.24$, and $g_z = 2.01$; Ni-B, $g_x = 2.31$, $g_y = 2.16$, and $g_z = 2.01$). These values are in good agreement with those previously reported for [NiFe]-hydrogenases [118], although relatively more Ni-B than was evident in the data presented by DerVartanian *et al.* [244] is consistently observed. The exact ratio of Ni-A to Ni-B varies between preparations: in the spectra shown, the ratio is $\approx$ 1:3 for Hyd-1 and 1:4 for Hyd-2.

The spectra of Hyd-2 contain no signals apart from those arising from Ni-A, Ni-B, and $[3Fe\text{-}4S]^+$, and are similar to those of the [NiFe]-hydrogenases from *Desulfovibrio*

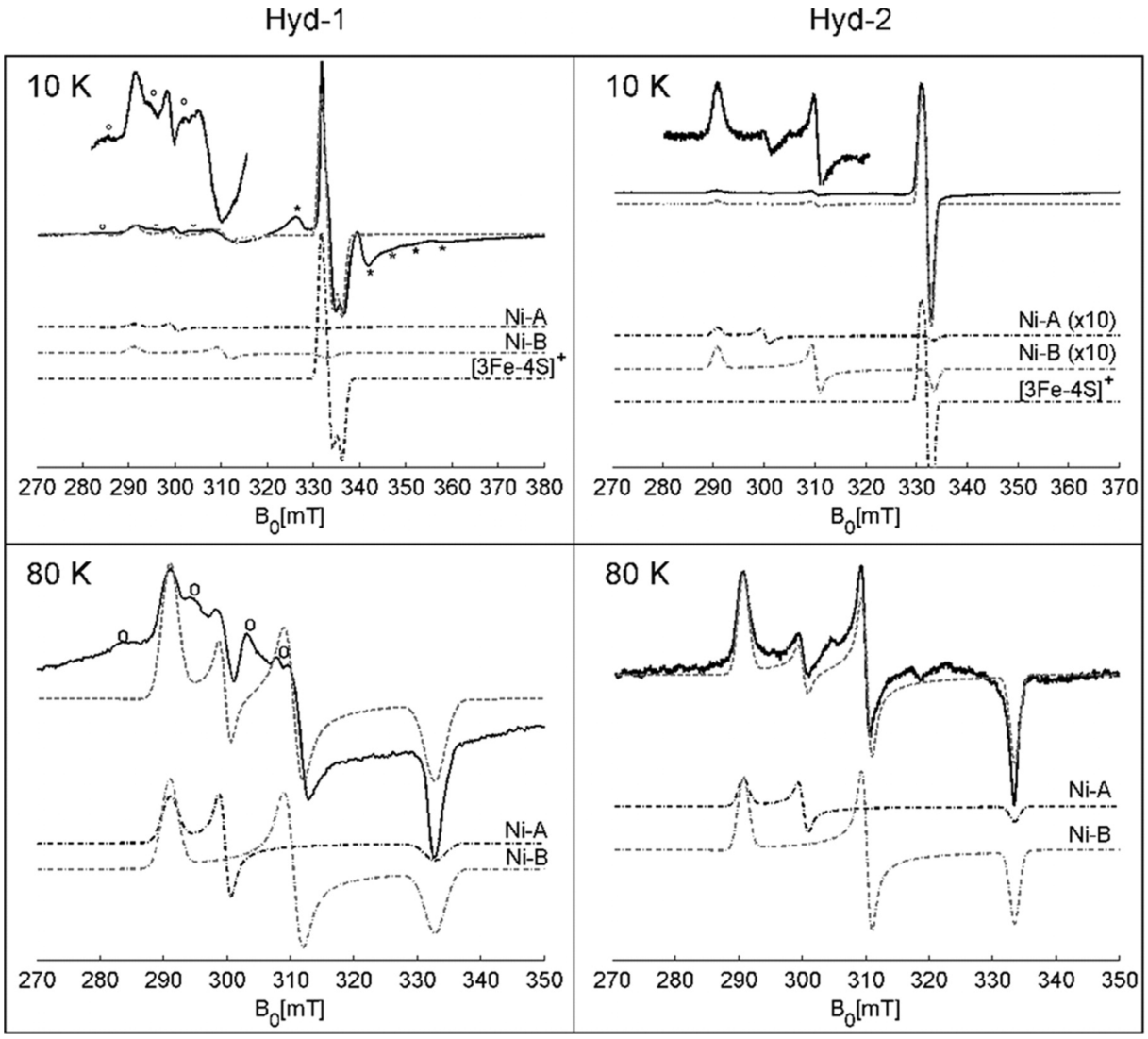


Figure 5.6: **X-band CW EPR spectra of as-isolated Hyd-1 and Hyd-2.** Simulations are shown as dotted lines and g values are as follows: (Hyd-1 and Hyd-2) Ni-A $g_{x,y,z}$ = 2.31, 2.24, 2.01; Ni-B $g_{x,y,z}$ = 2.31, 2.16, 2.01; $[3Fe\text{-}4S]^+$ (Hyd-1/Hyd-2), $g_{x,y,z}$ = 2.03/2.03, 2.01/2.02, 2.00/2.01. When necessary, spectra were baseline subtracted using a baseline spectrum recorded under the same conditions as the spectrum of the enzyme sample. * and ^{o} denote peaks resulting from interaction of the high potential centre with the active site (see text and Chapter 6). Measurement conditions: (10 K) mw power 0.13 mW; modulation amplitude 0.6 mT; (80 K) mw power 2.0 mW; modulation amplitude 1.0 mT (Hyd-1)/0.5 mT (Hyd-2). Figure taken from ref. [83].

species [242, 245–247]. In contrast, the spectra of Hyd-1 contain several other peaks around the $[3Fe\text{-}4S]^+$ cluster region at g = 2.06, 1.96, 1.93, 1.91, and 1.87 (denoted with an asterisk in Fig. 5.6) as well as around the peaks arising from Ni-A and Ni-B at g = 2.36, 2.27, and 2.21 (indicated with an open circle). These features have been

observed previously for [NiFe]-hydrogenases from *Allochromatium vinosum* [195, 241, 248, 249], *Thiocapsa roseopersicina* [243], and most recently *Ralstonia eutropha* (*Re*-MBH) [82] and *Aquifex aeolicus* (*Aa* Hase I) [16]. Contrary to *Re*-MBH [82, 88] and *Aa* Hase I [16] however, Ni-A is found to be present in as-isolated *E. coli* Hyd-1. This is confirmed by chronoamperometry experiments of as-isolated Hyd-1 and Hyd-2, which show the presence of the *Unready* state [83].

The presence of a 'split' signal at $g = 2.01$ for Hyd-1 is similar to that observed for the membrane-bound hydrogenases from *R. eutropha* [82] and *A. aeolicus* [16, 250]. In contrast, the relatively simple spectrum of Hyd-2 resembles hydrogenases from *Desulfovibrio* [242, 245–247], which are strict anaerobes. The EPR signatures of the as-isolated enzymes are thus consistent with Hyd-1 belonging to the O_2-tolerant hydrogenases and Hyd-2 belonging to the standard hydrogenases. The nature of the O_2 tolerance in Hyd-1 is the subject of Chapter 6.

5.3.2 The EPR-active reduced Ni states in *E. coli* Hyd-1 and Hyd-2

The light sensitivity of the Ni-C state was first observed in *A. vinosum* hydrogenase [212] through EPR spectroscopy and has since been reported for standard [NiFe]-hydrogenases from many different species, including *D. gigas* [200, 213, 214], *Thiocapsa roseopersicina* [251] and *D. vulgaris* Miyasaki F [218]. By monitoring the stretching frequencies of the CO and CN^- ligands to Fe in the active site, the transition between Ni-C and Ni-L has also been observed *via* FTIR [206, 207, 252, 253]. In some [NiFe]-hydrogenases more than one Ni-L state has been reported depending on the length of illumination of the Ni-C state [214, 218]. Figure 5.7 shows that H_2-reduced *E. coli* Hyd-2 undergoes a similar transition from Ni-C to Ni-L (and *vice versa*).

Reduced samples of Hyd-2 prepared in ambient light and measured at 80 K typically contain a mixture of Ni-C and Ni-L, resulting in a spectrum similar to the central black spectrum in Fig. 5.7. Illumination of the sample outside the EPR cavity with visible

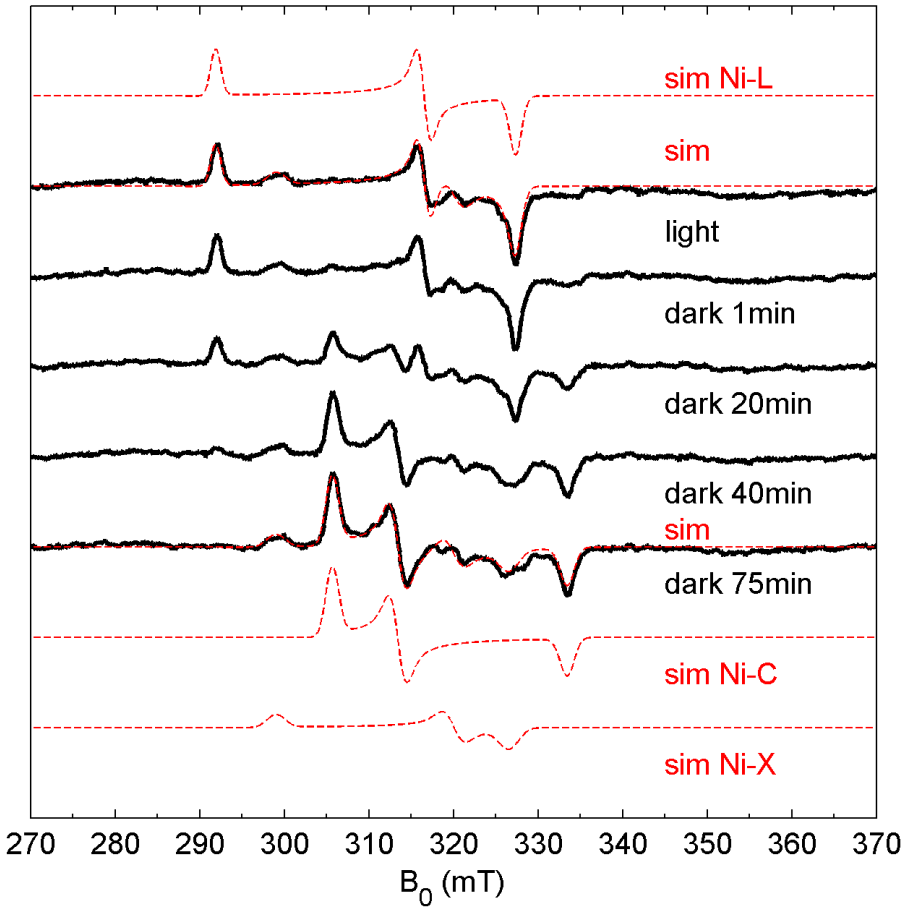


Figure 5.7: **X-band CW EPR spectra showing the conversion of Ni-L to Ni-C in H_2-reduced Hyd-2 (80 K).** 'Light' refers to the initial condition of the sample, which was prepared by illuminating the sample with visible light outside the cavity at 77 K; 'dark' refers to the sample kept in the dark in the spectrometer's resonator at 120 K for the number of minutes indicated before returning the temperature to 80 K before measurement. Simulations are shown as red dotted lines for Ni-C ($g_{x,y,z}$ = 2.194, 2.137, 2.011), Ni-L ($g_{x,y,z}$ = 2.297, 2.119, 2.048) and Ni-X ($g_{x,y,z}$ = 2.242, 2.095, 2.053); overall simulations of the 'light' sample containing Ni-L and Ni-X only, and of the 'dark' sample containing Ni-C and Ni-X are also included. Measurement conditions: mw power 2 mW, mw frequency 9.389 GHz, modulation amplitude 1 mT, temperature 80 K.

light at 77 K (immersed in liquid N_2) yields 100% Ni-L, and only one Ni-L species with $g_{x,y,z}$ = 2.297, 2.119, 2.048 could be detected. Leaving the sample in the dark at 120 K for increasing lengths of time[2] gradually results in the conversion to Ni-C with $g_{x,y,z}$ = 2.194,

[2]The time indications in Fig. 5.7 are approximate as it did not always take exactly the same amount of time to increase the temperature from 80 K to 120 K and then to reduce it to 80 K again before measurement. Furthermore the fast increase to 120 K temporarily results in a local temperature at the sample above 120 K. A quantitative investigation of the conversion of Ni-L to Ni-C is presented in Section 5.3.4.

2.139, 2.011. The g values of Ni-C and Ni-L in *E. coli* Hyd-1 are similar to those reported for other catalytic standard [NiFe]-hydrogenases [200, 212, 218, 251]. Both the spectra of Ni-L and Ni-C show additional EPR signals from a species henceforth named Ni-X which can be simulated with $g_{x,y,z}$ = 2.242, 2.095, 2.053.[3] Interestingly, a species with almost identical g values has been observed in the cytoplasmic H_2-sensing regulatory [NiFe]-hydrogenase from *R. eutropha* (*Re*-RH) [254]. Upon reduction with H_2, *Re*-RH forms Ni-C ($g_{x,y,z}$ = 2.19, 2.13, 2.01) which transforms into Ni-L ($g_{x,y,z}$ = 2.24, 2.09, 2.045) when illuminated at 30 K. Only after several hours at 200 K in the dark did the Ni-C state re-appear. A shorter period of time (15 minutes) resulted in a transient state with $g_{x,y,z}$ = 2.30, 2.069, 2.045 [254]. The g values observed for Ni-L in *R. eutropha* RH are unusual compared to those found in catalytic [NiFe]-hydrogenases, but are almost identical to those of the Ni-X species in *E. coli* Hyd-2. However, contrary to the observation made for Ni-L of *R. eutropha* RH, Ni-X was found to be insensitive to illumination with white light and the spectrum of Ni-X (measured at 120 K, not shown) remained unchanged when a H_2-reduced sample of Hyd-2 was left in the dark at 200 K for 12 hours. As additional purification procedures of the Hyd-2 enzyme sample (see Section 5.2) did not result in disappearance of the Ni-X signals and given the coincidence in g values with *R. eutropha* RH, it is concluded that Ni-X is very unlikely to be an impurity.

Contrary to *E. coli* Hyd-2, no Ni-C or Ni-L signals were observed in H_2-reduced *E. coli* Hyd-1 (not shown). However, at a considerably less negative potential of −200 mV, Ni signals with rather atypical g values appear, as can be seen by comparison with the Ni-C and Ni-L spectra of Hyd-2 and their difference spectrum, of which a simulation is included (Fig. 5.8).

When the same sample of enzyme is reduced further to -323 mV (Fig. 5.8), these Ni signals disappear and only signals of very small intensity remain (in addition to the methyl/benzyl viologen mediator peak at g = 2 marked with an asterisk in Fig. 5.8). Subtraction of the spectrum of the -323 mV sample from that of the -200 mV sample,

[3]Ni-X g_x is broad and sometimes appears to be composed of two peaks; an average value is taken in this case.

results in a 'clean' Ni spectrum of which the g_y component seems to be 'split' (note the 'inverted' viologen peak due to subtraction of the low-potential spectrum). This spectrum can be well-simulated with two different sets of rhombic g values which only differ slightly in g_y: $g_{x,y,z} = 2.332, 2.149, 2.047$ and $g_{x,y,z} = 2.332, 2.137, 2.047$. Importantly, the signals remain unchanged when the sample is illuminated at low temperatures or left in the

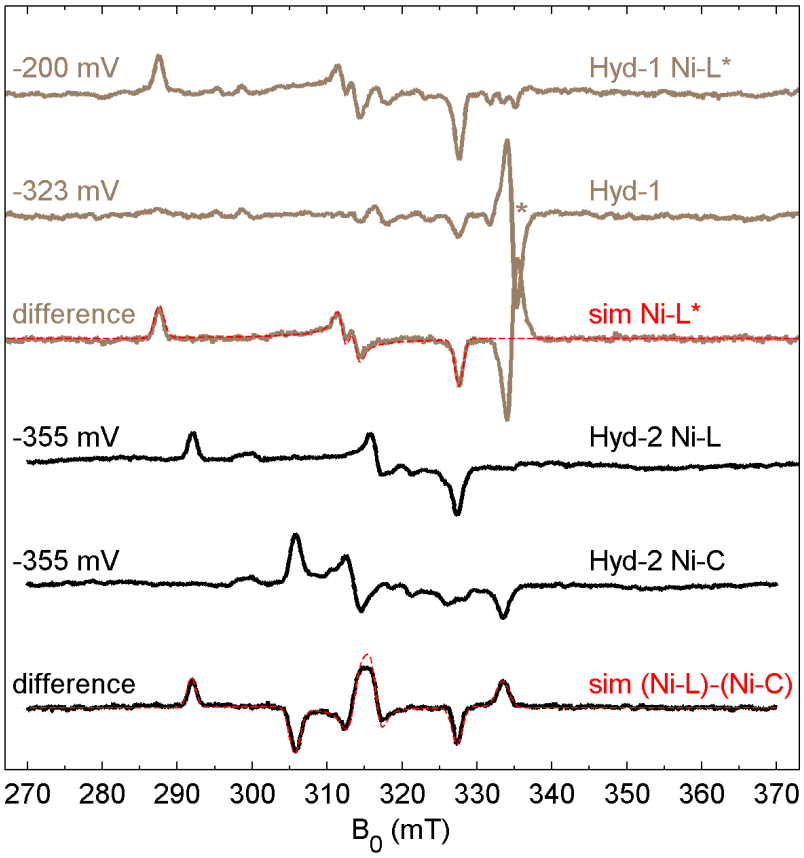


Figure 5.8: **X-band CW EPR spectra comparing the Ni species in low-potential Hyd-1 and Hyd-2 (80 K).** The difference spectra of the Hyd-1 −200 mV minus the −323 mV spectra, and the 'light' (Ni-L) minus 'dark' (Ni-C) spectra of Hyd-2 (both at −355 mV) are denoted as 'difference'. The Hyd-2 spectra result from a sample reduced under hydrogen; Hyd-1 samples were reduced chemically with dithionite in the presence of mediators (see 5.2). Simulations are shown for the difference spectra. Hyd-1 Ni-L* was simulated with two different g_y values (1:1 ratio of Ni-L*$_1$ $g_{x,y,z} = 2.332, 2.149, 2.047$ and Ni-L*$_2$ $g_{x,y,z} = 2.332, 2.137, 2.047$). The relative amounts of Ni-L*$_1$ and Ni-L*$_2$ varies between preparations. Hyd-2 Ni-L and Ni-C were simulated with the parameters given in Fig. 5.7. The peak at $g = 2$ marked with an asterisk results from benzyl viologen. Measurement conditions: (Hyd-1) mw power 2 mW, mw frequency 9.384 GHz, modulation amplitude 1 mT; (Hyd-2) see Fig. 5.7. Figure taken from Roessler *et al.*, *Journal of the American Chemical Society*, vol. 134, pp. 15581-15594, 2012.

dark at 250 K for two hours (spectra not shown). Because the g values are a mixture of typical values found for Ni-C and Ni-L (for which the (Ni-L)−(Ni-C) difference spectrum of Hyd-2 in Fig. 5.8 can be taken as a guidance), this Ni species, which is consistently observed in samples from different preparations, is named Ni-L*. As will be seen from the EPR potential titrations of native Hyd-1 and Hyd-1 variants in Chapter 6 (Section 6.3.2), Ni-L* is at approximately maximal intensity at −185 mV (at pH 6). For comparison, Ni-C in the standard *D. vulgaris* Miyasaki F [NiFe]-hydrogenase is at maximal intensity at ≈ −300 mV at pH 5.4 and ≈ −380 mV at pH 6.8 [255] (as determined *via* FTIR), *i.e.* at considerably lower potential than Ni-L* in *E. coli* Hyd-1. Even the O_2-tolerant hydrogenase *Aa* Hase I, for which the midpoint potentials of all Ni species are reported to be shifted to considerably higher potentials compared to standard hydrogenases, shows Ni-C at a maximal intensity at ≈ -270 mV at pH 6.4 [250]. Consequently, the unusually high potential at which Ni-L* is most intense, its g values and its light insensitivity are unprecedented in catalytic [NiFe]-hydrogenases.

In order to compare the reactivity of the catalytically active states in Hyd-1 and Hyd-2, electrochemical experiments were carried out to determine the H/D isotope effect on catalytic H_2 oxidation (Fig. 5.9). The preparation of the enzyme used for PFE experiments was identical to that used for EPR experiments. While enzyme assay methods have failed to detect an isotope effect because of the insufficient driving force for H_2 oxidation of typically used dyes such as methyl viologen [256, 257], Lamle *et al.* [258] have shown that chronoamperometry experiments are well suited for detailed studies because the driving force can be varied easily. The potential at which the chronoamperometry experiments in Fig. 5.9 were carried out was determined according to the E_{switch} values of Hyd-1 and Hyd-2 (see Fig 10.1 in Appendix 10.2). The potential was held constant throughout the experiments and chosen such that neither Hyd-1 nor Hyd-2 undergo high potential anaerobic inactivation (formation of the *Ready*/Ni-B state). The normalised catalytic oxidation current for a hydrogenase film of Hyd-1 and Hyd-2 at 37 ^{o}C and at 10 ^{o}C at pH 6 drops by a constant fraction as the headgas is changed repeatedly between H_2 and

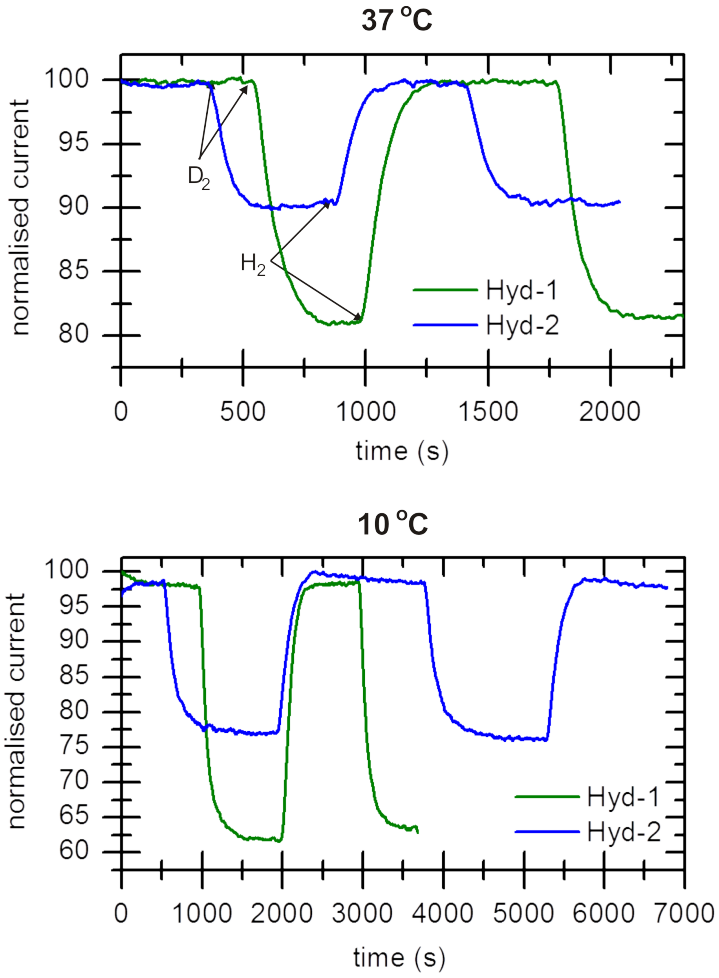


Figure 5.9: **The kinetic isotope effect in *E. coli* Hyd-1 *vs* Hyd-2.** Chronoamperometry experiments were recorded under 100% H_2 or D_2 (as indicated with arrows) at 300 (standard cubic centimetres) min^{-1}. The potential was held constant at -207.5 mV (37 ^{o}C) or -107.5 mV (10 ^{o}C), pH 6. Average kinetic isotope effect (H_2/D_2): (37 ^{o}C) 1.23 (Hyd-1) and 1.11 (Hyd-2); (10 ^{o}C) 1.58 (Hyd-1) and 1.29 (Hyd-2).

D_2. The average values for the kinetic isotope effect are 1.23 for Hyd-1/1.11 for Hyd-2 at 37 ^{o}C, and 1.58 for Hyd-1/1.29 for Hyd-2 at 10 ^{o}C. Thus, as for *A. vinosum* hydrogenase [258], the kinetic isotope effect is small. However, it is significantly larger for Hyd-1 than for Hyd-2. The decrease in the effect at higher temperature is expected as the rate determining step is shifted towards interfacial electron transfer which is less sensitive to H/D substitution [258].

Although the potential dependence of the isotope effect was not determined, Lamle *et al.* [258] showed that the effect decreases with decreasing potential as the driving force

for H_2 oxidation is decreased. Because E_{switch} is more positive for Hyd-1 than for Hyd-2 (Fig. 10.1 in Appendix 10.2), the difference between E_{switch} and the potential value chosen for the experiments in Fig. 5.9 (which was the same for Hyd-1 and Hyd-2) is larger for Hyd-1 than for Hyd-2. Consequently, the isotope effect is expected to increase for Hyd-1 if experiments are carried out at a potential with the same 'distance' from E_{switch} as for Hyd-2. The experiments in Fig. 5.9 therefore clearly show that H_2 bond cleavage or the transfer of a substrate proton is significantly more rate limiting in Hyd-1 than in Hyd-2.

The Ni-C and Ni-L states of Hyd-2 are now examined more closely and compared to similar states found in [NiFe]-hydrogenases from different species before returning to the Ni-L* state in Hyd-1.

5.3.3 The temperature and frequency dependence of Ni-C in *E. coli* Hyd-2

The temperature dependence of the Ni-C state in Hyd-2 is shown in Fig. 5.10.
The reduced Hyd-2 sample was warmed to 200 K in the dark for 30 minutes, which converted almost all Ni-L to Ni-C. Above 40 K all signals are due to Ni as the reduced Fe-S clusters relax too rapidly to be detected, and the spectrum remains unchanged between 80 K and 40 K. Besides the dominant Ni-C species, a small amount of Ni-L and Ni-X (see above and simulations in Fig. 5.10) are also present. With the appearance of the Fe-S clusters below 30 K, the g_y peak of Ni-C broadens and is practically invisible at 7.5 K while the Ni-C g_x peak intensifies. Previous studies on many standard [NiFe]-hydrogenases, for example from *D. gigas* [177, 245, 259], *D. vulgaris* Miyasaki F [260], *A. vinosum* [212, 261], have shown that the Ni-C state interacts strongly with the reduced proximal [4Fe-4S] cluster and that this interaction, mainly an exchange rather than dipolar interaction [177, 262] is responsible for the changes in the spectrum of Ni-C also observed in *E. coli* Hyd-2 as the temperature is lowered. The Fe-S cluster signals observed in reduced [NiFe]-hydrogenases are thought to arise from a complex magnetic interaction between the reduced proximal, medial and distal clusters and the origin of this signal in

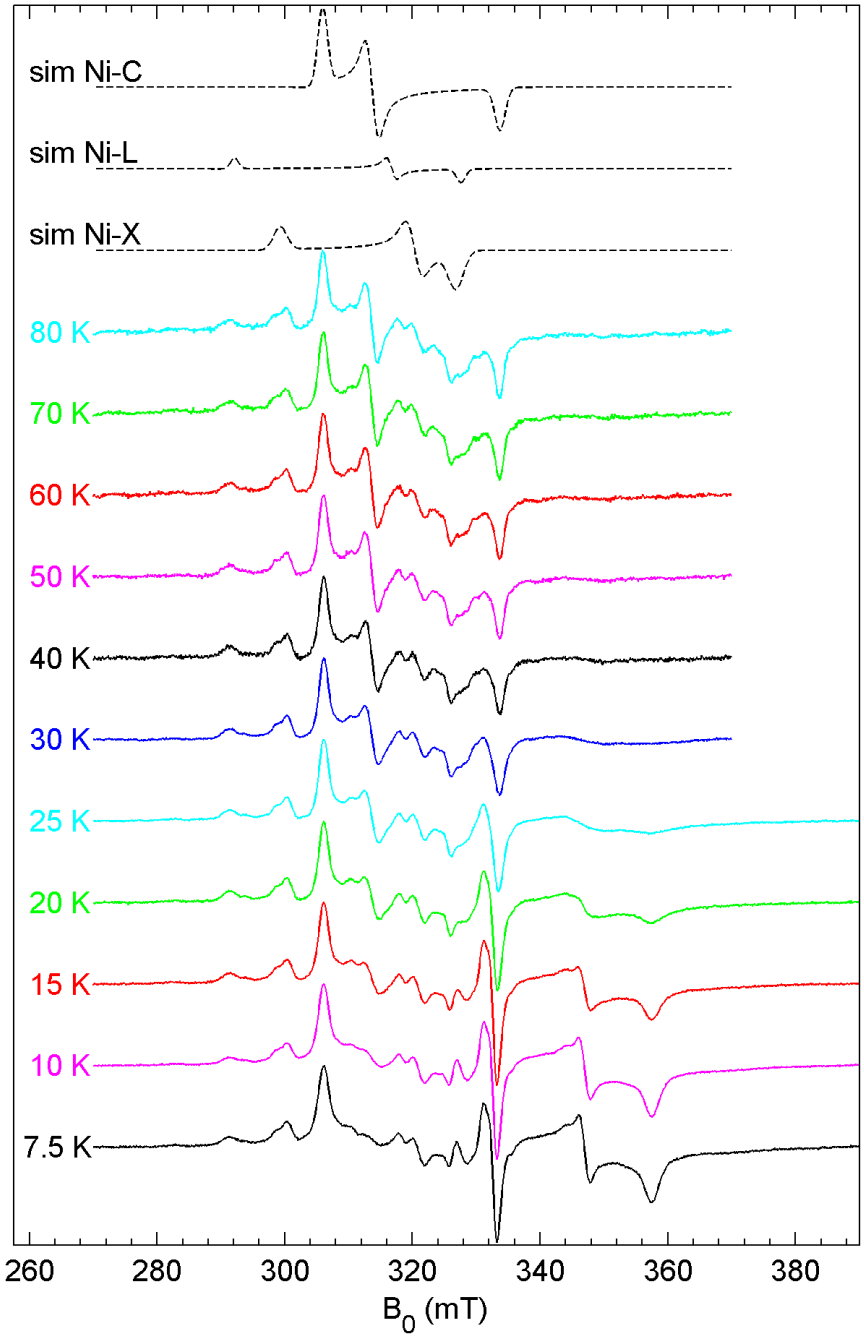


Figure 5.10: **X-band CW EPR spectra showing the temperature dependence of Hyd-2 Ni-C.** Simulations of the (uncoupled) Ni-C, Ni-L and Ni-X states are shown as dotted lines. See Fig. 5.7 for simulation parameters; Ni-X g_x is taken as an average value of the two peaks observed at this field positions in the spectra at all temperatures. Measurement conditions: mw power 2 mW (80 K to 25 K), 0.5 mW (20 K to 10 K), 0.13 mW (7.5 K); modulation amplitude 1 mT (all), mw frequency 9.392 GHz (all). Spectra were scaled to the same maximum intensity to allow easy comparison at different temperatures.

O_2-tolerant hydrogenases is the subject of Chapter 8, where it will be shown that the distal cluster is in a $S > 1/2$ spin ground state. In Hyd-2 the co-purified 16-Fe ferredoxin (HybA, Fig. 5.3) may also contribute to the observed Fe-S cluster signal. The peak centered at $g = 2.02$ was not always of the same magnitude in different H_2 or D_2 reduced samples of Hyd-2. Given its g values and temperature dependence is it unlikely to be an organic radical species.

The numerical first derivatives of the W-band two-pulse echo detected field sweeps of both the oxidised and reduced forms of Hyd-2 are compared to the corresponding X-band CW spectra in Fig. 5.11. The oxidised Hyd-2 W-band derivative spectrum allows a more accurate determination of the g values of the oxidised [3Fe-4S] cluster ($g_{x,y,z} = 2.028, 2.018, 2.013$) and confirms that there is no magnetic interaction between this cluster and the active site. Background signals from the W-band cavity Cu^{2+} and Mn^{2+} (Section 3.5.3) are indicated. The W-band sample was activated under H_2 prior to anaerobic oxidation and hence only shows the presence of Ni-B.

The W-band spectrum of reduced Hyd-2 reveals Ni-C signals that are not broadened or split by the reduced proximal cluster. Furthermore, the Fe-S cluster peaks at $g = 1.94$ and $g = 1.87$ are frequency-independent and therefore intrinsic g values more likely to arise from one Fe-S cluster species rather than a complex magnetic interaction between several reduced clusters (Chapter 8). As can be seen by a small amount of Ni-B present, the sample re-oxidised slightly as it was made, even though it was frozen as soon as possible following H_2 reduction. The narrow signal at $g = 2.02$ could result from a small fraction of re-oxidised [3Fe-4S] cluster, but even though the g values coincide, the linewidths are considerably broader than in the $[3Fe\text{-}4S]^+$ signal of the oxidised sample. Furthermore, this peak was also observed in some X-band samples (Fig. 5.10), which did not re-oxidise. An almost identical signal is observed in reduced samples of the [NiFe]-hydrogenase from *D. vulgaris* Miyasaki F and Fichtner *et al.* [218] assigned it to the *reduced* [3Fe-4S] cluster. Given that the $[3Fe\text{-}4S]^0$ cluster is thought to have a $S = 2$ ground state [202], and given that this signal is not always found to be present in reduced samples of Hyd-2 (and indeed

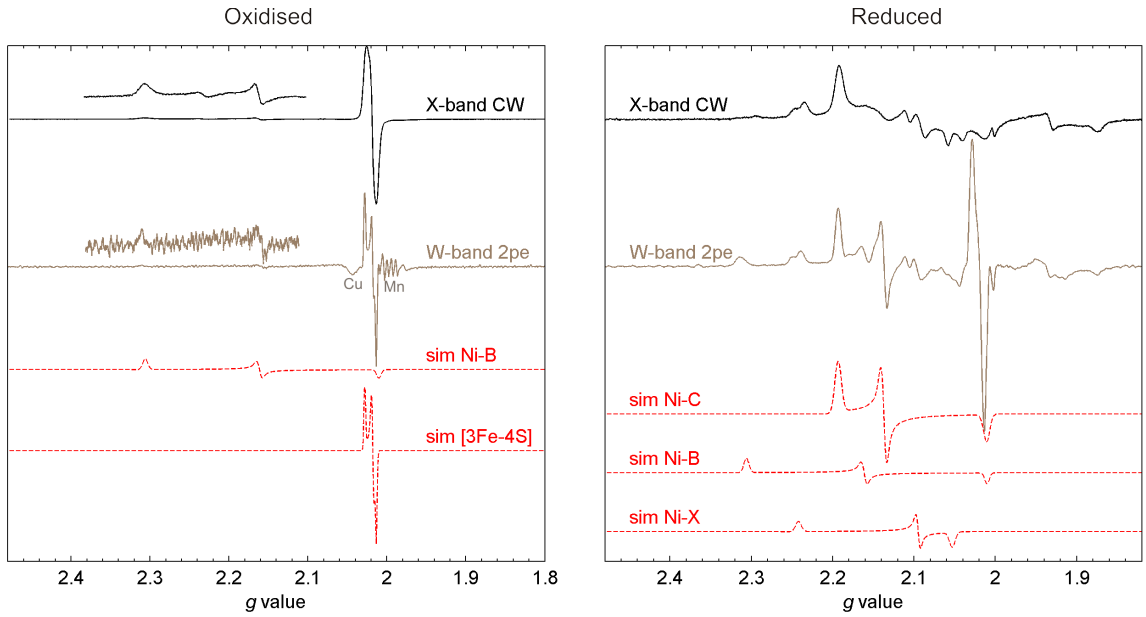


Figure 5.11: **Comparison of oxidised and reduced Hyd-2 at X-band and W-band frequencies.** W-band spectra are the numerical first derivative of two-pulse echo-detected field sweeps (2pe). The oxidised X-band CW spectrum results from an as-isolated sample containing as small amount of Ni-A. The oxidised W-band spectrum is from a sample that was anaerobically oxidised after activation under hydrogen. Insets show a magnification of the Ni region (x10). Reduced spectra result from samples reduced under hydrogen. The W-band sample re-oxidised slightly and shows the presence of a small amount of Ni-B (as well as Ni-X and Ni-C). Simulations are shown as dotted red lines. The peaks observed at $g = 1.87$ and $g = 1.94$ results from reduced [4Fe-4S]$^{+}$ species (see text). Measurement conditions: (X-band CW oxidised) mw power 2 mW, mw frequency 9.382 GHz, modulation amplitude 0.5 mT, temperature 20 K; (W-band oxidised) pulse sequence $\pi/2$ -τ - π - τ - echo, with $\pi/2 = 32$ ns, $\pi = 64$ ns, τ 180 ns; shot repetition time 7 ms, temperature 3.1 K, mw frequency 93.898 GHz, 2-step phase cycle, background subtracted, approximate protein concentration 200 μM; (X-band reduced) mw power 2 mW, mw frequency 9.386 GHz, modulation amplitude 0.5 mT, temperature 15 K; (W-band reduced) pulse sequence $\pi/2$ -τ - π - τ - echo, with $\pi/2 = 32$ ns, $\pi = 64$ ns, τ 140 ns; shot repetition time 1 ms, temperature 8.5 K, mw frequency 93.913 GHz. The field was calibrated at X-band and the W-band field was adjusted accordingly. The g values for the simulations are as follows: ([3Fe-4S]$^{+}$) $g_{x,y,z} = 2.028, 2.018, 2.013$; (Ni-A) $g_{x,y,z} = 2.306, 2.234, 2.010$; (Ni-B) $g_{x,y,z} = 2.306, 2.162, 2.010$; (Ni-C) $g_{x,y,z} = 2.194, 2.137, 2.011$; (Ni-X) $g_{x,y,z} = 2.242, 2.095, 2.053$ where g_x is taken as an average value of the two peaks observed in this field region. These are consistent with the values obtained from X-band measurements but in some cases could be determined with greater accuracy.

other standard [NiFe]-hydrogenases), it is concluded that the origin of this signal cannot be assigned to [3Fe-4S]^{0}. The Ni-X species, which is found in reduced, but not in oxidised samples, does not appear to interact with the proximal [4Fe-4S]$^{+}$ cluster, unlike Ni-C, as

its g values remain unchanged at X- and W-band frequencies.

The interconversion of Ni-C and Ni-L in Hyd-2 is now investigated in more detail.

5.3.4 Ni-C *vs* Ni-L in *E. coli* Hyd-2

The conversion from Ni-L to Ni-C in H_2-reduced Hyd-2 was monitored by measuring the increasing intensity of the Ni-C g_x signal intensity with time at 120 K, 125 K and 130 K. An example of such an experiment at 120 K is given in Fig. 5.12.

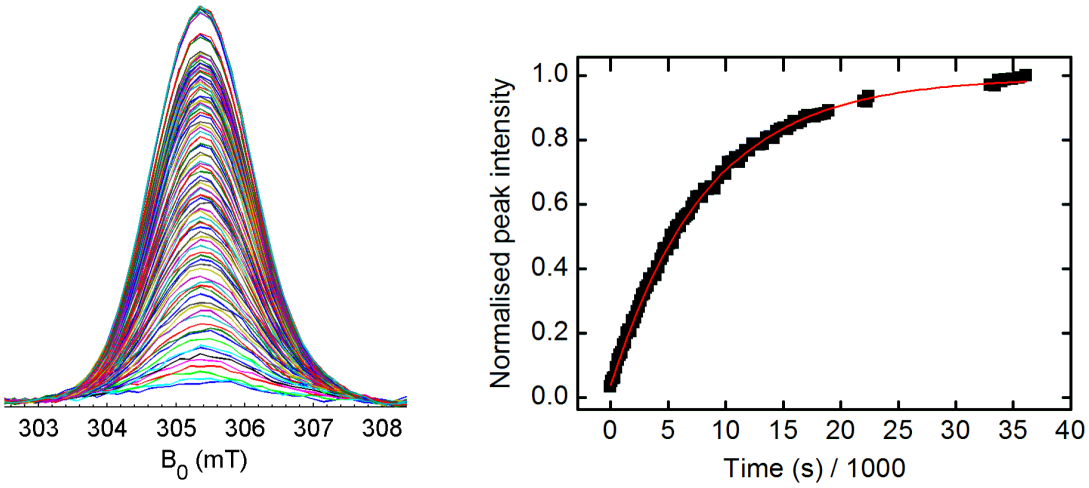


Figure 5.12: **Conversion of Ni-L to Ni-C in Hyd-2, monitored through the increasing peak intensity of Ni-C g_x.** (*Left*) X-band CW EPR spectra of the Ni-C g_x peak increasing in intensity the longer the sample is left in the dark. (*Right*) Intensity of the Ni-C g_x peak against time. The single exponential fit to the experimental data is shown in red. These experiments were performed by Rosalind Davies (University of Oxford).

The peak intensities as a function of time were fitted to a single exponential function,

$$y = a(1 - e^{-kt}) + b \tag{5.1}$$

where k is the rate of conversion of Ni-L to Ni-C. The variable b was necessary to account for the incomplete conversion of Ni-C to Ni-L before the experiment was commenced (complete conversion to Ni-L is only achieved upon illumination at lower temperatures than are feasible for a manageable timescale for this experiment). Table 5.2 summarises the rates of interconversion and the half lives of the Ni-L species ($\tau = 1/k$) at the three different temperatures. As expected, the rate of conversion increases as the temperature is increased.

Table 5.1: **Rate constants for the conversion of Ni-L to Ni-C in *E. coli* Hyd-2.** Rate constants were obtained as shown in Fig. 5.12 and all data were fitted with an error of less than 4% of the rate constant.

T (K)	1000/T	k x 10^4 (s^{-1})	τ_H (s)
120	8.33	1.20	8330
125	8.00	4.22	2370
130	7.69	11.90	840

The temperature dependence of the rate constants k follows the Arrhenius equation

$$k = A_0 \ \exp(-\frac{E_a}{RT}) \tag{5.2}$$

where A_0 is the pre-exponential factor (s^{-1}), R is the universal gas constant (8.3145 J K^{-1} mol^{-1}), E_a is the activation energy (kJ mol^{-1}) and T is the temperature in Kelvin (Fig. 5.13). The activation for the conversion of Ni-L to Ni-C in Hyd-2 is found to be $E_a = 30 \pm 1$ kJ mol^{-1} and $A_0 = 10^9$ s^{-1}.

Compared to the [NiFe]-hydrogenases from *D. vulgaris* Miyasaki F and *D. gigas*, both the activation energy and the pre-exponential factor are considerably smaller in *E. coli* Hyd-2 (Table 5.2). The smaller A_0 relative to the *D. vulgaris* enzyme indicates a lower

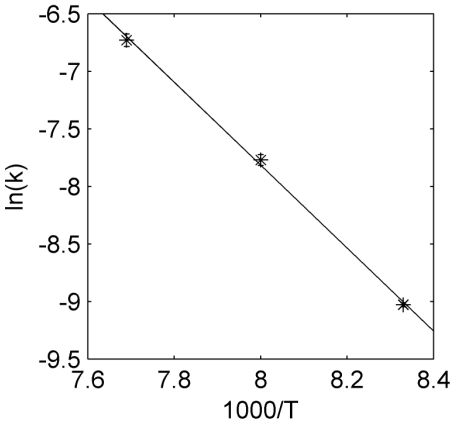


Figure 5.13: **Arrhenius plot (ln(k) against 1000/T) for the conversion of Ni-L to Ni-C in H_2-reduced Hyd-2.** See Table 5.2 for values of the rate constants at different temperatures.

probability of collision between the active site Ni and hydrogen. The Arrhenius equation was employed here to allow direct comparison with values reported in the literature. Strictly, transition state theory is more appropriate for the condensed phase where 'collisions' are not very meaningful. The rate constant for the reaction k is then given by the Eyring equation

$$k = \frac{k_B T}{h} \exp\left(\frac{\Delta S^{\ddagger}}{R}\right) \exp\left(\frac{-\Delta H^{\ddagger}}{RT}\right) \tag{5.3}$$

where k_B is the Boltzmann constant, h is Planck's constant and $\Delta S^{\ddagger}$ and $\Delta H^{\ddagger}$ are the standard entropy and enthalpy of activation, respectively ($\ddagger$ refers to the formation of the transition state). Application of the logarithmic transform leads to

$$\ln \frac{k}{T} = \frac{-\Delta H^{\ddagger}}{R} \frac{1}{T} + \ln\left(\frac{k_B T}{h}\right) + \frac{\Delta S^{\ddagger}}{R}. \tag{5.4}$$

$\Delta H^{\ddagger}$ and E_a are therefore identical and $\Delta S^{\ddagger} = -73$ J K^{-1} mol^{-1}. Thus, entropy decreases upon achieving the transition state, consistent with an associative mechanism for the conversion of Ni-L to Ni-C.

The structural differences between Ni-C and Ni-L in Hyd-2 are now investigated further using hyperfine spectroscopy. In 2003, Brecht *et al.* [194] used HYSCORE and ENDOR to

Table 5.2: **Comparison of the activation energies/enthalpies for the interconversion between Ni-L and Ni-C in standard [NiFe]-hydrogenases**.

[NiFe]-hydrogenase	$E_a/\Delta H^{\ddagger}$ (kJ mol^{-1})	A_0 (s^{-1})	$\Delta S^{\ddagger}$ (J K^{-1} mol^{-1})
D. vulgaris Miyasaki F [253]	46	10^{12}	-
D. gigas [263]	36 ± 3	-	-
E. coli Hyd-2	30 ± 1	10^{9}	−73 ± 1

provide the first experimental evidence that the Ni-C state in the regulatory H_2-sensing [NiFe]-hydrogenase from *R. eutropha* (*Re*-RH) contains a bridging hydride whereas in the Ni-L state the bridging position remains empty. In *Re*-RH the Fe-S clusters do not complicate the interpretation of the EPR spectra because they remain oxidised under conditions where the Ni-C or Ni-L states are visible [254, 264]. Even though the active site in this hydrogenase is thought to be structurally similar to that in catalytic [NiFe]-hydrogenases, there are differences; for instance, no EPR signals are observed in the oxidised *Re*-RH and the Ni-L g values differ from those reported in standard hydrogenases and coincide with those of Ni-X in Hyd-2 (see above). The exchangeable proton at the active site could be directly observed in D_2O-exchanged and D_2-reduced samples of *Re*-RH in the Ni-C state using HYSCORE. Similar signals (albeit less clearly resolved) were later observed in the catalytic *D. vulgaris* Miyasaki F hydrogenase [260], leading to the conclusion that electronic structure of the Ni-C state in regulatory and catalytic hydrogenases is the same. However, studies of the Ni-C state in the O_2-tolerant *Aa* Hase I revealed that the hydride is probably less strongly bound and farther from the active site Ni [265].

Samples of Hyd-2 reduced by D_2 or H_2 were prepared to determine whether any exchangeable protons are present at the active site in this enzyme. The HYSCORE spectra of the D_2-reduced sample in the Ni-C state at the g_x and g_y field positions (Fig. 5.14, right column) show a ridge centered at the ^{2}H Larmor frequency. A tentative simulation is overlaid onto the experimental data obtained at the g_y orientation. The red curve corresponds to correlations between the single quantum transitions between the two m_S

manifolds (ss), the pink to correlations of the single-quantum frequency of one m_S manifold to the double-quantum frequency of the other m_S manifold (sd) and the black to correlations between the double-quantum frequencies (dd). The simulation takes into account orientation selection but no attempt is made to calculate peak intensities, which are difficult to predict especially in samples with inhomogeneous broadening [126]. In the absence of the sd and dd transitions, it is difficult to determine the hyperfine tensor. Pulse X-band ENDOR measurements were attempted but these were not successful, most likely because of the enhanced relaxation rate of Ni-C due to interaction with the proximal Fe-S cluster and the fast nuclear relaxation compared to the timescale of the pulse ENDOR experiment. Förster *et al.* [260] found that only CW ENDOR experiments on extremely high protein concentrations were feasible on a sample of *D. vulgaris* Miyasaki F containing Ni-C largely uncoupled to the proximal Fe-S cluster; pulse ENDOR measurements remained unsuccessful. The HYSCORE spectra obtained here are very similar to those of *Aa* Hase I [265] where the anisotropic and isotropic parts of the hyperfine tensor (determined from Q-band ENDOR measurements) were found to be considerably smaller than those obtained for *Re*-RH [194], which was attributed to a weaker binding of the hydride [265]. Although no CW ENDOR or pulse Q-band ENDOR experiments could be carried out to characterise, further, the exchangeable protons in *E. coli* Hyd-2, the HYSCORE measurements indicate that the hyperfine tensor is similar to that determined for *Aa* Hase I and therefore it is reasonable to propose that the Ni-C state of Hyd-2 also only contains a weakly bound hydride in the bridging position.

The spectra of the H_2- and D_2-reduced samples recorded at the g_x orientation show strong peaks along the diagonal at 0.5, 1.2 and 1.7 MHz (Fig. 5.14, bottom row). These peaks, where the two smallest frequencies (ν_0 and ν_-) add up to the largest frequency (ν_+), were also observed in HYSCORE spectra of the *D. vulgaris* hydrogenase [260] and are indicative of a $I = 1$ nucleus (^{14}N) in the 'exact cancellation' condition, where the hyperfine and nuclear Zeeman interaction cancel each other out in one of the m_S manifolds and the three observed frequencies give the quadrupole interaction [266] (see Chapter 2,

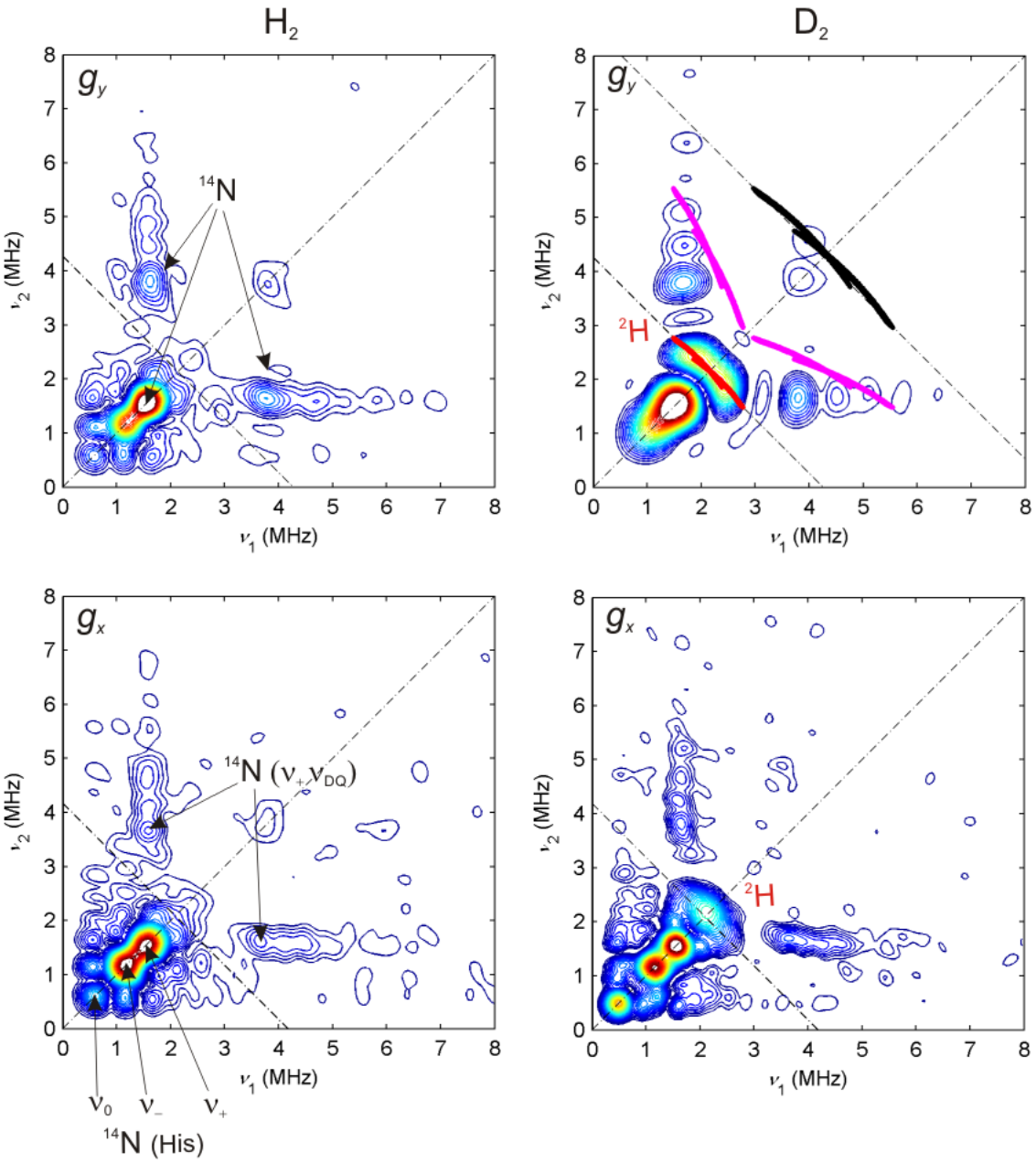


Figure 5.14: **X-band HYSCORE spectra (^{14}N/^{2}H region) of Ni-C in H_2-reduced (left) and D_2-reduced (right) *E. coli* Hyd-2 at g_y (top) and g_x (bottom) orientations.** Measurement conditions: (D_2 g_y) $\pi/2 = 20$ ns, $\pi = 16$ ns, τ 128 ns, shot repetition time 3 ms, 9.734 GHz, 324.1 mT, 80 points, 8-step phase cycle; (D_2 g_x) $\pi/2 = 20$ ns, $\pi = 16$ ns, τ 128 ns, shot repetition time 3 ms, 9.746 GHz, 319.2 mT, 160 points, 8-step phase cycle; (H_2 g_y) $\pi/2 = 16$ ns, $\pi = 16$ ns, τ 128 ns, shot repetition time 1 ms, 9.764 GHz, 325.2 mT, 160 points, 8-step phase cycle; (H_2 g_x) $\pi/2 = 16$ ns, $\pi = 16$ ns, τ 128 ns, shot repetition time 1 ms, 9.764 GHz, 318.0 mT, 160 points, 8-step phase cycle. All measurements were recorded between 2.6 and 2.7 K. The orientations g_y and g_x refer to the Ni-C state (see Fig. 5.7). The ^{2}H ridge in the top right spectrum was simulated with A = [-1.0, 0.5, -1.9] and $g_{x,y,z}$ = 2.194, 2.137, 2.011.

Section 2.6.3). The ^{14}N nucleus giving rise to this pattern has previously been identified to belong to the ϵ nitrogen of a histidine (His88) which forms a hydrogen bond to one of the bridging cysteines (Cys549) of the [NiFe] center in the hydrogenase from *D. vulgaris* Miyasaki F. From sequence alignments (Fig. 5.15) it is therefore predicted that His68 forms a hydrogen bond to Cys549 in *E. coli* Hyd-2 (for which there is no crystal structure to date). The lower-intensity cross peaks also visible at the g_y orientation relate the double-quantum transition at 3.7 MHz to the ν_+ transition at 1.6 MHz.[4] Again, these signals are also observed in the hydrogenase from *D. vulgaris* Miyasaki F [260] and *Aa* Hase I [265].

```
                                  68                        549
E. coli Hyd-2                CGVCTTTHALSSVR [...] HSFDPCMACAVH
D. vulgaris Miyasaki F       CGVCTYTHALASTR [...] HSFDPCIACGVH
A. aeolicus Hase I           CGVCTSIHALASLR [...] HSFDPCLACSTH
```

Figure 5.15: **Multiple sequence alignment showing sections of the large subunits in *E. coli* Hyd-2, *D. vulgaris* Miyasaki F and *A. aeolicus* Hase I.** The numbering is given for *E. coli* Hyd-2. Alignments were generated using the program ClustalW2 [267].

In the absence of a strongly coupled hydride in Hyd-2 Ni-C, and given that the Ni-L state is thought to differ from Ni-C not only through the absence of a bridging hydride but also through protonation of one of the terminal cysteines of the Ni ion [226], attempts were made to distinguish the Ni-C and Ni-L states in the proton region of the spectrum. The HYSCORE spectra in Fig. 5.16 were all carried out at the same field position (g_x of Ni-C) to allow a direct comparison. Short time traces and low temperatures (2.7 K) were required, suggesting that the proton coherences relax very fast. The corresponding spectra of H_2- and D_2-reduced samples are almost super-imposable. The signal-to-noise ratio in the spectra from the D_2-reduced sample are inferior, presumably because of the strong modulation caused by deuterium nuclei. The spectra of Ni-C and Ni-L only differ by the presence of an additional peak at approximately 16.5 MHz on the diagonal in the Ni-C state, which cannot at present be assigned. The peak was also observed at different orientations (spectra not shown).

[4]Due to the short time traces required, it is difficult to apply windowing functions without losing resolution, and artifacts arise due to truncation of the time domain. The double quantum peaks therefore appear broad.

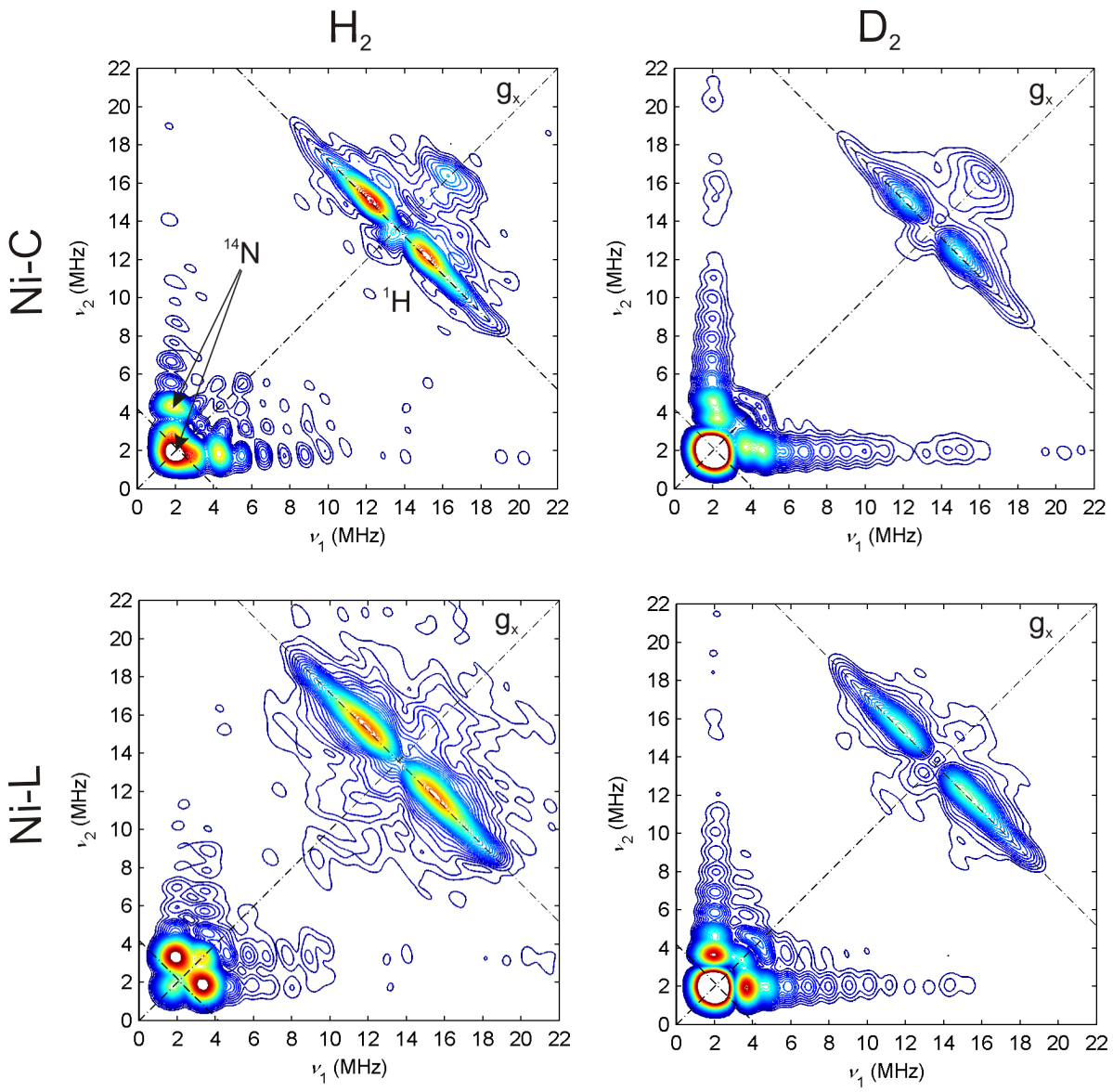


Figure 5.16: **X-band HYSCORE spectra (^{1}H region) of Ni-C (top) and Ni-L (bottom) in H_2-reduced (left) and D_2-reduced (right) *E. coli* Hyd-2 at the g_x orientation.** Measurement conditions: (D_2 Ni-C) $\pi/2$ = 16 ns, π = 16 ns, τ 128 ns, shot repetition time 1 μs, 9.730 GHz, 316.9 mT, 80 points, 8-step phase cycle; (D_2 Ni-L) $\pi/2$ = 16 ns, π = 16 ns, τ 128 ns, shot repetition time 1 μs, 9.747 GHz, 317.4 mT, 60 points, 8-step phase cycle; (H_2 Ni-C) $\pi/2$ = 16 ns, π = 16 ns, τ 128 ns, shot repetition time 1 μs, 9.764 GHz, 318.0 mT, 60 points, 8-step phase cycle; (H_2 Ni-L) $\pi/2$ = 16 ns, π = 16 ns, τ 128 ns, shot repetition time 1 μs, 9.746 GHz, 317.4 mT, 60 points, 8-step phase cycle. All measurements were recorded between 2.6 and 2.7 K. The orientation g_x refers to the Ni-C state (see Fig. 5.7).

5.3.5 The EPR-active reduced state in *E. coli* Hyd-1: Outlook

The spectrum of a sample of *E. coli* Hyd-1 reduced to -200 mV at 15 K (Fig. 5.17), a potential at which Ni-L* is visible, shows that the reduced Fe-S cluster signals are much more well defined than those of standard hydrogenases, as previously observed for the O_2-tolerant *Aa* Hase I [84] and *Re*-MBH [82].

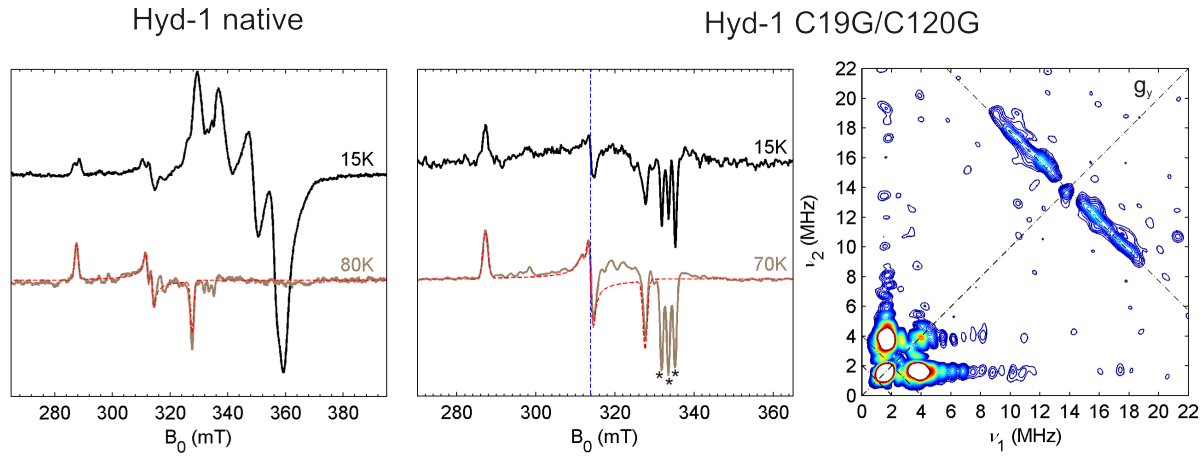


Figure 5.17: **X-band CW EPR spectra of *E. coli* Hyd-1 native (left) and C19G/C120G (centre) at low potentials and HYSCORE spectrum of Ni-L* in Hyd-1 C19G/C120G at the g_y orientation (right).** Measurement conditions: (Hyd-1 native) mw power 2 mW, mw frequency 9.385 GHz, modulation amplitude 1 mT (15 K and 80 K); ; (Hyd-1 C19G/C120G) mw power 2 mW, mw frequency 9.385 GHz, modulation amplitude 0.5 mT (15 K) or mw power 8 mW, mw frequency 9.382 GHz, modulation amplitude 1 mT (70 K); (HYSCORE Hyd-1 C19G/C120G) $\pi/2$ = 16 ns, π = 16 ns, τ 128 ns, shot repetition time 5 ms, 9.737 GHz, 324.4 mT, 75 points, 8-step phase cycle, 2.7 K. Unidentified peaks are marked with asterisks (see text).

It will be shown in Chapter 8 that this signal originates from the reduced proximal and medial clusters only, as the distal cluster is in a higher spin state and difficult to detect with EPR. The splitting of Ni-L* g_x at low temperatures (15 K spectrum in Fig. 5.17) is due to a dipolar interaction with the reduced proximal cluster (see Chapter 8, Section 8.3.3) and is similar to that of the Ni-L species of *D. gigas*, *D. fructosovorans* and *Dm. baculatum* [214] but rather different to that of Ni-C [177]. The central spectrum in Fig 5.17 originates from a variant Hyd-1, in which cysteines 19 and 120 at the proximal cluster were changed to glycine residues, reduced to a similar potential as the native Hyd-1 enzyme. This variant is introduced in detail in the following Chapter, Section

6.1.2. Ni-L* remains unsplit at low temperatures (both the proximal and distal clusters now have $S > 1/2$ ground states and are very difficult to detect, as will be shown in Chapter 8), so that a structural characterisation of this state using HYSCORE ought to be easier compared to the native enzyme. The three sharp peaks marked with asterisks in Fig. 5.17 are only observed in preparations of Hyd-1 (and variants) but never in Hyd-2. Similar peaks have been observed in *Aa* Hase I [16, 265], *Re*-MBH [82] and the soluble hydrogenase from *R. eutropha* [268]. They may be associated with degradation of the enzyme but the Fe-S clusters are unlikely to be damaged since there was essentially no $g = 4.3$ signal corresponding to the presence of free Fe^{3+} which would originate from cluster degradation (see wide-field sweep spectra of the C19G/C120G variant in Fig. 10.2 in the Appendix). The proton region of the HYSCORE spectrum of the Hyd-1 C19G/C120G variant measured at the g_y orientation (Fig 5.17, right) shows greater similarity with the Hyd-2 Ni-L spectra although it was difficult to obtain good quality spectra since the proton coherences were found to be similarly fast-relaxing, probably due to the reduced high-spin clusters.

5.4 Discussion and future work

The EPR signatures of the oxidised and reduced forms of *E. coli* Hyd-1 and Hyd-2 are consistent with their electrochemical characterisation [83] that places Hyd-1 into the family of O_2-tolerant hydrogenases, able to sustain catalytic activity in the presence of O_2 and strongly biased towards H_2 oxidation, and Hyd-2 into the family of standard, O_2-sensitive hydrogenases, capable of both H_2 oxidation and H_2 production. The contrasting properties of Hyd-1 and Hyd-2 are already being exploited in possible technological applications: The ability of Hyd-1 to catalyse H_2 oxidation in the presence of O_2 makes it an appropriate catalyst for small enzyme-based fuel cells [269]; Hyd-2 can be coupled to a CO dehydrogenase *via* a conducting graphite particle and this system catalyses the 'water-gas-shift' reaction (the formation of CO_2 and H_2 from CO and H_2O) with much

higher efficiency than the technologies currently used in industry [42].

However, important differences exist not only between Hyd-1 and Hyd-2, but also between Hyd-1 and other characterised O_2-tolerant hydrogenases, and between Hyd-2 and other standard hydrogenases. Firstly, reduced Hyd-1 was found to form an EPR-visible state of the active site Ni at an usually high potential. Secondly, electrochemical kinetic isotope effect experiments revealed that H_2 cleavage or the transfer of a substrate proton is more rate-limiting in Hyd-1 than in Hyd-2. Thirdly, the Ni-C state in Hyd-2 was found to contain, at best, a weakly bound hydride in the bridging position, contrary to the strongly bound hydride found in the Ni-C states of the regulatory *R. eutropha* hydrogenase [194] and the catalytic *D. vulgaris* Miyasaki F enzyme [260] and more comparable to the Ni-C state of the O_2-tolerant *Aa* Hase I [265]. Furthermore, the activation energy for the conversion of Ni-L to Ni-C in Hyd-2 was found to be lower than values reported for other standard hydrogenases. These findings are now discussed in more detail.

The reduced Ni species in Hyd-1 (Ni-L*) contrasts with those in other O_2-tolerant [NiFe]-hydrogenases. Saggu *et al.* [82] reported that the dimeric form of *Re*-MBH (which is comparable to the Hyd-1 complex studied here) forms a mixture of Ni-C and Ni-L states when the enzyme is incubated under H_2. Unusually, compared to standard hydrogenases, the Ni-C state was found to be formed under normal daylight conditions and did not convert to Ni-C in the dark [82]. On the other hand, the over-expressed trimeric form of this enzyme, which includes the membrane-integral cytochrome *b* and is isolated still bound to the membrane, only showed Ni-C in 80 K EPR spectra following reduction with H_2. A mixture of three Ni-L states appeared upon illumination with white light at 80 K [82], thereby mirroring the standard hydrogenases. Because the dimer, but not the trimer, also contained an EPR-silent inactive state (detected through FTIR), the authors concluded that only in its native environment (as a trimer) is the *Re*-MBH enzyme fully catalytically active, and that Ni-L is not a physiologically relevant state. It would therefore be informative to study the trimeric from of *E. coli* Hyd-1 (which includes HyaB, HyaA and HyaC attached to the membrane, see Fig. 5.3). However, the natural expression

level of Hyd-1 and Hyd-2 is too low for successful EPR measurements of entire membrane fractions (obtained from a Hyd-2/Hyd-3 or a Hyd-1/Hyd-3 knockout strain of *E. coli*)[5]. Unlike the hydrogenase-maturation process of *R. eutropha*, that of *E. coli* is not well understood and over-expression is therefore extremely difficult. Nonetheless, important differences exist between the EPR spectroscopic characteristics of the dimeric forms of *E. coli* Hyd-1 and *Re*-MBH, and the Ni-L* state with its light-insensitivity and unusual g values remains unprecedented. It is interesting to note that Hyd-2 exhibits 'normal' Ni-C and Ni-L signals even though it is, like Hyd-1, isolated detached from the membrane.

The cytochrome *b*-containing complex of Hydrogenase-I from *A. aeolicus* (*i.e.* the trimer) was found to form Ni-C upon reduction with H_2 [265]. However, a Ni-L state with g values ($g_{x,y,z}$ = 2.34, 2.15, 2.05) similar to Ni-L* of Hyd-1 was present in spectra at 70 K (in the dark) without prior illumination, and a pure Ni-C spectrum was only observed at 100 K in the dark [265]. This suggests that in *Aa* Hase I the energy barrier for the conversion of Ni-L into Ni-C is lower than for standard hydrogenases and indeed, Pandelia *et al.* [265] proposed that Ni-C of *Aa* Hase I contains a more weakly bound hydride. The apparently greater stability of the Ni-L state in this enzyme and the failure to detect a Ni-C state in *E. coli* Hyd-1 point towards a greater importance of the Ni-L state than previously assumed. In addition to EPR measurements, FTIR studies of Hyd-1 in the Ni-L* state would be highly informative. In particular, it would be interesting to establish whether the CO and CN^- stretching frequencies are comparable to those of the Ni-C or Ni-L states of other [NiFe]-hydrogenases or rather different, indicating a change in the electronic structure of the active site.

Several arguments point towards a structural similarity of Hyd-1 Ni-L* with Ni-L rather than Ni-C (hence it is named Ni-L*). Firstly, the g values are similar to the light-induced state Ni-L2 of *Dm. baculatum* [NiFe-Se]-hydrogenase [214] and Ni-L1 of *Aa* Hase I [265]. Secondly, the splitting pattern at low temperatures due to magnetic interaction with the reduced proximal cluster (see Chapter 8, Section 8.3.3) is similar

[5]The knockout strains were provided by Prof. Frank Sargent, University of Dundee.

to that of Ni-L in hydrogenases from other species [214] but rather different to that of Ni-C [177]. Finally, HYSCORE spectra of Hyd-1 Ni-L* resemble those of Hyd-2 Ni-L more than those of Hyd-2 Ni-C. Because of the presence of fast-relaxing reduced Fe-S clusters, the interpretation of these HYSCORE measurements is treated with caution. Nonetheless it is interesting that the HYSCORE spectra of Hyd-2 Ni-C resemble those of *Aa* Hase I Ni-C which was concluded to contain a weakly bound hydride [265]. This finding correlates with the lower activation energy required for the conversion of Ni-L to Ni-C in Hyd-2 compared to other enzymes and the apparently greater stability of Ni-L in *Aa* Hase I. It could therefore be possible that the activation energy in Hyd-1 is even smaller, such that Ni-C is a state so transient that it cannot be observed.

Recently, Lill and Siegbahn [229] proposed a mechanism using theoretical methods, which for the first time includes the Ni-L state in the catalytic cycle of [NiFe]-hydrogenases. As shown in Fig. 5.18, the authors came to the conclusion that only the first step of the cycle involves heterolytic cleavage of H_2, yielding Ni-C. Subsequently, catalysis proceeds through oxidative addition to Ni-L, so that both Ni-C and Ni-L are intermediates in the catalytic cycle.

This work on the *E. coli* Hyd-1 and Hyd-2 enzymes provides an experimental indication that Ni-L is not simply an artifact induced by light, but could be an intermediate in the catalytic cycle of [NiFe]-hydrogenases.

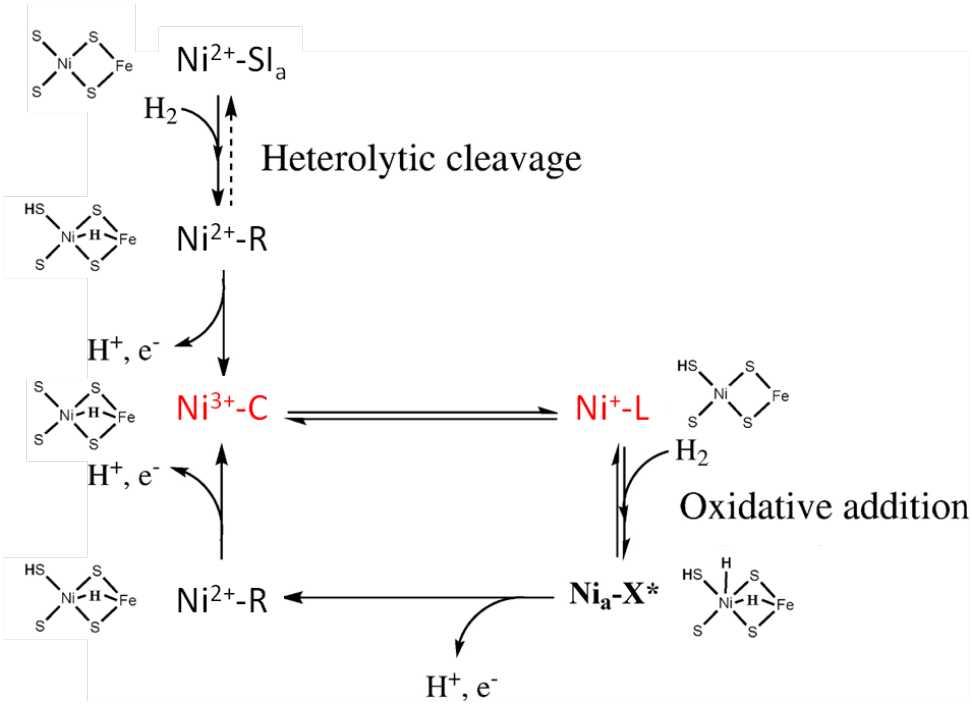


Figure 5.18: **Mechanism for H_2 cleavage in [NiFe]-hydrogenases proposed by Lill and Siegbahn [229] based on theoretical work, which includes Ni-L as an intermediate.** The nomenclature has been changed to that used in this thesis, with the exception of the Ni_a-X^* state which is unprecedented. EPR-active states are shown in red. The structural correspondence of the states is also included. Figure adapted with permission from ref. [229]. Copyright 2009 American Chemical Society.

Chapter 6

O_2-tolerance in [NiFe]-hydrogenases and the role of supernumerary cysteines at the proximal Fe-S cluster

All protein film electrochemistry experiments were carried out by Dr. Alison Parkin and Dr. Rhiannon Evans (Oxford). The C19G, C120G and C19G/C120G variants of *E. coli* Hyd-1 were made by Dr. Michael Lukey, as reported in his DPhil Thesis [136]. I am grateful to Elena Nomerotskaia for help with the isolation of native Hyd-1, and the C19G, C120G and C19G/C120G variant enzymes. The *Salmonella* Hyd-5 enzyme was prepared by Dr. Alison Parkin and Elena Nomerotskaia. EPR sample preparations and measurements were carried out with the help of Rosalind Davies under my supervision. Part of the work described in this Chapter has been published [89, 138, 270].

Abstract

The work in this Chapter aims to define what EPR spectral features are a fingerprint of O_2 tolerance in [NiFe]-hydrogenases.

Oxygen-tolerant [NiFe]-hydrogenases contain two 'supernumerary' cysteines at their proximal Fe-S cluster. These residues are glycines in standard hydrogenases. The individual and collective impact these cysteines have on the EPR spectra is investigated with studies of the C19G, C120G and C19G/C120G variants of *E. coli* Hyd-1. The results are discussed in the context of the reactivity of these enzymes with O_2. O_2 tolerance is largely conferred by a single cysteine (C19) and replacement of this amino acid with glycine removes the ability of the enzyme to function even in 1% O_2 [89]. However, the C19G variant is still capable of forming an additional paramagnetic species at high potentials so far attributed to be a characteristic of O_2-tolerant hydrogenases. This species has been assigned to the proximal Fe-S cluster undergoing a second redox transition at high potential [16], which provides a 'rescue' electron to the active site when O_2 attacks. The EPR signals of the Fe-S clusters in the four Hyd-1 enzymes, studied as a function of potential, are discussed in light of the recent crystal structures of O_2-tolerant [NiFe]-hydrogenases.

Investigation of the active-site Ni species formed following exposure to O_2 reveals that only the native Hyd-1 enzyme makes the Ni-B state exclusively, which can reactivate quickly to rejoin the catalytic cycle. C19G and C19G/C120G form O_2-inactivated EPR-silent Ni states in addition to Ni-A and Ni-B.

Finally, in light of the studies of *E. coli* Hyd-1, the EPR spectroscopic features of the O_2-tolerant hydrogenase-5 from *Salmonella enterica* serovar Typhimurium are characterised.

6.1 Introduction

6.1.1 Background to O_2 tolerance in [NiFe]-hydrogenases

Oxygen-tolerant catalytic [NiFe]-hydrogenases have been subject to intense research because their ability to remain functional in the presence of O_2 may be useful in the development of future H_2 technologies [75, 76, 269, 271, 272].

Electrochemical experiments of one of the best-characterised O_2-tolerant [NiFe]-hydrogenases, *Re*-MBH (the membrane-bound hydrogenase from *R. eutropha*), have shown that during H_2 oxidation, the enzyme survives O_2 by forming only the inactive *Ready* state, in which O_2 has been fully reduced and which reactivates very rapidly to rejoin the catalytic cycle [240]. In contrast, electron deficiency during O_2 attack results, at best, in the *Unready* state which reactivates only very slowly [224, 273, 274], and this state is formed in addition to *Ready* upon O_2 attack in standard hydrogenases. The contrasting response to O_2 of O_2-tolerant *E. coli* Hyd-1, and the standard hydrogenase *E. coli* Hyd-2 was shown in Chapter 5 (Section 5.1.3). The *Unready* and *Ready* kinetically defined states have been associated with the spectroscopically defined states Ni-A and Ni-B that are distinguished by EPR [118] and infrared [226] spectroscopy (see Chapter 5, Section 5.1.2). However, while Ni-B and *Ready* are widely regarded essentially as synonymous, the association between Ni-A and *Unready* is less certain, especially since [NiFeSe]-hydrogenases have been shown to form *Unready* states which are not Ni-A [275, 276].

Because of the damage that O_2 causes at the active site, numerous studies have focused on elucidating the origin of O_2 tolerance by addressing how an O_2 molecule might be prevented from attacking the [NiFe] centre [263, 277–280]. Site-directed mutagenesis has been conducted both in the O_2-tolerant *Re*-MBH [86], as well as the standard hydrogenase from *D. fructosovorans* [263, 277–280], and the effect on O_2 tolerance of the residue substitutions was tested. Most notably, the substitution of valine-74 (valine-78 in *E. coli* Hyd-1, see Fig. 6.1) for a cysteine in the [NiFe]-hydrogenase from *D. fructosovorans*,

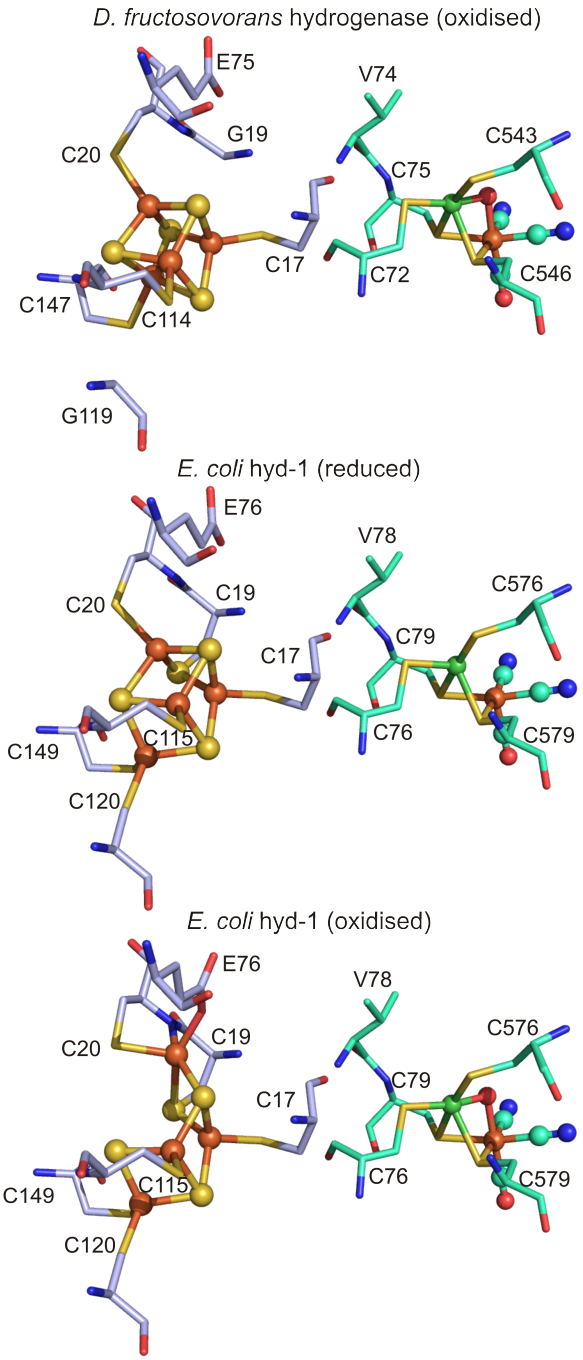


Figure 6.1: **The proximal cluster and active site and their amino acid environment in *D. fructosovorans* [NiFe]-hydrogenase (*Df* Hase, top) and *E. coli* Hyd-1 in the reduced (centre) and oxidised (bottom) forms.** Small subunit residues have a blue carbon backbone, while the Fe-S cluster is shown in stick-and-sphere representation. Large subunit residues have a green carbon backbone and the [NiFe] active site with Fe, its CO and CN^- ligands and Ni are in stick-and-sphere representation. The two terminal Ni-ligating cysteines and the Ni-Fe bridging μ-cysteines are also shown, as are valine-78 (*Ec* Hyd-1)/valine-74 (*Df* Hase) of the large subunit and glutamate-76 (*Ec* Hyd-1)/glutamate-75 (*Df* Hase). PDB: 1YRQ (*D. fructosovorans*), 3UQY and 3USC (*E. coli* Hyd-1). Only one of the conformers of the oxidised state of *E. coli* Hyd-1 is shown here (see Chapter 7 and ref. [18]).

a fully conserved residue in all [NiFe]-hydrogenases, resulted in a significant increase in O_2 tolerance [280]. Although this is an interesting finding, a cysteine residue is not found in this position in either standard or O_2 tolerant [NiFe]-hydrogenases and the study therefore reveals nothing about the physiological origin of O_2 tolerance in catalytic [NiFe]-hydrogenases.

Recent investigations have shown that at least part of the answer to the origins of O_2 tolerance in respiratory [NiFe]-hydrogenases is found in the small subunit containing the Fe-S electron transfer centres [16, 82, 88, 89, 281]. Notably, all O_2-tolerant [NiFe]-hydrogenases characterised to date exhibit a complex multiline Fe-S cluster EPR spectrum under oxidising conditions [16, 82–85, 88]. Through EPR redox titrations and Mössbauer spectroscopy of *Aa* Hase I (*Aquifex aeolicus* Hydrogenase I), Pandelia *et al.* showed that the proximal cluster is able to undergo *two* sequential redox transitions over a physiologically relevant potential range and that the 'overoxidised' proximal cluster is responsible for the complex multiline EPR spectrum formed at high potentials [16]. The proximal cluster should thus allow the delivery of rescue electrons to the active site when O_2 attacks, a prerequisite for the formation of the harmless Ni-B state. The authors further proposed that the cluster's unusual redox behaviour could be due to a unique coordination at one Fe subsite, which may recruit an extra cysteine [16]; O_2 tolerant membrane-bound hydrogenases contain two conserved cysteines (C19 and C120 in HyaA, the small subunit of *E. coli* Hyd-1) at the proximal Fe-S cluster that correspond to conserved glycines in standard hydrogenases [16, 62, 82, 88] (Fig. 6.2).

X-ray absorption spectroscopy experiments of *Re*-MBH further indicated that the proximal cluster in O_2-tolerant hydrogenases has an unusual structure [281] and the recently published crystal structures of *H. marinus* MBH and *Re*-MBH prove that the cysteines indeed play a role in ligating the proximal cluster (Fig. 6.1). Goris *et al.* [88] showed that a C19G/C120G variant of *Re*-MBH was less O_2 tolerant both *in vivo* and *in vitro* compared to the native enzyme. Furthermore, the multiline EPR spectrum, attributed by Pandelia *et al.* [16] to arise from coupling between the medial [3Fe-4S]$^+$ cluster and

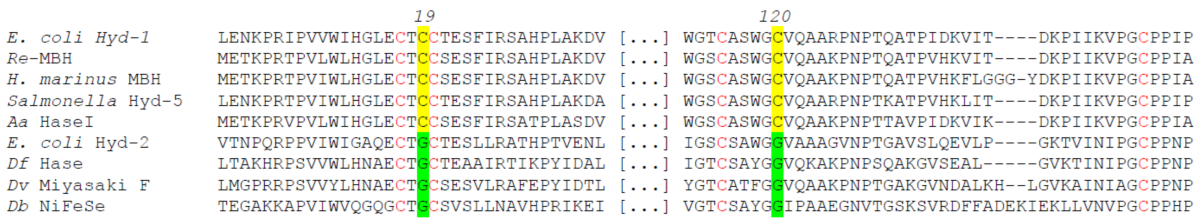


Figure 6.2: **Multiple sequence alignment of key sections of the small subunit in a selection of catalytic [NiFe(Se)]-hydrogenases.** The numbering is given for *E. coli* Hyd-1. *H. marinus* MBH = *Hydrogenovibrio marinus* [NiFe]-hydrogenase, *Df* Hase = *D. fructosovorans* [NiFe]-hydrogenase, *Dv* Miyasaki F = *D. vulgaris* Miyasaki F [NiFe]-hydrogenase, *Db* NiFeSe = *Desulfomicrobium baculatum* [NiFeSe]-hydrogenase. The cysteine residues shown in red coordinate the proximal cluster in both standard and O_2-tolerant [NiFe]-hydrogenases (C17, C20, C115 and C147 in *E. coli* Hyd-1 numbering). The supernumerary cysteines only found in O_2-tolerant enzymes are highlighted in yellow and the corresponding glycines in standard hydrogenases are highlighted in green. Sequence alignments were performed using the program ClustalW2 [267].

the proximal $[4Fe\text{-}4S]^{3+}$ cluster (which we now know is more correctly described by $[4Fe\text{-}3S]^{5+}$ [17]), was replaced by a simple $[3Fe\text{-}4S]^{+}$ cluster signal in the EPR spectrum of the C19G/C120G variant [88]. These publications call for a deconvolution of the individual and collective roles of the supernumerary cysteines in conveying O_2 tolerance.

Here, C19 and C120 in the small subunit of *E. coli* Hyd-1 are systematically exchanged for glycines and the resulting variants C19G, C120G and C19G/C120G are compared using EPR spectroscopy. In particular, the correlation between O_2 tolerance and the presence of the complex multiline EPR signal formed at high potentials, the formation of Ni species upon O_2 attack and the association between *Unready* and Ni-A (*vide supra*) is investigated, in close association with the electrochemical findings which were the work of Dr. Alison Parkin and Dr. Rhiannon Evans. The molecular biology to generate the variants was carried out by Dr. Michael Lukey.

Understanding the origins of O_2 tolerance in hydrogenases is not only important for potential technological applications but also has a potential impact on human health. *Salmonella enterica* serovar Typhimurium (hereafter *Salmonella*), a bacterium which is closely related to *E. coli*, causes numerous infections worldwide and is particularly dangerous and sometimes fatal to individuals whose immune system is already compromised,

as for example for AIDS patients [282]. Remarkably, Maier *et al.* found a 100% survival rate in mice infected with a variant strain of *Salmonella* in which the hydrogenases had been removed − in stark contrast with the 0% survival in mice infected with the native strain [283]. Possible vaccines for *Salmonella* infection may thus be developed if the origin of virulence stemming from its hydrogenase enzymes can be understood.

Similarly to *E. coli*, *Salmonella* is a facultative aerobe, evolved to grow under anaerobic conditions but able to function in the presence of O_2. A variety of enzymes tuned to operate under different conditions allow such metabolic flexibility in these bacteria [138]. Analogously to *E. coli* (Chapter 5, Section 5.1.3), anaerobic respiratory H_2 uptake in *Salmonella* is catalysed by Hyd-1 and Hyd-2, and Hyd-3 is responsible for H_2 evolution under fermentative conditions [232]. A third respiratory [NiFe]-hydrogenase (named Hyd-5), which has no direct homologue in *E. coli*, is expressed under aerobic conditions [138]. Electrochemical experiments carried out by Dr. Alison Parkin have shown that Hyd-5 is a H_2-uptake enzyme which is able to sustain H_2 oxidation in the presence of high levels of O_2 [138]. With the knowledge gained from the studies of the native and variant *E. coli* Hyd-1 enzymes, this chapter closes with the first EPR characterisation of Hyd-5 from *Salmonella enterica*.

6.1.2 Electrochemical characterisation of the proximal cluster of native *E. coli* Hyd-1 and variants C19G, C120G and C19G/C120G

Protein film electrochemistry is very well-suited for studying the reactions of hydrogenases with O_2: Soluble electron donors or acceptors that invariably react with O_2 are not required and the status of the enzyme can be monitored over many hours, since the catalytic current is directly proportional to the turnover frequency (and the coverage of active enzyme at the electrode surface) [89].

The effect of prolonged exposure to O_2 on the H_2 oxidation activity of native Hyd-1 and

the C19G, C120G and C19G/C120G variants is shown in Fig. 6.3, where the concentration of O_2 is varied while the H_2 concentration is maintained at 10%. Strikingly, while in the presence of 1% O_2 native Hyd-1 and C120G are able to sustain catalytic activity (the current reaches a plateau), the catalytic activity of C19G and C19G/C120G is almost completely abolished (the current continues to decrease and reaches a negligible value). Furthermore, the level of spontaneous recovery from O_2 inactivation is significant in native Hyd-1 and C120G (judging by final catalytic current compared to the initial current under 100% H_2) but negligible in C19G and C19G/C120G.[1] These chronoamperometry experiments establish that the O_2 tolerance of these enzymes lies in the order: native Hyd-1 > C120G >> C19G/C120G ≈ C19G. Whereas C120G resembles native Hyd-1 in having a high degree of O_2 tolerance, C19G and C19G/C120G are comparable to standard hydrogenases, which are highly sensitive to O_2 [89].

The cyclic voltammetry experiments in Fig. 6.4 show that potentials more negative than the 0 V used in Fig. 6.3 are necessary to drive recovery from exposure to O_2 (aerobic inactivation) in the case of C19G and C19G/C120G. After anaerobic inactivation (left panel) and aerobic inactivation (right panel), the potential was scanned from high to low values (red traces), followed by another complete cycle from low to high and back to low potentials (black traces). All enzymes show full recovery at 0 V following anaerobic inactivation, so that reactivation of *Ready* (Ni-B) is spontaneous at 0 V (the potential chosen for the experiments in Fig. 6.3). Following aerobic inactivation, native Hyd-1 and C120G recover at a relatively high potential, similar to that following anaerobic inactivation (see insets in Fig. 6.3 showing the derivative of the first reductive red scans). In contrast, most of the reactivation of aerobically generated states in C19G and C19G/C120G only occurs at much lower potentials. Therefore, prolonged O_2 exposure causes C19G/C120G and C19G, but not native Hyd-1 or (to any degree) C120G, to accumulate states that are reactivated only upon application of strongly reducing conditions [89].

[1] These experiments are complicated by slow and irreversible activity loss unrelated to reaction with O_2.

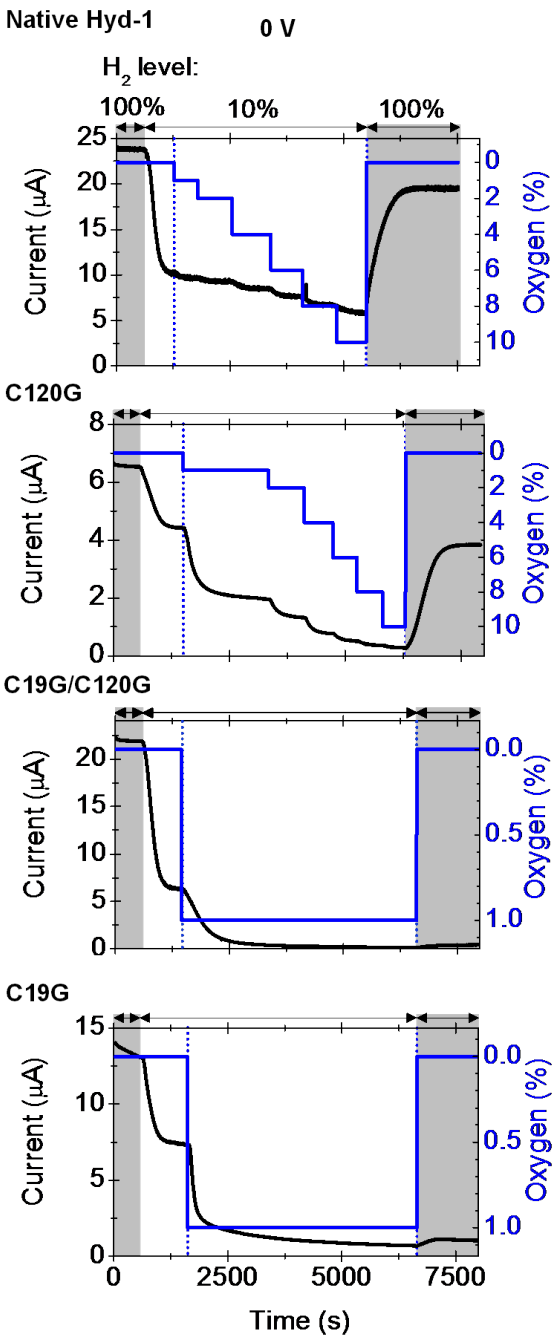


Figure 6.3: **Chronoamperometry experiments showing the response of native Hyd-1 and the proximal cluster variants to varying amounts of O_2.** Current-time traces recorded at 0 V, at pH 6, 30^{o}C, under a variable controlled H_2/O_2 headgas atmosphere with Ar as carrier gas (gas flow rate 1000 (standard cubic centimetres) min^{-1}). The O_2 concentration in is shown in blue and the recorded currents in black. Immediately prior to O_2 exposure currents were recorded at 100 % and 10 % H_2 and following exposure of each enzyme to O_2, anaerobicity was restored to 100 % as indicated by grey boxes. Hydrogen composition during O_2 exposure remained at 10 % as labeled in the upper most panel. The experiments shown in this Figure were carried out by Dr. Alison Parkin and Dr. Rhiannon Evans. Figure adapted from ref. [89]

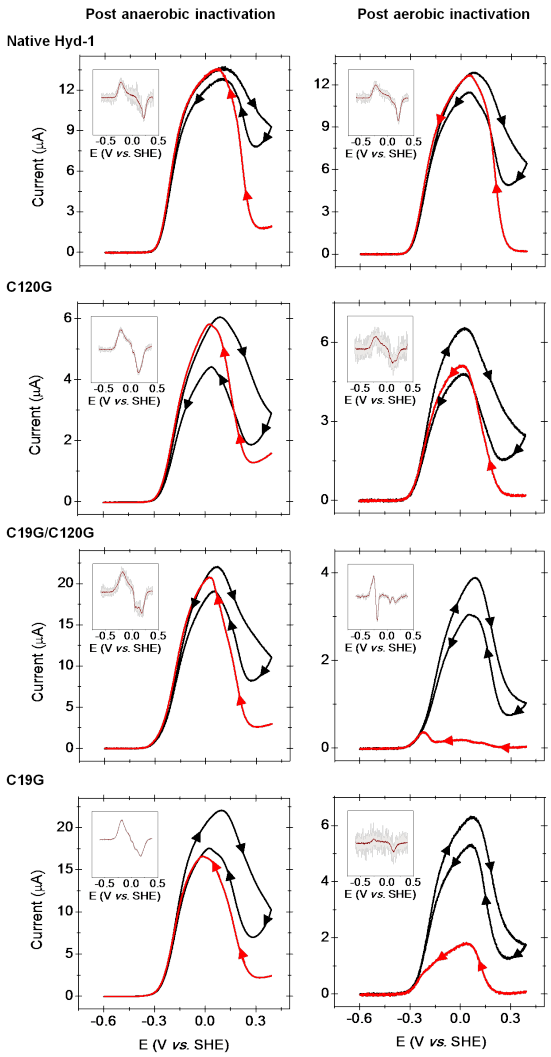


Figure 6.4: **Cyclic voltammograms showing re-activation of the anaerobically generated (left panel) and aerobically generated (right panel) inactive states of native Hyd-1 and the proximal cluster variants.** The insets show the derivative plots of the red traces. The scans were recorded under a headgas atmosphere of 100 % H_2 at pH 6.0, 30^{o}C, scan rate 0.1 mV s^{-1}. The anaerobic inactivation protocol was a potential poise at 0.39 V for 10,000 s, immediately followed by the re-activation potential sweep from 0.39 to -0.6 V (red trace). A second potential sweep was immediately initiated (black trace) to evaluate how much enzyme activity was recovered during the first sweep to low potential. The aerobic inactivation protocol was as follows: the electrode potential was first poised at 0 V with a gas flow of 10 % H_2 for 600 s, the atmosphere was changed to 10% O_2, 10 % H_2 for 2000 s. At 2600 s the electrode potential was raised to 0.39 V and at 3200 s the gas flow was changed back to 100% H2 for 1000 s to flush O_2 from the cell prior to the potential sweep from 0.39 to -0.6 V (red trace). This potential sweep was immediately continued (black trace) to evaluate how much activity was recovered during the first sweep to low potential. Arrows indicate the direction of the potential sweep. The total gas flow rate for all experiments was 300 (standard cubic centimeters)min^{-1}. The experiments shown in this Figure were carried out by Dr. Alison Parkin and Dr. Rhiannon Evans. Figure taken from ref. [89]

6.2 Methods

The concentration of as-isolated samples of all enzymes was determined using a Bradford assay [139] (Section 3.7). Spin quantifications were carried out as described in Section 3.3. All potential-adjusted EPR samples were prepared using the method described in Section 3.2.

6.2.1 Preparation of native and variant *E. coli* Hyd-1 EPR samples

As-isolated EPR samples (Fig. 6.5) were made by transferring $\approx$ 100 μL of enzyme in pH 7.5 buffer (20 mM Tris, 150 mM NaCl) to low-precision 4 mm quartz EPR tubes (Table 3.2) on the bench. To make the enzyme samples for the spectra shown in figures 6.6 and 6.7, bulk as-isolated hydrogenase samples were first activated under 100% H_2 at 37 ^{o}C with an initial injection of 0.4$-$0.6 μL of 400 μM sodium dithionite (Sigma Aldrich) and redox mediators (MV, BV, PMS, ITS, NQ and OHNQ, 40 μM each, Table 3.1). After equilibration to the $2H^+/H_2$ potential, half of the H_2-saturated enzyme was frozen for subsequent aerobic inactivation, and the other half was anaerobically inactivated: after flushing out the H_2 with Ar at 30 ^{o}C, the temperature was returned to 20 ^{o}C, the potential was raised to +78$\pm$2 mV by adding a substoichiometric amount of potassium ferricyanide (Sigma Aldrich), and the sample was withdrawn and frozen. The anaerobically inactivated native Hyd-1 sample (300 μL, sufficient to fill the resonator height) was transferred to a 4 mm high-precision EPR tube for accurate spin quantification (Fig. 6.6); all other samples were transferred to 4 mm low-precision tubes.

The aliquot of enzyme taken for aerobic inactivation was defrosted under the titration cell atmosphere and returned to the cell. The enzyme was exposed to 10% O_2 in Ar (total flow rate 100 (standard cubic centimeters) min^{-1}) at 30 ^{o}C for 4000 s, O_2 was flushed out of the cell with Ar until the potential was steady, the temperature was then returned to 20 ^{o}C, the potential was adjusted to +77$\pm$2 mV under Ar by adding sodium

dithionite, and the sample was withdrawn and frozen. All remaining native Hyd-1 or Hyd-1 C19G, C120G and C19G/C120G EPR samples result from titrations of as-isolated enzyme (containing MV, BV, PMS, ITS, NQ and OHNQ at 40 μM each) under Ar, using the method detailed in Section 3.2 (cell B), and withdrawal of ≈ 300 μL of enzyme solution at the desired potential into 4 mm high-precision EPR tubes. The order in which samples were taken are indicated in the figures showing EPR spectra of all titration samples.

6.2.2 Preparation of *Salmonella* Hyd-5 EPR samples

As-isolated enzyme containing the mediators MV, BV, PMS, ITS, NQ and OHNQ at 40 μM each was titrated (Section 3.2) to oxidising potentials and EPR samples were taken in the order +143, +265, +385 and +41 mV, with an error of $\pm$5 mV. The remaining enzyme solution was then reduced under H_2 for 4.5 h and a sample was taken at -340 ± 5 mV. The titration cell was then flushed with Ar and potassium ferricyanide was added to produce a final enzyme sample at -65 ± 5 mV. All EPR samples were prepared in MES buffer (Section 3.8) at 20^oC, withdrawn into 4 mm high-precision EPR tubes (Table 3.2) previously flushed with the gas mixture of the cell, and flash-frozen. *Salmonella* EPR samples were prepared by Rosalind Davis under my supervision.

6.2.3 EPR measurements

Continuous wave EPR measurements were carried out using an X-band (9-10 GHz) Bruker EMX spectrometer with an X-band super-high-sensitivity probehead equipped with a low-temperature helium flow cryostat (Section 3.5.1). Measurement conditions are provided in the figure legends. Background spectra were recorded under identical conditions and subtracted from the EPR spectrum of the enzyme sample. Data analysis was performed using the program EasySpin [116].

6.3 Results

6.3.1 The active site and O_2-tolerance

The as-isolated 80 K CW EPR spectra of native Hyd-1, C19G, C120G and C19G/C120G (Fig. 6.5) show the presence of both Ni-B and Ni-A (simulations are included and shown as dotted lined), as well as additional peaks which cannot be assigned.[2] The presence of both Ni-A and Ni-B was already noted for the native enzyme in Chapter 5 (Section 5.3.1) and the *Unready* state as well as the *Ready* state was also detected in electrochemical experiments of as-isolated Hyd-1 [83]. This contrasts with the presence of only a 'clean' Ni-B spectrum in as-isolated samples of O_2-tolerant *Re*-MBH [82, 88] and *Aa* Hase I [16]. In order to examine the EPR-detectable states formed by native Hyd-1 and the variants upon reaction with O_2, and because the as-isolated samples contain a significant amount of Ni-A, it was necessary to ensure complete activation before O_2 experiments were carried out.

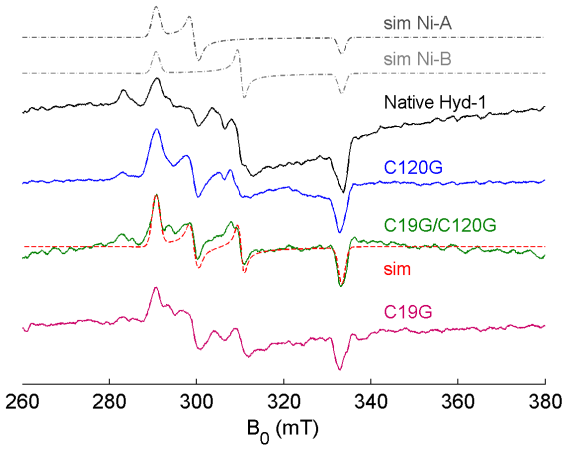


Figure 6.5: **X-band 9.39 GHz CW EPR spectra of as-isolated native Hyd-1 and the proximal cluster variants, 80 K.** Measurement conditions: mw power 8 mW; modulation amplitude 1 mT. Simulations (abbreviated to 'sim' and shown as dotted lines): Ni-A $g_{x,y,z}$ = 2.305, 2.238, 2.010; Ni-B $g_{x,y,z}$ = 2.305, 2.160, 2.010. The overall simulation of C19G/C120G is given in red. Figure adapted from ref. [89].

[2] As described below, reductive activation removes the additional peaks and only Ni-B (and Ni-A) signals are observed upon reoxidation. The additional peaks are therefore associated with additional *Unready* Ni species (see Section 6.4).

The activation was carried out under 100% H_2 at 37 ^{o}C and deemed complete when the potential reached a steady value and when no more Ni-A signals were observed after the potential was raised under H_2-free and O_2-free conditions (see Section 6.2.1). Activation of native Hyd-1 required 4 h, C120G required 8 h and C19G required 27 h. The C19G/C120G variant was especially slow to activate; as shown in Fig. 6.6, the sample treated with H_2 for 24 h still shows a weak Ni-A spectrum. Residual amounts of this state were only removed after 40 h of activation. Similarly, Ni-A was also still found to be present in samples of native Hyd-1 and the C19G and C120G variant enzymes after shorter activation times (not shown). The long activation time required for the Hyd-1 enzymes is highly unusual compared to standard hydrogenases, which usually require between 1 and 2 h 100% H_2 of activation. Indeed, a solution of the standard *E. coli* Hyd-2 is fully activated after 1 h under 100% H_2 at room temperature (see Chapter 5, Section 5.2.1).

After complete activation and anaerobic inactivation (equilibration of the potential to +78 mV), all enzymes showed clear Ni-B signals at 80 K (Fig. 6.6). Two Ni-B species with different g_x values (2.314 and 2.297) but (almost) identical g_y and g_z values are formed in all variants. Note also that g_y is slightly higher (2.173) compared to that of Ni-B in as-isolated enzymes samples ($g_y = 2.160$, Fig. 6.5). The g_x peaks are unlikely to arise from a single species coupling to Fe-S clusters since the latter are not detected at 80 K. The potential (+78 mV) was also carefully chosen such that a minimal number of Fe-S clusters are EPR active (*vide infra*, Section 6.3.2). The two different g_x values are consistently observed for samples following activation and anaerobic inactivation and at present the reason for this observation is not understood; it may be possible that two Ni species with slightly different ligand environments give rise to the observed EPR spectra. The spectra of activated enzymes also reveal much more homogeneous samples compared to the as-isolated enzyme EPR spectra (Fig. 6.5), which show many peaks in addition to those from Ni-A and Ni-B. A simulation for the Ni-B spectrum (red) of native Hyd-1 is shown in Fig. 6.6. For the native enzyme, the Ni-B signals amount to 0.6±0.2 spins per molecule of enzyme. However, this value is an underestimate because titrations show that

Ni-B is not fully formed at this potential (Section 6.3.2). Higher potentials could not be used to maximise the intensity of the Ni-B spectrum because Ni-B experiences enhanced relaxation as the high-potential proximal cluster becomes oxidised, as discussed below. Although a precise quantification of the Ni signals was only carried out for native Hyd-1, the values for the variants must be similar, because similar enzyme concentrations were used and signal-to-noise ratios are comparable in Fig. 6.6.

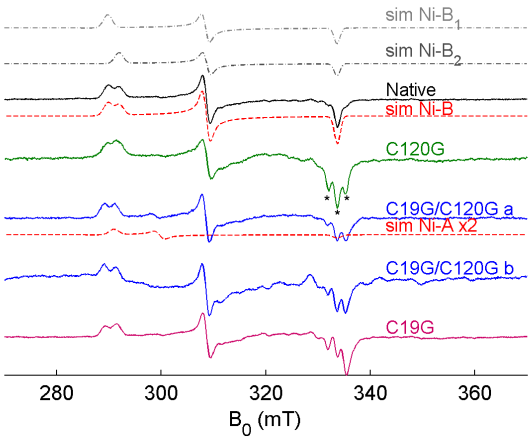


Figure 6.6: **X-band 9.39 GHz CW EPR spectra of anaerobically inactivated native Hyd-1 and the proximal cluster variants, 80 K.** Prior to inactivation, samples were activated under H_2 for 4 hours (native Hyd-1), 8 hours (C120G), 24 hours (C19G/C120G a), 27 hours (C19G) and and 40 hours (C19G/C120G b). The simulation of the spectrum of the anaerobically inactivated native Hyd-1 is shown in red (NiB_1 $g_{x,y,z}$ = 2.314, 2.174, 2.010, NiB_2 $g_{x,y,z}$ = 2.297, 2.172, 2.010). g values of the Ni-B species are comparable for the three variant enzymes. The C19G/C120G a spectrum shows a small amount of Ni-A (simulation of Ni-A shown in red, $g_{x,y,z}$ = 2.31, 2.24, 2.01). See Section 6.2.1 for details on sample preparation. Protein concentrations: Native Hyd-1 57.3 μM; other sample concentrations were between 50 and 60 μM. Unidentified peaks are marked with an asterisk. Measurement conditions: mw power 2 mW; modulation amplitude 1 mT. Figure adapted from ref. [89].

The unidentified peaks which are visible in all enzyme samples after H_2 treatment followed by anaerobic oxidation are marked with $*$ in the C120G spectrum in Fig. 6.6. The peaks are also observed in *Aa* Hase I [16, 265], *Re*-MBH [82] and the soluble hydrogenase from *R. eutropha* [268]. They may be associated with degradation of the enzyme and were previous mentioned in Chapter 5 (Section 5.3.5). However, there is no evidence of Fe-S cluster degradation because wide field-sweep EPR spectra of the anaerobically and

aerobically inactivated C19G/C120G variant (see Fig. 10.2 in the appendix) could not detect any significant peak at g ≈ 4.3, which would be indicative of free Fe^{3+}.

Figure 6.7 displays the 80 K CW EPR spectra of native Hyd-1 and the proximal cluster variants after exposure of activated enzyme to O_2. Native Hyd-1 shows a spectrum almost identical to that obtained from the anaerobically inactivated sample in Fig. 6.6, with similarly good signal-to-noise ratio and a comparable spin concentration, consisting solely of Ni-B. In contrast, a qualitative assessment of the g_y signals shows that samples of the C120G, C19G/C120G and C19G variants contain both Ni-A and Ni-B states. Despite enzyme concentrations similar to the native enzyme, the signal-to-noise ratio is much lower, strongly suggesting that the variant enzyme samples, particularly C19G and C19G/C120G, also contain EPR silent states. Quantitative assessment of the Ni-A:Ni-B ratio in Fig. 6.7 is complicated by two factors. First, precise potential control during aerobic inactivation of the EPR enzyme samples is not possible, and previous electrochemical

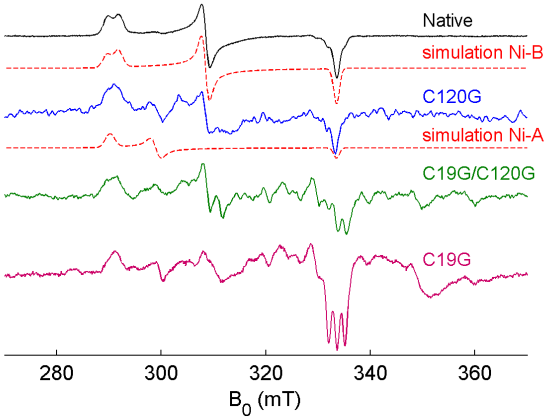


Figure 6.7: **X-band 9.39 GHz CW EPR spectra of aerobically inactivated native Hyd-1 and the proximal cluster variants, 80 K.** Prior to inactivation, samples were activated under H_2 for 4 hours (native Hyd-1), 8 hours (C120G), 24 hours (C19G/C120G a), 27 hours (C19G) and and 40 hours (C19G/C120G b). The simulation of the spectrum of the aerobically inactivated native Hyd-1 is shown in red (NiB_1 $g_{x,y,z}$ = 2.314, 2.174, 2.010, NiB_2 $g_{x,y,z}$ = 2.297, 2.172, 2.010). g values of the Ni-B species are comparable for the three variant enzymes. A simulation of Ni-A (in red, $g_{x,y,z}$ = 2.31, 2.24, 2.01) is shown for the C120G variant. See Section 6.2.1 for details on sample preparation. Protein concentrations were between 50 and 60 μM. Measurement conditions: mw power 2 mW; modulation amplitude 1 mT. Figure adapted from ref. [89].

studies of the [NiFe]-hydrogenase from *A. vinosum* show that formation of *Unready* is potential dependent [273]. Second, additional peaks (for example those marked with $*$ in Fig. 6.6) and broadened peaks prevented an accurate simulation of the spectra obtained after prolonged aerobic inactivation, and amounts could not be reliably assessed using only the g_y peak. Importantly, these spectra show that, on the basis of EPR alone, it is difficult to differentiate among the O_2 sensitivities of the different variants because more states than just Ni-A and Ni-B appear to be generated by reaction of the variants with O_2.

6.3.2 The high potential centre and O_2-tolerance

To investigate the correlation between the multiline EPR spectrum observed under oxidising conditions and O_2 tolerance, EPR redox titrations (see Section 3.2) were conducted on as-isolated samples of native Hyd-1, C120G, C19G/C120G and C19G, all at pH 6.

Native *E. coli* Hyd-1

The 15 K CW EPR spectra measured of the native Hyd-1 redox titration are shown in Fig. 6.8. For clarity, the Ni region of the spectra is magnified (Fig. 6.8, left).

A simple $[3Fe\text{-}4S]^+$ cluster signal is only observed at moderately high potentials (+145 mV) and this changes, upon further oxidation, into the more complex signals that are also observed for the O_2-tolerant hydrogenases *Re*-MBH [82, 88] and *Aa* Hase I [16]. Double integration (Section 3.3) of the Fe-S cluster signals at +385 mV yielded 2.0±0.3 spins per molecule of enzyme, consistent with the presence of a paramagnetic species in addition to the oxidised medial cluster. The Ni signals change with potential as the $[3Fe\text{-}4S]^+$ cluster signals transform into the complex multiline spectrum (Fig. 6.8, left), entailing that the additional paramagnetic species is located between the active site and the medial cluster.

Further evidence for the location of the additional paramagnetic species can be gained from the change in the 80 K spectra with increasing potential (Fig. 6.9): whereas Ni-B

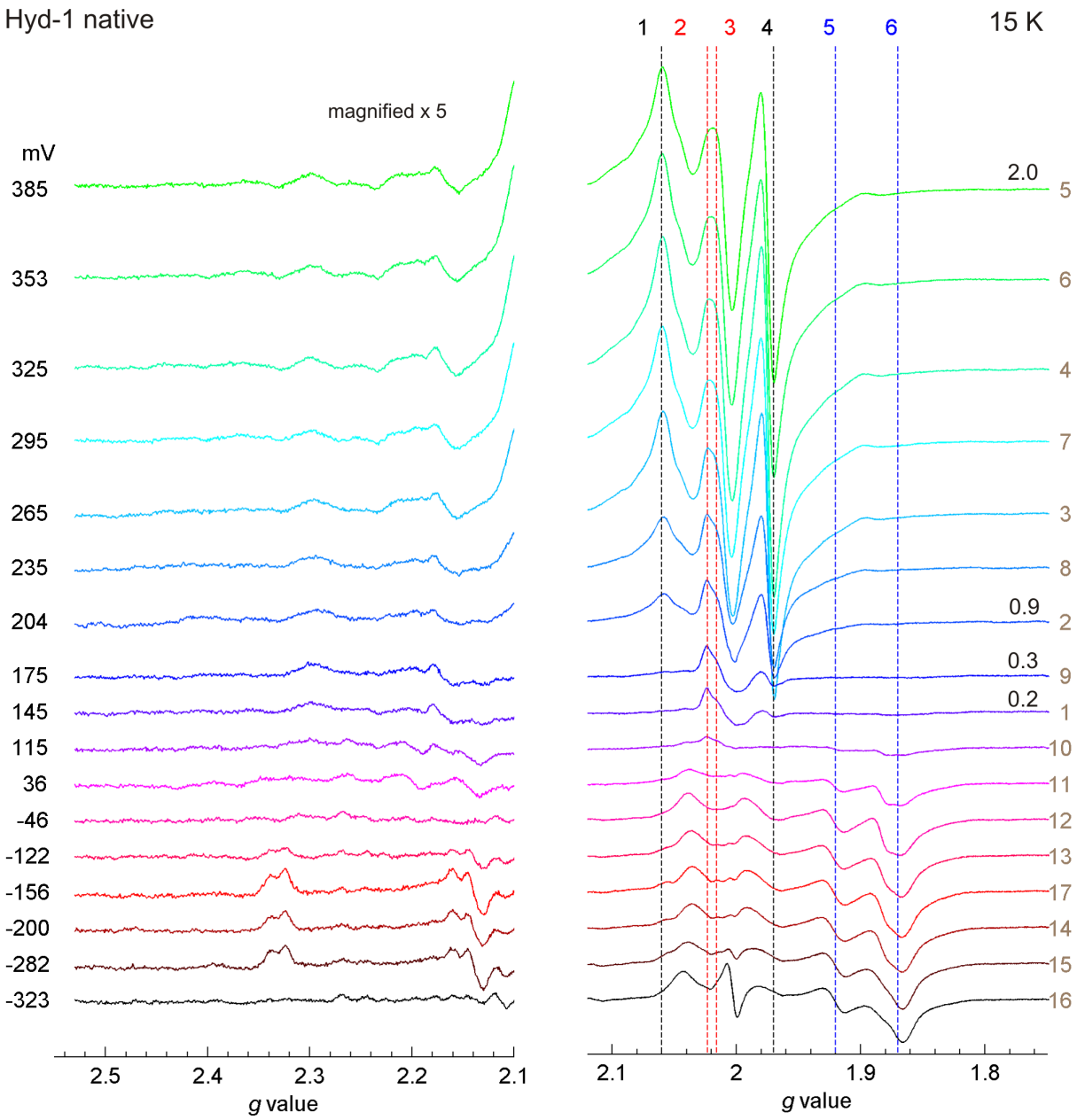


Figure 6.8: **X-band CW EPR spectra of potential titration of native Hyd-1 at 15 K.** The spacing between adjacent spectra is not proportional to the redox potential difference between the samples. The Ni region of the spectrum (left) was magnified 5-fold. Measurement conditions: mw frequency 9.385 GHz; mw power 2 mW; modulation amplitude 1 mT. Enzyme concentration: 24 μM. Annotations refer to the potential at which the sample was taken (in mV) and the order in which samples were taken (grey). Spin integrations of the Fe-S cluster region are given for the spectra at +204, +175 and +145 mV (black). Vertical lines indicate the peak heights monitored to extract mid-point potentials, see Fig. 6.14. Figure adapted from ref. [270].

signals can be clearly distinguished at 36 mV and at 145 mV, they are hardly visible at 385 mV (where only the phenazine methosulfate mediator peak is visible). Consequently, as the high potential centre become oxidised, the relaxation rate of Ni-B increases. Similar observations were reported for the *Aa* Hase I enzyme [16, 265] and these data on native *E. coli* Hyd-1 are entirely consistent with the assignment by Pandelia *et al.* of the high potential paramagnetic species to the 'overoxidised' proximal cluster [16].

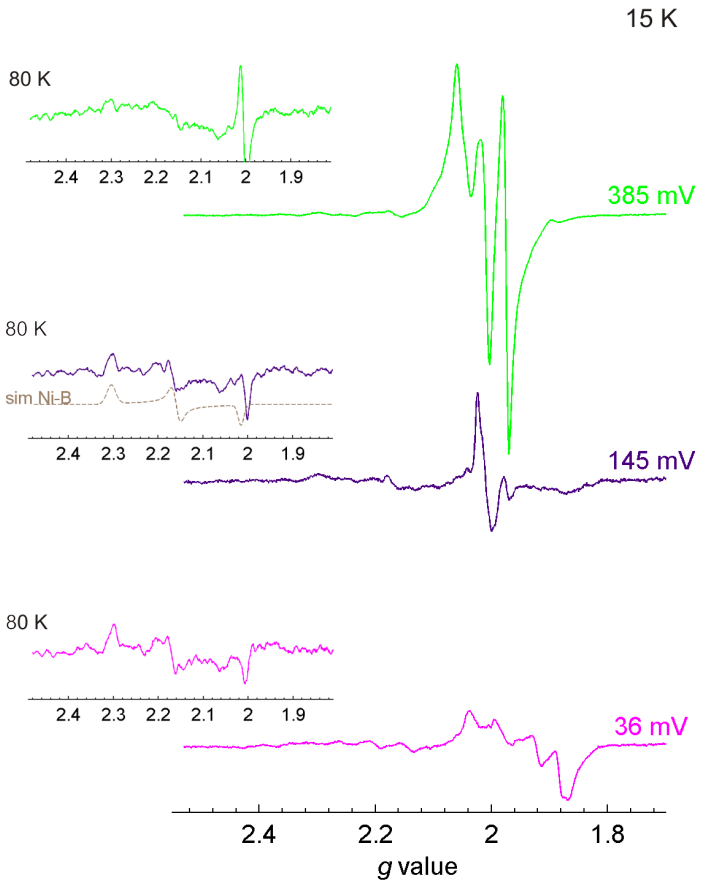


Figure 6.9: **X-band CW EPR spectra at 15 K and 80 K of native Hyd-1 poised at 385 mV, 145 mV and 36 mV.** For measurements of the 15 K data, see Fig. 6.8. Measurement conditions for 80 K spectra: mw power 2 mW, mw frequency 9.384 GHz, modulation amplitude 1 mT; simulation of Ni-B (dotted line) $g_{x,y,z}$ = 2.31, 2.16, 2.01. The peak at $g = 2$ in the 80 K spectra results from the mediator PMS.

The low potential changes in the CW EPR spectra are discussed in detail in Chapter 8, but it should be noted that at 36 mV Ni-B interacts with the *reduced* proximal $[4Fe\text{-}3S]^{3+}$ cluster and that, given the clear Ni-B spectra observed at 80 K, the relaxation behaviour

of Ni-B is dramatically different depending on whether it interacts with the reduced or the over-oxidised proximal cluster.

The C19G/C120G variant

In contrast to native Hyd-1, the C19G/C120G variant exhibits only the [3Fe-4S]$^+$ cluster signal at high potentials in low-temperature CW EPR spectra (Fig. 6.10, right). This signal grows in intensity as the medial cluster becomes oxidised. At 393 mV, the Fe-S cluster region of the spectrum integrated to 0.9±0.2 spin per molecule of enzyme, consistent with the presence of only one paramagnetic species. No significant changes are observed in the Ni region of the spectra at 15 K (Fig. 6.10, left) between 45 mV and 393 mV. This shows that there is no high potential EPR-visible paramagnetic species located in close proximity to the active site and, similar to standard hydrogenases (Section 5.3.3 in Chapter 5), any magnetic interactions between the oxidised medial cluster and the active site are negligible. Furthermore, the relaxation behaviour of the active site Ni species at high potentials is very different to that in native Hyd-1 at 15 K: the Ni signals for C19G/C120G became saturated at much lower microwave power (≤0.008 mW) than those for native Hyd-1 (≤0.12 mW).

The Ni-B g_y peak sharpens and shifts from 2.163 to 2.173 upon reduction and anaerobic reoxidation (see also Figures 6.5 and 6.6). Because no shifts are observed for other redox-active species in the potentiometric titration, the shift in Ni-B g_y cannot be attributed to hysteresis. Judging by the characteristic Ni-A g_y peak at 2.24, as-isolated preparations of C19G/C120G contain significantly more Ni-A than as-isolated samples of the native enzyme.

Intriguingly, no Fe-S cluster signals are present in the $g = 2$ region in low-potential spectra of C19G/C120G, in agreement with the spectra of the equivalent variant of *Re*-MBH [88]. Electrochemical measurements of aliquots of enzyme used to make the EPR samples of native Hyd-1 and the proximal cluster variants showed similar high activity and it is concluded that the Fe-S cluster are correctly assembled in all four enzymes

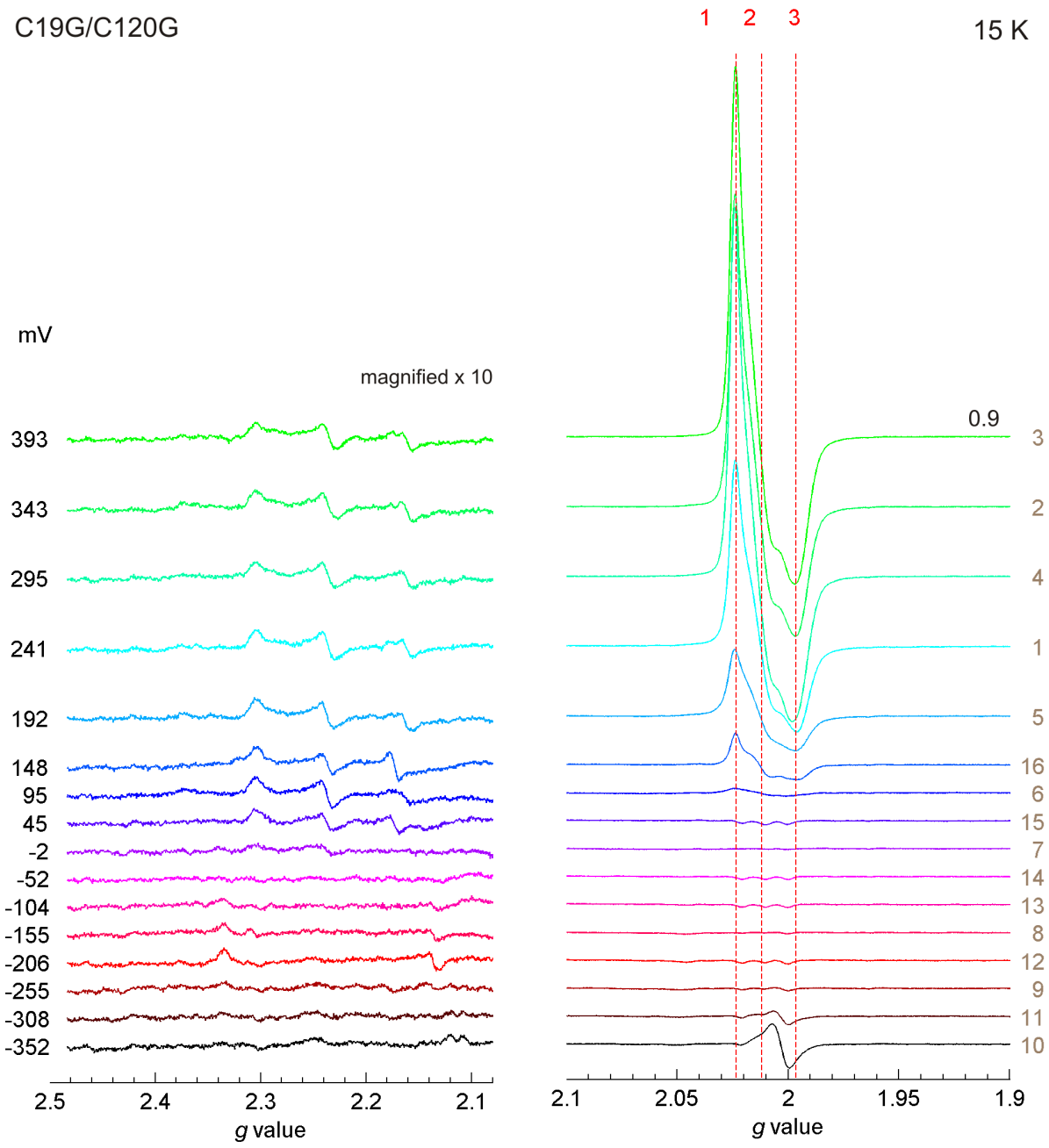


Figure 6.10: **X-band CW EPR spectra of potential titration of Hyd-1 C19G/C120G at 15 K.** The spacing between adjacent spectra is not proportional to the redox potential difference between the samples. The Ni region of the spectrum (left) was magnified 10-fold. Measurement conditions: mw frequency 9.385 GHz; mw power 2 mW; modulation amplitude 0.5 mT. Enzyme concentration: 21 μM. Annotations refer to the potential at which the sample was taken (in mV) and the order in which samples were taken (grey). The spin integration of the Fe-S cluster region is given for the spectrum at +393 mV (black). Vertical lines indicate the peak heights monitored to extract mid-point potentials, see Fig. 6.14. Figure adapted from ref. [270].

[89]. In Chapter 8 it will be shown that the reduced proximal cluster has a $S > 1/2$ spin ground state in all the proximal cluster variants, whereas its spin ground state is $S = 1/2$ in the native enzyme. The reduced distal cluster is EPR-invisible in *all* Hyd-1 enzymes.

The midpoint potentials of the Ni species in Hyd-1 C19G/C120G

Because the intensity of the signals arising from the active site Ni species is not complicated by nearby fast-relaxing proximal paramagnetic species, it is feasible to determine the midpoint potentials of the EPR-visible active site states in the C19G/C120G variant. The redox titration samples measured at 70 K are shown in Fig. 6.11 (left). Because the Ni-A g_x and Ni-B g_x peaks are essentially super-imposable, the midpoint potential of Ni-A and Ni-B was obtained by monitoring the intensity changes of the g_y peaks. However, as already noted, a shift in Ni-B g_y is observed following reduction and anaerobic reoxidation (henceforth Ni-B*). Furthermore, a shoulder appears at Ni-A/Ni-B g_x and the peak previously present at $g = 2.37$ has disappeared. The spectral changes observed upon chemical reduction or reduction with H_2 followed by anaerobic inactivation (Fig. 6.6) or oxidation are similar - with the exception that Ni-A is only recovered when the enzyme was chemically reduced. At lower potentials, a Ni species with unusual g values ($g_{x,y,z} = 2.33$, 2.14, 2.05) appears, which is named Ni-L* here and was discussed previously for native Hyd-1 (Chapter 5). Additional states of the active site (with Ni in the +2 oxidation state) are expected to be present, similar to other [NiFe]-hydrogenases (Section 5.1.2), but these are EPR-silent and can only be detected through infrared (IR) techniques [226]. The bell-shaped curve fit to the Ni-L* g_x peak intensities (Fig. 6.11, right) was obtained by taking the *apparent* midpoint potentials for the appearance and disappearance of Ni-L*.

In the absence of IR redox titrations, the EPR-silent products of reduction of Ni-A and Ni-B are unknown. From Fig. 5.1 in Chapter 5 the redox couples might be expected to be Ni-A/Ni-SU and Ni-B/Ni-SI_r. However, Ni-B in the O_2-tolerant *Aa* Hase I enzyme was found to be in equilibrium with the Ni-SI_a state. The midpoint potentials of the disappearance of Ni-A and Ni-B will therefore simply be referred to as E_m (Ni-A) and E_m

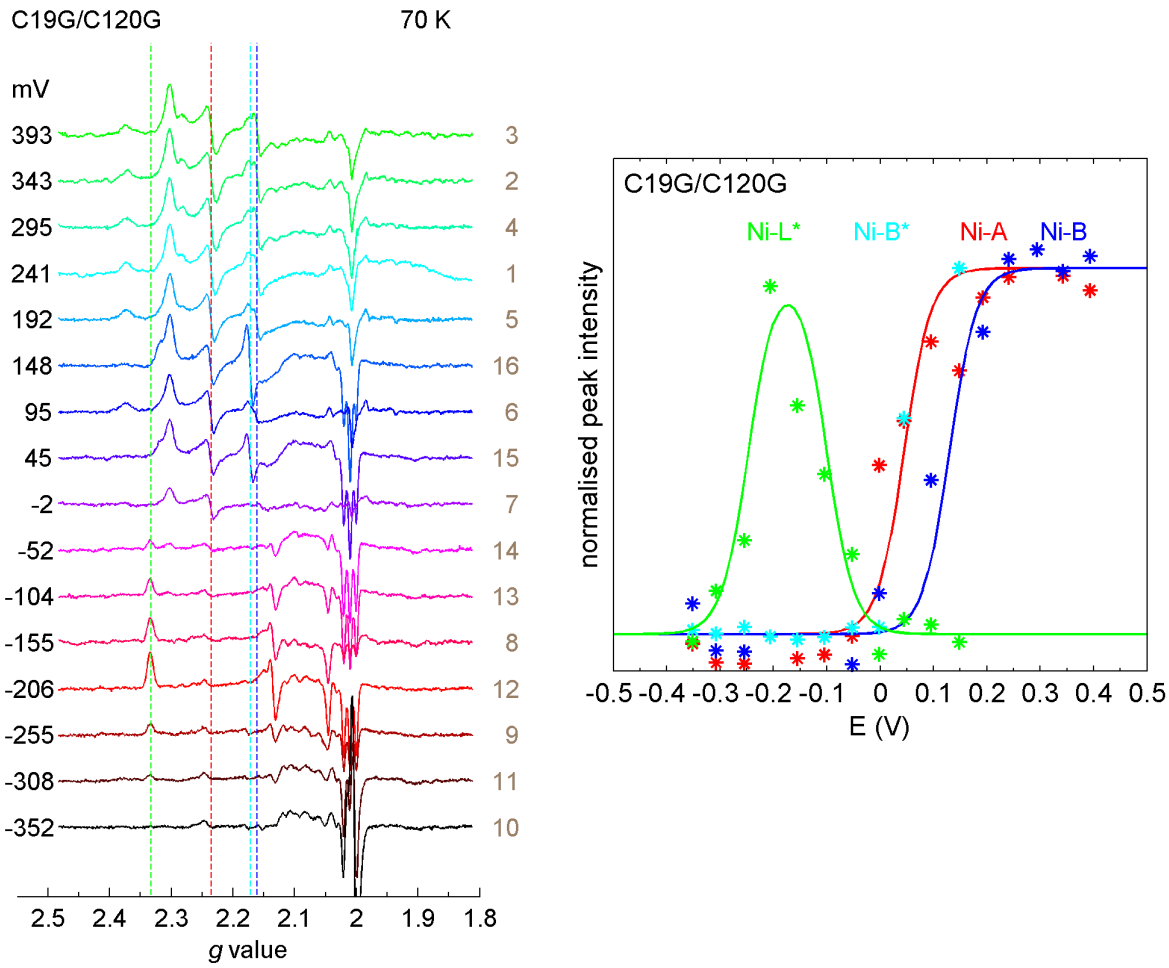


Figure 6.11: **X-band CW EPR spectra of potential titration of Hyd-1 C19G/C120G at 70 K (left) and corresponding Nernst plots of the observed Ni species.** (*Left*): Vertical dotted lines indicate the peak intensities used to compute the Nernst plots of Ni-A (g_y = 2.235), Ni-B (g_y = 2.161), Ni-B* (g_y = 2.172) and Ni-L* (g_x = 2.333). Approximate protein concentration: 21 μM (C19G/C120G). Measurement conditions: mw power 8 mW; modulation amplitude 1 mT, mw frequency 9.384 GHz. The resonator background (measured under identical conditions) was subtracted. (*Right*): Nernst plots of the Ni species observed resulting from the average peak intensities indicated in the titration graph (left). Midpoint potentials were as follows: E_m (Ni-A) = 45±30 mV, E_m (Ni-B) = 130±20 mV, E_m (Ni-B*) = 55 mV (tentative due to insufficient data points), E_m (Ni-L*) = −100 and −247±20 mV. Because the Nernst plots of the EPR-silent Ni species are unknown (these can only be determined *via* infrared spectroscopy) the midpoint potentials for Ni-L* are apparent values for the appearance and the disappearance of this state. Figure adapted from Evans *et al.*, *Journal of the American Chemical Society*, vol. 135, pp. 2694-2707, 2013.

(Ni-B). E_m (Ni-B*) refers to the midpoint of the formation of Ni-B after reduction and re-oxidation. Similarly, the two redox partners of Ni-L* are unknown and true midpoint

potentials can therefore not be determined. Consequently, it is most meaningful to note the potential at which the Ni-L* signals are at maximum intensity, which is ≈ -185 mV at pH 6. For comparison, midpoint potentials for Ni-A and Ni-B, and the potentials at which Ni-C is at maximum intensity in both standard hydrogenases and the O_2-tolerant *Aa* Hase I, are summarised in Table 6.1, both obtained *via* infrared (IR) methods and *via* CW EPR redox titrations. Generally, the potentials obtained for the C19G/C120G Hyd-1 variant are much higher than those reported for other [NiFe]-hydrogenases. An exception is the potential of Ni-C in *D. gigas* obtained *via* CW EPR [200] which is only slightly more negative than that of Ni-L* obtained here. However, it is noteworthy that the potentials at which the Ni-C signal in *D. gigas* is found to be at maximal intensity differ when measured with IR [211] or EPR [200] (Table 6.1). This is contrary to the theory that similar midpoint potentials result from both EPR and IR titrations [226] (see also Section 5.1.2). One difference in Table 6.1 between the IR and EPR titrations is that the EPR titration was carried out in the presence of H_2, whereas the IR titration was not. With the exception of the midpoint potentials of Ni-A and Ni-B in *A. vinosum* hydrogenase [203], which are also comparatively high and were carried out in the presence of H_2, all other potentials given in Table 6.1 result from titrations carried out in the absence of the enzymes' substrate. The potential of Ni-C in *Aa* Hase I is reported to be ≈ 100 mV higher than in standard hydrogenases, whereas the E_m Ni-B is reported to be similar [250]. In contrast, E_m Ni-B (and E_m Ni-B*) is also more positive in the C19G/C120G enzyme.

Table 6.1: **Comparison of the potentials of the EPR-visible active site species in [NiFe]-hydrogenases from different species.** * The potentials given for Ni-C correspond to the Ni-C signal at maximal intensity. [a] Values for pH 6 were extrapolated from pH 8.3 (Ni-A) and pH 7.7 (Ni-B and Ni-C) using the pH dependence given by the authors. [b] These titrations were performed in the presence of H_2 (all other titrations are performed in the absence of H_2). [c] Values at pH 6 for Ni-B and Ni-C were estimated from titration data at pH 5.4 and 6.8. [d] The potential of the formation of Ni-B after reduction and reoxidation is different and the low potential species is Ni-L* (see text).

Hydrogenase	E_m Ni-A (mV)	E_m Ni-B (mV)	Ni-C (mV)*	pH	method
Aa Hase I	-	−73	≈ −270	6.4	IR [250]
D. gigas	−119	−74	≈ −324	6.0	IR [211][a]
D. gigas	-	-	≈ −200	5.7	EPR [200][b]
D. vulgaris Miyasaki F	−96	−98	≈ −336	6.0	IR [255][c]
A. vinosum	+20	+32	-	6.0	EPR [203][b]
Ec Hyd-1 C19G/C120G	+45	+130	−185	6.0	EPR[d]
D. vulgaris Miyasaki F	-	−162.5	-	7.8	IR [255]
D. vulgaris Miyasaki F	−310	−230	-	7.7	EPR [284]

All variants of *E. coli* Hyd-1 presented here result from substitutions of residues which do not directly ligate the active Ni and Fe (Figures 6.1 and 6.2). In the absence of the possibility to carry out IR titrations, it has to be assumed that the potentials of the active site Ni species change insignificantly between different Hyd-1 enzymes.

6.3.3 The C19G variant

Like the double exchange variant, electrochemistry showed that the C19G variant is also incapable of sustaining catalytic activity in the presence of O_2 [89]. However, the EPR redox titration in Fig. 6.12 shows that the EPR spectra of the C19G and C19G/C120G variants are very different. Similar to native Hyd-1 (Fig. 6.8), only the oxidised $[3Fe\text{-}4S]^+$ cluster signal is observed at +145 mV (sample 1 of the titration). At higher potentials, the number of spins per molecule of the Fe-S cluster signal increases to 2.1±0.3 (at +384 mV) as a complex signal develops that differs from that observed in the native enzyme.

The splitting and shift of the Ni signals as the potential is raised indicates that the additional paramagnetic centre is located between the active site and the medial Fe-S cluster. Indeed, the Ni signals at 15 K show similar saturation properties to the native

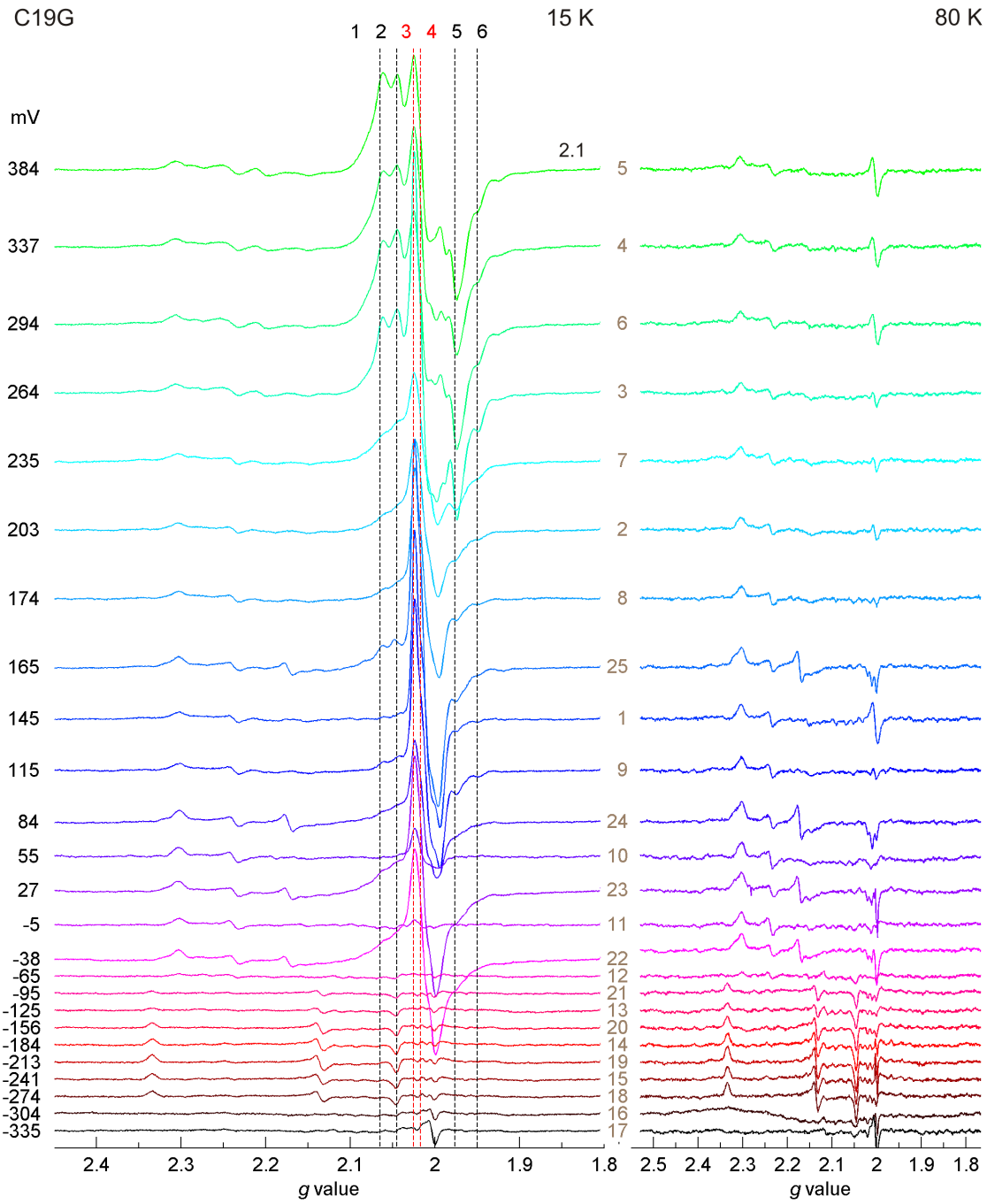


Figure 6.12: **X-band CW EPR spectra of potential titration of Hyd-1 C19G at 15 K (left) and at 80 K (right).** Measurement conditions: (15 K) mw frequency 9.385 GHz; mw power 2 mW; modulation amplitude 1 mT; (80 K) mw frequency 9.384 GHz; mw power 2 mW; modulation amplitude 1 mT. Enzyme concentration: 16 μM. Annotations refer to the potential at which the sample was taken (in mV) and the order in which samples were taken (grey). The spin integration of the Fe-S cluster region is given for the spectrum at +384 mV. Vertical lines indicate the peak heights monitored to extract mid-point potentials, see Fig. 6.14.The spin integration of the Fe-S cluster region is given for the spectrum at +384 mV (black). The spacing between adjacent spectra is not proportional to the redox potential difference between the samples.

enzyme - *i.e.* Ni-A and Ni-B relax much faster than in the C19G/C120G variant and only become saturated at mw powers greater than 0.12 mW. This explains the decreasing intensity of the Ni signals with increasing potentials in the 80 K spectra (Fig. 6.12, right) and a determination of the midpoint potentials of the EPR-visible Ni states of the active site using EPR titrations is therefore not feasible.

Similar to the C19G/C120G variant, Ni-B g_y shifts from 2.160 to 2.173 and the EPR signal sharpens significantly upon reduction and reoxidation. A shoulder also appears on the Ni-A/Ni-B g_x peak. The reoxidised Ni species is again referred to as Ni-B*. Contrary to the titrations of native Hyd-1 and C19G/C120G, the changes in the Fe-S cluster region of the spectra are not fully reversible. Although the high potential centre is reformed after reduction and anaerobic reoxidation (sample 24 at +84 mV and sample 25 at +165 mV in Fig. 6.12), it re-appears at a less oxidising potential (*e.g.* sample 22 *vs* sample 1), concomitantly with the appearance of the Ni-B* signals.

The spectra resulting from samples poised at low potentials are comparable to those of the C19G/C120G variant: the maximal intensity of Ni-L* is close to −200 mV (supporting the assumption that the midpoint potentials of the active Ni species change insignificantly between the different Hyd-1 enzymes) and no reduced Fe-S cluster signals are seen in the $g = 2$ region of the spectrum (see Chapter 8).

6.3.4 The C120G variant

The EPR titration of the O_2-tolerant C120G variant (Section 6.1.2) is summarised in Fig. 6.13. In electrochemical experiments this variant most resembles native Hyd-1 [89].

The medial $[3Fe\text{-}4S]^+$ cluster signal intensity increases as the potential is raised up to +175 mV but then the signal decreases as the potential is raised further (Fig. 6.13, right). At the same time, 'wings' appear on either side of the medial cluster signal and these broaden with increasing potentials. At +387 mV, the double integral of the Fe-S cluster signals amounts to 0.7±0.3 spin per molecule of enzyme, *i.e.* more similar to the C19G/C120G variant than native Hyd-1. A change in the Ni signals with increasing

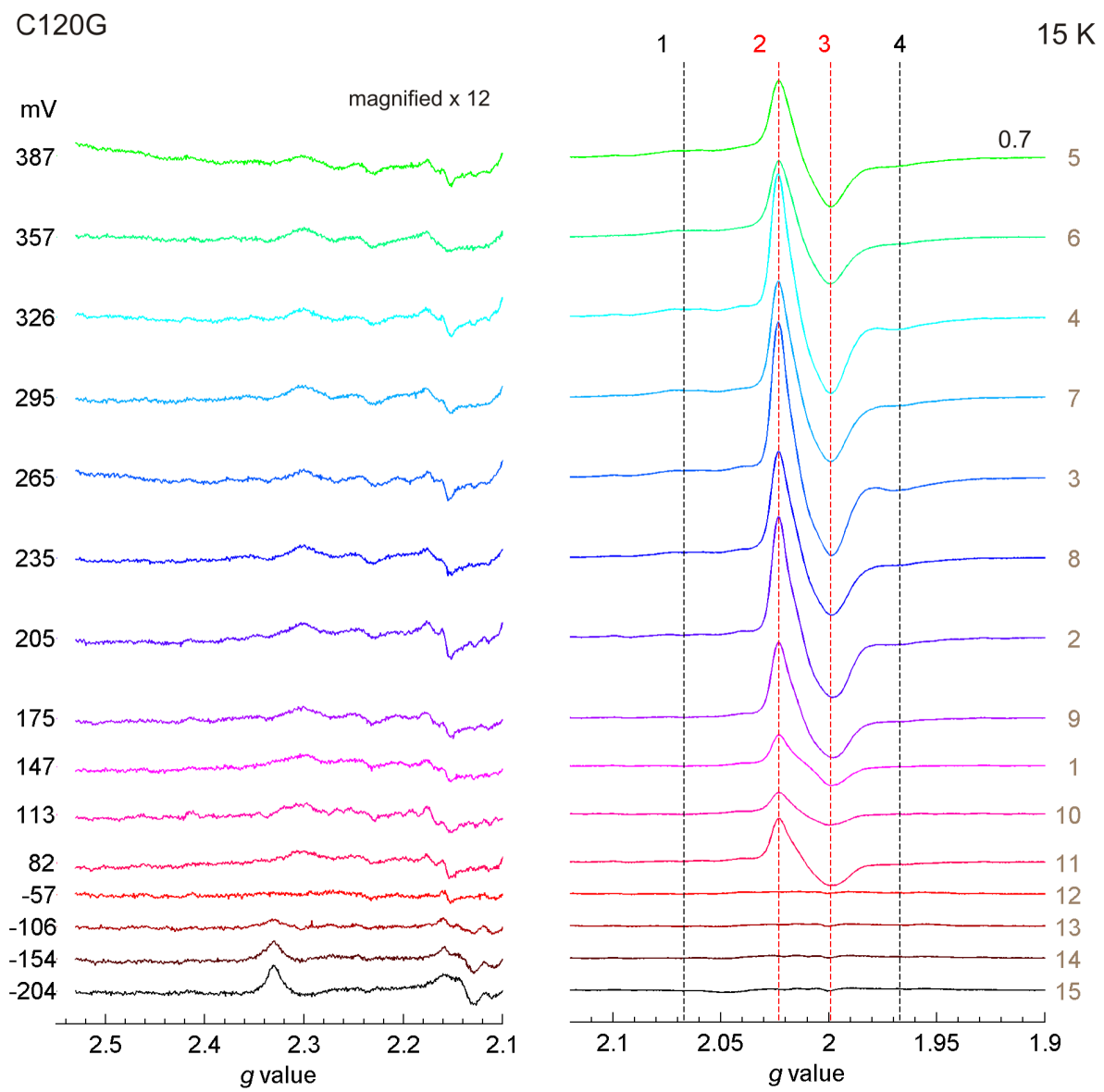


Figure 6.13: **X-band CW EPR spectra of potential titration of Hyd-1 C120G at 15 K.** The spacing between adjacent spectra is not proportional to the redox potential difference between the samples. The Ni region of the spectrum (left) was magnified 12-fold. Measurement conditions: mw frequency 9.385 GHz; mw power 2 mW; modulation amplitude 1 mT. Enzyme concentration: 14 μM. Annotations refer to the potential at which the sample was taken (in mV) and the order in which samples were taken (grey). The spin integration of the Fe-S cluster region is given for the spectrum at +387 mV (black). Vertical lines indicate the peak heights monitored to extract mid-point potentials, see Fig. 6.14.

potentials (Fig. 6.13, left) was difficult to ascertain in this variant; the derivative peak at $g = 2.15$ is unlikely to arise from Ni-B, as it is also present at lower potentials at which Ni-A and Ni-B are reduced (*e.g.* the spectrum at -57 mV). Ni-L* signals are present at

lower potentials and similarly to the C19G and C19G/C120G variants, no reduced Fe-S cluster signals are apparent (although subtle differences exist, as discussed in Chapter 8).

6.3.5 Summary of the supernumerary cysteine variants

Using the method described in Chapter 3 (Section 3.1), the peak intensities of the various Fe-S cluster species observed in the EPR titrations of native Hyd-1 and the C19G/C120G, C19G and C120G variants as a function of potential are summarised in Fig. 6.14. The peak positions in the CW EPR spectra (Figures 6.8, 6.10, 6.12 and 6.13) used to generate these plots are detailed in the legend of Fig. 6.14. All data points belonging to one species were fitted to one-electron redox transitions. In determining the Nernst plot of the C19G titration, the last four samples were omitted (see Section 6.3.3) and the data points resulting from these samples are shown as filled circles rather than asterisks. Because of the broadening of the 'wings' either side of the medial [3Fe-4S]$^+$ signal in C120G spectra from samples poised at increasingly high potential (Fig. 6.13), which are attributed to the oxidation of a high-potential species (HP), the two highest potential data points of HP in Fig. 6.14 (C120G) are almost certainly an underestimate. Therefore, the midpoint potential of the high-potential centre in C120G is tentative and could be much higher in reality. Determination of the area corresponding to each species should in principle yield more accurate midpoint potentials than monitoring peak intensities. However, in practice, trustworthy simulations and therefore deconvolution of the contributions of different clusters to observed Fe-S clusters signals is not presently possible.

With the exception of the C19G/C120G variant, obtaining the true midpoint potential of the medial cluster in native Hyd-1, C120G and C19G is not trivial. In these three enzymes the potential at which uncoupled [3Fe-4S]$^+$ cluster signals are observed at their maximal intensity does not correspond to the medial cluster being 100% oxidised (contrary to the C19G/C120G variant). The true midpoint potentials for the [3Fe-4S]$^{+/0}$ redox transition of native Hyd-1, C19G and C120G which are listed in Table 6.2 were estimated using spin integrations (Chapter 3, Section 3.3) as a guidance. As an example, the

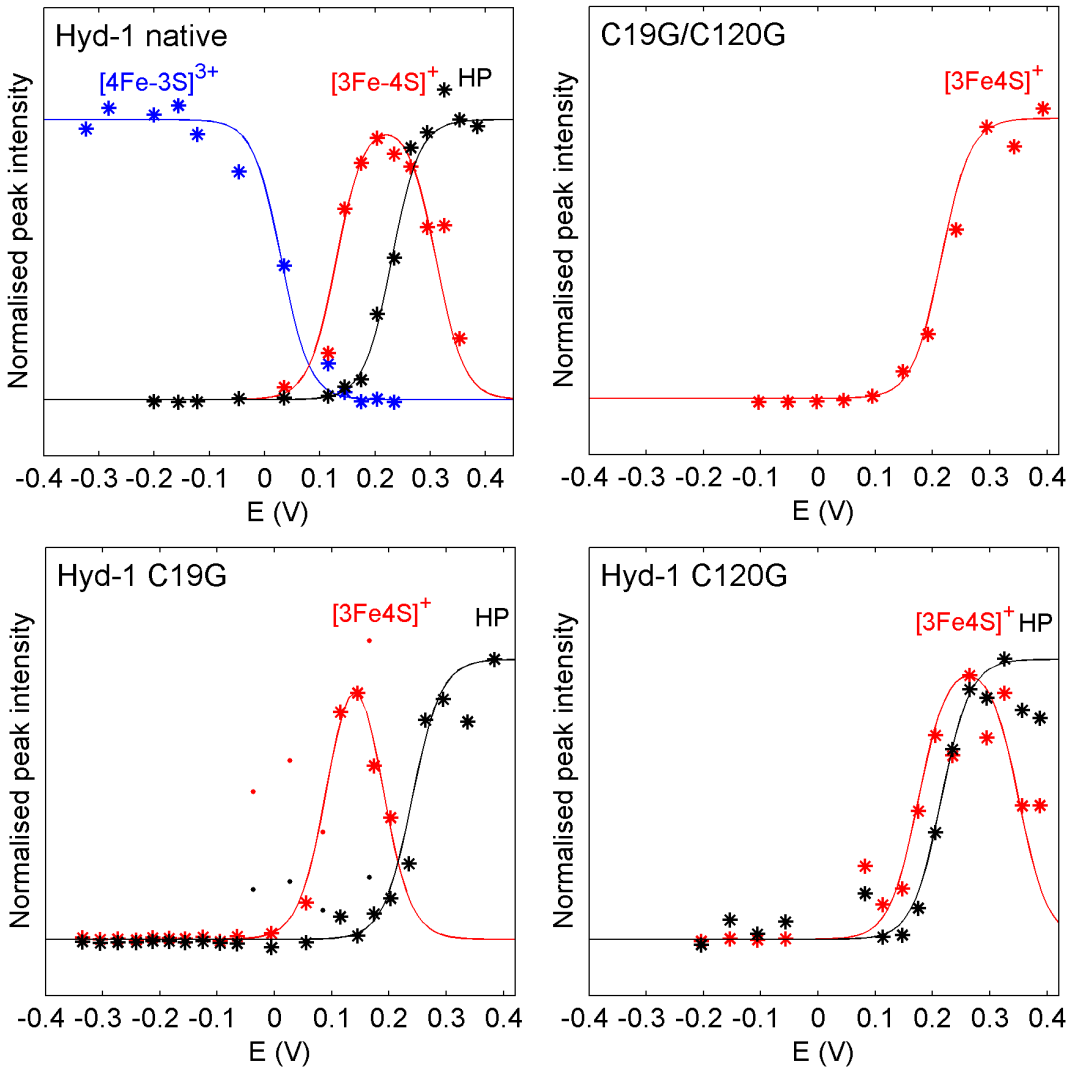


Figure 6.14: **Potentiometric titrations of the EPR-active Fe-S cluster species observed in native Hyd-1, C19G/C120G, C19G and C120G.** The peak positions in the CW EPR spectra used to give these plots were as follows: Native Hyd-1 (Fig. 6.8) $[4Fe\text{-}3S]^{3+}$ (peak 6, $g = 1.870$), $[3Fe\text{-}4S]^{+}$ (peak 2 minus peak 3, $g = 2.023$ minus $g = 2.016$), HP (peak 4, $g = 1.970$); C19G/C120G (Fig. 6.10) $[3Fe\text{-}4S]^{+}$ (g_y, $g = 2.017$ minus $g = 2.007$); C19G (Fig. 6.12) $[3Fe\text{-}4S]^{+}$ (peak 3, $g = 2.061$), HP (peak 1, $g = 2.025$); C120G (Fig. 6.13 $[3Fe\text{-}4S]^{+}$ (peak 2, $g = 2.072$), HP (peak 1, $g = 2.023$). The high-potential centre is labelled 'HP'. In the C19G plot, the last four samples of the titration are shown as · rather than as * (see text and Fig. 6.12).

procedure for native Hyd-1 is now explained. The Fe-S cluster region of the +204 mV spectrum (Fig. 6.8) integrates to 0.9 spin per molecule of enzyme. Given that the (true) midpoint potential of the high-potential centre was determined to be +230 mV (Fig. 6.14), this means that 26% of HP is oxidised at +204 mV, corresponding to 0.24 spin per

molecule. Consequently, 0.66 spin per molecule (or 66%) correspond to the oxidised medial cluster at +204 mV. Using the one-electron Nernst equation, the midpoint potential of the oxidised medial cluster is then +187 mV.[3] Similarly, the Fe-S cluster region of the spectrum at +175 mV integrates to 0.3 and that at +145 mV integrates to 0.2 spin per molecule, resulting in estimates of the midpoint potentials of the medial cluster of +200 mV and +181 mV, respectively. An average of these values yields the midpoint potential given in Table 6.2). Similar procedures were carried out for the C19G and C120G enzymes. Because the spin integrations carry considerable uncertainty (it is difficult to subtract the contribution from the EPR active Ni species accurately), the 'true' midpoint potentials for the medial Fe-S clusters provided in Table 6.2 have a relatively large error. However, inspection by eye of the normalised peak intensities of the different enzymes in Fig. 6.14 shows that the estimated (average) midpoint potentials for the $[3Fe\text{-}4S]^{+/0}$ reduction potential must be fairly accurate and that the potential at which the $[3Fe\text{-}4S]^{+}$ cluster signals are observed at their maximal intensity can be taken as a good quantity to estimate this parameter. Apparent midpoint potentials for the $[3Fe\text{-}4S]^{+/0}$ redox transition are also provided in Table 6.2, for comparison with values reported for other O_2-tolerant hydrogenases which are provided in this way (and often misleadingly called midpoint potentials). The red lines in Fig. 6.14 result from the *apparent* midpoint potential (the 'appearance' and 'disappearance' of the $[3Fe\text{-}4S]^{+}$ cluster signals). Fe-S cluster signals in the $g = 2$ region at low potentials are only observed in native Hyd-1 and this is discussed in detail in Chapter 8.

The midpoint potential of the high-potential centre in the native enzyme and that of the medial cluster in the C19G/C120G can be regarded as reference potentials. The reduction potentials of the high-potential paramagnetic centres (HP) are the same within experimental errors for native Hyd-1, C19G and C120G (Table 6.2).[4] The values are also comparable to those determined for the high potential centre in *Aa* Hase I (obtained at

[3]The Matlab code and a graphical example for determining these midpoint potentials is given in Appendix 10.3

[4]However, note that the midpoint potential for high-potential centre in C120G may be an underestimate, see Section 6.3.4.

Table 6.2: **Midpoint potentials of the EPR-active Fe-S clusters observed in native Hyd-1 and the supernumerary cysteine variants.** The midpoint potentials result from Fig. 6.14. For the medial cluster reduction potential two values are given: the apparent (app.) midpoint potential refers to the potential at which the observed [3Fe-4S]$^+$ cluster signal is at half its maximal intensity; the true midpoint potential refers to an estimate of the potential at which the medial is half oxidised and half reduced using spin integrations as a guide (see text). Note that the potentials given for the C19G variant do not take into account the samples 22-25 of the titration (Fig. 6.12). HP stands for high-potential centre. [a] The redox transition yielding this midpoint potential is assigned to the distal cluster in ref. [16]. See Chapter 8 for a discussion of the EPR-visible redox transitions at low potentials. The potentials for *Aa* Hase I (ref. [16]) were obtained at pH 6.4 *vs* the normal hydrogen electrode and those for *Re*-MBH and *R. metallidurans* CH34 were obtained at pH 7.0 [285]; all potentials for the Hyd-1 enzymes were obtained at pH 6.0.

Enzyme	HP	[3Fe-4S]$^{+/0}$(true)	[3Fe-4S]$^{+/0}$(app.)	[4Fe-3S]$^{4+/3+}_{\text{proximal}}$	[4Fe-4S]$^{2+/+}_{\text{distal}}$
Native Hyd-1	230±15	190±30	130±15	30±30	-
C19G/C120G	-	215±10	-	-	-
C19G	240±15	160±30	95±15	-	-
C120G	215±15	200±30	170±15	-	-
Aa Hase I [16]	232±20	-	78±20	98±20	−65±20 [a]
Re-MBH [285]	+160	-	+25	−60	−180 [a]
Rm CH34 [285]	+240	-	+100	+50	−80 [a]

pH 6.4, but the potential was found to be independent of pH [16]) and in the O_2-tolerant [NiFe]-hydrogenase from *Ralstonia metallidurans* [285]. However, E_m (HP) was reported to be considerably less positive in *Re*-MBH [285].

The *apparent* midpoint potentials of the medial Fe-S cluster in the *E. coli* enzymes and those reported for other O_2-tolerant native enzymes (Table 6.2) vary substantially. However, Table 6.2 shows that the apparent midpoint potential of the medial Fe-S cluster in C19G, C120G and native Hyd-1 is a significant underestimate of the true E_m values, which are almost comparable within experimental error. The E_m values for the [3Fe-4S]$^{+/0}$ redox transition appear to be unprecedentedly high. However, true and apparent midpoint potentials differ by as much as 65 mV (Table 6.2) and it is possible, for example, that the true E_m of the medial cluster in *R. metallidurans* hydrogenase would be similarly high after taking into account the pH dependence (the apparent midpoint potential was determined at pH 7 [285]). It would be interesting to compare the reduction potential of

the [3Fe-4S]$^{+/0}$ cluster in the C19G/C120G variant to that in the equivalent variant of *Re*-MBH, but this value has not been reported [88].

The reduction potentials of the medial cluster in standard [NiFe]-hydrogenases (which are 'true' midpoint potentials in the absence of the formation of a high potential paramagnetic species) are reported to vary between −80 and +65 mV, depending on the species [58, 202, 286, 287] (see also Section 8.1.1 in Chapter 8), and are thus much lower than the values determined in the *E. coli* enzymes here. The reduction potentials reported for the reduced Fe-S cluster(s) in other native O_2-tolerant [NiFe]-hydrogenases are included in Table 6.2 for completeness. The observation of only *one* low-potential redox transition in *E. coli* Hyd-1 is assigned to the [4Fe-3S]$^{4+/3+}$ transition of the proximal cluster (Chapter 8).

The changes in the Fe-S cluster and Ni signals (magnified in the insets in Fig. 6.15, with black vertical lines showing the positions of the g_x components of Ni-A and Ni-B (average), g_y of Ni-A and g_y of Ni-B) in native Hyd-1 and the three supernumerary-cysteine variants with increasingly high potential are summarised in Fig. 6.15: the order of O_2-tolerance (native Hyd-1 > C120G >> C19G/C120G ≈ C19G) established from electrochemical experiments (Section 6.1.2, ref. [89]) does not directly correlate with the ability of the enzyme to form a high potential paramagnetic species.

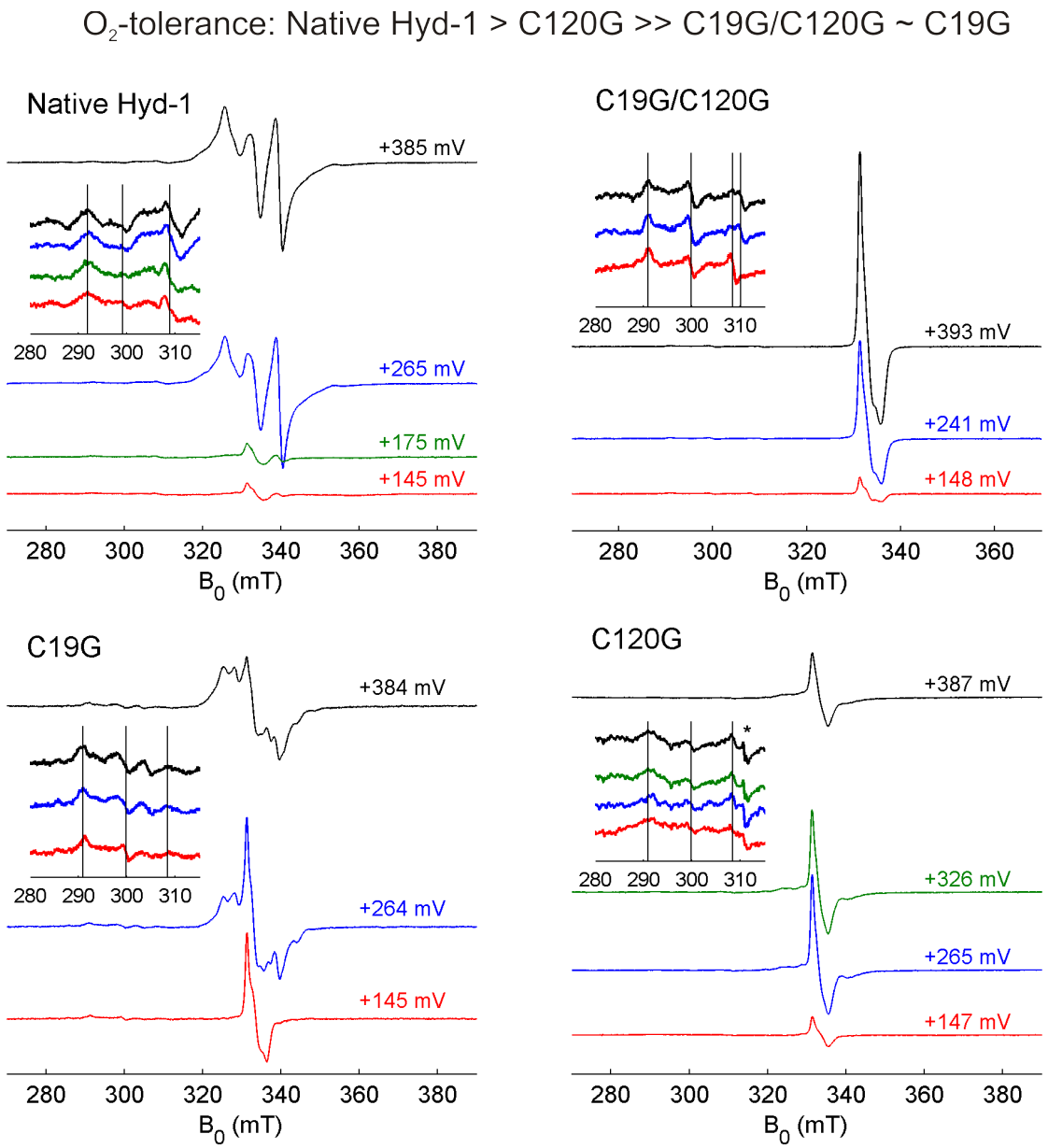


Figure 6.15: **Comparison of the 9.39 GHz CW EPR spectra at 15 K of Hyd-1 and proximal cluster variant 'as-isolated' enzyme samples poised at high potentials.** Vertical lines indicate the average g values of Ni-A/Ni-B g_x, Ni-A g_y, Ni-B g_y (from left of right). The fourth line in the C19G/C120G spectrum represents the shift in Ni-B g_y consistently observed (see text). The signal observed at $g = 2.15$ in the C120G variant is unlikely to arise from Ni-B and is marked as an asterisk (see text). Approximate protein concentrations: 24 μM (native), 14 μM (C120G), 21 μM (C19G/C120G), 16 μM (C19G). Measurement conditions: mw power 2 mW; modulation amplitude 1 mT (native) or 0.5 mT (C19G, C19G/C120G, C120G). Ni signals are saturated at 2 mW microwave power to different extents depending on the enzyme (see text). The resonator background (measured under identical conditions) was subtracted. Figure adapted from reference [89].

6.3.6 The EPR properties of an O_2-tolerant [NiFe]-hydrogenase from *Salmonella enterica*

The CW EPR spectra at 15 K of *Salmonella* Hyd-5 poised at different potentials are shown in Fig. 6.16. A signal with $g_{x,y,z} = 2.02, 2.01, 2.00$ is visible in the enzyme sample

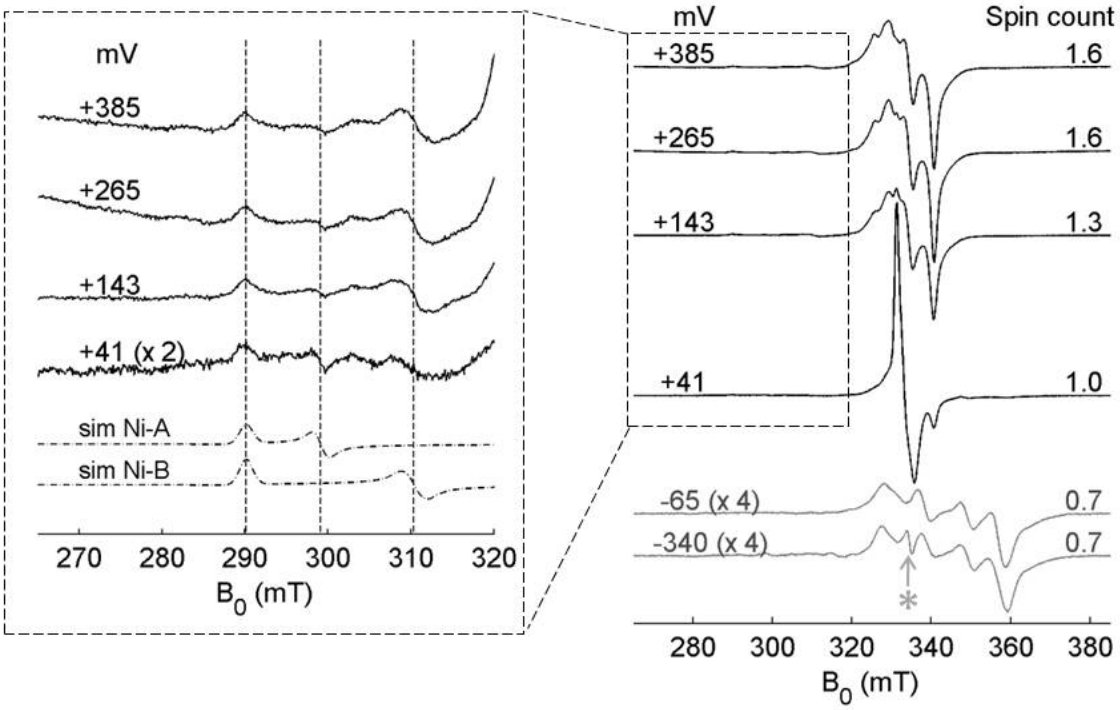


Figure 6.16: **CW EPR spectra of *Salmonella* Hyd-5 poised at different potentials.** (*Right*): Samples poised at different potentials as shown in mV. The number of spins per molecule of enzyme is indicated by the spin count (error ±0.2). Black spectra are from as-isolated potential-poised enzymes samples, grey spectra result from enzyme samples which have been H_2 reduced. g values: $[3Fe\text{-}4S]^+$ (+41 mV) $g_{x,y,z} = 2.02, 2.01, 2.00$; reduced Fe-S cluster(s) (−340 mV) $g = 2.05, 1.98, 1.92, 1.97$. The arrow with asterisk indicates reduced viologen mediator ($g = 2.00$). (*Left*): Magnification of the Ni region of selected spectra with simulations of Ni-A and Ni-B (dotted lines). Vertical lines indicate the positions of Ni-A/Ni-B $g_x = 2.31$ and Ni-B $g_y = 2.16$. Protein concentration: 25 μM. Measurement conditions: 15 K, mw power 2 mW; modulation amplitude 1 mT; mw frequency 9.374 GHz. The resonator background (measured under identical conditions) was subtracted. Samples were prepared by Rosalind Davies, University of Oxford. Figure reprinted from ref. [138], with permission from Elsevier.

poised at +41 mV, and is assigned to the oxidised $[3Fe\text{-}4S]^+$ medial cluster. Hyd-5 has been shown to contain three Fe-S clusters, similar to other respiratory [NiFe]-hydrogenases

[59]. The number of spins per molecule of enzyme increases with increasing potential, and the Fe-S cluster signal becomes more complex. At +385 mV, double integration yields 1.6±0.2 spins per molecule, indicating that in this enzyme, similar to (native) *E. coli* Hyd-1 (*vide supra*), *Re*-MBH [82, 88] and *Aa* Hase I [16], an additional paramagnetic species is formed at high potentials. Multiple sequence alignments (Fig. 6.2) show that two supernumerary cysteines are also present at the proximal cluster in *Salmonella*. EPR samples were prepared at selected potentials to allow comparison of the most important spectral changes with other [NiFe]-hydrogenases; a full titration to determine midpoint potentials was not carried out. However, the midpoint potential of the medial Fe-S cluster appears to be considerably lower than that in *E. coli* Hyd-1 (Fig. 6.8) because the spectrum at +41 mV, in which only a very small amount of the high-potential centre is oxidised, amounts to 1.0 spin per molecule, indicating that the medial cluster is essentially fully oxidised. In contrast, the reduction potential of the high-potential species may be more positive than that in *E. coli* Hyd-1 since the Fe-S cluster spectrum does not amount to a full 2 spins per molecule in the highest potential-poised sample. The magnification of the Ni region in the inset in Fig. 6.16 shows that as-isolated samples of *Salmonella* Hyd-5 contain both Ni-A and Ni-B, similar to *E. coli* Hyd-1, but contrary to *Re*-MBH and *Aa* Hase I which are reported to contain only Ni-B [16, 82, 84, 250]. The EPR spectra of Hyd-5 samples poised at low potentials (−65 mV and −340 mV) are very similar to those of equivalent samples of *E. coli* Hyd-1 (Fig. 6.8), *Re*-MBH [82, 285] and *Aa* Hase I [16, 84]. Both the Fe-S cluster signals in the spectra at −65 mV and −340 mV amounted to 0.7 spin per molecule, indicating that the EPR-visible clusters contributing to these signals were fully reduced at −65 mV. The origin of the Fe-S cluster EPR signals in low-potential samples of O_2-tolerant hydrogenases is investigated in Chapter 8.

6.4 Discussion and future work

Electrochemistry has shown that the ability of *E. coli* Hyd-1 to catalyse H_2 oxidation in the presence of O_2 depends crucially on the presence of a 'supernumerary' cysteine at position 19 in the small subunit, and to a lesser extent on the co-presence of a second cysteine at position 120 [89]. Protein film electrochemistry experiments have also revealed that native Hyd-1 produces only the *Ready* state (which is reactivated quickly at relatively high potentials) following prolonged exposure to O_2 (Section 6.1.2 [89]). Accordingly, the EPR spectrum obtained following exposure of activated native Hyd-1 to O_2 for 1 h, in the absence of H_2, shows only Ni-B. In contrast, a similar treatment of the C120G variant results in Ni-A as well as Ni-B, which agrees with PFE experiments [89]. In PFE, both the C19G and C19G/C120G variants are highly sensitive to trace amounts of O_2, and aerobic inactivation mainly results in *Unready* states that are only reactivated under strongly reducing conditions [89]. In conjunction with these experiments, the EPR spectra obtained following activation and exposure to O_2 suggest that species other than Ni-A and Ni-B are formed. It is highly unlikely that Fe-S cluster degradation occurred because no EPR signal at $g = 4.3$ is observed at 15 K, which would indicate the release of Fe^{3+}. The combined PFE [89] and EPR results therefore call for a reconsideration of the association between the spectroscopically defined Ni-A and the electrochemically (kinetically) defined *Unready* state [273]. This has already been noted for the [NiFeSe]-hydrogenase from *Desulfomicrobium baculatum*, which also reacts with O_2 to produce an inactive state that requires a low potential for activation but is not the spectroscopically established Ni-A [89, 275]. It is postulated that these non-Ni-A *Unready* states contain oxygenated cysteine species [276, 288], that may be difficult to distinguish spectroscopically but show up as additional electron density in crystallography [187, 224, 276, 289]. Importantly, the EPR and PFE [89] experiments of native Hyd-1, C120G, C19G/C120G and C19G presented here show that O_2 tolerance correlates strongly with the ability to maximise formation of the Ni-B/*Ready* state when O_2 attacks.

The EPR characterisation of the Hyd-1 enzymes reveals that there are structural

and/or electronic differences between as-isolated Ni-B and the Ni-B formed after anaerobic inactivation of H_2-activated enzyme or anaerobic reoxidation of chemically reduced enzyme (Ni-B*). First, the g_y value consistently shifts from $\approx$ 2.16 in Ni-B to $\approx$ 2.17 in Ni-B* and the peak sharpens (Figures 6.11, 6.10, 6.12). Interestingly, in the O_2-tolerant *Aa* Hase I, *Re*-MBH and *Rm* CH34 which are isolated containing only Ni-B, g_y is 2.17 [16, 82, 250, 285], whereas in standard hydrogenases, which contain a mixture of Ni-A and Ni-B in as-isolated samples, Ni-B g_y is typically $\approx$ 2.16 [82, 118]. Crystal structures of as-isolated O_2-tolerant and standard [NiFe]-hydrogenases do not report a difference between the observed Ni-B states [17, 59, 87]. The IR stretching frequencies of Ni-B in *Re*-MBH [82] and *Aa* Hase I [290] were not noted as being different to those observed in standard [NiFe]-hydrogenases [118, 226].

In addition, the g_x peak of Ni-B* in Hyd-1 and variants was found to be a 'doublet', as is clearly observed in the EPR spectra of anaerobically inactivated Hyd-1 samples which were previously fully activated to remove Ni-A (Fig. 6.6). As explained in Section 6.3.1, the apparent 'splitting' of g_x in Ni-B* is highly unlikely to result from a magnetic interaction with another paramagnetic species. Shoulders also appear on the g_x peak of Ni-A/Ni-B in as-isolated samples following *chemical* reduction and reoxidation (Fig. 6.11), consistent with two Ni-B* species with slightly different g_x values.

Second, the EPR titration showing the visible Ni species in the C19G/C120G variant at 70 K (Fig. 6.11) reveals that the midpoint potential of Ni-B* is substantially lower than that of Ni-B (by $\approx$ 75 mV), and more comparable to that of Ni-A (which remains unchanged following chemical reduction and reoxidation). A comparison of the midpoint potentials to those in native Hyd-1, C120G and C19G could not be provided by means of EPR titrations because the peak intensities of Ni-A and/or Ni-B at high potentials are affected by increased relaxation due to magnetic interaction with the high potential centre.

The reasons for the differences between Ni-B and Ni-B* remain elusive. Further insight may be provided by IR titrations. First, it should be established if two different Ni-B

states are observed, similar to the EPR titrations. Second, the redox partners of Ni-B and Ni-B* could be determined. The redox partner of Ni-B* is possibly Ni-SI_a, as was found to be the case for Ni-B in *Aa* Hase I [250], whereas the redox partner of Ni-B could be Ni-SI_r, similarly to standard hydrogenases [226]. Third, the midpoint potentials of Ni-B of activated and as-isolated enzymes samples should be compared as Table 6.1 revealed that midpoint potentials obtained in the presence and absence of H_2 differ significantly. Because of the large volumes of enzyme solution required and because of the extremely long activation times required for even small volumes of C19G/C120G (Section 6.3.1), it is not realistic to make this comparison using EPR titrations.

Since the midpoint potential of the Ni-B/Ni-SI_a couple in *Aa* Hase I [250] was found to be similar to that of Ni-B/Ni-SI_r in standard hydrogenases, it was concluded that the high E_{switch} value (the midpoint of reactivation, Section 5.1.3) found in O_2 tolerant hydrogenases cannot result from a high E_m of Ni-B [250]. Although the midpoint potential of Ni-B/Ni-B* in Hyd-1 C19G/C120G was found to be considerably more positive than that of Ni-B/Ni-SI_a in *Aa* Hase I, the results presented here lend support to the lack of direct correlation between E_m Ni-B (+130 mV in C19G/C120G) and E_{switch} (+180 mV in C19G/C120G [89]). Léger and co-workers [250] proposed that fast reactivation is responsible for the high E_{switch} value. It should also be noted that the very O_2-sensitive Hyd-1 C19G enzyme was found to have a high value for E_{switch} (Fig. 6.4 and ref. [89]), and this allows a more specific definition of the role of E_{switch} in determining O_2 tolerance. A high value of E_{switch} is important for rapid reactivation of Ni-B under mildly reducing conditions, but the Ni-B state must the product of O_2 inactivation [89].

The midpoint potential of the Ni-SI_a/Ni-C and the Ni-C/Ni-R couples in *Aa* Hase I were found to be considerably more positive (70-140 mV) than those in standard hydrogenases [250]. It was proposed that the positive shift in these two potentials contributes to the 'overpotential' for H_2 oxidation (see Section 5.1.3) observed in all O_2-tolerant hydrogenases characterised *via* PFE to date [83, 132, 250]. With the indications that Ni-L* is part of the catalytic cycle (Chapter 5), the high potential at which Ni-L* in Hyd-1

C19G/C120G is observed at maximum intensity (which is even higher than that of Ni-C in *Aa* Hase I, Table 6.1) lends support to this hypothesis. However, it is important to note that the overpotential for H_2 oxidation is not indicative of O_2 tolerance, since the O_2-sensitive Hyd-1 C19G and C19G/C120G variants exhibit similar overpotentials compared to the O_2-tolerant native Hyd-1 and Hyd-1 C120G (Fig. 6.4 and ref. [89]).

The EPR titrations of native Hyd-1, C19G, C19G/C120G and C120G show that there is no clear correlation between O_2 tolerance (determined from PFE experiments [89]) and the development of a multiline EPR spectrum at high potentials. However, the *reversibility* of the formation of this state may be crucial. The similarities and differences between the variants' Fe-S cluster EPR spectra are now examined in relation to the structural data most recently published for the native O_2-tolerant [NiFe]-hydrogenases from *R. eutropha* [87], *H. marinus* [17] and *E. coli* [18].

In *Aa* Hase I, the appearance of a complex signal at high potential has been interpreted as arising from spin coupling between the active-site Ni species, the oxidised medial [3Fe-4S]$^+$ cluster, and the superoxidised proximal cluster in the 3+ oxidation state [16]. It was therefore proposed that the proximal cluster in O_2-tolerant hydrogenases undergoes two redox transitions, one at high potential, as well as the 'normal' transition observed in standard hydrogenases [16]. The results presented here for native *E. coli* Hyd-1, as well as for the O_2-tolerant *Salmonella* Hyd-5, are consistent with this proposal. The crystal structures now determined at both low and high potentials of *E. coli* Hyd-1 [18] (see Fig. 6.1), together with those published for *H. marinus* MBH [17], leave no doubt that the proximal cluster in O_2-tolerant [NiFe]-hydrogenases is highly unusual and capable of two redox transitions over an unprecedented narrow potential range because of its unique structure and coordination. In fact, the proximal cluster is best described as a [4Fe-3S] cluster [17, 18, 281], in which the 4^{th} sulfur of the distorted cubane is provided by C19 (Fig. 6.1). The prediction that of the two supernumerary cysteines C19 plays the more important role therefore explains the electrochemical results of the C19G variant [89].

Thus, mechanistically, a key factor of O_2 tolerance in native enzymes is the ability of the proximal cluster to release two extra electrons to the active site [138, 290], because this avoids the formation of reactive oxygen species (Ni-A and other *Unready* states) and ensures the formation Ni-B/*Ready* only.

The challenge is now to reconcile the results of the proximal cluster variants with this mechanism. Despite its O_2 sensitivity, two paramagnetic species are present in high-potential samples of C19G. Because of the magnetic interaction with the active site Ni species, and the similar midpoint potential to that of the [4Fe-3S]$^{5+/4+}$ couple in the native enzyme, the second high-potential centre is most certainly the 'superoxidised' [4Fe-3S]$^{5+}$ cluster. Therefore, there are other criteria for protecting the enzyme from O_2, additional to the requirement for the proximal cluster to discharge an extra electron at high potentials (factor 1). The EPR titration of C19G shows that the spectral changes upon reduction and reoxidation are not fully reversible, although the [4Fe-3S]$^{5+}$ state is reformed, Fig 6.12. It is therefore postulated that sustained tolerance to O_2 is dependent on the *stability* of the [4Fe-3S]$^{5+}$ state of the proximal cluster (factor 2) and the ability of the proximal cluster to quickly re-set to the [4Fe-3S]$^{4+}$ state (factor 3), so that the cluster can participate in the normal catalytic cycle. From the EPR studies performed here, it appears that in C19G it is mainly factor 3 that is not fulfilled. It would be informative to activate and then anaerobically inactivate the O_2-inactivated enzyme (Fig. 6.7) to establish the reversibility of the O_2 inactivated states. Unfortunately, this is a highly infeasible experiment given how much the enzyme deteriorates during prolonged activation and inactivation procedures required.

Looking at the structure of native Hyd-1 (Fig. 6.17), the distance between Fe_4 and the S atom of C19 increases from 2.4 Å in the [4Fe-3S]$^{4+/3+}$ state (an acceptable bond length) to up to 2.9 Å in the [4Fe-3S]$^{5+}$ state (a distance too long to be a good bond).[5]

This lends support to the hypothesis that C19 is not required for the formation of the [4Fe-3S]$^{5+}$ state (although it may play a stabilising role), but that return to the

[5]As will be shown in the following Chapter, the C20-ligated Fe_4 exists in two conformations in the [4Fe-3S]$^{5+}$ state and the distance thus depends on which conformer is considered [18].

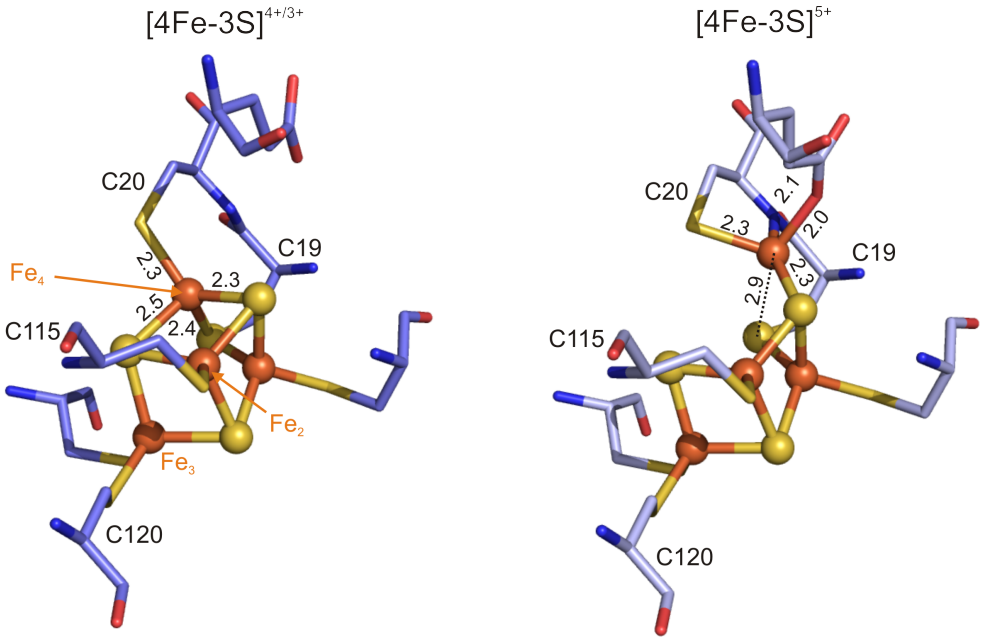


Figure 6.17: **The proximal cluster in its oxidised and reduced form in *E. coli* Hyd-1.** Distances result from the PDB files 3UQY (reduced form) and 3USC (oxidised form). Fe_4 exists in two conformations in the $[4Fe\text{-}3S]^{5+}$ state [18] and the distance in the oxidised state thus depends on which conformer is considered; only one conformation is shown here. Distances were obtained from the structure files using PyMOL. See Chapter 7 for further details.

$[4Fe\text{-}3S]^{4+/3+}$ states is difficult because of the absence of the sulfur of C19 available to stabilise Fe_4 in the C19G enzyme. It should be noted that the midpoint potential of the medial Fe-S cluster appears to be affected most by the C19G substitution. Although C19 is not in close proximity to the medial cluster, changes in the charge of relatively distant amino acids have previously been shown to have a dramatic effect on the midpoint potential of a Fe-S cluster [291]. Fe-S cluster midpoint potentials are also sensitive to the reduction potentials of neighbouring clusters [292]. Interestingly, the calculated true midpoint potentials of the $[3Fe\text{-}4S]^{+/0}$ couple in native Hyd-1 and all supernumerary cysteine variants are very positive, almost as high as those of the $[4Fe\text{-}3S]^{5+/4+}$ transitions, and certainly much higher than values reported for standard hydrogenases. The entire Fe-S cluster relay therefore may be tuned in O_2-tolerant hydrogenases to allow these enzymes to survive O_2. The Fe-S cluster transitions observed at lower potentials are discussed in

Chapter 8.

The considerably O_2-tolerant C120G variant does not appear to form the [4Fe-3S]$^{5+}$ state easily (even at +387 mV the EPR spectra mainly resembles that of an oxidised [3Fe-4S]$^{+}$ cluster and there are only small indications for the oxidation of another centre, Fig. 6.13). However, it is also possible that the oxidised product has a different conformation or spin state such that the magnetic coupling between the [4Fe-3S]$^{5+}$ state and the medial cluster/the active site Ni species is altered.

Substitution of both supernumerary cysteines with glycine removes the ability of the proximal cluster to enter the [4Fe-3S]$^{5+}$ state and also abolishes O_2 tolerance, as observed in the C19G/C120G variants of both *E. coli* Hyd-1 and *Re*-MBH [88]. The most obvious explanation is that in this enzyme, the proximal cluster really assumes the structure of the proximal cluster in standard hydrogenases.

Chapter 7

Characterisation of the unique [4Fe-3S] cluster in O_2-tolerant hydrogenases by HYSCORE

The *E. coli* Hyd-1 P242C and C19G/C120G/P242C variants were made by Dr. Michael Lukey and Dr. Rhiannon Evans (Oxford), respectively. Hyd-1 C19G/C120G/P242C EPR samples were prepared and measured by myself and Dr. Rhiannon Evans. Elena Nomerotskaia is gratefully acknowledged for help with enzyme purification. The computational calculations of Hyd-1 proximal cluster models (Fig. 7.2) were performed by Dr. Patricia Amara (Institut de Biologie Structurale, Grenoble) and Dr. Jean-Marie Mouesca (Laboratoire de Chimie Inorganique et Biologique, Grenoble). The program used for the simulation of the HYSCORE spectra was written by Dr. Jeffrey Harmer. Some of the HYSCORE measurements were carried out at the National EPR Research Facility & Service in Manchester and I would like to thank Daniel Sells and Dr. Floriana Tuna for valuable technical assistance during my stay. The work described in this Chapter has been published [270].

Abstract

The recent structures of the O_2-tolerant [NiFe]-hydrogenases *E. coli* Hyd-1 [18] and *H. marinus* MBH [17] at high potentials have revealed a directly bonded N ($^{14}N_{C20}$ in *E. coli* Hyd-1) to one of the Fe ions (Fe_4) in the unusual [4Fe-3S]$^{5+}$ proximal cluster, which plays a crucial role in rescuing the active site from the detrimental effects of O_2 [16, 88, 89].

The construction of a variant of *E. coli* Hyd-1 in which the medial [3Fe-4S] cluster has been converted to an EPR-silent [4Fe-4S] cluster enabled the detection of two strongly coupled nitrogen nuclei to Fe_4 *via* X-band HYSCORE. These ^{14}N peaks could not be observed clearly in native *E. coli* Hyd-1, presumably because of magnetic coupling to the paramagnetic medial [3Fe-4S]$^{+}$ cluster. A characterisation was thus only possible with the variant.

The larger ^{14}N coupling of $A = [11.5\ 11.5\ 16.0] \pm 1.5$ MHz characterises the Fe_4—$^{14}N_{C20}$ bond; the second coupling of $A = [2.8\ 4.6\ 3.5] \pm 0.3$ MHz is assigned to $^{14}N_{C19}$. Analyses of HYSCORE spectra were based on a $S = 1/2$ and $I = 1$ system, with consideration of the exchange coupling between the proximal [4Fe-3S]$^{5+}$ cluster and the [NiFe] active site. The results presented here present experimental evidence that Fe_4 is a valence-localised Fe^{3+} in the superoxidised proximal cluster, whose formation permits an additional 'rescue' electron to be transferred rapidly back to the active site upon O_2 attack.

7.1 Introduction

The crystal structures of three membrane-bound respiratory [NiFe]-hydrogenases, classified as O_2-tolerant, were recently solved [17, 18, 87]. These structures all reveal a unique proximal iron-sulfur cluster which lacks one of the inorganic sulfide ligands and is instead additionally coordinated by two supernumerary cysteine residues (Chapter 6). Importantly, the structures of *E. coli* Hyd-1 and *H. marinus* MBH, which were obtained both in oxidised and reduced forms in addition to the as-isolated form [17, 18], reveal a redox dependent conformational change of the proximal [4Fe-3S] cluster; the structure of *Re*-MBH was only obtained in the reduced state [87]. The reduced forms of the proximal cluster in all three enzymes are very similar and that in *E. coli* Hyd-1 is shown in Fig. 7.1 (right): the S atom of one of the supernumerary cysteines (C19) coordinates Fe_4 and Fe_1, while Fe_3 is ligated by the conserved C149 and the second supernumerary cysteine C120 only present in O_2 tolerant hydrogenases (*E. coli* Hyd-1 numbering is used here).

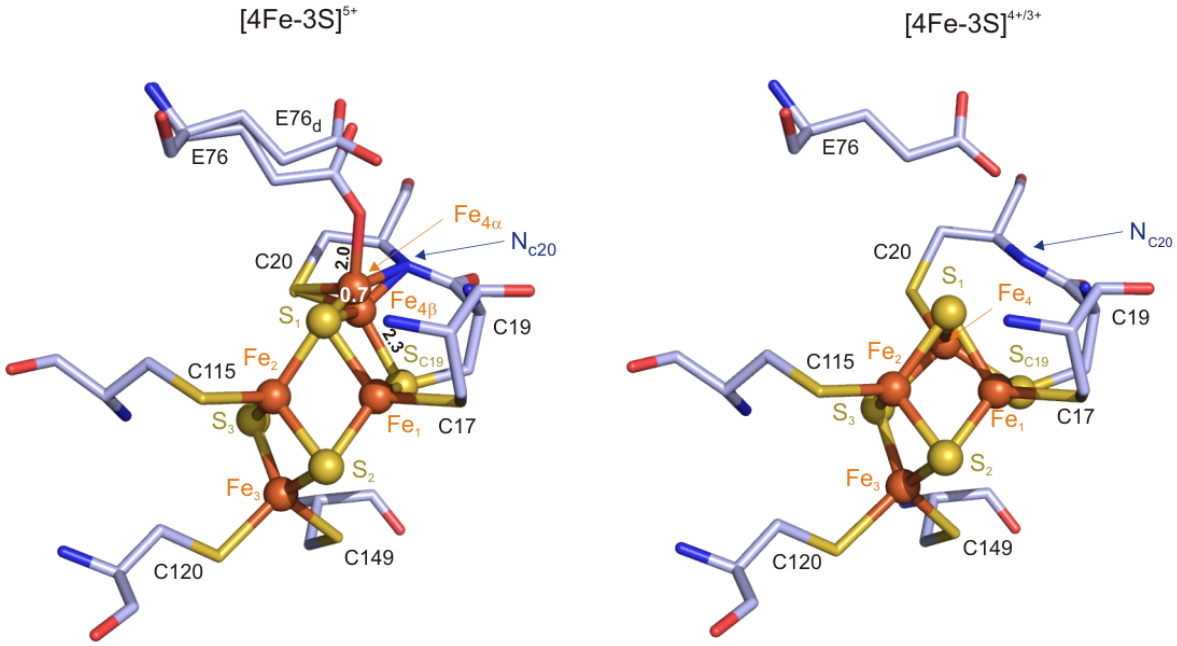


Figure 7.1: **The proximal cluster in its oxidised [4Fe-3S]$^{5+}$ conformations (3USC.PDB) and reduced [4Fe-3S]$^{4+/3+}$ form (3UQY.PDB) in *E. coli* Hyd-1.** In the oxidised state, different conformations of the Fe_4 ion are indicated with α and β and are separated by 0.7 Å; the conformer of Glu76 distant to the Fe-S cluster is denoted as $E76_d$, see ref. [18]. Bond distances of the Fe_4 closest to Glu76 or Cys19 are given in Å.

The most remarkable change in the oxidised form (Fig. 7.1, left) is the position of Fe_4, now no longer ligated by inorganic sulfide S_3, but instead by the backbone nitrogen of C20 [17, 18]. As can be seen in Fig. 7.1 (left), Volbeda and Amara *et al.* [18] found two different conformations of the Fe_4 and also of glutamate 76 in the oxidised from of the proximal cluster ($[4Fe\text{-}3S]^{5+}$) of *E. coli* Hyd-1. Although Shomura *et al.* [17] observed a change in the position of Fe_4 (Fe_2 in *Hm*-MBH) in reduced and oxidised states of the proximal cluster, the authors did not report different conformations of this Fe atom and Glu76 (Glu82 in *Hm*-MBH) in the $[4Fe\text{-}3S]^{5+}$ form of the cluster. However, following additional refinement of the *Hm*-MBH structure, Volbeda and Amara *et al.* [18] concluded that, similar to *E. coli* Hyd-1, different conformations of Fe_2 and Glu82 are also present in this enzyme. The different models that could correspond to the $[4Fe\text{-}3S]^{5+}$ proximal cluster proposed by Volbeda and Amara *et al.* [18] are shown in Fig. 7.2.

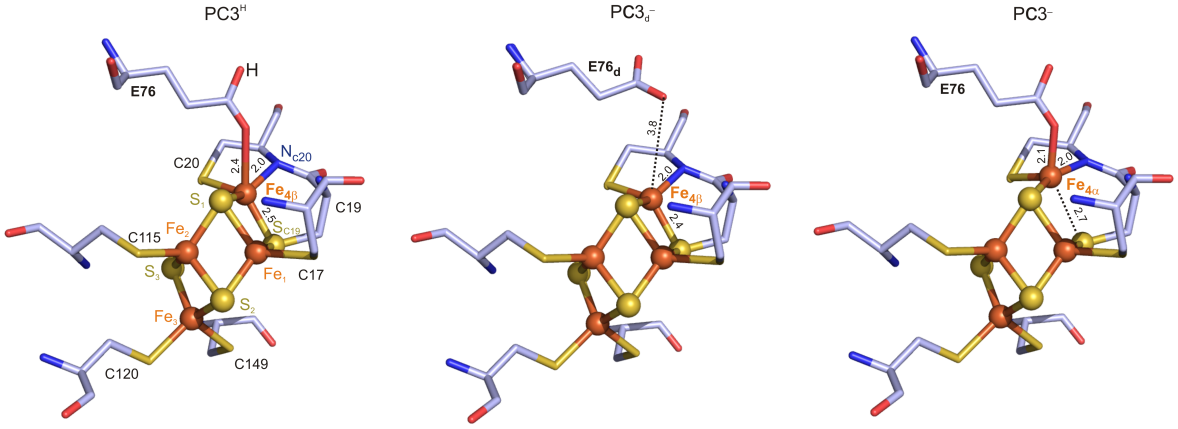


Figure 7.2: **Different models proposed for the proximal cluster in its oxidised in *E. coli* Hyd-1.** Models are based on the oxidised crystal structure of *E. coli* Hyd-1 (3USC.PDB). Distances refer to the geometry-optimised models given in ref. [18] and are very similar to those obtained from the crystal structure. Different conformations of the Fe_4 are indicated with α and β; the conformer of Glu76 distant do the Fe-S cluster is denoted as $E76_d$. The superscript ^{H} in $PC3^H$ refers to E76 being protonated; a $^-$ superscript refers to deprotonated E76 in $PC3^-_d$ and $PC3^-$. Subscript $_d$ symbolises the distant position of E76. See ref. [18] and text.

The models were calculated [18] based on the crystal structures, and Mössbauer and EPR data of the *A. aeolicus* Hase I enzyme [16]. The geometry-optimised models were constructed in order to assign electronic structures to the structurally defined $[4Fe\text{-}3S]^{5+}$

cluster and determine the protonation states of Glu76 [18]. Figure 7.2 shows the X-ray structural equivalent to the geometry optimised models (generated from 3USC.PDB), but the bond distances shown result from calculations and vary slightly from those in the crystal structure [18]. The three different models are distinguished by the positions of Glu76 and Fe_4, but N_{C20} is $\approx$ 2.1 Å from Fe_4 in all cases and is thus considered to be bonded and deprotonated [18]. $PC3^H$ is so-called because Glu76 is protonated. In this model Fe_4 is in a trigonal bipyramidal coordination. $PC3_d^-$ reflects the distal position of deprotonated Glu76 from the cluster and Fe_4 is in an approximately tetrahedral environment. Because of the change in conformation of Glu76, this residue was proposed to act as a base in deprotonating the backbone amide N of Cys20, and it is possible that the crystal structure (Fig. 7.1, left) reflects different intermediates (Fig. 7.2) in the transfer of the C20 amide proton by Glu76 to the active site [18].

The preferred models, $PC3^H$ and $PC3_d^-$, maintain electroneutrality in the transition from the $[4Fe\text{-}3S]^{4+}$ to the $[4Fe\text{-}3S]^{5+}$ state, as can be appreciated by considering the whole cluster environment, including the 6-Cys coordination and the negative charge on N_{C20} [18]. The additional negative charge on the backbone amide N_{C20} (or even in the entire C=O and N moiety reported to be nearly coplanar in the oxidised structure reported for *H. marinus* MBH [17]) was postulated to stabilise a higher oxidation state in the $[4Fe\text{-}3S]^{5+}$ state of the proximal cluster [17]. Quantum mechanics/molecular mechanics calculations [18] assign a 3+ oxidation state to Fe_4 in the $[4Fe\text{-}3S]^{5+}$ state of the proximal cluster, but characterisation of the electronic state of Fe_4 and the nature of the bond to N_{C20} remains to be determined. Furthermore, it remains to be ascertained which of the proposed models, $PC3^H$, $PC3_d^-$ or $PC3^-$ (Fig. 7.2), corresponds to the spectroscopically (EPR and Mössbauer) observed state.

If Fe_4 of the proximal cluster in high-potential samples of O_2-tolerant hydrogenases has unpaired electrons and thus spin density, it should be possible to detect spin density on N_{C20} using HYSCORE (Section 2.6.3), and from the magnetic couplings characterise the strength and nature of the Fe−N bond. N_{C20} should be strongly coupled and thus

easily distinguishable from other nearby backbone N atoms that are not directly bonded to the [4Fe-3S]$^{5+}$ cluster. Indeed, previous studies on systems containing Fe−N bonds have shown that the strongly coupled ^{14}N (*e.g.* hyperfine couplings of A = [6.2 7.6 8.4] MHz [293]) manifests itself as peaks in the (−,+) quadrant of the corresponding HYSCORE spectra, clearly distinguishable from remote N atoms which give rise to peaks in the (+,+) quadrant [293–296].

Here, samples poised at high potentials of both native *E. coli* Hyd-1 and Hyd-1 P242C, a variant in which the medial [3Fe-4S] cluster is converted to a [4Fe-4S] cluster (see also Chapter 8), are investigated *via* HYSCORE spectroscopy. Proline 242 in *E. coli* Hyd-1 occupies the position that a cysteine residue would occupy in a [NiFeSe]-hydrogenase, which contain medial [4Fe-4S] clusters [59]. The successful conversion of a medial [3Fe-4S] cluster into a [4Fe-4S] cluster in a [NiFe]-hydrogenase was first demonstrated for the O_2-sensitive hydrogenase from *D. fructosovorans* [58]. The advantage of the conversion of the medial [3Fe-4S] cluster into a [4Fe-4S] cluster in *E. coli* Hyd-1 would be a simplification of the coupling situation at high potentials because of 'removal' of one of the paramagnetic species. At high potentials, the paramagnetic species contributing to the observed EPR signals in native *E. coli* Hyd-1 are the [3Fe-4S]$^{+}$ medial cluster, the [4Fe-3S]$^{5+}$ proximal cluster and the oxidised active site Ni species [16, 82, 88, 285] (see Chapter 6). In the absence of a medial [3Fe-4S] cluster, *E. coli* Hyd-1 P242C poised at high potentials should only contain the [4Fe-3S]$^{5+}$ proximal cluster and the oxidised active site Ni species.

7.2 Methods

Total protein concentration was determined for as-isolated samples of enzyme by the method of Bradford [139] (Section 3.7) prior to potential adjustment for redox titration experiments. Spin quantifications were carried out as described in Section 3.3.

7.2.1 Preparation of EPR samples

All native Hyd-1 or Hyd-1 P242C, C19G/C120G and C19G/C120G/P242C EPR samples in Fig. 7.3 and 7.5 and result from titrations of as-isolated enzyme (containing MV, BV, PMS, ITS, NQ and OHNQ at 40 μM each) under Ar, using the method detailed in Section 3.2 (cell B), and withdrawal of ≈ 300 μL of enzyme solution at the desired potential into 4 mm high-precision EPR tubes (Section 3.2). The order in which samples were taken are indicated for the full titrations of native Hyd-1 and P242C (Fig. 7.3). The spectrum of C19G/C120G in Fig. 7.5 results from sample 3 of the full titration (see Fig. 6.10, Chapter 6) and that of C19G/C120G/P242C results from sample 5 of the full titration (not shown). The native Hyd-1 and Hyd-1 P242C samples for pulse EPR measurements were prepared by concentrating as-isolated enzyme (Millipore, centrifugal filter units 0.5 mL) in an anaerobic glove box (Glove Box Technology), anaerobic transferral to cell A (Fig. 3.3) on the bench, addition of 400 μM each of PMS, NQ and ITS and adjustment to the potential specified by addition of sub-μL quantities of 400 mM potassium ferricyanide. The deuterated Hyd-1 P242C sample was prepared in a similar way except that the buffer was exchanged for D_2O MES buffer (Section 3.8) until the aqueous composition was $> 99\%$ D^+ and 40 μM of each mediator were added because of the weaker sample concentration. The control sample was prepared by adding 10 mM ferricyanide to a buffer solution with 10 % glycerol (identical to that of the enzyme solution) containing 400 μM PMS, NQ and ITS. Samples were flash-frozen in 3.8 mm high-precision tubes (Section 3.2). The W-band Hyd-1 P242C sample was prepared in an anaerobic glove box (Glove Box Technology) using the methods described in Section 3.2 by adjusting ≈ 100 μL as-isolated enzyme (≈ 250 μM) containing 50 μM each PMS, NQ and ITS to +373 mV by addition of ferricyanide. An aliquot (1-2 μL) was transferred as quickly as possible to a W-band EPR tube. Although the potential was steady at +373 mV during as enzyme solution was transferred to the EPR tube, the potential of W-band samples was generally found to be less reliable than that of X-band samples (see also Chapter 8). Because no error margin can be given for this sample, the quoted potential should be considered to

be only approximate.

7.2.2 EPR measurements and analysis of HYSCORE spectra

Continuous wave EPR measurements were carried out using an X-band (9.1-9.9 GHz) Bruker EMX spectrometer with an X-band super-high-sensitivity probehead (Section 3.5.1). Measurement conditions are provided in the figure legends. Most pulsed measurements were carried out on a W-/X-band Bruker Elexsys 680 spectrometer using an X-band EN-4118 MD4 resonator or a W-band 600-1021H TeraFlex resonator. Some of the X-band HYSCORE measurements were carried out at the National EPR Research & Service in Manchester on a X-band Bruker 580 spectrometer with a MD4-W1007 resonator. All spectrometers were equipped with a low temperature helium flow cryostat (Oxford Instruments). The field was calibrated as described in Section 3.5.2. Simulations of the HYSCORE spectra were performed on an in-house program written by Dr. Jeffrey Harmer.

7.3 Results

7.3.1 Potential titrations of *E. coli* native and P242C variant Hyd-1

The CW EPR spectra of potential titrations of as-isolated native Hyd-1 and the P242C variant are presented in Fig. 7.3. Fe-S cluster and Ni signals were measured under non-saturating conditions. Since signals in the P242C variant samples were more easily saturated than in the native enzyme samples, a higher temperature of 20 K was chosen in order to measure at a reasonable mw power. The P242C variant signals did not change shape between 15 K and 20 K (not shown).

Whereas the oxidised medial cluster, uncoupled to the high potential centre (Section 6.3.2), is visible at +145 mV in native Hyd-1, the peaks corresponding to the $[3Fe\text{-}4S]^{+}$

cluster with $g_{x,y,z} = 2.03, 2.01, 2.00$ are not visible at any potential in the P242C titration. This indicates that the conversion of the medial cluster into an EPR-silent [4Fe-4S] cluster was successful.

In order to determine the number of redox transitions the EPR-visible Fe-S clusters undergo and to investigate the effect of the P242C mutation on their midpoint potentials, Nernst plots (Section 3.1) were constructed and are compared to those of native Hyd-1 in Fig. 7.4. The peak positions used are indicated in Fig. 7.3 and the resulting curves are well described by one-electro processes. As will be shown in Chapter 8, the low-potential redox transitions corresponds to the [4Fe-3S]$^{4+/3+}$ couple of the proximal cluster in both enzymes. The medial [4Fe-4S] cluster in Hyd-1 P242C appears to be EPR-silent and further evidence of this is provided in the following Chapter.

The red bell-shaped curve in Fig. 7.4 (left) results from a fit of the *apparent* midpoint potential of the 'appearance' and 'disappearance' of the [3Fe-4S]$^{+}$ cluster signals in native Hyd-1 and does not reflect the true midpoint potential of the [3Fe-4S]$^{+/0}$ redox couple (see Section 6.3.5, Chapter 6 and ref. [270]). Equivalent signals are not observed in Hyd-1 P242C, consistent with the absence of the [3Fe-4S] cluster. However, similar to the native enzyme, a high-potential redox transition corresponding to the development of a complex EPR signal is observed (black sigmoid $*$ in Fig. 7.4). In native Hyd-1, this redox transition with E_m = 230±15 mV was assigned to the proximal [4Fe-3S]$^{5+/4+}$ couple (Chapter 6). Because the proximal Fe-S cluster should be structurally and electronically the same in native Hyd-1 and the P242C variant, the high-potential redox transition in Hyd-1 P242C, with $E_m = 175\pm15$ mV is also assigned to the proximal [4Fe-3S]$^{5+/4+}$ couple (black sigmoid in Fig. 7.4, right). Differences in the Nernst plots of the high-potential redox transition were observed depending on the g value chosen and the data in Fig. 7.3 (right) result from peak intensities at $g = 2.062$ (peak 1 in Fig. 7.3). A spread of *ca.* 55 mV was found (Fig. 10.4) and this significant result is discussed later. The Fe-S cluster signals at +384 mV in the P242C variant (Fig. 7.3, right) integrated to +0.9±0.3 spins per molecule of enzyme, compared to 2.0±0.3 spins in the native enzyme at a similar potential. The spin

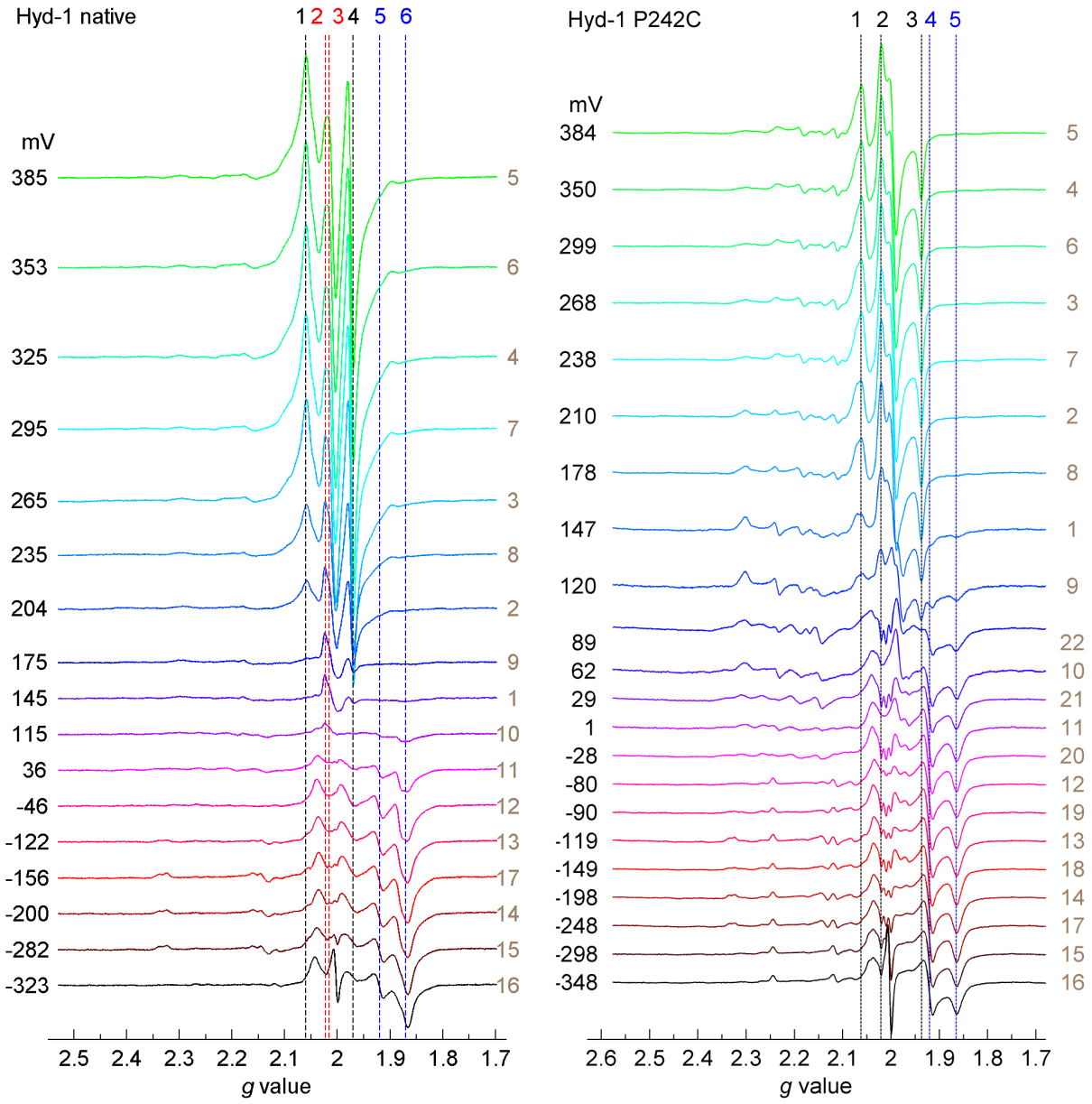


Figure 7.3: **CW EPR spectra of potential titrations of native Hyd-1 (left) and the P242C variant (right).** The spacing between adjacent spectra is not proportional to the redox potential difference between the samples. Measurement conditions: mw frequency 9.385 GHz (native), 9.375 GHz (P242C); mw power 2 mW (native), 0.5 mW (P242C); modulation amplitude 1 mT. Enzyme concentrations: 24 μM (native), 46 μM (P242C). Temperature: 15 K (native), 20 K (P242C). Annotations refer to the potential at which the sample was taken (left, in mV) and the order in which samples were taken (right, grey). Vertical lines indicate the peak heights monitored to extract mid-point potentials, see Fig. 7.4.

quantifications provide further evidence that the [3Fe-4S]$^+$ paramagnet is absent in Hyd-1 P242C poised at high potentials. In the absence of magnetic interactions with a medial

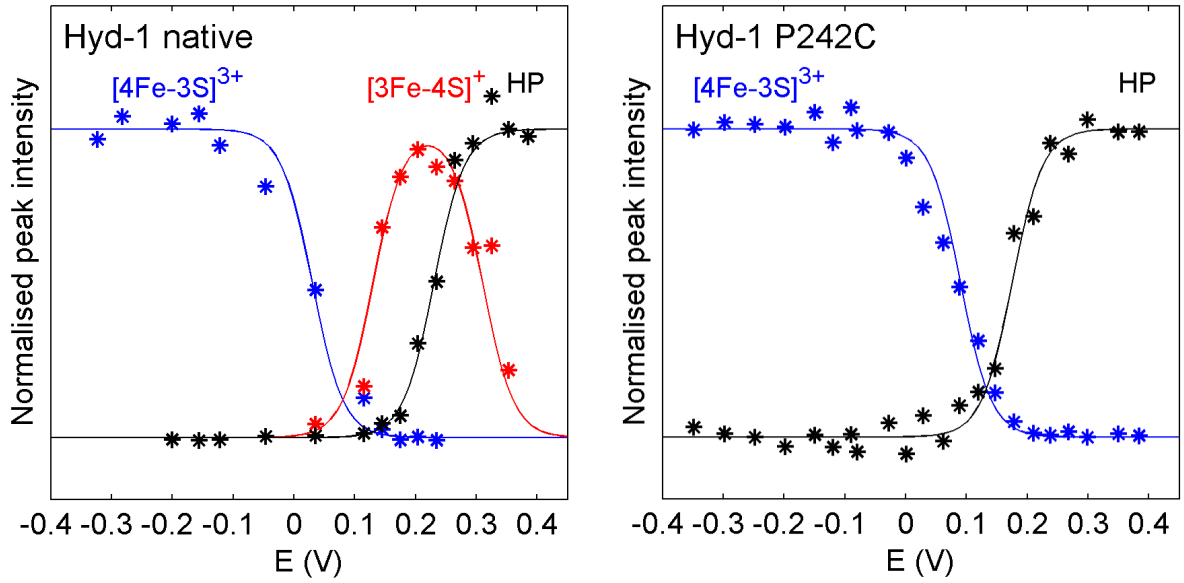


Figure 7.4: **Potentiometric titrations of the EPR-active species observed in native Hyd-1 (left) and the P242C variant (right).** The peak positions in the CW EPR spectra (labeled in Fig. 7.3) used to give these plots were as follows: Native Hyd-1 $[4Fe\text{-}3S]^{3+}$ (peak 6, $g = 1.870$), $[3Fe\text{-}4S]^{+}$ (peak 2 minus peak 3, $g = 2.023$ minus $g = 2.016$), HP (peak 4, $g = 1.970$); Hyd-1 P242C $[4Fe\text{-}3S]^{3+}$ (peak 5, $g = 1.865$), HP (peak 1, $g = 2.062$). Adapated from ref. [270].

$[3Fe\text{-}4S]^{+}$ cluster, one may expect a simpler Fe-S cluster signal with g values corresponding directly to the $[4Fe\text{-}3S]^{5+}$ cluster in the Hyd-1 P242C variant at high potentials. However, it has been shown that there is a large exchange interaction between the active site Ni species and the proximal $[4Fe\text{-}3S]^{5+}$ cluster, estimated to be $\approx$ 630 MHz in *A. aeolicus* Hase I [16]. Prior to the availability of the crystal structures of O_2-tolerant hydrogenases, Saggu *et al.* concluded from X-band and Q-band echo-detected EPR spectra of *Re*-MBH poised at high potentials that Ni-B (Ni-A is not observed in this enzyme) is coupled to *two* paramagnetic species, with exchange interactions of 780 and 550 MHz, neither of which is the medial $[3Fe\text{-}4S]^{+}$ cluster [297]. The high-potential $[4Fe\text{-}3S]^{5+}$ cluster EPR spectra of Hyd-1 P242C are indeed also strongly influenced by a large exchange coupling to both Ni-B and Ni-A (see below). The presence of Ni-A as well as Ni-B in as-isolated samples of Hyd-1 P242C is apparent from the characteristic Ni-A $g_y = 2.24$ peak in the EPR spectra between +62 and +147 mV (Fig. 7.3). Ni-A is also visible in 80 K EPR spectra of high-potential samples (Fig. 8.7, Chapter 8).

Conventional solution assays show that the activity of the P242C *E. coli* Hyd-1 variant (69±15 s^{-1}) is of the same order of magnitude as that of native enzyme (147±26 s^{-1}). Hyd-1 P242C is also highly active on an electrode, as revealed by protein film electrochemistry experiments.[1] In conjunction with the lack of the observation of a $[3Fe\text{-}4S]^{+/0}$ transition in EPR titration experiments and the integration of the Fe-S cluster signals in high-potential samples to only ≈ 1 spin per molecule of enzyme, it is concluded that the conversion of the medial cluster into a [4Fe-4S] cluster through the P242C point mutation in *E. coli* Hyd-1 was successful. In addition, given that the medial and distal Fe-S clusters in O_2-tolerant and standard hydrogenases are essentially identical [17, 18, 87], the conversion in *E. coli* Hyd-1 may also be inferred from the crystallographically proven conversion of the medial [3Fe-4S] to a [4Fe-4S] cluster through the same point mutation in the standard *D. fructosovorans* [NiFe]-hydrogenase [58].

7.3.2 Comparison of the EPR spectra of native Hyd-1 and the P242C, C129G/C120G/P242C and C19G/C120G variants at high potentials

In Chapter 6 is was shown that replacement of both supernumerary cysteines residues at the proximal cluster by glycines (Hyd-1 C19G/C120G) removed the ability of the proximal cluster to undergo the high-potential $[4Fe\text{-}3S]^{4+/5+}$ transition (a simple $[3Fe\text{-}4S]^{+}$ cluster signal was also observed for the equivalent variant of *Re*-MBH [88]). A variant in which the C19G/C120G and the P242C point mutations are combined should therefore result in the observation of *only* uncoupled active site Ni species in samples poised at high potentials.

Figure 7.5 summarises the X-band CW EPR spectra of native Hyd-1 and the P242C, C19G/C120G/P242C and C19G/C120G variants samples poised at potentials between +384 and +393 mV. The number of spins per molecule that the Fe-S cluster signals

[1] Methylene blue solution assays and PFE experiments were carried out by Dr. Rhiannon Evans, University of Oxford.

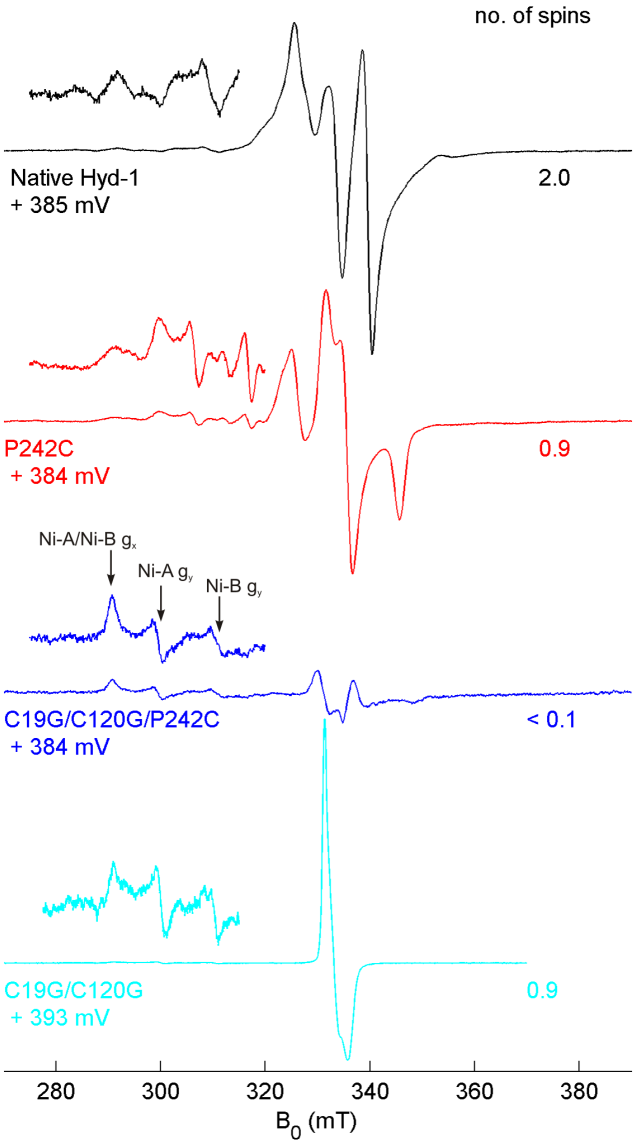


Figure 7.5: **X-band CW EPR spectra of native Hyd-1 (15 K), Hyd-1 P242C (20 K), Hyd-1 C19G/C120G/P242C (15 K) and Hyd-1 C19G/C120G (15 K) poised at high potentials.** The nickel region of the spectra is magnified in the insets. The C19G/C120G/P242C and C19G/C120G spectra show 'unsplit' Ni-A and Ni-B (see text), and the g values (Ni-A/Ni-B $g_x = 2.31$, Ni-A $g_y = 2.24$, Ni-B $g_y = 2.16$) are indicated for the C19G/C120G/P242C variant. The spin integrations of the Fe-S cluster signals are also shown (Native Hyd-1: 2.0±0.3, P242C: 0.9±0.3, C19G/C120G/P242C < 0.1, C19G/C120G 0.9±0.2 spins per molecule of enzyme). Measurement conditions: mw frequency 9.385 GHz (native & C19G/C120G), 9.375 GHz (P242C & C19G/C120G/P242C); mw power 2 mW (native, C19G/C120G/P242C & C19G/C120G), 0.5 mW (P242C)); modulation amplitude 1 mT (native, P242C & C19G/C120G/P242C), 0.5 mT (C19G/C120G). Enzyme concentrations: 24 μM (native), 46 μM (P242C), 22 μM (C19G/C120G/P242C), 21 μM (C19G/C120G). Spectra are not scaled by enzyme concentration and measurement conditions. Figure adapted from ref. [270].

integrated to are indicated to the right of the spectra. The Ni regions are magnified and shown as insets. While the Ni signals in native Hyd-1 and Hyd-1 P242C are 'split' by a very large exchange interaction of $\approx$ 600 MHz (see Section 7.3.5), those in the 'double' (C19G/C120G) and 'triple' (C19G/C120G/P242C) variant spectra are not. As previously discussed in Chapter 6 (Section 6.3.2) and similarly to standard hydrogenases (*e.g. E. coli* Hyd-2, Section 5.3.3), the spectrum of the double variant shows that any exchange or dipolar interactions between the medial [3Fe-4S]$^{+}$ cluster and the active site Ni-B and Ni-A are negligible. The Ni signals in the triple variant are very similar to those in the double variant and represent the intrinsic g values of Ni-A and Ni-B, as they are not shifted by exchange or dipolar electron-electron couplings (Fig. 7.5). The saturation properties of the Ni signals in the triple variant were similar to those in the double variant, which are saturated at 15 K and 2 mW mw power in the absence of the additional [4Fe-3S]$^{5+}$ paramagnet leading to the enhanced relaxation observed in the native enzyme (Section 6.3.2) and also in Hyd-1 P242C. The Ni signal characteristics of the C19G/C120G variant are thus evident in the 'triple' variant. Furthermore, the signals observed in the Fe-S cluster region only amounted to a negligible 0.08 spins per molecule of enzyme, showing that the characteristics of the P242C mutation are also evident in the triple variant. Solution assays and PFE experiments conducted on Hyd-1 C19G/C120G/P242C established that this enzyme is active, though considerably less so than native Hyd-1.[2] Consequently, the spectrum of the triple variant lends additional support to the successful conversion of the medial cluster in variants with the P242C point mutation.

No significantly larger EPR signal at $g = 4.3$ (indicative of free Fe^{3+} [298]) was detected in high-potential samples of native Hyd-1 and Hyd-1 P242C compared to the double and triple variants which lack the [4Fe-3S]$^{5+}$ paramagnet (spectra not shown). This indicates that Fe_4 in the [4Fe-3S]$^{5+}$ is not a separate electronic and magnetic entity from the rest of the Fe-S cluster.

[2]Solution assays conducted by Dr. Rhiannon Evans yielded a turnover of 16$\pm$3 s^{-1} at pH 6 and 25 ^{o}C using methylene blue to monitor H_2 oxidation.

The low-temperature Ni signals in native Hyd-1 and Hyd-1 P242C are significantly different and the deviation of the signals from the Ni-A and Ni-B g values (visible in the 'double' and 'triple' variant spectra) appears to be more significant in the P242C enzyme. Although P242C contains considerably more Ni-A than the native enzyme, the observed splitting is expected to be similar in both Ni-A and Ni-B if it is caused only by magnetic interaction with the proximal $[4Fe\text{-}3S]^{5+}$ cluster.

7.3.3 Detection of strong nitrogen couplings in high-potential Hyd-1 P242C

The X-band two-pulse echo-detected field sweeps of concentrated samples of native Hyd-1 and Hyd-1 P242C oxidised to +385 and +381 mV, respectively, are depicted in Fig. 7.6. Numerical derivatives of the absorption spectra are comparable to the X-band CW EPR spectra from the titration samples at similar potentials (shown in blue in Fig. 7.6).

Figure 7.7 depicts HYSCORE spectra measured at 15 K at field positions where the echo-signal intensity was maximal in both native Hyd-1 (top) and Hyd-1 P242C (centre). The blue and red lines in the (−,+) quadrant correspond to the approximate expected single and double quantum (dq) cross-peak positions, respectively, that are expected for a ^{14}N nucleus strongly ($|A| > 2|\nu_{mw}|$) coupled to the electron spin. Although cross-peaks are observed in the spectra of both enzymes, they are much clearer in the Hyd-1 P242C variant (even after taking into account the difference in samples concentrations and increasing the accumulation time accordingly for the native Hyd-1 sample). Furthermore, as discussed in Section 7.3.4, an additional strong ^{14}N coupling was revealed in matched HYSCORE measurements of P242C only. Lowering the temperature of the measurements to 10 K did not intensify the ^{14}N cross-peaks in native Hyd-1 HYSCORE spectra (not shown). Similarly, the ^{1}H couplings (peaks split around $\approx$ 15 MHz at this field position) are well-defined in Hyd-1 P242C as compared to the native enzyme, where only the nuclear Zeeman frequency peak is observed. Further measurements and analyses of the ^{14}N couplings was therefore conducted on the P242C variant (*vide infra*), where they are

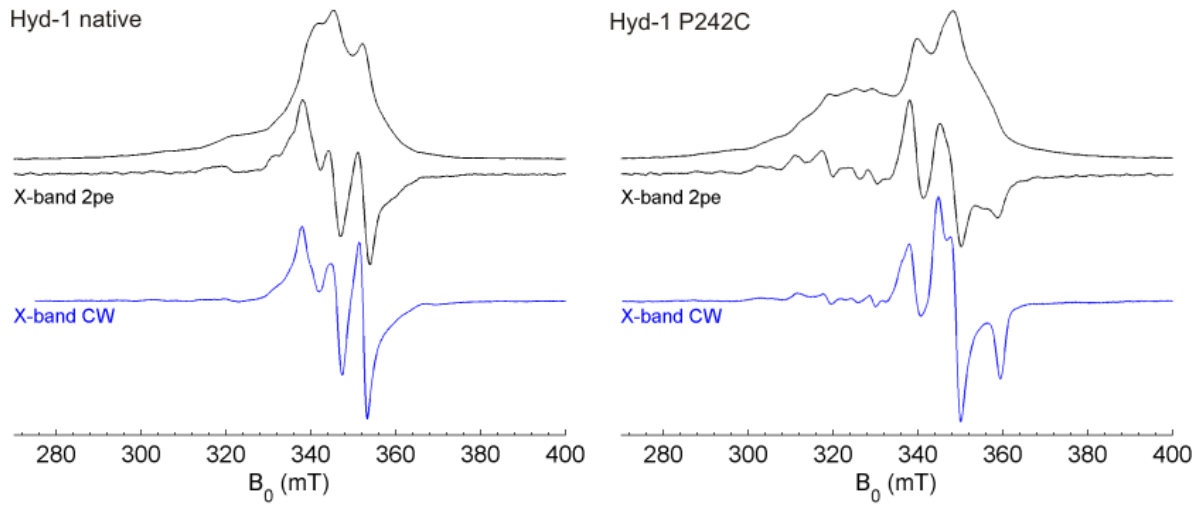


Figure 7.6: **X-band echo-detected and CW spectra of native Hyd-1 and the P242C variant poised at high potential.** The two-pulse echo-detected (2pe) field sweeps and their derivative spectra are shown in black. The native Hyd-1 sample was poised at + 385 mV and the P242C sample was poised at + 381 mV; enzyme concentrations were 378 μM (native) and 622 μM (P242C). Measurement conditions: mw frequency 9.741 GHz (native), 9.750 GHz (P242C); pulse sequence $\pi/2$ -τ - π - τ - echo where τ = 128 ns, $\pi/2$ = 20 ns, π = 40 ns; shot repetition time 2 ms, temperature: 15 K (native), 12.5 K (P242C). CW spectra (blue) are taken from Fig. 7.5 and measurements conditions are identical, but the mw frequencies were used to adjust the field axis of the 2pe sweeps to enable a direct comparison of the peak positions. Taken from ref. [270].

more easily detected, presumably because of the removal of a significant electron-electron interaction with the medial [3Fe-4S]$^{+}$ paramagnet. In a measurement at 345 mT at 10 K of a control sample (containing buffer, mediators and ferricyanide but no enzyme), no ^{14}N or ^{1}H couplings were detected (not shown).

To detect any nearby exchangeable proton(s), relating to the postulated deprotonation of N_{C20} by Glu76 [18] (Fig. 7.2), a deuterium-exchange sample of Hyd-1 P242C at high potential was also prepared. The HYSCORE spectrum obtained at the field position of the maximum EPR spectrum intensity is shown in Fig. 7.7 (bottom). Similarly to the sample prepared in H_2O, strongly coupled ^{14}N cross-peaks are detected. Because of the considerably weaker concentration of this sample, comparison of the ^{1}H proton region of the spectra (centre and bottom in Fig. 7.7) is not reliable (the signal-to-noise ratio is too low). However, the ^{2}H region of the spectrum of the deuterated P242C

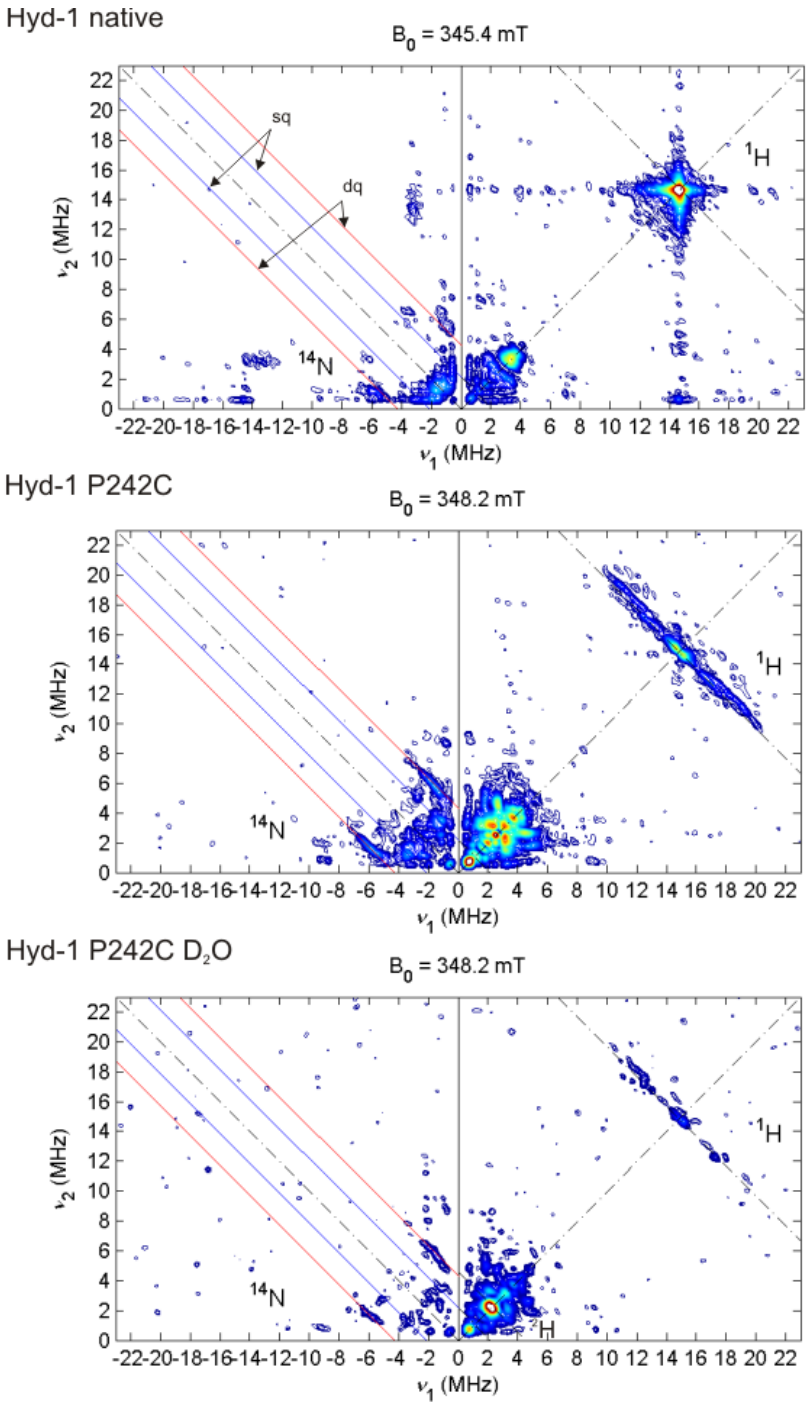


Figure 7.7: **X-band HYSCORE spectra of native Hyd-1, Hyd-1 P242C and deuterated P242C samples poised at high potential.** Measurement conditions: $\pi/2 = 16$ ns, $\pi = 16$ ns, 15 K, shot repetition time 1 ms, 150 points, 8-step phase cycle, $\tau = 108$ ns, 9.741 GHz (native), 9.750 GHz (P242C) and 9.740 GHz (P242C D_2O). The field positions at which the spectra were recorded correspond to the maximum intensities of the field sweeps in Fig. 7.6. Sample concentrations 378 μM (native), 622 μM (P242C), 22 μM (P242C D_2O). The deuterated P242C sample was poised at +405 mV. The approximate single (sq) and double quantum (dq) transition cross-peak positions expected for a strongly coupled ^{14}N nucleus are shown as blue and red lines in the (−,+) quadrant, respectively. Figure adapted from ref. [270].

sample reveals that the couplings to any exchangeable proton is, at most, 1 MHz (or < 6.5 MHz for a proton). As a rough estimate, with a conservative spin projection factor (see Section 4.4.1) of 1 on Fe_4 and using the electron-nucleus point-dipole formula, the small observed ^{2}H coupling implies that any exchangeable protons are at least 2.9 Å away. In calculations reproducing the EPR data of native *Aa* Hase I [16], Volbeda and Amara *et al.* [18] assigned a spin projection factor of 7/3 (typical for Fe^{3+} [3] to Fe_4 in the $[4Fe\text{-}3S]^{5+}$ proximal cluster). This would increase the minimum distance to Fe_4 of any exchangeable protons to approximately 3.8 Å.[3] This estimate suggests a limit on the closest exchangeable proton of 2.9 to 3.8 Å.

7.3.4 HYSCORE measurement of Hyd-1 P242C reveal three ^{14}N couplings

Further HYSCORE measurements reveal that couplings from *three* different ^{14}N nuclei are observed in Hyd-1 P242C and Fig. 7.8 provides an overview. The strong couplings N1 and N2 are identifiable by the (dq, dq) cross-peaks in the (−,+) quadrant which are sharp since they are broadened by the nuclear quadrupole interaction (NQI) only though second order contributions. The strongest coupling N1 could only be detected by matched HYSCORE experiments (Section 2.6.3, Fig. 2.10). As will be explained below, N1 and N2 are strongly coupled to the proximal $[4Fe\text{-}3S]^{5+}$ cluster while N3 is in close proximity to the active site [NiFe] centre.

Given the large exchange interaction J between the active site Ni species and the proximal Fe-S cluster, it is instructive to examine the dependence of the nuclear energy levels on J. Figure 7.9 shows an energy level diagram for two electron spins $S_1 = 1/2$ (the proximal Fe-S cluster, red transitions) and $S_2 = 1/2$ (active site Ni-B, blue transitions), with S_1 coupled to a nuclear spin of $I = 1$ (^{14}N) and an exchange interaction $J \cdot S_1 S_2$.

The corresponding nuclear energy levels as a function of J (Fig. 7.9, right) show that

[3] In this calculation the other Fe ions of the cluster and their spin projection factors were not taken into account and the distance given is therefore approximate.

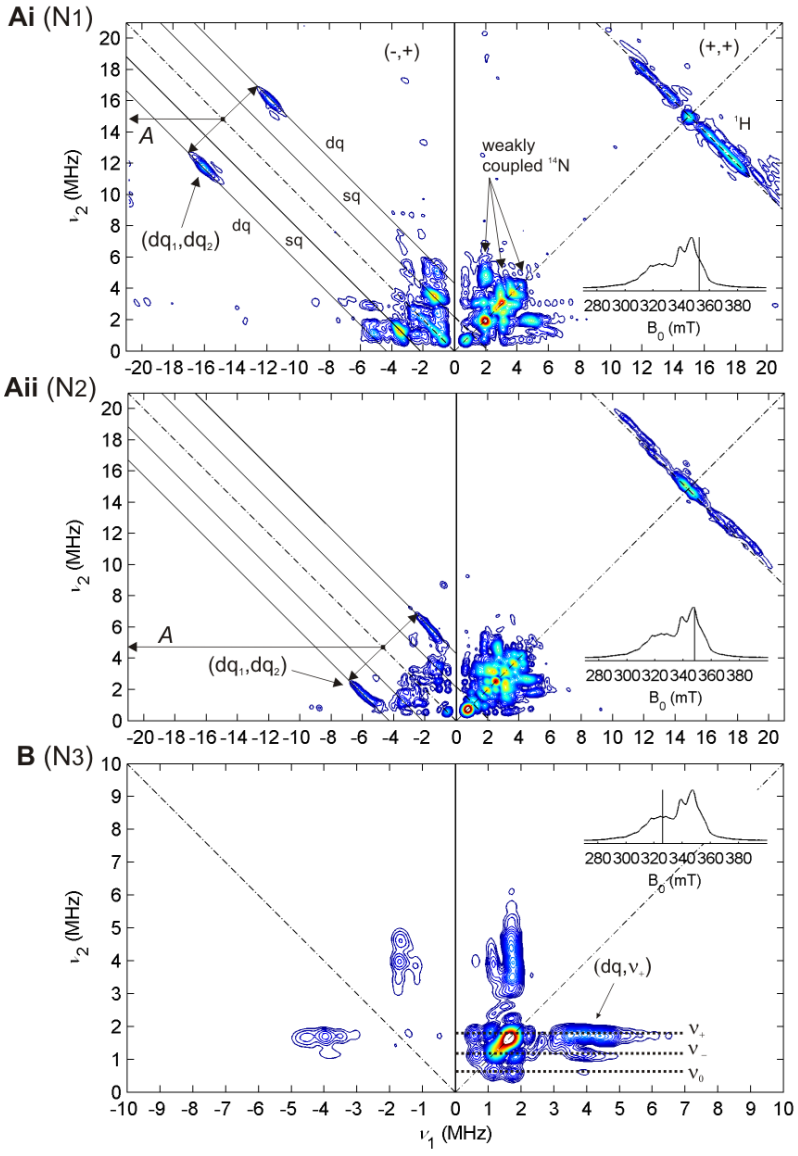


Figure 7.8: **X-band HYSCORE spectra showing the three different ^{14}N nuclei (N1, N2 & N3) observed in P242C at high potential.** (Ai) Measurement at 352.8 mT exemplifying the cross-peaks observed from strongly coupled N1 assigned to N_{C20}. (Aii) Measurement at 348.2 mT exemplifying the cross-peaks observed from strongly coupled N2 assigned to N_{C19}. An estimate for the effective hyperfine couplings (A) for N1 and N2 can be determined by inspecting the dq (double-quantum transition) cross-peaks (see also Figs. 7.13 & 7.14). (B) Measurement at 326.0 mT exemplifying the cross-peaks observed from weakly coupled N3 (in the exact cancellation condition) assigned to $^{14}N_{\epsilon}$ of His 83 (see also Figs. 7.10 & 7.13). Measurement conditions: (Ai) 9.728 GHz, 15 K, τ = 128 ns, matched pulses; (Aii & B) 9.737 GHz, 15 K, τ = 108 ns. Insets show the echo-detected field sweep spectra and the field positions for the HYSCORE measurements (vertical lines). Sample conditions: 622 μM, oxidized to +381 mV. Figure taken from ref. [270].

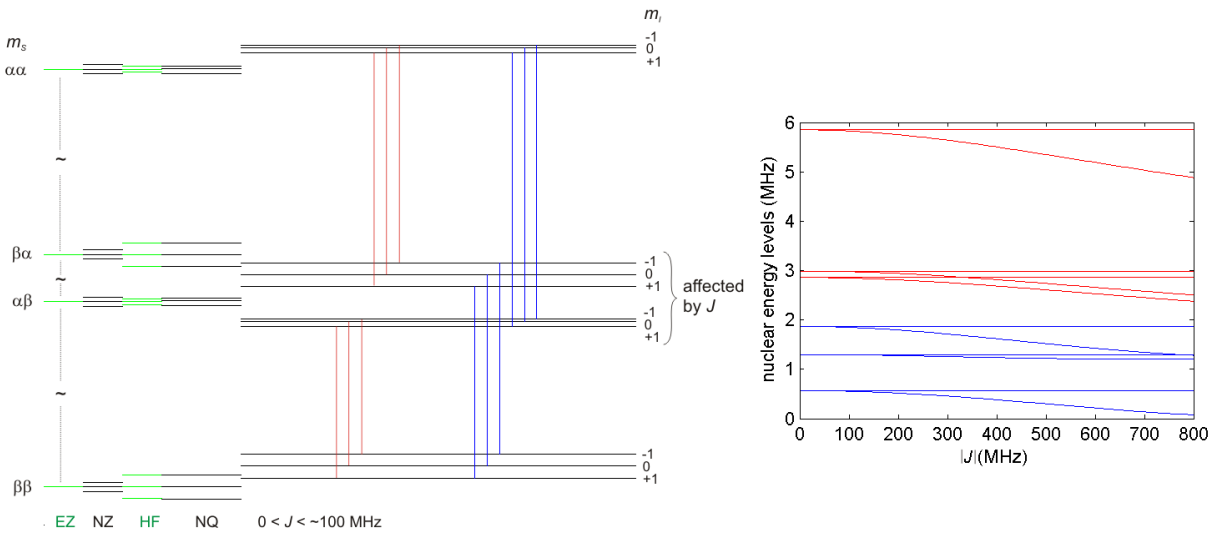


Figure 7.9: **Energy level diagram for a $S_1 = 1/2$, $S_2 = 1/2$ and $I = 1$ (^{14}N) system with an exchange interaction $J > 0$ between centres 1 and 2 and dependence of nuclear energy levels on J.** (*Left*) EZ = electron Zeeman interaction, NZ = nuclear Zeeman interaction, HF = hyperfine interaction, NQ = nuclear quadrupole interaction, J = exchange interaction between spins 1 and 2. The electron Zeeman splitting was rescaled to show the nuclear energy level splitting. EPR transitions for $\Delta m_S = \pm 1$ and $\Delta m_I = \pm 0$ are shown. Simulation parameters are as follows: $g_1 = 2.066$, 2.000, 1.937 (proximal Fe−S cluster *apparent* g values; see Table 7.3 for g values determined following EPR and HYSCORE measurements in Section 7.3.4); $A = [2.8\ 4.6\ 3.5] \pm 0.3$ MHz; $|e^2qQ|/h = 1.0 \pm 0.25$ MHz, $\eta = 0$; $g_2 = 2.30$, 2.16, 2.01 (Ni-B); $J = 20$ MHz; $B = 366.4$ mT with orientation $(1\ 1\ 1)/\sqrt{(3)}$. Red and blue transitions correspond to the proximal Fe-S cluster and the active site Ni species, respectively. (*Right*) Nuclear energy levels for the ^{14}N system (the α- and β-electron spin manifolds are in red and blue, respectively) as a function of $|J|$.

half of the energy levels are shifted once J exceeds ≈ 100 MHz; the other half is unaffected up to an exchange coupling of 800 MHz. The energy level diagram in Fig. 7.9 (left) thus applies for $J < 100$ MHz (see also Fig. 2.8). While the $\alpha\alpha$ and $\beta\beta$ states are unaffected, the spin-spin interaction mixes the $\alpha\beta$ and the $\beta\alpha$ states, altering their wavefunctions (which become linear combinations of $\alpha\beta$ and $\beta\alpha$) and thus their energies [299]. As J increases, the energy shifts of the central two 'triplets' in Fig. 7.9 (left) therefore become more pronounced, as seen in Fig. 7.9 (right). No predictions are made regarding the intensities of the transitions in the HYSCORE experiments. In the following simulations of the observed ^{14}N couplings, the exchange interaction between the active site Ni and the proximal Fe-S cluster is considered by examination of the effect of increasing J on the

observed cross-peaks.

The ^{14}N nucleus near the active site (N3)

Fig. 7.10 (top left) shows a measurement at a field position in the Ni-region of the EPR spectrum (see inset field sweeps), where the Fe-S cluster EPR transitions are off-resonance (*i.e.* only the active site contributes).

The observed ^{14}N cross-peaks resemble those observed in spectra of reduced *E. coli* Hyd-2 (Chapter 5, Fig. 5.14) where in agreement with other work on [NiFe]-hydrogenases [125, 260], they were attributed to Nϵ of His68 hydrogen-bonded to one of the active site Ni-Fe bridging cysteine Cys549. Figure 7.11 shows a structural model of His83 H-bonded to Cys579 in *E. coli* Hyd-1, together with a multiple sequence alignment of the relevant section of the large subunit in *E. coli* Hyd-1, *E. coli* Hyd-2, *D. vulgaris* Miyasaki [NiFe]-hydrogenase and *Aa* Hase I.

In the spectrum in Fig. 7.10, the exact cancellation condition is satisfactorily met; for the $I = 1$ nucleus the nuclear Zeeman and hyperfine frequency cancel each other out in one m_S manifold, allowing the nuclear quadrupole transitions (ν_0, ν_+ and ν_-) to be observed directly [125, 260] (Chapter 2, Section 2.6.3). These three peaks are apparent from the cross-peaks relating the ν_0, ν_+ and ν_- transitions to the double-quantum (ν_{dq}) transition in the other electron-spin manifold (labelled in Fig. 7.10, top row). The ν_- and ν_+ frequencies (0.6 and 1.7 MHz, respectively) were used to calculate the quadrupole coupling and the asymmetry parameter η, as explained in refs. [125, 297]. The quadrupole coupling $|e^2qQ|/h = 1.9$ MHz is similar to that previously obtained in the oxidised state of the O_2-tolerant *Re*-MBH [82] and oxidised and reduced states of the O_2-sensitive [NiFe]-hydrogenases from *D. vulgaris* and *D. gigas* [300, 301], as well as the Q67H variant of the H_2-sensor from *R. eutropha* which contains a hydrogen-bonded His to one of the [NiFe] bridging Cys residues that corresponds to a glutamine residue in the native enzyme [125]. The value obtained for η here (0.4) is in good agreement with values reported for *Re*-MBH ($\eta = 0.38$ [297]), *D. vulgaris* and *D. gigas* ($\eta \approx 0.4$ [300, 301]) and *Re* H_2-sensor Q67H

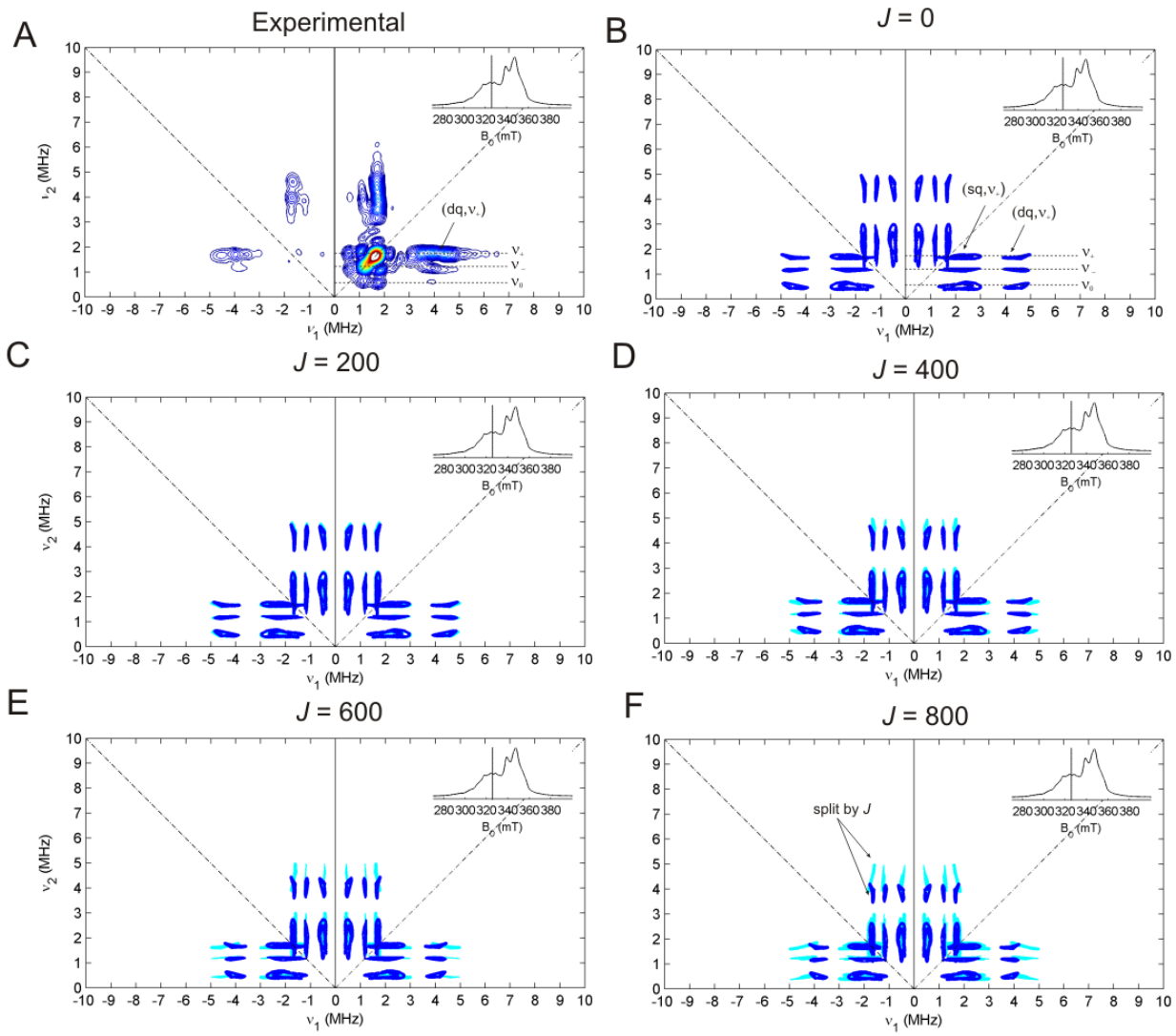
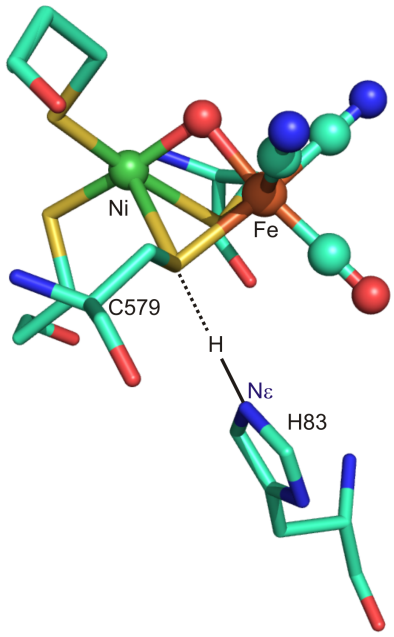


Figure 7.10: **X-band HYSCORE spectrum of P242C at high potential at B_0 = 326.0 mT with cross-peak position simulations as a function of the exchange coupling J between the $[4Fe\text{-}3S]^{5+}$ cluster and the active site Ni-A/Ni-B species.** The blue and cyan cross-peaks separate as J increases (see Panels B through F). The ^{14}N parameters were $|A|$ = [2.0 2.3 2.3] MHz, $|e^2qQ/h|$ = 1.9 MHz, and η = 0.40 (Table 7.1). Measurement conditions of spectrum (A) were: $t_{\pi/2}$ = 16 ns, t_π = 16 ns, τ = 108 ns, 15 K, shot repetition time 1 ms, 150x150 points, 8-step phase cycle; mw frequency 9.7374 GHz. Sample conditions: 622 μM, oxidized to +381 mV. Figure taken from ref. [270].



	83	579
E. coli Hyd-1	CGVCTGVHALASVY [...]	HSFDPCLACSTH
E. coli Hyd-2	CGVCTTTHALSSVR [...]	HSFDPCMACAVH
D. vulgaris Miyasaki F	CGVCTYTHALASTR [...]	HSFDPCIACGVH
A. aeolicus Hase I	CGVCTSIHALASLR [...]	HSFDPCLACSTH

Figure 7.11: **The active site of *E. coli* Hyd-1 showing the H-bonding between bridging Cys579 and Nϵ of His83 and multiple sequence alignment of key regions of the large subunit in different [NiFe]-hydrogenases.** The oxidised structure of *E. coli* Hyd-1 was used (3USC.PDB). The position of the H atom in the hydrogen bond between Cys579 and Nϵ of His83 is approximate. The conserved His83 and Cys579 in O_2-tolerant (*E. coli* Hyd-1, *A. aeolicus* Hase I) and standard [NiFe]-hydrogenases (*E. coli* Hyd-2 and *D. vulgaris* Miyasaki F) are highlighted in yellow. *E. coli* numbering is shown. Alignments used the program ClustalW2 [267].

($\eta = 0.53$ [125]). A comparison of A_{iso}, $|e^2qQ|/h$ and η for different [NiFe]-hydrogenases is summarised in Table 7.1. Once the quadrupole coupling and asymmetry parameter were obtained, the hyperfine principal values were determined to be $|A|$ = [2.0 2.3 2.3] MHz (note that the nuclear Zeeman frequency $\nu = 1.00$ MHz at 326 mT, so $2|\nu| \approx |A|$).

Simulations of the experimental spectrum in Fig. 7.10 (see also Fig. 7.13) were necessary to take into account the exchange interaction between the active site Ni and the Fe-S cluster:

$$\mathcal{H}_{tot} = \mathcal{H}_{EZ}^{FeS} + \mathcal{H}_{EZ}^{Ni} + \mathcal{H}_J + \mathcal{H}_{NZ} + \mathcal{H}_{HF} + \mathcal{H}_{NQ} \tag{7.1}$$

Table 7.1: **Hyperfine and nuclear quadrupole parameters for ^{14}N of H-bonded His to active site [NiFe]-bridging Cys in *E. coli* Hyd-1 compared to other [NiFe]-hydrogenases.** The state of the active site is indicated in brackets. [a] indicates that A_{iso} was estimated from the relationship $|A| = 2\nu_N$ for the exact cancellation condition. [b] indicates that the values were estimated from the double-quantum transition in the non-cancelled spin manifold $\nu_{dq}^{\pm} = [(\nu_N \pm |A|/2)^2 + \zeta^2]^{1/2}$ where $\zeta = (e^2qQ/4h)(3+\eta^2)^{1/2}$ [125, 297]. *Re*-RH Q67H designates a variant of the regulatory hydrogenase from *R. eutropha* in which the native Glu67 was replaced by a His residue (see Chapter 5 for details). Table adapted from ref. [270].

[NiFe]-hydrogenase	A_{iso} (MHz)	A (MHz)	T (MHz)	e^2qQ/h (MHz)	η
Hyd-1 P242C (Ni-A/Ni-B)	1.9	[2.0 2.3 2.3]	[−0.2 0.1 0.1]	1.9	0.4
Aa Hase I (Ni-C) [302]	1.54	[1.22 1.33 2.07]	[−0.3 −0.2 0.5]	1.92	0.40
Re-MBH (Ni-B) [297]	1.4-1.6	-	-	1.94	0.38
D. vulgaris (Ni-A) [125, 301]	$\approx 1.9^b$	-	-	1.90±0.03	0.34±0.04
D. vulgaris (Ni-B) [297]	1.4-1.6	-	-	1.9	0.37
D. gigas (Ni-A & Ni-C) [300]	$\approx 1.8^a$	-	-	1.9	0.4
E. coli Hyd-2 (Ni-C) (Ch. 5)	$\approx 1.8^b$	-	-	1.9	0.52
Re-RH Q67H (Ni-C) [125]	$\approx 1.83^b$	-	-	1.79±0.04	0.53±0.06

In equation 7.1, the ^{14}N nuclear Zeeman, hyperfine and nuclear quadrupole interactions are associated with the [NiFe] spin (or with the [4Fe-3S]$^{5+}$ cluster spin, see below) and diagonalisation of Eq. 7.1 to find the energy levels enabled the HYSCORE cross-peak positions to be calculated exactly; no peak intensities were calculated. As J increases (Fig. 7.10), long peaks running parallel to the axes are observed and any splitting would only be resolved when J gets very large. Since no splitting of the cross-peaks is observed experimentally, the simulations establish an upper limit of $J < 800$ MHz. The insensitivity of the HYSCORE cross-peak positions for this type of nucleus to the magnitude of J explains why similar spectra and magnetic parameters have been reported for numerous different hydrogenases in both the reduced state (Ni-C coupled to the reduced proximal [4Fe-3S]$^{3+}$ or [4Fe-4S]$^{+}$ cluster) and the oxidised state (Ni-A and/or Ni-B coupled to the proximal [4Fe-3S]$^{5+}$ cluster in O_2-tolerant hydrogenases), as summarised in Table 7.1.

The two ^{14}N nuclei strongly coupled to the proximal Fe-S cluster

Initial estimates of the hyperfine couplings for N1 and N2 can be made from the first-order equation of the dq nuclear frequencies:

$$dq^{\alpha,\beta} \approx |A \mp 2\nu_{14_N}|, \tag{7.2}$$

where A is the hyperfine coupling, as indicated in Fig. 7.8 Ai and Aii. However, frequency calculations using equation 7.1 are again necessary to examine the influence of J. Simulated dq cross-peaks were therefore plotted as a function of J and compared to the experimental HYSCORE spectrum, as exemplified for N2 in Fig. 7.12. This plot shows how the dq cross-peaks are split by the exchange coupling for J values of 0, 200, 400, 600 and 800 MHz, and indicates that the exchange interaction between the active site Ni species and the proximal [4Fe-3S]$^{5+}$ cluster is at most 400 MHz, as larger J values would result in a resolved splitting which is not observed experimentally. A similar plot for the N1 cross peaks places a limit of $J < 200$ MHz (not shown).

The magnetic parameters for N2 were obtained by fitting primarily the dq cross-peaks at different field positions (Fig. 7.13). Although sq signals for N2 are observed, these are difficult to assign since very intense peaks from 'free' peptide backbone nitrogens appear in the same region of the spectrum ($\approx \nu_1$,$\nu_2 < 5$ MHz, see also Chapter 8, Section 8.4.3). The nuclear quadrupole parameters determined for N2 are summarised in Table 7.2.

As shown in Fig. 7.14, no cross-peaks from N1 were observed at the low-field side of the Fe-S EPR spectrum and this important observation is discussed in Section 7.3.5. The lack of sq cross-peaks prevented the nuclear quadrupole interaction parameters to be determined for N1. The sq signals are broadened to first order by the NQI and thus presumably too weak to be detected given that the dq cross-peaks (only broadened through second order contributions) are already weak and required matched pulses to be observed. The limited field range over which N1 dq cross-peaks are observed (Fig. 7.14) means that the error for the hyperfine coupling A (Table 7.2) is relatively large.

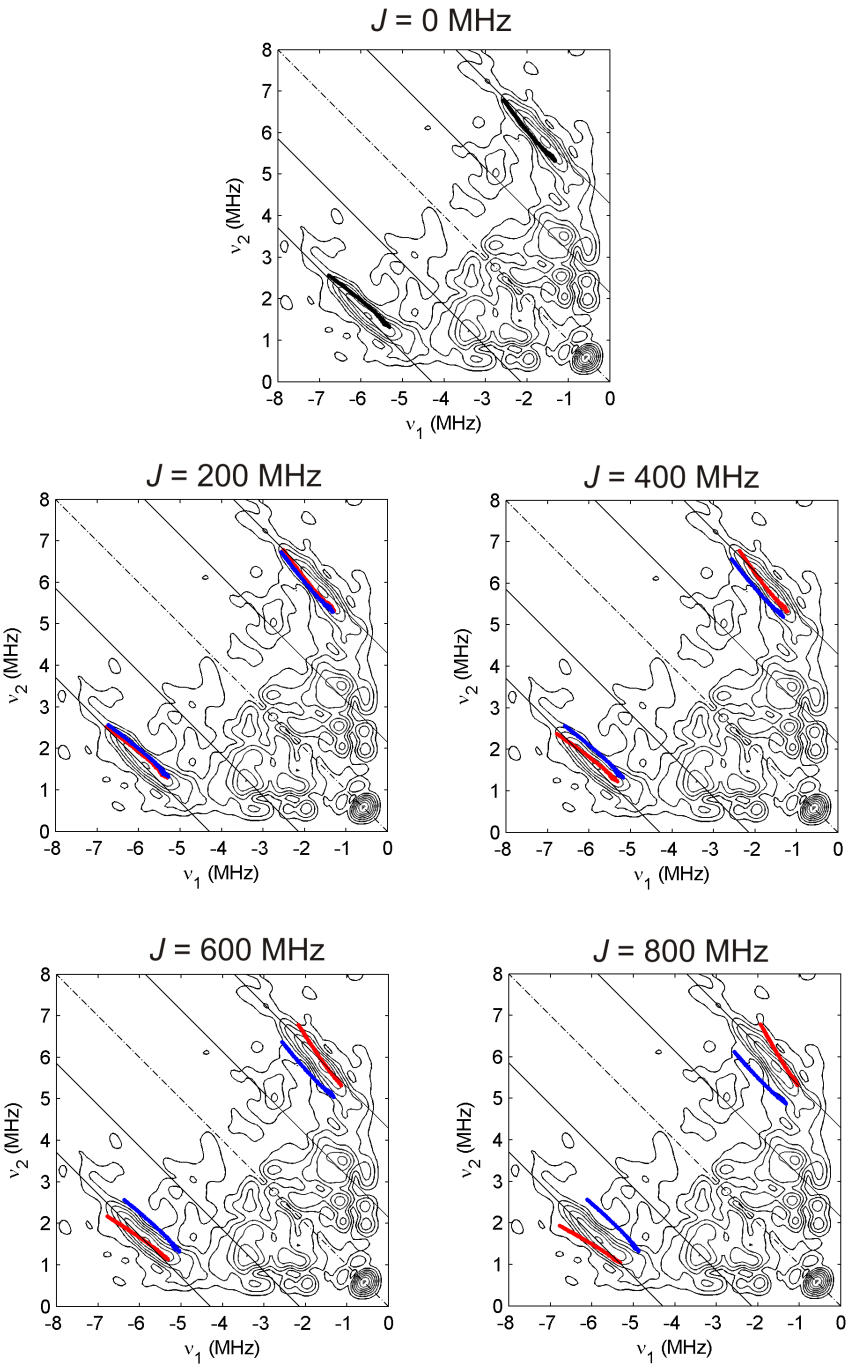


Figure 7.12: **X-band HYSCORE spectrum of P242C at high potential, at B_0 = 348.2 mT, with simulations of only the dq cross-peaks as a function of the exchange coupling J between the proximal $[4Fe\text{-}3S]^{5+}$ cluster and the active site Ni-A/Ni-B species.** Parameters for the strongly coupled N2 are given in Table 7.2 (A = [2.8, 4.6, 3.5] MHz, $|e^2qQ/h|$ = 1.0 MHz, η = 0). Measurement conditions of the experimental spectrum (black) were: $t_{\pi/2}$ = 16 ns, t_π = 16 ns, τ = 120 ns, 15 K, shot repetition time 1 ms, 150x150 points, 8-step phase cycle, mw frequency 9.7497 GHz. Sample conditions: 622 μM, oxidized to +381 mV. The dependence of the calculated dq cross-peaks as a function of J for N1 is similar (not shown). Taken from ref. [270].

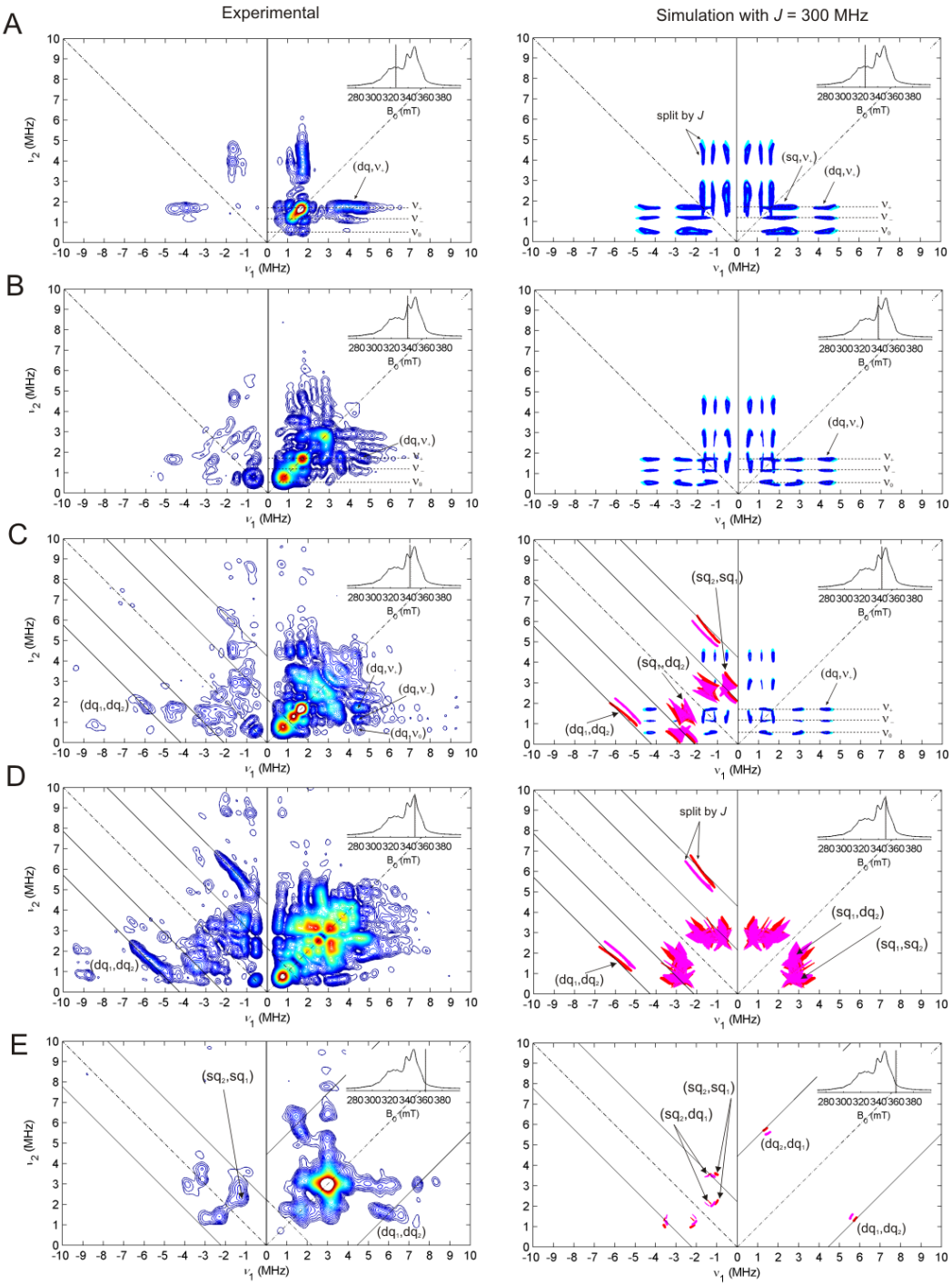


Figure 7.13: **X-band HYSCORE spectra of P242C poised at high potential showing the field dependence of the N2 & N3 couplings.** Field positions are indicated in the insets. Simulations for the weakly coupled N3 (blue/cyan) and the strongly coupled N2 nucleus (red/magenta) were calculated using the parameters given in Table 7.2 and include a $J = 300$ MHz coupling between the active site Ni species and the proximal $[4Fe\text{-}3S]^{5+}$ cluster (for the J dependence, see Figures 7.12 and 7.10). Selected transitions are labelled; ν_0, ν_-, ν_+ indicate the transition frequencies in the exact cancellation condition of the cancelled spin manifold, and sq/dq indicates double-quantum/single-quantum transitions. The black solid lines separated by 2ν (14^N) and 4ν (14^N) indicate the approximate positions of the sq and dq cross-peaks, respectively. Measurement conditions: $t_{\pi/2} = 16$ ns, $t_\pi = 16$ ns, $\tau = 108$ ns, 15 K, shot repetition time 1 ms, 150 points, 8-step phase cycle; field positions and mw frequencies: (A) 326.0 mT, 9.7374 GHz (B) 339.0 mT, 9.7497 GHz (C) 343.7 mT, 9.7372 GHz (D) 348.2 mT, 9.7497 GHz (E) 361.0 mT, 9.7497 GHz. Sample conditions: 622 μM, +381 mV. Figure taken from ref. [270].

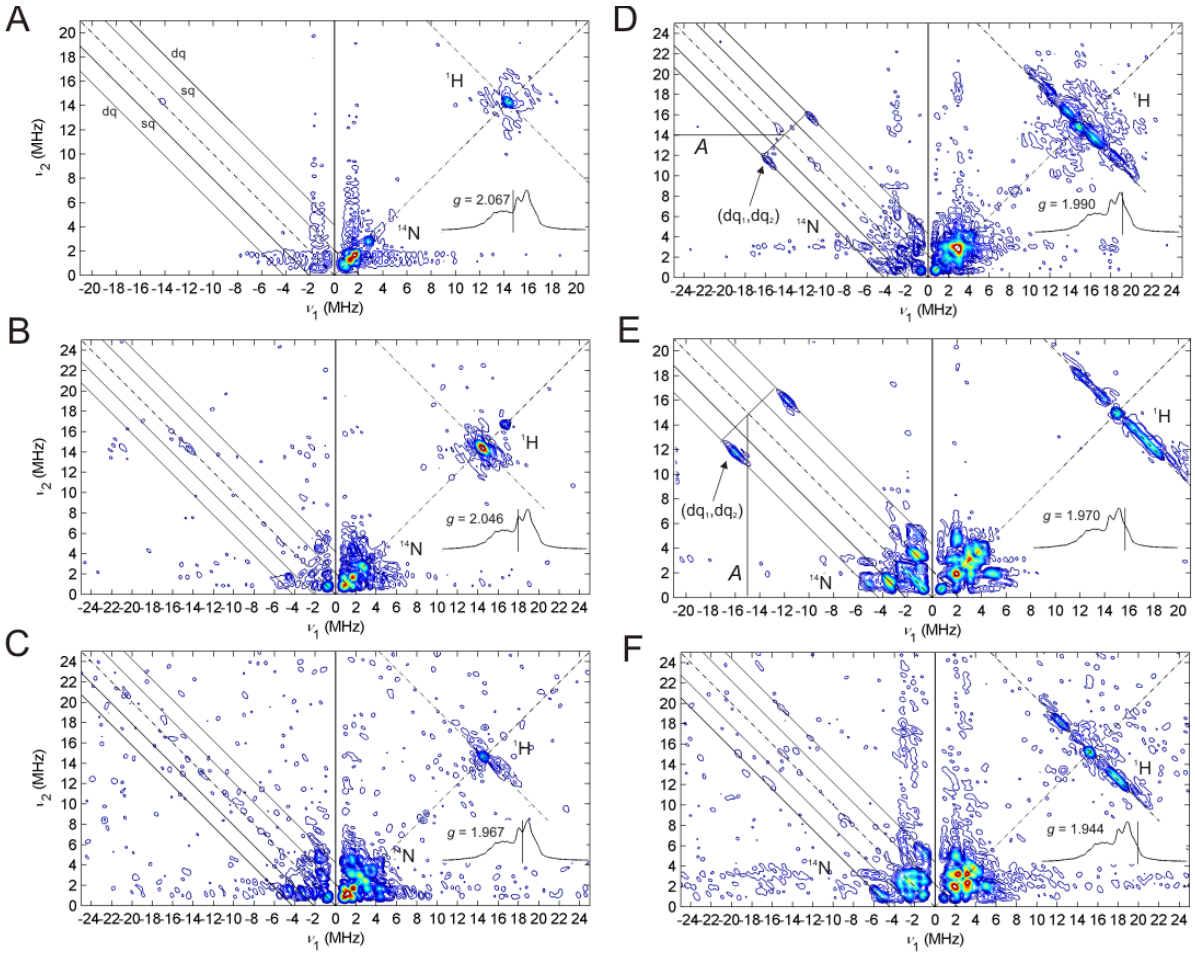


Figure 7.14: **X-band HYSCORE spectra of P242C poised at high potential showing the field dependence of the N1 coupling.** Field positions are indicated in the insets. The black solid lines separated by 2^{14}N and 4^{14}N indicate the approximate positions of the sq and dq cross-peaks, respectively. Measurement conditions: (all) $t_{\pi/2}$ = 48 ns, t_π = 16 ns, 15 K, shot repetition time 0.5 ms, 8-step phase cycle; field positions and mw frequencies and other parameters: (A) 336.0 mT, 9.7216 GHz, τ = 128 ns, 90x90 points (B) 339.7 mT, 9.7280 GHz, τ = 112 ns, 90x90 points (C) 353.4 mT, 9.7279 GHz, τ = 128 ns, 90x90 points (D) 350.0 mT, 9.7463 GHz, τ = 128 ns, 175x175 points (E) 352.8 mT, 9.7280 GHz, τ = 128 ns, 90x90 points (F) 357.5 mT, 9.7279 GHz, τ = 128 ns, 90x90 points. Note that the scales are not all identical (due to different Nyquist frequencies in different experiments). Sample conditions: 622 μM, oxidized to +381 mV. The hyperfine parameters for N1 given in Table 7.2 were determined by inspecting the double-quantum transition cross-peaks (dq) in spectra D & E. In the absence of observable dq cross-peaks over a wider field range, the orientation of the hyperfine tensor is unknown and its principal values are approximate (and thus quoted from lowest to highest in Table 7.2). Additional HYSCORE measurements with different τ values and matched pulse lengths were measured at the field positions at which spectra A-C were recorded, but no cross-peaks attributable to N1 (or proton cross-peaks other than those at the ^{1}H nuclear Zeeman frequency) were visible (spectra not shown). Figure taken from ref. [270].

Table 7.2: **Hyperfine and nuclear-quadrupole parameters for $^{14}N_{C20}$ coupling to Fe_4 in *E. coli* Hyd-1 P242C and comparison with other strongly coupled ^{14}N nuclei reported in the literature.** Guanine N1/MoaA refers to the binding of guanine N1 to [4Fe-4S] cluster II of *S*-Adenosylmethionine-dependent enzyme MoaA. Average values for A_{iso}, A and η are given from ref. [303]; *Aa* IspH/inhibitor refers to the pyridine inhibitor binding of the [4Fe-4S] protein of *A. aeolicus* IspH (LytB). [a] Distance in proposed modeled structure in ref. [303]. [b] This distance was calculated based on quantum-mechanically geometry-optimised coordinates of the $[(Fe_4S_4)(SMe_4)_3(pyr)]^{2-}$ (model of IspH + inhibitor BPH-293 given in ref. [293]. [c] The crystal structure of the oxidised form of *Re*-MBH has not yet been published. [d] Error in each value ±1.5 MHz.

^{14}N nucleus	A_{iso} (MHz)	A (MHz)	e^2qQ/h (MHz)	η	T (MHz)	Fe-N bond length (Å)
N1 of P242C (Fe−S)	13.0	[11.5 11.5 16.0][d]	-	-	[-1.5 -1.5 3.0]	2.1/2.2
N2 of P242C (Fe−S)	3.6	[2.8 4.6 3.5]	|1.0|	0	[-0.8 1.0 -0.1]	3.1
Guanine N1/MoaA [303]	3.5	[1.2 5.4 4.1]	-3.0	0	[-2.3 1.9 0.6]	1.94[a]
Aa IspH/inhibitor [293]	7.4	[6.2 7.6 8.4]	3.0	-	[-1.2 0.2 1.0]	1.95[b]
N_{C20} of *Re* MBH [304]	14.6	[11.4 14.1 18.2]	-	-	[-3.2 -0.5 3.6]	N/A[c]

The limit on the exchange coupling J obtained from the dq cross-peaks of N1 and N2 in the HYSCORE spectra shows that a high-potential Fe-S species is present with a small exchange coupling to the [NiFe] active site. However, the high-potential X-band CW EPR spectra exhibit Ni-A and Ni-B signals that are split by a very large J (≈ 600 MHz) from the nearby $[4Fe\text{-}3S]^{5+}$ proximal cluster (Fig. 7.5). The HYSCORE and CW EPR data can therefore only be reconciled if the high-potential Fe-S signals arise from at least two species. This possibility is explored in the next section.

7.3.5 Model of the 'superoxidised' P242C EPR spectra

Figure 7.15 shows the experimental EPR spectra at X-band (A) and W-band (B) from P242C poised at high-potential, along with the simulations which comprise Ni-A and Ni-B coupled to two Fe-S species (conformers, see Section 7.4) labelled HP1 and HP2; the exchange coupling scheme employed is HP1—Ni-A (J_{1A}), HP1—Ni-B (J_{1B}) and HP2—Ni-A (J_{2A}) and HP2—Ni-B (J_{2B}), in which it is anticipated that $J_{1A} \approx J_{1B}$ and $J_{2A} \approx J_{2B}$. As shown in Table 7.3, HP1 has very small exchange couplings to both Ni-A and Ni-B, and nitrogen nuclei N1 and N2 detected by HYSCORE are thus assigned to HP1. Conformer HP2 has large exchange couplings to the active site, and this gives rise to the observed signals at X-band which are considerably shifted from their g-value resonant

positions. Figure 7.15 presents both absorption and first derivative representations, and simulations for the individual components and their sum. These simulations convincingly demonstrate that a four-component model is able to account for the data. The experimental spectral width and intensity at both mw frequencies is well described and the weak spectral wings apparent in the X- and W-band absorption spectra are modeled. As noted above, no cross-peaks from N1 in HYSCORE spectra measured at the low-field side of the Fe-S EPR spectrum were detected. The lack of observed N1 cross-peaks provides further support for the model because the EPR simulations predict that only HP2 is present at low field. The detailed information obtained from the simulations is made possible by the P242C variant, which removes the exchange couplings to the medial cluster present in native Hyd-1. Exhaustive efforts to simulate the EPR data with only one Fe-S paramagnetic center were unsuccessful.[4]

Table 7.3: g **values for the proximal [4Fe-3S]$^{5+}$ cluster and exchange interaction with the active site in O_2-tolerant [NiFe]-hydrogenases.** [a] Simulation parameters for Ni-A: $g_{x,y,z}$ = 2.31, 2.24, 2.01; Euler angles (−2.81, 2.30, 2.41) radians and Ni-B: $g_{x,y,z}$ = 2.31, 2.15, 2.01; Euler angles (−2.81, 2.30, 2.41) radians; Euler angles were based on reference [305]. $J_{1A/B}/J_{2A/B}$ designate the exchange couplings between Ni-A/Ni-B and HP1/HP2, respectively (Fig. 7.15). The simulations included an electron dipole-dipole interaction between each HP and [NiFe] pair, with the unique principal value axis taken to be directed between the two centers with a coupling of (−17,−17,+34) MHz. This coupling was determined using coordinates from reference [18] (3USC.PDB) in conjunction with the point-dipolar model, employing an $S = 1/2$ spin for the [NiFe] site and using the four spin projection factors listed in ref. [18] to model the Fe-S spin. g values and Euler angles for HP1 and HP2 are given for the best simulation, but are not unique. [b] The two exchange couplings J belong to one spin system where Ni-B is coupled to two X^{ox} species [297]. g_e stands for the free electron g value (2.00). Table taken from ref. [270].

[NiFe]-hydrogenase	[4Fe-3S]$^{5+}$ g values (Euler angles, radians)	J (MHz)
Re-MBH [297]	$\approx g_e$	780 & 550 [b]
Aa Hase I [16]	2.010, 2.015, 1.990	630
E. coli Hyd-1 [18]	2.043, 2.031, 2.007	-
P242C HP1 [a] [270]	2.008, 1.990, 1.933 (2.36, 0.79, 2.36)	< 40 (J_{1A} & J_{1B})
P242C HP2 [a] [270]	2.000, 1.955, 2.018 (0.79, 1.57, 2.36)	600 (J_{2A} & J_{2B})

[4]Not only could no N1 signals be detected in the HYSCORE spectra where only HP2 is present, but no protons signals besides the matrix line are present either (Fig. 7.14). These HYSCORE spectra resemble the behaviour observed for native Hyd-1 where a large exchange coupling, presumably with the medial [3Fe-4S]$^{+}$ cluster, prevents detection of coupled nearby nuclei (Fig. 7.7).

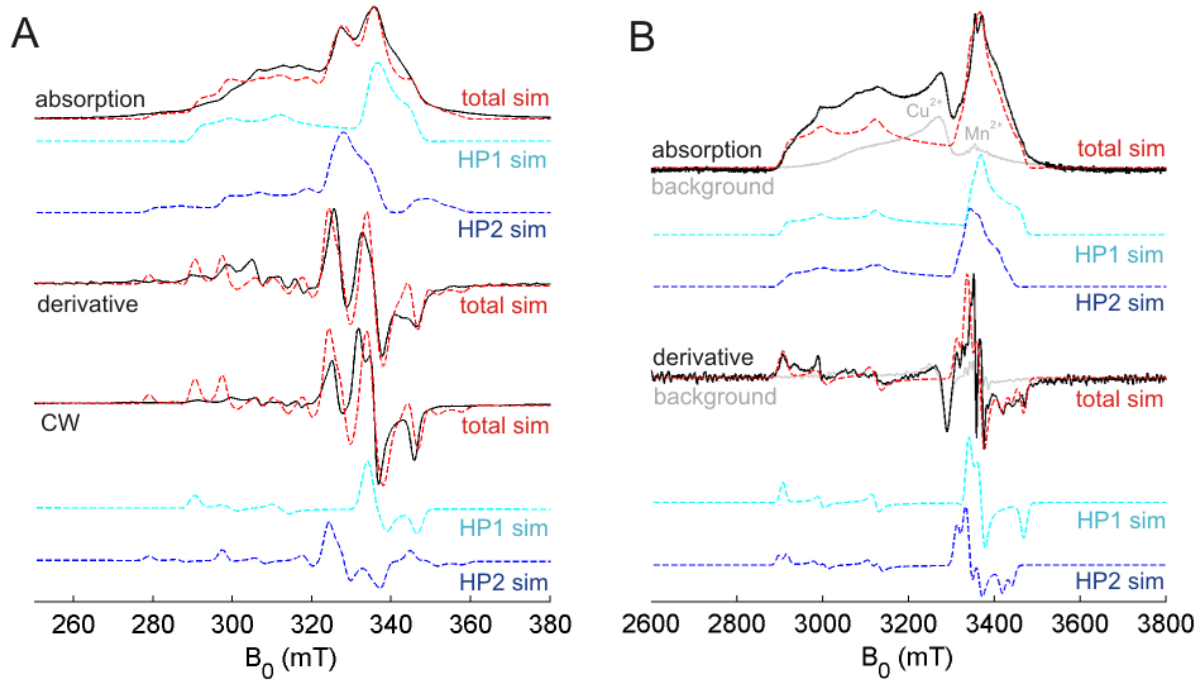


Figure 7.15: **Simulation of EPR spectra of P242C poised at high potential in terms of a four component model.** (A) X-band echo-detected EPR (top, black), its derivative (middle, black) and CW EPR (bottom, black) spectra and their simulation; HP1−Ni-A + HP1−Ni-B (cyan), HP2−Ni-A + HP2−Ni-B (blue), and their total (red); HP1 and HP2 denote the two conformations of the proximal $[4Fe\text{-}3S]^{5+}$ cluster. Equal contributions of HP1 and HP2 are assumed, and the Ni-A:Ni-B ratio is 1:2 as determined by X-band CW EPR measurements at 125 K [270]. (B) Corresponding W-band data. The 1^{st} derivative experimental spectrum (bottom) was obtained by numerical differentiation of the absorption spectrum (top). The background spectra (grey) refer to a sample containing buffer only; note that the Cu^{2+} and Mn^{2+} peaks result from W-band probehead contaminations rather than impurities in the buffer (see Section 3.5.3). Measurement and sample conditions: (X-band) mw power 0.5 mW, modulation amplitude 1 mT, 20 K, 622 μM, +381 mV; (W-band) pulse sequence $\pi/2 - \tau - \pi - \tau - echo$ where τ = 180 ns (P242C) or 220 ns (background), $t_{\pi/2}$ = 32 ns, t_{π} = 64 ns, shot repetition time 5 ms, mw frequency 93.855 GHz (P242C), 93.900 GHz (background), 3 K, 250 μM, approx. +373 mV. The P242C W-band sample was measured in the central region (g = 2.34 to 1.91) with more accumulations to improve the signal-to-noise. Simulation parameters are given in Table 7.3. Figure taken from ref. [270].

7.4 Discussion

The X- and W-band EPR and X-band HYSCORE data of the P242C variant poised at high potential (Fig. 7.15) clearly show that two different conformations of the proximal [4Fe-3S]$^{5+}$ cluster are present, a result which is fully consistent with the crystal structure data for the native enzyme revealing two conformations for the [4Fe-3S]$^{5+}$ cluster [18]. HYSCORE measurements of a deuterated samples of Hyd-1 P242C allowed the determination of a approximate limit on the distance of exchangeable protons from the unpaired electron spins. The lack of detection of exchangeable protons in close proximity is in agreement with the models proposed by Volbeda and Amara *et al.* [18] (Fig. 7.2). A more reliable and precise limit on the minimum distance from the unpaired electron spins would be necessary to assign models (PC3^H, PC3$_d^-$ and PC3$^-$) to the observed conformers on the basis of exchangeable protons. Detailed information about the exchangeable protons could in principle be obtained through assignment of the non-exchangeable proton couplings first, similarly to previous studies on the [4Fe-4S]$^{3+}$ cluster in *Ectothiorhodospira holophila* [306] or the [2Fe-2S]$^+$ cluster in palustrisredoxin-B from *Rhodopseudomonas palustris* [175]. Such assignments of the non-exchangeable protons would require additional HYSCORE and ENDOR measurements of deuterated P242C.

The presence of two paramagnetic conformers of the superoxidised proximal cluster reinforces its dynamic nature, and the EPR studies indicate that conformer HP2 has a strong electronic pathway to the active site, whereas HP1 is by comparison relatively electronically 'insulated'. It is now almost certain that Glu76 plays an important mechanistic role and Fe_4 can be imagined as oscillating between between Glu76 and Cys19 shifting its position by 0.7 Å, as shown in Fig. 7.1 (left). Whether Glu76 deprotonates N_{C20} and contributes to the transferral of the resulting proton to the active site [18] remains to be answered. Proton transfer from a glutamate residue is certainly not unprecedented: In cytochrome c oxidase, the P_R to F transition is induced by a proton transfer from Glu286 in the *R. sphaeroides* enzyme to the heme-copper centre [307].

Confidence in the four-component EPR model and the magnetic parameters is only

made possible because the P242C variant eliminates the couplings to the medial cluster $[3Fe\text{-}4S]^+$ paramagnet. X-band HYSCORE cross-peaks from strongly coupled ^{14}N nuclei are sensitive to the exchange interaction which allow the nitrogen nuclei N1 and N2 to be assigned to conformer HP1. Any strongly coupled ^{14}N signal from HP2 could not be detected, presumably a result of fast relaxation due to the presence of the strong exchange interaction. Note that HYSCORE experiments on native Hyd-1 also failed to detect any strong ^{14}N couplings, or ^{1}H couplings $>$ 1MHz which must be present, presumably also because of the large exchange interaction with the medial cluster and resultant fast relaxation. Experiments at higher mw frequencies may be able to mitigate this relaxation problem [297, 304]. The presence of two conformers of the proximal cluster, which cannot have exactly the same physical properties, offers an explanation for why the potentiometric titrations for P242C show a field dependence of the $[4Fe\text{-}3S]^{5+/4+}$ couple (Fig. 10.4). The magnetic parameters for N1 and N2 are summarized in Table 7.2 and compared to data reported for Fe−N bonds in three other Fe-S systems — the nitrogen of a guanine substrate binding to a $[4Fe\text{-}4S]^+$ cluster of the S-adenosyl-methionine-dependent enzyme MoaA (Guanine N1/MoaA) [303], a pyridine inhibitor binding to the $[4Fe\text{-}4S]^+$ protein IspH (LytB) from *Aquifex aeolicus* (*Aa* IspH/inhibitor) [293], and the proximal cluster in *Re*-MBH, for which recent $^{14/15}N$ Q-band ENDOR data were assigned to the amide nitrogen coordinating Fe_4 (also Fe_4 in *Re*-MBH) — the first EPR data presented for the Fe−N bond in the superoxidised cluster in an O_2-tolerant [NiFe]-hydrogenase [304]. The largest coupling N1 can be unambiguously assigned to N_{C20} since it is covalently bonded to Fe_4 (Fe_4—N_{C20} = 2.1 Å, Table 7.2); Fe_4 carries a large spin density and thus a transfer of spin density to the N_{C20} orbitals gives rise to the large experimental hyperfine coupling. This coupling can be separated into an isotropic and an anistropic part,

$$(A_1, A_2, A_3) = A_{iso} + (-T, -T, 2T), \tag{7.3}$$

where the anisotropy of the hyperfine coupling is axial within experimental error (Table 7.2). Using the N1 coupling in Table 7.2 yields A_{iso} = 12.5-13.5 MHz and T = 0.5-2.5 MHz.

The isotropic hyperfine coupling characterises the s-orbital nature of the Fe_4—N_{C20} bond via the fraction of spin density f_{2s} residing in the 2s orbital of N_{C20}, which can be estimated from

$$f_{2s} = a_{iso} 2S / a^0_{2s}, \tag{7.4}$$

where $a^0_{2s} \approx 1811$ MHz is the coupling for unit spin density in a nitrogen 2s orbital [308] and S = 5/2 for Fe^{3+}. The fundamental hyperfine coupling matrix **a** describes the interaction of the nitrogen with the spin of the isolated Fe^{3+} ion and is related to the experimental hyperfine coupling matrix **A** using the spin projection factor k derived from the spin-coupling model [180, 309],

$$\mathbf{A} = k\mathbf{a} \tag{7.5}$$

An estimate of the spin projection factors of the high-potential proximal cluster irons are reported in reference [18]; $k_1 = -88/81$; $k_2 = +10/9$; $k_3 = -110/81$; $k_4 = +7/3$, where Fe_4 is formally assigned the 3+ oxidation state. Consequently, with A_{iso} = 12.5-13.5 MHz and $k_4 = 7/3$, Eq. 7.4 and 7.5 yield a_{iso} = 5.36-5.79 MHz and f_{2s} = 1.5-1.6%. A similar value of $f_{2s} \approx 3$ % was found for the histidine nitrogen coordinating Fe^{3+} ($S = 5/2$) in aquometmyoglobin [310].

The anisotropic part of the hyperfine coupling consists of a direct dipolar coupling to the Fe-S cluster spin, and a local part due to nitrogen p-orbital spin density, $\mathbf{T} = \mathbf{T}_{dip} + \mathbf{A}_p$. The dipolar part $\mathbf{T}_{dip}$ would be expected to be large since N_{C20} is very close to the paramagnetic cluster and, in particular, subsite Fe_4 with a large spin projection factor. This contribution can be estimated using the point-dipolar formula

$$\mathbf{T}_{dip} = \frac{\mu_0 \mu_B \mu_N g_e g_N}{4\pi h} \sum_j k_j \frac{3\mathbf{n}_j \mathbf{n}_j^T - 1}{r_j^3}, \tag{7.6}$$

where $\mathbf{T}_{dip}$ is the dipolar matrix, $\mathbf{n}_j$ and r_j are the nitrogen-(k_j of Fe_j) unit row vector and distance, respectively, and T indicates a transpose. Substituting the four k_i values into

Eq. t 7.6 yields a dipolar matrix with principal values of [−1.6, −1.6, 3.2] MHz where the unique axis (with principal value $2T_{dip} = 3.2$ MHz) points essentially along the Fe_4—N_{C20} vector. This result is consistent with the size of the anisotropy observed experimentally (Eq. 7.3, mean anisotropic coupling [−1.5, −1.5, 3.0] MHz) and thus the 3+ assignment of the Fe_4 oxidation state. Any remaining anisotropy is due to p-orbital spin density and should be small as is now discussed. The crystal structure reveals that the N_{C20} bond angle CNC = 119.5^o (for both conformers), which suggests a sp^n hybrid orbital bonding scheme with n ≈ 2. In such a case, the ratio f_{2p}/f_{2s} is ≈ 2, where f_{2p} is the p-orbital spin density (for sp^2:$f_{2p}/f_{2s} = 2$ with bond angle CNC = 120^o) [310, 311]. It is thus instructive to make an estimate of the p-orbital spin density from the experimental hyperfine coupling to check that it is consistent with this expectation. The hyperfine coupling due to a p-orbital contribution can be estimated if an axial experimental hyperfine interaction is assumed where the unique axis points along the Fe_4—N_{C20} vector with value $A_{iso} + 2T_{dip} + 2A_p$ (this implies a σ-orbital contribution, and that the π-orbital contribution is small). The spin density in the p-orbital is then given by

$$f_{2p} = a_p 2S/a^0_{2p}, \tag{7.7}$$

where $a^0_{2p} \approx 55$ MHz is the coupling for unit spin density in a nitrogen 2p orbital [308]. With a_p = 0-0.38 MHz, f_{2p} = 0-3.5% (excluding negative a_p values). Recalling that f_{2s} = 1.5-1.6% it can be concluded that within error the experimental ratio is consistent with $f_{2p}/f_{2s} \approx 2$. The approximate hyperfine coupling analysis presented here is thus in accord with the expected p- and s-orbital contributions for a sp^n hybrid orbital picture, where the spin density predominately resides in a σ-orbital.

The second largest coupling N2 is assigned to N_{C19}, which is approximately 3.1 Å from Fe_4 [18] and using Eq. 7.6 leads to T_{dip} = [−0.6,−0.4,1.0] MHz, which compares favorably with the experimental values for N2 given in Table 7.2. Because HYSCORE data place an upper limit on the exchange coupling of $J < 400$ MHz for the paramagnetic center coupled to N2, it cannot be assigned to conformer HP2. The assignment of N1 (N_{C20}) and

N2 (N_{C19}) is consistent with Fe_4 being in the 3+ oxidation state and the spin coupling scheme and spin projection factors k_j given in reference [18], i.e. with k_4 around +7/3. The experiments conducted here therefore lend support to the proposition by Volbeda and Amara *et al.* based on QM/MM calculations that Fe_4 is the Fe ion changing oxidation state from +2 to +3 in the oxidation of the proximal cluster from $[4Fe\text{-}3S]^{4+}$ to $[4Fe\text{-}3S]^{5+}$ [18]. This is also expected based on the changes in the coordination environment of Fe_4 from an all 'soft' sulfur coordination to the addition of 'hard' electronegative ligands in the $[4Fe\text{-}3S]^{5+}$ state (Fig. 7.1) [17, 18]. The nitrogen hyperfine couplings to the $[4Fe\text{-}4S]^{+}$ clusters reported in references [293] and [303] are significantly smaller than N1 (see Table 7.2), even though the N-atom is also coordinated to a Fe of the cluster. The small dipolar part of the ^{14}N hyperfine coupling in these cases is likely due to the small spin projection factors which is estimated to be $k < |1.5|$ for Fe^{2+} or $Fe^{2.5+}$ in the 'normal' reduced ferredoxin-type $[4Fe\text{-}4S]^{+}$ clusters [180] found in Guanine N1/MoaA and *Aa* IspH/inhibitor.

The third ^{14}N coupling observed was assigned to Nϵ of His83 of the large subunit, which is hydrogen bonded to the Ni-Fe bridging Cys546. This coupling has been reported for several standard [NiFe]-hydrogenases as well as O_2-tolerant *Re*-MBH and provides a further indication that the active site and its environment are very similar in standard and O_2-tolerant hydrogenases and that differences in the enzymes' response to O_2 do not stem, significantly, from differences in the active site, as already suggested by the crystal structures of *Re*-MBH, *H. marinus* MBH and *E. coli* Hyd-1 [17, 18, 87]. A similar conclusion was reached by Saggu *et al.* [297] who compared the O_2-tolerant *Re*-MBH and the standard *D. vulgaris* Miyasaki F [NiFe]-hydrogenase active sites through Q-band ENDOR measurements.

In summary, the P242C variant has proved to be extremely useful in resolving the properties of the superoxidised proximal cluster. The EPR and HYSCORE data have shown that two conformations, already revealed in the crystal structure of native Hyd-1, have strikingly different exchange couplings to the active site. Furthermore the work presented here provides experimental evidence that a localized Fe(III) subsite is produced

upon superoxidation as a result of a rearrangement that generates a bond between that Fe and a deprotonated peptide nitrogen — a strong π-donor. The striking similarity of the oxidised and reduced forms of the nitrogenase P cluster [17, 34, 312] with the proximal cluster found in O_2-tolerant hydrogenases [17, 18] (see also Chapter 1, Fig. 1.2) entails that mechanistic details revealed for the latter might provide important mechanistic clues for the mechanism of N_2 fixation by nitrogenase.

Chapter 8

The spin state of the distal iron-sulfur cluster in O_2-tolerant [NiFe]-hydrogenases

The *E. coli* P242C, C19G, C120G and C19G/C120G variants were constructed by Dr. Michael Lukey [136]. The *Salmonella* Hyd-5 enzyme was prepared by Dr. Alison Parkin and Elena Nomerotskaia and the EPR sample was made by Rosalind Davies under my supervision. Protein purifications were carried out with the help of Elena Nomerotskaia. I am also grateful to Dr. Jeffrey Harmer for many helpful discussions and for providing the HYSCORE simulation program. Part of the work described in this chapter has been published [270].

Abstract

The iron-sulfur cofactor relay in [NiFe]-hydrogenases, which consists of a proximal [4Fe-4S] or [4Fe-3S], a medial [3Fe-4S] and a distal [4Fe-4S] cluster in relation to the active site, is of paramount importance for understanding the nature of electron-transfer in these enzymes. Upon reduction, a complex EPR spectrum due to Fe-S clusters is typically observed. Its origin is not very well understood but it is generally accepted to arise from a magnetic interaction between all three reduced clusters. The signal is more well-defined in O_2-tolerant hydrogenases (which are able to function in the presence of O_2) and remarkably similar in *Aquifex aeolicus* Hydrogenase I, *Ralstonia eutropha* membrane-bound hydrogenase, *Salmonella enterica* Hydrogenase-5 and *E. coli* Hydrogenase-1. By comparison of the EPR signals of the Fe-S clusters in *E. coli* Hyd-1, as well as a variant in which the medial [3Fe-4S] cluster is exchanged for a [4Fe-4S] cluster, it will be shown that the distal cluster in O_2-tolerant hydrogenases has an EPR-silent high-spin ground state. This finding is supported by studies on additional proximal cluster variants of Hyd-1. The $[4Fe\text{-}4S]^{+}$-$[4Fe\text{-}4S]^{2+}$ redox transition of the distal cluster is not observed in EPR titrations of either the native or the variant enzymes and the midpoint potential of the distal cluster is therefore not known. The implications for electron transfer in hydrogenases are discussed.

8.1 Introduction

The work described in this Chapter aims to understand the origin of the 'complex interaction signal' observed in the EPR spectra of O_2-tolerant [NiFe]-hydrogenase samples poised at low potentials. This requires an unambiguous answer as to whether both the reduced proximal $[4Fe\text{-}3S]^{3+}$ and the reduced distal $[4Fe\text{-}4S]^{+}$ clusters contribute to the signal and if these clusters are in the $S = 1/2$ ground spin state. The *E. coli* species has already proven itself to be amenable to point mutations invaluable in furthering our understanding of the involvement of the electron transfer relay in the response of [NiFe]-hydrogenases to oxygen (Chapter 6). EPR studies of the proximal and medial cluster variants of *E. coli* Hyd-1, which were introduced in Chapters 6 and 7, should therefore also shed light on the nature of the electron transfer chain at low potentials.

8.1.1 Previous studies of the Fe-S cluster relay at low potentials

[NiFe]-hydrogenases from many different species have been studied at low potential using EPR (mainly CW), following reduction with the enzymes' substrate H_2 or with reducing agents such as sodium dithionite. The origin of the EPR-active Ni signals, Ni-C and Ni-L, is well documented (see Chapter 5) but the observed Fe-S cluster signals arising from the small subunit are complicated. To date, there is no consensus on which reduced Fe-S clusters (potentially up to two $[4Fe\text{-}4S]^{+}$ and one $[3Fe\text{-}4S]^{0}$ cluster in standard hydrogenases and one $[4Fe\text{-}3S]^{3+}$, one $[3Fe\text{-}4S]^{0}$ and one $[4Fe\text{-}4S]^{+}$ cluster in O_2-tolerant [NiFe]-hydrogenases) contribute to the observed signals. The following paragraphs provide an overview of the literature on this subject for O_2-sensitive (standard) hydrogenases, which have been studied for over three decades, and the more recent developments for the O_2-tolerant hydrogenases.

Standard (O_2-sensitive) [NiFe]-hydrogenases

A summary of the midpoint potentials of the Fe-S clusters in standard [NiFe]-hydrogenases reported in the literature is given in Table 8.1. For completeness, values reported for the $[3Fe\text{-}4S]^{+/0}$ transition are also included.

Table 8.1: **Midpoint potentials of Fe-S clusters reported for standard [NiFe]-hydrogenases.** The method used to obtain the E_m values is indicated, as well as the reference the values were taken from. [a]In this work the cluster with the lower midpoint potential was tentatively assigned to be the proximal cluster. [b]No data in support of the E_m values are provided in this paper. *D. vulgaris* H. stands for *D. vulgaris* Hildenborough. See text for controversy in the assignment of observed mid-point potentials to redox transitions of Fe-S clusters.

	E_m (mV)				
Species	$[4Fe\text{-}4S]^{2+/+}_{distal}$	$[4Fe\text{-}4S]^{2+/+}_{proximal}$	$[3Fe\text{-}4S]^{+/0}_{medial}$	ref.	method
A. vinosum	−301	−301	−30	[286]	PFE
D. gigas		−320	−70	[202, 245]	EPR
D. gigas	−340	−290		[202]	Mössbauer
D. gigas	−315	−445[a]		[205]	UV-vis
D. vulgaris H.	−315	−315	−80	[287]	EPR
D. fructosovorans	−340	−340	+65	[58][b]	EPR

In all cases, the observed EPR signal from samples at low potentials is attributed to a complex magnetic interaction between several paramagnetic centres, which may include the medial $[3Fe\text{-}4S]^0$ cluster in the $S = 2$ state [202] as well as the active site Ni and one or two reduced [4Fe-4S] clusters with $S = 1/2$ ground states. Because of the splitting of the Ni signals observed at low temperatures, it is generally accepted that at least the reduced *proximal* Fe-S cluster is observed [200, 202, 214, 245, 247, 259, 284]. The only detailed quantitative description of the magnetic interactions between the Ni centre and the proximal $[4Fe\text{-}4S]^+$ was performed for the *D. gigas* enzyme, first by approximating the reduced [4Fe-4S] cluster as a point dipole [262], and then by taking into account the delocalisation of the magnetic moment [177] within the cluster using the local spin model [162] (see also Section 4.2.1). These simulations were mainly based on the Ni-region of the spectra since the reduced Fe-S cluster peaks observed in standard hydrogenases are

so broad. While the authors acknowledge that additional complex effects such as the reduced medial and distal clusters and any uncoupled [4Fe-4S]$^+$ cluster are not taken into account, the experimental data are still quite well described over a range of frequencies (X-, S- and Q-band) by simulations based on magnetic interactions between the Ni centre and the proximal [4Fe-4S]$^+$ cluster alone [177].

However, despite the consensus on the proximal cluster contribution to the 'complex interaction signal', there is disagreement in the literature about the contribution of the distal cluster. Most information about the reduced Fe-S clusters has been derived from X-band CW EPR and studies have mainly been performed with standard hydrogenases, in particular from the *Desulfovibrio* species, of which the *D. gigas* enzyme is probably the most extensively studied: EPR titrations of the low potential Fe-S cluster species in *D. gigas* hydrogenase fit a one-electron reduction curve, suggesting that only *one* transition occurs (unless both the midpoint potentials of the proximal and distal clusters are identical); strong cooperativity between two reduced [4Fe-4S]$^+$ clusters should fit a two-electron redox process [200, 202]. On this basis, it was postulated that only a single [4Fe-4S]$^+$ cluster is reduced [200]. In contradiction, Patil *et al.* [287] found that the 'development of the complex EPR signal' at low potentials better fitted a two-electron rather than a one-electron process in EPR titrations of the *D. vulgaris* enzyme, leading the authors to the conclusion that *two* strongly cooperating reduced [4Fe-4S] clusters are observed in the [NiFe]-hydrogenase from this species. However, Asso *et al.* later showed that the EPR spectra of reduced samples from *D. gigas* and *D. vulgaris* are very similar [284], and a different number of reduced [4Fe-4S] clusters contributing to this signal [200, 287] is therefore surprising and appears contradictory.

Double integration of the EPR signals as a method of determining whether one or two clusters are observed has proven to be very difficult because of the broadness of the signals [198]. Teixeira *et al.* only observed 0.5 spins per molecule in the *D. gigas* enzyme and this was attributed to *two* reduced [4Fe-4S] clusters because a more simple rhombic g matrix was observed at slightly higher potentials (integrating to 0.1 spins per molecule of

enzyme) [245]. An additional problem is that the magnetic interaction observed with the EPR active Ni species (Ni-C or Ni-L) complicates spin counting and assignment of the observed peaks, as either a result of splitting due to spin-spin interaction or corresponding to intrinsic g values. Teixeira *et al.* later observed *two* redox transitions with Mössbauer spectroscopy, but EPR studies still pointed towards only *one* visible redox transition [202]. Nevertheless the existence of an EPR-invisible $S = 3/2$ cluster was ruled out because Mössbauer spectra were "quite different" from those of $S = 3/2$ $[4Fe\text{-}4S]^{+}$ clusters, and no $S = 3/2$ signal could be detected in EPR; the broad Fe-S cluster signal observed was postulated to involve both reduced [4Fe-4S] clusters with very similar reduction potentials [202]. Following UV-vis stoichiometric titrations of the *D. gigas* hydrogenase Roberts and Lindahl concluded that two $[4Fe\text{-}4S]^{2+/+}$ transitions are observed [205]. Non-turnover protein film electrochemistry (Section 3.4) of the CO-inhibited *A. vinosum* enzyme was consistent with two $[4Fe\text{-}4S]^{2+/+}$ redox processes, with identical midpoint potentials [286].

O_2-tolerant [NiFe]-hydrogenases

Compared to standard hydrogenases, the Fe-S cluster 'complex interaction signal' is much better resolved and has sharper CW EPR features in low potential samples of all O_2-tolerant [NiFe]-hydrogenases characterised so far: *E. coli* Hyd-1 [244], *Re*-MBH [82, 88, 285, 313], *Aa* Hase I [16, 84] and *H. marinus* MBH [85]. The latter enzyme has not been extensively characterised and is not discussed further here. Despite some controversy in the literature, the current consensus is that both the proximal and distal 4Fe clusters contribute to the complex signal observed at low potentials. The first redox titration of *Re*-MBH yielded a single redox curve at low potential, attributed to two clusters with identical (or very similar) midpoint potentials [313]. A 'biphasic' redox curve was later obtained by Knüttel *et al.* [285] for the same enzyme, and relative spin quantifications also led the authors to conclude that two reduced 4Fe clusters are observed. In contrast, Saggu *et al.* [82] found that the complex signal in *Re*-MBH integrated to 0.5-0.8 spins per molecule and because of the lack of any splitting of the Ni signals at

low temperatures, the authors concluded that only one reduced 4Fe cluster is observed, most likely the distal cluster (too distant to cause splitting of the Ni signals). However, no full redox titrations were performed. Most recently, in relation to the unusual role of the proximal cluster (see Chapter 6), the same team of researchers reverted to favouring the proposition by Knüttel *et al.* of two reduced 4Fe clusters observed at low potential [88], though without providing further evidence. The only comprehensive study of the redox transitions of the Fe-S clusters of any other O_2-tolerant [NiFe]-hydrogenase was recently published by Pandelia *et al.* who attributed the complex signal in *Aa* Hase I to an "interaction pattern of a reduced proximal and a distal cluster ($S = 1/2$) mediated by the high spin [3Fe-4S]^0 cluster ($S = 2$)" [16]. The number of spins per molecule that this signal integrated to was however not provided [16]. Very little data are currently published for *E. coli* Hyd-1, but the low-potential Fe-S cluster spectra obtained *via* hydrogen or dithionite reduction were reported to integrate to approximately one spin per molecule of enzyme [244].

The midpoint potentials reported for O_2-tolerant [NiFe]-hydrogenases are much higher compared to standard hydrogenases and a summary of the available data and proposed assignments to structurally defined clusters are given in Table 8.2. For completeness, the midpoint potentials of the high-potential centre (HP), the second redox transition of the proximal cluster [4Fe-3S]$^{5+/4+}$ (see Chapter 6), are also included.

Table 8.2: **Midpoint potentials of Fe-S clusters reported for O_2-tolerant [NiFe]-hydrogenases.** All E_m values were determined *via* EPR. HP stands for high potential centre (see Chapter 6). Note that the potentials reported for the medial cluster are apparent rather than true midpoint potentials (see Chapter 6, Section 6.3.5).

	E_m (mV)				
Species	$[4Fe\text{-}4S]^{2+/+}_{distal}$	$[4Fe\text{-}3S]^{4+/3+}_{proximal}$	$[3Fe\text{-}4S]^{+/0}_{medial}$	HP	ref.
A. aeolicus	−78	+87	+68	+232	[16]
R. eutropha H16	−180	−60	+25	+160	[285]
R. metallidurans CH34	−80	+50	+100	+240	[285]

The midpoint potentials of the Fe-S clusters in standard [NiFe]-hydrogenases from

A. vinosum and *D. fructosovorans*, and those in the O_2-tolerant hydrogenases *Re*-MBH and *Aa* Hase I are compared in Fig. 8.1. The proximal [4Fe-3S] cluster in O_2-tolerant hydrogenases is capable of *two* redox transitions (see Chapter 6). The $[4Fe\text{-}3S]^{5+/4+}$ transition, thought to occur as a protection against O_2 attack [16, 88, 89], is shown as a dotted line.

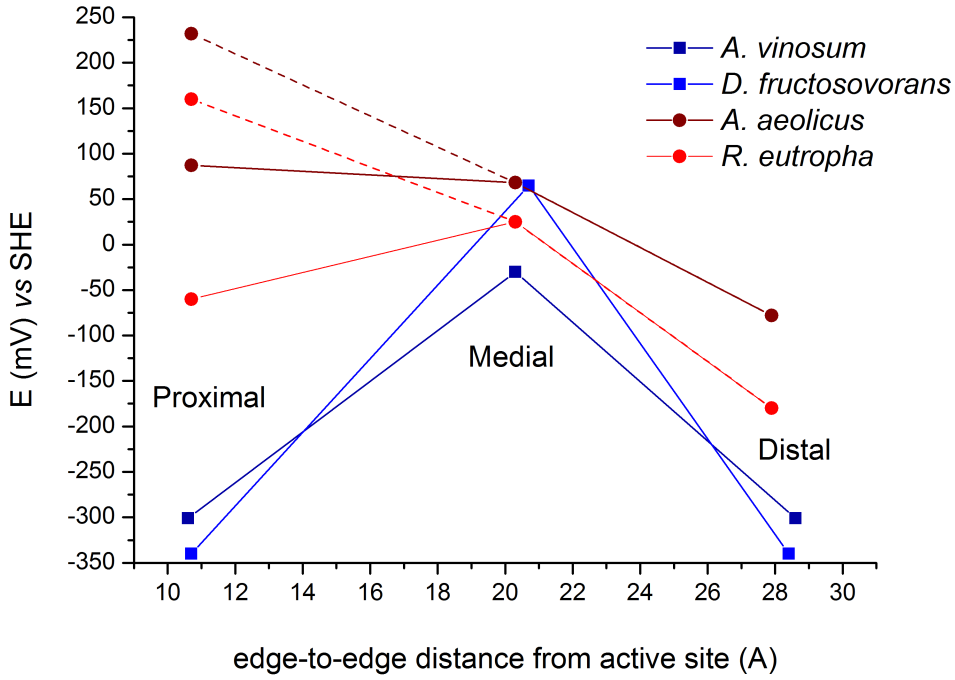


Figure 8.1: **Comparison of the midpoint potentials of the Fe-S cluster in standard and O_2-tolerant [NiFe]-hydrogenases.** The $[4Fe\text{-}3S]^{4+}$-$[4Fe\text{-}3S]^{5+}$ transition in the O_2-tolerant hydrogenases is shown as a dotted line. The distance of the Fe-S clusters from the active site are the shortest edge-to-edge distances obtained from the crystal structures of those enzymes (*A.vinosum* 3MYR, *D. fructosovorans* 1FRV, *R. eutropha* 3RGW). Distances for the *A. aeolicus* Fe-S clusters were taken to be the same as those in *R. eutropha*. Note that the midpoint potentials for the medial cluster in *Re*-MBH and *Aa* Hase I are apparent midpoint potentials and most certainly a substantial underestimate of the true midpoint potentials (see Section 6.3.5 in Chapter 6).

8.1.2 Previous site-directed mutagenesis studies of the electron transfer relay

The majority of site-directed mutagenesis studies of [NiFe]-hydrogenases have targeted the active site and the proposed gas channels (Sections 1.2.2 and 6.1.1), with the aim of addressing the mechanisms of proton transfer to and from the active site, the roles of conserved residues close to the active site and the origin of O_2-tolerance. Four mutagenesis studies are documented which investigate the Fe-S cluster electron transfer to and from the active site (*vide infra*).

In 1998, Rousset *et al.* converted the medial [3Fe-4S] cluster in the *D. fructosovorans* [NiFe]-hydrogenase into a [4Fe-4S] cluster [58]. A proline residue occupies position 238, a potential ligand to the 'empty' iron site of the medial cluster in the *D. fructosovorans* enzyme. This position is occupied by a cysteine in [NiFeSe]-hydrogenases, which contain medial [4Fe-4S] clusters [59]. In viologen dye assays, the P238C exchange was shown to only have a small effect on the catalytic activity of the enzyme, despite the dramatic 300 mV decrease in the midpoint potential of the converted medial cluster. This may be because viologen dyes need not transfer electrons *via* Fe-S relays but could react more directly with the active site. The authors state that the midpoint potentials of the proximal and distal clusters are identical and not significantly changed in the P238C variant ($E_m = -380$ mV) compared to the wild-type enzyme ($E_m = -340$ mV). Low potential spectra were reported to correspond to three spins per molecule of enzyme, implying that all three [4Fe-4S] clusters have a $S = 1/2$ ground state [58].

The reverse mutation of a medial [4Fe-4S] to a [3Fe-4S] cluster was achieved in the [NiFeSe]-hydrogenase of *Methanococcus voltae* [314]. The three [4Fe-4S] clusters in the native enzyme are believed to have identical midpoint potentials of -370 mV and the C205P variant contained a medial [3Fe-4S] cluster with a midpoint potential of $E_m = 60$ mV [314]. In the absence of titration data and quantification of the observed EPR signals at low potential no further comparison with the mutation performed by Rousset *et al.* can

be made.

The role of the unusual ligating His residue of the distal [4Fe-4S] cluster in [NiFe]-hydrogenases (Section 1.2.2) was probed by Dementin *et al.* [60] in the [NiFe]-hydrogenase from *D. fructosovorans*. Histidine 184 was substituted for Cys or Gly. Although the change in coordination slowed down the first-order electron transfer to and from the distal cluster, protein stability, active site chemistry, proton transfer and cluster assembly were found to be unaffected. The latter was concluded from X-band CW EPR measurements: the spectra of the wild-type and mutant enzymes were very similar. Reduction of the [4Fe-4S] cluster(s) in the H184C mutant corresponded to a one-electron transition with a midpoint potential of −310 mV. The Fe-S cluster signals of the reduced H184C mutant was reported to contain 1.4 times more spins per molecule compared to the wild-type enzyme at −420 mV. The Ni-C signal was found to be split completely suggesting that the proximal cluster was fully reduced and Dementin *et al.* concluded that the distal cluster must have been at least partially reduced [60].

Recently, Goris *et al.* [88] performed the first mutagenesis studies in an O_2-tolerant hydrogenase, by exchanging C19 and C120 (conserved residues in O_2-tolerant hydrogenases) for glycines (conserved residues in O_2-sensitive hydrogenases) at the proximal cluster in *Re*-MBH, as already discussed in Chapter 6. Surprisingly, no signals at all were observed in the CW EPR spectrum of the H_2-reduced sample of the C19G/C120G variant.

8.2 Methods

8.2.1 EPR sample preparation

E. coli Hyd-1 and variants, and *Salmonella* Hyd-5 were isolated as detailed in Section 3.6.2. Potential adjustments were carried out on as-isolated enzyme solutions (unless otherwise specified), using the method described in Section 3.2. The native Hyd-1 and Hyd-2 P242C enzymes samples used for the titrations in Fig. 8.4 both contained 40 μM each of MV, BV, PMS, ITS, NQ, OHNQ (Table 3.1).

To make the activated samples for the spectra in Fig. 8.2 and the anaerobically inactivated samples for the spectra shown in Fig. 8.9, the as-isolated enzyme samples were first activated under 100% H_2 at 37 ^{o}C with an initial injection of 0.4-0.6 μL sodium dithionite (Sigma Aldrich) and 40 μM each of the mediators MV, BV, PMS, ITS, NQ, OHNQ (Table 3.1). After equilibration to the H^+/H_2 potential, the temperature was returned to 20 ^{o}C and the 'activated' samples withdrawn. For the remaining enzyme, H_2 was flushed out with Ar at 30 ^{o}C, the temperature returned to 20^{o}C, the potential raised to 78$\pm$2 mV by adding substoichiometric amounts of potassium ferricyanide (Sigma Aldrich) and the 'anaerobically inactivated' samples were withdrawn.

The low-potential native Hyd-1 samples for pulsed EPR measurements were prepared in an anaerobic glove box (Glove Box Technologies) using the methods described in Section 3.2 by activating $\approx$ 200 μL as-isolated enzyme in 100% H_2 at 37 ^{o}C for two hours before returning the temperature to 20 ^{o}C. Then 1-2 μL of the solution was transferred as quickly as possible to a W-band EPR tube, approximately 80 μL of the enzyme solution was transferred to a 3.8 mm tube, and finally an aliquot of approximately 50 μL was transferred to a 3 mm tube for DEER measurements. An aliquot of the remaining enzyme was retained to determine the protein concentration *via* a Bradford assay (Section 3.7). The pulsed EPR samples of Hyd-1 C19G and C120G (Fig. 8.18) were prepared in a similar way, except that the starting volume was 100 μL and only the 3.8 mm sample was prepared. The exact concentration of the samples was not determined but is estimated to be at least 300 μM. The low-potential Hyd-1 P242C sample for pulsed EPR measurements was prepared in an anaerobic glove box (Glove Box Technologies) using the methods described in Section 3.2 by adjusting $\approx$ 150 μL as-isolated enzyme containing 200 μM each of the mediators MV, BV, PMS, ITS, NQ, OHNQ (Table 3.1) to $-$250 mV by addition of sodium dithionite. Then 1-2 μL of the solution were transferred as quickly as possible to a W-band EPR tube; the potential was re-adjusted, and approximately 80 μL of the enzyme solution was transferred to a 3.8 mm tube. The concentration of this sample is approximate because several samples (of known concentration) were pooled and concentrated

anaerobically to the desired volume. The sample of Hyd-1 C19G/C120G (Fig. 8.18) was prepared in the same way, except that the potential was adjusted to −200 mV and only a 3.8 mm sample was required. The exact concentration of this sample was not determined but is estimated to be at least 300 μM.

8.2.2 EPR measurements

For the spectrometers and resonators used, see Section 3.5. The field was calibrated as explained in Section 3.5.2. Spin quantification was carried out as described in Section 3.3. Measurement conditions are given in the figure legends. The details of the DEER experiments described in Section 8.4.4 are as follows: Four-pulse experiments (Section 2.6.5) employed pulse lengths of $t_\pi/t_{\pi/2}$ = 40 ns / 40 ns, t_π = 20 ns. A variable τ_1 time (from 180-204 ns) was applied to dampen nuclear modulations, and the time τ_2 was 1.2 μs. Experiments were carried out with ω_A = 9.638 GHz, and ω_B = 9.737 GHz at 368.0 mT and 353.8 mT. Three-pulse experiments (Section 2.6.5) employed pulse lengths of $t_\pi/t_{\pi/2}$ = 40 ns / 40 ns, t_π = 20 ns. A variable τ_1 time (from 180-204 ns) was applied to dampen nuclear modulations, and the time τ_2 was 1.5 μs or 1.0 μs. Experiments were carried out with ω_A = 9.319 GHz, and ω_B = 9.411 GHz at 346.7 mT. All experiments were carried out at 2.7 K with a shot repetition time of 2 ms.

8.3 Results (Part I)

8.3.1 Native and variant *E. coli* Hyd-1 and *Salmonella* Hyd-5 compared at low potentials

The X-band CW EPR spectra at 15 K of H_2-reduced samples of the proximal cluster variants and native *E. coli* Hyd-1 are shown in Fig. 8.2. Strikingly, no EPR signals were observed in this field range in any of the proximal cluster variants, other than a small amount of reduced methyl and benzyl viologen mediator at $g = 2$ (see Section 6.1.2 for an

introduction to the C19G, C120G and C19G/C120G variants). A similar observation was made for the C19G/C120G variant of *Re*-MBH [NiFe]-hydrogenase [88]. Electrochemical measurements of aliquots of enzyme used to make the H_2-activated EPR samples of native Hyd-1 and the three proximal cluster variants showed similar high activity, excluding the possibility of incorrectly assembled Fe-S clusters.[1]

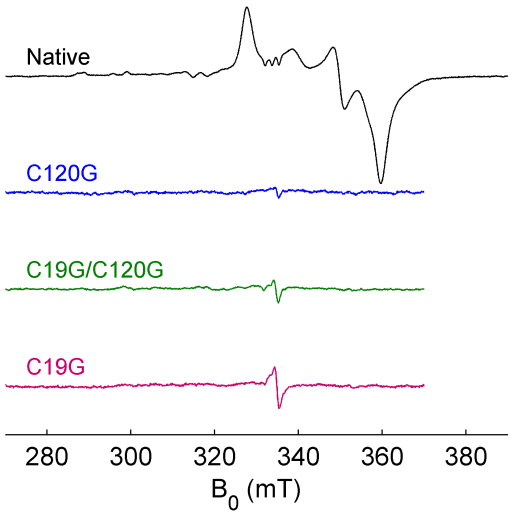


Figure 8.2: **Comparison of the X-band CW EPR spectra at 15K of native Hyd-1 and proximal variant enzyme samples after activation under H_2.** Activation under 100 % H_2 at 37 °C of native Hyd-1 required 4 hours, C120G required 8 hours, C19G required 27 hours and C19G/C120G required 40 hours (see Section 8.2 for full details of sample preparation). The solution temperature was returned to 20 °C before EPR samples were taken. Approximate protein concentration: 50-60 μM. Measurement conditions: mw power 2 mW (all), modulation amplitude 1 mT (all), mw frequency 9.390 GHz (native, C19G), 9.388 GHz (C120G), 9.383 GHz (C19G/C120G). Adapted from ref. [89].

The following possibilities could explain the lack of EPR signals in the proximal variant low potential EPR spectra. First, the potentials of both clusters could be shifted to much lower potentials compared to the native enzyme, and this could be outside the experimentally accessible potential range. Second, the change of coordination around the proximal cluster could cause the spin ground state of that cluster to change from $S = 1/2$ to a higher spin state. The latter explanation implies that the distal cluster

[1]This is further supported by conventional solution assays, carried out by Dr. Rhiannon Evans and Dr. Alison Parkin, using BV as an electron acceptor: Hyd-1 59±3, C19G/C120G 29±3, C19G 15±1, C120G 41±1 μmol H_2 min^{-1} mg^{-1} [89].

is never observed, not even in the native enzyme. Alternatively, if the distal cluster is present in the $S = 1/2$ state in the native enzyme, the lack of any signal in the C19G, C120G and C19G/C120G variants would have to result from the mutation(s) near the proximal cluster also affecting the spin ground state of the distal cluster, which is more than 20 Å away.

As a first step, it is instructive to compare the CW EPR spectra of native *E. coli* Hyd-1, the medial cluster Hyd-1 variant P242C and the *Salmonella* Hyd-5 (Section 6.3.6) enzymes at low potentials (Fig. 8.3). While the Fe-S cluster spectrum of the *Salmonella* hydrogenase is almost identical to that of *E. coli* Hyd-1 and that of the other characterised O_2-tolerant [NiFe]-hydrogenases, the spectrum of the *E. coli* P242C variant differs and can be simulated with a single species with an anisotropic rhombic g tensor (red dotted line in Fig. 8.3). In the Ni region of the spectra, a species with $g_x = 2.24(5)$ and $g_y = 2.11(5)$ is present in Hyd-1 P242C, *Salmonella* Hyd-5 and to a lesser extent in native Hyd-1 (g_z is masked by the Fe-S cluster signals but from Fig. 8.7 $g_z = 2.05$). The amount of this species varied with sample preparation but was always found to be less prominent in native Hyd-1. A species with $g_{x,y,z} = 2.242,\ 2.095,\ 2.053$ was found to be present in reduced samples of *E. coli* Hyd-2 and has been named Ni-X (see Chapter 5, Section 5.3.2). Because of the similarity in g values and given that it is also observed only in low-potential samples of native Hyd-1, Hyd-1 variants and *Salmonella* Hyd-5, the species is also referred to as Ni-X in these enzymes.[2]

All the Fe-S cluster spectra integrated to approximately one spin per molecule of enzyme, as indicated in Fig. 8.3. The signal heights reached maximum intensities at the given potentials (see Section 8.3.2 for native Hyd-1 and Hyd-1 P242C and Section 6.3.6 for *Salmonella* Hyd-5), showing that the species were fully reduced. For comparison, the spectrum of H_2-reduced *Re*-MBH was reported to integrate to 0.5-0.8 spins per molecule [82]. Rousset *et al.* [58] reported the Fe-S cluster spectra of the medial cluster vari-

[2]The light dependence of Ni-X was not investigated in native *E. coli* Hyd-1, Hyd-1 variants and *Salmonella* Hyd-5. However, Ni-X in *E. coli* Hyd-2 has similar g values and was found to be light-independent (Section 5.3.2).

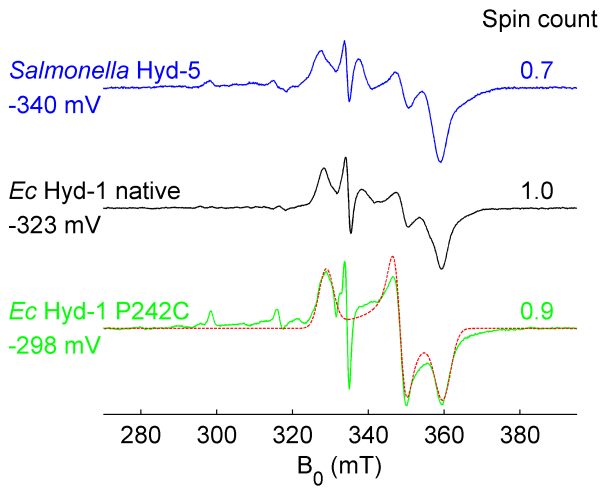


Figure 8.3: **Comparison of the low potential CW EPR spectra of *E. coli* Hyd-1 native and P242C variant, and *Salmonella* Hyd-5.** The potentials at which the samples were taken is indicated, as well as the number of spins per molecule to which the spectra integrated (± 0.2). Measurement conditions: mw power 2 mW (all), modulation amplitude 1 mT (all), mw frequency 9.374 GHz (*Salmonella* Hyd-5), 9.385 GHz (*E. coli* Hyd-1 native), 9.375 GHz (*E. coli* Hyd-1 P242C). The radical peak at $g = 2$ results from redox mediators (benzyl viologen). Simulation parameters for the Hyd-1 P242C [4Fe-3S]$^{3+}$ cluster(red dotted line): $g_x = 2.035$, $g_y = 1.923$, $g_z = 1.862$. Enzyme concentrations: 25 μM (*Salmonella* Hyd-5), 24 μM (*E. coli* Hyd-1), 46 μM (*E. coli* Hyd-1 P242C). Spectra are scaled by enzyme concentration. The *Salmonella* Hyd-5 sample was prepared by Dr. Alison Parkin and Rosalind Davies.

ant ([3Fe-4S] to [4Fe-4S] intended) in the standard *D. fructosovorans* [NiFe]-hydrogenase (Section 8.1.2) to integrate to three spins per molecule of enzyme. In contrast, the spin integrations observed for native *E. coli* Hyd-1, Hyd-1 P242C and *Salmonella* Hyd-5 are consistent with just one reduced cluster in the $S = 1/2$ ground state.

8.3.2 Potential titrations of *E. coli* native and P242C variant Hyd-1

Figure 8.4 shows the CW EPR spectra of potential titrations of native Hyd-1 and the P242C variant. This Figure was previously shown in Chapter 7 (Fig. 7.3) in the context of the spectral changes occurring at high potentials. It is reproduced here for easy referral in later sections of this chapter.

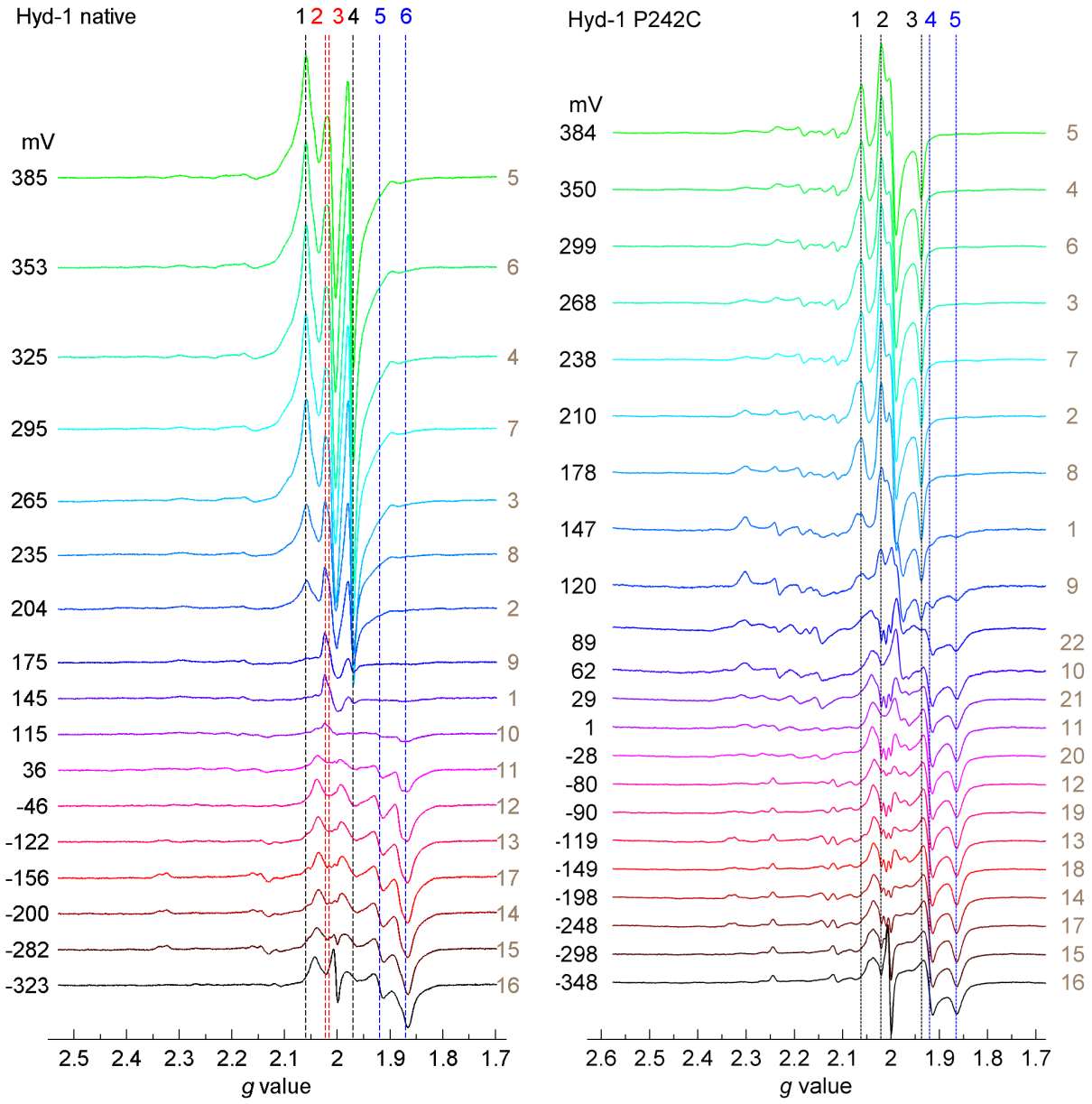


Figure 8.4: **CW EPR spectra of potential titrations of native Hyd-1 (*left*) and the P242C variant (*right*).** The spacing between adjacent spectra is not proportional to the redox potential difference between the samples. Measurement conditions: mw frequency 9.385 GHz (native), 9.375 GHz (P242C); mw power 2 mW (native), 0.5 mW (P242C); modulation amplitude 1 mT. Enzyme concentrations: 24 μM (native), 46 μM (P242C). Temperature: 15 K (native), 20 K (P242C). Annotations refer to the potential at which the sample was taken (*left*, in mV) and the order in which samples were taken (*right*, grey). Vertical lines indicate the peak heights monitored to extract mid-point potentials, see Fig. 8.5. This Figure is identical to Fig. 7.3 in Chapter 7.

Spin quantification of the Fe-S cluster regions in the high and low potential spectra of Native Hyd-1 and the P242C variant (Fig 8.4) are summarised in Table 8.3.

Table 8.3: **Spin integrations of native Hyd-1 and the P242C variant of Fe-S cluster signals at high and low potentials.** Spin integrations refer to the spectra in Fig. 8.4.

	Hyd-1 native	Hyd-1 P242C
High potential	2.0±0.3 (+ 385 mV)	0.9±0.3 (+ 384 mV)
Low potential	1.0±0.2 (- 323 mV)	0.9±0.2 (- 348 mV)

Even though the error margin on these values is reasonably large (because accurate subtraction of the Ni signal contribution to the spectra is difficult), the ratio of high to low-potential spectra is 2 in native Hyd-1, but 1 in the medial cluster variant. The high potential Fe-S cluster spectra of native Hyd-1 result from the oxidised medial cluster and the oxidised proximal $[4Fe\text{-}3S]^{5+}$ cluster (or high potential centre, HP) whereas those of Hyd-1 P242C result from HP alone, as discussed in Chapter 7. Consequently, the spin intensities at low potentials strongly suggest that the reduced medial $[4Fe\text{-}4S]^{+}$ is not observed in the P242C variant.

The EPR-visible Fe-S cluster redox transitions observed in Fig. 8.4 are summarised in Fig. 8.5 (Fig. 7.4 in Chapter 7). As with native Hyd-1, only *one* redox transition is observed at low potentials in the P242C variant. This contrasts with *two* transitions reported for the native *Aa* Hase I enzyme [16] and will be discussed in more detail later.

The midpoint potentials of the EPR-active Fe-S clusters for both enzymes are compared in Table 8.4. Amino acid substitutions near the medial cluster shift the midpoint potentials of the observed [4Fe-4S] and the high potential centre closer together. Compared to standard hydrogenases, the midpoint potentials of all redox transitions are much higher (see Table 8.1 and references therein) and more comparable to the values reported for O_2-tolerant hydrogenases (Table 8.2). The observed EPR signals of the $[4Fe\text{-}4S]^{+}$ or $[4Fe\text{-}3S]^{3+}$ cluster need to be unambiguously assigned and this is the subject of the following Section.

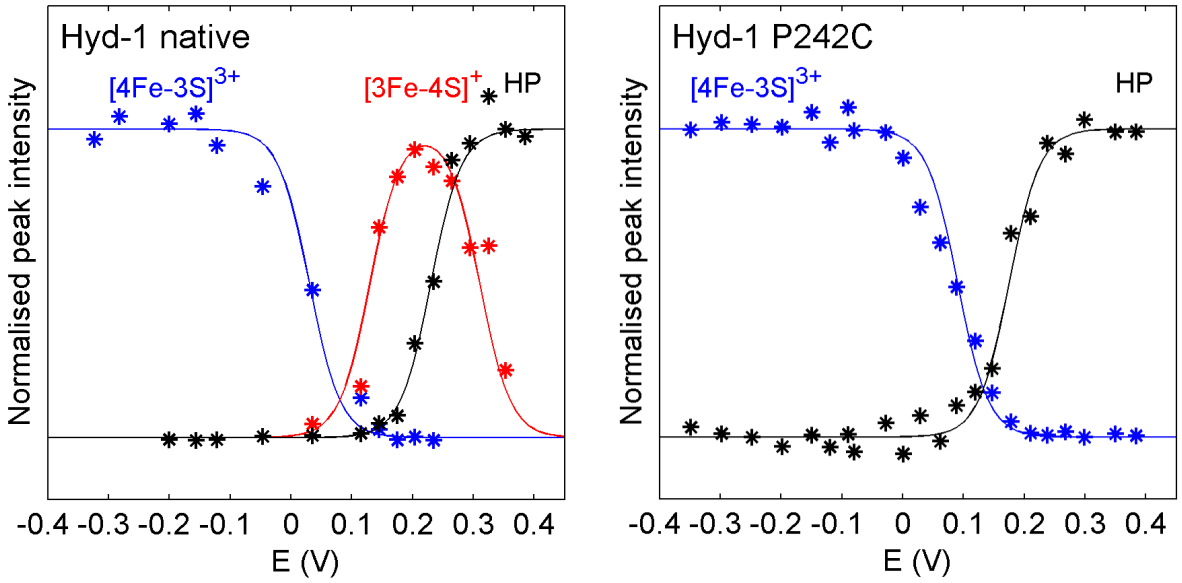


Figure 8.5: **Potentiometric titrations of the EPR-active species observed in native Hyd-1 (*left*) and the P242C variant (*right*).** The peak positions in the CW EPR spectra (labeled in Fig. 8.4) used to give these plots were as follows: Native Hyd-1 $[4Fe\text{-}3S]^{3+}$ (peak 6, $g = 1.870$), $[3Fe\text{-}4S]^{+}$ (peak 2 minus peak 3, $g = 2.023$ minus $g = 2.016$), HP (peak 4, $g = 1.970$); Hyd-1 P242C $[4Fe\text{-}4S]^{+}$ (peak 5, $g = 1.865$), HP (peak 1, $g = 2.062$). See text for assignment of the blue redox transitions. This Figure is identical to Fig. 7.4 in Chapter 7.

Table 8.4: **Midpoint potentials of the EPR-active Fe-S clusters observed in native Hyd-1 and Hyd-1 P242C.** The midpoint potentials for HP and the $[4Fe\text{-}3S]^{4+/3+}$ couple (see text) result from Fig. 8.5; the 'true' midpoint potential of the medial cluster $[3Fe\text{-}4S]^{+/0}$ couple was obtained as explained in Chapter 6, Section 6.3.5.

	E_m (mV)		
Enzyme	$[4Fe\text{-}3S]^{4+/3+}$	$[3Fe\text{-}4S]^{+/0}$	HP
Hyd-1 native	$+30 \pm 30$	$+190 \pm 30$	$+230 \pm 15$
Hyd-1 P242C	$+90 \pm 20$	-	$+175 \pm 15$

8.3.3 Interactions with the active site Ni species

A magnification of the Ni region of titration samples of native Hyd-1 and the P242C variant (measured at 15 K and 20 K, respectively), is given in Fig. 8.6. The five selected potentials represent the following situations (from uppermost to lowest): (1) the HP centre and inactive Ni species are fully oxidised, as is the medial [3Fe-4S] cluster in native Hyd-1; (2) the HP centre is largely reduced but the distal [4Fe-4S] or proximal [4Fe-3S]

cluster is not yet reduced (the potential at which this occurs differs for the two enzymes), the medial cluster is still partially oxidised in native Hyd-1; (3) the [4Fe-4S] or [4Fe-3S] cluster is partially reduced and the inactive Ni species are still partially oxidised, the medial cluster is reduced; (4) the [4Fe-4S] or [4Fe-3S] cluster and active Ni species (Ni-L*) are reduced; (5) the [4Fe-4S] or [4Fe-3S] cluster is reduced and so is Ni-X (more prominent in P242C Hyd-1). Although the Ni signals of native Hyd-1 and Hyd-1 P242C differ at high potentials (top two spectra) (see Chapter 6), they are remarkably similar at lower potentials (bottom three spectra).

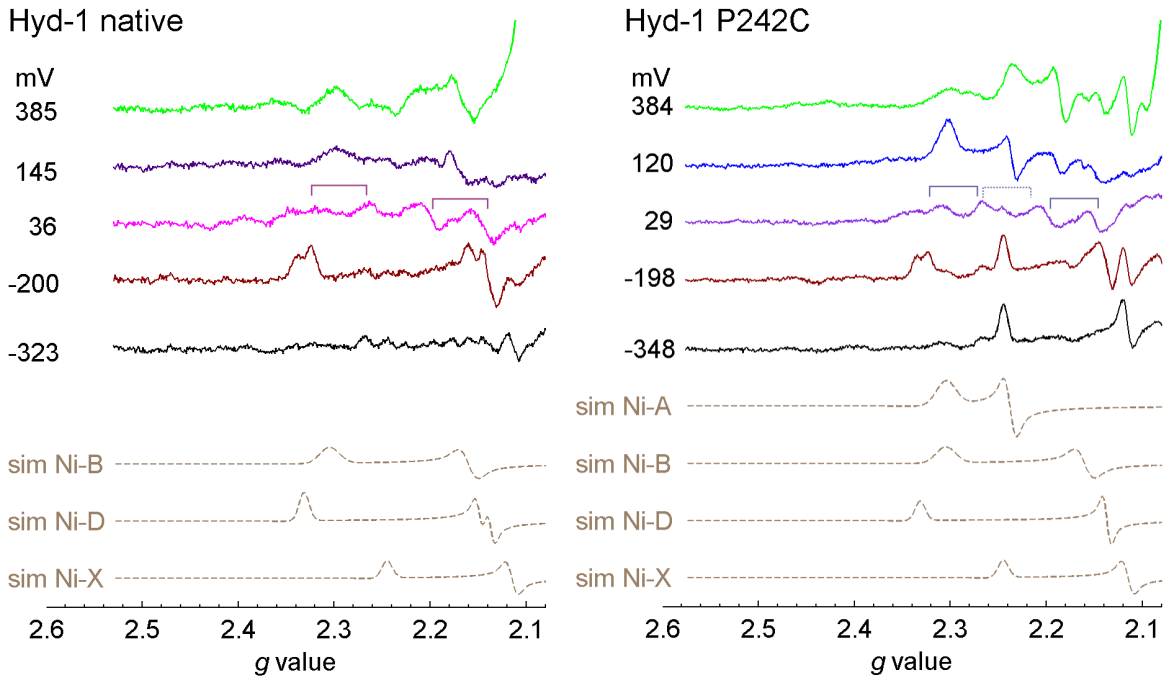


Figure 8.6: **CW EPR spectra of Ni signals of native Hyd-1 (15 K) and Hyd-1 P242C (20 K) at selected potentials.** Spectra were magnified from Fig. 8.4 and colours corresponding to potentials are the same in the two Figures. See Fig. 8.4 for measurement conditions. Horizontal bars refer to the symmetric splitting of Ni-A (Hyd-1 P242C) or Ni-B (native Hyd-1 and Hyd-1 P242C) g_x and g_y due to interaction with the reduced proximal $[4Fe\text{-}3S]^{3+}$ cluster (see text). Simulations of the 'unsplit' Ni species are included as dotted lines: Ni-A $g_{x,y,z}$ = 2.31, 2.24, 2.01; Ni-B $g_{x,y,z}$ = 2.31, 2.16, 2.01; Ni-L* $g_{x,y,z}$ = 2.332, 2.149/2.137, 2.047 (see Section 5.3.2); Ni-X $g_{x,y,z}$ = 2.24(5), 2.11(5), 2.05.

At ≈ 30 mV, the visible [4Fe-4S] or [4Fe-3S] cluster is almost completely reduced in

Hyd-1 P242C and partially reduced in native Hyd-1 (Fig. 8.5). Ni-B and Ni-A are still (at least partially) oxidised at this potential though the Ni species are not immediately identifiable at 15/20 K because the signals are split (simulations of the 'unsplit' Ni species are included in Fig. 8.6). The midpoint potentials for the EPR-active Ni species were given for the C19G/C120G variant (Chapter 6, Section 6.3.2) and it is assumed that these do not change significantly between different Fe-S cluster variants of Hyd-1 because amino acid exchanges are remote from the active site. This is supported by the 80 K spectra of the $\approx$ 30 mV samples of native Hyd-1 and the medial cluster variant which show uncoupled Ni-A and Ni-B due to faster relaxation of the Fe-S clusters at this temperature (Fig. 8.7).

The 80 K spectrum of native Hyd-1 at 36 mV contains very little Ni-A (judging from the magnitude of the $g_y = 2.24$ peak in Fig. 8.7) and the g_x and g_y of Ni-B are split symmetrically and to the same extent into two components of similar intensity, as indicated on Fig. 8.6. This suggests that an isotropic exchange interaction between the active site and the reduced distal [4Fe-4S] cluster or the reduced proximal [4Fe-3S] cluster is responsible for this splitting. The spectrum is remarkably similar to that of *Aa* Hase I obtained under similar conditions [16]. The magnitude of the isotropic exchange between the active site Ni-B and the reduced [4Fe-4S]/[4Fe-3S] cluster is $\approx$ 110 MHz - almost identical to the value of 108 MHz reported for the *A. aeolicus* enzyme [16]. The spectrum of Hyd-1 P242C is also very similar to both that of the native enzyme and that of *Aa* Hase I and the exchange interaction between Ni-B and $[4Fe\text{-}4S]^{+}/[4Fe\text{-}3S]^{3+}$ is $\approx$ 100 MHz. It is difficult to quantify the magnitude of the exchange interaction of Ni-A with the reduced Fe-S cluster. However, the split Ni-A signals appear to be buried under the split Ni-B signals (indicated as dotted horizontal bar in Fig. 8.6 for Ni-A g_y), suggesting that the exchange interactions of $[4Fe\text{-}4S]^{+}/[4Fe\text{-}3S]^{3+}$ with Ni-A and Ni-B are of similar magnitude. In standard hydrogenases such an exchange interaction is normally observed between the reduced proximal cluster and the active site Ni-C (because the proximal [4Fe-4S] cluster is reduced at lower potentials compared to the cluster observed

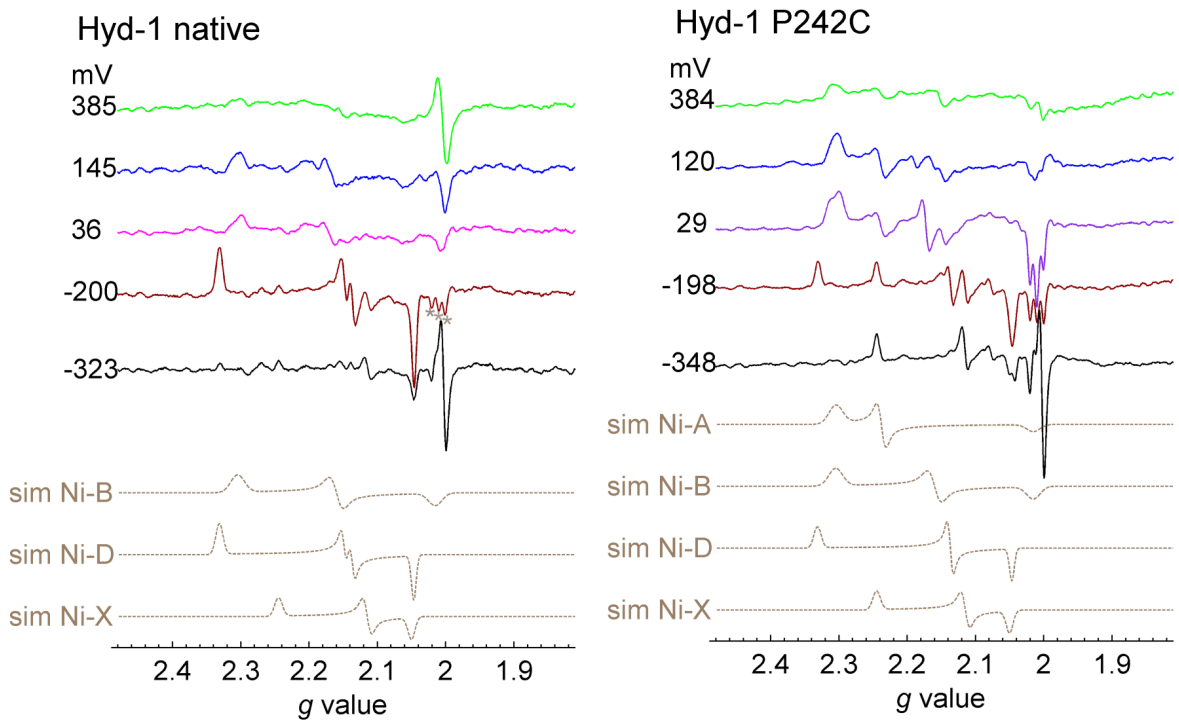


Figure 8.7: **CW EPR spectra of Ni signals of native Hyd-1 and Hyd-1 P242C at selected potentials (80 K).** Spectra correspond to the low-temperature measurements in Fig. 8.6. The radical signals at $g = 2$ in the native Hyd-1 spectra result from mediators (phenazine methosulfate at high potential and benzyl/methyl viologen at low potential). Measurement conditions: (Hyd-1 native) mw power 2 mW, mw frequency 9.384 GHz, modulation amplitude 1 mT; (Hyd-1 P242C) mw power 8 mW, mw frequency 9.375 GHz, modulation amplitude 1 mT. Simulations of the Ni species are included as dotted lines: Ni-A $g_{x,y,z} = 2.31, 2.24, 2.01$; Ni-B $g_{x,y,z} = 2.31, 2.16, 2.01$; Ni-L* $g_{x,y,z} = 2.332, 2.149/2.137, 2.047$ (see Section 5.3.2); Ni-X $g_{x,y,z} = 2.24(5), 2.11(5), 2.05$. The three peaks marked with an asterisk are unidentified; they may be associated with degradation of the enzyme but are unlikely to result from damage to the Fe-S clusters (see Section 5.3.5).

here). For the [NiFe]-hydrogenase from *D. gigas* the exchange coupling was determined to be 120 MHz [262]. At high potential, the Ni signals are not split by interaction with the medial cluster in the C19G/C120G variant at high potential and in standard hydrogenases (Chapter 5, Section 5.3.3); therefore, the splitting of Ni-B (and Ni-A) observed in native Hyd-1 and the P242C variant at $\approx$ 30 mV must be due to interaction with the reduced proximal [4Fe-3S]$^{3+}$ cluster. The splitting of Ni-B at similar potentials in *Aa* Hase I was also attributed to arise from the reduced proximal cluster [16]. The low-potential redox transition observed in native Hyd-1 and Hyd-1 P242C therefore arises from the proximal

[4Fe-3S] cluster.

At potentials below approximately −80 mV, Hyd-1 P242C shows signals at $g_x = 2.24(5)$, $g_y = 2.11(5)$ and $g_z = 2.05$ (Ni-X, *vide supra*) which are present at a much smaller intensity in native Hyd-1. As with the native enzyme, the Ni species which is observed at maximum intensity at ≈ -200 mV has g values that more closely resemble Ni-L rather than Ni-C. As for native Hyd-1, it is named Ni-L* here. As shown in Fig. 8.6, a splitting of approximately 49 MHz in native Hyd-1 and 42 MHz in Hyd-1 P242C is observed in the g_x component of Ni-L*, showing that Ni-L* is magnetically coupled to another species. This splitting disappears at high temperatures (Fig. 8.7). In contrast, the 'splitting' of the g_y component seen in native Hyd-1 is also present at 80 K (Fig. 8.7) and therefore cannot be attributed to an interaction with another paramagnetic centre. Given the anisotropy of the observed splitting, it is most likely due to a dipolar interaction rather than an (isotropic) exchange interaction (Section 2.4). A splitting of this magnitude in g_x can only arise from the proximal cluster; the distal cluster is too far away from the active site. Even with spin projection factors with unreasonably large magnitudes (+1.83 and −1.33, Section Chapter 4 Section 4.4.1) for the ferrous and mixed valence Fe pairs in the reduced [4Fe-4S] cluster, a maximum splitting of 5 MHz could result from a dipolar interaction of Ni-L* with the distal cluster. Reasonable spin projection factors (for ferredoxin-type clusters) are calculated to give rise to a value of 40-50 MHz for the dipolar interaction between the proximal cluster and Ni-B/Ni-A. Intercluster distances were taken from the crystal structure of *E. coli* Hyd-1 and the method described in Chapter 4 was used to calculate these estimates. Like the splitting of Ni-L*, a similar anisotropic splitting of the Ni-L signals was found for the standard [NiFe]-hydrogenases from *D. gigas* and *D. fructosovorans*, and the [NiFeSe]-hydrogenase from *Dm. baculatum*, which was also attributed to predominantly dipolar (rather than exchange) coupling with the reduced proximal cluster [214]. Despite significant differences in light sensitivity and g values of the Ni-L species in standard [NiFe(Se)]-hydrogenases compared to Ni-L* observed in *E. coli* Hyd-1 and variants (Chapter 5, Section 5.3.2), the nature of the splitting observed at

low temperatures is a further indication that Ni-L* is more structurally similar to Ni-L than Ni-C. As previously stated, no signals from reduced clusters are seen in the $g = 2$ region of the spectra of the low potential samples of the proximal cluster variants. In many spectra of native Hyd-1 and variant samples three peaks around $g = 2$ are observed (as exemplified in Fig. 8.7, marked with asterisks); they may be associated with degradation of the enzyme but are unlikely to result from damage to the Fe-S clusters (see Section 5.3.5). Further evidence for the splitting in Ni-L* g_x arising from an interaction with the reduced proximal $[4Fe\text{-}3S]^{3+}$ cluster is provided by examining the proximal cluster variants at low temperature, poised at a potential where Ni-L* is observed at or near maximal intensity (Fig. 8.8).

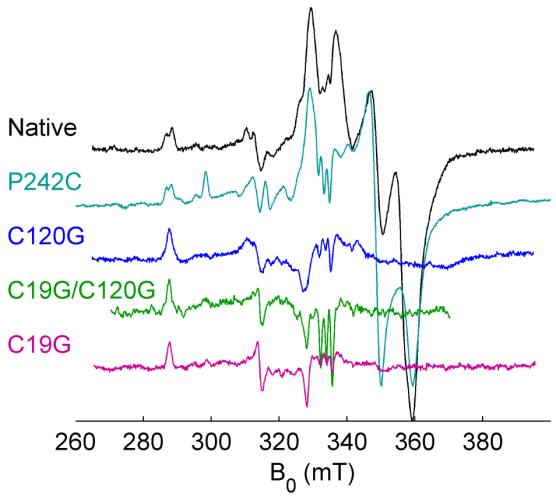


Figure 8.8: **X-band CW EPR spectra of native Hyd-1 and variants comparing low-potential Ni signals.** Samples were taken at the following potentials: Native -200 mV; P242C -198 mV; C120G -204 mV; C19G/C120G -206 mV; C19G -184 mV. Measurement conditions (mw power, modulation amplitude, temperature): native (2 mW, 1 mT, 15 K), P242C (0.5 mW, 1 mT, 20 K), C120G (2 mW, 1 mT, 15 K), C19G/C120G (2 mW, 1 mT, 15 K), C19G (2 mW, 1 mT, 15 K). Figure taken from ref. [270].

Ni-L* g_x in not split in any of the proximal cluster variants (C19G, C120G and C19G/C120G) and the spectra measured at 15 K look almost identical. Consequently the splitting of Ni-L* in native Hyd-1 (and the P242C variant) must arise from the interaction with the reduced proximal cluster. Note that a broad feature detected in the C120G

variant between 345 - 375 mT (indiscernible in the C19G and C19G/C120G variants) indicates a small amount of reduced Fe-S cluster (see below).

The question that now remains is whether the Ni-A/Ni-B signals are split in the proximal cluster variants, as they are for the native and P242C Hyd-1 enzymes (Fig. 8.6). Figure 8.9 compares C19G, C120G and the double variant at a potential at which the proximal cluster (if visible) should be partially reduced while Ni-A/Ni-B is still largely oxidised. Samples were activated under hydrogen and then anaerobically inactivated in order to obtain only Ni-B (see Section 8.2), although the spectrum of C19G/C120G shows that a small amount of Ni-A remained.[3] The 15 K spectra reveal that a small fraction of the medial [3Fe-4S] cluster is oxidised in the C19G and C120G variants. However, there is no direct magnetic interaction between the medial cluster and the active site (Chapter 6, Section 6.3.2), therefore the splitting of Ni-B observed in the C120G variant must arise from exchange coupling with the small amount of reduced proximal cluster in the $S = 1/2$ ground state (*vide supra*). Indeed, uncoupled Ni-B signals are observed for the C120G variant at 80 K (consistent with the disappearance of the reduced $[4Fe\text{-}3S]^{3+}$ cluster at higher temperatures). In contrast, the Ni signals remain practically unchanged between 15 K and 80 K in the C19G and the C19G/C120G variants. The 'doublet' Ni-B g_x peaks does not result from interaction with another paramagnetic centre since it persists at 80 K, at which temperature no Fe-S signals are detected. This change in the Ni-B signal is consistently observed following activation under hydrogen. The presence of two g_x peaks and only one g_y and g_z peak was explained by the existence of two different Ni-B species (Chapter 6, Section 6.3.1). Titrations of C19G and C19G/C120G have shown that across the whole potential range over which Ni-A and Ni-B are visible, no splitting is observed at 15 K (see Chapter 6, Section 6.3.2). The splitting pattern of Ni-B observed in C120G (Fig. 8.9 15 K, green trace) is very similar to the native and the P242C enzymes, but it is also evident that some uncoupled Ni-B is present. It therefore appears that the C120G mutation alone results in a proximal cluster with a physical mixture [315] of spin ground

[3]The C19G/C120G variant has proven to be especially difficult to activate (see Chapter 6, Section 6.3.1).

states ($S = 1/2$ and a higher spin state), while the C19G and C19G/C120G mutations result in a proximal cluster with a pure $S > 1/2$ ground state.

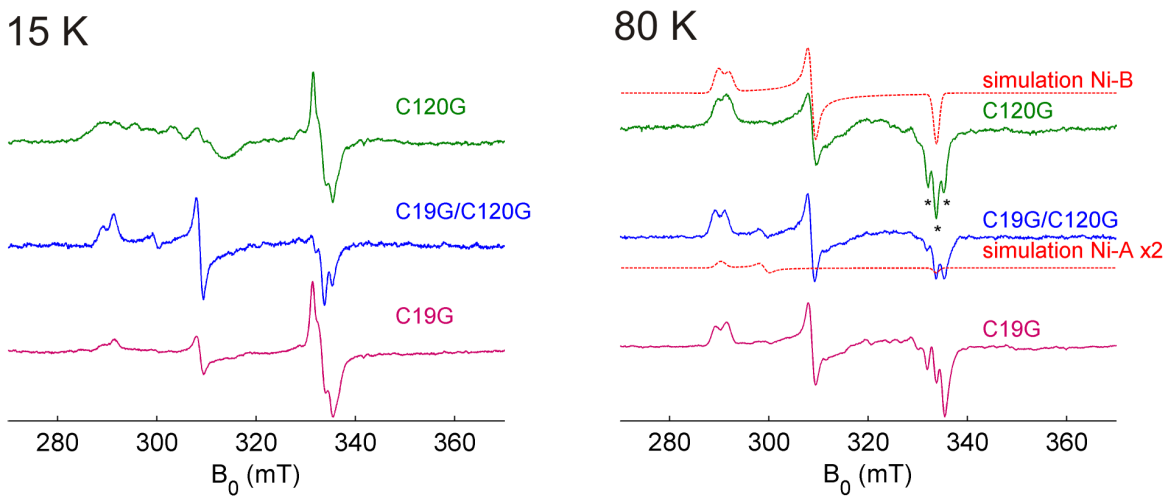


Figure 8.9: **15 K and 80 K CW EPR spectra of native Hyd-1 and proximal cluster variants poised at 77±2 mV following anaerobic inactivation.** Prior to inactivation, samples were activated under H_2 for 4 hours (native Hyd-1), 8 hours (C120G), 24 hours (C19G/C120G)and 27 hours (C19G). The simulation of the spectrum of the anaerobically activated native Hyd 1 is shown in red (NiB_1 $g_{x,y,z}$ = 2.314, 2.174, 2.010, NiB_2 $g_{x,y,z}$ = 2.297, 2.172, 2.010). g values of the Ni-B species are comparable for the three variant enzymes. See Section 8.2 for details on sample preparation. Approximate protein concentration: 50-60 μM. Measurement conditions: (15 K) mw power 2 mW, modulation amplitude 0.5 mT; (80 K) mw power 2 mW, modulation amplitude 1 mT. Unidentified peaks are marked with an asterisk.

8.3.4 Temperature dependence of the low-potential signal in native Hyd-1 and Hyd-1 P242C

The shape of the Fe-S cluster signals in the low-potential samples of native Hyd-1 changes remarkably as a function of temperature (Fig. 8.10). The same H_2-reduced sample was measured under non-saturating conditions at temperatures between 40 K and 3.3 K and the spectrum gradually changes from four apparent g values into an almost axial spectrum at 3.3 K. Similar spectra measured at 6 K/5 K have been reported for the [NiFe]-hydrogenase from *A. aeolicus* [16, 84] although signals were not examined in that case as

a function of temperature. Concomitantly with the broadening of the Fe-S cluster signals with increasingly higher temperatures, the splitting of Ni-L* g_x gradually decreases until it is absent at 40 K (Fig. 8.10, right).

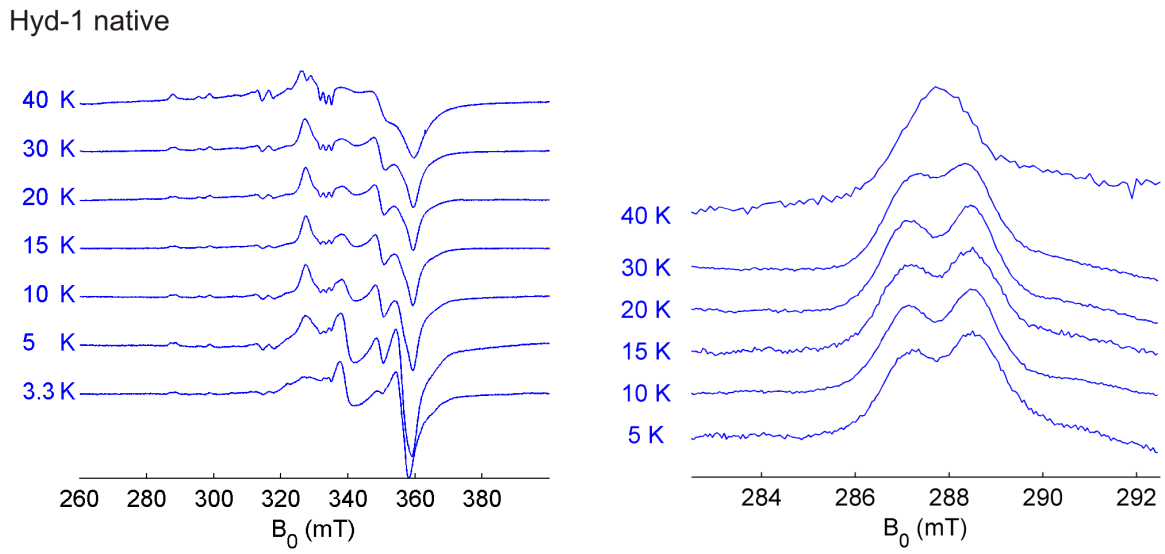


Figure 8.10: **Native Hyd-1: temperature dependence of low-potential species. (*Left*): full CW EPR spectra measured under non-saturating conditions (see text), (*right*): Ni-L* g_x = 2.33.** Measurement conditions: *Left* mw power 2 mW (40 K, 30 K), 0.5 mW (20 K, 15 K), 0.12 mW (10 K), 32 μW (5 K), 8 μW (3.3 K); modulation amplitude 1 mT (all). (*Right*): 2 mW (40 K, 30 K, 20 K, 15 K), 0.12 mW (10 K, 5 K); modulation amplitude 0.5 mT (all except 1 mT at 40 K); mw frequency 9.381 GHz; sample concentration 555 μM; potential - 355 mV. Adapted from [270].

By contrast, a similar temperature-dependence study of a sample of the Hyd-1 P242C variant poised at -250 mV (a potential at which the observed [4Fe-4S] or [4Fe-3S] cluster is fully reduced, see Fig. 8.5) reveals that the rhombic Fe-S cluster signal does not change shape as the temperature is decreased. Because of the slower relaxation of the Fe-S species in this enzyme, no spectrum could be recorded at 3.3 K under non-saturating conditions. Consequently, the Fe-S signals remain sharp to higher temperatures compared to native Hyd-1. The splitting of Ni-L* g_x vanishes at and above 40 K (Fig. 8.11, right), similar to the native enzyme.

The spin integrations of spectra across the temperature range studied are summarised for both native Hyd-1 and the P242C variant in Table 8.5. Relative values with respect to the double integral of the 40 K spectra are tabulated. Calculated values refer to the change

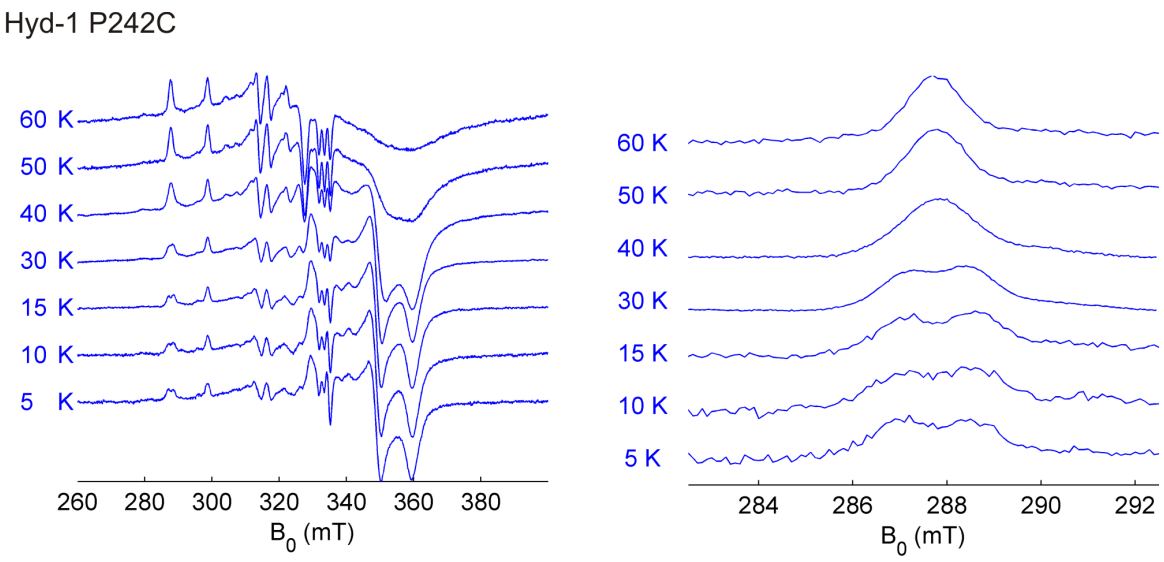


Figure 8.11: **Hyd-1 P242C: temperature dependence of low-potential species. (*Left*): full CW EPR spectra measured under non-saturating conditions (see text), (*right*): Ni-L* g_x = 2.33.** Measurement conditions: *Left* mw power 2 mW (60 K, 50 K, 30 K), 8 mW (40 K), 32 μW (15 K), 8 μW (10 K, 5 K); modulation amplitude 1 mT (all). *right* 2 mW (60 K, 50 K, 30 K), 8 mW (40 K), 32 μW (15 K), 8 μW (10 K), 0.5 μW, 5 K); modulation amplitude 0.5 mT (40 K, 30 K), 1 mT (60 K, 50 K, 15 K, 10 K, 5 K); approximate sample concentration 300 μM, potential - 250 mV. Figure adapted from ref. [270].

in signal intensity expected according to the Boltzmann distribution and are also given with respect to 40 K, using equation 8.3. For a simple two-level system, the fractional population of the upper state (N_{upper}) with respect to the lower state (N_{lower}) is given by equation 8.1:

$$N_{upper}/N_{lower} = \exp\{-(\Delta E/kT)\} \tag{8.1}$$

The fractional excess of the lower energy level (F_l) is then:

$$F_l = \frac{N_{lower} - N_{upper}}{N_{lower} + N_{upper}} = \frac{1 - \exp\{-(\Delta E/kT)\}}{1 + \exp\{-(\Delta E/kT)\}} \tag{8.2}$$

Consequently, for a given temperature T_1 and T_2:

$$\frac{F_l(T_1)}{F_l(T_2)} \simeq \frac{T_2}{T_1} \tag{8.3}$$

The last column in Table 8.5 gives the values measured for a $Cu(ClO_4)_2$ standard sample, which follows the Boltzmann distribution (Appendix Fig. 10.5). No low lying $S \neq 1/2$ excited states are present in Cu^{2+} [316]. Calculated values using equation 8.2 differed from those listed using equation 8.3 by less than 0.5%, so the approximate equation 8.3 was used. The copper sample was measured to ensure that the temperature displayed by the temperature controller corresponds to the true temperature of the sample, as well as to gauge differences between calculated and experimental values in a 'model' sample compared to 'unknown' Hyd-1 samples where the excited states are unknown.

Table 8.5: **Temperature dependence of Hyd-1 native and P242C double integrals of low-potential CW EPR spectra, compared to a $Cu(ClO_4)_2$ standard and values expected from the Boltzmann distribution.** Measurement conditions for Hyd-1 native and P242C are as detailed in Figures 8.10 (*left*) and 8.10 (*left*), respectively. Conditions for $Cu(ClO_4)_2$: mw power 8 μW (40 K, 30 K, 20 K), 2 μW (15 K, 10 K); modulation amplitude 1 mT (all); sample concentration 200 μM. − indicates that the sample was not measured at this temperature. Table taken from ref. [270].

Temperature (K)	calculated	experimental ratios *vs* 40 K		
		Hyd-1 native	Hyd-1 P242C	$Cu(ClO_4)_2$
60	0.7	-	0.7	-
50	0.8	-	0.8	-
40	1.0	1.0	1.0	1.0
30	1.3	1.3	1.4	1.4
20	2.0	1.7	-	2.0
15	2.7	2.3	2.9	2.8
10	4.0	3.7	4.6	4.1
5	8.0	8.0	8.0	-
3.3	12.1	13.1	-	-

The largest error for both native Hyd-1 and the P242C variant is within 15% of the calculated values, compared to 7% for the $Cu(ClO_4)_2$ sample. Experimental ratios are calculated from double integration of the entire spectrum because in the absence of accurate simulations of the Ni signals it is impossible to subtract the contribution from the Ni species. One source of error is the difficulty in measuring the Ni signals under non-

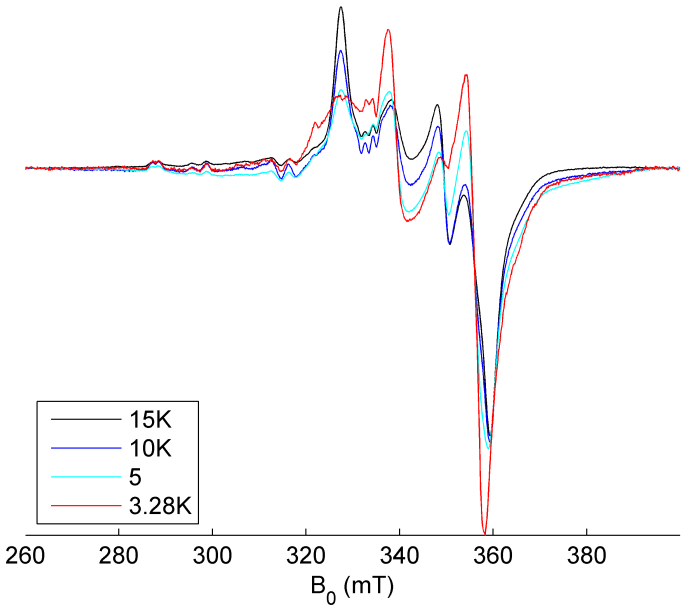


Figure 8.12: **Temperature dependence of low potential native Hyd-1 X-band CW EPR spectra scaled by the Boltzmann distribution.** Measurement conditions: mw power 0.5 mW (15 K), 0.12 mW (10 K), 32 μW (5 K), 8 μW (3.3 K); modulation amplitude 1 mT (all); sample concentration 555 μM. Spectra are scaled by mw power and the Boltzmann distribution.

saturating conditions at low temperatures.[4] The values in Table 8.5 therefore have a slight dependence on mw power. Comparing the spin integrations of the $Cu(ClO_4)_2$ and two enzyme samples to the calculated values leads to the conclusion that only one species is present at all temperatures. Given that absolute spin integrations yielded approximately one spin per molecule of enzyme at 15 K/20 K for Hyd-1 native/P242C (Fig. 8.4), the temperature dependence study is another piece of evidence that the Fe-S signals arise from either the reduced distal $[4Fe\text{-}4S]^{+}$ cluster or the reduced proximal $[4Fe\text{-}3S]^{3+}$ cluster, or both. The spectra of native Hyd-1 between 15 K and 3.3 K scaled by the Boltzmann distribution therefore show the transformation of one species rather than the appearance of another (Fig. 8.12).

Consequently, the transformation of the spectrum of native Hyd-1 low-potential sam-

[4]This is less problematic for native Hyd-1 which was prepared at a potential at which the Ni signals are very small.

ples into a quasi-axial spectrum at decreasing temperature is *not* due to another very fast-relaxing $S = 1/2$ species appearing, although the shape and temperature dependence still remains to be understood. Since no simple rhombic g matrix is observed, a hypothesis that is consistent with all extant data is that the reduced medial cluster in the $S = 2$ ground state [202] interacts with the $S = 1/2$ proximal $[4Fe\text{-}3S]^{3+}$ cluster, yielding the 'complex interaction signal'.

8.4 Results (Part II)

Pulsed EPR studies, primarily on native Hyd-1 and the P242C variant, were conducted to probe the following features in the 'low-potential' X-band CW EPR spectra: 1) the unusual shape and temperature dependence of native Hyd-1 spectra compared to the medial cluster variant; 2) the frequency dependence of the observed signals and therefore assignment of intrinsic g values; 3) evidence for non $S = 1/2$ ground state Fe-S clusters. These studies aided the design of further pulsed experiments which could establish the ligand environment of the observed Fe-S cluster(s) to aid its/their assignment.

8.4.1 X-band and W-band field sweeps

The X-band CW measurements of H_2-reduced samples of native Hyd-1 showed a temperature dependent transformation of the Fe-S-cluster signal shape (Fig. 8.10). In two-pulse echo-detected measurements of the same sample (Fig. 8.13), the echo intensity (measured under non-saturating conditions) was found to decay extremely sharply with increasing temperature. At 2.7 K the spectrum is almost axial, as also observed at low temperatures in X-band CW EPR. However, Fig 8.13 shows that at 7 K the signal looks nothing like the corresponding CW spectrum and essentially consists of contributions from the resonator background (mainly Cu^{2+} at this mw frequency); the Fe-S cluster signal decays within 100 ns, the deadtime. Consequently, no clear separation of two species or two spectral components is possible in pulsed measurements through variation of the temperature.

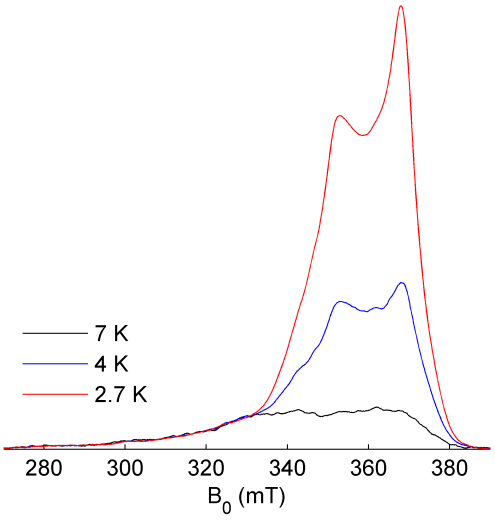


Figure 8.13: **Temperature dependence of H_2-reduced native Hyd-1 X-band two-pulse echo-detected field sweeps.** Measurement conditions: pulse sequence $\pi/2-\tau-\pi-\tau$ - echo, with $\pi/2 = 16$ ns, $\pi = 32$ ns, τ 180 ns; shot repetition time 3 ms (7 K, 4 K), 6 ms (2.7 K); mw frequency 9.738 GHz. Spectra are scaled by the video gain.

Measurements of the spin-spin relaxation time (T_2)[5] at 3 K of reduced native Hyd-1 are shown in Fig. 8.14 (the Hyd-1 P242C trace will be discussed later). ESEEM (Section 2.6.2) modulations from ^{14}N nuclei are largely suppressed when longer pulses are used ($\pi/2 = 40$ ns, black trace). T_2 measurements at 7 K yielded similar traces (not shown). Subsequent field sweeps were therefore recorded with $\pi/2 = 40$ ns to minimise distortions from ^{14}N modulations. As exemplified by the two single exponential fits to the black experimental trace, the spin-spin relaxation of the Fe-S cluster species in reduced native Hyd-1 is biphasic with time constants of approximately 75 ns and 100 ns.

The full field sweep of reduced native Hyd-1 as a function of τ at 2.7 K is depicted in Fig. 8.15 and selected field sweeps are normalised to highlight the change in signal shape with τ. The trend with increasing τ is comparable to that observed with increasing temperature: Short τ values produce an almost axial spectrum where the background contribution is negligible whereas the background becomes comparatively larger as the τ value is increased (despite the high sample concentration). A typical background spectrum

[5]Strictly speaking this is the phase memory time (T_m), see Section 2.6.6.

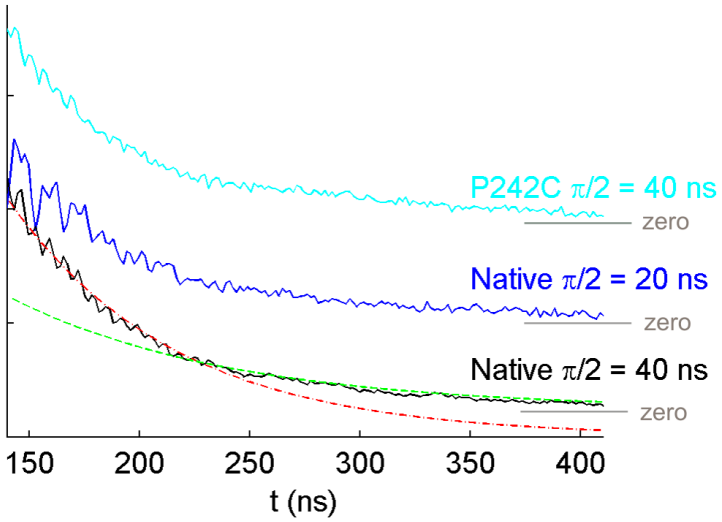


Figure 8.14: **T2 measurements of low-potential native Hyd-1 and the P242C variant at X-band (3 K).** Measurement conditions: shot repetition time 5 ms (all); mw frequency 9.739 GHz (black, blue), 9.747 GHz (cyan); field positions 330 mT (Hyd-1 native), 361 mT (Hyd-1 P242C); pulse sequence $\pi/2 - \tau - \pi - \tau$ - echo where the initial τ is 180 ns and is increased in 8 ns steps and $\pi/2 = 40$ ns, $\pi = 80$ ns (cyan, black) or $\pi/2 = 20$ ns, $\pi = 40$ ns (blue). Dotted lines are single exponential decay fits to the black trace, with T = 75 ns (red) and T = 100 ns (green). Sample concentrations: 555 μM (native Hyd-1), $\approx$ 300 μM (Hyd-1 P242C).

is included in Fig. 8.15 (*right*). The derivative of the summed field sweeps at different τ values are compared to the X-band CW data at the end of this section.

Compared to native Hyd-1, the spin-lattice relaxation time (T_1) is remarkably longer in the reduced medial cluster P242C variant and field sweeps could therefore be recorded at significantly higher temperatures (7 K *vs* 2.7 K). This is in agreement with the lower mw power saturation characteristics at higher temperatures that were required in X-band CW EPR measurements of this variant (see Fig. 8.4). Also, similar to the X-band CW measurements, two-pulse echo-detected field sweeps were found to change little with temperature (not shown) and 7 K was chosen for investigating the effect of τ because at this temperature the echo intensity was sufficiently high to yield a good signal-to-noise ratio without requiring an unmanageable accumulation time (very fast shot repetition times are possible). Interestingly, the T_2 (T_m) traces of this variant were also found to

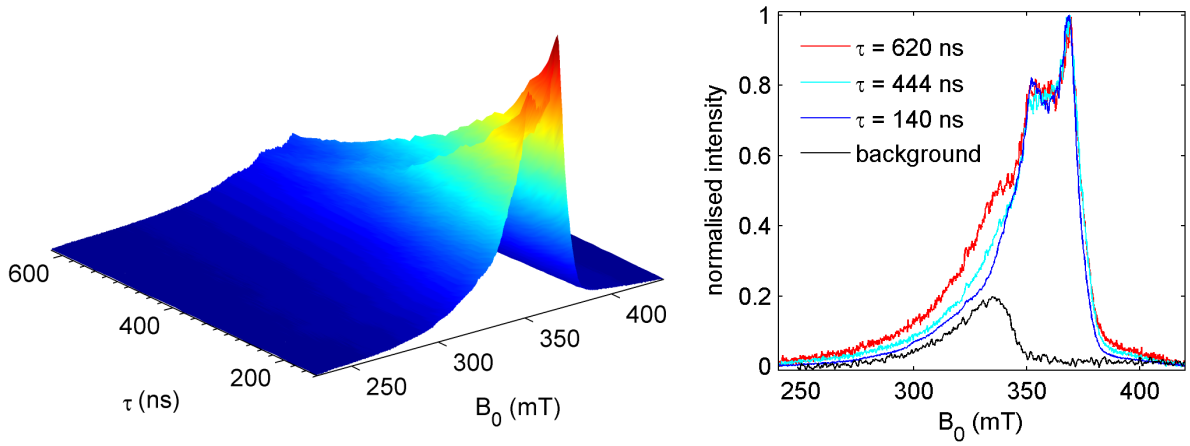


Figure 8.15: **H_2-reduced native Hyd-1 X-band two-pulse echo-detected field sweeps with variable τ at 2.7 K.** Measurement conditions: (native Hyd-1) pulse sequence $\pi/2 - \tau - \pi - \tau$ - echo where τ is varied between 140 ns and 620 ns in 16 ns increments and $\pi/2 = 40$ ns, $\pi = 80$ ns; mw frequency 9.743 GHz; shot repetition time 5 ms; sample concentration 555 μM; potential - 355 mV; (background) $\pi/2$ -τ - π - τ - echo where $\pi/2 = 16$ ns, $\pi = 32$ ns, $\tau = 188$ ns; mw frequency 9.803 GHz; shot repetition time 2 ms.

be biexponential and very similar to those measured for native Hyd-1. A representative trace measured at 7 K is shown in Fig. 8.14. This also argues against the native Hyd-1 spectra arising from two reduced Fe-S cluster species (with different T_2 relaxation times). Two-pulse echo-detected field sweeps of Hyd-1 P242C with variable τ (Fig. 8.16) are consistent with one rhombic g matrix. The origin of the clearly visible modulation of the peak between $\approx$ 320-340 mT is unexplained (and also convoluted by background Cu contributions). The nuclear frequencies could in principle be examined as a function of τ but the two-pulse ESEEM experiment is unsuitable for this purpose because the primary echo decays with the short phase memory time which is very short. A three-pulse ESEEM experiment which is only dependent on T_1 and in which the echo decays with the transverse nuclear relaxation time but not with the phase memory time would be more suitable. The purpose of the experiment chosen here was to establish whether different species (if more than one is present) are apparent at different τ values: This was not found to be the case for either native Hyd-1 or the P242C variant.

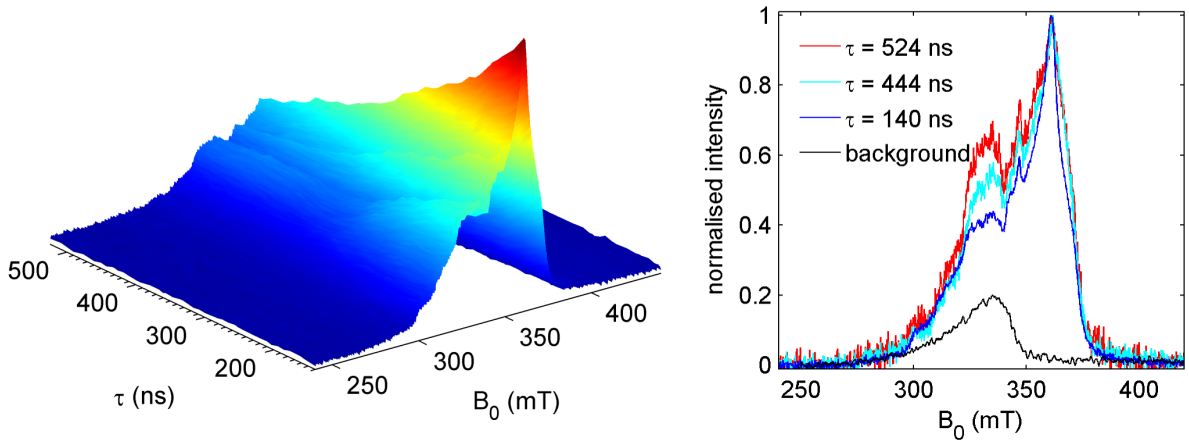


Figure 8.16: **Reduced Hyd-1 P242C X-band two-pulse echo-detected field sweeps with variable τ at 7 K.** Measurement conditions: (Hyd-1 P242C) pulse sequence $\pi/2 - \tau - \pi - \tau$ - echo where τ is varied between 140 ns and 524 ns in 16 ns increments and $\pi/2 = 40$ ns, $\pi = 80$ ns; mw frequency 9.747 GHz; shot repetition time 5 ms; sample concentration ≈ 300 μM; potential - 355 mV; temperature 7 K; (background) $\pi/2$ -τ - π - τ - echo where $\pi/2 = 16$ ns, $\pi = 32$ ns, $\tau = 188$ ns; mw frequency 9.803 GHz; shot repetition time 2 ms; temperature 2.7 K.

W-band two-pulsed echo-detected field sweeps of both reduced native Hyd-1 and Hyd-1 P242C were also conducted to examine the frequency dependence of the Fe-S cluster peaks observed. W-band CW sweeps were attempted but were rather unsuccessful as lines were not well-defined, presumably because the spectra are very broad and the sample concentration is still comparatively low so that detection *via* the modulation amplitude method is poor.

The resonator Mn^{2+} and Cu^{2+} peaks were subtracted from the two-pulse echo detected field sweeps as best as possible (see Section 3.5.3) and the resulting numerical derivative spectra are compared to the CW and pulse X-band spectra in Fig. 8.17 on a g-value scale.

Surprisingly, even at 3 K the peaks observed in reduced native Hyd-1 at W-band can be well-simulated with just *one* rhombic g matrix ($g_{x,y,z} = 2.045, 1.916, 1.865$). This is in contrast with the pulsed X-band spectrum (cyan) that very much resembles that of low-temperature X-band CW spectra (top blue trace, 3.2 K). At higher temperatures the echo intensity at W-band decreased very rapidly, making spectra with good signal-

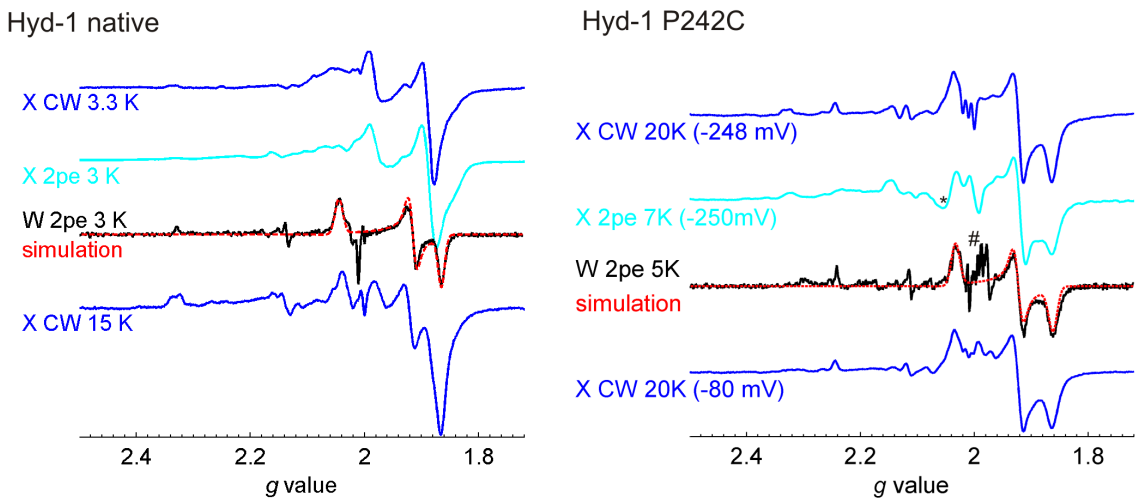


Figure 8.17: **Comparison of X- and W-band field sweeps of low-potential native Hyd-1 and the P242C variant.** 2pe stands for 'two-pulse echo-detected field sweep', 'X' for 'X-band', 'W' for 'W-band'. X-band spectra correspond to measurements previously shown in this Chapter: The X-band CW samples measured at 15 K (native) and 20 K (P242C) are taken from the titration samples in Fig. 8.4; the X-band CW sample at 3.3 K is taken from Fig. 8.10; the 2pe X-band measurements correspond to the numerical first derivatives summed over all τ values of the measurements shown in Figures 8.15 and 8.16. The Cu^{2+} background peak is indicated with an asterisk and the Mn^{2+} background peaks are marked with # (see Section 3.5.3). W-band spectra (black) result from background subtracted numerical derivatives of absorption spectra. W-band sample and background measurement conditions: (native) $\pi/2 = 32$ ns, $\tau = 180$ ns, 93.839 GHz, shot repetition time 5 μs, 2-step phase cycle; (P242C) see Fig. 3.8. W-band sample concentrations: (native) 555 μM, (P242C) $\approx$ 300 μM. Adapted from ref. [270].

to-noise ratio more time-consuming to record. However, the shape of the field sweep did not change at 8.5 K. Pandelia *et al.* simulated Q-band measurements of the reduced *Aa* Hase I hydrogenase with *two* uncoupled 4Fe clusters, concluding that the medial $S = 2$ $[3Fe\text{-}4S]^0$ spin relaxes too fast to be detectable in pulsed measurements [16]. While Q-band measurements for reduced *E. coli* Hyd-1 were not available in this study, they should be very similar to those of *Aa* Hase I, because of the similarity in the X-band CW spectra of the two enzymes (as well as those of *Re*-MBH [82, 88]). The W-band measurement of reduced *E. coli* Hyd-1 is not consistent with the presence of both the reduced proximal and distal clusters in low-potential samples of O_2-tolerant hydrogenases.

The Ni species present in Fig. 8.17 is Ni-L* and the g_x and g_y values are consistent with those observed in X-band CW spectra (bottom blue trace, 15 K); the g_z peak is

masked under the Fe-S cluster peaks. The echo-detected pulse X-band and W-band measurements result from samples made from the same enzyme batch reduced under hydrogen to -355 mV. As expected, the cyan trace (from the pulsed X-band sample) therefore contains very little Ni-L*. The presence of clear Ni-L* signals in the W-band measurement (black trace) indicates that the potential of the sample is probably close to -200 mV (the potential at which Ni-L* is at or close to maximum intensity, Fig. 8.4), rather than the nominal value of -355 mV; *i.e.* the potential increased during sample preparation. However, even if the potential is $\approx$ 150 mV higher than anticipated, the [4Fe-3S] cluster is still fully reduced (see Fig. 8.5). Usefully, the W-band signals of Ni-L* confirm further that the splitting of the g_x peak at X-band is due to a dipolar interaction with the reduced proximal cluster since it is obscured by the much larger linewidths at W-band frequencies. The peak at $g = 2.01$ (also observed in P242C Hyd-1 W-band spectra) is currently unexplained; it is highly unlikely to result from a Ni species since only Ni-L* is present and X-band CW measurements at high temperatures have shown that Ni-L* $g_z = 2.05$.

The Fe-S cluster peaks in W-band measurements of the Hyd-1 P242C variant can also be simulated with a single rhombic g matrix ($g_{x,y,z}$ = 2.035, 1.923, 1.862), whose g values differ slightly from those in native Hyd-1 ($g_{x,y,z}$ = 2.045, 1.916, 1.865). Due to the increased Mn^{2+} contribution in the background at the time at which this sample was measured (compared to native Hyd-1), the $g = 2$ region is masked by the manganese hyperfine peaks. An additional derivative peak is probably present at $g = 1.976$ (masked by the Mn^{2+} background signals) and is currently unexplained. However, it is likely to arise from high-potential species as peaks in this region are also observed in X-band CW measurements of higher potential samples (Fig. 8.4). The observed Ni signals again indicate that the potential of the W-band sample is higher than the nominal -250 mV because Ni-B and Ni-X are present, rather than Ni-L* and Ni-X which would be expected at -250 mV. Indeed Ni-L* is seen in the pulsed X-band sample (cyan), and the corresponding X-band CW spectrum is given for comparison (top blue trace). The Cu^{2+} background contributes

significantly to the pulsed X-band spectrum, as can be seen from the characteristic peak at $g = 2.07$ (marked with an asterisk). Similar to the native Hyd-1 sample, the variant W-band sample also appears to be at a potential $\approx$ 150-170 mV more positive than the pulse X-band sample made from the same enzyme solution. However, the Nernst plots indicate that the Fe-S cluster species are fully reduced even at -80 mV (Fig. 8.5). The exchange interaction between Ni-B and the reduced proximal cluster observed clearly at X-band is too small to be apparent at W-band since the linewidth is dominated by g strain and Ni-B appears as 'unsplit'.

Pulsed measurements in the $g = 2$ region, in particular measurements at W-band, further support the presence of only the proximal or only the distal cluster in the $S = 1/2$ ground state in both the native enzyme and the medial cluster variant.

8.4.2 Wide X-band field sweeps of the proximal cluster variants

To investigate the presence of peaks arising from higher spin states of reduced Fe-S clusters, pulsed EPR field sweeps over a wide field range were also conducted for low-potential samples of native Hyd-1 and the medial and proximal cluster variants.

In all reduced Hyd-1 enzymes from several different sample preparations, broad peaks are observed up to 800 mT at low temperatures. A summary of the two-pulse echo-detected field sweeps at 2.7 K at four different τ values between 140 and 188 ns is given in Fig. 8.18. As exemplified by the C19G/C120G variant, for which no $S = 1/2$ signals are detected, the echo intensity at $g = 1.88$ (*i.e.* in the Fe-S cluster region of the spectrum at 370 mT) increases exponentially as the temperatures is lowered (Fig. 8.19). The spin-lattice relaxation time of these $S > 1/2$ species is less than 2 ms at 2.7 K - compared to $\approx$ 5 ms for the $S = 1/2$ species at 3 K in native Hyd-1 and 7 K in Hyd-1 P242C. All measurements in Fig. 8.18 were measured under the same conditions to compare signals arising from higher spin states directly. The $S = 1/2$ peaks in the $g = 2$ region for native Hyd-1 and Hyd-1 P242C were therefore (deliberately) heavily saturated and cut off. Spectra in which these peaks are not cut off are given in Appendix 10.5 Fig. 10.6.

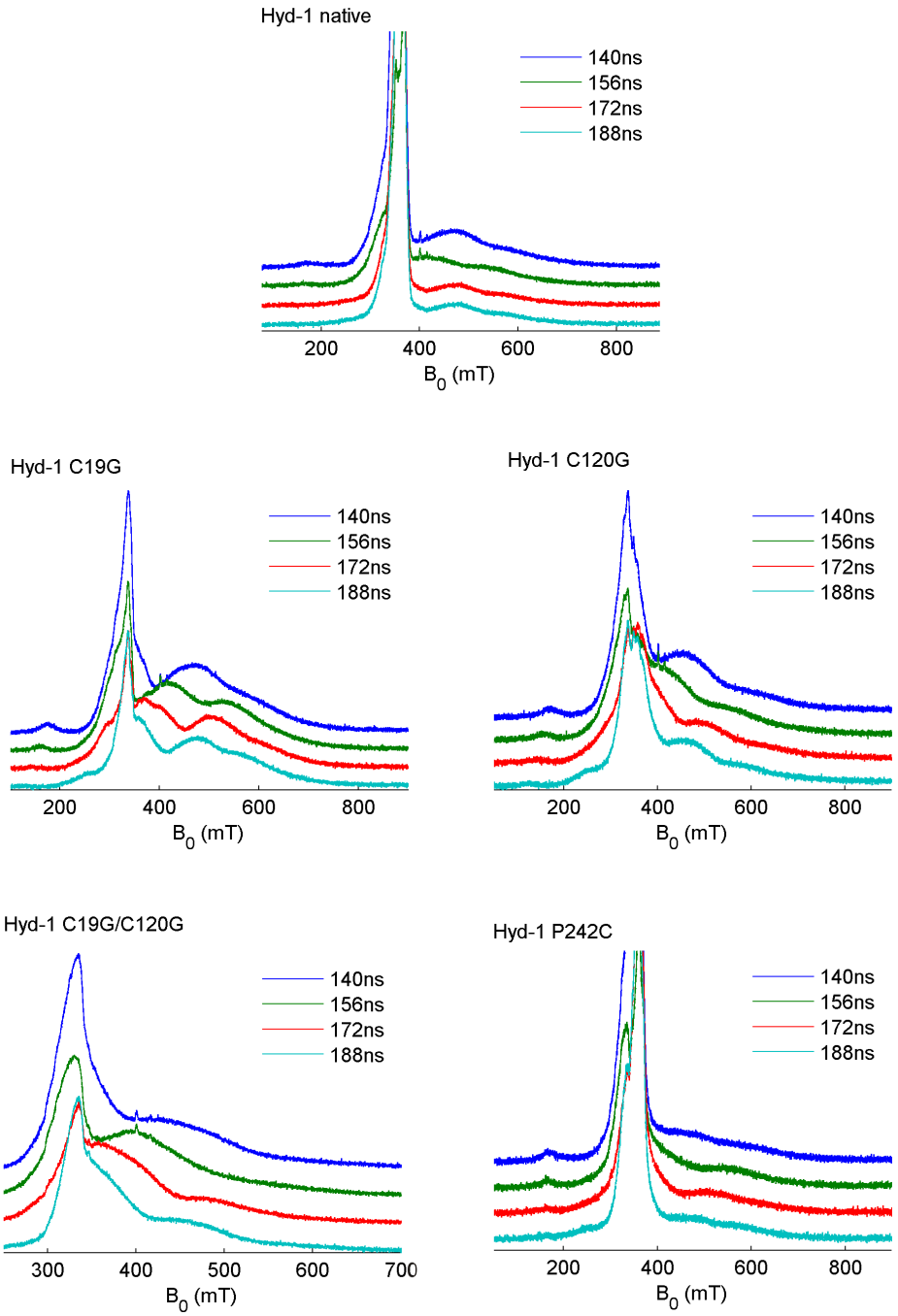


Figure 8.18: **X-band two-pulse echo-detected wide field sweeps of native Hyd-1 and variants (2.7 K).** Sample potentials: −355 mV (native, C19G, C120G, H_2-reduced), −200 mV (C19G/C120G, dithionite-reduced), −250 mV (P242C, dithionite-reduced). Measurement conditions: pulse sequence $\pi/2$ - τ - π - τ - echo where τ is varied between 140 ns and 188 ns in 16 ns increments and $\pi/2$ = 16 ns, π = 32 ns; mw frequency 9.740 GHz (native, C19G, C120G), 9.745 GHz (P242C), 9.740 GHz (C19G/C120G); shot repetition time 2 ms. The $g = 2$ region in the native Hyd-1 and Hyd-1 P242C spectra was cut off because these peaks were deliberately saturated (see text). Adapted from ref. [270].

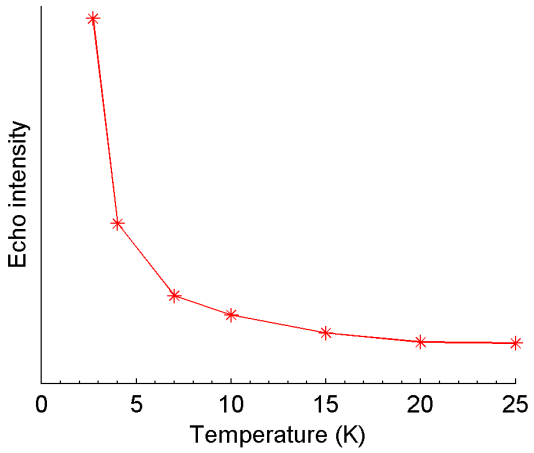


Figure 8.19: **Echo intensity of low-potential Hyd-1 C19G/C120G as a function of temperature (X-band).** Field sweeps were recorded over the range 369.5-370.5 mT (g = 1.88) at 2.7, 4, 5, 10, 15, 20 and 25 K. The average intensity (corresponding to the average echo intensity) was plotted as a function of the temperature. Measurement conditions: mw frequency 9.740 GHz; shot repetition time 4 ms; pulse sequence $\pi/2 - \tau - \pi - \tau$ - echo with $\pi/2$ = 16 ns and τ = 180 ns.

Small peaks between g = 5.5 (τ = 188 ns, 127 mT) and g = 4 (τ = 140 ns, 174 mT) are present in all spectra,[6] and since peaks at around g = 5 were shown to be indicative of $S = 3/2$ species [298], this indicates that $S = 3/2$ species are present in these reduced Hyd-1 samples. Given that the low-field peaks are also present in Hyd-1 P242C, they result at least in part from the reduced distal cluster. The shift in the low and high field peaks with τ may arise from the ^{14}N nuclear modulations (which are very pronounced especially when short pulses are employed). Strong pulses were required to obtain a significant signal-to-noise ratio for these field sweeps. Quantification of a [4Fe-4S]$^{+}$ cluster with $S = 3/2$ ground state is difficult. Lanciano *et al.* [317] developed a method in which the temperature dependence of the ratio of the area under low-field Kramers doublets in the FS0 center of the *E. coli* NarGHI nitrate reductase was used to determine the percentage of the cluster in the $S = 3/2$ ground state. However, given the low signal-to-noise ratio already at 2.7 K in the hydrogenase samples studied here, this method is not feasible. The signals are likely to result from more than one $S > 1/2$ species, complicating the analysis

[6]The field sweep range for the C19G/C120G sample was narrower and did not include this region.

further. A quantification of the higher spin state peaks was therefore not attempted. However, even in the absence of a definitive assignment, the broad peaks observed over an extremely wide field range in pulse EPR measurements are inexplicable by $S = 1/2$ species and provide further evidence for the hypothesis that the distal cluster is in a higher spin state. While X-band CW measurements did not reveal peaks that can be attributed to $S = 3/2$ states in low potential samples,[7] the low-temperature pulsed measurements do indicate that at least some of the reduced [4Fe-4S]/[4Fe-3S] clusters are present in this ground state.

8.4.3 There is no direct evidence for the reduced distal cluster contributing to the low-potential Fe-S spectrum

All evidence so far suggests that the reduced proximal but not the distal cluster contributes the 'complex interaction signal' observed at low potentials in the $g = 2$ region of CW EPR spectra of native Hyd-1 (and other O_2-tolerant [NiFe]-hydrogenases [16, 82, 84, 88]). Furthermore it appears that the proximal cluster is solely responsible for the rhombic spectrum observed in Hyd-1 P242C. Like all [NiFe]-hydrogenases crystallised so far, the distal cluster in *E. coli* Hyd-1 is coordinated by three Cys residues and one His residue (Section 1.2.2). If the reduced distal cluster has a $S = 1/2$ ground state, it ought to be possible to detect the directly coordinating nitrogen *via* HYSCORE (Section 2.6.3) or ENDOR (Section 2.6.4) because its coupling is expected to be anisotropic and much stronger than that of a backbone nitrogen to the electron spin. Indeed, this was shown to be the case in two recent studies of [4Fe-4S] clusters with directly ligating nitrogen atoms: Wang *et al.* [293] investigated the inhibitor binding of pyridine derivatives to the [4Fe-4S] protein *A. aeolicus* IspH (LytB) *via* HYSCORE and showed that signals in the $(-,+)$ quadrant (^{14}N single and double quantum transitions) arise from the pyridine derivative directly binding to the [4Fe-4S] cluster rather than from any (more remote)

[7] these may be undetectable due to the modulation amplitude detection method, similar to the lack of clear Fe-S cluster signals in W-band CW measurements

protein residues; Lees *et al.* [303] used ENDOR to show that guanine binds to the [4Fe-4S] cluster II of the S-Adenosylmethionine-Dependent Enzyme MoaA *via* N1 of the purine ring. The directly coordinating His nitrogen in Rieske-type [2Fe-2S] proteins [294] and ferric heme proteins [295, 296] were also shown to result in single and double-quantum cross-peaks in the (−,+) quadrant of HYSCORE measurements. Peaks in the (−,+) quadrant of HYSCORE spectra indicative of strong coupling (large A_{iso} of ^{14}N) appear to be present in systems containing Fe−N bonds in general and are therefore expected to be visible in HYSCORE measurements of reduced native Hyd-1 and Hyd-1 P242C provided the distal cluster contributes to the observed Fe-S cluster signals. Furthermore, the Fe−N bond in the proximal [4Fe-3S]$^{5+}$ cluster could be detected *via* HYSCORE (strong ^{14}N peaks in the (−,+) quadrant) especially clearly in the P242C variant, as shown in Chapter 7.

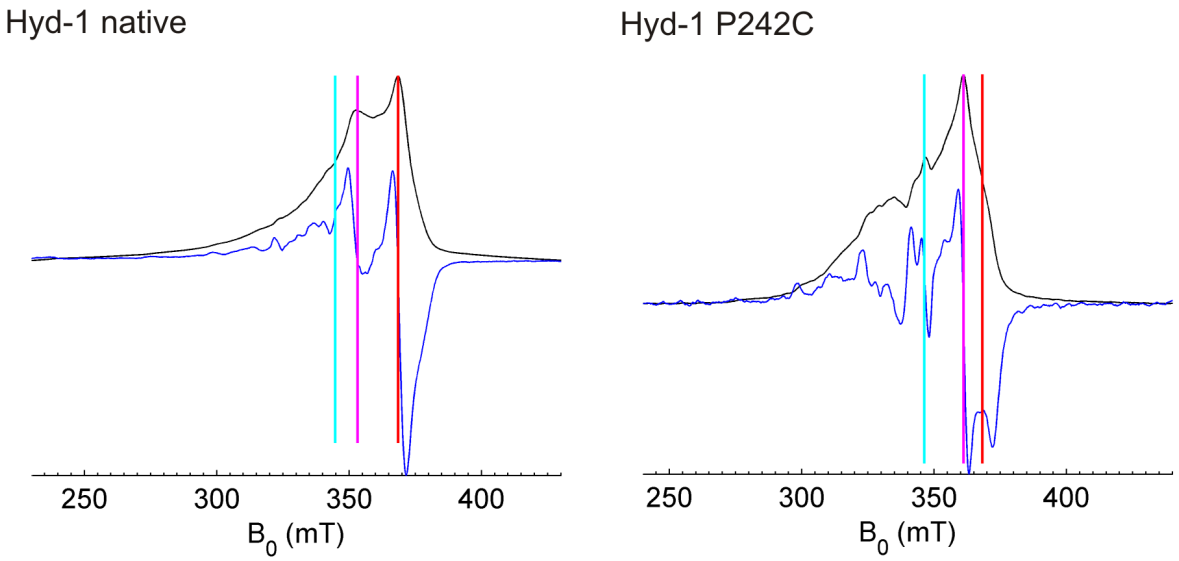


Figure 8.20: **X-band two-pulse echo-detected field sweeps of native Hyd-1 and Hyd-1 P242C poised at low potential: HYSCORE field positions.** Measurement conditions: (Hyd-1 native) $\pi/2 = 40$ ns, $\pi = 80$ ns, τ was varied from 140 to 524 ns in 16 ns increments, 3 K, shot repetition time 5 ms, 9.743 GHz; (Hyd-1 P242C) $\pi/2 = 40$ ns, $\pi = 80$ ns, τ was varied from 140 to 620 ns in 16 ns increments, 7 K, shot repetition time 5 μs, 9.747 GHz. The field sweeps shown are summed over all τ values and included at two-step phase cycle. The numerical first derivatives of the field sweep spectra (black) are given (blue). Vertical lines indicate the field positions of the HYSCORE experiments in Figures 8.21 and 8.22.

The field positions at which HYSCORE spectra were recorded are indicated on the field sweep spectra of native Hyd-1 and Hyd-1 P242C (summed over many τ values) in Fig. 8.20. Because of the occurrence of *blind spots* in the HYSCORE experiment (inherent to all pulse EPR experiments based on the nuclear coherence generator $\pi/2$ - τ - $\pi/2$) [111] spectra with different τ values have to be recorded. Following the field sweep experiments described in Section 8.4.1, the temperatures chosen for the HYSCORE experiments were 2.7 K and 7 K for the native and P242C enzymes, respectively. A summary of the typical HYSCORE spectra obtained is given in Figures 8.21 and 8.22; the remaining set is in Appendix 10.5. In both enzymes, peaks are only visible in the (+,+) quadrant (reflecting weakly coupled nuclear spins, Section 2.6.3). The blue and red lines in the (−,+) quadrant correspond to the approximate single and double-quantum transition cross-peak positions, respectively, that would be expected from a strongly coupled ^{14}N. Clearly, unlike the above mentioned examples of HYSCORE measurements containing Fe−N bonds, no peaks are observed at any field position and any τ value in reduced native and medial cluster variant Hyd-1 samples. The peaks around 14-15 MHz (depending on the field position) in the (+,+) quadrant correspond to couplings to the many nearby protons. The peaks centred at $\approx$ +4 MHz (A_{iso} = 0.9 MHz, e^2qQ/h = 3.25 MHz and A_{iso} = 0.9 MHz, e^2qQ/h = 3.8 MHz, simulations are included in 8.23) are the ^{14}N double quantum transitions of the protein backbone. Wang *et al.* [293] observed these in the inhibited [4Fe-4S] *A. aeolicus* protein *in addition* to the single and double quantum transitions in the (−,+) quadrant. The modulations from these backbone nitrogens is rather strong and could in principle mask that from a directly coordinating N atom. Measurements with τ values that result in blind spots ($A_{blind} = \frac{n}{\tau}$ where n = 1,2,3...) at the backbone nitrogen frequencies were therefore also performed (see Appendix 10.5) but no peaks became apparent in the (−,+) quadrant either. Even in experiments with very long accumulation times (12 h) no additional peaks appeared out of the noise. The HYSCORE experiments therefore provide no evidence for a directly coordinating nitrogen atom to the Fe-S cluster that is responsible for the signals observed in the $g = 2$ region in reduced native Hyd-1

and Hyd-1 P242C.

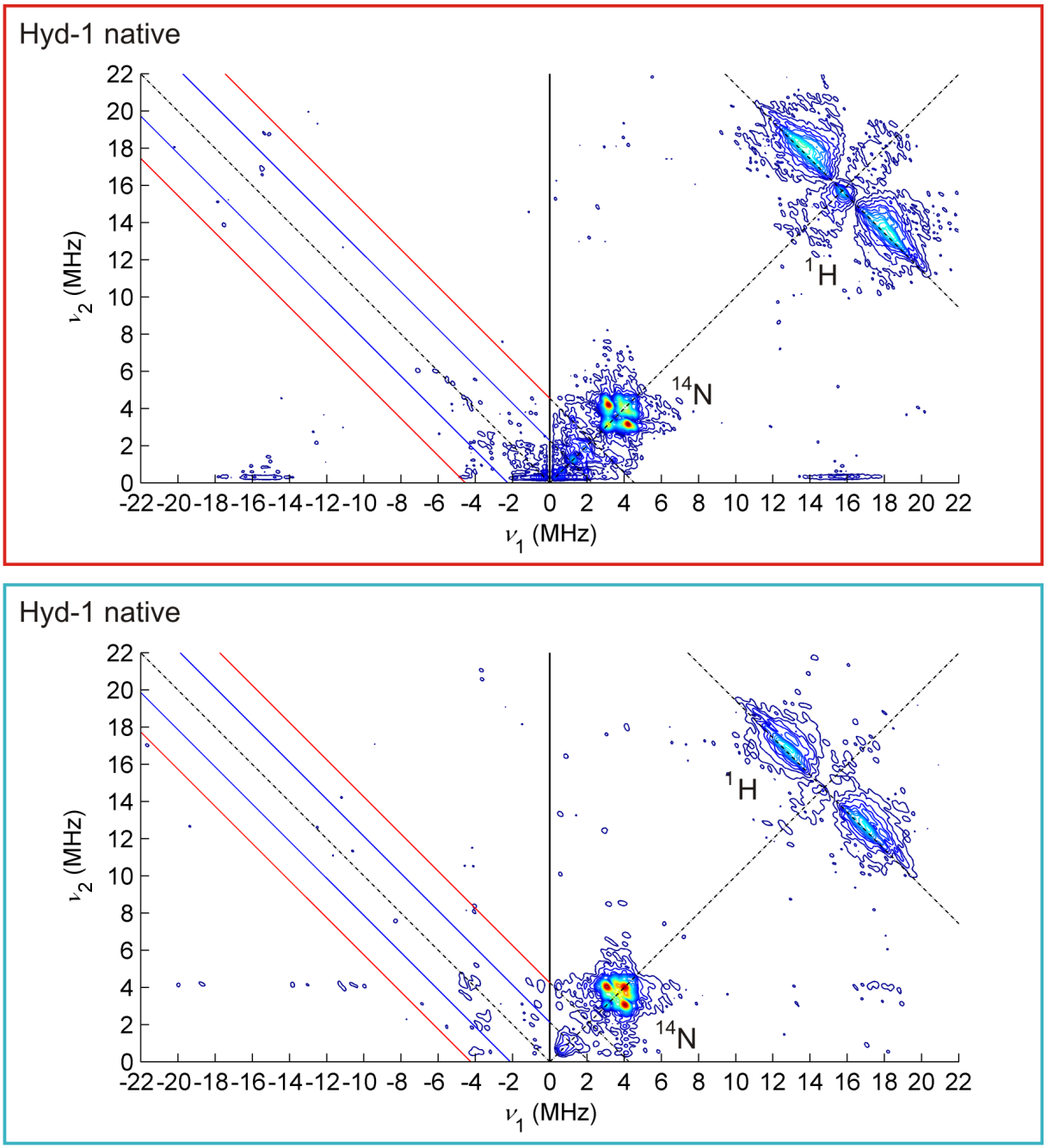


Figure 8.21: **X-band HYSCORE spectra of H_2-reduced native Hyd-1 (- 355 mV).** Measurement conditions: $\pi/2 = 16$ ns, $\pi = 16$ ns, 2.7 K, shot repetition time 5 ms, 150 points, 8-step phase cycle, (*Top*): 368.4 mT, $\tau = 112$ ns, 9.738 GHz, (*Bottom*): 344.7 mT, $\tau = 120$ ns, 9.738 GHz. The coloured boxes refer to the field positions indicated with similarly coloured lines in Fig. 8.20 (*left*). Sample concentration 555 μM.

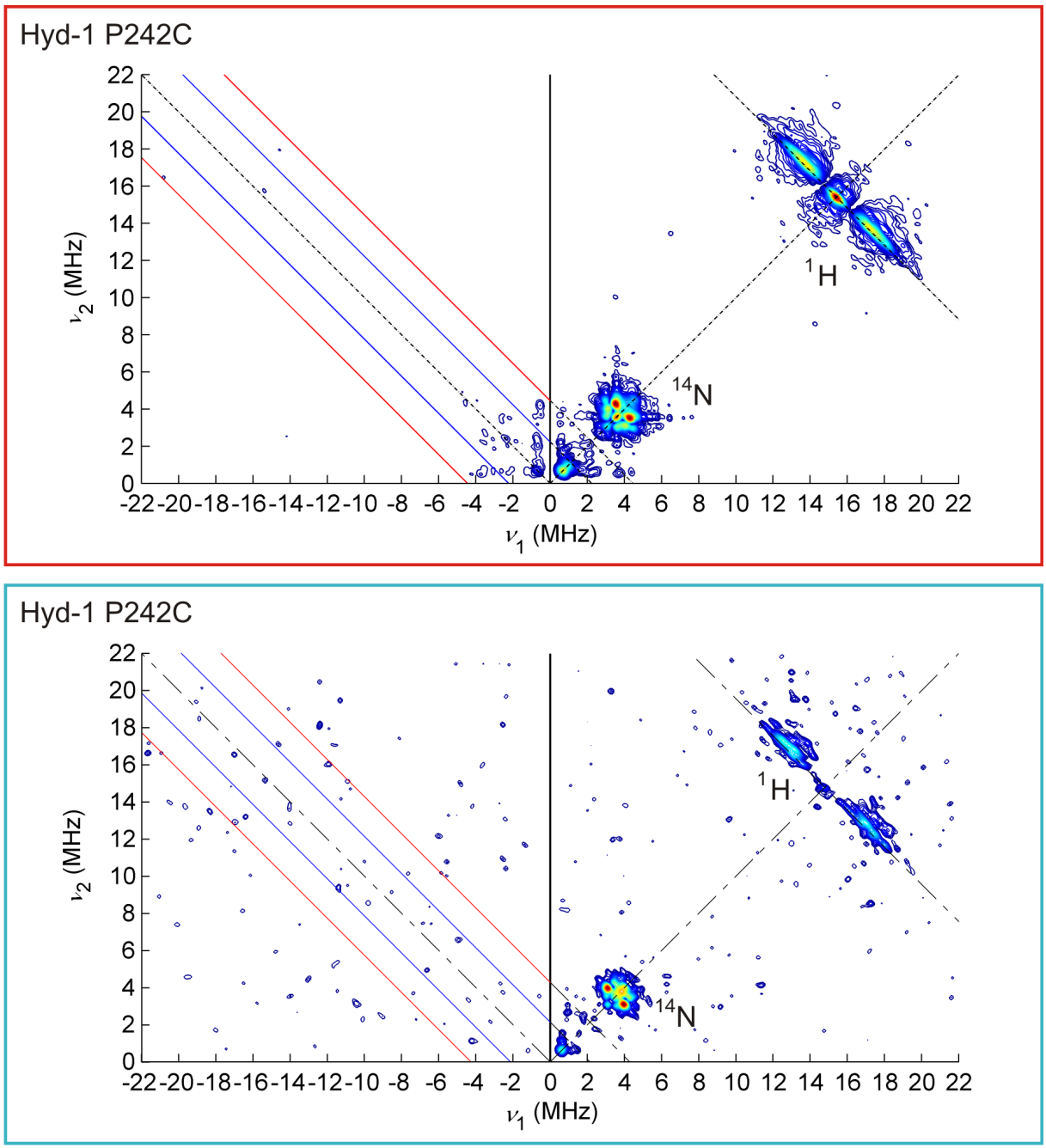


Figure 8.22: **X-band HYSCORE spectra of reduced Hyd-1 P242C (- 250 mV).** Measurement conditions: $\pi/2 = 16$ ns, $\pi = 16$ ns, 7 K, shot repetition time 5 ms, 150 points, 8-step phase cycle, (*Top*): 368.2 mT, $\tau = 116$ ns, 9.746 GHz, (*Bottom*): 346.2 mT, $\tau = 120$ ns, 9.746 GHz. The coloured boxes refer to the field positions indicated with similarly coloured lines in Fig. 8.20 (*right*). Sample concentration approximately 300 μM.

Because the ^{14}N peaks observed in the (+,+) quadrant are isotropic (the dipolar contribution is expected to be small because the gyromagnetic ratio of ^{14}N is small), they are expected to arise from spin density delocalisation through bonds (rather than through space). They must also arise from coupling to the observed $S = 1/2$ species, which appears to be the proximal [4Fe-3S]$^{3+}$ cluster. The directly ligating amino acids of the proximal cluster are all cysteines and the next nearest ligands do not have nitrogen-containing side-chains. The observed peaks therefore most certainly result mainly from the backbone nitrogens. Simulations of the two sets of ^{14}N double-quantum transitions at three different field positions, together with the experimental spectra of both enzymes (zoomed to the low frequency region), are shown in Fig. 8.23. The simulation parameters (A_{iso} = 0.9 MHz, e^2qQ/h = 3.25 MHz, η = 0.45; A_{iso} = 0.9 MHz, e^2qQ/h = 3.8 MHz, η = 0.45), where the η value is tentative (in the absence of a more extensive set of data at different field positions), are in excellent agreement with a general trend in the combination of e^2qQ/h and η reported for backbone ^{14}N couplings [318, 319]. It is not clear why *two* slightly different sets of backbone nitrogen couplings are observed but neither set can account for a directly ligating histidine bonding through N(δ). Even the more weakly interacting N(δ) of a histidine ligand with a quinone radical in photosystem II [318] (weaker compared to the directly bonding N(δ) of the ligating His in the distal cluster of hydrogenases) was found to have very different nuclear quadrupole parameters (e^2qQ/h = 1.47-1.58 and η = 0.71-0.78, depending on pH) to those obtained here. In the example in the literature which is most similar to the histidine-coordinated distal [4Fe-4S]$^{+}$ cluster in hydrogenases, *i.e.* a pyridine derivative ligating a [4Fe-4S]$^{+}$ cluster [293], the HYSCORE spectra show the strongly coupled nitrogen peaks in the (−,+) quadrant (which are not observed here), but also exhibit backbone nitrogen peaks that are very similar to those in Fig. 8.23[8]. Furthermore, HYSCORE spectra of the reduced *D. vulgaris* hydrogenase [260], also measured at field positions where the Fe-S cluster transitions are resonant, resemble those in Fig. 8.23. However, the authors attributed

[8]No nuclear quadrupole parameters for the backbone nitrogen peaks are provided in the paper by Wang *et al.* [293]

the origin of the observed ^{14}N peaks to His235 (*D. vulgaris* numbering) coordinating the proximal cluster and the His188 coordinating the distal cluster [260]; this is a misassignment because the proximal cluster is not coordinated by a histidine residue.

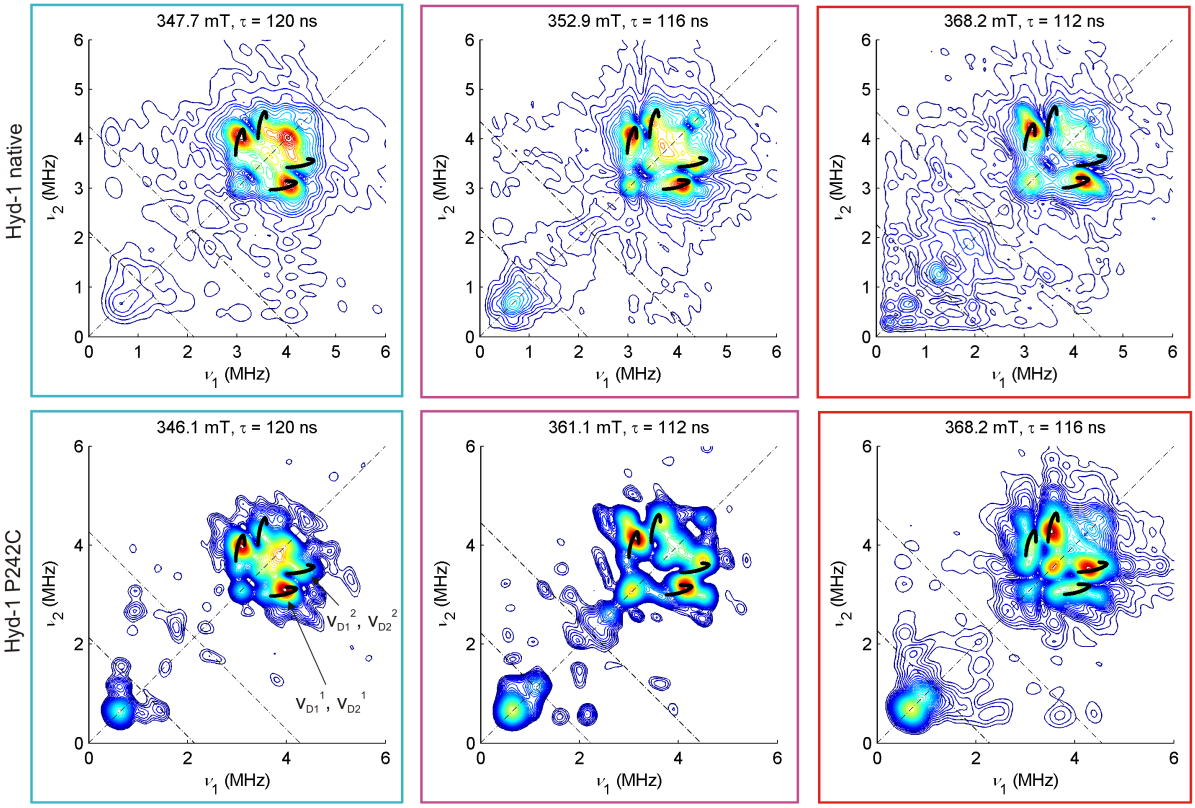


Figure 8.23: **X-band HYSCORE spectra in reduced native Hyd-1 and Hyd-1 P242C and simulations of ^{14}N peaks.** For measurements conditions of the experimental HYSCORE spectra, see Figures 8.21, 8.22, 10.7 and 10.9. The field positions are indicated in the field sweeps of Fig. 8.20. For the simulations, the following parameters were used for the two sets of ^{14}N peaks (labelled with arrows): (1) $A_{iso} = 0.9$ MHz, $e^2qQ/h = 3.25$ MHz, $\eta = 0.45$; (2) $A_{iso} = 0.9$ MHz, $e^2qQ/h = 3.8$ MHz, $\eta = 0.45$. The η values are tentative only. The coloured boxes refer to the field positions indicated with similarly coloured lines in Fig. 8.20.

For completeness, ENDOR (Section 2.6.4) measurements were also conducted, even though it is unlikely for the coupling to be so large or isotropic so that it would remain undetected in HYSCORE experiments. A Davies ENDOR experiment was attempted at 368.4 mT on the native Hyd-1 sample at 2.7 K. However, the initial π pulse could not invert the echo and nothing was detected in the ENDOR trace after 1.5 h of measurement. The failure to invert the magnetisation could in principle result from the T_1 time being

too short. However, T_1 at 2.7 K for the reduced native Hyd-1 sample is approximately 5 ms and thus a more likely explanation is spectral spin diffusion since the local spin concentration in the sample is high: The spins excited by the pulse (with resonance frequencies near ω_{mw}) mix with the (many) spins not excited by the pulse *via* the flip-flop term of the dipolar coupling Hamiltonian [111]. Although Davies ENDOR is often the ENDOR method of choice when the couplings are large, Mims ENDOR is more sensitive (particularly for small hyperfine couplings when the phase memory time is sufficiently long so that τ can be optimally adjusted) [126] and a so Mims ENDOR experiment at 368.2 mT on the native Hyd-1 sample at 2.7 K was also measured, but no strongly coupled nitrogen signal could be detected in this experiment either (not shown).

HYSCORE measurements were also conducted on the H_2-reduced native Hyd-1 and C19G variant samples at high field (500 mT) where signals from non $S = 1/2$ ground state Fe-S clusters are observed (see Fig. 8.18). Because of the high nuclear Zeeman frequency at this field position, the backbone nitrogen peaks are most likely weaker compared to measurements at lower field values — the contrary might be expected for a strongly coupled nitrogen even though it is difficult to predict the appearance of the HYSCORE spectra if the spin manifold is unknown. There is no evidence for the presence of a strongly coupled nitrogen in the spectra in Fig. 8.24, which would have allowed unambiguous assignment of the broad features observed at high fields to the distal cluster. However, the presence of backbone ^{14}N peaks in the (+,+) quadrant at 500 mT, well out of the field range of a 'normal' $S = 1/2$ ground state $[4Fe\text{-}4S]^+$ cluster, does confirm that the broad high-field peaks (see also Fig. 8.18) do indeed arise from the protein. Three-pulse ESEEM measurements were initially taken to ensure that the HYSCORE spectra were not measured with an unfavourable τ value (*i.e.* peaks hidden under blind spots). A three-pulse ESEEM measurement at 500 mT with $\tau = 108$ ns, at the same field position and with the same τ value as the HYSCORE measurements in Fig. 8.24, yielded similar results to those conducted at 400, 450 and 600 mT with different τ values (spectra not shown).

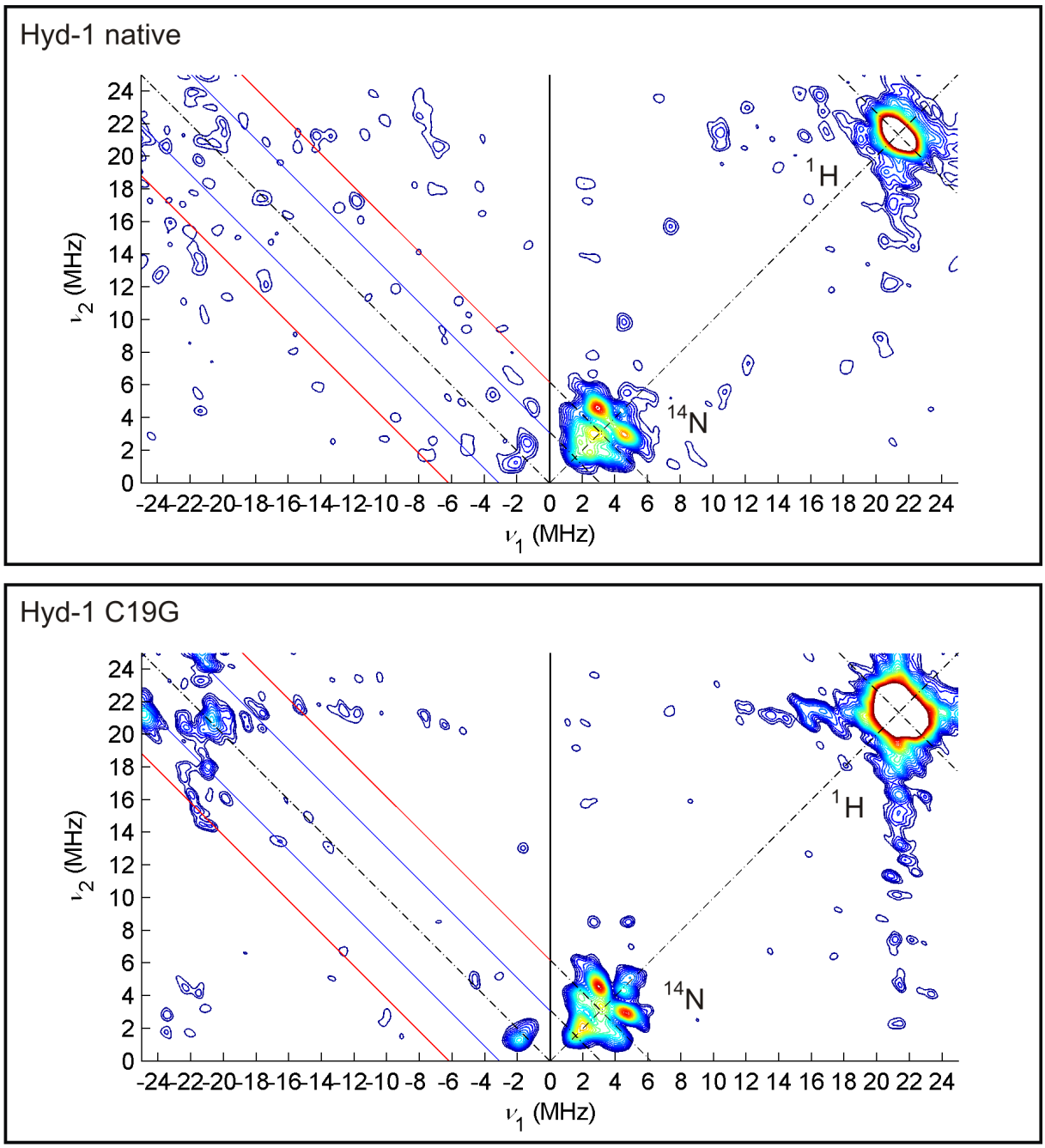


Figure 8.24: **X-band HYSCORE spectra of reduced native Hyd-1 and Hyd-1 C19G at 500 mT (2.7 K).** Measurement conditions: $\pi/2 = 16$ ns, $\pi = 8$ ns, 2.7 K, shot repetition time 0.5 ms, 80 points, 8-step phase cycle, 500.0 mT, $\tau = 108$ ns, 9.723 GHz (native) or 9.718 GHz (C19G). See to Fig. 8.18 for field sweeps of these samples at 2.7 K. The proton peaks were cut off to allow better visualisation of the ^{14}N peaks. Adapted from ref. [270].

8.4.4 Are there dipolar interactions between the proximal and distal clusters?

In native *E. coli* Hyd-1, the edge-to-edge distance between the proximal and distal clusters is 24 Å (Fig. 8.25). If both clusters are in the $S = 1/2$ ground state in low-potential sam-

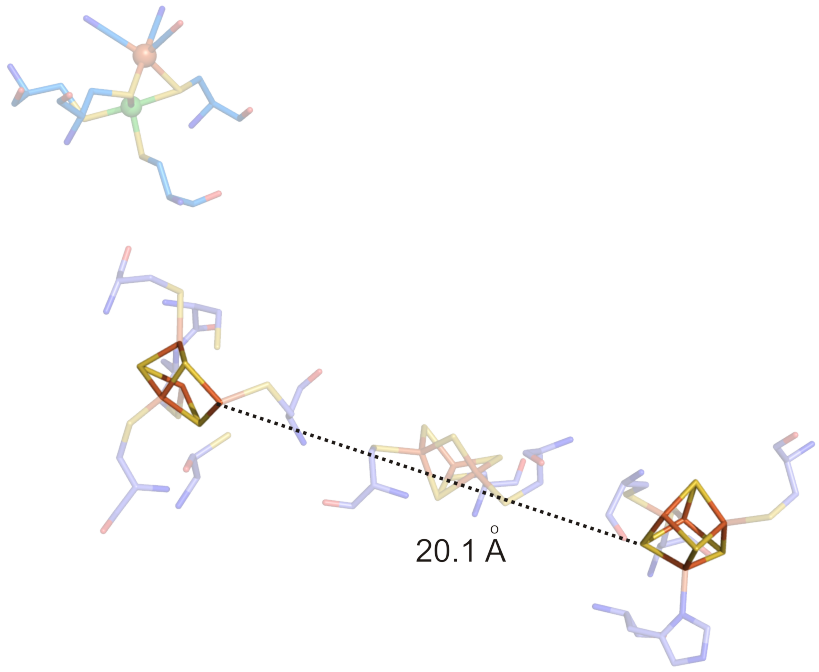


Figure 8.25: **Distance between the proximal and distal clusters in *E. coli* Hyd-1.** The shortest edge-to-edge distance is indicated; the longest edge-to-edge distance is 27.6 Å (not labelled).

ples of Hyd-1, it should therefore be possible to measure the dipolar interaction between them using the DEER experiment (Section 2.6.5). Although the analysis of DEER traces resulting from dipolar interactions between Fe-S clusters is complicated (see Section 4.2), the mere observation of a modulation could only result from both the proximal and distal clusters with $S = 1/2$ ground states. The distance between the proximal and reduced clusters is in the ideal range for DEER experiments. In NADH:ubiquinone oxidoreductase (complex I), the DEER traces almost exclusively reflected the dipolar interaction between the N2 and N4 clusters which are 22.9 Å apart (shortest edge-to-edge distance in *T. thermophilus* complex I), even though other clusters are also reduced and in the

$S = 1/2$ ground state (see Chapter 4).

No DEER modulation could be observed in experiments at different field positions and pump/detection pulse frequencies (spectra not shown, see Section 8.2 for measurement details). It is unlikely that no DEER effect was seen because the pump pulse was not resonant with the pump spin spectrum or because an insufficient number of spins was excited by the detection pulse sequence in *all* the experiments carried out. Because the reduced medial [3Fe-4S]^0 cluster could have a dramatic effect on the relaxation rates, 3-pulse DEER experiments were also carried out, but these also yielded traces with a simple exponential decay and no modulation. The failure to detect any dipolar interaction therefore also supports the presence of only one reduced Fe-S $S = 1/2$ cluster.

8.5 Discussion and further work

In summary, the above results have shown that only *one* reduced Fe-S cluster is EPR-visible in low-potential samples of O_2-tolerant [NiFe]-hydrogenases:

1. Both native Hyd-1 and the P242C variant CW EPR spectra from low potential samples integrate to only one spin per molecule of enzyme in the Fe-S cluster $g = 2$ region across the whole temperature range over which Fe-S cluster signals are visible.

2. Potentiometric titrations of native Hyd-1 and the medial cluster P242C variant exhibit only one redox transition at low potentials. The possibility of one [4Fe-4S]$^{2+/+}$ transition and one [4Fe-3S]$^{3+/4+}$ transition with exactly the same midpoint potential is impossible because of point 1.

3. A simple rhombic g matrix is observed in all low-potential P242C variant EPR spectra. A simple rhombic g matrix is also observed for reduced native Hyd-1 at W-band.

4. No dipolar interaction was observed between the proximal and distal clusters even though these are at an ideal distance for the DEER experiment.

Additionally, the following points indicate that the proximal cluster has a $S = 1/2$ ground state but that the distal cluster has higher spin ground state:

5. No $S = 1/2$ Fe-S signals are observed in the reduced proximal cluster variants C19G and C19G/C120G, and only very small signals are observed in the C120G variant. This contrasts with EPR spectra of the reduced medial cluster variant, where a rhombic EPR signal amounts to one spin per molecule of enzyme.

6. Exchange and dipolar interactions with Ni-A/Ni-B and Ni-L* respectively are detectable and of a magnitude which is only consistent with arising from the proximal but not the distal cluster.

7. HYSCORE experiments could not detect a directly coordinating nitrogen strongly coupling to the observed $S = 1/2$ ground state cluster, as would be expected if the $S = 1/2$ cluster was the His-ligated distal cluster.

8. Signals from higher spin states could be detected in pulse EPR field sweeps in native Hyd-1 and the proximal and medial cluster variants.

The X-band CW spectra at various potentials for the *Aa* Hase I [16], *Re*-MBH [82, 88], *E. coli* Hyd-1 and *Salmonella* Hyd-5 enzymes are strikingly similar, and the C19G/C120G variants of *Re*-MBH [88] and *E. coli* Hyd-1 have almost identical spectra (Section 8.3.1). This may be expected since sequence alignments and crystal structures of the as-isolated enzymes show that the cofactor arrangement and their ligation is highly conserved (see Fig. 10.10 in Appendix 10.5). The origin of the observed EPR signals is therefore very likely to be the same for all O_2-tolerant [NiFe]-hydrogenases and it is expected that — if similar variants of *Aa* Hase I and *Re*-MBH could be isolated and characterised — similar spectra to those measured for *E. coli* Hyd-1 would be obtained.

The conclusions presented here are in conflict with the recent paper by Pandelia *et al.* [16], who concluded that both the proximal and distal clusters contribute to the low-potential Fe-S cluster signals observed. However, Pandelia's assignment is only based on a

CW EPR titration of the native *Aa* Hase I hydrogenase. In that publication, the EPR signals assigned to the reduced proximal cluster are extremely small (even at their maximum intensity) and not significantly above the noise level. Although no spin quantification is provided, by eye these signals can only account for at most 0.1 spins per molecule. With the additional information from the titration of the medial cluster variant *E. coli* Hyd-1 enzyme in particular, the low-potential transition assigned by Pandelia *et al.* to the distal cluster is re-assigned to the proximal cluster [4Fe-3S]$^{4+/3+}$ transition.

Progress can therefore be made in understanding the origin of the 'complex interaction signal' observed in all low-potential samples of O_2-tolerant hydrogenases. While the proximal cluster interacts with the paramagnetic Ni species at the active site, any spin at the medial cluster site does not. We know from the high potential spectra of the C19G/C120G *E. coli* Hyd-1 variant (see Chapter 6, Section 6.3.2) and the *Re*-MBH variant [88] that any exchange or dipolar interaction between the medial cluster and the active site Ni species are negligible, and this is also the case for standard hydrogenases which lack the high-potential centre (Chapter 5, Section 5.3.3). Similarly, the medial and distal cluster spins may be expected to interact, but not the proximal and distal clusters. Thus, at least to a good approximation, only the magnetic coupling between the spins of direct neighbours is significant. The proposal by Pandelia *et al.* [16] that the low-potential 'complex interaction signal' observed in O_2-tolerant hydrogenases arises from "two reduced proximal and distal clusters ($S = 1/2$) mediated by the high spin [3Fe-4S]^0 cluster ($S = 2$)" [16] can therefore be simplified as arising from the reduced proximal ($S = 1/2$) and medial ($S = 2$) cluster only. One possible explanation for the temperature dependence of the X-band CW EPR spectra is that the exchange interaction between the proximal and medial clusters is modulated as a function of temperature by a change in the T_1 relaxation time of the medial cluster ($S = 2$). Because the W-band spectrum has no resolved exchange splitting, the exchange coupling is likely to be less than ≈ 700 MHz — a feasible upper limit given the spacing between the turning points of the X-band EPR spectra. Since the reduced medial cluster parameters are unknown, this

interpretation cannot currently be verified though simulations of the CW EPR data. The X-band CW spectra of native Hyd-1 at different temperatures (Fig. 8.10) suggest another possibility for the origin of the 'complex interaction signal': *i.e.* an excited $S = 1/2$ state could also be populated. Both the ground and excited states would have to originate from the same species so that a decrease in temperature would cause an increased population of the ground state while the overall number of spins remains invariant as a function of temperature. While this scenario may explain the observed X-band data, a similar 'transformation' should also occur at W-band. The afore-mentioned explanation is therefore more consistent with all extant data.

The titration data of native Hyd-1 show that the shape of the 'complex interaction signal' observed clearly below approximately 30 mV not only changes with temperature but also (more subtly) with potential. This is also apparent in titrations of *Aa* Hase I [16]. However, in the medial cluster variant P242C the appearance of the rhombic g matrix is unaffected by both temperature and potential. Given that this difference is caused by changes to the medial cluster, it seems unlikely that coupling to active site paramagnetic Ni species with decreasing potential (Ni-B to Ni-L*) is responsible for the observed potential dependent change in signal shape in native Hyd-1. Again, involvement of the medial cluster is more likely as the [3Fe-4S]$^{+/0}$ redox transition is not complete at 30 mV in native Hyd-1 (Fig. 8.5). However, the way in which the medial cluster spin leads to the observed spectral changes remains elusive.

The data presented here are in agreement with previous publications on O_2-tolerant [NiFe]-hydrogenases, but interpreted differently. However, the data are not entirely consistent with previous work on O_2-sensitive hydrogenases. In particular, Rousset *et al.* [58] reported the presence of three reduced [4Fe-4S]$^+$ $S = 1/2$ clusters in the medial cluster P238C variant of *D. fructosovorans*, but only the reduced proximal cluster is observed in the corresponding variant of *E. coli* Hyd-1, *i.e.* both the medial (all Cys-ligated) and distal (3 Cys, 1 His ligands) clusters in this variant must be in a high spin ground state. Consequently, no midpoint potential can be obtained for the medial cluster in Hyd-1

P242C. The value reported for the medial [4Fe-4S] cluster in ref. [58] was over 300 mV more negative then the value for the medial [3Fe-4S] cluster in the native enzyme. In *E. coli* Hyd-1 P242C the proximal cluster [4Fe-3S]$^{4+/3+}$ transition was found to be 60 mV more positive than that in the native enzyme. Rousset *et al.* [58] report that the midpoint potentials of the proximal and distal clusters (which are identical) decrease from -340 mV in the native *D. fructosovorans* enzyme to -380 mV in the medial cluster variant. Given the proximity of the Pro residue to the proximal cluster ($\approx$ 13 Å), it is not surprising that the redox potentials of the proximal cluster are affected by the P242C mutation at the medial cluster.

The X-band CW and pulse EPR data over a wide field range show that higher spin states are present in native Hyd-1 and all the variants studied. Assignment of the observed signals to a particular Fe-S cluster is not an easy task. It is possible that even over a very wide field range no clear EPR signals are observed from a reduced cluster that must exist. For instance, in nitrate reductase 40 % of the His-ligated [4Fe-4S]$^{+}$ cluster FS0 was shown to be in the $S = 3/2$ ground state in the native enzyme [317, 320], but substitution of the ligating His for a Ser residue removed all EPR signals in the $g = 5$ region that were present in the wild type enzyme [317], and no additional signals appeared in either the $g = 2$ region [321] nor at other field positions [317]. The signals in the $g = 2$ region were found to be almost identical in the native, H50S and H50C mutants of *E. coli* nitrate reductase (these arise from the three other reduced [4Fe-4S] clusters in the $S = 1/2$ ground state) and no change was observed in the spin intensity measurements [321]. It is possible that paramagnetic Fe-S cluster species are not detected because the mw frequency source range is limited. For example, if the zero-field splitting is larger than 10 GHz, no peaks will be detectable even at zero field because the mw frequency is not sufficiently high. Comparatively low spin concentrations and very broad EPR spectra can also make the detection of high-spin species very difficult. The mutation of a Cys to a Ser residue in an all Cys coordinated [4Fe-4S] cluster in *E. coli* fumarate reductase resulted in a change from low to high-spin ($S = 3/2$) [322]. The situation in *E. coli* Hyd-1 is similar as both

C19 and C120 ligate the proximal cluster (Fig 6.1, Chapter 6).

Other techniques could help elucidate the origin of the observed high-spin EPR signals. Parallel mode EPR would unambiguously establish whether signals originate from an integer or a half-integer spin and thus from a reduced [4Fe-4S] cluster or a reduced [3Fe-4S] cluster. For example, the $g = 5.0$ peak observed in active [FeFe]-hydrogenase from *D. vulgaris* could be assigned to the H-cluster in the $S = 3/2$ state rather than originating from an $S = 2$ species [298]. Magnetic circular dichroism has proven to be a valuable tool for distinguishing between high-spin and low-spin $[4Fe\text{-}4S]^{+}$ clusters and also $[3Fe\text{-}4S]^{0}$ clusters (see for example [323]). Magnetisation studies have also been successfully used to determine the spin state of the [4Fe-4S] cluster in the Fe protein of the *A. vinelandii* nitrogenase, in conjunction with Mössbauer and EPR spectroscopy [324].

Perhaps it is not so surprising that the distal cluster in O_2-tolerant [NiFe]-hydrogenases has a high-spin ground state. Although the factors leading to high-spin ground states in [4Fe-4S] clusters are not very well understood, mutation of one of the Cys in an all Cys-ligated $[4Fe\text{-}4S]^{+}$ cluster with $S = 1/2$ ground state leads to a higher spin state (see above), and high-spin $[4Fe\text{-}4S]^{+}$ clusters reported in the literature are not all Cys coordinated, but are typically ligated by three Cys residues and one different amino acid: Examples include the FS0 cluster in nitrate reductase (three Cys and one His) [320], the 'labile' [4Fe-4S] cluster (ligated by three Cys and one Asp) in *Desulfovibrio africanus* ferredoxin III [325, 326][9] and the [4Fe-4S] cluster (ligated by three Cys and one Asp) in *P. furiosus* ferredoxin [327]. The ligation of the cluster in the latter protein has been extensively studied [323] and remarkably in the D14C variant the $[4Fe\text{-}4S]^{+}$ cluster was found to be exclusively in the $S = 1/2$ ground state. Similarly, the 'labile' $[4Fe\text{-}4S]^{+}$ cluster in *D. africanus* also changed from a $S = 3/2$ ground state in the native protein to a $S = 1/2$ ground state in the D14C variant [326]. It would therefore be very interesting to see what the result of an equivalent mutation for the distal cluster in *E. coli* Hyd-1 would be: Would the substitution of the directly ligating His for a Cys residue change the spin state of this

[9] *D. africanus* ferredoxin III contains two [4Fe-4S] clusters. One of these is named the 'labile cluster' because of its ability to convert reversibly to to a [3Fe-4S] cluster under oxidising conditions [325].

cluster to $S = 1/2$? Such a mutation has been made in the standard [NiFe]-hydrogenase from *D. fructosovorans* in which the distal cluster is believed to be in the $S = 1/2$ ground state even in the native enzyme [58]. It is therefore surprising that the low potential CW EPR spectrum of the H184C mutant was reported to integrate to 1.4 time more [4Fe-4S] clusters per molecule of enzyme than the wild type enzyme [60], an observation that would appear more consistent with the distal cluster changing from a higher spin state in the native enzyme to a $S = 1/2$ ground state in the H184C mutant. Given the much more well-defined reduced Fe-S cluster signals in O_2-tolerant [NiFe]-hydrogenases, it may be possible to investigate the Fe-S cluster signals in such a distal cluster variant of *E. coli* Hyd-1 in considerably more detail.

An important consequence of the distal cluster being in a higher spin state in O_2-tolerant hydrogenases is that we do not know its reduction potential. Protein film electrochemistry has been used to determine the reduction potential of Fe-S clusters in the standard *A. vinosum* hydrogenase [286]. However, this method is only possible if the catalytic activity of the enzyme can be fully inhibited. Carbon monoxide is a strong inhibitor of standard hydrogenases [132], but not of O_2-tolerant hydrogenases [83, 290, 328] and no other inhibitor capable of fully abolishing catalytic activity has yet been discovered. In principle, it should possible to inhibit catalytic activity by depriving the enzyme of substrate by carrying out PFE cyclic voltammetry experiments (Section 3.4) in the presence of Ar only — Hyd-1 essentially produces no H_2 even in the absence of H_2 [83]. However, such experiments have so far not been conclusive.[10] If the distal cluster H187C mutation in *E. coli* Hyd-1 indeed resulted in a $S = 1/2$ ground state distal cluster, the midpoint potential could be determined by EPR redox titrations. It cannot be assumed that the variant cluster has the same potential as in the native enzyme but comparison of the native enzyme and distal variant's EPR spectra will permit deconvolution of what signals and spin-spin interactions in the native enzyme are due to the native distal cluster. Determining how these distal cluster related spectral fingerprints change with potential should

[10]Personal communication with Dr. Alison Parkin, University of Oxford

permit an approximate indirect determination of the midpoint potential of the distal cluster in the native enzyme. Latest developments in theoretical methods [329, 330] may also lead to reliable calculations of reduction potentials of Fe-S clusters in large proteins (for which high-resolution crystal structures are available) in the near future. However, clusters with unusual ligation motifs, such as the distal cluster in [NiFe]-hydrogenases, still present a major challenge.[11]

The finding that the distal cluster in O_2-tolerant hydrogenases (and perhaps in all [NiFe]-hydrogenases) has a high-spin ground state also calls for a re-evaluation of the consensus that $S = 1/2$ is the most common ground state in reduced [4Fe-4S] clusters in large enzymes in general.

[11]Personal communication with Professor Toshiko Ichiye, Georgetown University, Washington, USA.

Chapter 9

Summary and Conclusions

The application of DEER spectroscopy to the complete hydrophilic domain of complex I housing the electron-transfer Fe-S centres has resolved a debate of over 30 years regarding the assignment of the known reduction potentials to structurally defined Fe-S clusters (Chapter 4). Importantly, the successful application of DEER to such an unprecedented number of delocalised metal centres has relied on over 30 years of research, which narrowed the number of possible assignments down to just three models. The correct assignment leads to an alternating occupancy of the electron transfer chain during turnover, and brings us one step closer towards understanding how electron transfer occurs so efficiently in this important enzyme of the respiratory chain. With NADH binding at the FMN and electron transfer relatively well understood, numerous questions remain regarding quinone binding and proton translocation across the membrane. The recent crystal structures of the entire complex I comprising both the hydrophilic and hydrophobic domains are an important step towards elucidating the latter.

Oxygen-tolerant respiratory [NiFe]-hydrogenases have been subjected to intense research and the work described in this thesis contributes towards the identification and characterisation of the unique Fe-S cluster proximal to the active site. This [4Fe-3S] cluster is capable of a double role owing to its ability to access *three* oxidation states [16]: one-electron transfer during catalysis and two-electron release to rescue the active site

from detrimental attack by O_2 (Chapter 6). The crystal structures of three O_2-tolerant [NiFe]-hydrogenases from different species [17, 18, 87], including *E. coli* Hyd-1 which is investigated in this thesis, reveal that changes in redox state are accompanied by conformational changes of the cluster, which bear striking similarities with the P-cluster in nitrogenase. Crystallography shows that a peptide amide nitrogen coordinates the proximal cluster at high potentials [17, 18]. HYSCORE studies of a variant of *E. coli* Hyd-1 enabled determination of the electronic state of the Fe atom binding the peptide amide N, and the nature of the Fe−N bond (Chapter 7).While theoretical studies on *E. coli* Hyd-1 lead to the conclusion that the N-coordinated Fe is the atom that loses an electron to generate the 'overoxidised' proximal cluster state [18], further studies will be necessary to determine the valence delocalisation patterns of this novel cluster. It is now clear that O_2 tolerance in membrane-bound [NiFe]-hydrogenases primarily stems from intriguing engineering of the proximal cluster of the electron transfer relay [17, 18, 87]. However, puzzles regarding the active site still remain: studies of the Ni signals of *E. coli* Hyd-1 revealed an unusual species at moderately low potentials (Chapter 5). Concomitant studies of the standard *E. coli* Hyd-2 lead to the tentative conclusion that this species (named Ni-L*) resembles Ni-L, a species generally considered to be an artifact induced by illumination at low temperatures, and question the exclusion of Ni-L from the catalytic cycle. Further studies and additional techniques will be necessary to probe the structure and electronic nature of Ni-L*.

The investigations in Chapter 8 reveal that the distal [4Fe-4S] cluster in O_2-tolerant [NiFe]-hydrogenases (and possibly in *all* membrane-bound [NiFe]-hydrogenases) is not EPR visible. Instead, the Fe-S signal observed at low potentials should be assigned to the reduced proximal cluster. This conclusion is contrary to the current consensus and has implications for our understanding of the energy landscape of the electron-transfer relay of these enzymes, since the reduction potential of the distal cluster is then no longer known.

It is interesting to compare the two types of enzymes investigated in this thesis.

Clearly, complex I and [NiFe]-hydrogenases cope with O_2 in very different ways: while the reactive oxygen species formed at the FMN in complex I are released into solution, O_2 is trapped at the active site in hydrogenases, and a special Fe-S cluster design is required to 'salvage' the active site. At least two Fe-S clusters in intact complex I have never been observed *via* EPR. The finding that the distal cluster in O_2-tolerant [NiFe]-hydrogenases is in a $S \neq 1/2$ ground state and EPR invisible raises the possibility that many more Fe-S clusters than previously thought, including $[4Fe\text{-}4S]^+$ clusters generally accepted to prevail in the $S = 1/2$ ground state, remain hidden. Just as many Fe-S clusters remained hidden until more discriminating spectroscopic techniques than UV-visible spectroscopy were available [4], maybe many more Fe-S clusters are still unobserved because even EPR can become a very difficult technique as soon as the ground state is not $S = 1/2$.

Although we have come a long way in the 12 years since Helmut Beinert's lecture held at the 9th International Conference on Biological Inorganic Chemistry, the title of his lecture remains true: "Iron-sulfur proteins: ancient structures, still full of surprises" [4].

Chapter 10

Appendices

10.1 The Nernst equation

For a redox component A undergoing the n-electron reduction

$$A_{ox} + ne^- = A_{red} \tag{10.1}$$

and a redox component B undergoing the n-electron oxidation:

$$B_{red} = B_{ox} + ne^- \tag{10.2}$$

the complete oxidation-reduction reaction is:

$$A_{ox} + B_{red} = A_{red} + B_{ox} \tag{10.3}$$

The equilibrium constant is given by

$$K = \frac{[A_{ox}][B_{red}]}{[A_{red}][B_{ox}]} \tag{10.4}$$

and the standard free energy of the reaction

$$\Delta G^0 = -nF\Delta E^0 \tag{10.5}$$

where F is the Faraday constant (96.493 JV^{-1}) and ΔE^0 is the redox potential difference between the two half cells in equations 10.1 and 10.2 under standard conditions (unit activities and pH 0).

Under non-standard conditions, the free energy is given by

$$\begin{aligned} \Delta G &= \Delta G^0 + RT \ln K \\ &= -nF\Delta E \end{aligned} \tag{10.6}$$

where ΔE is the redox potential difference between the two half cells in equations 10.1 under non-standard conditions.

Therefore

$$\begin{aligned}
\Delta E &= \Delta E_0 - \frac{RT}{nF}\ln\frac{[A_{ox}][B_{red}]}{[A_{red}][B_{ox}]} \\
&= \Delta E_0 - \frac{RT}{nF}\ln\frac{[B_{red}]}{[B_{ox}]} + \frac{RT}{nF}\ln\frac{[A_{red}]}{[A_{ox}]} \\
&= E_{0(B)} - \frac{RT}{nF}\ln\frac{[B_{red}]}{[B_{ox}]} - \left(E_{0(A)} - \frac{RT}{nF}\ln\frac{[A_{red}]}{[A_{ox}]}\right) \\
&= E_B - E_A
\end{aligned} \tag{10.7}$$

where the reduction potential of A (or B) the reduction potential of A, E_A is thus given by the Nernst equation

$$E_A = E_{0(A)} - \frac{RT}{nF}\ln\frac{[A_{red}]}{[A_{ox}]}. \tag{10.8}$$

10.2 Appendix to Chapter 5

The temperature dependence of E_{switch} in *E. coli* Hyd-1 and Hyd-2 is shown in Fig. 10.1.

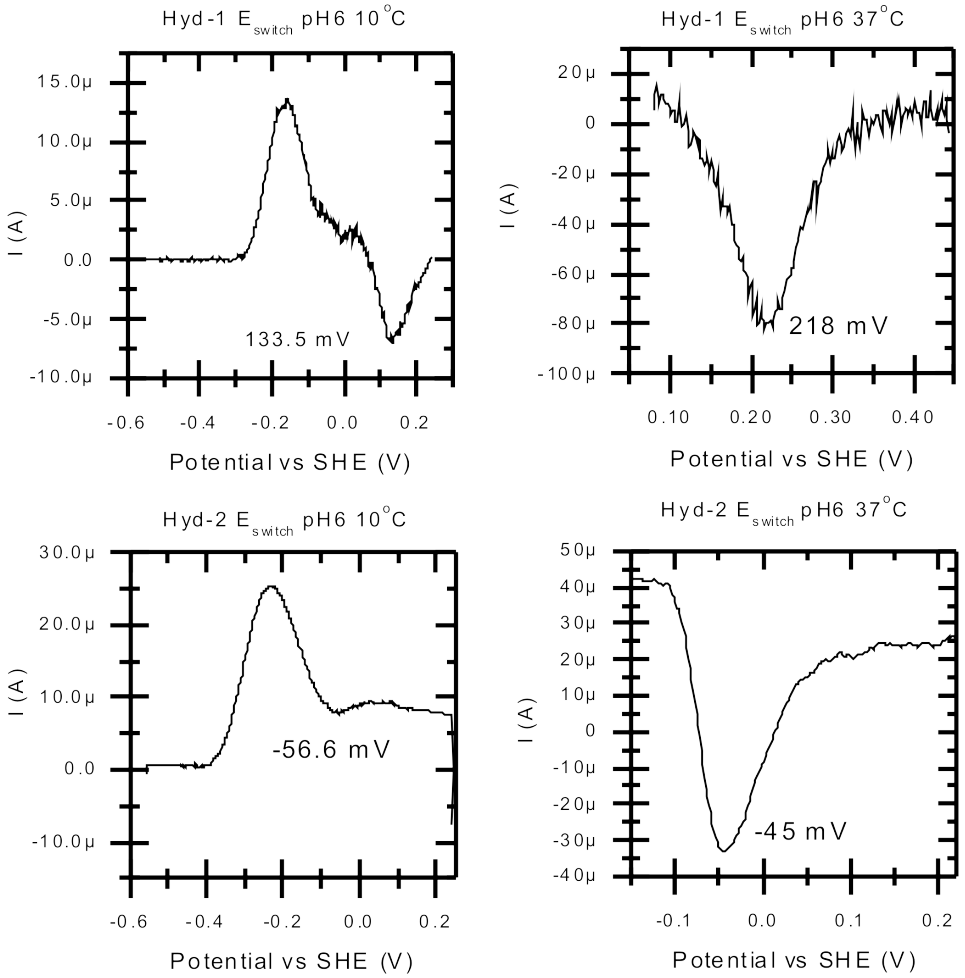


Figure 10.1: **E_{switch} at 37 ^{o}C and 10 ^{o}C of *E. coli* Hyd-1 and Hyd-2 at pH 6** Cyclic voltammetry experiments were recorded following activation of the enzymes under 100 % H_2 or D_2 (as indicated with arrows) at 300 (standard cubic centimetres) min^{-1}, scan rate 0.5 mV s^{-1}.

10.3 Appendix to Chapter 6

Wide field-sweep EPR spectra of the anaerobically and aerobically inactivated C19G/C120G variant of *E. coli* Hyd-1 are shown in Fig. 10.2. Essentially no signal is at $g = 4.3$ (indicative of free Fe^{3+}) is detected.

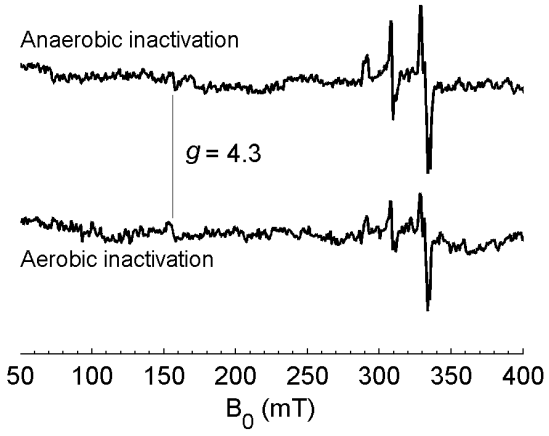


Figure 10.2: **X-band 9.39 CW EPR spectra of C19G/C120G samples following anaerobic and aerobic inactivation at +78 ± 2 mV, 15 K**
Prior to inactivation, samples were activated under H_2 for 40 hours. For full details of sample preparation see Methods 6.2.1 in Chapter 6. Approximate protein concentration: 50-60 μM. Measurement conditions: mw power 2 mW; modulation amplitude 0.5 mT. Taken from ref. [89].

Method for calculating true midpoint potentials in Hyd-1 enzymes forming a high potential species

The Matlab code written to calculate true midpoint potential for the medial [3Fe-4S]$^{+/0}$ redox transition is given in below. It makes use of the Nernst equation for a one-electron process (Section 10.1).

```
clc
close all
clear all

% to calculate true midpoint potentials for medial cluster in enzymes with HP

n=1; %number of electrons
F=96485; R=8.31447; T=293; %constants
f=n*F/(R*T); %units C/J = 1/V ie. must convert to V

% Nernst plot for HP
E_FeS = 0.230;  % midpoint potential for HP
E_ap=[-0.1:0.01:0.4];
I_FeS = 1./(1+exp(-f*(E_ap - E_FeS)));

figure (1), clf
   set(gcf, 'Units', 'centimeters','Position',[2 10 10 10] , 'PaperPositionMode',
'auto');
   set(gca,'units','centimeters','position',[1.5 1.1 8 8])
plot (E_ap, I_FeS, 'k');

I_FeS = 1./(1+exp(-f*(E_ap - E_FeS)));

% potential E1 at defined number of spins per molecule S (less or equal to 1)
E1=0.204;
S=0.9;

hhh=vline(E1, 'k--');

% percentage of oxidised HP centre
R1=1./(1+exp(-f*(E1 - E_FeS)))
% number of spins corresponding to HP centre
S1=R1*S
hhh=hline(R1, 'k--');

% number of spins corresponding to 3Fe cluster
S2=S-S1
hhh=hline(S2, 'r--');
% percentage/number of spin of reduced 3Fe cluster
R2=1-S2
% estimated midpoint potential of 3Fe cluster
E2=-log((1-R2)/R2)/f+E1

%just to check calculation is right...
hhh=vline(E2, 'g--');
hhh=hline(0.5, 'g--');

I_FeS2 = 1./(1+exp(-f*(E_ap - E2)));

hold on
plot (E_ap, I_FeS2, 'r');
xlabel('E (V)');
ylabel('fraction of oxidised cluster');
legend ('HP centre', 'medial cluster', 'location', 'NW');
text(0.22, 0.1, 'E_1');
text(0.15, 0.45, 'E_2', 'color', 'g');
filename = ('Figures/Nernst_EmCalculation');  print ('-f1', '-dpng', '-r300', filename);
```

The Matlab code includes the variables used to generate the plot in Fig. 10.3.

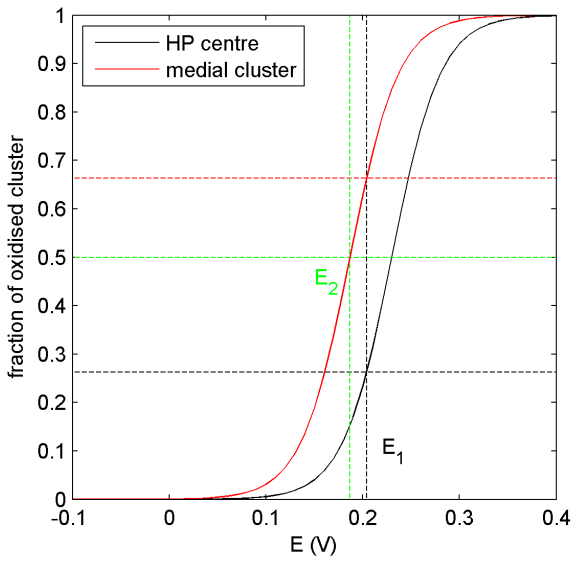


Figure 10.3: **Calculated one-electron Nernst plot for HP with E_m +230 mV and deduced plot for medial cluster based on the information that at E_1 the spin integration of the FeS cluster signals is 0.9.** For this particular example, as stated in the main text, the percentage of oxidised HP at E_1 is 26 % (as indicated by the horizontal black dotted line); and the percentage of oxidised medial cluster is 66 %, as indicated by the horizontal red dotted line (taking into account that the spin integration is 0.9 spins per molecule at E_1). The true midpoint potential of the medial cluster (red curve) in this case is E_2 = 187 mV. Taken from ref. [270].

10.4 Appendix to Chapter 7

Nernst plots for native *E. coli* Hyd-1 and the P242C variant

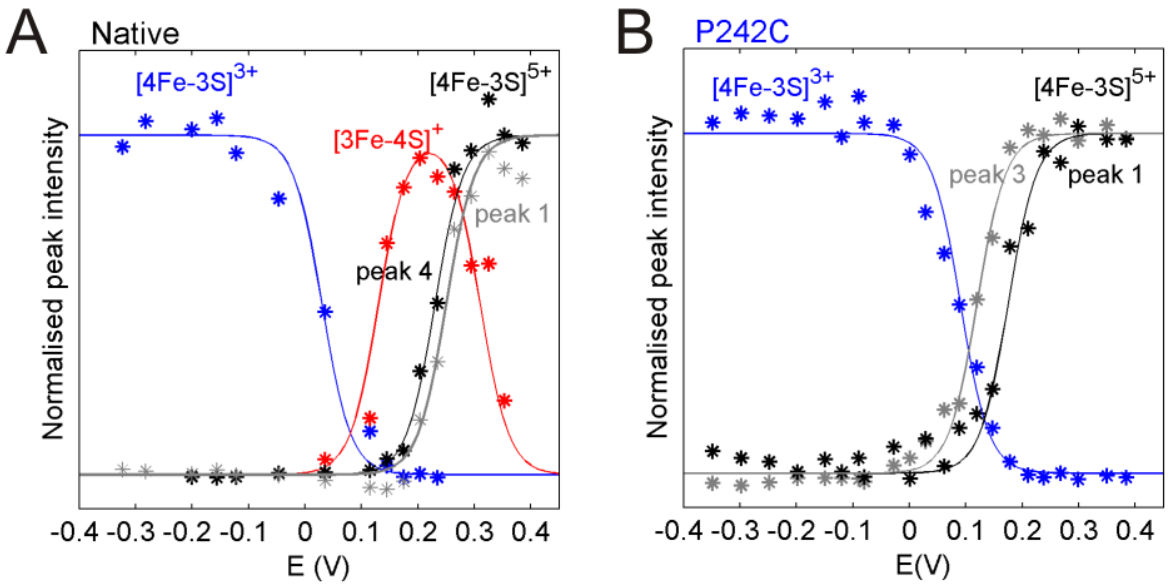


Figure 10.4: **Nernst plots for native Hyd-1 and for P242C showing the spread in reduction potential for the [4Fe-3S]$^{5+/4+}$ (HP) couple.** Black and blue curves were determined as detailed in Fig. 7.4. Grey data points and fitted curves result from monitoring alternative peak positions in the high-potential Fe-S cluster spectra (Fig. 7.3) and illustrate the 'spread' in reduction potential for the HP reduction in Hyd-1 P242C; E_m (peak 1, native) = +250±15 mV and E_m (peak 3, P242C) = +120±15 mV. Adapted from ref. [270].

10.5 Appendix to Chapter 8

Temperature dependence of the $Cu(ClO_4)_2$ standard, showing that this sample follows the Boltzmann distribution

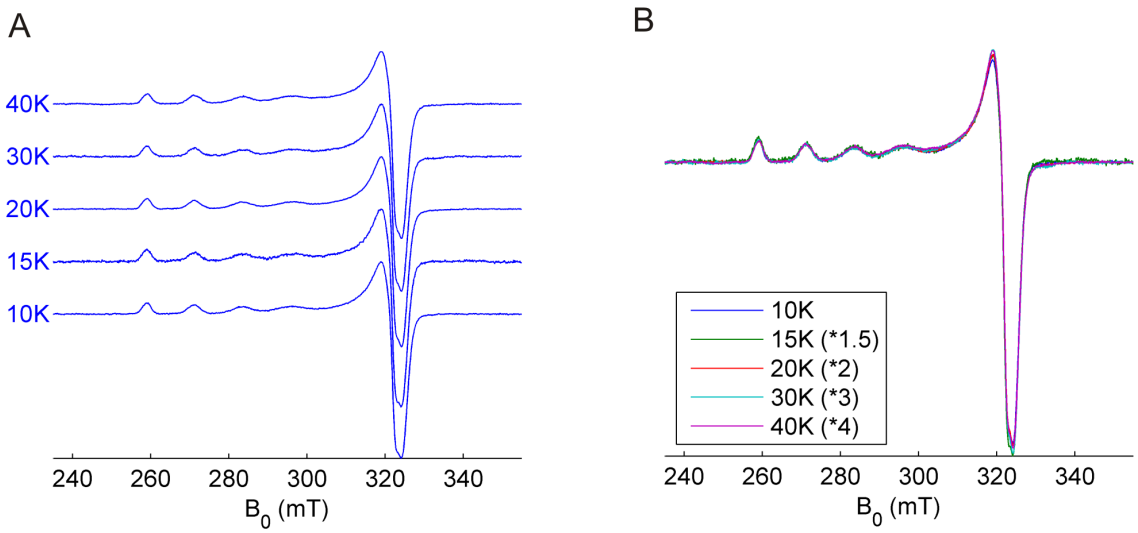


Figure 10.5: **Temperature dependence of $Cu(ClO_4)_2$ CW EPR spectra, measured under non-saturating conditions.** In A, all spectra are scaled to an intensity of 1; in B, spectra are scaled by the factor expected from the Boltzmann temperature dependence of the system. Measurement conditions: mw power 8 μW (40 K, 30 K, 20 K), 2 μW (15 K, 10 K); modulation amplitude 1 mT (all); sample concentration 200 μM.

X-band two-pulse echo-detected wide field sweeps of native Hyd-1 and the P242C variant

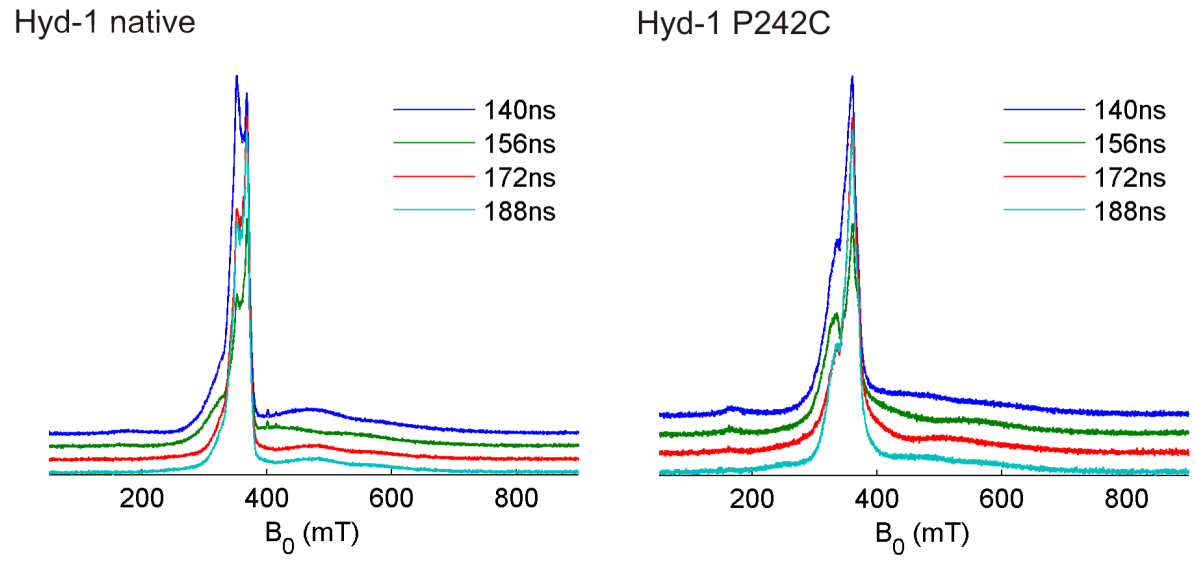


Figure 10.6: **X-band two-pulse echo-detected wide field sweeps of native Hyd-1 and Hyd-1 P242C (2.7 K).** Sample potentials: -355 mV (native H_2-reduced), -250 mV (P242C, dithionite-reduced). Measurement conditions: pulse sequence $\pi/2$ -τ - π - τ - echo where τ is varied between 140 ns and 188 ns in 16 ns increments and $\pi/2$ = 16 ns, π = 32 ns; mw frequency 9.740 GHz (native), 9.745 GHz (P242C); shot repetition time 2 ms.

Additional HYSCORE spectra of native Hyd-1 and Hyd-1 P242C reduced samples

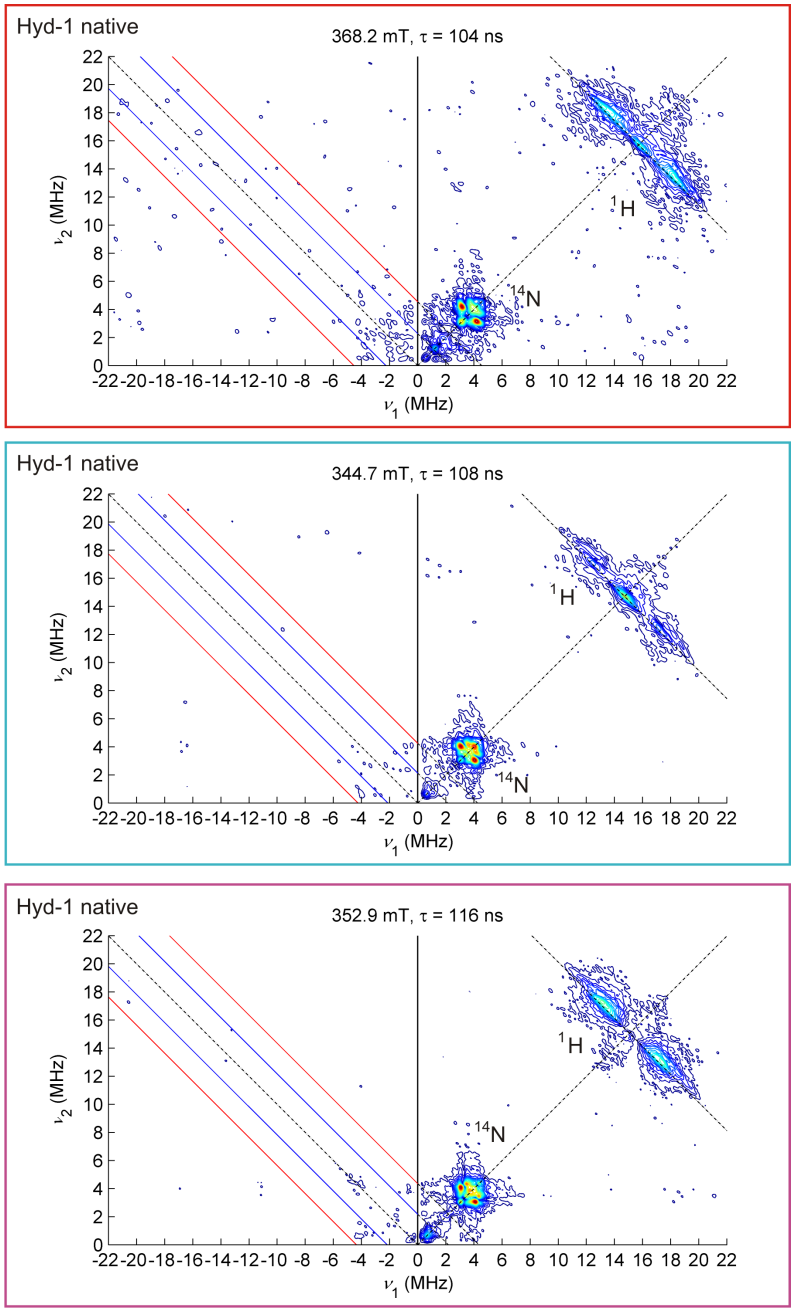


Figure 10.7: **X-band HYSCORE spectra of H_2-reduced native Hyd-1 (- 355 mV).** Measurement conditions: $\pi/2 = 16$ ns, $\pi = 16$ ns, 2.7 K, shot repetition time 5 ms, 150 points, 8-step phase cycle, (*Top*): 368.2 mT, $\tau = 104$ ns, 9.738 GHz, (*Centre*): 344.7 mT, $\tau = 108$ ns, 9.738 GHz, (*Bottom*): 352.9 mT, $\tau = 116$ ns, 9.738 GHz. The coloured boxes refer to the field positions indicated with similarly coloured lines in Fig. 8.20 (left) in Chapter 8.

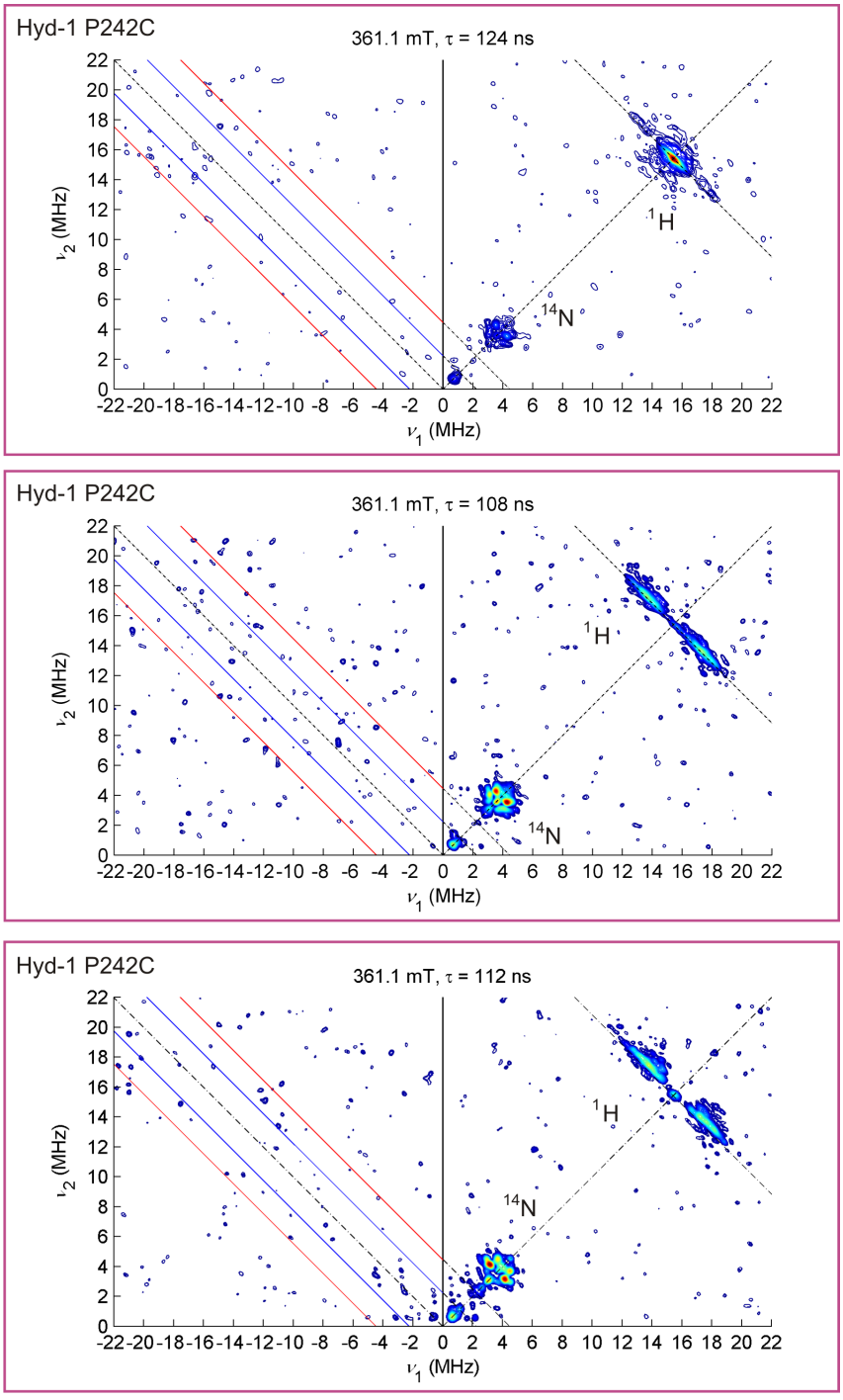


Figure 10.8: **X-band HYSCORE spectra of reduced Hyd-1 P242C (- 250 mV)** Measurement conditions: $\pi/2 = 16$ ns, $\pi = 16$ ns, 7 K, shot repetition time 5 ms, 150 points, 8-step phase cycle, (*Top*): 361.1 mT, $\tau = 124$ ns, 9.746 GHz, (*Centre*): 361.1 mT, $\tau = 108$ ns, 9.746 GHz, (*Bottom*): 361.1 mT, $\tau = 112$ ns, 9.746 GHz. The coloured boxes refer to the field positions indicated with similarly coloured lines in Fig. 8.20 (right) in Chapter 8.

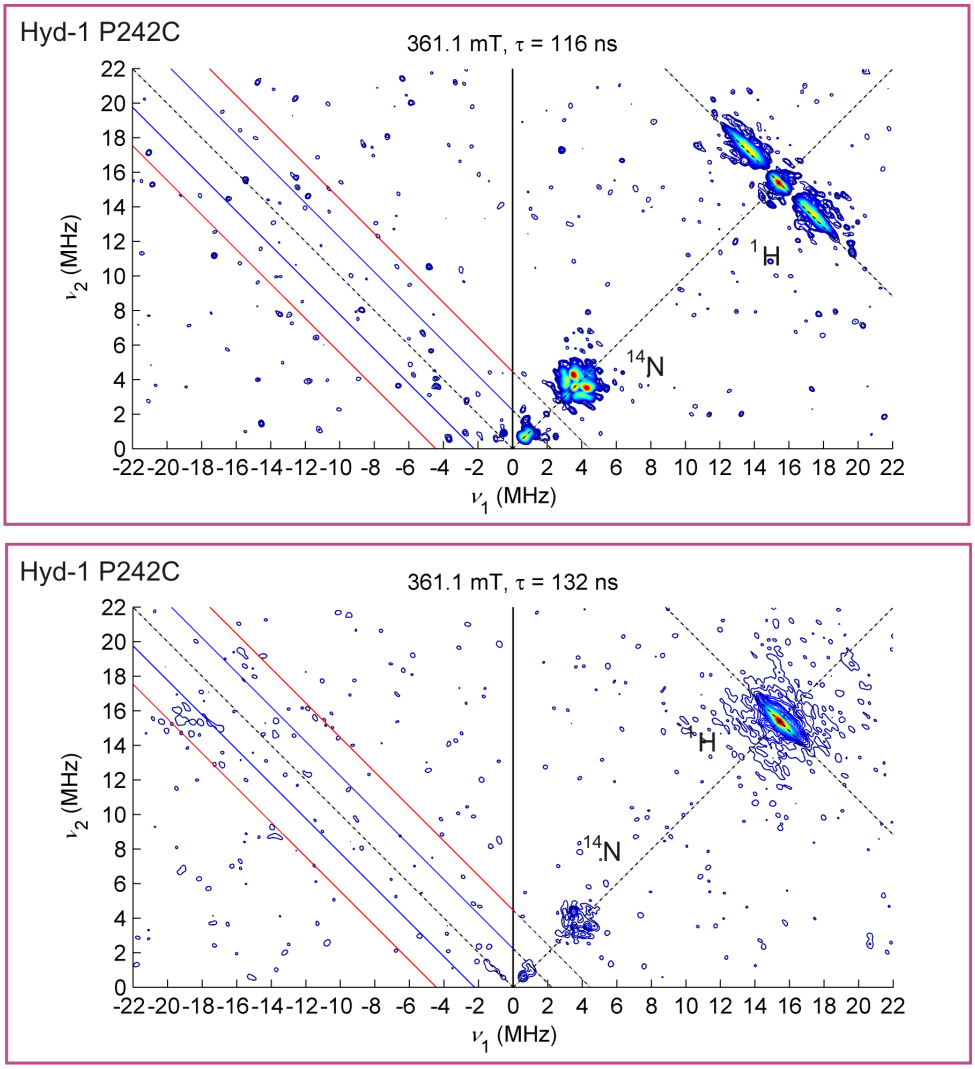


Figure 10.9: **X-band HYSCORE spectra of reduced Hyd-1 P242C (- 250 mV)** Measurement conditions: $\pi/2 = 16$ ns, $\pi = 16$ ns, 7 K, shot repetition time 5 ms, 150 points, 8-step phase cycle, (*Top*): 361.1 mT, $\tau = 116$ ns, 9.746 GHz, (*Bottom*): 361.1 mT, $\tau = 132$ ns, 9.746 GHz. The coloured boxes refer to the field positions indicated with similarly coloured lines in Fig. 8.20 (right) in Chapter 8.

Multiple sequence alignments of the small subunit of O_2-tolerant catalytic [NiFe]-hydrogenases



Figure 10.10: **Multiple sequence alignment of the small subunit O_2-tolerant [NiFe]-hydrogenases** The residues directly ligating the Fe-S clusters are highlighted (yellow for the proximal cluster, pink for the medial cluster, cyan for the distal cluster). Alignments were performed using the program ClustalW2 [267].

Bibliography

[1] H. Beinert and R. H. Sands, "Studies on succinic and DPNH dehydrogenase preparations by paramagnetic resonance (EPR) spectroscopy," *Biochemical and Biophysical Research Communications*, vol. 3, pp. 41–46, 1960.

[2] H. Beinert and R. H. Sands, "Biological Applications Involving Iron," in *Foundations of Modern EPR* (G. R. Eaton, S. Eaton, and K. M. Salikhov, eds.), pp. 379–409, World Scientific Publishing, 1998.

[3] J. F. Gibson, D. O. Hall, J. H. M. Thornley, and F. R. Whatley, "The iron complex in spinach ferredoxin," *Proceedings of the National Academy of Sciences*, vol. 56, pp. 987–990, 1966.

[4] H. Beinert, "Iron-sulfur proteins: ancient structures, still full of surprises," *Journal of Biological Inorganic Chemistry*, vol. 5, pp. 2–15, 2000.

[5] H. Beinert, R. H. Holm, and E. Münck, "Iron-Sulfur Clusters: Nature's Modular, Multipurpose Structures," *Science*, vol. 277, pp. 653–659, 1997.

[6] W. Lovenberg, *Iron-Sulfur Proteins*, vol. I & II. Academic Press, New York, 1973.

[7] L. Noodleman, C. Peng, D. Case, and J. Mouesca, "Orbital interactions, electron delocalization and spin coupling in iron-sulfur clusters," *Coordination Chemistry Reviews*, vol. 144, pp. 199–244, 1995.

[8] E. L. Bominaar, C. Achim, S. A. Borshch, J. J. Girerd, and E. Münck, "Analysis of Exchange Interaction and Electron Delocalization as Intramolecular Determinants of Intermolecular Electron-Transfer Kinetics," *Inorganic Chemistry*, vol. 36, pp. 3689–3701, 1997.

[9] F. Malatesta, F. Nicoletti, V. Zickermann, B. Ludwig, and M. Brunori, "Electron entry in a CuA mutant of cytochrome c oxidase from *Paracoccus denitrificans*. Conclusive evidence on the initial electron entry metal center," *FEBS Letters*, vol. 434, pp. 322–324, 1998.

[10] J. S. Rieske, D. H. MacLennan, and R. Coleman, "Isolation and properties of an iron-protein from the (reduced coenzyme Q)-cytochrome C reductase complex of the respiratory chain," *Biochemical and Biophysical Research Communications*, vol. 15, pp. 338–344, 1964.

[11] M. B. Robin and P. Day, *Mixed Valence Chemistry-A Survey and Classification*, vol. 10 of *Advances in Inorganic Chemistry*, pp. 247–422. Elsevier, 1968.

[12] J. M. Berg and R. H. Holm, "Structures and Reactions of Iron-Sulfur Protein Clusters and Their Synthetic Analogs," in *Iron-Sulfur Proteins*, Wiley-Interscience, 1982.

[13] L. Banci, I. Bertini, S. Ciurli, S. Ferretti, C. Luchinat, and M. Piccioli, "The electronic structure of iron-sulfur $[Fe_4S_4]^{3+}$ clusters in proteins. An investigation of the oxidized high-potential iron-sulfur protein II from *Ectothiorhodospira vacuolata*," *Biochemistry*, vol. 32, pp. 9387–9397, 1993.

[14] E. L. Bominaar, Z. Hu, E. Muenck, J.-J. Girerd, and S. A. Borshch, "Double Exchange and Vibronic Coupling in Mixed-Valence Systems. Electronic Structure of Exchange-Coupled Siroheme-$[Fe_4S_4]^{2+}$ Chromophore in Oxidized *E. Coli* Sulfite Reductase," *Journal of the American Chemical Society*, vol. 117, pp. 6976–6989, 1995.

[15] H. A. Heering, Y. B. M. Bulsink, W. R. Hagen, and T. E. Meyer, "Reversible Super-Reduction of the Cubane $[Fe_4S_4]^{(3+,2+,1+)}$ in the High-Potential Iron-Sulfur Protein Under Non-Denaturing Conditions," *European Journal of Biochemistry*, vol. 232, pp. 811–817, 1995.

[16] M.-E. Pandelia, W. Nitschke, P. Infossi, M.-T. Giudici-Orticoni, E. Bill, and W. Lubitz, "Characterization of a unique [FeS] cluster in the electron transfer chain of the oxygen tolerant [NiFe] hydrogenase from *Aquifex aeolicus*," *Proceedings of the National Academy of Sciences of the United States of America*, vol. 108, pp. 6097–6102, 2011.

[17] Y. Shomura, K.-S. Yoon, H. Nishihara, and Y. Higuchi, "Structural basis for a [4Fe-3S] cluster in the oxygen-tolerant membrane-bound [NiFe]-hydrogenase," *Nature*, vol. 479, pp. 253–256, 2011.

[18] A. Volbeda, P. Amara, C. Darnault, J.-M. Mouesca, A. Parkin, M. M. Roessler, F. A. Armstrong, and J. C. Fontecilla-Camps, "X-ray crystallographic and computational studies of the O_2-tolerant [NiFe]-hydrogenase 1 from *Escherichia coli*," *Proceedings of the National Academy of Sciences of the United States of America*, vol. 109, pp. 5305–5310, 2012.

[19] J. L. C. Duff, J. L. J. Breton, J. N. Butt, F. A. Armstrong, and A. J. Thomson, "Novel Redox Chemistry of [3Fe4S] Clusters: Electrochemical Characterization of the All-Fe(II) Form of the [3Fe4S] Cluster Generated Reversibly in Various Proteins and Its Spectroscopic Investigation in *Sulfolobus acidocaldarius* Ferredoxin," *Journal of the American Chemical Society*, vol. 118, pp. 8593–8603, 1996.

[20] J. Hirst, G. N. L. Jameson, J. W. A. Allen, and F. A. Armstrong, "Very Rapid, Cooperative Two-Electron/Two-Proton Redox Reactions of [3Fe-4S] Clusters: Detection and Analysis by Protein-Film Voltammetry," *Journal of the American Chemical Society*, vol. 120, pp. 11994–11999, 1998.

[21] J. Frazzon and D. R. Dean, "Formation of iron-sulfur clusters in bacteria: an emerging field in bioinorganic chemistry," *Current Opinion in Chemical Biology*, vol. 7, pp. 166–173, 2003.

[22] T. A. Rouault and W.-H. Tong, "Iron-sulphur cluster biogenesis and mitochondrial iron homeostasis," *Nature Reviews Molecular Cell Biology*, vol. 6, pp. 345–351, 2005.

[23] D. C. Johnson, D. R. Dean, A. D. Smith, and M. K. Johnson, "Structure, function, and formation of biological iron-sulfur clusters," *Annual Review of Biochemistry*, vol. 74, pp. 247–281, 2005.

[24] K. S. Hagen, J. G. Reynolds, and R. H. Holm, "Definition of reaction sequences resulting in self-assembly of $[Fe_4S_4(SR)_4]^{2-}$ clusters from simple reactants," *Journal of the American Chemical Society*, vol. 103, pp. 4054–4063, 1981.

[25] R. Holm, "Trinuclear Cuboidal and Heterometallic Cubane-Type Iron-Sulfur Clusters: New Structural and Reactivity Themes in Chemistry and Biology," *Advances in Inorganic Chemistry*, vol. 38, pp. 1–71, 1992.

[26] J. Gloux, P. Gloux, H. Hendriks, and G. Rius, "EPR study of the $[Fe_4S_4]^+$ and $[Fe_4S_4]^{3+}$ states in gamma-irradiated crystals of $(Bu_4N)_2[Fe_4S_4(SPh)_4]$. g Tensors in relation to the geometry of the 4Fe-4S core," *Journal of the American Chemical Society*, vol. 109, pp. 3220–3224, 1987.

[27] J. Gloux, P. Gloux, B. Lamotte, J.-M. Mouesca, and G. Rius, "The Different $[Fe_4S_4]^{3+}$ and $[Fe_4S_4]^+$ Species Created by gamma Irradiation in Single Crystals of the $(Et_4N)_2[Fe_4S_4(SBenz)_4]$ Model Compound: Their EPR Description and Their Biological Significance," *Journal of the American Chemical Society*, vol. 116, pp. 1953–1961, 1994.

[28] J. Gloux and P. Gloux, "EPR Study of the $[Fe_4S_4]^+$ State in Single Crystals of $(Et_4N)_3[Fe_4S_4(SCH_2Ph)_4]$: g-Tensors of Kramers Doublets of the S = 3/2 Ground State," *Journal of the American Chemical Society*, vol. 117, pp. 7513–7519, 1995.

[29] L. Le Pape, B. Lamotte, J.-M. Mouesca, and G. Rius, "Paramagnetic States of Four Iron-Four Sulfur Clusters. 2. Proton ENDOR Study of a 1+ State in an Asymmetrical Cluster," *Journal of the American Chemical Society*, vol. 119, pp. 9771–9781, 1997.

[30] M. M. Werst, M. C. Kennedy, A. L. P. Houseman, H. Beinert, and B. M. Hoffman, "Characterization of the iron-sulfur $[Fe_4S_4]^+$ cluster at the active site of aconitase by iron-57, sulfur-33, and nitrogen-14 electron nuclear double resonance spectroscopy," *Biochemistry*, vol. 29, pp. 10533–10540, 1990.

[31] S. J. Lloyd, H. Lauble, G. S. Prasad, and C. D. Stout, "The mechanism of aconitase: 1.8 Å resolution crystal structure of the S642a:citrate complex," *Protein science : a publication of the Protein Society*, vol. 8, pp. 2655–2662, 1999.

[32] J.-H. Jeoung and H. Dobbek, "Carbon Dioxide Activation at the Ni,Fe-Cluster of Anaerobic Carbon Monoxide Dehydrogenase," *Science*, vol. 318, pp. 1461–1464, 2007.

[33] O. Einsle, F. A. Tezcan, S. L. A. Andrade, B. Schmid, M. Yoshida, J. B. Howard, and D. C. Rees, "Nitrogenase MoFe-Protein at 1.16 Å Resolution: A Central Ligand in the FeMo-Cofactor," *Science*, vol. 297, pp. 1696–1700, 2002.

[34] J. W. Peters, M. H. B. Stowell, S. M. Soltis, M. G. Finnegan, M. K. Johnson, and D. C. Rees, "Redox-Dependent Structural Changes in the Nitrogenase P-Cluster," *Biochemistry*, vol. 36, pp. 1181–1187, 1997.

[35] P. Atkins, T. Overton, J. Rourke, M. Weller, and F. Armstrong, *Shriver & Atkins Inorganic Chemistry*. Oxford University Press, fourth ed., 2006.

[36] J. M. Berg, J. L. Tymoczko, and L. Stryer, *Biochemistry*. Freeman, sixth ed., 2007.

[37] M. M. Werst, M. C. Kennedy, H. Beinert, and B. M. Hoffman, "Oxygen-17, proton, and deuterium electron nuclear double resonance characterization of solvent, substrate, and inhibitor binding to the iron-sulfur [4Fe-4S]$^+$ cluster of aconitase," *Biochemistry*, vol. 29, pp. 10526–10532, 1990.

[38] A. H. Robbins and C. D. Stout, "Structure of activated aconitase: Formation of the [4Fe-4S] clusterin the crystal," *Proceedings of the National Academy of Sciences of the United States of America*, vol. 68, pp. 3639–3643, 1988.

[39] M. H. Emptage, "Aconitase: evolution of the active site picture," *ACS Symposium Series*, vol. 372, pp. 343–371, 1988.

[40] S. W. Ragsdale, "Life with Carbon Monoxide," *Critical Reviews in Biochemistry and Molecular Biology*, vol. 39, pp. 165–195, 2004.

[41] T. W. Woolerton, S. Sheard, E. Pierce, S. W. Ragsdale, and F. A. Armstrong, "CO_2 photoreduction at enzyme-modified metal oxide nanoparticles," *Energy Environmental Science*, vol. 4, pp. 2393–2399, 2011.

[42] O. Lazarus, T. W. Woolerton, A. Parkin, M. J. Lukey, E. Reisner, J. Seravalli, E. Pierce, S. W. Ragsdale, F. Sargent, and F. A. Armstrong, "Water-Gas Shift Reaction Catalyzed by Redox Enzymes on Conducting Graphite Platelets," *Journal of the American Chemical Society*, vol. 131, pp. 14154–14155, 2009.

[43] D. C. Rees and J. B. Howard, "The Interface Between the Biological and Inorganic Worlds: Iron-Sulfur Metalloclusters," *Science*, vol. 300, pp. 929–931, 2003.

[44] N. Khoroshilova, C. Popescu, E. Münck, H. Beinert, and P. J. Kiley, "Iron-sulfur cluster disassembly in the FNR protein of *Escherichia coli* by O_2: [4Fe-4S] to [2Fe-2S] conversion with loss of biological activity," *Proceedings of the National Academy of Sciences of the United States of America*, vol. 94, pp. 6087–6092, 1997.

[45] C. V. Popescu, D. M. Bates, H. Beinert, E. Münck, and P. J. Kiley, "Mössbauer spectroscopy as a tool for the study of activation/inactivation of the transcription regulator FNR in whole cells of *Escherichia coli*," *Proceedings of the National Academy of Sciences of the United States of America*, vol. 95, pp. 13431–13435, 1998.

[46] O. Warburg, *Heavy metal prosthetic groups and enzyme action*. Clarendon Press, Oxford, 1949.

[47] A. Volbeda, M.-H. Charon, C. Piras, E. C. Hatchikian, M. Frey, and J. C. Fontecilla-Camps, "Crystal structure of the nickel-iron hydrogenase from *Desulfovibrio gigas*," *Nature*, vol. 373, pp. 580–587, 1995.

[48] C. R. D. Lancaster, A. Kröger, M. Auer, and H. Michel, "Structure of fumarate reductase from *Wolinella succinogenes* at 2.2 Å resolution," *Nature*, vol. 402, pp. 377–385, 1999.

[49] H. Dobbek, V. Svetlitchnyi, L. Gremer, R. Huber, and O. Meyer, "Crystal Structure of a Carbon Monoxide Dehydrogenase Reveals a [Ni-4Fe-5S] Cluster," *Science*, vol. 293, pp. 1281–1285, 2001.

[50] M. G. Bertero, R. A. Rothery, M. Palak, C. Hou, D. Lim, F. Blasco, J. H. Weiner, and N. C. J. Strynadka, "Insights into the respiratory electron transfer pathway from the structure of nitrate reductase A," *Nature Structural and Molecular Biology*, vol. 10, pp. 681–687, 2003.

[51] L. A. Sazanov and P. Hinchliffe, "Structure of the Hydrophilic Domain of Respiratory Complex I from *Thermus thermophilus*," *Science*, vol. 311, pp. 1430–1436, 2006.

[52] C. C. Page, C. C. Moser, X. Chen, and P. L. Dutton, "Natural engineering principles of electron tunnelling in biological oxidation-reduction," *Nature*, vol. 402, pp. 47–52, 1999.

[53] H. B. Gray and J. R. Winkler, "Long-range electron transfer," *Proceedings of the National Academy of Sciences of the United States of America*, vol. 102, pp. 3534–3539, 2005.

[54] S. S. Skourtis, I. A. Balabin, T. Kawatsu, and D. N. Beratan, "Protein dynamics and electron transfer: Electronic decoherence and non-Condon effects," *Proceedings of the National Academy of Sciences of the United States of America*, vol. 102, pp. 3552–3557, 2005.

[55] O. Miyashita, M. Y. Okamura, and J. N. Onuchic, "Interprotein electron transfer from cytochrome c_2 to photosynthetic reaction center: Tunneling across an aqueous interface," *Proceedings of the National Academy of Sciences of the United States of America*, vol. 102, pp. 3558–3563, 2005.

[56] B. M. Hoffman, L. M. Celis, D. A. Cull, A. D. Patel, J. L. Seifert, K. E. Wheeler, J. Wang, J. Yao, I. V. Kurnikov, and J. M. Nocek, "Differential influence of dynamic processes on forward and reverse electron transfer across a protein-protein interface," *Proceedings of the National Academy of Sciences of the United States of America*, vol. 102, pp. 3564–3569, 2005.

[57] E. Yavin, A. K. Boal, E. D. A. Stemp, E. M. Boon, A. L. Livingston, V. L. O'Shea, S. S. David, and J. K. Barton, "Protein DNA charge transport: Redox activation of a DNA repair protein by guanine radical," *Proceedings of the National Academy of Sciences of the United States of America*, vol. 102, pp. 3546–3551, 2005.

[58] M. Rousset, Y. Montet, B. Guigliarelli, N. Forget, M. Asso, P. Bertrand, J. C. Fontecilla-Camps, and E. C. Hatchikian, "[3Fe-4S] to [4Fe-4S] cluster conversion in *Desulfovibrio fructosovorans* [NiFe] hydrogenase by site-directed mutagenesis," *Proceedings of the National Academy of Sciences of the United States of America*, vol. 95, pp. 11625–11630, 1998.

[59] J. C. Fontecilla-Camps, A. Volbeda, C. Cavazza, and Y. Nicolet, "Structure/Function Relationships of [NiFe]- and [FeFe]-Hydrogenases," *Chemical Reviews*, vol. 107, pp. 4273–4303, 2007.

[60] S. Dementin, V. Belle, P. Bertrand, B. Guigliarelli, G. Adryanczyk-Perrier, A. L. De Lacey, V. M. Fernandez, M. Rousset, and C. Léger, "Changing the Ligation of the Distal [4Fe4S] Cluster in NiFe Hydrogenase Impairs Inter- and Intramolecular Electron Transfers," *Journal of the American Chemical Society*, vol. 128, pp. 5209–5218, 2006.

[61] P. M. Vignais and A. Colbeau, "Molecular biology of microbial hydrogenases," *Current Issues in Molecular Biology*, vol. 6, pp. 159–188, 2004.

[62] P. M. Vignais and B. Billoud, "Occurrence, classification, and biological function of hydrogenases: an overview," *Chemical Reviews*, vol. 107, pp. 4206–4272, 2007.

[63] E. Garcin, X. Vernede, E. C. Hatchikian, A. Volbeda, M. Frey, and J. C. Fontecilla-Camps, "The crystal structure of a reduced [NiFeSe] hydrogenase provides an image of the activated catalytic center," *Structure*, vol. 7, pp. 557–566, 1999.

[64] M. Adams, "Organometallic iron: the key to biological hydrogen metabolism," *Current Opinion in Chemical Biology*, vol. 4, pp. 214–220, 2000.

[65] Y. Montet, P. Amara, A. Volbeda, X. Vernede, E. C. Hatchikian, M. J. Field, M. Frey, and J. C. Fontecilla-Camps, "Gas access to the active site of Ni-Fe hydrogenases probed by X-ray crystallography and molecular dynamics," *Nature Structural and Molecular Biology*, vol. 4, pp. 523–526, 1997.

[66] V. H. Teixeira, A. M. Baptista, and C. M. Soares, "Pathways of H_2 toward the active site of [NiFe]-hydrogenase," *Biophysical Journal*, vol. 91, pp. 2035–2045, 2006.

[67] J. Cohen, K. Kim, P. King, M. Seibert, and K. Schulten, "Finding Gas Diffusion Pathways in Proteins: Application to O_2 and H_2 Transport in *Cp*I [FeFe]-Hydrogenase and the Role of Packing Defects," *Structure*, vol. 13, pp. 1321–1329, 2005.

[68] J. Cohen, K. Kim, M. Posewitz, M. L. Ghirardi, K. Schulten, M. Seibert, and P. King, "Molecular dynamics and experimental investigation of H_2 and O_2 diffusion in [Fe]-hydrogenase," *Biochemical Society Transactions*, vol. 33, pp. 80–82, 2005.

[69] A. Volbeda and J. C. Fontecilla-Camps, "Structure-function relationships of nickel-iron sites in hydrogenase and a comparison with the active sites of other nickel-iron enzymes," *Coordination Chemistry Reviews*, vol. 249, pp. 1609–1619, 2005.

[70] A. K. Jones, E. Sillery, S. P. J. Albracht, and F. A. Armstrong, "Direct comparison of the electrocatalytic oxidation of hydrogen by an enzyme and a platinum catalyst," *Chemical Communications*, no. 8, pp. 866–867, 2002.

[71] N. M. Marković, C. A. Lucas, B. N. Grgur, and P. N. Ross, "Surface Electrochemistry of CO and H_2/CO Mixtures at Pt(100) Interface: Electrode Kinetics and Interfacial Structures," *The Journal of Physical Chemistry B*, vol. 103, pp. 9616–9623, 1999.

[72] A. Le Goff, V. Artero, B. Jousselme, P. D. Tran, N. Guillet, R. Métayé, A. Fihri, S. Palacin, and M. Fontecave, "From Hydrogenases to Noble Metal-Free Catalytic Nanomaterials for H_2 Production and Uptake," *Science*, vol. 326, pp. 1384–1387, 2009.

[73] M. L. Helm, M. P. Stewart, R. M. Bullock, M. R. DuBois, and D. L. DuBois, "A Synthetic Nickel Electrocatalyst with a Turnover Frequency Above 100,000 s^{-1} for H_2 Production," *Science*, vol. 333, pp. 863–866, 2011.

[74] E. Reisner, J. C. Fontecilla-Camps, and F. A. Armstrong, "Catalytic electrochemistry of a [NiFeSe]-hydrogenase on TiO_2 and demonstration of its suitability for visible-light driven H_2 production," *Chemical Communications*, no. 5, pp. 550–552, 2009.

[75] E. Reisner, D. J. Powell, C. Cavazza, J. C. Fontecilla-Camps, and F. A. Armstrong, "Visible Light-Driven H_2 Production by Hydrogenases Attached to Dye-Sensitized TiO_2 Nanoparticles," *Journal of the American Chemical Society*, vol. 131, pp. 18457–18466, 2009.

[76] B. Friedrich, J. Fritsch, and O. Lenz, "Oxygen-tolerant hydrogenases in hydrogen-based technologies," *Current Opinion in Biotechnology*, vol. 22, pp. 358–364, 2011.

[77] H. Krassen, A. Schwarze, B. Friedrich, K. Ataka, O. Lenz, and J. Heberle, "Photosynthetic Hydrogen Production by a Hybrid Complex of Photosystem I and [NiFe]-Hydrogenase," *ACS Nano*, vol. 3, pp. 4055–4061, 2009.

[78] C. E. Lubner, P. Knörzer, P. J. Silva, K. A. Vincent, T. Happe, D. A. Bryant, and J. H. Golbeck, "Wiring an [FeFe]-hydrogenase with photosystem I for light-induced hydrogen production.," *Biochemistry*, vol. 49, pp. 10264–10266, 2010.

[79] M. Heinnickel, D. A. Bryant, and J. H. Golbeck, "Wiring photosystem I for electron transfer to a tethered redox dye," *Energy and Environmental Science*, vol. 4, pp. 2428–2434, 2011.

[80] T. Buhrke, O. Lenz, N. Krauss, and B. Friedrich, "Oxygen Tolerance of the H_2-sensing [NiFe] Hydrogenase from *Ralstonia eutropha* H16 Is Based on Limited Access of Oxygen to the Active Site," *Journal of Biological Chemistry*, vol. 280, pp. 23791–23796, 2005.

[81] O. Duché, S. Elsen, L. Cournac, and A. Colbeau, "Enlarging the gas access channel to the active site renders the regulatory hydrogenase HupUV of *Rhodobacter capsulatus* O_2 sensitive without affecting its transductory activity," *FEBS Journal*, vol. 272, pp. 3899–3908, 2005.

[82] M. Saggu, I. Zebger, M. Ludwig, O. Lenz, B. Friedrich, P. Hildebrandt, and F. Lendzian, "Spectroscopic Insights into the Oxygen-tolerant Membrane-associated [NiFe] Hydrogenase of *Ralstonia eutropha* H16," *Journal of Biological Chemistry*, vol. 284, pp. 16264–16276, 2009.

[83] M. J. Lukey, A. Parkin, M. M. Roessler, B. J. Murphy, J. Harmer, T. Palmer, F. Sargent, and F. A. Armstrong, "How *Escherichia coli* is equipped to oxidize hydrogen under different redox conditions," *Journal of Biological Chemistry*, vol. 285, pp. 3928–3938, 2010.

[84] M. Brugna-Guiral, P. Tron, W. Nitschke, K.-O. O. Stetter, B. Burlat, B. Guigliarelli, M. Bruschi, and M. T. Giudici-Orticoni, "[NiFe] hydrogenases from the hyperthermophilic bacterium *Aquifex aeolicus*: properties, function, and phylogenetics," *Extremophiles*, vol. 7, pp. 145–157, 2003.

[85] K.-S. Yoon, K. Fukuda, K. Fujisawa, and H. Nishihara, "Purification and characterization of a highly thermostable, oxygen-resistant, respiratory [NiFe]-hydrogenase from a marine, aerobic hydrogen-oxidizing bacterium *Hydrogenovibrio marinus*," *International Journal of Hydrogen Energy*, vol. 36, pp. 7081–7088, 2011.

[86] M. Ludwig, J. A. Cracknell, K. A. Vincent, F. A. Armstrong, and O. Lenz, "Oxygen-tolerant H_2 Oxidation by Membrane-bound [NiFe] Hydrogenases of *Ralstonia* Species," *Journal of Biological Chemistry*, vol. 284, pp. 465–477, 2009.

[87] J. Fritsch, P. Scheerer, S. Frielingsdorf, S. Kroschinsky, B. Friedrich, O. Lenz, and C. M. Spahn, "The crystal structure of an oxygen-tolerant hydrogenase uncovers a novel iron-sulphur centre," *Nature*, vol. 479, pp. 249–252, 2011.

[88] T. Goris, A. F. Wait, M. Saggu, J. Fritsch, N. Heidary, M. Stein, I. Zebger, F. Lendzian, F. A. Armstrong, B. Friedrich, and O. Lenz, "A unique iron-sulfur cluster is crucial for oxygen tolerance of a [NiFe]-hydrogenase," *Nature Chemical Biology*, vol. 7, pp. 310–318, 2011.

[89] M. J. Lukey, M. M. Roessler, A. Parkin, R. M. Evans, R. A. Davies, O. Lenz, B. Friedrich, F. Sargent, and F. A. Armstrong, "Oxygen-Tolerant [NiFe]-Hydrogenases: The Individual and Collective Importance of Supernumerary Cysteines at the Proximal Fe-S Cluster," *Journal of the American Chemical Society*, vol. 133, pp. 16881–16892, 2011.

[90] J. Hirst, "Towards the molecular mechanism of respiratory complex I," *Biochemical Journal*, vol. 425, pp. 327–339, 2010.

[91] J. Carroll, I. M. Fearnley, J. M. Skehel, R. J. Shannon, J. Hirst, and J. E. Walker, "Bovine Complex I Is a Complex of 45 Different Subunits," *Journal of Biological Chemistry*, vol. 281, pp. 32724–32727, 2006.

[92] U. Brandt, "Energy Converting NADH: Quinone Oxidoreductase (Complex I)," *Annual Review of Biochemistry*, vol. 75, pp. 69–92, 2006.

[93] T. Clason, T. Ruiz, H. Schägger, G. Peng, V. Zickermann, U. Brandt, H. Michel, and M. Radermacher, "The structure of eukaryotic and prokaryotic complex I," *Journal of Structural Biology*, vol. 169, pp. 81–88, 2010.

[94] G. Yakovlev, T. Reda, and J. Hirst, "Reevaluating the relationship between EPR spectra and enzyme structure for the iron-sulfur clusters in NADH:quinone oxidoreductase," *Proceedings of the National Academy of Sciences of the United States of America*, vol. 104, pp. 12720–12725, 2007.

[95] J. M. Berrisford and L. A. Sazanov, "Structural Basis for the Mechanism of Respiratory Complex I," *Journal of Biological Chemistry*, vol. 284, pp. 29773–29783, 2009.

[96] M. S. King, M. S. Sharpley, and J. Hirst, "Reduction of Hydrophilic Ubiquinones by the Flavin in Mitochondrial NADH:Ubiquinone Oxidoreductase (Complex I) and Production of Reactive Oxygen Species," *Biochemistry*, vol. 48, pp. 2053–2062, 2009.

[97] R. G. Efremov, R. Baradaran, and L. A. Sazanov, "The architecture of respiratory complex I," *Nature*, vol. 465, pp. 441–445, 2010.

[98] C. Hunte, V. Zickermann, and U. Brandt, "Functional Modules and Structural Basis of Conformational Coupling in Mitochondrial Complex I," *Science*, vol. 329, pp. 448–451, 2010.

[99] M.-C. Kao, E. Nakamaru-Ogiso, A. Matsuno-Yagi, and T. Yagi, "Characterization of the Membrane Domain Subunit NuoK (ND4L) of the NADH-Quinone Oxidoreductase from *Escherichia coli*," *Biochemistry*, vol. 44, pp. 9545–9554, 2005.

[100] A. Schapira, "Human complex I defects in neurodegenerative diseases," *Biochimica et Biophysica Acta - Bioenergetics*, vol. 1364, pp. 261–270, 1998.

[101] S. DiMauro and E. A. Schon, "Mitochondrial Respiratory-Chain Diseases," *The New England Journal of Medicine*, vol. 348, pp. 2656–2668, 2003.

[102] J. Smeitink, L. van den Heuvel, and S. DiMauro, "The genetics and pathology of oxidative phosphorylation," *Nature Reviews Genetics*, vol. 2, pp. 342–352, 2001.

[103] T. M. Dawson and V. L. Dawson, "Molecular Pathways of Neurodegeneration in Parkinson's Disease," *Science*, vol. 302, pp. 819–822, 2003.

[104] R. S. Balaban, S. Nemoto, and T. Finkel, "Mitochondria, Oxidants, and Aging," *Cell*, vol. 120, pp. 483–495, 2005.

[105] L. Kussmaul and J. Hirst, "The mechanism of superoxide production by NADH:ubiquinone oxidoreductase (complex I) from bovine heart mitochondria," *Proceedings of the National Academy of Sciences of the United States of America*, vol. 103, pp. 7607–7612, 2006.

[106] T. Pohl, T. Bauer, K. Dörner, S. Stolpe, P. Sell, G. Zocher, and T. Friedrich, "Iron-Sulfur Cluster N7 of the NADH: Ubiquinone Oxidoreductase (Complex I) Is Essential for Stability but Not Involved in Electron Transfer," *Biochemistry*, vol. 46, pp. 6588–6596, 2007.

[107] E. Nakamaru-Ogiso, T. Yano, T. Yagi, and T. Ohnishi, "Characterization of the Iron-Sulfur Cluster N7 (N1c) in the Subunit NuoG of the Proton-translocating NADH-quinone Oxidoreductase from *Escherichia coli*," *Journal of Biological Chemistry*, vol. 280, pp. 301–307, 2005.

[108] D. Esterházy, M. S. King, G. Yakovlev, and J. Hirst, "Production of Reactive Oxygen Species by Complex I (NADH:Ubiquinone Oxidoreductase) from *Escherichia coli* and Comparison to the Enzyme from Mitochondria," *Biochemistry*, vol. 47, pp. 3964–3971, 2008.

[109] N. M. Atherton, *Principles of Electron Spin Resonance*. Ellis Horwood Limited, 1993.

[110] J. A. Weil and J. R. Bolton, *Electron Paramagnetic Resonance*. Wiley, second ed., 2007.

[111] A. Schweiger and G. Jeschke, *Principles of pulse electron paramagnetic resonance*. Oxford University Press, 2005.

[112] G. R. Eaton, S. Eaton, and K. M. Salikhov, *Foundations of Modern EPR*. World Scientific Publishing, 1998.

[113] G. Jeschke, *Kurze Einführung in die elektronparamagnetische Resonanzspektroskopie*. http://www.epr.ethz.ch/education/epr2007.pdf: Universität Konstanz, 2007.

[114] S. A. Goudsmit, "The Discovery of the Electron Spin," in *Foundations of Modern EPR* (G. R. Eaton, S. Eaton, and K. M. Salikhov, eds.), pp. 1–12, World Scientific Publishing, 1998.

[115] P. J. Hore, J. A. Jones, and S. Wimperis, *NMR: The Toolkit*. Oxford University Press, 2000.

[116] S. Stoll and A. Schweiger, "EasySpin, a comprehensive software package for spectral simulation and analysis in EPR," *Journal of Magnetic Resonance*, vol. 178, pp. 42–55, 2006.

[117] S. Stoll, *EasySpin*, http://www.easyspin.org, 2011.

[118] W. Lubitz, E. Reijerse, and M. van Gastel, "[NiFe] and [FeFe] Hydrogenases Studied by Advanced Magnetic Resonance Techniques," *Chemical Reviews*, vol. 107, pp. 4331–4365, 2007.

[119] A. Abragam and M. H. L. Pryce, "Theory of the Nuclear Hyperfine Structure of Paramagnetic Resonance Spectra in Crystals," *Proceedings of the Royal Society of London. Series A. Mathematical and Physical Sciences*, vol. 205, pp. 135–153, 1951.

[120] W. R. Hagen, "EPR spectroscopy as a probe of metal centres in biological systems," *Dalton Transactions*, no. 37, pp. 4415–4434, 2006.

[121] B. J. Hales, *EPR and ENDOR Spectroscopies*, Louisiana State University.

[122] Bruker BioSpin, *Pulse EPR*. http://www.bruker-biospin.com/pulse.html, 2011.

[123] G. Jeschke, R. Rakhmatullin, and A. Schweiger, "Sensitivity Enhancement by Matched Microwave Pulses in One- and Two-Dimensional Electron Spin Echo Envelope Modulation Spectroscopy," *Journal of Magnetic Resonance*, vol. 131, pp. 261–271, 1998.

[124] J. Forrer, I. García-Rubio, R. Schuhmam, R. Tschaggelar, and J. Harmer, "Cryogenic Q-band (35GHz) probehead featuring large excitation microwave fields for pulse and continuous wave electron paramagnetic resonance spectroscopy: Performance and applications," *Journal of Magnetic Resonance*, vol. 190, pp. 280–291, 2008.

[125] T. Buhrke, M. Brecht, W. Lubitz, and B. Friedrich, "The H_2 sensor of *Ralstonia eutropha*: biochemical and spectroscopic analysis of mutant proteins modified at a conserved glutamine residue close to the [NiFe] active site," *Journal of Biological Inorganic Chemistry*, vol. 7, pp. 897–908, 2002.

[126] C. Calle, A. Sreekanth, M. V. Fedin, J. Forrer, I. Garcia-Rubio, I. A. Gromov, D. Hinderberger, B. Kasumaj, P. Léger, B. Mancosu, G. Mitrikas, M. G. Santangelo, S. Stoll, A. Schweiger, R. Tschaggelar, and J. Harmer, "Pulse EPR Methods for Studying Chemical and Biological Samples Containing Transition Metals," *Helvetica Chimica Acta*, vol. 89, pp. 2495–2521, 2006.

[127] A. D. Milov, K. M. Salikhov, and M. D. Shchirov, "Use of the double resonance in electron spin echo method for the study of paramagnetic center spatial distribution in solids," *Fizika Tverdogo Tela*, vol. 23, pp. 975–982, 1981.

[128] R. Cammack, "Redox states and potentials," *Bioenergetics*, pp. 85–109, 1995.

[129] P. L. Dutton, "Redox potentiometry: Determination of midpoint potentials of oxidation-reduction components of biological electron-transfer systems," *Methods in Enzymology*, vol. 54, pp. 411–435, 1978.

[130] R. C. Prince, S. J. G. Linkletter, and Dutton, "The thermodynamic properties of some commonly used oxidation-reduction mediators, inhibitors and dyes, as determined by polarography," *Biochimica et Biophysica Acta - Bioenergetics*, vol. 635, pp. 132–148, 1981.

[131] P. Wardman, "Reduction Potentials of One-Electron Couples Involving Free Radicals in Aqueous Solution," *Journal of Physical and Chemical Reference Data*, vol. 18, pp. 1637–1755, 1989.

[132] K. A. Vincent, A. Parkin, and F. A. Armstrong, "Investigating and Exploiting the Electrocatalytic Properties of Hydrogenases," *Chemical Reviews*, vol. 107, pp. 4366–4413, 2007.

[133] A. J. Bard and L. R. Faulkner, *Electrochemical Methods: Fundamentals and Applications*. Wiley, New York, 1980.

[134] W. Hofbauer and R. Bittl, "A Novel Approach to Separating EPR Lines Arising from Species with Different Transition Moments," *Journal of Magnetic Resonance*, vol. 147, pp. 226–231, 2000.

[135] M. M. Roessler, M. S. King, A. J. Robinson, F. A. Armstrong, J. Harmer, and J. Hirst, "Direct assignment of EPR spectra to structurally defined iron-sulfur clusters in complex I by double electron-electron resonance," *Proceedings of the National Academy of Sciences of the United States of America*, vol. 107, pp. 1930–1935, 2010.

[136] M. J. Lukey, *The Uptake [NiFe]-Hydrogenases of* Escherichia coli. PhD thesis, Oxford University, Balliol College, 2010.

[137] A. Dubini, "How bacteria get energy from hydrogen: a genetic analysis of periplasmic hydrogen oxidation in *Escherichia coli*," *International Journal of Hydrogen Energy*, vol. 27, pp. 1413–1420, 2002.

[138] A. Parkin, L. Bowman, M. M. Roessler, R. A. Davies, T. Palmer, F. A. Armstrong, and F. Sargent, "How *Salmonella* oxidises H_2 under aerobic conditions," *FEBS Letters*, vol. 586, pp. 536–544, 2012.

[139] M. Bradford, "A rapid and sensitive method for the quantitation of microgram quantities of protein utilizing the principle of protein-dye binding," *Analytical Biochemistry*, vol. 72, pp. 248–254, 1976.

[140] P. K. Glasoe and F. A. Long, "Use of glass electrodes to measure acidities in deuterium oxide," *The Journal of Physical Chemistry*, vol. 64, pp. 188–190, 1960.

[141] D. L. Williams-Smith, R. C. Bray, M. J. Barber, A. D. Tsopanakis, and S. P. Vincent, "Changes in apparent pH on freezing aqueous buffer solutions and their relevance to biochemical electron-paramagnetic-resonance spectroscopy," *The Biochemical Journal*, vol. 167, pp. 593–600, 1977.

[142] J. E. Lovett, A. M. Bowen, C. R. Timmel, M. W. Jones, J. R. Dilworth, D. Caprotti, S. G. Bell, L. L. Wong, and J. Harmer, "Structural information from orientationally selective DEER spectroscopy," *Physical Chemistry Chemical Physics*, vol. 11, pp. 6840–6848, 2009.

[143] T. Ohnishi, "Iron-sulfur clusters/semiquinones in Complex I," *Biochimica et Biophysica Acta - Bioenergetics*, vol. 1364, pp. 186–206, 1998.

[144] T. Ohnishi and E. Nakamaru-Ogiso, "Were there any "misassignments" among iron-sulfur clusters N4, N5 and N6b in NADH-quinone oxidoreductase (complex I)?," *Biochimica et Biophysica Acta - Bioenergetics*, vol. 1777, pp. 703–710, 2008.

[145] T. Reda, C. D. Barker, and J. Hirst, "Reduction of the Iron-Sulfur Clusters in Mitochondrial NADH:Ubiquinone Oxidoreductase (Complex I) by Eu^{II}-DTPA, a Very Low Potential Reductant," *Biochemistry*, vol. 47, pp. 8885–8893, 2008.

[146] J. Hirst, J. Carroll, I. M. Fearnley, R. J. Shannon, and J. E. Walker, "The nuclear encoded subunits of complex I from bovine heart mitochondria.," *Biochimica et Biophysica Acta*, vol. 1604, pp. 135–150, 2003.

[147] T. Yano, W. R. Dunham, and T. Ohnishi, "Characterization of the $\Delta\mu H^+$ -Sensitive Ubisemiquinone Species (SQNf) and the Interaction with Cluster N2: New Insight into the Energy-Coupled Electron Transfer in Complex I," *Biochemistry*, vol. 44, pp. 1744–1754, 2005.

[148] T. Maly, F. MacMillan, K. Zwicker, N. Kashani-Poor, U. Brandt, and T. F. Prisner, "Relaxation filtered hyperfine (REFINE) spectroscopy: a novel tool for studying overlapping biological electron paramagnetic resonance signals applied to mitochondrial complex I," *Biochemistry*, vol. 43, pp. 3969–3978, 2004.

[149] A. Cernescu, T. Maly, and T. F. Prisner, "2D-REFINE spectroscopy: Separation of overlapping hyperfine spectra," *Journal of Magnetic Resonance*, vol. 192, pp. 78–84, 2008.

[150] T. Maly, K. Zwicker, A. Cernescu, U. Brandt, and T. F. Prisner, "New pulsed EPR methods and their application to characterize mitochondrial complex I," *Biochimica et Biophysica Acta - Bioenergetics*, vol. 1787, pp. 584–592, 2009.

[151] L. Euro, D. A. Bloch, M. Wikström, M. I. Verkhovsky, and M. Verkhovskaya, "Electrostatic Interactions Between FeS Clusters in NADH:Ubiquinone Oxidoreductase (Complex I) from *Escherichia coli*," *Biochemistry*, vol. 47, pp. 3185–3193, 2008.

[152] V. D. Sled', T. Friedrich, H. Leif, H. Weiss, S. W. Meinhardt, Y. Fukumori, M. W. Calhoun, R. B. Gennis, and T. Ohnishi, "Bacterial NADH-quinone oxidoreductases: Iron-sulfur clusters and related problems," *Journal of Bioenergetics and Biomembranes*, vol. 25, pp. 347–356, 1993.

[153] V. D. Sled, N. I. Rudnitzky, Y. Hatefi, and T. Ohnishi, "Thermodynamic Analysis of Flavin in Mitochondrial NADH:Ubiquinone Oxidoreductase (Complex I)," *Biochemistry*, vol. 33, pp. 10069–10075, 1994.

[154] M. Uhlmann and T. Friedrich, "EPR Signals Assigned to Fe/S Cluster N1c of the *Escherichia coli* NADH:Ubiquinone Oxidoreductase (Complex I) Derive from Cluster N1a," *Biochemistry*, vol. 44, pp. 1653–1658, 2005.

[155] Y. Zu, S. Di Bernardo, T. Yagi, and J. Hirst, "Redox Properties of the [2Fe-2S] Center in the 24 kDa (NQO2) Subunit of NADH:Ubiquinone Oxidoreductase (Complex I)," *Biochemistry*, vol. 41, pp. 10056–10069, 2002.

[156] T. Yano, T. Yagi, V. D. Sled, and T. Ohnishi, "Expression and Characterization of the 66-Kilodalton (NQO3) Iron-Sulfur Subunit of the Proton-translocating NADH-Quinone Oxidoreductase of *Paracoccus denitrificans*," *Journal of Biological Chemistry*, vol. 270, pp. 18264–18270, 1995.

[157] A. Vinogradov, "Energy-dependent Complex I-associated ubisemiquinones in submitochondrial particles," *FEBS Letters*, vol. 370, pp. 83–87, 1995.

[158] G. Jeschke, "Direct Conversion of EPR Dipolar Time Evolution Data to Distance Distributions," *Journal of Magnetic Resonance*, vol. 155, pp. 72–82, 2002.

[159] Y.-W. Chiang, P. P. Borbat, and J. H. Freed, "Maximum entropy: A complement to Tikhonov regularization for determination of pair distance distributions by pulsed ESR," *Journal of Magnetic Resonance*, vol. 177, pp. 184–196, 2005.

[160] G. Jeschke, "Distance Measurements in the Nanometer Range by Pulse EPR," *ChemPhysChem*, vol. 3, pp. 927–932, 2002.

[161] O. Schiemann and T. F. Prisner, "Long-range distance determinations in biomacromolecules by EPR spectroscopy.," *Quarterly Reviews of Biophysics*, vol. 40, pp. 1–53, 2007.

[162] P. Bertrand, C. More, B. Guigliarelli, A. Fournel, B. Bennett, and B. Howes, "Biological polynuclear clusters coupled by magnetic interactions: From the point dipole approximation to a local spin model," *Journal of the American Chemical Society*, vol. 116, pp. 3078–3086, 1994.

[163] C. Elsässer, M. Brecht, and R. Bittl, "Pulsed Electron-Electron Double Resonance on Multinuclear Metal Clusters: Assignment of Spin Projection Factors Based on the Dipolar Interaction," *Journal of the American Chemical Society*, vol. 124, pp. 12606–12611, 2002.

[164] C. Elsässer, M. Brecht, and R. Bittl, "Treatment of spin-coupled metal-centres in pulsed electron-electron double-resonance experiments," *Biochemical Society Transactions*, vol. 33, pp. 15–19, 2005.

[165] J. Telser, H.-I. Lee, and B. M. Hoffman, "Investigation of exchange couplings in $[Fe_3S_4]^+$ clusters by electron spin-lattice relaxation," *Journal of Biological Inorganic Chemistry*, vol. 5, pp. 369–380, 2000.

[166] T. A. Kent, B. H. Huynh, and E. Münck, "Iron-sulfur proteins: spin-coupling model for three-iron clusters," *Proceedings of the National Academy of Sciences of the United States of America*, vol. 77, pp. 6574–6576, 1980.

[167] C. C. Moser, J. M. Keske, K. Warncke, R. S. Farid, and P. L. Dutton, "Nature of biological electron transfer," *Nature*, vol. 355, pp. 796–802, 1992.

[168] B. Guigliarelli, C. More, P. Bertrand, and J. P. Gayda, "g-tensor calculation for Fe[III] triads: Application to the 3Fe clusters in iron-sulfur proteins," *The Journal of Chemical Physics*, vol. 85, pp. 2774–2778, 1986.

[169] H. Winkler, "Spin fluctuation rates from Moessbauer spectra of high-spin ferrous rubredoxin," *Physics Letters A*, vol. 69, pp. 360–363, 1979.

[170] I. Moura, B. H. Huynh, R. P. Hausinger, J. Le Gall, A. V. Xavier, and E. Muenck, "Moessbauer and EPR Studies of Desulforedoxin from *Desulfovibrio gigas*," *Journal of Biological Chemistry*, vol. 255, pp. 2493–2498, 1980.

[171] M. Orio and J.-M. Mouesca, "Variation of Average g Values and Effective Exchange Coupling Constants among [2Fe-2S] Clusters: A Density Functional Theory Study of the Impact of Localization (Trapping Forces) versus Delocalization (Double-Exchange) as Competing Factors," *Inorganic Chemistry*, vol. 47, pp. 5394–5416, 2008.

[172] M. S. Sharpley, R. J. Shannon, F. Draghi, and J. Hirst, "Interactions between Phospholipids and NADH:Ubiquinone Oxidoreductase (Complex I) from Bovine Mitochondria," *Biochemistry*, vol. 45, pp. 241–248, 2006.

[173] R. Kappl, M. Ebelshäuser, F. Hannemann, R. Bernhardt, and J. Hüttermann, "Probing electronic and structural properties of the reduced [2Fe-2S] cluster by orientation-selective 1H ENDOR spectroscopy: Adrenodoxin versus rieske iron-sulfur protein," *Applied Magnetic Resonance*, vol. 30, pp. 427–459, 2006.

[174] R. J. Gurbiel, P. E. Doan, G. T. Gassner, T. J. Macke, D. A. Case, T. Ohnishi, J. A. Fee, D. P. Ballou, and B. M. Hoffman, "Active Site Structure of Rieske-Type Proteins: Electron Nuclear Double Resonance Studies of Isotopically Labeled Phthalate Dioxygenase from *Pseudomonas cepacia* and Rieske Protein from *Rhodobacter capsulatus* and Molecular Modeling Studies of a Rieske Center," *Biochemistry*, vol. 35, pp. 7834–7845, 1996.

[175] J. A. B. Abdalla, A. M. Bowen, S. G. Bell, L. L. Wong, C. R. Timmel, and J. Harmer, "Characterisation of the paramagnetic $[2Fe\text{-}2S]^+$ centre in palustrisredoxin-B (PuxB) from *Rhodopseudomonas palustris* CGA009: g-matrix determination and spin coupling analysis," *Physical Chemistry Chemical Physics*, vol. 14, pp. 6526–6537, 2012.

[176] A. Kamlowski, A. van der Est, P. Fromme, and D. Stehlik, "Low temperature EPR on Photosystem I single crystals: orientation of the iron-sulfur centers F_A and F_B," *Biochimica et Biophysica Acta - Bioenergetics*, vol. 1319, pp. 185–198, 1997.

[177] P. Bertrand, P. Camensuli, C. More, and B. Guigliarelli, "A Local Spin Model To Describe the Magnetic Interactions in Biological Molecules Containing $[4Fe\text{-}4S]^+$ Clusters. Application to Ni-Fe Hydrogenases," *Journal of the American Chemical Society*, vol. 118, pp. 1426–1434, 1996.

[178] B. Guigliarelli, P. Bertrand, and J. P. Gayda, "Contribution of the fine structure terms to the g values of the biological Fe(III)-Fe(II) clusters," *The Journal of Chemical Physics*, vol. 85, pp. 1689–1692, 1986.

[179] J. T. Sage, Y. M. Xia, P. G. Debrunner, D. T. Keough, J. De Jersey, and B. Zerner, "Moessbauer analysis of the binuclear iron site in purple acid phosphatase from pig allantoic fluid," *Journal of the American Chemical Society*, vol. 111, pp. 7239–7247, 1989.

[180] J. M. Mouesca, L. Noodleman, D. A. Case, and B. Lamotte, "Spin Densities and Spin Coupling in Iron-Sulfur Clusters: A New Analysis of Hyperfine Coupling Constants," *Inorganic Chemistry*, vol. 34, pp. 4347–4359, 1995.

[181] W. R. Dunham, A. J. Bearden, I. T. Salmeen, G. Palmer, R. H. Sands, W. H. Orme-Johnson, and H. Beinert, "The two-iron ferredoxins in spinach, parsley, pig adrenal cortex, *Azotobacter vinelandii*, and *Clostridium pasteurianum*: Studies by magnetic field Mössbauer spectroscopy," *Biochimica et Biophysica Acta - Bioenergetics*, vol. 253, pp. 134–152, 1971.

[182] E. Münck and C. Popescu, "Mössbauer studies of exchange coupled cluster assemblies in biological systems," *Hyperfine Interactions*, vol. 126, pp. 59–67, 2000.

[183] G. Jeschke, M. Sajid, M. Schulte, and A. Godt, "Three-spin correlations in double electron-electron resonance," *Physical Chemistry Chemical Physics*, vol. 11, pp. 6580–6591, 2009.

[184] A. Waletko, K. Zwicker, A. Abdrakhmanova, V. Zickermann, U. Brandt, and S. Kerscher, "Histidine 129 in the 75-kDa Subunit of Mitochondrial Complex I from *Yarrowia lipolytica* is Not a Ligand for $[Fe_4S_4]$ Cluster N5 but is Required for Catalytic Activity," *Journal of Biological Chemistry*, vol. 280, pp. 5622–5625, 2005.

[185] J. A. Birrell, G. Yakovlev, and J. Hirst, "Reactions of the Flavin Mononucleotide in Complex I: A Combined Mechanism Describes NADH Oxidation Coupled to the Reduction of $APAD^+$, Ferricyanide, or Molecular Oxygen," *Biochemistry*, vol. 48, pp. 12005–12013, 2009.

[186] H. R. Bridges, E. Bill, and J. Hirst, "Mössbauer spectroscopy on respiratory complex I: the iron-sulfur cluster ensemble in the NADH-reduced enzyme is partially oxidized," *Biochemistry*, vol. 51, pp. 149–158, 2012.

[187] V. Yankovskaya, R. Horsefield, S. Törnroth, C. Luna-Chavez, H. Miyoshi, C. Léger, B. Byrne, G. Cecchini, and S. Iwata, "Architecture of Succinate Dehydrogenase and Reactive Oxygen Species Generation," *Science*, vol. 299, pp. 700–704, 2003.

[188] M. R. Gunner and B. Honig, "Electrostatic control of midpoint potentials in the cytochrome subunit of the *Rhodopseudomonas viridis* reaction center," *Proceedings of the National Academy of Sciences of the United States of America*, vol. 88, pp. 9151–9155, 1991.

[189] J. Alric, J. Lavergne, F. Rappaport, A. Verméglio, K. Matsuura, K. Shimada, and K. V. P. Nagashima, "Kinetic Performance and Energy Profile in a Roller Coaster Electron Transfer Chain: A Study of Modified Tetraheme-Reaction Center Constructs," *Journal of the American Chemical Society*, vol. 128, pp. 4136–4145, 2006.

[190] W. Nitschke and S. M. Dracheva, *Reaction center-associated cytochromes*, pp. 775–805. Kluwer Academic Publishers, 1995.

[191] C. C. Moser, T. A. Farid, S. E. Chobot, and P. L. Dutton, "Electron tunneling chains of mitochondria," *Biochimica et Biophysica Acta - Bioenergetics*, vol. 1757, pp. 1096–1109, 2006.

[192] M. L. Verkhovskaya, N. Belevich, L. Euro, M. Wikström, and M. I. Verkhovsky, "Real-time electron transfer in respiratory complex I," *Proceedings of the National Academy of Sciences of the United States of America*, vol. 105, pp. 3763–3767, 2008.

[193] C. I. Ragan and E. Racker, "Resolution and Reconstitution of the Mitochondrial Electron Transport System," *Journal of Biological Chemistry*, vol. 248, pp. 6876–6884, 1973.

[194] M. Brecht, M. van Gastel, T. Buhrke, B. Friedrich, and W. Lubitz, "Direct Detection of a Hydrogen Ligand in the [NiFe] Center of the Regulatory H_2-Sensing Hydrogenase from *Ralstonia eutropha* in Its Reduced State by HYSCORE and ENDOR Spectroscopy," *Journal of the American Chemical Society*, vol. 125, pp. 13075–13083, 2003.

[195] S. P. J. Albracht, E. G. Graf, and R. K. Thauer, "The EPR properties of nickel in hydrogenase from *Methanobacterium thermoautotrophicum*," *FEBS Letters*, vol. 140, pp. 311–313, 1982.

[196] R. Cammack, D. Patil, R. Aguirre, and E. Hatchikian, "Redox properties of the ESR-detectable nickel in hydrogenase from *Desulfovibrio gigas*," *FEBS Letters*, vol. 142, pp. 289–292, 1982.

[197] J. LeGall, P. O. Ljungdahl, I. Moura, H. D. Peck, A. V. Xavier, J. J. G. Moura, M. Teixera, B. H. Huynh, and D. V. DerVartanian, "The presence of redox-sensitive nickel in the periplasmic hydrogenase from *Desulfovibrio gigas*," *Biochemical and Biophysical Research Communications*, vol. 106, pp. 610–616, 1982.

[198] V. Fernandez, "ESR-detectable nickel and iron-sulphur centres in relation to the reversible activation of *Desulfovibrio gigas* hydrogenase," *Biochimica et Biophysica Acta - General Subjects*, vol. 883, pp. 145–154, 1986.

[199] M. Teixeira, I. Moura, A. V. Xavier, D. V. DerVartanian, L. J. LeGall, H. D. Peck, B. H. Huynh, and J. J. G. Moura, "*Desulfovibrio gigas* Hydrogenase: Redox Properties of the Nickel and Iron-Sulfur Centers," *European Journal of Biochemistry*, vol. 130, pp. 481–484, 1983.

[200] R. Cammack, D. Patil, E. Hatchikian, and V. Fernandez, "Nickel and iron-sulphur centres in *Desulfovibrio gigas* hydrogenase: ESR spectra, redox properties and interactions," *Biochimica et Biophysica Acta - Protein Structure and Molecular Enzymology*, vol. 912, pp. 98–109, 1987.

[201] J. M. C. C. Coremans, J. W. Van der Zwaan, and S. P. J. Albracht, "Redox behaviour of nickel in hydrogenase from *Methanobacterium thermoautotrophicum* (strain Marburg). Correlation between the nickel valence state and enzyme activity," *Biochimica et Biophysica Acta - Protein Structure and Molecular Enzymology*, vol. 997, pp. 256–267, 1989.

[202] M. Teixeira, I. Moura, A. V. Xavier, J. J. Moura, J. LeGall, D. V. DerVartanian, H. D. Peck, and B. H. Huynh, "Redox intermediates of *Desulfovibrio gigas* [NiFe] hydrogenase generated under hydrogen. Mössbauer and EPR characterization of the metal centers," *Journal of Biological Chemistry*, vol. 264, pp. 16435–16450, 1989.

[203] J. M. Coremans, J. W. van der Zwaan, and S. P. Albracht, "Distinct redox behaviour of prosthetic groups in ready and unready hydrogenase from *Chromatium vinosum*," *Biochimica et Biophysica Acta*, vol. 1119, pp. 157–168, 1992.

[204] L. M. Roberts and P. A. Lindahl, "Analysis of Oxidative Titrations of *Desulfovibrio gigas* Hydrogenase; Implications for the Catalytic Mechanism," *Biochemistry*, vol. 33, pp. 14339–14350, 1994.

[205] L. M. Roberts and P. A. Lindahl, "Stoichiometric reductive titrations of *Desulfovibrio gigas* hydrogenase," *Journal of the American Chemical Society*, vol. 117, pp. 2565–2572, 1995.

[206] K. A. Bagley, E. C. Duin, W. Roseboom, S. P. J. Albracht, and W. H. Woodruff, "Infrared-Detectable Group Senses Changes in Charge Density on the Nickel Center in Hydrogenase from *Chromatium vinosum*," *Biochemistry*, vol. 34, pp. 5527–5535, 1995.

[207] A. J. Pierik, W. Roseboom, R. P. Happe, K. A. Bagley, and S. P. J. Albracht, "Carbon Monoxide and Cyanide as Intrinsic Ligands to Iron in the Active Site of [NiFe]-Hydrogenases," *Journal of Biological Chemistry*, vol. 274, pp. 3331–3337, 1999.

[208] R. P. Happe, W. Roseboom, A. J. Pierik, S. P. J. Albracht, and K. A. Bagley, "Biological activition of hydrogen," *Nature*, vol. 385, p. 126, 1997.

[209] F. Dole, A. Fournel, V. Magro, E. C. Hatchikian, P. Bertrand, and B. Guigliarelli, "Nature and Electronic Structure of the Ni-X Dinuclear Center of *Desulfovibrio gigas* Hydrogenase. Implications for the Enzymatic Mechanism," *Biochemistry*, vol. 36, pp. 7847–7854, 1997.

[210] J. E. Huyett, M. Carepo, A. Pamplona, R. Franco, I. Moura, J. J. G. Moura, and B. M. Hoffman, "57Fe Q-Band Pulsed ENDOR of the Hetero-Dinuclear Site of Nickel Hydrogenase: Comparison of the NiA, NiB, and NiC States," *Journal of the American Chemical Society*, vol. 119, pp. 9291–9292, 1997.

[211] A. L. de Lacey, E. C. Hatchikian, A. Volbeda, M. Frey, J. C. Fontecilla-Camps, and V. M. Fernandez, "Infrared-Spectroelectrochemical Characterization of the [NiFe] Hydrogenase of *Desulfovibrio gigas*," *Journal of the American Chemical Society*, vol. 119, pp. 7181–7189, 1997.

[212] J. van der Zwaan, S. Albracht, R. Fontijn, and E. Slater, "Monovalent nickel in hydrogenase from *Chromatium vinosum* Light sensitivity and evidence for direct interaction with hydrogen," *FEBS Letters*, vol. 179, pp. 271–277, 1985.

[213] R. Williams, R. Cammack, and E. C. Hatchikian, "Studies of light-induced nickel EPR signals in *Desulfovibrio gigas* hydrogenase," *Faraday Transactions*, vol. 90, pp. 2921–2924, 1994.

[214] M. Medina, E. C. Hatchikian, and R. Cammack, "Studies of light-induced nickel EPR signals in hydrogenase: comparison of enzymes with and without selenium," *Biochimica et Biophysica Acta - Bioenergetics*, vol. 1275, pp. 227–236, 1996.

[215] G. Boison, O. Schmitz, B. Schmitz, and H. Bothe, "Unusual Gene Arrangement of the Bidirectional Hydrogenase and Functional Analysis of Its Diaphorase Subunit HoxU in Respiration of the Unicellular Cyanobacterium *Anacystis nidulans*," *Current Microbiology*, vol. 36, pp. 253–258, 1998.

[216] H.-J. Fan and M. B. Hall, "A Capable Bridging Ligand for Fe-Only Hydrogenase: Density Functional Calculations of a Low-Energy Route for Heterolytic Cleavage and Formation of Dihydrogen," *Journal of the American Chemical Society*, vol. 123, pp. 3828–3829, 2001.

[217] S. Foerster, M. Stein, M. Brecht, H. Ogata, Y. Higuchi, and W. Lubitz, "Single Crystal EPR Studies of the Reduced Active Site of [NiFe] Hydrogenase from *Desulfovibrio vulgaris* Miyazaki F," *Journal of the American Chemical Society*, vol. 125, pp. 83–93, 2002.

[218] C. Fichtner, M. Gastel, and W. Lubitz, "Wavelength dependence of the photoinduced conversion of the Ni-C to the Ni-L redox state in the [NiFe] hydrogenase of *Desulfovibrio vulgaris* Miyazaki F," *Physical Chemistry Chemical Physics*, vol. 5, pp. 5507–5513, 2003.

[219] Y. Higuchi, T. Yagi, and N. Yasuoka, "Unusual ligand structure in NiFe active center and an additional Mg site in hydrogenase revealed by high resolution X-ray structure analysis," *Structure*, vol. 5, pp. 1671–1680, 1997.

[220] V. Fernandez, R. Aguirre, and E. Hatchikian, "Reductive activation and redox properties of hydrogenase from *Desulfovibrio gigas*," *Biochimica et Biophysica Acta - Protein Structure and Molecular Enzymology*, vol. 790, pp. 1–7, 1984.

[221] A. Volbeda, E. Garcin, C. Piras, A. L. de Lacey, V. M. Fernandez, E. C. Hatchikian, M. Frey, and J. C. Fontecilla-Camps, "Structure of the [NiFe] Hydrogenase Active Site: Evidence for Biologically Uncommon Fe Ligands," *Journal of the American Chemical Society*, vol. 118, pp. 12989–12996, 1996.

[222] P. M. Matias, C. M. Soares, L. M. Saraiva, R. Coelho, J. Morais, J. Le Gall, and M. A. Carrondo, "[NiFe] hydrogenase from *Desulfovibrio desulfuricans* ATCC 27774: gene sequencing, three-dimensional structure determination and refinement at 1.8 Å and modelling studies of its interaction with the tetrahaem cytochrome c_3," *Journal of Biological Inorganic Chemistry*, vol. 6, pp. 63–81, 2001.

[223] H. Ogata, S. Hirota, A. Nakahara, H. Komori, N. Shibata, T. Kato, K. Kano, and Y. Higuchi, "Activation Process of [NiFe] Hydrogenase Elucidated by High-Resolution X-Ray Analyses: Conversion of the Ready to the Unready State," *Structure*, vol. 13, pp. 1635–1642, 2005.

[224] A. Volbeda, L. Martin, C. Cavazza, M. Matho, B. W. Faber, W. Roseboom, S. P. J. Albracht, E. Garcin, M. Rousset, and J. C. Fontecilla-Camps, "Structural differences between the ready and unready oxidized states of [NiFe] hydrogenases," *Journal of Biological Inorganic Chemistry*, vol. 10, pp. 239–249, 2005.

[225] M. Carepo, D. L. Tierney, C. D. Brondino, T. C. Yang, A. Pamplona, J. Telser, I. Moura, J. J. G. Moura, and B. M. Hoffman, "^{17}O ENDOR Detection of a Solvent-Derived Ni-(OHx)-Fe Bridge That Is Lost upon Activation of the Hydrogenase from *Desulfovibrio gigas*," *Journal of the American Chemical Society*, vol. 124, pp. 281–286, 2001.

[226] A. L. De Lacey, V. M. Fernandez, M. Rousset, and R. Cammack, "Activation and Inactivation of Hydrogenase Function and the Catalytic Cycle: Spectroelectrochemical Studies," *Chemical Reviews*, vol. 107, pp. 4304–4330, 2007.

[227] P. E. M. Siegbahn, J. W. Tye, and M. B. Hall, "Computational Studies of [NiFe] and [FeFe] Hydrogenases," *Chemical Reviews*, vol. 107, pp. 4414–4435, 2007.

[228] J. M. Keith and M. B. Hall, "Potential Hydrogen Bottleneck in Nickel-Iron Hydrogenase," *Inorganic Chemistry*, vol. 49, pp. 6378–6380, 2010.

[229] S. O. Lill and P. E. M. Siegbahn, "An Autocatalytic Mechanism for NiFe-Hydrogenase: Reduction to Ni(I) Followed by Oxidative Addition," *Biochemistry*, vol. 48, pp. 1056–1066, 2009.

[230] A. Volbeda and J. C. Fontecilla-Camps, "The active site and catalytic mechanism of NiFe hydrogenases," *Dalton Transactions*, no. 21, pp. 4030–4038, 2003.

[231] G. Sawers, "The hydrogenases and formate dehydrogenases of *Escherichia coli*," *Antonie van Leeuwenhoek*, vol. 66, pp. 57–88, 1994.

[232] R. G. Sawers and D. H. Boxer, "Purification and properties of membrane-bound hydrogenase isoenzyme 1 from anaerobically grown *Escherichia coli* K12," *European Journal of Biochemistry*, vol. 156, pp. 265–275, 1986.

[233] S. P. Ballantine and D. H. Boxer, "Isolation and characterisation of a soluble active fragment of hydrogenase isoenzyme 2 from the membranes of anaerobically grown *Escherichia coli*," *European Journal of Biochemistry*, vol. 156, pp. 277–284, 1986.

[234] R. G. Sawers, S. P. Ballantine, and D. H. Boxer, "Differential expression of hydrogenase isoenzymes in *Escherichia coli* K-12: evidence for a third isoenzyme," *Journal of Bacteriology*, vol. 164, pp. 1324–1331, 1985.

[235] L. Forzi and R. Sawers, "Maturation of [NiFe]-hydrogenases in *Escherichia coli*," *BioMetals*, vol. 20, pp. 565–578, 2007.

[236] T. V. Laurinavichene and A. A. Tsygankov, "H_2 consumption by *Escherichia coli* coupled via hydrogenase 1 or hydrogenase 2 to different terminal electron acceptors," *FEMS Microbiology Letters*, vol. 202, pp. 121–124, 2001.

[237] M. W. Adams and D. O. Hall, "Purification of the membrane-bound hydrogenase of *Escherichia coli*.," *The Biochemical Journal*, vol. 183, pp. 11–22, 1979.

[238] A. K. Jones, S. E. Lamle, H. R. Pershad, K. A. Vincent, S. P. J. Albracht, and F. A. Armstrong, "Enzyme Electrokinetics: Electrochemical Studies of the Anaerobic Interconversions between Active and Inactive States of *Allochromatium vinosum* [NiFe]-hydrogenase," *Journal of the American Chemical Society*, vol. 125, pp. 8505–8514, 2003.

[239] F. A. Armstrong and S. P. J. Albracht, "[NiFe]-hydrogenases: spectroscopic and electrochemical definition of reactions and intermediates," *Philosophical Transactions of the Royal Society A: Mathematical, Physical and Engineering Sciences*, vol. 363, pp. 937–954, 2005.

[240] J. A. Cracknell, A. F. Wait, O. Lenz, B. Friedrich, and F. A. Armstrong, "A kinetic and thermodynamic understanding of O_2 tolerance in [NiFe]-hydrogenases," *Proceedings of the National Academy of Sciences of the United States of America*, vol. 106, pp. 20681–20686, 2009.

[241] S. P. J. Albracht, M. L. Kalkman, and E. C. Slater, "Magnetic interaction of nickel(III) and the iron-sulphur cluster in hydrogenase from *Chromatium vinosum*," *Biochimica et Biophysica Acta - Bioenergetics*, vol. 724, pp. 309–316, 1983.

[242] W. V. Lalla-Maharajh, D. O. Hall, R. Cammack, K. K. Rao, and J. Le Gall, "Purification and properties of the membrane-bound by hydrogenase from *Desulfovibrio desulfuricans*," *The Biochemical Journal*, vol. 209, pp. 445–454, 1983.

[243] R. Cammack, K. L. Kovacs, J. McCracken, and J. Peisach, "Spectroscopic characterization of the nickel and iron-sulphur clusters of hydrogenase from the purple photosynthetic bacterium *Thiocapsa roseopersicina.*," *European Journal of Biochemistry*, vol. 182, pp. 363–366, 1989.

[244] M. DerVartanian, "Electron Paramagnetic Resonance (EPR) Studies on Hydrogenase-1 (HYD1) Purified from a Mutant Strain (AP6) of *Escherichia coli* Enhanced in HYD1," *Biochemical and Biophysical Research Communications*, vol. 227, pp. 211–215, 1996.

[245] M. Teixeira, I. Moura, A. V. Xavier, H. B. Hanh, D. V. DerVartanian, H. D. Peck, J. LeGall, and J. J. G. Moura, "Electron paramagnetic resonance studies on the mechanism of activation and the catalytic cycle on the nickel-containing hydrogenase from *Desulfovibrio gigas*," *Journal of Biological Chemistry*, vol. 260, pp. 8942–8950, 1985.

[246] C. V. Romão, I. A. C. Pereira, A. V. Xavier, J. Legall, and M. Teixeira, "Characterization of the [NiFe] Hydrogenase from the Sulfate Reducer *Desulfovibrio vulgaris* Hildenborough," *Biochemical and Biophysical Research Communications*, vol. 240, pp. 75–79, 1997.

[247] C. E. Hatchikian, A. S. Traore, V. M. Fernandez, and R. Cammack, "Characterization of the nickel-iron periplasmic hydrogenase from *Desulfovibrio fructosovorans*," *European Journal of Biochemistry*, vol. 187, pp. 635–643, 1990.

[248] S. Albracht, J. van der Zwaan, and R. Fontijn, "EPR Spectrum at 4, 9 and 35 GHz of hydrogenase from *Chromatium vinosum*. Direct evidence for spin-spin interaction between Ni(III) and the ironsulphur cluster," *Biochimica et Biophysica Acta - Bioenergetics*, vol. 766, pp. 245–258, 1984.

[249] S. Albracht, R. Fontijn, and J. van der Zwaan, "Destruction and reconstitution of the activity of hydrogenase from *Chromatium vinosum*," *Biochimica et Biophysica Acta - Protein Structure and Molecular Enzymology*, vol. 832, pp. 89–97, 1985.

[250] M.-E. Pandelia, V. Fourmond, P. Tron-Infossi, E. Lojou, P. Bertrand, C. Léger, M.-T. Giudici-Orticoni, and W. Lubitz, "Membrane-Bound Hydrogenase I from the Hyperthermophilic Bacterium *Aquifex aeolicus*: Enzyme Activation, Redox Intermediates and Oxygen Tolerance," *Journal of the American Chemical Society*, vol. 132, pp. 6991–7004, 2010.

[251] J. P. Whitehead, R. J. Gurbiel, C. Bagyinka, B. M. Hoffman, and M. J. Maroney, "The hydrogen binding site in hydrogenase: 35-GHz ENDOR and XAS studies of the nickel-C (reduced and active form) and the Ni-L photoproduct," *Journal of the American Chemical Society*, vol. 115, pp. 5629–5635, 1993.

[252] O. Schröder, B. Bleijlevens, T. de Jongh, Z. Chen, T. Li, J. Fischer, J. Förster, C. Friedrich, K. Bagley, S. Albracht, and W. Lubitz, "Characterization of a cyanobacterial-like uptake [NiFe]-hydrogenase: EPR and FTIR spectroscopic studies of the enzyme from *Acidithiobacillus ferrooxidans*," *Journal of Biological Inorganic Chemistry*, vol. 12, pp. 212–233, 2007.

[253] M.-E. Pandelia, L. J. Currell, H. Gorner, and W. Lubitz, "FTIR study on the light sensitivity of the [NiFe] hydrogenase from *Desulfovibrio vulgaris* Miyazaki F: Ni-C to Ni-L photoconversion, kinetics of proton rebinding and H/D isotope effect," *Physical Chemistry Chemical Physics*, vol. 11, pp. 8680–8683, 2009.

[254] M. Bernhard, T. Buhrke, B. Bleijlevens, A. L. De Lacey, V. M. Fernandez, S. P. J. Albracht, and B. Friedrich, "The H_2 Sensor of Ralstonia eutropha," *Journal of Biological Chemistry*, vol. 276, pp. 15592–15597, 2001.

[255] C. Fichtner, C. Laurich, E. Bothe, and W. Lubitz, "Spectroelectrochemical Characterization of the [NiFe] Hydrogenase of *Desulfovibrio vulgaris* Miyazaki F," *Biochemistry*, vol. 45, pp. 9706–9716, 2006.

[256] P. Bertrand, F. Dole, M. Asso, and B. Guigliarelli, "Is there a rate-limiting step in the catalytic cycle of [Ni-Fe] hydrogenases?," *Journal of Biological Inorganic Chemistry*, vol. 5, pp. 682–691, 2000.

[257] N. A. Zorin, B. Dimon, J. Gagnon, J. Gaillard, P. Carrier, and P. M. Vignais, "Inhibition by Iodoacetamide and Acetylene of the H-D-Exchange Reaction Catalyzed by *Thiocapsa roseopersicina* Hydrogenase," *European Journal of Biochemistry*, vol. 241, pp. 675–681, 1996.

[258] S. E. Lamle, K. A. Vincent, L. M. Halliwell, S. P. J. Albracht, and F. A. Armstrong, "Hydrogenase on an electrode: a remarkable heterogeneous catalyst," *Dalton Transactions*, no. 21, pp. 4152–4157, 2003.

[259] R. Cammack, D. S. Patil, and V. M. Fernandez, "Electron-spin-resonance/electron-paramagnetic-resonance spectroscopy of iron-sulphur enzymes.," *Biochemical Society transactions*, vol. 13, pp. 572–578, 1985.

[260] S. Foerster, M. Gastel, M. Brecht, and W. Lubitz, "An orientation-selected ENDOR and HYSCORE study of the Ni-C active state of *Desulfovibrio vulgaris* Miyazaki F hydrogenase," *Journal of Biological Inorganic Chemistry*, vol. 10, pp. 51–62, 2005.

[261] J. W. Van der Zwaan, S. P. J. Albracht, R. D. Fontijn, and P. Mul, "On the anomalous temperature behaviour of the EPR signal of monovalent nickel in hydrogenase," *European Journal of Biochemistry*, vol. 169, pp. 377–384, 1987.

[262] B. Guigliarelli, C. More, A. Fournel, M. Asso, E. C. Hatchikian, R. Williams, R. Cammack, and P. Bertrand, "Structural organization of the Ni and (4Fe-4S) centers in the active form of *Desulfovibrio gigas* hydrogenase. Analysis of the magnetic interactions by electron paramagnetic resonance spectroscopy," *Biochemistry*, vol. 34, pp. 4781–4790, 1995.

[263] P.-P. Liebgott, S. Dementin, C. Léger, and M. Rousset, "Towards engineering O_2-tolerance in [Ni-Fe] hydrogenases," *Energy and Environmental Science*, vol. 4, pp. 33–41, 2011.

[264] A. Pierik, "Characterization of the active site of a hydrogen sensor from *Alcaligenes eutropha*," *FEBS Letters*, vol. 438, pp. 231–235, 1998.

[265] M.-E. Pandelia, *[NiFe] hydrogenases from* Desulfovibrio vulgaris *Miyasaki F and* Aquifex aeolicus *studied by FTIR, EPR and electrochemical techniques: Redox intermediates, O_2/CO sensitivity and light-induced effects*. PhD thesis, Technische Universität Berlin, 2009.

[266] H. L. Flanagan and D. J. Singel, "Analysis of ^{14}N ESEEM patterns of randomly oriented solids," *The Journal of Chemical Physics*, vol. 87, pp. 5606–5616, 1987.

[267] R. Chenna, H. Sugawara, T. Koike, R. Lopez, T. J. Gibson, D. G. Higgins, and J. D. Thompson, "Multiple sequence alignment with the Clustal series of programs," *Nucleic Acids Research*, vol. 31, pp. 3497–3500, 2003.

[268] M. Horch, L. Lauterbach, M. Saggu, P. Hildebrandt, F. Lendzian, R. Bittl, O. Lenz, and I. Zebger, "Probing the active site of an O_2-tolerant NAD^+-reducing [NiFe]-hydrogenase from *Ralstonia eutropha* H16 by in situ EPR and FTIR spectroscopy.," *Angewandte Chemie International Edition*, vol. 49, pp. 8026–8029, 2010.

[269] A. F. Wait, A. Parkin, G. M. Morley, L. dos Santos, and F. A. Armstrong, "Characteristics of Enzyme-Based Hydrogen Fuel Cells Using an Oxygen-Tolerant Hydrogenase as the Anodic Catalyst," *The Journal of Physical Chemistry C*, vol. 114, pp. 12003–12009, 2010.

[270] M. M. Roessler, R. M. Evans, R. A. Davies, J. Harmer, and F. A. Armstrong, "EPR spectroscopic studies of the Fe-S clusters in the O_2-tolerant [NiFe]-hydrogenase Hyd-1 from *E. Coli*, and characterization of the unique [4Fe-3S] cluster by HYSCORE," *Journal of the American Chemical Society*, vol. 134, pp. 15581–15594, 2012.

[271] M. L. Ghirardi, M. C. Posewitz, P. C. Maness, A. Dubini, J. Yu, and M. Seibert, "Hydrogenases and Hydrogen Photoproduction in Oxygenic Photosynthetic Organisms," *Annual Review of Plant Biology*, vol. 58, pp. 71–91, 2007.

[272] C. Tard and C. J. Pickett, "Structural and Functional Analogues of the Active Sites of the [Fe]-, [NiFe]-, and [FeFe]-Hydrogenases," *Chemical Reviews*, vol. 109, pp. 2245–2274, 2009.

[273] S. E. Lamle, S. P. J. Albracht, and F. A. Armstrong, "Electrochemical Potential-Step Investigations of the Aerobic Interconversions of [NiFe]-Hydrogenase from *Allochromatium vinosum*: Insights into the Puzzling Difference between Unready and Ready Oxidized Inactive States," *Journal of the American Chemical Society*, vol. 126, pp. 14899–14909, 2004.

[274] S. E. Lamle, S. P. J. Albracht, and F. A. Armstrong, "The Mechanism of Activation of a [NiFe]-Hydrogenase by Electrons, Hydrogen, and Carbon Monoxide," *Journal of the American Chemical Society*, vol. 127, pp. 6595–6604, 2005.

[275] A. Parkin, G. Goldet, C. Cavazza, J. C. Fontecilla-Camps, and F. A. Armstrong, "The difference a Se makes? Oxygen-tolerant hydrogen production by the [NiFeSe]-hydrogenase from *Desulfomicrobium baculatum*," *Journal of the American Chemical Society*, vol. 130, pp. 13410–13416, 2008.

[276] M. C. Marques, R. Coelho, A. L. De Lacey, I. A. Pereira, and P. M. Matias, "The three-dimensional structure of [NiFeSe] hydrogenase from *Desulfovibrio vulgaris* Hildenborough: a hydrogenase without a bridging ligand in the active site in its oxidised, "as-isolated" state," *Journal of Molecular Biology*, vol. 396, pp. 893–907, 2010.

[277] S. Dementin, F. Leroux, L. Cournac, A. L. Lacey, A. Volbeda, C. Léger, B. Burlat, N. Martinez, S. Champ, L. Martin, O. Sanganas, M. Haumann, V. M. Fernández, B. Guigliarelli, J. C. Fontecilla-Camps, and M. Rousset, "Introduction of Methionines in the Gas Channel Makes [NiFe] Hydrogenase Aero-Tolerant," *Journal of the American Chemical Society*, vol. 131, pp. 10156–10164, 2009.

[278] F. Leroux, S. Dementin, B. Burlat, L. Cournac, A. Volbeda, S. Champ, L. Martin, B. Guigliarelli, P. Bertrand, J. Fontecilla-Camps, M. Rousset, and C. Léger, "Experimental approaches to kinetics of gas diffusion in hydrogenase," *Proceedings of the National Academy of Sciences of the United States of America*, vol. 105, pp. 11188–11193, 2008.

[279] P.-P. P. Liebgott, F. Leroux, B. Burlat, S. Dementin, C. Baffert, T. Lautier, V. Fourmond, P. Ceccaldi, C. Cavazza, I. Meynial-Salles, P. Soucaille, J. Carlos, B. Guigliarelli, P. Bertrand, M. Rousset, and C. Léger, "Relating diffusion along

the substrate tunnel and oxygen sensitivity in hydrogenase," *Nature Chemical Biology*, vol. 6, pp. 63–70, 2009.

[280] P.-P. Liebgott, A. L. de Lacey, B. Burlat, L. Cournac, P. Richaud, M. Brugna, V. M. Fernandez, B. Guigliarelli, M. Rousset, C. Léger, and S. Dementin, "Original Design of an Oxygen-Tolerant [NiFe] Hydrogenase: Major Effect of a Valine-to-Cysteine Mutation near the Active Site," *Journal of the American Chemical Society*, vol. 133, pp. 986–997, 2010.

[281] J. Fritsch, S. Löscher, O. Sanganas, E. Siebert, I. Zebger, M. Stein, M. Ludwig, A. L. De Lacey, H. Dau, B. Friedrich, O. Lenz, and M. Haumann, "[NiFe] and [FeS] cofactors in the membrane-bound hydrogenase of *Ralstonia eutropha* investigated by X-ray absorption spectroscopy: insights into O_2-tolerant H_2 cleavage," *Biochemistry*, vol. 50, pp. 5858–5869, 2011.

[282] M. A. Gordon and S. M. Graham, "Invasive Salmonellosis in Malawi," *Journal of Infections in Developing Countries*, vol. 2, pp. 438–442, 2008.

[283] R. J. Maier, A. Olczak, S. Maier, S. Soni, and J. Gunn, "Respiratory Hydrogen Use by *Salmonella enterica* Serovar Typhimurium Is Essential for Virulence," *Infection and Immunity*, vol. 72, pp. 6294–6299, 2004.

[284] M. Asso, B. Guigliarelli, T. Yagi, and P. Bertrand, "EPR and redox properties of *Desulfovibrio vulgaris* Miyazaki hydrogenase: Comparison with the NiFe enzyme from *Desulfovibrio gigas*," *Biochimica et Biophysica Acta - Protein Structure and Molecular Enzymology*, vol. 1122, pp. 50–56, 1992.

[285] K. Knüttel, K. Schneider, A. Erkens, W. Plass, A. Mueller, E. Bill, and A. X. Trautwein, "Redox properties of the metal centers in the membrane-bound hydrogenase from *Alcaligenes eutropha* CH34," *Bulletin of the Polish Academy of Sciences, Chemistry*, vol. 42, pp. 495–510, 1994.

[286] H. R. Pershad, J. L. C. Duff, H. A. Heering, E. C. Duin, S. P. J. Albracht, and F. A. Armstrong, "Catalytic Electron Transport in *Chromatium vinosum* [NiFe]-Hydrogenase: Application of Voltammetry in Detecting Redox-Active Centers and Establishing That Hydrogen Oxidation Is Very Fast Even at Potentials Close to the Reversible H^+/H_2 Value," *Biochemistry*, vol. 38, pp. 8992–8999, 1999.

[287] D. S. Patil, J. J. Moura, S. H. He, M. Teixeira, B. C. Prickril, D. V. DerVartanian, H. D. Peck, J. LeGall, and B. H. Huynh, "EPR-detectable redox centers of the periplasmic hydrogenase from *Desulfovibrio vulgaris*," *Journal of Biological Chemistry*, vol. 263, pp. 18732–18738, 1988.

[288] M. Y. Darensbourg and W. Weigand, "Sulfoxygenation of Active Site Models of [NiFe] and [FeFe] Hydrogenases - A Commentary on Possible Chemical Models of Hydrogenase Enzyme Oxygen Sensitivity," *Europeran Journal of Inorganic Chemistry*, vol. 2011, no. 7, pp. 994–1004, 2011.

[289] P. Atkins, T. Overton, J. Rourke, M. Weller, and F. Armstrong, *Shriver and Atkins' Inorganic Chemistry*. Oxford University Press, 2010.

[290] M.-E. Pandelia, P. Infossi, M. T. Giudici-Orticoni, and W. Lubitz, "The Oxygen-Tolerant Hydrogenase I from *Aquifex aeolicus* Weakly Interacts with Carbon Monoxide: An Electrochemical and Time-Resolved FTIR Study," *Biochemistry*, vol. 49, pp. 8873–8881, 2010.

[291] K. Chen, C. A. Bonagura, G. J. Tilley, J. P. McEvoy, Y.-S. Jung, F. A. Armstrong, C. D. Stout, and B. K. Burgess, "Crystal structures of ferredoxin variants exhibiting large changes in [Fe-S] reduction potential," *Nature Structural and Molecular Biology*, vol. 9, pp. 188–192, 2002.

[292] A. Parkin, *Electrochemical Investigations of Electrocatalysis by Microbial Oxidoreductases*. PhD thesis, Oxford University, Jesus College, 2008.

[293] W. Wang, J. Li, K. Wang, T. I. Smirnova, and E. Oldfield, "Pyridine Inhibitor Binding to the 4Fe-4S Protein *A. aeolicus* IspH (LytB): A HYSCORE Investigation," *Journal of the American Chemical Society*, vol. 133, pp. 6525–6528, 2011.

[294] S. Dikanov, A. Shubin, A. Kounosu, T. Iwasaki, and R. Samoilova, "A comparative, two-dimensional ^{14}N ESEEM characterization of reduced [2Fe-2S] clusters in hyperthermophilic archaeal high- and low-potential Rieske-type proteins," *Journal of Biological Inorganic Chemistry*, vol. 9, pp. 753–767, 2004.

[295] M. Fittipaldi, I. Garcia-Rubio, F. Trandafir, I. Gromov, A. Schweiger, A. Bouwen, and S. Van Doorslaer, "A Multi-Frequency Pulse EPR and ENDOR Approach to Study Strongly Coupled Nuclei in Frozen Solutions of High-Spin Ferric Heme Proteins," *The Journal of Physical Chemistry B*, vol. 112, pp. 3859–3870, 2008.

[296] E. Vinck and S. V. Doorslaer, "Analysing low-spin ferric complexes using pulse EPR techniques: a structure determination of bis (4-methylimidazole)(tetraphenylporphyrinato)iron(iii)," *Physical Chemistry Chemical Physics*, vol. 6, pp. 5324–5330, 2004.

[297] M. Saggu, C. Teutloff, M. Ludwig, M. Brecht, M.-E. Pandelia, O. Lenz, B. Friedrich, W. Lubitz, P. Hildebrandt, F. Lendzian, and R. Bittl, "Comparison of the membrane-bound [NiFe] hydrogenases from *R. eutropha* H16 and D. vulgaris Miyazaki F in the oxidized ready state by pulsed EPR," *Physical Chemistry Chemical Physics*, vol. 12, pp. 2139–2148, 2010.

[298] W. R. Hagen, W. A. Berg, W. M. Dongen, E. J. Reijerse, and P. J. Kan, "EPR spectroscopy of biological iron-sulfur clusters with spin-admixed S= 3/2," *Faraday Transactions*, vol. 94, pp. 2969–2973, 1998.

[299] P. J. Hore, *Nuclear Magnetic Resonance*. Oxford Chemistry Primers, Oxford University Press, 1995.

[300] A. Chapman, R. Cammack, C. Hatchikian, J. McCracken, and J. Peisach, "A pulsed EPR study of redox-dependent hyperfine interactions for the nickel centre of *Desulfovibrio gigas* hydrogenase," *FEBS Letters*, vol. 242, pp. 134–138, 1988.

[301] M. Brecht, M. Stein, O. Trofanchuk, F. Lendzian, R. Bittl, Y. Higuchi, and W. Lubitz, "Magnetic resonance and related phenomena, vol II," *Technische Universität Berlin*, pp. 818–819, 1998.

[302] M.-E. Pandelia, P. Infossi, M. Stein, M.-T. Giudici-Orticoni, and W. Lubitz, "Spectroscopic characterization of the key catalytic intermediate Ni-C in the O_2-tolerant [NiFe] hydrogenase I from *Aquifex aeolicus*: evidence of a weakly bound hydride," *Chemical Communications*, vol. 48, pp. 823–825, 2012.

[303] N. S. Lees, P. Hänzelmann, H. L. Hernandez, S. Subramanian, H. Schindelin, M. K. Johnson, and B. M. Hoffman, "ENDOR Spectroscopy Shows That Guanine N1 Binds to [4Fe-4S] Cluster II of the S-Adenosylmethionine-Dependent Enzyme MoaA: Mechanistic Implications," *Journal of the American Chemical Society*, vol. 131, pp. 9184–9185, 2009.

[304] C. Teutloff, J. Löwenstein, J. Fritsch, S. Frielingsdorf, O. Lenz, F. Lendzian, and R. Bittl, "Pulse EPR on the iron-sulfur clusters of the membrane-bound hydrogenase from *Ralstonia eutropha*," in *The 45th Annual International Meeting of the EPR Spectroscopy Group of the Royal Society of Chemistry*, University of Manchester, 2012.

[305] O. Trofanchuk, M. Stein, C. Geßner, F. Lendzian, Y. Higuchi, and W. Lubitz, "Single crystal EPR studies of the oxidized active site of [NiFe] hydrogenase from *Desulfovibrio vulgaris* Miyazaki F," *Journal of Biological Inorganic Chemistry*, vol. 5, pp. 36–44, 2000.

[306] R. Kappl, S. Ciurli, C. Luchinat, and J. Hüttermann, "Probing Structural and Electronic Properties of the Oxidized $[Fe_4S_4]^{3+}$ Cluster of *Ectothiorhodospira halophila* iso-II High-Potential Iron-Sulfur Protein by ENDOR Spectroscopy," *Journal of the American Chemical Society*, vol. 121, pp. 1925–1935, 1999.

[307] P. Brzezinski and R. Gennis, "Cytochrome c oxidase: exciting progress and remaining mysteries," *Journal of Bioenergetics and Biomembranes*, vol. 40, pp. 521–531, 2008.

[308] J. Morton and K. Preston, "Atomic parameters for paramagnetic resonance data," *Journal of Magnetic Resonance*, vol. 30, pp. 577–582, 1978.

[309] A. Bencini and D. Gatteschi, *EPR of Exchange Coupled Systems*. Springer Verlag, 1990.

[310] C. P. Scholes, A. Lapidot, R. Mascarenhas, T. Inubushi, R. A. Isaacson, and G. Feher, "Electron nuclear double resonance (ENDOR) from heme and histidine nitrogens in single crystals of aquometmyoglobin," *Journal of the American Chemical Society*, vol. 104, pp. 2724–2735, 1982.

[311] G. M. Zhidomirov, P. V. Schastnev, and N. D. Chuvylkin, *Quantum Chemical Calculations of Magnetic Resonance Parameters: Free Radicals*. Nauka, Sibirskoe Otdelenie, 1978.

[312] K. Grubel and P. L. Holland, "New Iron-Sulfur Clusters Help Hydrogenases Tolerate Oxygen," *Angewandte Chemie International Edition*, vol. 51, pp. 3308–3310, 2012.

[313] K. Schneider, D. Patil, and R. Cammack, "ESR properties of membrane-bound hydrogenases from aerobic hydrogen bacteria," *Biochimica et Biophysica Acta - Protein Structure and Molecular Enzymology*, vol. 748, pp. 353–361, 1983.

[314] R. Bingemann and A. Klein, "Conversion of the central [4Fe-4S] cluster into a [3Fe-4S] cluster leads to reduced hydrogen-uptake activity of the F420-reducing hydrogenase of *Methanococcus voltae*," *European Journal of Biochemistry*, vol. 267, pp. 6612–6618, 2000.

[315] M. J. Carney, G. C. Papaefthymiou, K. Spartalian, R. B. Frankel, and R. H. Holm, "Ground spin state variability in $[Fe_4S_4(SR)_4]^{3-}$. Synthetic analogs of the reduced clusters in ferredoxins and other iron-sulfur proteins: cases of extreme sensitivity of electronic state and structure to extrinsic factors," *Journal of the American Chemical Society*, vol. 110, pp. 6084–6095, 1988.

[316] G. Giugliarelli, "Simulation of EPR spectra of Cu^{2+} complexes with statistical distribution of the g-factor and hyperfine splitting," *Chemical Physics*, vol. 98, pp. 115–122, 1985.

[317] P. Lanciano, A. Savoyant, S. Grimaldi, A. Magalon, B. Guigliarelli, and P. Bertrand, "New Method for the Spin Quantitation of $[4Fe\text{-}4S]^+$ Clusters with $S = 3/2$. Application to the FS0 Center of the NarGHI Nitrate Reductase from *Escherichia coli*," *The Journal of Physical Chemistry B*, vol. 111, pp. 13632–13637, 2007.

[318] Y. Deligiannakis, J. Hanley, and A. W. Rutherford, "1D- and 2D-ESEEM Study of the Semiquinone Radical Q_A^- of Photosystem II," *Journal of the American Chemical Society*, vol. 121, pp. 7653–7664, 1999.

[319] S. Grimaldi, F. MacMillan, T. Ostermann, B. Ludwig, H. Michel, and T. Prisner, "$QH^{\cdot -}$ Ubisemiquinone Radical in the bo_3-Type Ubiquinol Oxidase Studied by Pulsed Electron Paramagnetic Resonance and Hyperfine Sublevel Correlation Spectroscopy," *Biochemistry*, vol. 40, pp. 1037–1043, 2001.

[320] R. A. Rothery, M. G. Bertero, R. Cammack, M. Palak, F. Blasco, N. C. J. Strynadka, and J. H. Weiner, "The Catalytic Subunit of *Escherichia coli* Nitrate Reductase A Contains a Novel [4Fe-4S] Cluster with a High-Spin Ground State," *Biochemistry*, vol. 43, pp. 5324–5333, 2004.

[321] A. Magalon, M. Asso, B. Guigliarelli, R. A. Rothery, P. Bertrand, G. Giordano, and F. Blasco, "Molybdenum Cofactor Properties and [Fe-S] Cluster Coordination in *Escherichia coli* Nitrate Reductase A: Investigation by Site-Directed Mutagenesis of the Conserved His-50 Residue in the NarG Subunit," *Biochemistry*, vol. 37, pp. 7363–7370, 1998.

[322] A. T. Kowal, M. T. Werth, A. Manodori, G. Cecchini, I. Schroeder, R. P. Gunsalus, and M. K. Johnson, "Effect of cysteine to serine mutations on the properties of

the [4Fe-4S] center in *Escherichia coli* fumarate reductase," *Biochemistry*, vol. 34, pp. 12284–12293, 1995.

[323] P. S. Brereton, R. E. Duderstadt, C. R. Staples, M. K. Johnson, and M. W. W. Adams, "Effect of Serinate Ligation at Each of the Iron Sites of the $[Fe_4S_4]$ Cluster of *Pyrococcus furiosus* Ferredoxin on the Redox, Spectroscopic, and Biological Properties," *Biochemistry*, vol. 38, pp. 10594–10605, 1999.

[324] P. A. Lindahl, E. P. Day, T. A. Kent, W. H. Orme-Johnson, and E. Münck, "Mössbauer, EPR, and magnetization studies of the Azotobacter vinelandii Fe protein. Evidence for a $[4Fe\text{-}4S]^{1+}$ cluster with spin S = 3/2," *Journal of Biological Chemistry*, vol. 260, pp. 11160–11173, 1985.

[325] S. J. George, F. A. Armstrong, E. C. Hatchikian, and A. J. Thomson, "Electrochemical and spectroscopic characterization of the conversion of the 7Fe into the 8Fe form of ferredoxin III from *Desulfovibrio africanus*. Identification of a [4Fe-4S] cluster with one non-cysteine ligand," *Biochemical Journal*, vol. 264, pp. 275–284, 1989.

[326] J. L. Busch, J. L. Breton, B. M. Bartlett, F. A. Armstrong, R. James, and A. J. Thomson, "[3Fe-4S] $\leftrightarrow$ [4Fe-4S] cluster interconversion in *Desulfovibrio africanus* ferredoxin III: properties of an Asp14 $\rightarrow$ Cys mutant," *The Biochemical Journal*, vol. 323, pp. 95–102, 1997.

[327] R. E. Duderstadt, P. S. Brereton, M. W. W. Adams, and M. K. Johnson, "A pure S = 3/2 $[Fe_4S_4]^+$ cluster in the A33Y variant of *Pyrococcus furiosus* ferredoxin," *FEBS Letters*, vol. 454, pp. 21–26, 1999.

[328] K. A. Vincent, J. A. Cracknell, O. Lenz, I. Zebger, B. Friedrich, and F. A. Armstrong, "Electrocatalytic hydrogen oxidation by an enzyme at high carbon monoxide or oxygen levels," *Proceedings of the National Academy of Sciences of the United States of America*, vol. 102, pp. 16951–16954, 2005.

[329] S. Niu and T. Ichiye, "Density functional theory calculations of redox properties of iron-sulphur protein analogues," *Molecular Simulation*, vol. 37, pp. 572–590, 2011.

[330] Y. Luo, S. Niu, and T. Ichiye, "Understanding Rubredoxin Redox Sites by Density Functional Theory Studies of Analogues," *The Journal of Physical Chemistry A*, vol. 116, pp. 8918–8924, 2012.